Title

Improving understanding and monitoring of levee seepage and subsidence using polarimetric and interferometric synthetic aperture radar for disaster risk management in the Sacramento-San Joaquin Delta

Author

An, Karen

Publication Date

2020

Peer reviewed|Thesis/dissertation

UNIVERSITY OF CALIFORNIA

Los Angeles

Improving understanding and monitoring of levee seepage and subsidence using polarimetric and interferometric synthetic aperture radar for disaster risk management in the Sacramento-San Joaquin Delta

A dissertation submitted in partial satisfaction of the

requirements for the degree Doctor of Philosophy

in Geography

by

Karen An

2020

ABSTRACT OF THE DISSERTATION

Improving understanding and monitoring of levee seepage and subsidence

using polarimetric and interferometric synthetic aperture radar

for disaster risk management in the Sacramento-San Joaquin Delta

by

Karen An

Doctor of Philosophy in Geography

University of California, Los Angeles, 2020

Professor Yongwei Sheng, Chair

Interferometric synthetic aperture radar (InSAR) technology allows for detailed monitoring of levee and delta subsidence, while polarimetric SAR (PolSAR) can detect levee seepage. The dissertation first reviews the history of microwave remote sensing and its basic principles before focusing on case studies of land subsidence (Chapter 1). Northern California's Sacramento-San Joaquin Delta has an exemplar earthen levee system that protects the area from flooding. The region supports part of the water supply for 25 million residents and contributes billions to the state's economy from agriculture. However, historical drainage for farming has

caused continued subsidence of Delta islands, and threatens their vulnerable levees. Aging flood infrastructure needs to be closely monitored as metropolitan areas globally face increasing inundation risk from sea level rise. To augment traditional ground survey, InSAR is shown to efficiently quantify elevation change along levees with continuous spatial coverage (Chapter 2). Evidence of settling from historic breaks is investigated using a vertical velocity map and time-series of cumulative displacement from data acquired by the UAVSAR (Uninhabited Aerial Vehicle SAR) L-band instrument, during 2009-2015. Previous field studies lack continuous subsidence maps across islands that display local complexities (Chapter 3). Traditional lidar surveys, land cover, elevation, and soil organic matter datasets are compared to explain small-scale subsidence. Threats to levee infrastructure include seepage, which occurs when water moves below the structure, weakening structural integrity. Seeps can be detected using PolSAR, which is sensitive to changes in dielectric constant and surface roughness. Since wet soil has a much higher dielectric constant than dry soil, seepage is shown to be detectable with a polarimetric ratio. The California Aqueduct in the San Joaquin Valley is chosen as a dry testbed to investigate polarimetric seep signatures, and the procedure is also applied to Twitchell Island in the Delta (Chapter 4). The potential to combine SAR and GIS visualization makes instruments like UAVSAR optimal to study deltas. UAVSAR's airborne capability can be utilized during disasters to detect structural damage and flood extent (Chapter 5). UAVSAR is also the prototype for the upcoming NASA-ISRO satellite, and detailed monitoring and response will be attainable for flood infrastructure globally.

The dissertation of Karen An is approved.

Scott Joseph Brandenberg

Kyle C. Cavanaugh

Cathleen E. Jones

Michael Edward Shin

Yongwei Sheng, Committee Chair

University of California, Los Angeles

2020

This dissertation is dedicated to my lifelong sidekick, Kenneth.

He truly saw how the sausage gets made.

And without his help, this hot dog would never have been born.

TABLE OF CONTENTS

CHAPTER 1: A review on the application of radar interferometry for land subsidence

Abstract……1

Introduction……..2

Principles of interferometry…….4

Step-by-step InSAR processing……8

Limitations of differential interferometry……..10

Past land subsidence studies using InSAR…….14

Measuring land subsidence in dry regions……....15

Measuring land subsidence in wet regions……....18

Dissertation Outline……...……22

Figures……26

References……..28

CHAPTER 2: Radar interferometry offers new monitoring approach for critical flood control infrastructure

Abstract……..34

Introduction……35

Materials and Methods……...39

Study Site……39

The UAVSAR Synthetic Aperture Radar……40

LiDAR Surveys……...41

GPS Data……...41

UAVSAR Time Series Processing……..42

Levee Oriented Moving Window Average…….44

Results……45

Levee Subsidence……...45

Historic Levee Breaks……47

Levee Settling Immediately After Repair……...49

Discussion……..50

Levee Subsidence……...51

Levee Settling After Repairs……...53

Uncertainties & Challenges……...55

Conclusions……56

Figures……59

Supplementary Figures……..65

References……..72

CHAPTER 3: Current-day subsidence within the Sacramento-San Joaquin Delta and its relationship to elevation, soil organic matter and land use practices

Abstract…….....82

Introduction……84

History of the Delta……85

Radar Interferometry…….88

Materials and Methods……...90

UAVSAR…….90

GIS Datasets……..91

Lidar Surveys…….92

Extensometer Data…….93

InSAR Methodology……...93

Uncertainty……94

Results……96

Sherman Island……...98

Twitchell Island……100

Bradford Island and Webb Tract…….101

Jersey Island and Bethel Tract……102

Venice Island and Empire Tract……..……103

Holland Tract and Bacon Island……..104

Jones Tract……...105

Ryer Island and Grand Island……..105

Canal Ranch Tract, Brack Tract, and Terminous Tract……..106

Discussion……107

Lidar Comparison……107

Percent Soil Organic Matter Comparison……...109

Elevation Comparison…….110

Land Cover Comparison……..112

Conclusions……..113

Figures……..115

Supplementary Figures……141

References……164

CHAPTER 4: Using PolSAR indices and decomposition products to identify increased soil moisture for levee seepage detection of California water conveyance systems

Abstract……170

Introduction……..171

Polarimetric Synthetic Aperture Radar (PolSAR)……...174

Challenges of Measuring Soil Moisture with Remote Sensing……....178

California Conveyance Systems……...181

Materials and Methods…….182

UAVSAR……...182

NDWI……...184

GIS Datasets……185

Manual Seep Detection……186

Google Earth Engine……...189

GIS Preparation……...190

Results……..190

California Aqueduct…….190

Sacramento Delta – Twitchell Island……...199

Discussion……....204

California Aqueduct…….204

Sacramento Delta – Twitchell Island……...209

Conclusions……..210

Figures……..214

References……446

CHAPTER 5: Developing open source flood disaster response toolkits and tutorials using UAVSAR and NISAR-simulated data

Abstract……451

Introduction……..452

Materials and Methods……454

Disaster Prevention…….456

Disaster Response……458

New Techniques……...460

Expected Results……..462

Figures……..464

References……468

CHAPTER 6: Dissertation Summary……..473

LIST OF FIGURES

Chapter 1

Figure 1: Viewing geometry of airborne radar instrument……26

Figure 2: UAVSAR-derived subsidence in New Orleans, Louisiana……27

Chapter 2

Figure 1: Overview of study area……...59

Figure 2: Levee subsidence on Sherman Island……60

Figure 3: Levee subsidence on other islands……61

Figure 4: Historic levee breaks……..62

Figure 5: Most recent Delta levee break……63

Figure 6: Recent levee impact……64

Figure S1: GPS time series for Sherman Island stations……...65

Figure S2: GPS-LOS conversion……...66

Figure S3: Overview vertical velocity map……...67

Figure S4: Overview uncertainty map……...68

Figure S5: Sensitivity analysis of InSAR and lidar datasets……..69

Figure S6: Levee oriented moving window average……70

Figure S7: More historic levee breaks……...71

Chapter 3

Figure 1: Study area of Sacramento-San Joaquin Delta……..115

Figure 2: Lidar differential……...116

Figure 3: Vertical velocity rates……...…117

Figure 4: Mean subsidence rates for crops, elevation, and soil classes……...119

Figure 5: Sherman Island profile…….121

Figure 6: Sherman Island mean subsidence plots and extensometer comparison……...122

Figure 7: Twitchell Island profile……124

Figure 8: Twitchell Island mean subsidence plots……...125

Figure 9: Bradford Island and Webb Tract profile……..126

Figure 10: Bradford Island and Webb Tract mean subsidence plots……...127

Figure 11: Jersey Island and Bethel Tract profile……129

Figure 12: Jersey Island and Bethel Tract mean subsidence plots……...130

Figure 13: Venice Island and Empire Tract profile…….132

Figure 14: Holland Tract and Bacon Island profile…….133

Figure 15: Holland Tract and Bacon Island mean subsidence plots……134

Figure 16: Jones Tract profile……..136

Figure 17: Ryer Island and Grand Island profile…….137

Figure 18: Ryer Island and Grand Island mean subsidence plots……138

Figure 19: Canal Ranch Tract, Brack Tract, and Terminous Tract profile……..140

Figure S1: Soil organic matter map……141

Figure S2: Lidar digital elevation map……142

Figure S3: Vertical rate uncertainty map……143

Figure S4: Regional mean subsidence rates for top crop classes……144

Figure S5: Regional mean subsidence rates for elevation classes……...…145

Figure S6: Regional mean subsidence rates for soil classes……147

Figure S7: Bouldin Island profile……149

Figure S8: Bouldin Island mean subsidence plots……...150

Figure S9: Brack Tract mean subsidence plots……151

Figure S10: Brannan Island profile……..152

Figure S11: Brannan Island mean subsidence plots……....153

Figure S12: Canal Ranch Tract mean subsidence plots……...154

Figure S13: Empire Tract mean subsidence plots……155

Figure S14: Jones Tract mean subsidence plots……..156

Figure S15: Mandeville Island profile……157

Figure S16: Mandeville Island mean subsidence plots……158

Figure S17: McDonald Tract and Medford Island profile……...159

Figure S18: Palm Tract and Orwood Tract profile……..160

Figure S19: Palm Tract and Orwood Tract mean subsidence plots…….161

Figure S20: Venice Island mean subsidence plots……...163

Chapter 4

Figure 1: Study area overview for California Aqueduct and Seeps 1-3……..214

Figure 2: Aqueduct Seeps 1-3 Google Earth imagery…….216

Figure 3: Aqueduct Seeps 1-3 legends for NDWI and PolSAR data products……219

Figure 4: Aqueduct Seeps 1-3 NDWI……..220

Figure 5: Aqueduct Seeps 1-3 HH single polarization……228

Figure 6: Aqueduct Seeps 1-3 VV single polarization……230

Figure 7: Aqueduct Seeps 1-3 HV/HH ratio……232

Figure 8: Aqueduct Seeps 1-3 VV/HH ratio……234

Figure 9: Aqueduct Seeps 1-3 copolarization phase……236

Figure 10: Aqueduct Seeps 1-3 entropy……...238

Figure 11: Aqueduct Seeps 1-3 anisotropy……..…240

Figure 12: Aqueduct Seeps 1-3 mean alpha angle……...242

Figure 13: Study area overview for Aqueduct Seep 4…….244

Figure 14: Aqueduct Seep 4 Google Earth imagery……245

Figure 15: Aqueduct Seep 4 legends for NDWI and PolSAR data products……...248

Figure 16: Aqueduct Seep 4 NDWI……249

Figure 17: Aqueduct Seep 4 HH single polarization……...265

Figure 18: Aqueduct Seep 4 VV single polarization……...267

Figure 19: Aqueduct Seep 4 HV/HH ratio……...269

Figure 20: Aqueduct Seep 4 VV/HH ratio……...271

Figure 21: Aqueduct Seep 4 copolarization phase……...273

Figure 22: Aqueduct Seep 4 entropy……...275

Figure 23: Aqueduct Seep 4 anisotropy……...277

Figure 24: Aqueduct Seep 4 mean alpha angle……279

Figure 25: Aqueduct Study area overview for Seep 5……281

Figure 26: Aqueduct Seep 5 Google Earth imagery……282

Figure 27: Aqueduct Seep 5 legends for NDWI and PolSAR data products……...285

Figure 28: Aqueduct Seep 5 NDWI……286

Figure 29: Aqueduct Seep 5 HH single polarization……...302

Figure 30: Aqueduct Seep 5 VV single polarization……...304

Figure 31: Aqueduct Seep 5 HV/HH ratio……...306

Figure 32: Aqueduct Seep 5 VV/HH ratio……...308

Figure 33: Aqueduct Seep 5 copolarization phase……...310

Figure 34: Aqueduct Seep 5 entropy……...312

Figure 35: Aqueduct Seep 5 anisotropy……...314

Figure 36: Aqueduct Seep 5 mean alpha angle……316

Figure 37: Study area overview for Twitchell Island and Seeps 1-3……...318

Figure 38: Twitchell Seeps 1-3 Google Earth imagery……...320

Figure 39: Twitchell Seeps 1-3 legends for NDWI and PolSAR data products……..327

Figure 40: Twitchell Seeps 1-3 NDWI……328

Figure 41: Twitchell Seeps 1-3 VV/HH ratio for Line 05519…….339

Figure 42: Twitchell Seeps 1-3 VV/HH ratio for Line 15502…….344

Figure 43: Twitchell Seeps 1-3 VV/HH ratio for Line 33502…….349

Figure 44: Twitchell Seeps 1-3 VV/HH ratio for Line 23518…….354

Figure 45: Study area overview for Twitchell Seep 4…….359

Figure 46: Twitchell Seep 4 Google Earth imagery……360

Figure 47: Twitchell Seep 4 legends for NDWI and PolSAR data products……...367

Figure 48: Twitchell Seep 4 NDWI…….368

Figure 49: Twitchell Seep 4 VV/HH ratio for Line 05519……..379

Figure 50: Twitchell Seep 4 VV/HH ratio for Line 15502……..384

Figure 51: Twitchell Seep 4 VV/HH ratio for Line 33502……..389

Figure 52: Twitchell Seep 4 VV/HH ratio for Line 23518……..394

Figure 53: Study area overview for Twitchell Seep 5…….399

Figure 54: Twitchell Seep 5 Google Earth imagery……400

Figure 55: Twitchell Seep 5 legends for NDWI and PolSAR data products……...408

Figure 56: Twitchell Seep 5 NDWI…….409

Figure 57: Twitchell Seep 5 VV/HH ratio for Line 05519……..420

Figure 58: Twitchell Seep 5 VV/HH ratio for Line 15502……..425

Figure 59: Twitchell Seep 5 VV/HH ratio for Line 15503……..430

Figure 60: Twitchell Seep 5 VV/HH ratio for Line 33502……..435

Figure 61: Twitchell Seep 5 VV/HH ratio for Line 23518……..440

Figure 62: Field photos of Twitchell Seep 5……445

Chapter 5

Figure 1: Vertical velocity rate map for critical flood infrastructure in New Orleans, LA…….464

Figure 2: Single vertical polarization image for prisons in Otey, Texas…….465

Figure 3: Single vertical polarization image for bridge in Lake Houston……...466

Figure 4: Unwrapped InSAR phase product for Hurricane Harvey……467

LIST OF TABLES

Chapter 3

Table 1: Summary table of average island subsidence……118

Chapter 4

Table 1: Summary table for seep detection parameters……...205

ACKNOWLEDGEMENTS

To my committee members, thank you for all of the insightful comments and feedback you have provided my research over the years. I appreciate the time and effort spent to help improve upon my work. A special thank you to Cathleen Jones, from whom I learned everything about radar science from and whose patience and encouragement have been integral to this work and my well-being.

To all of my family and friends who have been wondering for years if this day would ever come, it's finally happened – I've graduated! Thank you for always reminding me this day would come. A special thanks,

- To my mom and dad, who put their daughters before themselves since we were born. Their loyalty, kindness, and humor motivate all of my ambitions.
- To my sissy Sharon, whose courage, strong will, and coolness I aspire to imitate.
- To my partner in crime (and legal activities) Kenneth, everything is for you.
- To my lifelong pal Jenny, who has been by my side since 4th grade, you are my chosen family.
- To my sweet 96 year old gōnggong, you are evidence that happiness is the true secret to longevity. This guy loves McDonald's breakfast every morning.
- To my hip and cool auntie Xiao Hui, I miss you and your friendship daily. I can't wait to return to Taiwan to eat my weight in pineapple cakes.
- To Oliver and Charlie for decreasing my blood pressure and accompanying me on all-nighters.
- And lastly, to Beyoncé for inspiring us all.

Permissions

- Cathleen E. Jones granted permission for the reprint of copyrighted material, Figure 1 in Chapter 1. This figure is printed in: Jones, C. E., Dudas, J., Bawden, G. W. (2016). Application of remote sensing to assessment of water conveyance infrastructure integrity. In R. L. Anderson and H. Ferriz (Eds.), Applied Geology in California, Special Publication 26. Association of Environmental and Engineering Geologists, Star Publishing Company.
- Figure 2, Chapter 1 and Figure 1, Chapter 5 are reprinted with permission by Cathleen E. Jones and Karen An from: Jones, C. E., An, K., Blom, R. G., Kent, J. D., Ivins, E. R., & Bekaert, D. (2016). Anthropogenic and geologic influences on subsidence in the vicinity of New Orleans, Louisiana. Journal of Geophysical Research: Solid Earth, 121(5), 3867-3887.
- Chapter 2 is a version of: An, K., Jones, C., Bekaert, D., & Bennett, V. (2020). Radar interferometry offers new monitoring approach for critical flood control infrastructure. In review.

Coauthor contributions

Chapter 2 – Cathleen E. Jones, David P.S. Bekaert, and Victoria Bennett are the coauthors and all contributed to reviewing the paper. Cathleen E. Jones and Karen An wrote the majority of the text. Cathleen E. Jones and David P.S. Bekaert processed the time series product and vertical velocity map used in the paper, and Karen An contributed. Victoria Bennett collected the GPS data for Sherman Island, and wrote the corresponding section about the data.

Chapter 3 – Cathleen E. Jones, David P.S. Bekaert, and Karen An contributed to processing the same vertical velocity map as used in Chapter 2. Steven Deverel contributed comments and provided the soil organic matter dataset and Sherman Island extensometer data.

For all chapters, the authors thank Joel Dudas from the California Dept. of Water Resources for important information about the Sacramento-San Joaquin levee system and GIS datasets.

Funding

This work was supported by the UCLA Graduate Research Mentorship Fellowship and the NASA Earth and Space Science Fellowship. This work was also supported in part by the Jet Propulsion Laboratory, California Institute of Technology, under a contract with the National Aeronautics and Space Administration. Funding for data acquisition and analysis was also supported in part by the California Dept. of Water Resources and the Dept. of Homeland Security. Any use of trade, firm, or product names is for descriptive purposes only and does not imply endorsement by the U.S. Government.

KAREN AN

Education
University of California, Los Angeles
Geography, Ph.D. Candidate, Teaching Associate
University of California, Los Angeles (2015)
Geography, M.A., Teaching Assistant and Associate
University of California, Irvine (2013)
Environmental Science, B.S. (Minor in Information & Computer Science) with Departmental Honors

Honors & Awards
2017-2020 NASA Earth and Space Science Fellowship (NESSF)
2015-2016 UCLA Graduate Research Mentorship Fellowship
2013 UCI Graduation with Departmental Honors
2013 UCI Undergraduate Research/Departmental Service Award in Earth System Science
2010-2013 UCI Dean's Honor List

Teaching Experience
Geography 1: Earth's Physical Environment – Fall 2014
Geography 5: People & Earth's Ecosystems – Winter 2015, Spring 2015, Fall 2015, Winter 2016
Geography 170: Advanced Geographic Information Systems (GIS) – Spring 2016
Geography 172: Remote Sensing Digital Image Processing and Analysis – Spring 2018

List of Publications & Presentations
An, K., Jones, C. E., Bekaert, D. P. S., Bennett, V. (in review) Radar interferometry offers new monitoring approach for critical flood control infrastructure.

An, K., Jones, C. E., Bekaert, D. P. S., et al. (in prep.) Current-day subsidence within the Sacramento-San Joaquin Delta and its relationship to elevation, soil organic matter and land use practices.

Bekaert, D. P., Jones, C. E., An, K., & Huang, M. H. (2019). Exploiting UAVSAR for a comprehensive analysis of subsidence in the Sacramento Delta. *Remote sensing of environment*, *220*, 124-134.

Jones, C. E., An, K., Blom, R.G., Kent, J.D., Ivins, E.R., Bekaert, D. (2016), Anthropogenic and geologic influences on subsidence in the vicinity of New Orleans, Louisiana, J. Geophys. Res. Solid Earth, 121, 3867–3887.
(also adapted for Environmental Science Journal for Teens, January 2017)

Jones, C., Simard, M., Rangoonwala, A., Ramsey III, E., Bekaert, D. & An, K. (2018) "Oh, That Sinking Feeling: Observations Of Landscape Change In The Mississippi River Delta Jones". GSA Annual Meeting (presentation).

Jones, C. E., Bekaert, D., & An, K. (2017). From flood to drought: Utilizing sar to assess the status of levees and aqueducts. In *2017 IEEE International Geoscience and Remote Sensing Symposium (IGARSS)* (pp. 5889-5892). IEEE.

An, K., Jones, C., Bekaert, D. (2017) “Levee Seepage Detection in the Sacramento-San Joaquin Delta Using Polarimetric SAR”. AGU Fall Meeting (presentation).

Jones, C. E., Sharma, P., Dudas, J., Bekaert, D., An, K., & Deverel, S. “Radar Remote Sensing of Subsidence in the Sacramento-San Joaquin Delta”. Delta Levee Science Meeting (poster).

Bekaert, D., Jones, C., An, K., & Huang, M. H. (2016). Large-scale time-series InSAR analysis of the Sacramento-San Joaquin delta subsidence using UAVSAR. In *Fringe 2017 Workshop*.

An, K., Jones, C.E., Bekaert, D., Dudas, J., (2016) “Assessment of earthen levee stability for management and response: A NASA-DHS-California Dept. Water Resources collaboration”, AGU Fall Meeting (presentation).

An, K., Jones, C.E., Blom, R.G., Kent, J.D., Ivins, E.R. (2015) “InSAR Remote Sensing of Localized Surface Subsidence in New Orleans, LA,” AGU Fall Meeting. (poster)

An, K., Reager, J., Famiglietti, J. (2013) Estimating a Global Hydrological Carrying Capacity Using GRACE Observed Water Stress, AGU Fall Meeting. (poster)

An, K., Reager, J., & Famiglietti, J.S. (2013) "The Human Implications of NASA's GRACE Satellite: Estimating a Global Hydrological Carrying Capacity", UROP Symposium, University of California, Irvine, 18 May. (presentation)

CHAPTER ONE

A review on the application of radar interferometry for land subsidence

Abstract

Since the first instruments in the 1950s, imaging radars and the synthetic aperture radar (SAR) instruments that followed have been monitoring small and large scale surface processes on Earth and throughout our solar system with great accuracy and precision. Interferometric SAR (InSAR) technology has allowed for detailed monitoring of earthquakes, volcanoes, glaciology, landslides, ocean processes, and more. In particular, the contribution of InSAR to studies of small scale elevation displacement, namely land subsidence, has allowed scientists to monitor potentially hazardous locations around the world. This chapter reviews a brief history of microwave remote sensing, and explains the basic principles and limitations of InSAR before focusing on case studies that have used interferometry to monitor land subsidence in different environments. The high spatial resolution offered by today's airborne instruments will be compared to the first SAR images from early spaceborne missions. The progress of using this technology for such a wide variety of applications has made InSAR an indispensable tool in earth science remote sensing, and the queue of future spaceborne missions reflects the continuation of this trend. Emerging applications of InSAR also point to more direct comparisons with field datasets and informative geographic information systems (GIS) data to explain the intricate features seen in SAR datasets.

Introduction

The history of microwave remote sensing began in the 19th century when scientists such as Maxwell and Hertz first began to study the relationships between electricity and magnetism. Their work, along with others, has helped shaped modern radio, television, microwave ovens, and the field of microwave remote sensing that exists today. The development of radar devices was instrumental during World War II, when the idea of echolocation was used to determine the distance of targets relating to the time delay of an echo. This helped pave the way for the first Radio Detection and Ranging (RADAR) device in 1935 by Scottish scientist Robert Watson-Watt that was able to detect aircraft targets using pulses of microwaves (Woodhouse, 2006). After the war ended, microwave applications continued with the military but meteorologists also began to conduct research using ground based radar instruments to study the atmosphere and storm events. Radio astronomy also became an emerging field as scientists studied passively sensed microwave signals from space, leading to the discoveries of phenomena such as quasars, pulsars, and the background cosmic radiation resulting from the Big Bang (Woodhouse, 2006).

The first imaging radars in the 1950s, such as the Side-Looking Airborne Radar (SLAR), highlighted the navigational abilities of radar since it is able to "see" through clouds and even darkness. In 1952, Carl Wiley developed a method using the Doppler shift in echoes to synthesize higher resolution (Woodhouse, 2006). This method is now referred to as aperture synthesis and is the basis for modern synthetic aperture radar (SAR) instruments that use active microwave remote sensing techniques. Traditionally, longer wavelength (higher resolution) instruments required very large antennas, but SAR instruments are able to mimic this thanks to Wiley's work. Spaceborne SAR satellites have allowed for continuous global monitoring of many changing processes on Earth. Early spaceborne radar satellites such as Cosmos 243 and

Nimbus-5 evolved into high resolution radiometers that can measure rainfall, vertical profiles of temperature, and more. Spaceborne SAR instruments orbit the earth at 200-800 km altitude with an average 25 m^2 spatial resolution and swath widths of 50-100 km (Bamler and Hartl, 1998). The first spaceborne imaging radars didn't exist until the 1970s, with Seasat in 1978 being one of the earliest active sensors studying the ocean (sea surface winds, temperatures, wave heights, etc.). This was the first SAR data that was appropriate for interferometry purposes, though not many interferograms were generated from the data since few scientists had access to the data and processing was expensive and unintuitive (Bamler and Hartl, 1998). ERS 1 and 2 from the European Space Agency followed, and provided a decade of data on the ocean and atmosphere. Since then, dozens of passive and active microwave instruments have collected data about the Earth and other planets in our solar system.

Interferometric synthetic aperture radar (InSAR) methods involve taking the phase difference either between two SAR images from different measurement times, or two SAR images taken at the same time from different antenna positions. This can also be referred to as differential InSAR (D-InSAR) or repeat track interferometry. InSAR studies have in particular become widespread in recent years after ERS-1 launched in 1991, which had good stability, calibration, orbit accuracy, and baseline control, and the Shuttle Imaging Radar SIR-C/X-SAR in 1994, which was a high performance SAR with multi-frequency and polarization capabilities (Bamler and Hartl, 1998). These missions, along with SRTM from the Shuttle Imagine Radar line (discussed below), allowed for a breakthrough in the field of SAR interferometry. InSAR research allows for high resolution monitoring of surface deformation from earthquakes, glaciology, land subsidence, landslides, and other geophysical processes across large areas that are often inaccessible by field surveys. InSAR has even been used to measure surface

deformation caused by nuclear test site detonations (Vincent, 2003). The advantages with remote sensing instruments also include having frequent and non-invasive measurements, which helps lessen the strain on resources. Differential InSAR (DInSar) has also allowed for centimeter to millimeter level precision in measuring surface displacements over large temporal and spatial scales. Spaceborne SAR instruments have grown in number in recent decades, and can offer data with global coverage, independent of sun illumination and meteorological conditions.

This chapter reviews the applications of InSAR for surface deformation, land subsidence in particular, and discuss the challenges with extracting this type of information. Section 1 first conducts a review of the principles of interferometry by explaining some basic terminology in relation to a typical radar instrument's viewing geometries. The steps of InSAR processing and limitations to differential interferometry are also discussed in this section. Section 2 discusses past studies of land subsidence using InSAR and compares the different types of instrumentation used, among varying study areas in terms of typical coherence, also called phase variance. For instance, dry areas tend to be less challenging than wet areas that often have less coherence due to the dielectric properties of water. The section also discusses emerging applications of InSAR that are being used to monitor subsidence along critical levee infrastructure, in areas such as New Orleans, Louisiana and the Sacramento-San Joaquin Delta in California. The chapter concludes in the third section with a brief discussion of upcoming SAR missions that will help continue the legacy of such high resolution monitoring of the Earth's surface.

1. Principles of interferometry

RADAR, which stands for Radio Detection and Ranging, is based on echolocation, where a signal is transmitted and then measured by the time when it is received. Synthetic aperture radar instruments are able to produce such high geometric resolutions by "synthetically"

achieving a longer antenna than what is physically onboard the instrument. This is done by employing side-looking geometry and pulse compression techniques (Bamler and Hartl, 1998). Such geometries have made SAR interferometry less intuitive to understand than traditional optical remote sensing instruments. A typical strip-map mode SAR imaging geometry describes an instrument at an altitude H above the surface (Bamler and Hartl, 1998). The instrument travels along the track, or azimuth (along the x-axis) and sends and/or receives radar echoes in a side-looking fashion along the range direction (along the y-axis). A more detailed schematic of the instrument geometry can be seen in Figure 1 (Jones, 2016). The head-on view shows, in this case an airborne instrument, traveling directly out of the page. The instrument is side-looking, and therefore sends out electromagnetic pulses in the line-of-sight direction, also called the slant range or look direction. This line-of-sight forms an angle with the nadir direction, called the look angle or incidence angle. As denoted by the figure, these terms occur in the cross track direction, or the range direction as described in the previous figure. Objects closest to the instrument occur in the near range and those farther occur in the far range. These boundaries represent the image swath size, which is usually tens of kilometers for instruments with less than 10 meters resolution (Jones, 2016). It is shown here that the ground resolution Δ_g is usually larger than the slant range resolution Δ_s. This is a result of raw imagery being recorded using radar coordinates, with axes displayed along the flight direction. Therefore, the resulting pixels are not equivalent when projected onto the surface. In the side view panel, the azimuth resolution Δ_a is equal to the ground resolution. Here, the instrument is traveling across the page in the along track, or azimuth direction.

Besides strip-map mode, instruments can also employ ScanSAR mode, which transmits its pulses in bursts, or spotlight mode, which only images certain patches as directed. These

different modes can alter the image resolution, where range resolution is determined by pulse duration and azimuth resolution is determined and limited by antenna footprint size (Bamler and Hartl, 1998). Different imaging modes have different tradeoffs concerning spatial and temporal resolution. For example, since only certain patches are covered in spotlight mode, repeat visit time can occur more often. The different wavelengths of SAR instruments are commonly referred to by their military codenames: X-band (3 cm), C-band (6 cm), S-band (9 cm), and L-band (24 cm). The wavelength of an instrument determines its antenna size, signal bandwidth, and baseline size. The bandwidth can also determine range resolution and phase noise, but is limited by cost and regulations. The most obvious difference in radar backscatter can be seen between longer wavelengths like L-band that can penetrate through forest canopy, and short wavelengths such as C-band, which will scatter from near the top of the canopy by leaves and branches. Some popular missions with varying wavelengths include: TerraSAR-X and COSMO-Skymed in X-band, Radarsat, Sentinel-1, Envisat, and ERS for C-band, and ALOS/PALSAR and UAVSAR for L-band (Jones, 2016).

The images formed from SAR data are based on the phase and amplitude, having to do with time delay and energy respectively, of the return echoes from Earth's surface. The most well-known InSAR application was to generate DEMs (digital elevation models) of Earth's surface. A common method for this reconstruction is across-track interferometry, which utilizes two SAR sensors flying on parallel tracks and slightly different view angles to reconstruct each surface point's location in space (with knowledge of the look angle) (Bamler and Hartl, 1998). Whereas traditional radar applications only utilized the amplitude portion of a single image, interferometric methods have allowed for time-varying analysis by using the phase difference from at least two images. This phase value is derived from the number of cycles, or wavelengths

that have traveled between the return object and the instrument receiver. If something differs about the object or the surface has moved, this changes the phase signal for the second radar image over the same area. Depending on the wavelength of the instrument, even if the soil has grown a couple centimeters from increased moisture, this will cause a phase shift in the image (Bamler and Hartl, 1998). An interferogram is formed by subtracting these images to display the phase difference between the acquisitions over the same area, a technique called repeat pass interferometry. The temporal baseline, or time difference between acquisitions, can range from days to weeks, though anything longer may cause decorrelation due to changes of the surface (Smith, 2002).

Decorrelation can negatively affect the quality of an interferogram, and is caused when two sets of radar signals, taken at different times over the same area, experience different interactions with the surface. Factors on the ground such as vegetation, water, wind, soil moisture, etc. can impact radar scattering. Provided high coherence, however, differential interferometry can measure surface displacements with millimeter scale accuracy since radar instruments employ centimeter scale wavelengths (Bamler and Hartl, 1998). Coherence limited regions would therefore be better studied using an instrument with longer wavelength, such as L-band since it is longer than small leaves or vegetation that would cause more decorrelation in shorter wavelengths. On the other hand, if baseline limitation is more of a concern, a shorter wavelength would be more suitable since longer wavelengths require larger baselines (Bamler and Hartl, 1998). Analyzing SAR data has been described as an inverse problem since much signal processing is required to make sense of the data and form a useful image.

Step-by-step InSAR processing

At the first step of processing raw SAR images are single look complex (SLC) images, which contain the highest spatial resolution. Each cell contains complex numbers of the phase and amplitude of the received signal. To reduce speckle, which looks like grainy noise in an SLC image, the next processing step is usually to multilook the image by averaging over several pixels, which will reduce the spatial resolution. Speckle can be caused by the combination backscatter from many small scale objects on the surface with different shapes and points (Jones, 2016). InSAR processing will produce an interferogram and a coherence map. The interferogram contains a product of the amplitude from the 2 SAR images used to create the interferogram, and a phase difference from the 2 SAR images. The coherence map shows any differences that may have occurred between the acquisitions used to produce the interferogram, which can be used to interpret the interferogram itself. From these products, an unwrapped phase product can be produced, which contains values that are linearly related to actual displacement values.

Since the phase range for an interferogram is only from 0 to 2π, the interferogram must be unwrapped to achieve values greater than 2π. A 2π radians difference in phase between acquisitions is equivalent to surface displacement of half the wavelength that was received. This method is equivalent to summing up contour line elevations on a topographic map (Smith, 2002). This can even be done visually by counting the "phase wraps", equivalent to 2π radians, relative to a stable area in the image. If the study area has lost coherence, which may be common after large displacements such as earthquakes and volcanoes, common applications of InSAR, then GPS (Global Positioning System) data may be required. Using a GPS station's location as the phase reference, one can obtain the actual displacement value from the interferogram. InSAR only measures the relative surface displacement from some location in the image. This location,

called the phase reference, must be subtracted from the entire image to derive values of relative displacement. Therefore, the temporal baseline between acquisitions should be catered to the application at hand. The amount of displacement that has occurred should be realistic. For example one would expect small rates for land subsidence, and any large anomalies should be attributed to phase unwrapping errors (Jones, 2016).

Since interferograms only measure displacement that has occurred between at least two acquistions, one cannot pinpoint when during that temporal baseline the deformation occurred, though there are time series methods that can help remedy this, described below. In addition, InSAR instruments are measuring changes only in the side-looking line-of-sight direction of their antenna, and so are measuring a combination of horizontal and vertical displacements (Jones, 2016). For example, if two antenna or instruments are imaging the same point on the ground from opposite directions, the amount of land subsidence measured will not differ because it is in the vertical field. On the other hand, if tension or compression (horizontal movements of the surface) are measured from these opposing instruments, the directions will be reversed for each instrument (Jones, 2016). This can be helped by having multiple look directions over an area, though this is more applicable for airborne instruments.

Additional knowledge about the study area, for example whether it is dominated by vertical movements such as groundwater extraction, is also helpful in discerning horizontal and vertical displacements. If no ground motion has occurred, then the conversion to elevation is only based on the baseline, instrument height, and look angle. If ground motion has occurred, then the topographic signal must be isolated from the interferogram in order to produce a map of ground displacement. This is done by subtracting a known DEM. The longer the baseline, the higher resolution DEM must be used to subtract this topographic signal. Precision for InSAR

displacement is on the millimeter scale since phase changes are measured on scales of a fraction of a wavelength (centimeter scale). On the other hand, precision for DEMs generated from SAR are on the meter scale because these values are due largely to differences in baseline.

There are also time series methods for InSAR to reduce noise by using several SAR images taken at different times. One method is called persistent scatterer interferometry (PS-InSAR). This method creates dozens of interferograms in order to identify stable scatterers on the ground, such as telephone poles, buildings, freeways, etc. These permanent scatterers act as a virtual GPS network since each point has its own phase change history without decorrelation issues (Galloway and Hoffmann, 2007). PS-InSAR is best suited for urban environments, where many of these scatterers exist, versus a more rural and unpopulated study area. The advantages of this method are that temporal decorrelation and atmospheric effects won't contribute to the InSAR processing errors. However, the environmental limitations and lack of spatial continuity may be drawbacks compared to a continuous interferogram made with traditional InSAR methods. Another method is called small baseline subsets (SBAS). This method uses a linear least squares fit over temporally overlapping interferograms to derive displacement rates, and is a better alternative than PS-InSAR for less coherent areas such as agricultural fields (Jones, 2016).

Limitations of differential interferometry

The phase difference between the SAR images that compose an interferogram is made up of different components: actual surface displacement, atmospheric changes, topographic contributions, instrument noise, and other surface property changes (Galloway and Hoffmann, 2007). The challenge with InSAR analysis is disentangling all these factors to isolate surface displacement. Generally, the signal-to-noise ratio of an instrument is dependent on instrument power, surface reflectivity, and image coherence, which is usually the limiting factor and

depends on orbital distance between acquisitions and the amount of time between acquisitions (Galloway and Hoffmann, 2007). The main limitation of InSAR applications is loss of coherence between data acquisitions, which can be caused by vegetation growth, agricultural activity, change in terrain type, and especially occurs in coastal humid regions. Loss of coherence, also referred to as incoherence or loss of correlation, is caused by surface changes that are not discernable to the radar from changes in location. This is caused by surface roughness and surface material altering the radar backscatter in a significant way between acquisitions (Jones, 2016). Coherence is not only a measure for interferogram quality, but also can be used for image classification. The presence of water also causes the image to decorrelate in mere milliseconds due to small wave ripples, which act as small waves (Bamler and Hartl, 1998). Agricultural fields that have been watered or plowed is a common loss of coherence for active farmlands. Even desert regions in the southwest U.S. are susceptible to loss of coherence during the summer monsoon season (Heywood et al., 2002).

Atmospheric effects from water vapor, pressure, and temperature changes can also play a role in disrupting interferometric phase changes and being misconstrued as surface deformation. This occurs because atmospheric water vapor disrupts and slows the velocity of transmitted radar waves (Woodhouse, 2006). This issue is only relevant for repeat pass interferometry where different atmospheric conditions may exist between acquisitions, since for single pass images, there is a constant phase shift across the image (Woodhouse, 2006). Having multiple images from repeat track interferometry can help to identify atmospheric artifacts since these objects will not persist over time.

Repeat SAR acquisitions are ideally flown on the same repeat orbits to avoid topographic noise, but the terrain can still have a significant effect on the radar signal. During InSAR

processing, as described above, a DEM is often used to correct for terrain effects. However, the efficacy of this depends largely on the quality of the DEM, the availability of which depends on the study region. Scattering distortions from topography can occur through foreshortening and lay-over. Foreshortening causes mountain slopes tilting towards the sensor to look contracted, while slopes tilting away from the sensor look stretched (Bamler and Hartl, 1998). Lay-over occurs when the slope angle equals or exceeds the look angle, which is the angle made from the line-of-sight and nadir line from the instrument. In general, topographic noise is more apparent in spaceborne data while aircraft motion is more apparent in airborne data (Jones, 2016).

The incidence angle of an instrument also plays a role in the value of radar backscatter. Typically, the larger the incidence angle, the weaker the radar backscatter since reflectivity from scatterers decreases with increasing incidence angle. For InSAR applications, it is recommended to use an incidence angle such as 45° that balances effects from foreshortening and lay-over (Bamler and Hartl, 1998). For other applications, such as for oceanic science, larger incidence angles are more appropriate. For example, the ERS missions were flown with very steep incidence angles, and so its images are not appropriate for high terrain areas (Bamler and Hartl, 1998).

Additionally, the baseline, or short distance between SAR antenna positions, plays a role in topographic sensitivity. As the baseline increases, more phase cycles can be introduced into the final interferogram, even when no ground motion has occurred (Smith, 2002). This means that interferograms with shorter baselines are more appropriate for ground surface motion studies. This angular difference for the antennas is called the baseline, whereas the time period between the acquisitions that form an interferogram taken at different times is called the temporal baseline. For repeat pass interferometry, the baseline refers to the offset that an

instrument platform may have between acquisitions. This varies from meters to hundreds of meters for airborne and spaceborne instruments, respectively (Jones, 2016). Images taken at different frequencies have what is called a spectral baseline (Bamler and Hartl, 1998). Older radar instruments such as ERS and Radarsat were not designed with high repeat track accuracy, and so not many SAR images were suitable for interferogram generation. As more studies display the utilities of InSAR, instruments are being designed with higher repeat track accuracies between acquisitions with this application in mind.

Since interferometric SAR measures change in the line-of-sight, many scientists focus on decomposing the signal to horizontal displacements for applications such as land subsidence. This can be difficult to resolve because usually additional information, such as from a nearby GPS station, is needed to create three-dimensional displacement data. This translation can also be done by comparing ascending and descending acquisitions over a similar time period, but such data may not be readily available. Other limiting factors to using InSAR, which could be said of many remote sensing applications, include data availability, data processing, and lack of *in situ* datasets. Today, many commercial instruments boast high resolution (1-meter) SAR imagery, such as TerraSAR-X and Cosmo-SkyMed, though images can be expensive to acquire and may not be available in the desired study location. Depending on the application, C-band and L-band instruments such as ALOS, Radarsat-2, and Sentinel may offer sufficient data, though the temporal availability may be sparse over long periods. Data processing can also be a challenge, especially for the average remote sensing scientist, who may find the previously explained SAR processing unintuitive. Casual applications of InSAR seem to be lacking in traditional hydrogeology studies, which would be greatly augmented with such spatially rich data, some examples of which are discussed in the next section.

2. Past land subsidence studies using InSAR

InSAR has evolved in recent decades from a technology invented by the military to an accepted tool used for remote sensing studies of the Earth's surface. The span of InSAR applications to Earth science include topics of volcanism (Hooper et al., 2004, Pritchard and Simons, 2004), earthquakes (Simons et al., 2002, Pollitz et al., 2001), ice-sheet dynamics (Rignot and Kanagaratnam, 2006, Shepherd et al., 2012), topography (Bürgmann et al., 2000), and land subsidence (Amelung et al., 1999, Galloway et al., 1998). Even smaller-scale land deformation from landslides and sediment erosion/deposition can be observed by InSAR (Smith, 2002). These types of studies are able to augment existing field observations that may be costly or unfeasible. Airborne SAR instruments also have the capability of assisting emergency response teams during a disaster event by quickly creating flood inundation maps or an earthquake signature (Hensley et al., 2012). InSAR can offer high resolution products on the meter scale, where individual trees can be seen, and the power of interferometry, where detailed movements are shown in the earthflow signatures not obvious from an individual SAR image. InSAR is also a powerful tool in creating digital elevation models, such as the widely used DEM from the Shuttle Radar Topography Mission (SRTM) in 2000 (Van, 2001). Described as a "breakthrough in remote sensing of topography", the SRTM products provide 30-meter spatial resolution of elevation for most of the globe (excluding the high latitudes and polar regions). This mission was made possible by using a single-pass C-band interferometer which collected imagery from two different positions simultaneously in time (Van, 2001). The applications which this global DEM has influenced include the fields of ecology, geology, geophysics, and more.

One of the most common applications of interferometry is measuring land subsidence. The most common cause of land subsidence, the gradual settling or sudden sinking of the

surface, is caused by aquifer compaction from over-drafting (USGS, 2000). The most well-known example of this is seen in the San Joaquin Valley, California where the land surface has sunk up to 30 feet in some areas. In 1991, the National Research Council estimated that the U.S. annual cost for subsidence related damage and flooding was over $125 million (Galloway et al., 1999). Other well known cases of subsidence include aquifer compaction in Mexico City with up to 2 feet of subsidence per year, agricultural drainage in the western Netherlands, and collapse features on the Yucatan Peninsula from rainwater infiltration (Galloway et al., 1999). This is concerning for water resource management since groundwater, which is stored in these aquifers, is being extracted at much faster rates than it is naturally replenished. Furthermore, the size of the aquifer in terms of how much water volume it can hold is also decreased due to compaction (USGS, 2000). Other causes of subsidence include mining activities, soil drainage, soil compaction, sinkholes, and more (National Research Council, 1991). Land subsidence has been observed in many agricultural and industrial sites around the world. In drained soils that are primarily composed of organic carbon, subsidence occurs due to the microbial activity of decomposing carbon to carbon dioxide and water (USGS, 2000). Land subsidence can even lead to sinkholes, when subsurface cavities collapse in a short time period (hours), which can cause widespread damage.

Measuring land subsidence in dry regions

As detailed previously, loss of coherence in InSAR products is most challenging in wet areas such as the Mississippi Delta. This section contains a review of a variety of study areas with different climates and a discussion of how scientists have dealt with different conditions impacting the radar returns. “Sensing the ups and downs of Las Vegas…” by Amelung et al. (1999) was an important contribution to the field that sought to explain subsidence features in a

hydrological context. The study compares interferograms created from the ERS satellite for the summer and winter seasons from 1992-1997, to in situ groundwater level data in the Las Vegas Valley. The authors found a maximum subsidence rate of 19 cm during the time period and was able to relate physical phenomena, such as water table levels and clay thickness, to patterns exhibited in the interferograms. In the Las Vegas Valley, two subsidence features were identified: a bowl in the northwest and an elongated bowl in the valley center. The northwest subsidence bowl was experiencing continuous declines in groundwater levels, which caused subsequent compaction, especially during the summer. This result shows the advantages of having time series data, by being able to measure a change rate of land elevation and isolating seasonal rates. Knowledge of human activities in the area such as groundwater extraction also helps to explain and even validate the many signals that can appear in an interferogram. The central subsidence bowl was found to be bounded by faults and experienced residual compaction from slowly draining aquitards. This result shows the advantage of obtaining spatially continuous and high resolution data to be able to observe such distinct patterns over the same area.

Amelung et al. also compared their InSAR results with field leveling measurements from a borehole extensometer to provide information about the elastic deformation of the aquifer system. This data, combined with the interferograms and groundwater well level time-series helps to paint a complete picture of the land subsidence and its drivers in Las Vegas Valley. There is a need for more InSAR studies to incorporate such datasets about the study area to explain features and rates seen from the interferometry. However, Amelung et al. admit that an exact match is not expected since the interferogram measures total subsidence and their extensometer data only show surface compaction. The authors also mention that it is difficult to

obtain reliable leveling data since historically, these surveys are infrequently made, but having field measurements still helps to constrain errors in interferogram processing. Different instruments employing different wavelength bands could help to provide more information to this problem. The paper concludes by saying that some of the deformation is elastic and fully recoverable. This is an interesting topic for water management and conservation groups, on whether groundwater depletion in this area is a geological risk, though water scarcity is likely the larger concern for these groups.

Nearby in the Mojave Desert, California, Galloway et al. (1998) also used interferometric SAR to measure land subsidence from groundwater depletion. The authors describe the Mojave as an ideal place to collect SAR data due to the stable soil moisture conditions, slow plant growth, and lack of agricultural activity, all of which can contribute to decorrelation. However, the authors do mention potential atmospheric effects from seasonal flooding of a nearby lake, but would require further comparison with additional interferograms. Like the previous study, Galloway et al. used ERS-1 data to create interferograms to show surface deformation from 1993-1995, and compare the data with geologic maps, known aquifer properties, groundwater levels, and land use information. The authors found that subsidence rates increased after seasonal groundwater level decreases, also seen in borehole extensometer observations. However, extensometer data is only able to capture a portion of the total measured subsidence since some compaction occurs deep below the instrument. GPS stations and InSAR data can help to supplement these measurements.

Galloway et al. also explain the principles of aquifer system deformation. Changes between the pore fluid pressure and aquifer system compression are based on effective stress principles. A change in the pore fluid pressure will cause an equal change in the effective stress

on an aquifer system, which will compress or expand in response. When the effective stress increases past the maximum effective stress, this can result in a permanent reduction of how much volume the aquifer system can hold. It should also be noted that there is an expected lag time between any aquifer compaction and expansion due to groundwater activities depending on the underlying aquifer geology. Subsidence from compaction in slow draining systems can continue for decades to centuries (Galloway and Hoffmann, 2007). The land subsidence in this region is not only an indicator of how much groundwater extraction has occurred, but can also cause geologic hazards. In Antelope Valley, land subsidence has caused earth fissures to erupt, contributing to flooding and erosion issues in the region. Knowledge of where compaction is occurring is not only useful for garnering information about hazards such as fissures and groundwater management, but can also offer information about basin sediments and hydrogeology.

Measuring land subsidence in wet regions

In dry regions such as the Mojave Desert, studies have measured sub-centimeter errors in the path length due to atmospheric effects (Goldstein, 1995). In more humid regions with less coherence, past studies have averaged multi-temporal observations to remove atmospheric effects (Zebker et al., 1997). New Orleans, Louisiana is one of these places and is of particular interest as a highly populated coastal delta experiencing rising sea levels, extreme flood events, and natural and anthropogenic drivers of subsidence. Jones et al. (2016) uses an airborne radar instrument called UAVSAR (Uninhabited Aerial Vehicle Synthetic Aperture Radar) from NASA (National Aeronautics and Space Administration) to measure subsidence rates in the greater New Orleans area. This section will focus on studies that have utilized UAVSAR to demonstrate the progress of radar technology since the previous studies.

Many complicated processes have helped to mold the New Orleans landscape and can make it difficult to differentiate between natural and human processes, such as sediment compaction, ocean currents, sea level rise, land subsidence, and human activities such as groundwater extraction (Dokka, 2011). This geologic history began with the Mississippi River transporting billions of tons of mud and sand from the interior continent and depositing at the river mouth, which has resulted in a combination of streams, levees, swamps, marshes, and lakes forming the delta plain (Snowden et al., 1980). These delta sediments are loosely arranged, organically rich and easily compressible. Such a complex and wet region would be difficult for a traditional C-band spaceborne radar to study, but the use of UAVSAR in the Jones et al. study showed the success of and importance of monitoring subsidence in coastal deltas. UAVSAR is an airborne polarimetric radar instrument from NASA that has been used to measure deformation from earthquakes, volcanoes, subsidence, glacier movement, etc. (Hensley et al., 2012). This is an L-band (23.8 cm wavelength) airborne sensor with high signal-to-noise ratio, repeat flight track accuracy, and high range resolution (1.67 m) (Hensley et al., 2011). The benefits of radar instruments include their ability to see through smoke, haze, clouds, and that data can be collected during the day or night. This adaptability is especially relevant during disaster events that may include stormy weather, inhibiting traditional visual surveys of damage. UAVSAR's high spatial resolution and L-band's long temporal coherence for InSAR allow it to be an appropriate tool for delta subsidence monitoring. In general, airborne SAR instruments can produce sub-meter range resolution terrain maps, though tend to be an order of magnitude costlier than spaceborne SAR data (Bamler and Hartl, 1998).

Jones et al. (2016) found that with more than half of Louisiana's drinking water being dependent on groundwater, extraction of these resources along with high oil and gas production

contributed to localized subsidence in New Orleans. This increases the vulnerability of levee failure during intense storms such as Hurricane Katrina in 2005, before which rapid subsidence had already been identified and contributed to the failing levees and catastrophic flooding (Dixon et al., 2006). An interferogram made from UAVSAR acquisitions from 2009-2012 was combined with local geographic information systems (GIS) data to help identify the sources of subsidence and mask out unrelated features such as surface water. The highest vertical velocity rates (15-30 mm/yr) were observed at the NASA Michoud Assembly Facility associated with a major power plant extracting groundwater for industrial purposes. In western New Orleans, the Norco area contained up to 40 mm/yr of subsidence due to chemical plants refining crude oil for gasoline, and also large groundwater withdrawals for cooling water. These features are shown in Figure 2, where the top panel shows the bull's-eye feature from the interferogram indicating subsidence and the bottom panel shows GIS point layers of active water wells confirming chemical industry as the cause for subsidence. This figure also helps to show the contrast in spatial resolution from previous studies using ERS data at 90 meters resolution and UAVSAR data at about 6 meters resolution. Many other notable features such as the: Bonnet Carré Spillway, Mississippi River Gulf Outlet canal, and levee lines along the Lower 9th Ward are also showing concerning rates of subsidence. The authors also found that housing construction dates, soil type differences, and buried beach sands seemed to have modest correlations with patterns seen in UAVSAR. Current hurricane protection and coastal restoration efforts still have not incorporated late 20th century water level and geodetic data into their projections. This study showed by using SAR interferometry and local GIS datasets, areas of subsidence can be identified in a more efficient and economical manner, especially for emergency response applications.

Another study by Sharma et al. (2016) also used UAVSAR to monitor subsidence on Sherman Island in the Sacramento-San Joaquin Delta ("the Delta") in northern California. Sherman Island was chosen as the focus of the study since it helps to control the salinity gradient traveling in from the San Francisco Bay. The authors found subsidence rates of 0-5 cm/yr from 2009-2014, assuming the subsidence is linear. Levee systems throughout the country play a crucial role in flood protection for citizens, infrastructure, and agricultural land that is vital to the livelihood of these regions. The Delta is the largest estuary in the western U.S. (over 2500 km^2) and contains over 1,500 km of earthen levees that protect the 65 islands in the area from flooding, primarily caused by subsidence over the past 150 years (Service, 2007). These waterways also supply irrigation water for about 1 million hectares of agricultural land, and serve as a main water supply for 23 million California residents (Service, 2007). Many of these islands are 10-25 feet below sea level, and the levees that surround them are only 1 foot above the 100-year flood elevation, sitting atop compressible peat and organic clay soils (Ingebritsen et al., 2000). Levee damage can be attributed to a variety of factors, including: floods, tidal currents, subsidence due to groundwater withdrawal and mining, plate motion, seismic events, and even rodent burrowing (Jones et al., 2016). Threats to the infrastructure include cracking, slope instability, wave wash, erosion, sinkholes, boils, seepage, and subsidence (Jones et al., 2016). Seepage occurs when there is water movement below the structure, which can weaken the levee and develop into a boil, leading to complete failure of the levee (Jones et al., 2016). Localized subsidence from soil compaction also destabilizes the structure and can lead to failure.

Sharma et al. found that areas with higher organic soil content on Sherman Island contained higher subsidence rates, and that these areas also tended to have lower elevation. This might be an indication of ongoing subsidence over longer time periods. The authors were able to

make such comparisons by directly visualizing soil and elevation data next to the interferogram. The resolution that UAVSAR offers also allows measurement of movement on the levees themselves. The authors also found on a levee section that had undergone several repairs was experiencing loading due to the addition of fill material. Again, the variety of contributing factors to subsidence requires additional data about the water table, soil type, land use, etc. that this study compares the interferometry results with.

SAR monitoring of widespread subsidence has been accomplished in many studies, but applying this to individual levees is an emerging topic because it requires high spatial resolution and a wide imaging swath, both of which which UAVSAR offers. Many InSAR studies have shown their utility in measuring land subsidence in dry and urban environments. These studies have been limited in agricultural and naturally wet areas due to decorrelation for shorter radar wavelengths. Jones et al. (2016) and Sharma et al. (2016) were able to study these types of regions by using UAVSAR's longer wavelength (L-band) data, which is collected at short, regular intervals. By performing time-series methods for low coherence areas on these acquisitions, decorrelation is decreased and the remaining interferogram reflects more accurately the surface deformation. The Sharma et al. study also validates the UAVSAR rates with power pole measurements, extensometer rates, and other datasets as similarly done in past InSAR studies. Subsidence quantification is a necessary objective for coastal communities around the world experiencing relative sea level rise as these deltaic lands are the last barrier against flood damage.

3. Dissertation Outline

Since the first instruments in the 1950s, imaging radars and the synthetic aperture radar (SAR) instruments that followed have been monitoring small and large scale surface processes

on Earth and throughout our solar system with great accuracy and precision. Interferometric SAR (InSAR) technology has allowed for detailed monitoring of earthquakes, volcanoes, glaciology, landslides, ocean processes, and more. While other remote sensing methods, such as LiDAR (Light Detection and Ranging), are able to measure surface displacements by subtraction of elevation values over multiple acquisitions, InSAR is able to measure displacement without the initial elevation value, and with higher accuracy (Jones, 2016). Long term monitoring with InSAR over vulnerable urban centers should be considered since these areas tend to maintain interferometric coherence better over time. In particular, the contribution of InSAR to studies of land subsidence has allowed scientists to monitor potentially hazardous locations around the world. Emerging applications of InSAR also point to more direct comparisons with field datasets and informative geographic information systems (GIS) data to explain the intricate features seen in SAR datasets.

The high spatial resolution of today's airborne instruments has improved by at least a factor of 10 from the first SAR images created by early spaceborne missions. The progress of using this technology for such a wide variety of applications has made InSAR an indispensable tool in earth science remote sensing, and the queue of future spaceborne missions reflects the continuation of this trend. UAVSAR is the airborne prototype for NISAR, and the work presented can help to identify correct instrument modes pre- and post-disasters. This work also shows how NISAR will meet the mission objectives for benefitting resource management and damage assessment during natural hazards. UAVSAR applications can be designed for emergency response situations after a flood event or earthquake to allow resources, as in the Sacramento-San Joaquin Delta, to focus on the levees most likely damaged (Hensley et al., 2012). Chapter 2 previews the capability of monitoring levees using high resolution L-band

sensors using the Sacramento Delta as a case study. Chapter 3 ventures into the Delta island interiors and investigates small-scale subsidence features as compared with a GIS repository.

The polarization, or direction, of the waves being transmitted and received by SAR instruments also has great potential to be combined with traditional InSAR applications. PolSAR, or polarimetric SAR, can allow for separation of scattering mechanisms, which can indicate different surface properties. SAR instruments emit horizontally polarized and vertically polarized waves, usually denoted by H and V respectively. Fully polarized instruments use HH, VV, HV, and VH denotations to signify the transmitted wave for the first letter and the received wave direction for the second letter. The horizontal field is close to the horizontal line of the ground surface while the vertical field is perpendicular to the horizontal field and look direction. Different objects on the surface, water, buildings, vegetation, etc., will react differently to the polarized waves, and therefore can offer useful identification from their scattering properties. In the past, missions did not possess sufficient bandwidth to transmit and store data from all these polarizations, but newer instruments such as UAVSAR, which is also airborne and can store data onboard, are fully polarized and can produce such datasets.

Polarimetric methods have also introduced the possibility of identifying levee seepage locations, which can be automated for emergency response. Hensley et al. (2011) also used UAVSAR to detect soil moisture for a campaign in Canada that was to be used as supporting material for the Soil Moisture Active Passive (SMAP) satellite, whose radar has since failed. Such high priority missions also relay the importance of being able to remotely sense soil moisture, not just for levee monitoring, but other hydrological applications. Hensely et al. were able to measure soil moisture changes using interferometric phase change, and observed agreement with model predictions. This study helped to validate the methodology of using

polarimetric interferometry to measure soil moisture over an area that was mostly agricultural land (similar to the Sacramento Delta), and shows the increasing interest in space-borne SAR satellites. In order to retrieve volumetric soil moisture content and surface height, Oh (2004) presented a semi-empirical polarimetric backscattering model for bare soil surfaces in Korea. Soil moisture is an important component in hydrological processes and can inform on agricultural processes as well. Chapter 4 compares a variety of PolSAR datasets and optical imagery to determine the viability of levee seep detection for the California Aqueduct and Delta levees.

InSAR has variety of applications and can be unintuitive to understand, but is powerful in terms of spatial resolution and surface displacement measurements, especially for studying small scale features such as levees. The future developments of combining the high spatial resolution and accuracy of InSAR with the descriptive capabilities of PolSAR hold a promising future for an all-encompassing remote sensing tool. The airborne capabilities of UAVSAR and emergency response applications outlined by the NISAR mission preview future disaster protocol. Chapter 5 outlines future work to be done using UAVSAR and NISAR-simulated data on previous major floods, such as Hurricane Harvey in the Gulf Coast, in preparation for final NISAR products. Chapter 6 is a summary of the dissertation. The integration of InSAR, PolSAR, and GIS datasets can help monitor small-scale subsidence and seepage for critical flood infrastructure around the world.

Figures

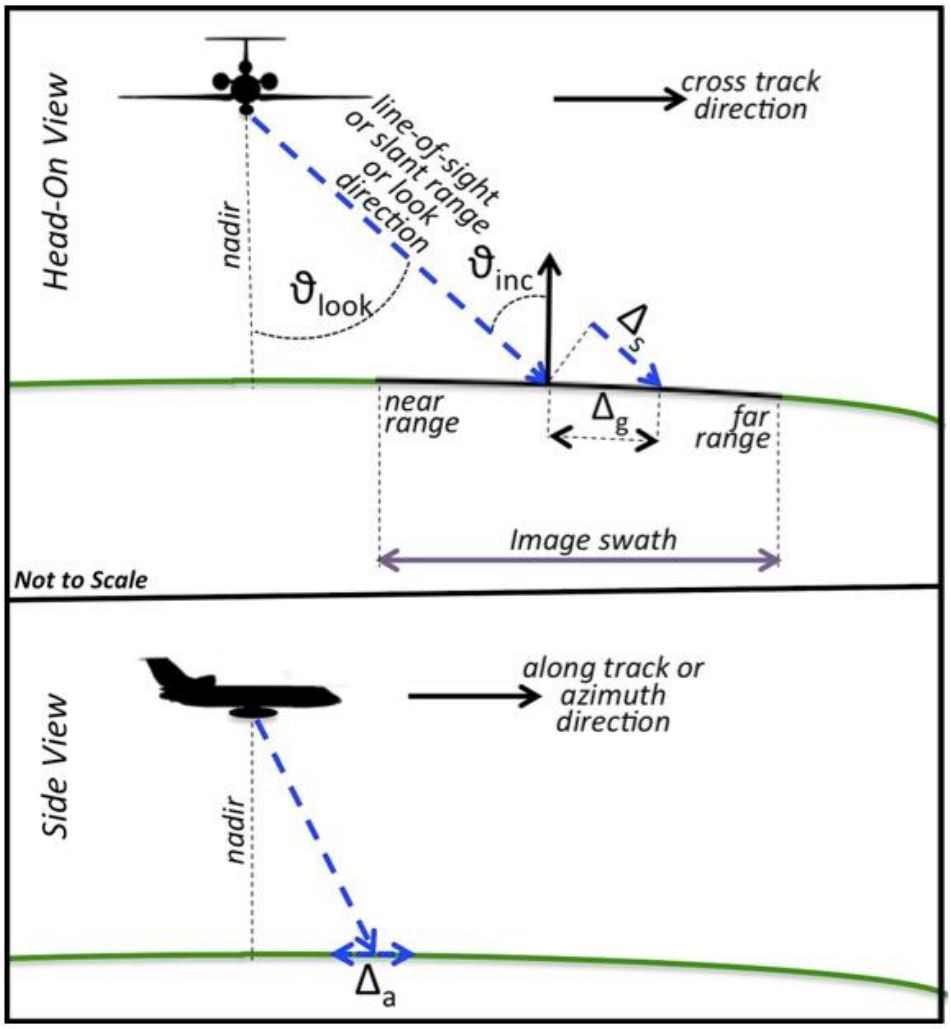

Figure 1: From Jones, 2016 "A practical guide to synthetic aperture radar interferometry (InSAR) for engineering and environmental geologists". These sketches describe the viewing geometry of an airborne radar instrument, with the aircraft flying out of the page in the top panel, and flying across the page in the bottom panel.

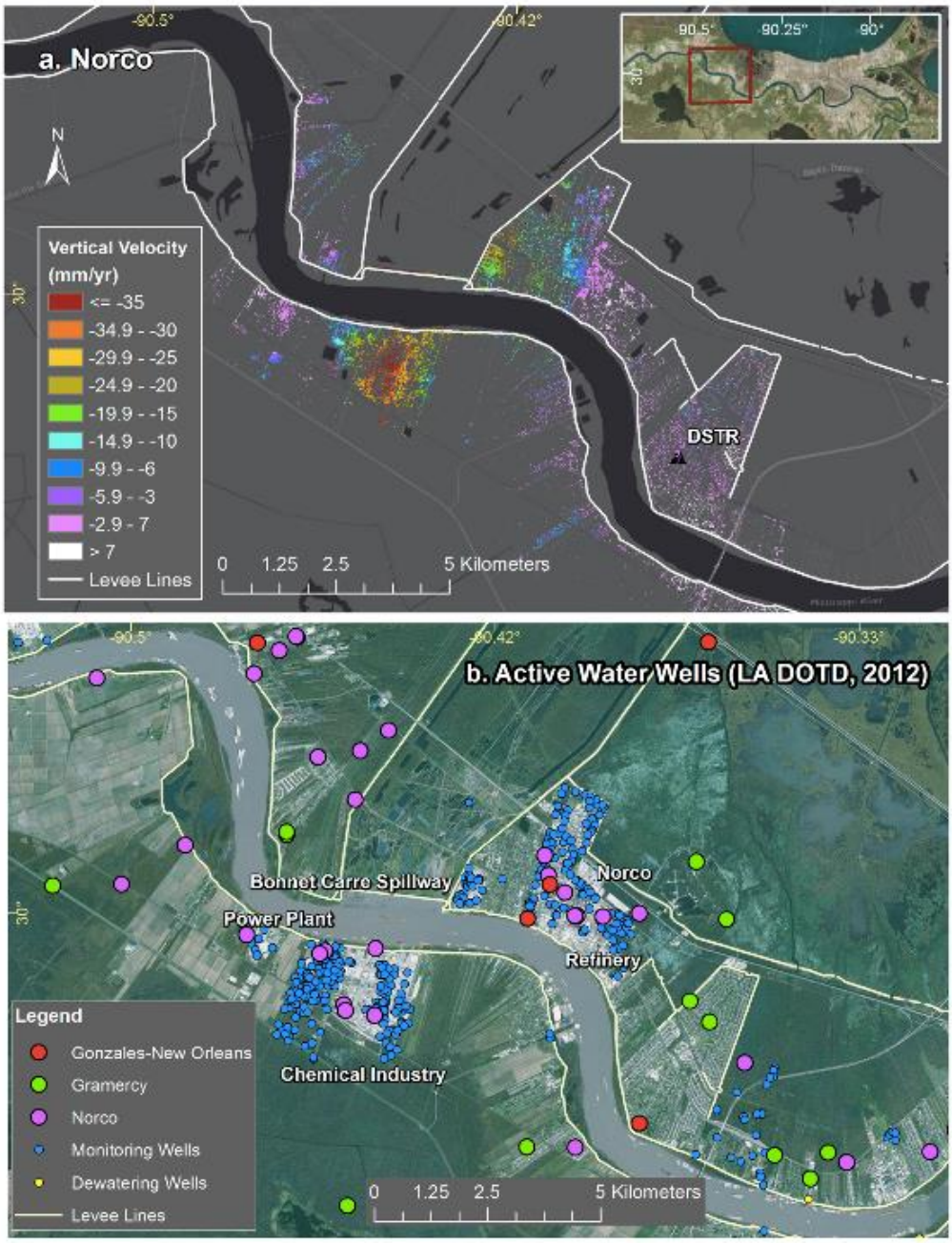

Figure 2: From Jones et al. (2016) "Anthropogenic and geologic influences on subsidence in the vicinity of New Orleans, Louisiana". UAVSAR interferogram from 2009-2012, with the top panel showing land subsidence from chemical industry activity and the bottom panel showing GIS water well locations to explain above features.

References

Amelung, F., Galloway, D. L., Bell, J. W., Zebker, H. A., & Laczniak, R. J. (1999). Sensing the ups and downs of Las Vegas: InSAR reveals structural control of land subsidence and aquifer-system deformation. *Geology*, *27*(6), 483-486.

Bamler, R., & Hartl, P. (1998). Synthetic aperture radar interferometry. Inverse Problems, 14(4), R1. iop.

Bürgmann, R., Rosen, P. A., & Fielding, E. J. (2000). Synthetic aperture radar interferometry to measure Earth's surface topography and its deformation. *Annual review of earth and planetary sciences*, *28*(1), 169-209.

Dixon, T. H., Amelung, F., Ferretti, A., Novali, F., Rocca, F., Dokka, R., ... & Whitman, D. (2006). Space geodesy: Subsidence and flooding in New Orleans. Nature, 441(7093), 587-588.

Dokka, R. K. (2011). The role of deep processes in late 20th century subsidence of New Orleans and coastal areas of southern Louisiana and Mississippi. Journal of Geophysical Research: Solid Earth, 116(B6).

Galloway, D. L., & Hoffmann, J. (2007). The application of satellite differential SAR interferometry-derived ground displacements in hydrogeology. Hydrogeology Journal, 15(1), 133-154.

Galloway, D. L., Hudnut, K. W., Ingebritsen, S. E., Phillips, S. P., Peltzer, G., Rogez, F., & Rosen, P. A. (1998). Detection of aquifer system compaction and land subsidence using interferometric synthetic aperture radar, Antelope Valley, Mojave Desert, California. *Water Resources Research*, *34*(10), 2573-2585.

Galloway, D. L., Jones, D. R., & Ingebritsen, S. E. (1999). Land subsidence in the United States (Vol. 1182). US Geological Survey.

Goldstein, R. (1995). Atmospheric limitations to repeat-pass interferometry. *Geophysical Research Letters,* 22(18), 2517-2520.

Hensley, S., Michel, T., Van Zyl, J., Muellerschoen, R., Chapman, B., Oveisgharan, S., ... & Mladenova, I. (2011, July). Effect of soil moisture on polarimetric-interferometric repeat pass observations by UAVSAR during 2010 Canadian Soil Moisture campaign. In Geoscience and Remote Sensing Symposium (IGARSS), 2011 IEEE International (pp. 1063-1066). IEEE.

Hensley, S., Jones, C., & Lou, Y. (2012). Prospects for operational use of airborne polarimetric SAR for disaster response and management. In Geoscience and Remote Sensing Symposium (IGARSS), 2012 IEEE International (pp. 103-106). IEEE.

Heywood, C. E., Galloway, D. L., & Stork, S. V. (2002). Ground displacements caused by aquifer-system water-level variations observed using interferometric synthetic aperture radar near Albuquerque, New Mexico (No. 2002-4235).

Hooper, A., Zebker, H., Segall, P., & Kampes, B. (2004). A new method for measuring deformation on volcanoes and other natural terrains using InSAR persistent scatterers. *Geophysical research letters*, *31*(23).

Ingebritsen, S. E., Ikehara, M. E., Galloway, D. L., & Jones, D. R. (2000). Delta subsidence in California: the sinking heart of the state (No. 005-00). Geological Survey (US).

Jet Propulsion Laboratory. (n.d.). In Mission to Earth: Seasat. Retrieved from https://www.jpl.nasa.gov/missions/seasat/

Jones, C. E., Bawden, G., Deverel, S., Dudas, J., Hensley, S., & Yun, S. H. (2012). Study of movement and seepage along levees using DINSAR and the airborne UAVSAR instrument. In SPIE Remote Sensing (pp. 85360E-85360E). International Society for Optics and Photonics.

Jones, C. E., An, K., Blom, R. G., Kent, J. D., Ivins, E. R., & Bekaert, D. (2016). Anthropogenic and geologic influences on subsidence in the vicinity of New Orleans, Louisiana. Journal of Geophysical Research: Solid Earth, 121(5), 3867-3887.

Jones, C. E., Dudas, J., Bawden, G. W. (2016). Application of remote sensing to assessment of water conveyance infrastructure integrity. In R. L. Anderson and H. Ferriz (Eds.), Applied Geology in California, Special Publication 26. Association of Environmental and Engineering Geologists, Star Publishing Company.

Jones, C. E. (2016). A practical guide to synthetic aperture radar for engineering and environmental geologists. In R. L. Anderson and H. Ferriz (Eds.), Applied Geology in California, Special Publication 26. Association of Environmental and Engineering Geologists, Star Publishing Company. In press.

National Research Council (1991). Mitigating losses from land subsidence in the United States: Washington, D. C., National Academy Press, 58 p.

Pollitz, F. F., Wicks, C., & Thatcher, W. (2001). Mantle flow beneath a continental strike-slip fault: Postseismic deformation after the 1999 Hector Mine earthquake. *Science*, *293*(5536), 1814-1818.

Pritchard, M. E., & Simons, M. (2004). An InSAR-based survey of volcanic deformation in the central Andes. *Geochemistry, Geophysics, Geosystems*, *5*(2).

Rignot, E., & Kanagaratnam, P. (2006). Changes in the velocity structure of the Greenland Ice Sheet. *Science*, *311*(5763), 986-990.

Service, R. (2007). Environmental restoration. Delta blues, California style. Science (New York, N.Y.), 317(5837), 442–5. doi:10.1126/science.317.5837.442

Sharma, P., Jones, C. E., Dudas, J., Bawden, G. W., & Deverel, S. (2016). Monitoring of subsidence with UAVSAR on Sherman Island in California's Sacramento–San Joaquin Delta. Remote Sensing of Environment, 181, 218-236.

Shepherd, A., Ivins, E. R., Geruo, A., Barletta, V. R., Bentley, M. J., Bettadpur, S., ... & Horwath, M. (2012). A reconciled estimate of ice-sheet mass balance. *Science*, *338*(6111), 1183-1189.

Simons, M., Fialko, Y., & Rivera, L. (2002). Coseismic deformation from the 1999 Mw 7.1 Hector Mine, California, earthquake as inferred from InSAR and GPS observations. *Bulletin of the Seismological Society of America*, *92*(4), 1390-1402.

Smith, L. C. (2002). Emerging applications of interferometric synthetic aperture radar (InSAR) in geomorphology and hydrology. Annals of the Association of American Geographers, 92(3), 385-398.

Snowden, J. O., Ward, W. C., & Studlick, J. R. J. (1980). Geology of greater New Orleans: its relationship to land subsidence and flooding.

Van Zyl, J. J. (2001). The Shuttle Radar Topography Mission (SRTM): a breakthrough in remote sensing of topography. Acta Astronautica, 48(5-12), 559-565.

Vincent, P., Larsen, S., Galloway, D., Laczniak, R. J., Walter, W. R., Foxall, W., & Zucca, J. J. (2003). New signatures of underground nuclear tests revealed by satellite radar interferometry. Geophysical Research Letters, 30(22).

Woodhouse, I. H. (2005). Introduction to microwave remote sensing. CRC press.

Zebker, H. A., Rosen, P. A., & Hensley, S. (1997). Atmospheric effects in interferometric synthetic aperture radar surface deformation and topographic maps. Journal of geophysical research: solid earth, 102(B4), 7547-7563.

CHAPTER TWO

Radar interferometry offers new monitoring approach for critical flood control infrastructure

Abstract

Aging flood infrastructure systems will need to be closely monitored as metropolitan areas globally face increasing inundation risk from sea level rise. To augment traditional ground survey, synthetic aperture radar (SAR) is shown to efficiently quantify elevation change along earthen levees with continuous spatial coverage. The study area, California's Sacramento-San Joaquin Delta, has an exemplar earthen levee system that protects the region from flooding. We investigate evidence of settling from historic levee breaks and small-scale subsidence features with a vertical velocity map and time-series of cumulative displacement derived from data acquired by the UAVSAR (Uninhabited Aerial Vehicle Synthetic Aperture Radar) L-band SAR, during 2009-2015. Comparison between radar and lidar maps (2007 and 2017) show that typical laser elevation surveys can miss subsidence features in the presence of normal maintenance activities. Historic levee break sites show more stable conditions due to the nature of repairs, and can be monitored using the SAR time series product. The time series product is able to monitor levee conditions over time, showing fast settling immediately after a levee repair that eventually becomes more stable. SAR information helps monitor the efficacy of repairs and targeted improvements to decrease the risk of levee breaks. In light of the upcoming NASA-ISRO SAR satellite mission, for which UAVSAR is the prototype, detailed monitoring will be attainable for levees worldwide.

Introduction

With ten percent of the global population living in low elevation coastal regions (less than ten meters above sea level), coastal land loss will continue with more frequent flooding as sea levels rise (McGranahan et al., 2007; Tebaldi et al., 2012; Buchanan et al., 2016). Global extreme coastal water level exposure is estimated to affect 190 million people by 2100, three times as many people as previously estimated (Kulp et al., 2019). It is widely suggested that the sustainability of coastal areas will depend on engineered solutions (Tessler et al., 2015; Wuebbles et al., 2017). For example, in Manila, Philippines, there is a $6 million flood management plan that includes building a new dam in an upper catchment area (The World Bank, 2017). Ho Chi Minh City, Vietnam has a $4.4 billion project for tide control plans and building more dikes and reservoirs (Global Construction Review, 2016). Almost 400 km of higher seawalls have been erected in Japan since the 2011 Thoku earthquake and tsunami (Reuters, 2018). However, these structures may be built on compressible soils or areas already subsiding and will need continual monitoring. More than 70% of people currently exposed to permanent inundation or flooding live in Asian countries where there is a great need for data on the height and condition of levees and seawalls (Kulp et al., 2019). The importance of monitoring such coastal hazards is prioritized in the U.S. National Academy of Sciences' 2017 Decadal Survey for Earth Science and Applications from Space (National Academy of Sciences, 2018), which acknowledges the risk of increased storm activity to coastal areas protected by infrastructure to be a significant societal challenge.

Man-made levees are typically earthen embankments or concrete floodwalls, designed to divert the flow of water during a major flood event, storm surge, and seasonal high water (American Society of Civil Engineers, 2017). Even in areas where flooding is infrequent, and

particularly those with dry climates, levees are often an integral part of a conveyance system that provides water to locations distant from the source. Sinking deltas such as the Ganges-Brahmaputra in Bangladesh, the second largest in the world, experience extreme sediment starvation from levees and dams built to combat flooding (Schmidt, 2015). The levees in Jakarta, Indonesia's largest city, are challenged by intense groundwater withdrawal that has accelerated clay compaction. In 2007, this led to catastrophic flooding in Jakarta, leaving 200,000 people displaced (Schmidt, 2015). In 2005, Hurricane Katrina caused catastrophic levee and floodwall failure in New Orleans, resulting in over $200 billion in property damage and over 1 million people displaced (U.S. Army Corps of Engineers). In addition to protecting coastal cities, inland areas are often protected from riverine floods by levees. The United States contains an estimated 30,000 documented miles of levees, and up to 100,000 undocumented miles, with nearly two-thirds of Americans living in a county with at least one levee (American Society of Civil Engineers, 2017). In the U.S., 97% of the levees documented in the USACE National Levee Database are earthen structures, with the remaining 3% composed of concrete floodwalls (American Society of Civil Engineers, 2017). The USACE Levee Safety Program accounts for levees that protect millions of people and $1.3 trillion in property from flood damage, but the National Levee Database (NLD) received a "D" grade from the American Society of Civil Engineers' 2017 Infrastructure Report Card, indicating poor conditions based on engineering inspections and risk assessments. The grade shows a majority of the system experiencing significant deterioration at the end of their service life and large risk for failure (American Society of Civil Engineers, 2017).

Despite the importance of maintaining levees, methods of assessing their conditions remain largely ground-based with sparse spatial and temporal coverage, in most cases relying on

day-to-day monitoring accomplished through visual surveys made by people driving or walking along the levees, augmented by measurements made at discrete locations (Weir, 1950; Broadbent et al., 1960; Prokopovich, 1985). Inclinometers and extensometers placed in bore holes are used to measure horizontal and vertical movement within the levee prism, and electromagnetic or seismic-based measurement identify the type of material within and beneath the levee (Rojstaczer & Deverel, 1993). Although modernized geodetic methods employing Global Position System (GPS) and Light Distancing and Ranging (LiDAR) are now used in many areas, theodolite surveys with or without electronic distancing capability are still used. All of the surveying methods commonly used for determining changes in the position of a levee or land surface rely on differencing surface contours measured at different times, which is limited by the precision and accuracy of the method employed. Furthermore, most methods are labor intensive, making it effectively impossible to obtain a continual long-term, regional view of levee conditions. Those methods that do allow more rapid acquisition over large areas, namely airborne lidar and orthophotogrammetry, have significantly poorer accuracy than can be achieved across smaller areas in ground-based surveys, so it can take many years to detect even relatively large velocities of 1-2 cm/yr or identify areas that are moving significantly relative to adjacent areas (Jones et al., 2016).

In contrast, it is possible to use a different remote sensing technique, namely synthetic aperture radar (SAR) interferometry (InSAR), to measure surface displacement directly across large areas at one time with far greater accuracy than is possible with traditional methods. InSAR satellite acquisitions are routine and can be used to measure how the structure is changing over time. In contrast, spaceborne lidars do not have the spatial resolution needed for levee monitoring (Markus et al., 2017), and airborne lidar surveys can be costly and hence infrequent.

Differential interferometric synthetic aperture radar (DInSAR) allows for frequent and non-invasive measurements with centimeter to millimeter level precision (Amelung et al., 1999; Hooper et al., 2004). InSAR has been used previously to some extent for levee health monitoring (Jones et al., 2016), particularly making use of multiple polarizations of the radar pulses (Sehat et al., 2014), applying InSAR time series analysis in urban settings (Lanari et al., 2004; Chaussard et al., 2014), or being used to monitor the swelling and shrinkage of levees associated with meteorological conditions (Özer et al., 2019). The surface position surveys have largely used persistent scatterer InSAR (PSInSAR) to look at levees with hard surfaces and at a limited number of locations in urban areas (Dixon et al., 2006; Brooks et al., 2012). The main limitation is that short wavelength SARs (X, C band) experience rapid temporal decorrelation (Zebker & Villasenor, 1992), and so are challenged to detect small movements or distinguish surface movement below vegetation, while the longer wavelength SAR instruments (L-band) available in the past have not had the resolution to image the levees directly. This limitation can be addressed with L-band instruments such as UAVSAR (Uninhabited Aerial Vehicle Synthetic Aperture Radar) (Fore et al., 2015), and the upcoming NISAR mission for a spaceborne L-band radar (Rosen et al., 2017).

A high resolution map of cumulative elevation change as a function of time is derived from UAVSAR data for the period 2009-2015 for the Sacramento-San Joaquin Delta ("the Delta"). The ground settling rates at historic and recent levee impacts and breaks, and large subsidence signals across the Delta are complemented with a lidar differential of surveys from 2007 and 2017 (California Department of Water Resources, 2007; California Department of Resources, 2017). Development of robust remote sensing methods for quantitative determination

of earthen levee status, particularly those accessible at low cost and with global coverage, would have a significant effect on reducing risk to life and property throughout the world.

Materials and Methods

Study Site

In this study, an InSAR time series approach to monitoring the conditions of an earthen levee system in the Sacramento-San Joaquin Delta is evaluated and compared to airborne lidar-based monitoring. The Sacramento-San Joaquin Delta, the largest estuary in the western U.S. (4,800 km^2), formed in the late 1800s as a freshwater tidal marsh east of the San Francisco Bay at the confluence of the Sacramento and San Joaquin Rivers. Drainage for agriculture has formed 65 low-lying islands surrounded by 1,800 km of levees (Service, 2007). However, these agricultural practices eventually led to ongoing land subsidence, mainly caused by aerobic microbial oxidation of soil carbon (Ingebritsen et al., 2000). Where land subsidence has reduced the island elevation below tide levels, the levees continuously hold back water, in contrast to more typical riverine levees that do so only during high flow events. The aging levees effectively maintain the channel system that conveys fresh water to 3 million acres of farmland and part of the water supply for 25 million residents (Ingebritsen et al., 2000; Service, 2007).

The Delta levees are a useful exemplar of other levee systems around the world because they are earthen embankments, typically constructed from compacted soil and covered with grass, gravel, stone, asphalt, or concrete to prevent erosion (American Society of Civil Engineers, 2017). An extensive network of drainage ditches that feed groundwater to pumping stations helps to prevent flooding, but levee breaks in the Delta have become commonplace in the last century (Deverel et al., 2016). Repair costs for these breaks range from $43 to $243 million and in some cases force total abandonment of the island (Bates & Lund, 2013). The Delta

is also near many major seismic faults (Figure 1), with the San Francisco Bay region predicted to experience a 6.0 or larger earthquake at 98% probability by 2043 (Aagaard et al., 2016), putting the levees at risk of soil liquefaction (Deverel et al., 2016).

The UAVSAR Synthetic Aperture Radar

UAVSAR is a quad-polarized, L-band (23.8 cm wavelength) airborne synthetic aperture radar (SAR) instrument, flown in a pod carried by a NASA G-III aircraft. The instrument operates at an altitude of 12.5 km, with a bandwidth of 80 MHz and a center frequency of 1.2575 GHz. The image swath is 22 km wide, and the incidence angles range from 22°−67°. The instrument spatial resolution is 0.8 m (along flight-line) by 1.7 m (along the line-of-sight (LOS)) (Bekaert et al., 2019). The longer wavelength, high spatial resolution, and flexibility in acquisition geometry make UAVSAR an advantageous instrument for monitoring levee systems. Nine flight lines cover the majority of the legal Delta boundary (Figure 1). Each line was acquired between 52 to 60 times from July 2009 to October 2015. To minimize artifacts due to aircraft motion, the aircraft is actively controlled to stay within 5 m of the planned flight path. During post-processing image offsets are determined, the flight track is corrected, and the datasets are re-processed. Using measurements of aircraft position and 3-D acceleration during post-processing achieves 8 mm precision, but residual position errors of 0 to 5 cm can persist in the image. These artifacts can appear as linear ramps perpendicular to the flight direction, which are removed in processing, or bands in the along-flight direction. The latter are not removed but are reduced by averaging in the InSAR time series processing. InSAR only measures surface displacement in the line-of-sight direction, so having multiple look directions eliminates the effect of levee orientation on line-of-sight measurements.

LiDAR Surveys

The California Department of Water Resources (CA DWR) conducted two lidar surveys over the Delta legal boundary 10 years apart, in 2007 and 2017. The most common use of lidar is to generate high precision digital surface models, which can be used to study forest canopy structure, archaeological sites, and landslide risk (Dubayah & Drake, 2000; Chase et al., 2012; Jaboyedoff et al., 2012). Lidar is able to measure surface changes such as subsidence between two events, but if surface material has been added, lidar will measure the net of all sources of elevation change. Elevation was collected at 0.5-1-meter spacings (vertical datum NAVD88, geoid model Geoid03 Continental US). For the 2007 survey, the vertical accuracy was calculated to be 15 cm at 90% confidence and less than 18.5 cm at 95% confidence (California Department of Water Resources, 2007). For the 2017 survey, the measured vertical accuracy was 10.7 cm at 95% confidence level (California Department of Water Resources, 2017). A differential was calculated between the surveys to compare with the InSAR time series cumulative displacement, which was collected over a shorter time period, 2009-2015, with more frequent measurements. The differential was calculated as the 2017 elevation minus the 2007 elevation, and divided over 10 years, hereafter known as lidar vertical velocity. Since there are only two data acquisitions, the rates calculated should not be considered linear over the time period, but rather an indicator of average cumulative change between two snapshots in time.

GPS Data

On one of the most important Delta islands, our team commissioned GPS (Global Positioning System) stations to measure elevation changes from April 2015 to July 2017. Three stand-alone continuously monitoring GPS stations were installed along the setback levee on Sherman Island in April 2015. These stations were anchored to the ground surface using a 3-feet

deep concrete pedestal. The locations of the GPS stations are shown in Figure 2C. Each station contains a Novatel ProPak 6 receiver and a dual-frequency GPS plus GLONASS pinwheel antenna. The ProPak 6 is a high performance Global Navigation Satellite System (GNSS) receiver capable of tracking different combinations of GNSS signal and integrated L-Band on 240 channels. The receivers have a built-in cellular modem and are connected to the ATT network for remote data transmission. The reference frame was NAD83CSRS and the raw GPS data time series for each station can be found in the supplementary material in Figure S1. The GPS station data was also normalized and projected into the line-of-sight for more direct comparison with the InSAR product's time series for individual flight lines. This conversion is based on the decomposition of the east-north components of a UAVSAR flight line. See Figure S2 in the supplementary material for details.

UAVSAR Time Series Processing

The first spatially comprehensive map of modern subsidence rates (vertical velocity) in the Delta was reported in Bekaert et al. (2019). The reported vertical velocities show the Delta to be subsiding by 9.2 +/- 4.4 mm/yr on average in 2009-2015, with high variability across islands. The same UAVSAR dataset is utilized for this study, but clipped and smoothed along the levees for a separate analysis on levee conditions. The time series product, with values for each acquisition date, is used to present the plots of cumulative displacement over time, and the vertical velocity map is used to visualize the spatial patterns of subsidence. Included below is a summary of how the vertical velocities were generated, with full details in Bekaert et al. (2019).

Using the Small Baseline Subset (SBAS) time-series processing algorithm (Berardino et al., 2002) and the GIAnT toolkit (Agram et al., 2013), the cumulative LOS (line-of-sight) displacement time series and uncertainty are calculated from unwrapped interferograms. The

derived displacements are relative to different reference points for each flight track, with the reference location selected based on high coherence and amplitude/phase stability. In the process of combining the data together to form a single map, the InSAR results are re-referenced to 24 GNSS stations within the scene extent as a tie-in for the mosaicked flight swaths. The GNSS products used are from the Nevada Geodetic Laboratory and have horizontal rate uncertainties up to 0.3 mm/yr (Blewitt et al., 2013). Consistency is required in the swath overlap regions to solve for reference corrections in a single inversion strategy. Broad-scale horizontal movement from nearby faults is removed from the rates. For the final combined map, the GNSS rates are used to remove long wavelength artifacts (ramps, tilts), while the InSAR rates constrain local variability. By implementing a planar correction for each flight line when constraining the flight swath overlap regions, tropospheric delay and residual position errors are further reduced. Vertical velocity maps from the different flight lines are combined with a weighted average, allowing areas with overlapping pixels to have lower uncertainty. The corresponding uncertainties are calculated using a jackknife approach. A full propagation of errors is included, with an RMSE of 7.7 mm/yr between GNSS rates and the vertical velocities. See Figure S3-S4 for the vertical velocity and uncertainty maps for the major central Delta islands obtained from Bekaert et al. (2019).

Atmospheric corrections were also applied using the ERA-Interim global atmospheric model (Doin et al., 2009) using a modified version of the TRAIN toolbox (Bekaert et al., 2015). The modifications made were to integrate the refractivity from the surface to the aircraft altitude and incorporate time-of-day of acquisitions. Localized systematic noise from ground fog or low lying clouds was also considered. Monthly temperatures from Sacramento were used to estimate

atmospheric delay from 100% humidity at 1 km above the ground (Younes, 2016), and the values ranged from 0.63 to 2.10 mm, which is well within the estimated accuracy of the data.

To evaluate whether the residual of the InSAR and lidar vertical velocities (v_{InSAR} and v_{LiDAR}, respectively) is larger than the uncertainty, the following expression was applied:

$$\left|v_{InSAR} - v_{LiDAR}\right| \leq \sqrt{{\sigma_{v_{InSAR}}}^2 + {\sigma_{v_{LiDAR}}}^2} \quad (1)$$

where $\sigma_{v_{InSAR}}$ is the 1-sigma uncertainty calculated for the InSAR vertical velocities (as stated above) and $\sigma_{v_{LiDAR}}$ is 10.7 mm/yr, which is the 1-sigma uncertainty as calculated from the vertical accuracy reported from the lidar datasets (California Department of Water Resources, 2007; California Department of Water Resources, 2017). If the expression is true, then the InSAR and lidar vertical velocities measured are consistent within both datasets' uncertainties. Across the entire Delta legal boundary, where there are both lidar and SAR data, 99.8% of pixels showed agreement (see Figure S5 for the visual comparison of these results and Bekaert, et al. (2019) for scaling information).

Levee Oriented Moving Window Average

A collection of GIS (geographic information systems) datasets was used to investigate past levee break locations and identify areas which may be experiencing levee settling. The datasets provided are: levee anatomy (CA DWR), historic levee breaks (CA DWR), and repair and seepage locations (CA DWR). The levee anatomy vector datasets differentiate portions of the levee as the levee crown, levee landside and waterside slopes, and toe ditch and berm. The final map of vertical velocity was clipped to the boundaries of this combined anatomy to isolate the values for the levees only. Past levee break locations provided by the DWR are used to identify areas that could be settling after repair work. The levee anatomy layer was used to mask

the InSAR vertical velocity map in Esri's ArcMap 10.6. Next, equally spaced points were generated along the levee crown/centerline and visually inspected for accuracy for each island. These points were indexed and used to calculate a moving window average of the vertical velocities. Each window is uniquely generated by searching for the nearest points along the waterside levee and landside levee boundaries. A best-fitting window is generated for each levee centerline point. This is done to ensure that a consistent length of the levee is averaged at each step, between 70-100 m. Unlike a traditional moving window, the generated window is levee-oriented, i.e., it modifies its orientation with respect to a levee's location on an island. Since the levee's landside and waterside slope vary in width and shape across an island, a static window would not capture the actual levee section for all locations. For more details, see Figure S6 in the supplementary material. This moving average window is used to reduce noise in the dataset, while retaining the major patterns of the original velocity map. Both the vertical velocity and the uncertainty estimates were calculated with the adaptable sliding window.

Results

The average vertical velocities calculated from InSAR on the levees within the Delta legal boundary range from -77 to 14 mm/yr, showing high variability island to island.

Levee Subsidence

Below, the largest subsidence signal in the Delta is presented alongside GPS station data and the lidar vertical velocity map. Other subsidence signals in the Delta are also investigated, and the rates of settling between historic and recent levee breaks and impacts (where the levee was struck by a vessel) are also compared with the lidar surveys. The section of levee showing the highest rates of subsidence across the Delta is located in southwestern Sherman Island, with up to -160 mm/yr of subsidence (Figure 2A). The full resolution from the unsmoothed vertical

velocity map is shown in Figure 2A, and the smoothed levee-specific results in Figure 2C. From the smoothed results, it can be seen that one portion of the levee is experiencing the highest rate of subsidence, and this rate gradually decreases on either side of the section. Nearby this section is the 1969 levee break, indicated in Figure 2A-C southeast of the subsidence feature, which shows more stable conditions consistent with levee sections further from the location of maximum rate. Figure 2B shows the lidar vertical velocity results for the same area. Lidar shows a large increase in elevation that coincides spatially with the highest subsidence signal from the InSAR results, though each are still within the datasets' uncertainty bounds. Independent of auxiliary information, one would infer from the lidar data that no subsidence was occurring at this location. In fact, the elevation increase is likely due to the continual addition of fill to maintain the elevation in this area.

The large subsidence signal is also confirmed by three GPS stations from our team, the locations of which are shown in Figure 2C. The smoothed InSAR results and the InSAR LOS time series of the three GPS locations (Figure 2D), shows that Station 1 and 2 have the higher rates of displacement compared with Station 3. Comparing this to the projected LOS rates for the GPS station data (Figure 2E), Station 1 also has the highest cumulative displacement. Station 2 has a very similar InSAR LOS time series to Station 1, but is closer to Station 3 when looking at the GPS LOS time series. In both datasets, Station 3 shows the least amount of vertical displacement.

Some other major subsidence signals across the Delta are shown in Figure 3. In Figure 3A, there is a long stretch of subsidence along the northern section of Webb Tract that matches exactly with the elevation gain seen in the lidar vertical velocity map in Figure 3B. From the original InSAR rate map, Figure 3A shows these large subsidence signals in close proximity to

the levee. The largest subsidence feature on the west measures up to -56 mm/yr. Like the Sherman Island example, the InSAR measures actual deformation at the surface while the lidar shows an elevation gain at the same site. Known repair work occurred along this levee section for toe ditch cleaning and seepage control. On Jersey Island (Figure 3C), a large signal of up to -47 mm/yr of subsidence is seen close to the levee with another large subsidence feature more inland. In this case, the lidar surveys in Figure 3D agree with the InSAR results and also show significant elevation loss. The features are not identical, but both datasets show the highest rates of subsidence close to the levee and extending inland. For a different section of Sherman Island shown in Figure 3E-F, three large subsidence features close to the levee are shown. These features also show up as elevation loss in the lidar data in Figure 3F, with the easternmost example exhibiting the highest elevation loss in both the InSAR and lidar, up to -48 mm/yr.

As discussed in the Methods section, a measure of sensitivity for the InSAR and lidar residuals against their uncertainties was evaluated. For the scaled $\sigma_{v_{InSAR}}$ sensitivity result (Figure S5), when only looking at the central islands (as shown in Figure S3-S4), 0.17% of pixels for island interiors disagreed in sensitivity while 2.45% of pixels for the levees disagreed in sensitivity. This indicates that the InSAR and lidar datasets are more than 14 times as likely to be out of each other's uncertainty bounds on the levees as on island interiors. Areas of disagreement coincide with large InSAR subsidence features like on Sherman Island that are masked by repair work's elevation gain in the lidar vertical velocity map.

Historic Levee Breaks

In Figure 4, sections of four Delta islands that are the sites of past levee breaks are shown. At each of these sites, the area of previous repair of a levee break is evident in the velocity map as being more stable than its surroundings. These rates differ between the three

examples, from -2 up to 8 mm/yr, but relative to each location's surroundings, the levee break point shows the least amount of subsidence. For each location, the subsidence rates increase gradually as you move away from the levee break point on either side. This is likely due to the method used for levee repairs, in which solid material such as rocks or fill are added to the levee break site and also extend to unimpacted levee on both sides. Over time, this material, depending on its contents, begins to settle and becomes more stable. As seen in Figure 4B-D, scour (or blowout) ponds directly adjacent to the breaks were formed during flooding, as water scooped up layers of peat and penetrated island interiors deep enough to maintain permanent seepage (CALFED Bay-Delta Program, 2000).

The most recent levee break occurred in 2004 on Jones Tract, as seen in Figure 5. In the optical imagery basemap, a large land scar inland also shows the path of flooding that occurred during this massive event. At the break point, the InSAR-derived rates measure -8 to -6 mm/yr of settling, which is much higher than those for the older break sites shown in Figure 4, likely due to this levee break being fairly recent in time. Like the other levee break examples in Figure 4, Jones Tract also displays a similar pattern of gradually higher subsidence/settling rates moving away from the break location. However, here the pattern is not as smooth with large sections of the levee showing high rates of settling, up to -14 mm/yr on the western side and -9 mm/yr on the eastern section. In Figure 5B, the lidar vertical velocity between 2007 and 2017 is shown for the Jones Tract break. Here, a larger value means that the elevation has increased from 2007 to 2017, which is seen in the red pixel sections on either side of the break point. At the break, there is an elevation change of -2.6 mm/yr to 0.6 mm/yr, and on either side of the break, an elevation increase of up to 24 mm/yr.

This location of pattern is coincident with the settling pattern seen in the InSAR, but with opposite trends in elevation change. Due to repair work adding material, InSAR settling (negative value) is observed as lidar elevation increase (positive value). The lidar surveys measure net elevation change, including added fill material between acquisitions, and not the ongoing settling since the repairs were administered. In fact, where the InSAR shows the least amount of settling at the break site, the lidar shows less elevation gain. On either side of the break where InSAR shows faster rates of settling, the lidar shows more elevation gain. Although the west side of the impact shows more subsidence from InSAR, it has less elevation gain in the lidar compared to the east side of the impact. It is confirmed in Google Earth that extensive repair work occurred in this area, especially on the eastern side, between October 2011 and May 2012 that matches the elevation gain features seen in the lidar. This may also explain the trend seen in Figure 5C of increased displacement around 2011-2012 for the area. This breach on Jones Tract flooded the island with over 150,000 acre-feet of water and required 3 weeks for repair, costing about $90 million to repair, with the actual repair costing $30-$40 million and the remaining costs for property damage (U.S. Army Corps of Engineers; Deverel et al., 2016).

Levee Settling Immediately After Repair

On August 27, 2009, a 175 m bulk carrier ship collided into the north side of Bradford Island, damaging 45 m of the levee with significant cracks. Figure 6A shows an optical image one month after the impact, with repair work indicated by the bare earth section of the levee. In the InSAR results shown in Figure 6C, this repaired section is experiencing rapid settling, with rates from -19 to -31 mm/yr. Here, the opposite pattern is seen from the historic levee break examples, where at the impact site the highest rate of settling is seen, and with rate decreasing on either side. Over time, the reverse trend should be expected with the repair site showing the most

stable rates. The trend is seen in the InSAR LOS time series in Figure 6B, where pixels at the impact site are experiencing more displacement than its surroundings. There is an initially high rate of settling for the whole area between 2009 and 2012, relative to later years. The lidar vertical velocity map in Figure 6D shows an elevation increase at the repair site that is also apparent at older levee break sites, but with a higher rate of 42 mm/yr since the initial repairs occurred in 2009 between the lidar acquisitions. We also see a section of elevation loss in Figure 6D west of the impact site that corresponds to higher subsidence rates in Figure 6C and is outside of the repaired levee section.

Discussion

Like the levees enclosing New Orleans, the Sacramento Delta levees are under constant hydrostatic stress even between high water events because the islands lie beneath mean sea level. A measurable indicator and predictor of levee conditions in the Delta relevant to water resource management is land subsidence on or near a levee, which can be highly spatially variable, depending on soil characteristics and land practices. The largest contributor to land subsidence in the Delta is microbial soil oxidation, especially for dry peat soil used for agriculture in island interiors. However, for the levees, the structures sit atop these soft, compressible peat layers and experience subsidence, or settlement, primarily from consolidation and secondary compression. The added force from the levees causes water to be squeezed out of the soil, a slow process due to the low hydraulic conductivity of the peat (Reinert et al., 2014).

The InSAR-based methodology presented here can be used to quantify contemporary subsidence rates in a spatially comprehensive and consistent manner independent of levee orientation. High resolution levee monitoring allows for managers to focus traditional surveys on sections of the levee most likely to be experiencing subsidence. The centimeter-to-millimeter

level displacement accuracy can also detect precursors to levee failure unidentified by typical visual inspections.

Levee Subsidence

Sherman Island is the westernmost island in the Delta, and thus helps control the salinity gradient between brackish water entering from the San Francisco Bay and freshwater resources to the east. In 1972, a levee failure on an adjacent island, Brannan, caused a salinity intrusion that stopped water exports from the Delta, and over 350 million m^3 of freshwater was released from reservoirs to reduce saline conditions (Deverel et al., 2016). Sherman Island was one of the earliest reclaimed islands in the late 1800s, and today is mostly pasture area, with some active corn and alfalfa sites (Boryan et al., 2011). This island has experienced five major inundation events since 1900 and two levee breaks, one of which is shown in Figure 2. The 1969 break site is the more stable stretch of levee due to the method of repair. First, rocks were used to fill the break, which do not experience the same compression as only adding fill material. Later in 2007, the levee was broadened and more fill material was added at this site. Knowing the settling rates in between these two repairs would be helpful when adding sufficient material to maintain levee height after the initial rapid settling.

The largest signal of subsidence in the Delta is observed on Sherman Island at the test site, measuring up to 160 mm/yr. This subsidence signal is also confirmed by the GPS stations, which show Station 1 having the largest displacement trend. Both the InSAR and GPS time series show Station 1 having the highest displacement and Station 3 measuring the least. The GPS stations are also located more inland (outside the levee mask), and may not be capturing the full extent of deformation occurring on the levee structure itself. GPS time series data are needed as ground-truth for the InSAR product, but only capture movement at a single point, and an

extensive network of stations across all islands is not feasible. This comparison demonstrates the need for continual SAR data collection over the Delta. The large subsidence feature also coincides with the lidar data in Figure 6 showing a large increase in elevation, up to 45 mm/yr, of repair work. If relying solely on decadal lidar surveys, the vertical velocity would not measure settling in any area where fill was added, i.e., would be sensitive to repair work, whereas an InSAR time series product as processed in this study shows actual subsidence. Since radar backscatter is sensitive to changes in surface roughness and dielectric properties, if fill material is added there would be a loss of coherence in the SAR data due to the difference in material (Jones et al., 2016). Low coherence pixels are not included in the time series processing, and thus the final vertical velocity map is a result of acquisitions showing true surface movement (subsidence/uplift). As shown in Figure 2D, multiple acquisitions allow for continual measurements of such sites experiencing intense subsidence. Especially for areas where the land behind the levee lie significantly below mean sea level, such as islands in the central Delta, knowledge of ongoing subsidence rates for the levees is critical for administration of maintenance resources.

In Figure 3, Webb Tract showed a similar result to Sherman Island, with elevation gain in the lidar and elevation loss in the InSAR. Again, a large subsidence signal is being masked by repair work in the lidar vertical velocity map. Therefore, lidar cannot be the sole survey used when measuring elevation change to identify at-risk levees in areas with ongoing maintenance. Where there is major subsidence but not extensive repair work, lidar does agree with elevation loss in the examples on Jersey and Sherman Island. At both sites, the lidar matches well with the InSAR for the location and intensity of large subsidence features. However, it can be argued that areas receiving repair work have been deemed a priority by levee managers, and thus especially

need settling rate information. It is promising that UAVSAR is able to identify subsiding levees, especially in such a coherence challenged area such as the Delta, regardless of ongoing addition of fill material on the levees. The location of such large subsidence features can be communicated to levee managers as possible points of vulnerability that require further inspection.

Levee Settling After Repairs

With about 160 levee breaches in the past century and repairs costing tens of millions of dollars, close monitoring of levee conditions vulnerable to breaches is vital (Bates & Lund, 2013). Levee failure usually occurs during a high water event that causes overtopping or erosion, but can also occur during a normal day from internal degradation due to an ongoing seep, slumping, cracking, or animal burrowing. Close monitoring of areas in proximity to previous levee breaks (e.g., Figure 4) is important since these levee sections have already proved to be vulnerable in the past. Though these sites do not seem to be subsiding currently, the repairs are often made atop less stable levees or compressible peat and sandy soils, and the surrounding area for each levee break do show subsidence based on our results.

As seen from the results, observations of subsidence initially following repairs are more likely temporary loading on organic soils from the addition of fill during the levee repair. For the most recent levee break in the Delta (Figure 5), this short-term settling is especially apparent when compared to older levee breaks, with rates up to 24 mm/yr, whereas the 1955 break on Empire Tract is only settling up to 4 mm/yr. The same pattern of more stable breaks is seen at 20 different locations across the Delta (see Figure S7 in the supplementary material). Having such information about levee break locations allows differentiation between temporary settling from a repair and ongoing, long-term subsidence. Over time, repair tactics have also changed, and

depending on the material added, the repaired break may show different rates of settling. Continual InSAR satellite measurements over a levee system can help identify subsiding sections before a levee breaks or overtops, and let water managers know areas most susceptible to failure. After a repair, InSAR can help evaluate the efficacy of the repair method by measuring the rate of settling from different materials being added. Depending on the underlying soil, the response to loading from the fill material will vary for different sites.

In 2009, a shipwreck occurred on Bradford Island 12 days before the start of the InSAR time series, resulting in serious cracking of the levee. The levee portion did not break due to immediate repair work of adding sand, silt, and clay to stabilize the levee. Since this event occurred close to the start of the InSAR time series, it allows for the observation of initial rates of settling after the repair, up to -30 mm/yr, the largest value of all the historic levee break examples in this study. This indicates that rates of settling are highest directly after a levee repair and begin to decrease over time on a timescale of approximately three years. Such information can benefit levee managers in monitoring an administered repair to ensure that the settling that occurs is short-term and does not indicate long term subsidence for an already vulnerable area.

This monitoring method can be applied to other levee systems as well with the launch of NISAR. A similar analysis was conducted using UAVSAR-derived vertical velocities in New Orleans, LA (Jones et al., 2016). Here, levees that also protect from high water events such as the Bonnet Carré Spillway, Mississippi River-Gulf Outlet Canal showed concerning rates of subsidence. The levees near the Michoud Canal, which lie near the Inner Harbor Navigation Canal Surge Barrier, showed the maximum subsidence in the scene, up to 50 mm/yr. The potential of UAVSAR and NISAR to be used during emergency response will greatly aid the direction of resources after a large flood or earthquake (Rosen et al., 2017). For day-to-day

monitoring, the detection of small deformation features along the levee can lead to timely assessments before actual levee failure occurs. The results show that such InSAR time series products can measure long term deformation from subsidence, seasonal changes due to temperature and precipitation, and short term deformation from settling. These various timescales allow for detection of a variety of levee behaviors, such as long term uplift that can lead to piping, short term deformation from a high water event, and long term drought periods that can cause levee sliding (Özer et al., 2019).

Uncertainties & Challenges

Measuring deformation in a study area such as the Delta can be challenging, even with an L-band SAR instrument. There can be data processing errors from decorrelation of the baseline, temporal terrain decorrelation, co-registration errors, or noise from volume scattering in vegetation (Hanssen, 2001). Systematic errors can arise from aircraft motion, tropospheric delay in the atmosphere, or land use change. Disturbances on the surface caused by farming activity (grazing, cultivation, etc.) can cause temporal decorrelation (Deverel et al., 2016). The time series methodology used with the SBAS technique generally averages out atmospheric noise during analysis, with random noise usually being reduced by the square root of the number of acquisitions. Each of the nine Delta stacks had over 50 acquisitions. UAVSAR also imaged the Delta at different times of day and over different seasons over six years, which would randomize the atmospheric noise.

Spaceborne radar satellites will experience most of the same challenges but with a higher noise level and a sensitivity to levee orientation since there will only be two look directions, namely from the ascending and descending paths. However, the instrument will have a more consistent repeat cycle and shorter acquisition interval that can allow for longer time series

products to be produced with maintained coherence. Having regular and frequent acquisitions will allow for the differentiation between short-term settling, seasonal changes, and land subsidence in dynamic deltas where levees experience frequent repairs. A common method to study man-made infrastructures such as dams or bridges is PSInSAR, but the coherent scatterers are usually found on surfaces without vegetation. For deltas with high agricultural activity and wet conditions, this means that PSInSAR scatterers would likely only be found along the waterside rip-rap slope of the levee, and not on the levee crown or land-side slope where subsidence can have different rates (Özer et al., 2019). The upcoming NISAR satellite will have longer wavelength than others in operation (L-band) that can help to improve coherence for such deltas and increase data coverage.

Conclusions

This study shows the feasibility of high resolution monitoring of a levee system using an L-band radar instrument, and contrasted InSAR- and lidar-based methods. The SAR and lidar observations are not always measuring the same physical process, with levee repair work in the lidar data often masking large subsidence signals seen in the SAR data. Though the lidar surveys offer high-resolution elevation data, they were shown to detect elevation gain at levee repair sites due to the addition of fill material. With a priori knowledge of repair sites, the InSAR time-series method is able to differentiate between short-term settling after a levee break and ongoing subsidence.

Some subsidence reversal may be possible through land-use practices that increase sediment accumulation or natural accretion in protected marshes (Bates & Lund, 2013). However, the “patch and pray” method of repairs is unsustainable, and so implementing InSAR-derived deformation detection can help targeted repair of levee locations showing initial signs of

failure. In the face of climate change, there is likely to be less winter snow and earlier spring snowmelt in California and precipitation decreases in southern California, causing greater dependence on groundwater (Luoma et al., 2015). Due to this water supply uncertainty, California water demands from the Delta are likely to increase in the future while water availability from the Delta will decrease and gain economic value (Lund, 2016). More frequent drought periods for California are also of concern since a levee break during a dry year will be more detrimental to the water supply. The U.S. has many levees non-compliant with standards, for which subsidence will worsen levee integrity. Using local tide gauge data, Bekaert et al. (2019) estimate that on average, subsidence rates in the Delta are a factor of 4.5 higher than sea level rise rates, which absent continual and increasing repairs likely result in more overtopping events in the Delta and increase erosion along the levees.

The method demonstrated is generally applicable for other deltas and low-lying coastal areas, protected by levees and flood-walls. With almost half a billion people living on or near deltas in the world's largest cities, the risk of coastal flooding and loss of infrastructure is ever imminent (Syvitski et al., 2009). The 10 million people a year that experience storm surge flooding live mostly on deltas in Asia from heavy precipitation and storms (Syvitski et al., 2009). In the coming decades more metropolitan areas will come under threat of flooding, possibly adding sea walls and levees as defense against sea level rise (Tessler et al., 2015; Wuebbles et al., 2017). These structures will be built upon compacting soils with reduced aggradation (common in deltas due to drainage or oil/gas extraction), and need continuous monitoring to maintain their integrity (Syvitski et al., 2009).

UAVSAR is the prototype for the upcoming NISAR satellite from NASA-ISRO, and this study previews the capability of the spaceborne L-band satellite to study similar levee systems

around the world. NISAR will image at instrument resolutions of 6-12 meters, with products available 1-2 days after observation and possibly within hours for disaster response (Rosen et al., 2017). Since NISAR is dual-polarized, utilization of the polarimetric radar (PolSAR) methods can amplify detection of levee vulnerabilities such as seepage (Sehat et al., 2014). In addition, automated creation of deformation maps for vulnerable levee systems will be more feasible with increased global and temporal coverage to identify anomalous conditions. As shown in this study, the technology has the capability of monitoring critical infrastructure before, during, and after a disaster event. Especially in areas of the world where traditional surveying is sparse or expensive, SAR remote sensing can offer detailed measurements crucial to the health of the levee system.

Figures

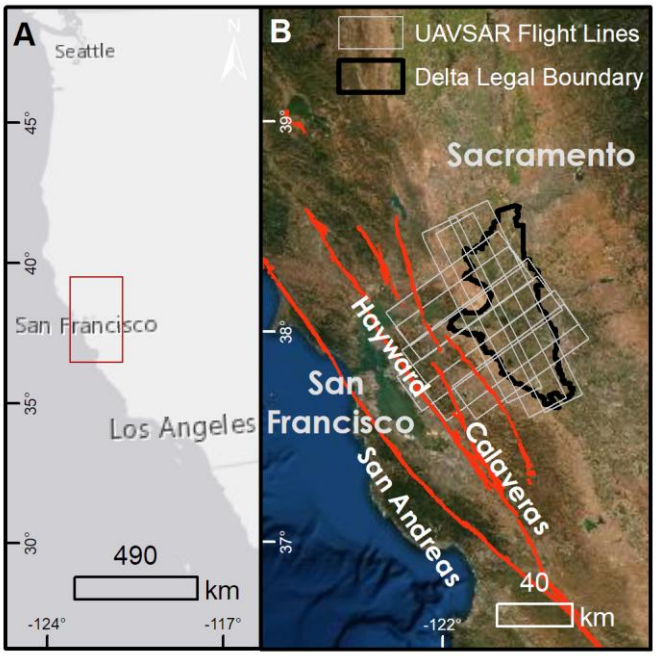

Figure 1: Overview of study area. The Sacramento-San Joaquin Delta is located in northern CA near many major faults (red lines). The coverage by UAVSAR is shown by the nine flight lines (grey polygons). In this study the SAR data are cropped to the legal delta boundary (black polygon) for overlap with the lidar surveys.

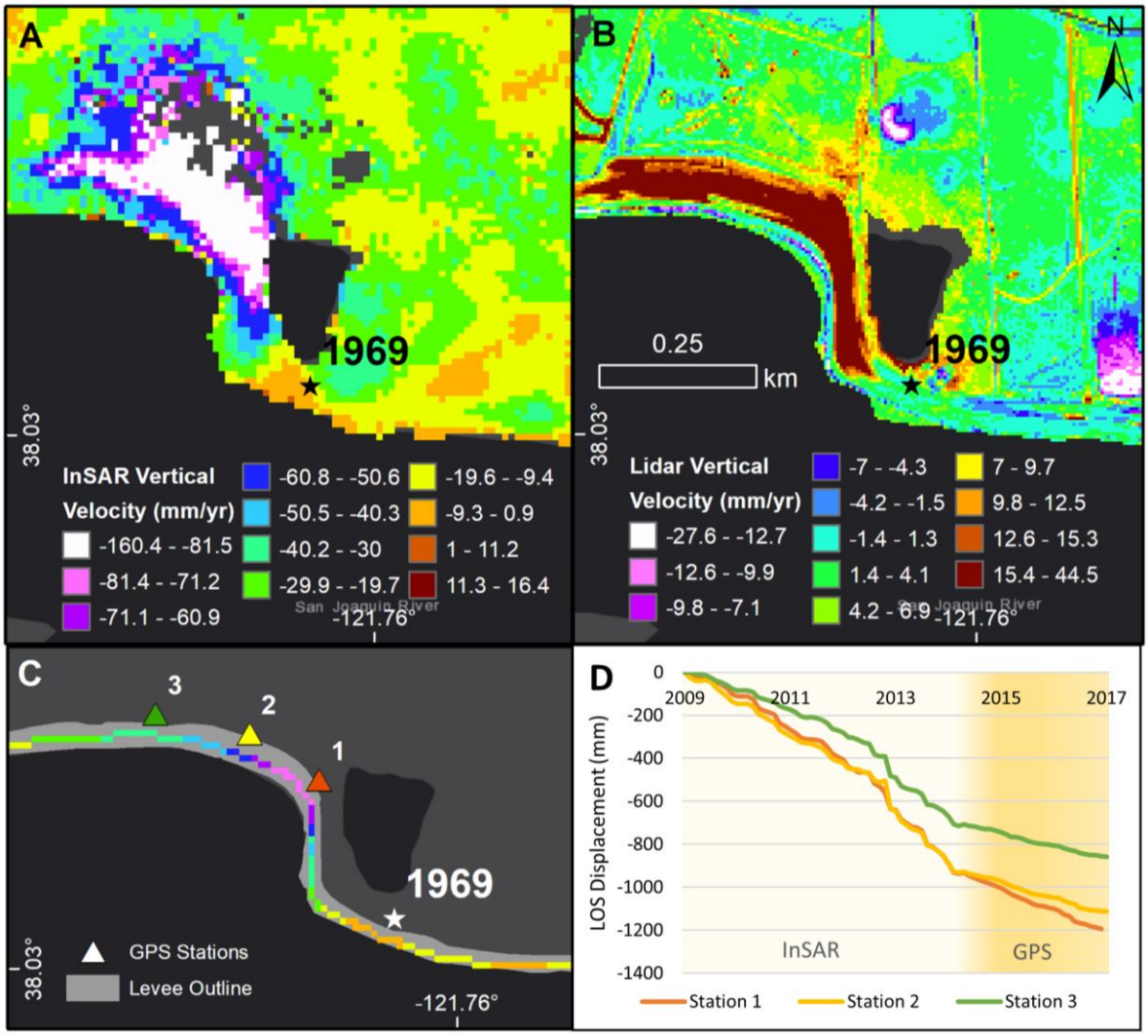

Figure 2: Levee subsidence on Sherman Island. (A) Vertical velocity map for southwestern levee section showing the greatest subsidence in the Delta, and a stable 1969 levee break. **(B)** Lidar vertical velocity for the same section showing large elevation gain. **(C)** Smoothed results of panel a showing levee outline (grey) that the moving window was applied to, and the three GPS stations (colored triangles). **(D)** LOS displacement from InSAR time series product for the GPS station locations for 2009-2015 and GPS time series for the three stations converted to LOS displacement for 2015-2017.

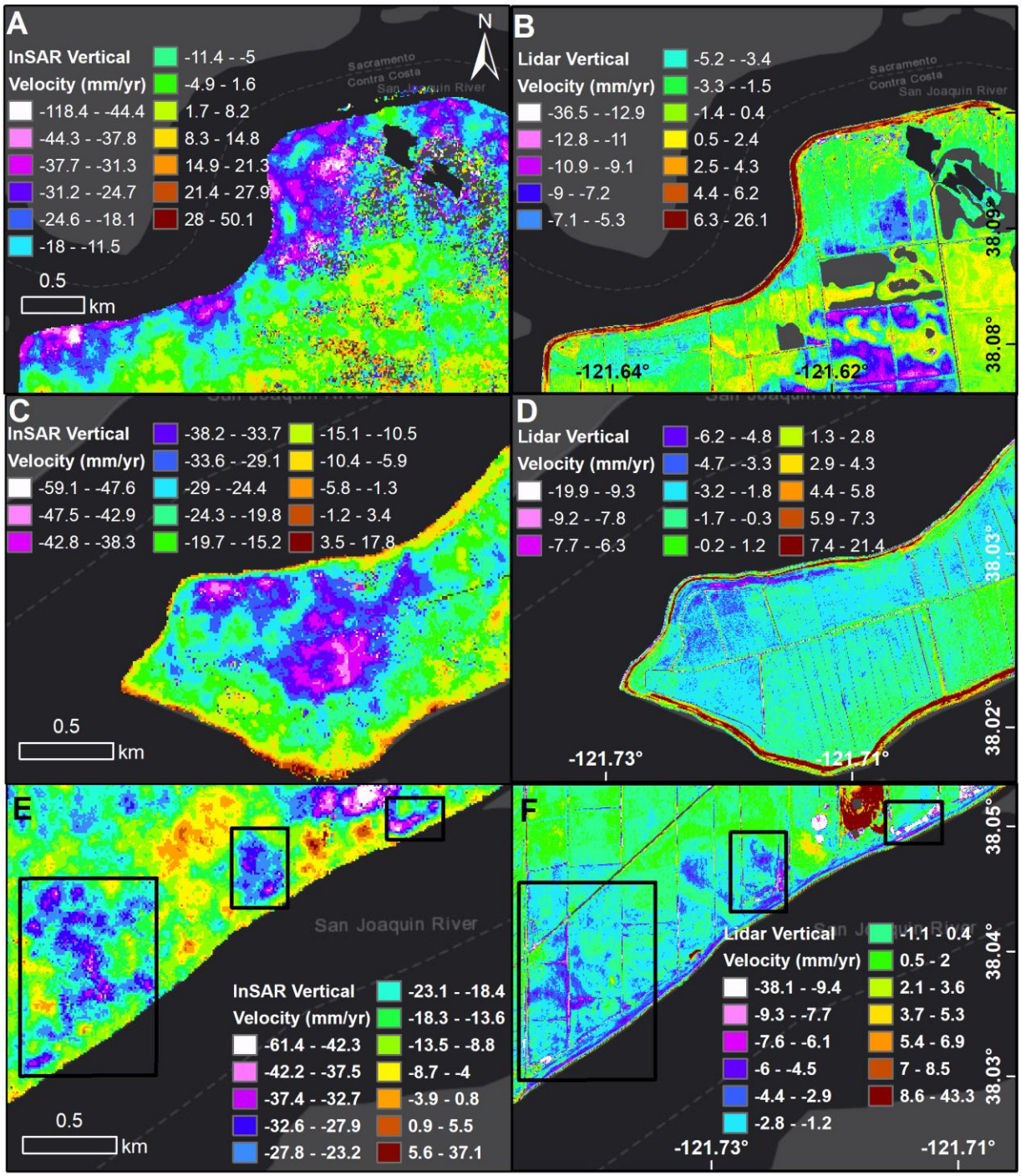

Figure 3: Levee subsidence on other islands. (A) Vertical velocity map showing subsidence along northern section of Webb Tract. **(B)** Lidar vertical velocity of same section of Webb Tract. **(C)** Vertical velocity map showing subsidence on Jersey Island. **(D)** Lidar vertical velocity of same area on Jersey Island. **(E)** Vertical velocity map of three large subsidence features along south section of Sherman Island. **(F)** Lidar vertical velocity of same area on Sherman Island.

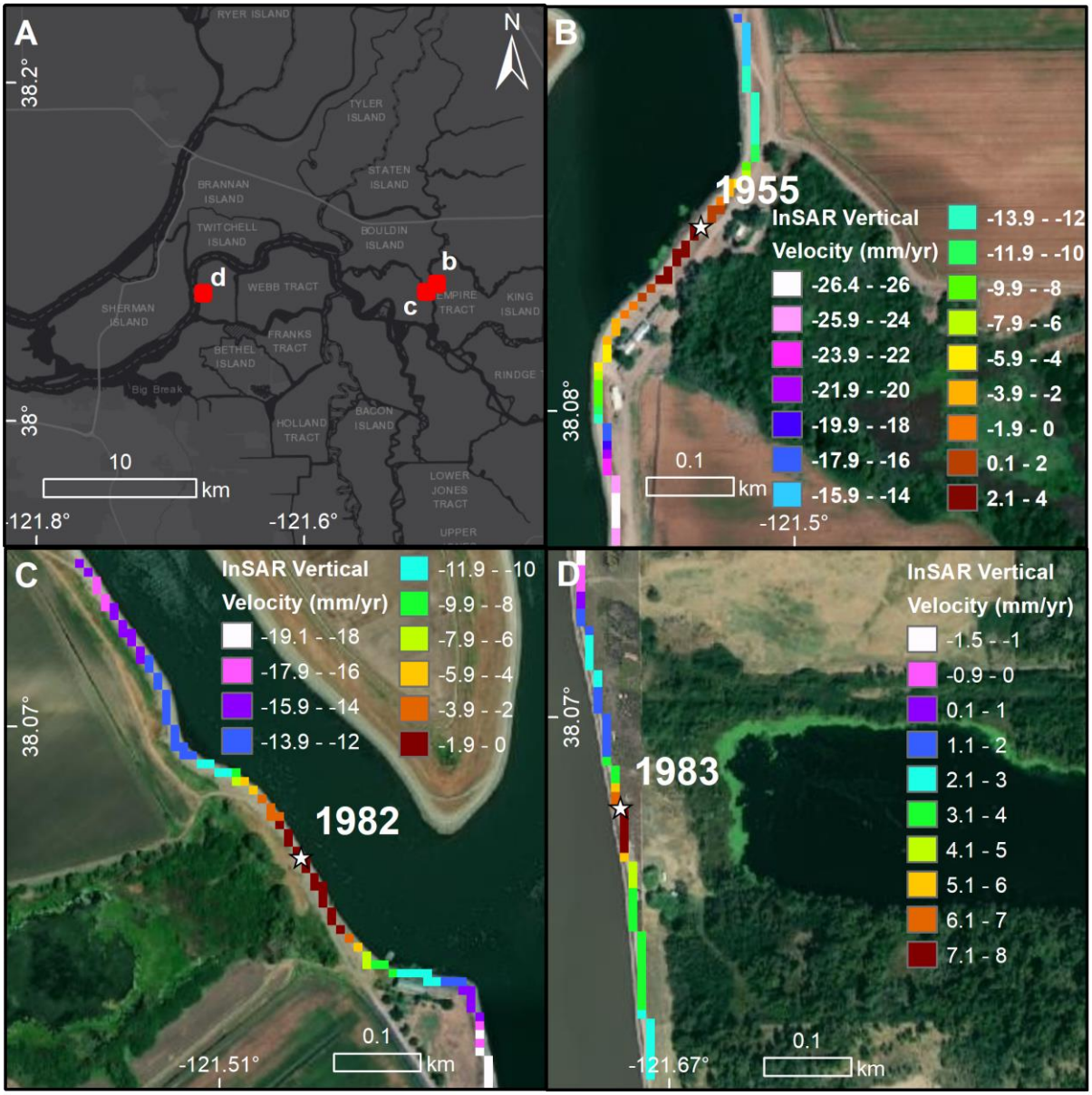

Figure 4: Historic levee breaks. (A) Overview of central Sacramento-San Joaquin Delta islands. **(B)** Vertical velocity map showing stable conditions at a 1955 break on Empire Tract. **(C)** Vertical velocity map showing stable conditions at a 1982 break on Venice Island. **(D)** Vertical velocity map showing stable conditions at a 1983 break on Bradford Island.

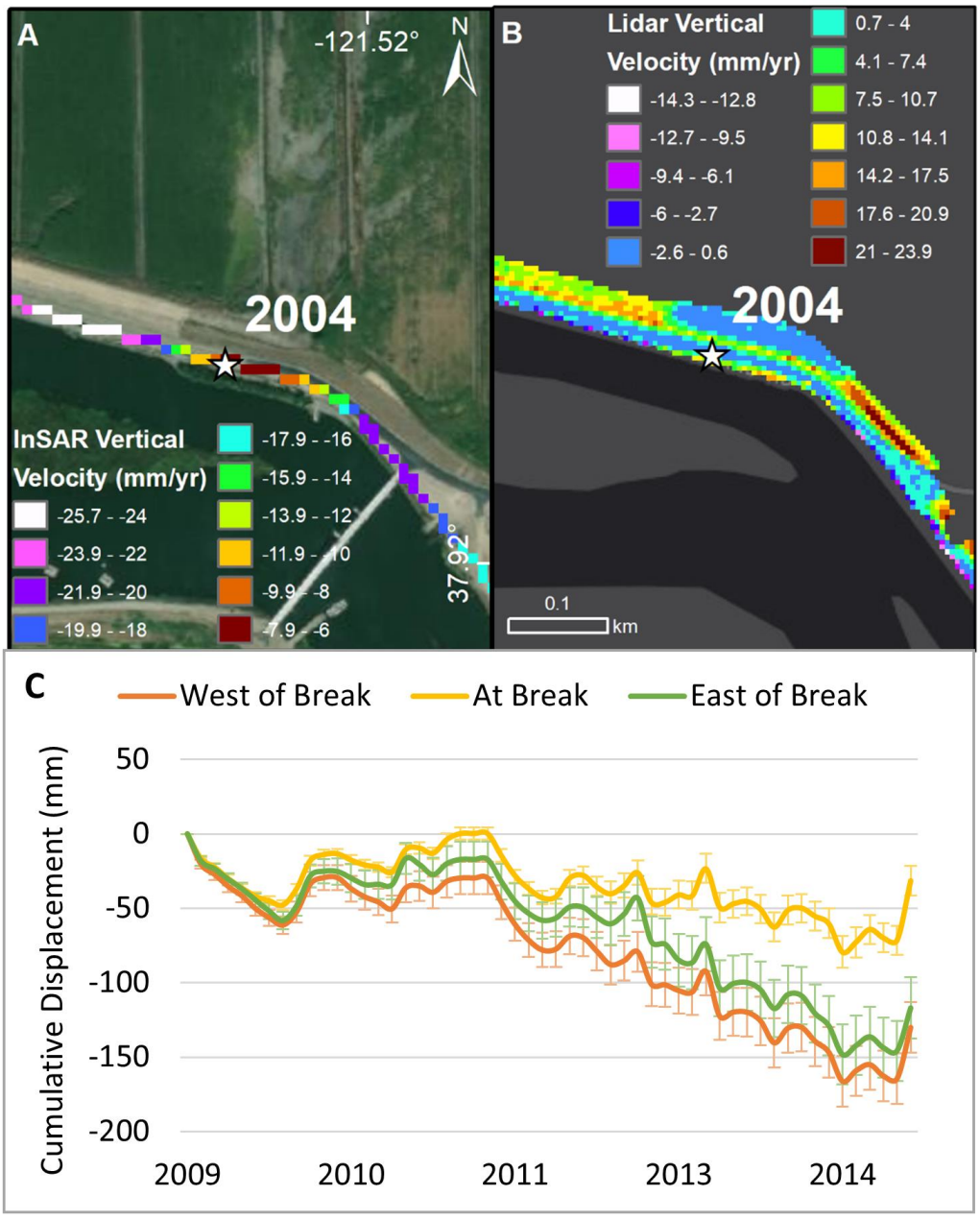

Figure 5: Most recent Delta levee break. (A) Vertical velocity map showing stable conditions at 2004 levee break on Jones Tract with flood scar inland. **(B)** Lidar vertical velocity showing high elevation gain on either side of break site. **(C)** LOS displacement from InSAR time series product for pixels to the west, east, and at the break site from 2009-2015.

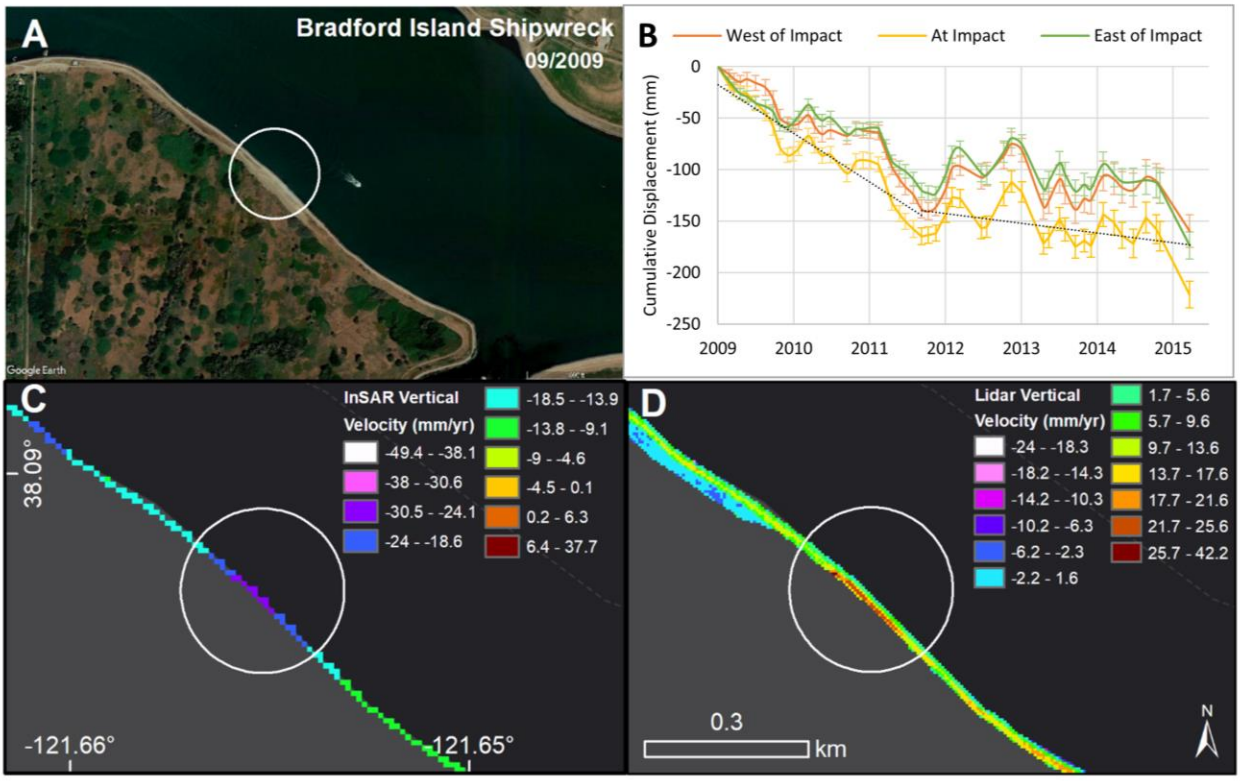

Figure 6: Recent levee impact. (A) Google Earth image of Bradford Island one month after shipwreck impact (circled). **(B)** LOS displacement from InSAR time series product for pixels to the west, east, and at the impact site from 2009-2015. **(C)** Vertical velocity map showing high subsidence values at the impact site. **(D)** Lidar vertical velocity showing high elevation gain at the impact site.

Supplementary Figures

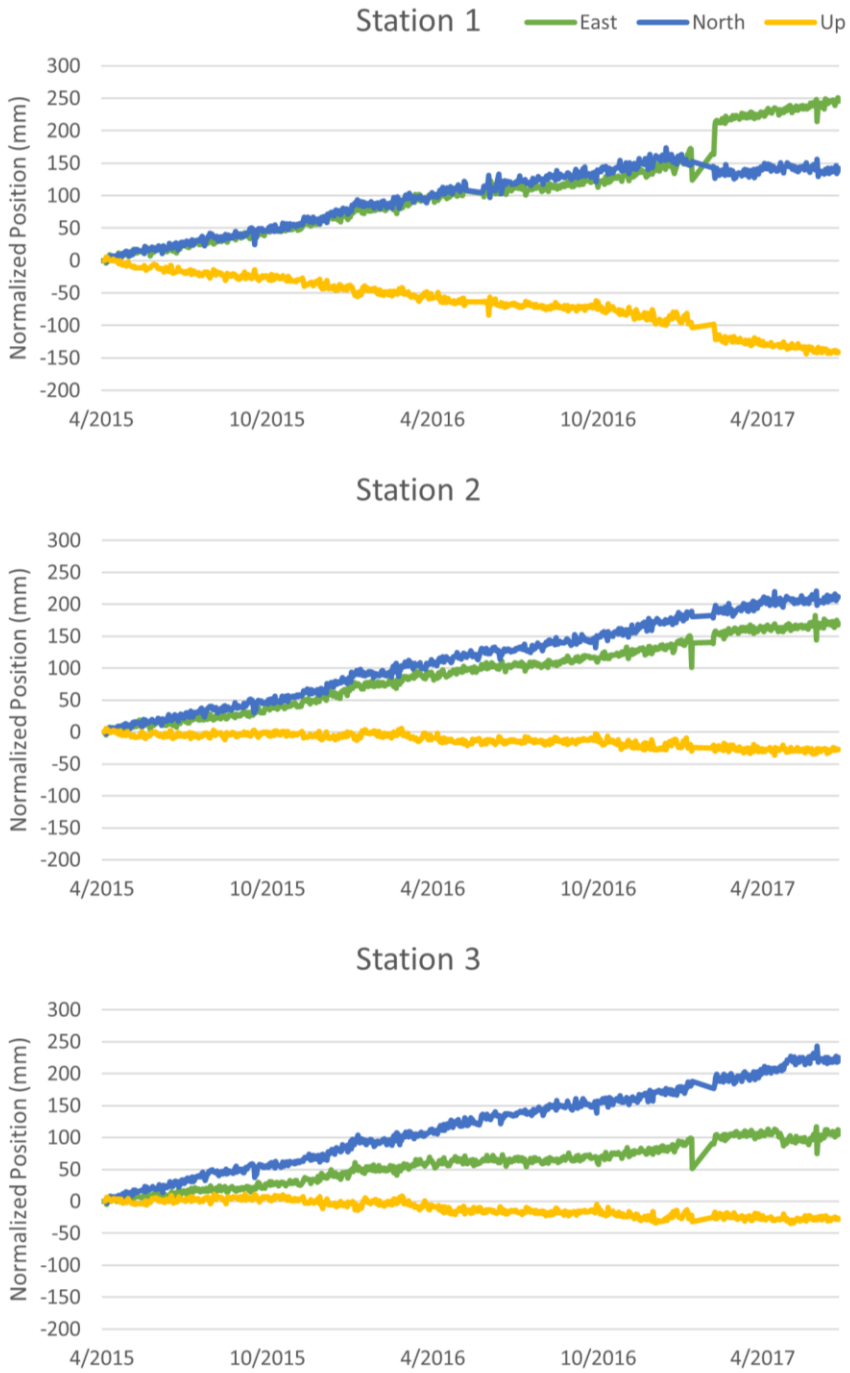

Figure S1: Original GPS time series. Raw time series (including data jumps) for the Sherman test site stations (locations shown in Fig. 2C). Positional change is normalized to the first data entry for visualization.

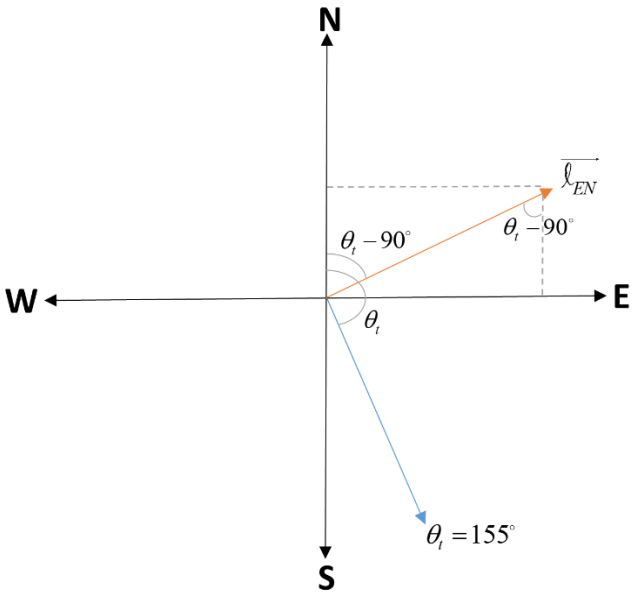

$$\begin{aligned} \ell_E &= \ell_{EN} \sin(\theta_t - 90^\circ) \\ \ell_N &= \ell_{EN} \cos(\theta_t - 90^\circ) \end{aligned} \tag{1}$$

$$\hat{\ell} = \frac{\vec{\ell}}{\ell}$$

$$\begin{aligned} \hat{\ell} &= -\cos\theta_i \hat{U} + \sin\theta_i \cos(\theta_t - 90^\circ)\hat{N} + \sin\theta_i \sin(\theta_t - 90^\circ)\hat{E} \\ \vec{\ell} &= -\ell \cos\theta_i \hat{U} + \ell \sin\theta_i \cos(\theta_t - 90^\circ)\hat{N} + \ell \sin\theta_i \sin(\theta_t - 90^\circ)\hat{E} \end{aligned} \tag{2}$$

$$\begin{aligned} \vec{d}_{GPS} &= d_U \hat{U} + d_N \hat{N} + d_E \hat{E} \\ \vec{d} \cdot \hat{\ell} &= -[d_U(-\cos\theta_i) + d_N \sin\theta_i \cos(\theta_t - 90^\circ) + d_E \sin\theta_i \sin(\theta_t - 90^\circ)] \end{aligned} \tag{3}$$

Figure S2: GPS-LOS conversion. A schematic of the projected east-north component for UAVSAR flight line 15502 where θ_t is the track angle from north and $\overrightarrow{\ell_{EN}}$ is the east-north vector. Eq. 1 shows the individual east and north components in terms of the east-north vector and the track angle. Eq. 2 solves for the unit vector $\hat{\ell}$ by dividing the vector $\vec{\ell}$ by its length ℓ. The unit vector is shown in terms of its east, north, and up vectors where θ_i is the incidence angle. Eq. 3 shows the GPS displacement vector in terms of its east, north, and up components. The dot product between this displacement vector and the unit vector is solved to convert the GPS positions to the UAVSAR line-of-sight displacements. A final negative is taken of this equation because the GIAnT program assigns the look direction as positive looking up from the target. The converted LOS values are shown in Fig. 2E.

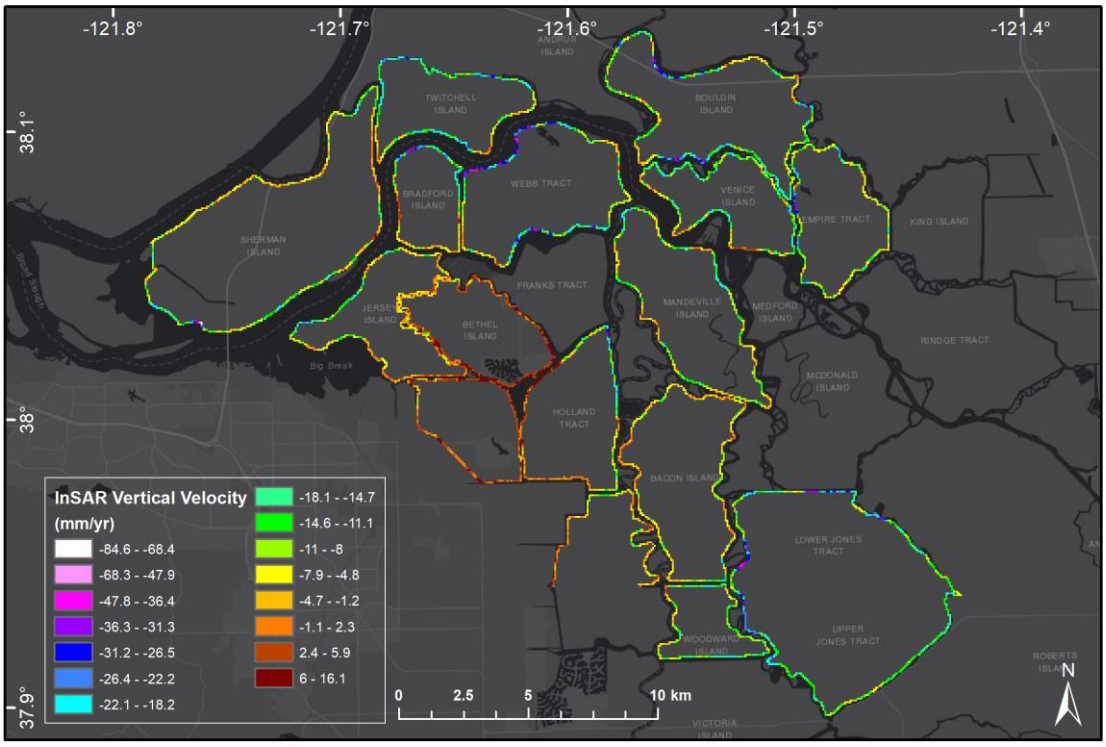

Figure S3: Overview vertical velocity map. Vertical velocity for the central and western Delta islands where blue and purple denote subsidence and orange and red areas show more stable or uplift areas. Pixel size is enlarged to 70 m for better visibility.

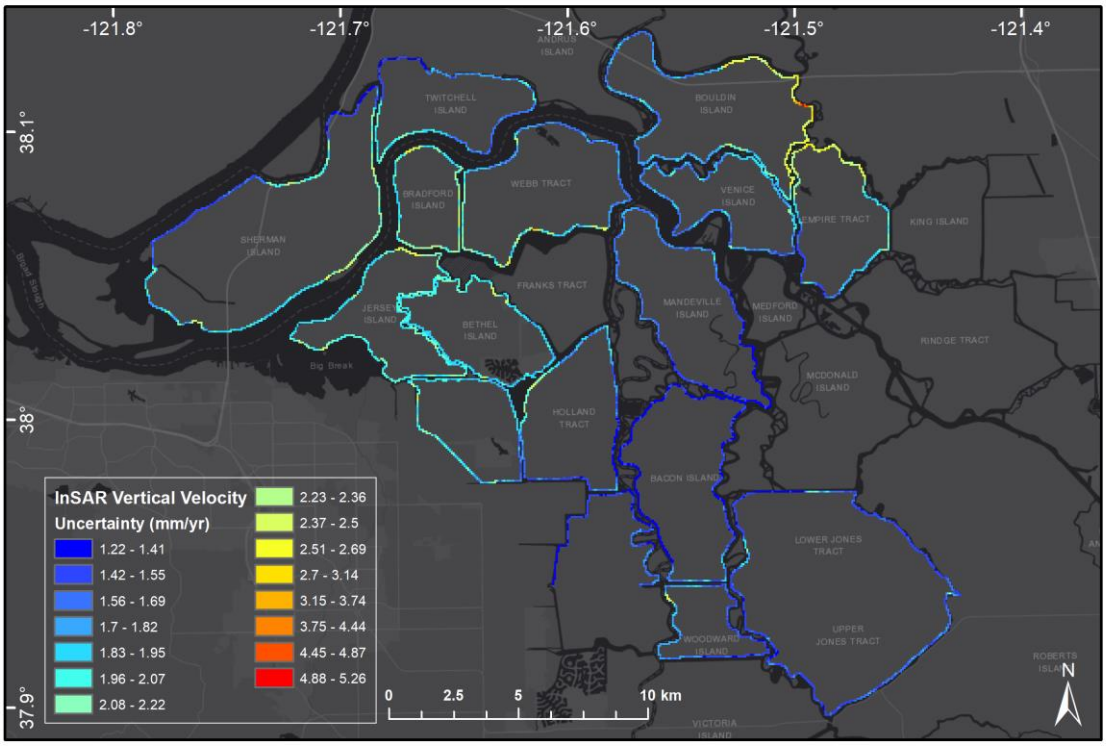

Figure S4: Overview uncertainty map. Vertical velocity uncertainty values for the central and western Delta islands where blue and purple denote lower uncertainty and orange and red areas show more uncertainty. Pixel size is enlarged to 70 m for better visibility.

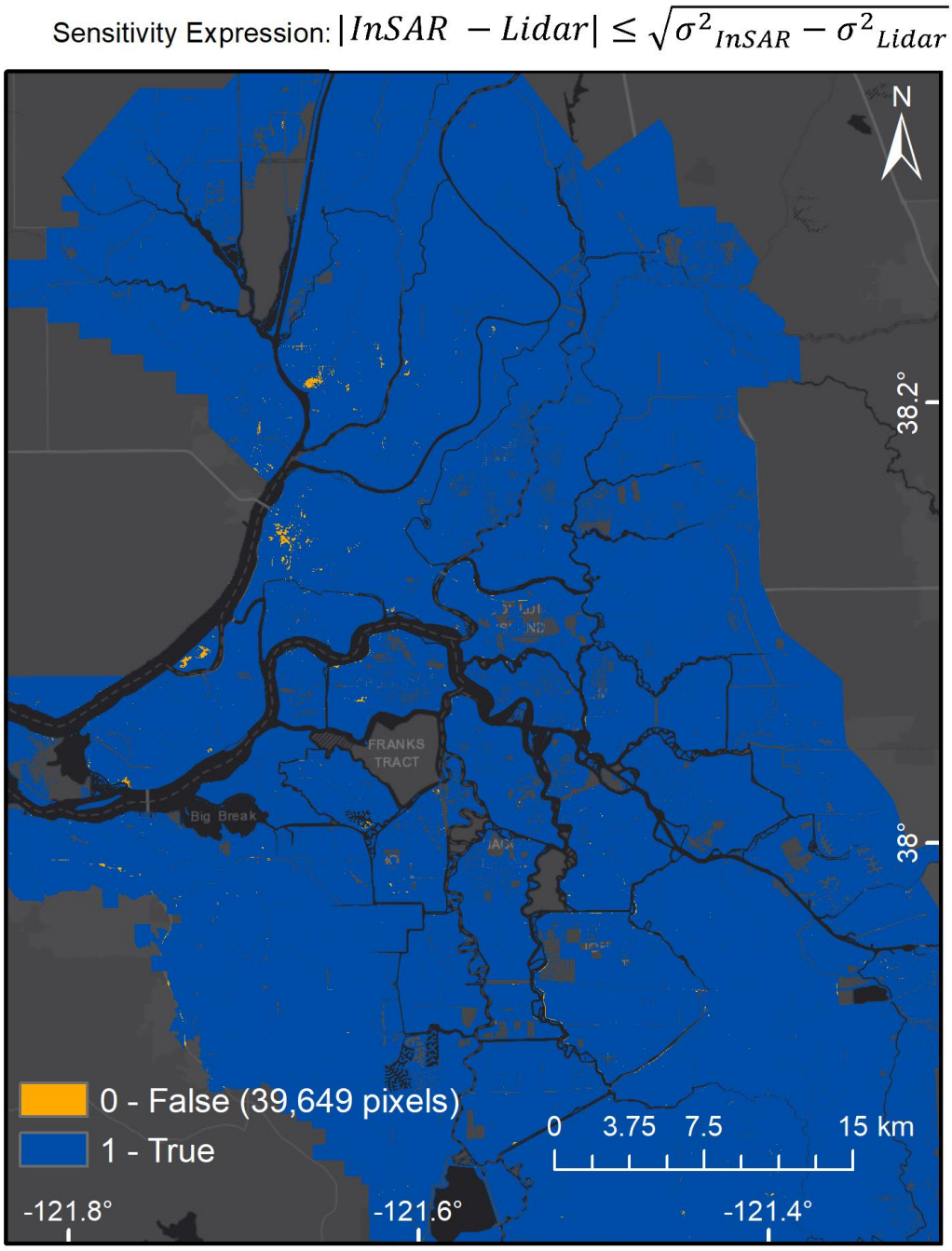

Figure S5: Sensitivity analysis. The sensitivity between the InSAR and lidar datasets was calculated using the above expression, where σ_{InSAR} is the 1-sigma uncertainty calculated for the InSAR vertical velocity rates (see Bekaert et al., 2019) and σ_{LiDAR} is 10.7 mm/yr, which is the 1-sigma uncertainty as calculated from the 95% confidence level values for vertical accuracy reported from the lidar datasets. Orange pixels show areas where the difference between InSAR and lidar is not within uncertainty bounds, and blue pixels show areas where the datasets are within each other's 1-sigma uncertainty bounds.

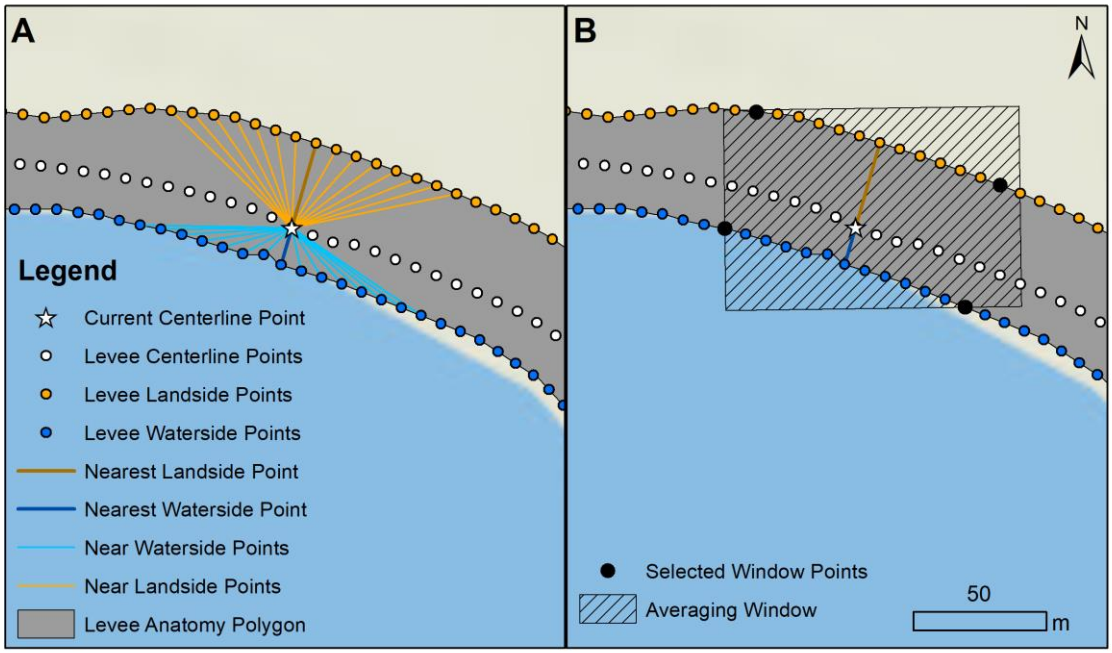

Figure S6: Levee oriented moving window average. (A) An example levee section on southwest Sherman Island showing the levee centerline (white), landside (orange), and waterside (blue) points generated from the levee anatomy polygon (grey). While working on the current centerline point (white star), the nearest landside and waterside points are located. (B) Counting six points away on both sides from the nearest landside and waterside points, the window border points of the averaging window are chosen (black). Based on these window points, a best-fit averaging window is generated.

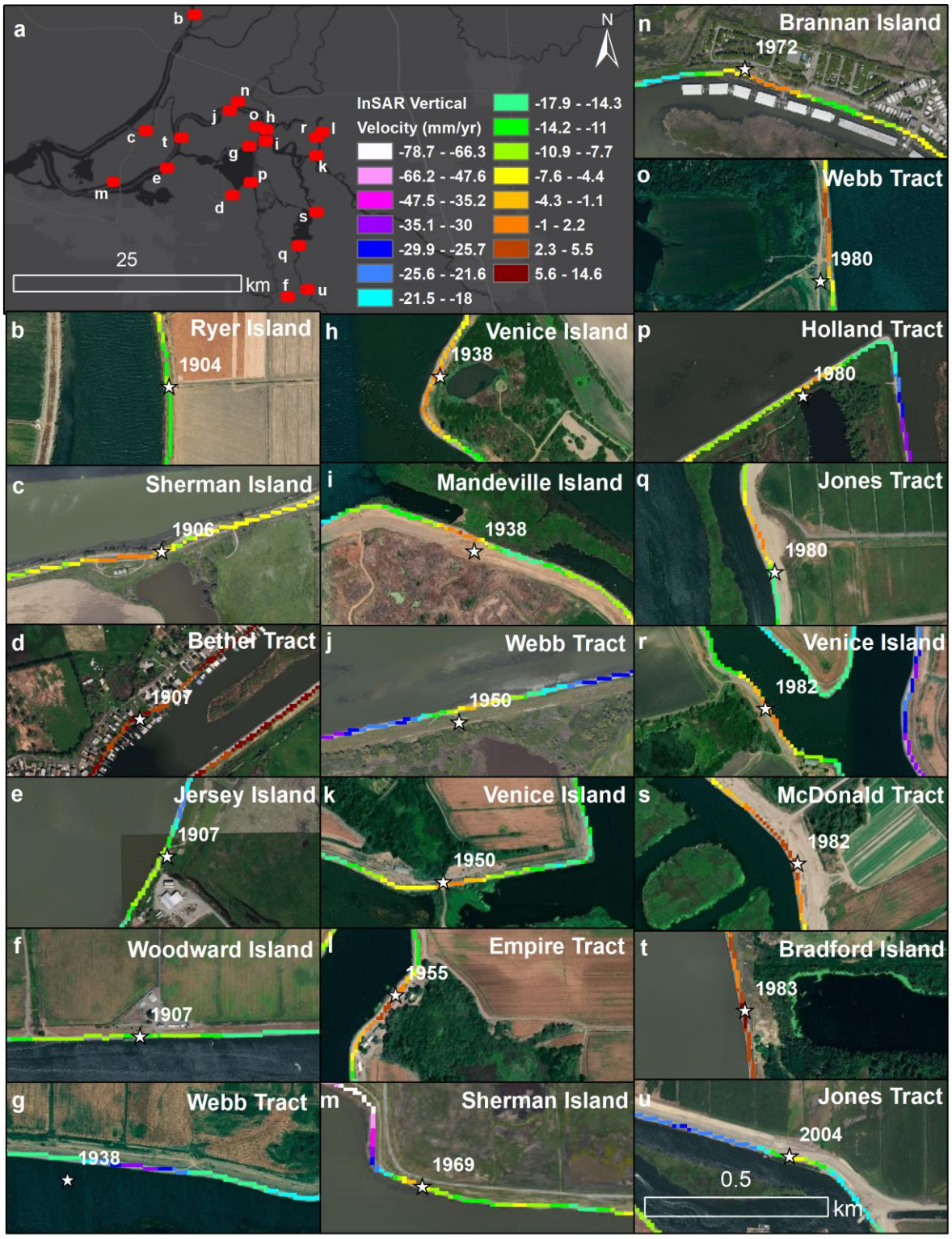

Figure S7: More historic levee breaks. (a) Overview of the Sacramento-San Joaquin Delta with locations of all levee breaks (red). (b-u) Vertical velocities showing more stable conditions at historic levee break throughout the Delta.

References

Aagaard, B. T., Blair, J. L., Boatwright, J., Garcia, S. H., Harris, R. A., Michael, A. J., et al. (2016). Earthquake outlook for the San Francisco Bay region 2014–2043 (Tech. Rep.). doi: 10.3133/fs20163020

Agram, P., Jolivet, R., Riel, B., Lin, Y., Simons, M., Hetland, E., et al. (2013). New radar interferometric time series analysis toolbox released. *Eos, Transactions American Geophysical Union*, 94(7), 69–70. doi: 10.1002/2013EO070001

Amelung, F., Galloway, D. L., Bell, J. W., Zebker, H. A., & Laczniak, R. J. (1999). Sensing the ups and downs of Las Vegas: InSAR reveals structural control of land subsidence and aquifer-system deformation. *Geology*, 27(6), 483–486. doi: 10.1130/0091-7613(1999)027<0483:STUADO>2.3.CO;2

American Society of Civil Engineers. (2017). ASCE 2017 Infrastructure Report Card (Tech. Rep.). Retrieved from https://www.infrastructurereportcard.org/cat-item/levees/

Bates, M. E., & Lund, J. R. (2013). Delta subsidence reversal, levee failure, and aquatic habitat—a cautionary tale. *San Francisco Estuary and Watershed Science*, 11(1). doi: 10.15447/sfews.2013v11iss1art1

Bekaert, D., Walters, R., Wright, T., Hooper, A., & Parker, D. (2015). Statistical comparison of InSAR tropospheric correction techniques. *Remote Sensing of Environment*, 170, 40–47. doi:

10.1016/j.rse.2015.08.035

Bekaert, D. P., Jones, C. E., An, K., & Huang, M.-H. (2019). Exploiting UAVSAR for a comprehensive analysis of subsidence in the Sacramento Delta. *Remote Sensing of Environment*, 220, 124–134. doi: 10.1016/j.rse.2018.10.023

Berardino, P., Fornaro, G., Lanari, R., & Sansosti, E. (2002). A new algorithm for surface deformation monitoring based on small baseline differential SAR interferograms. *IEEE Transactions on Geoscience and Remote Sensing*, 40(11), 2375–2383. doi: 10.1109/TGRS.2002.803792

Blewitt, G., Kreemer, C., Hammond, W. C., & Goldfarb, J. M. (2013). Terrestrial reference frame NA12 for crustal deformation studies in North America. *Journal of Geodynamics*, 72, 11–24. doi: 10.1016/j.jog.2013.08.004

Boryan, C., Yang, Z., Mueller, R., & Craig, M. (2011). Monitoring U.S. agriculture: the U.S. department of agriculture, national agricultural statistics service, cropland data layer program. *Geocarto International*, 26(5), 341–358. doi: 10.1080/10106049.2011.562309

Broadbent, F. E., et al. (1960). Factors influencing the decomposition of organic soils of the California delta. *Hilgardia*, 29, 587–612. doi: 10.3733/hilg.v29n13p587

Brooks, B. A, Bawden, G., Manjunath, D., Werner, C., Knowles, N., Foster, J., et al. (2012).

Contemporaneous Subsidence and Levee Overtopping Potential, Sacramento-San Joaquin Delta, California. San Francisco Estuary and Watershed Science, 10(1). Retrieved from https://escholarship.org/uc/item/15g1b9tm

Buchanan, M. K., Kopp, R. E., Oppenheimer, M., & Tebaldi, C. (2016). Allowances for evolving coastal flood risk under uncertain local sea-level rise. *Climatic Change*, 137(3-4), 347–362. doi: 10.1007/s10584-016-1664-7

CalFed Bay-Delta Program (1999). Ecosystem Restoration Program Plan Vol. 1 - Ecological Attributes of the San Francisco Bay-Delta Watershed. Programmatic EIS/EIR Technical Appendix. California Agencies. 345. Retrieved from https://digitalcommons.law.ggu.edu/caldocs_agencies/345

California Department of Water Resources, Delta-Suisun Marsh office (2007). 2007 Sacramento San Joaquin Delta LiDAR Acquisition. Retrieved from http://gisarchive.cnra.ca.gov/iso/ImageryBaseMapsLandCover/LIDAR/DeltaLIDAR2007/

California Department of Water Resources, Delta-Suisun Marsh office (2017). 2017 Sacramento San Joaquin Delta LiDAR Acquisition. Retrieved from http://gisarchive.cnra.ca.gov/iso/ImageryBaseMapsLandCover/LIDAR/DeltaLIDAR2017/

Chase, A. F., Chase, D. Z., Fisher, C. T., Leisz, S. J., & Weishampel, J. F. (2012). Geospatial revolution and remote sensing LiDAR in Mesoamerican archaeology. *Proceedings of the*

National Academy of Sciences, 109(32), 12916–12921. doi: 10.1073/pnas.1205198109

Chaussard, E., Wdowinski, S., Cabral-Cano, E., & Amelung, F. (2014). Land subsidence in central Mexico detected by ALOS InSAR time-series. *Remote Sensing of Environment*, 140, 94–106. doi: 10.1016/j.rse.2013.08.038

Deverel, S. J., Bachand, S., Brandenberg, S. J., Jones, C. E., Stewart, J. P., & Zimmaro, P. (2016). Factors and processes affecting delta levee system vulnerability. *San Francisco Estuary and Watershed Science*, 14(4). doi: 10.15447/sfews.2016v14iss4art3

Deverel, S. J., Ingrum, T., & Leighton, D. (2016). Present-day oxidative subsidence of organic soils and mitigation in the Sacramento-San Joaquin Delta, California, USA. *Hydrogeology Journal*, 24(3), 569–586. doi: 10.1007/s10040-016-1391-1

Dixon, T. H., Amelung, F., Ferretti, A., Novali, F., Rocca, F., Dokka, R., et al. (2006). Subsidence and flooding in New Orleans. *Nature*, 441(7093), 587. doi: 10.1038/441587a

Doin, M.-P., Lasserre, C., Peltzer, G., Cavali´e, O., & Doubre, C. (2009). Corrections of stratified tropospheric delays in SAR interferometry: Validation with global atmospheric models. *Journal of Applied Geophysics*, 69(1), 35–50. doi: 10.1016/j.jappgeo.2009.03.010

Dubayah, R. O., & Drake, J. B. (2000). Lidar remote sensing for forestry. *Journal of Forestry*, 98(6), 44–46. doi: 10.1093/jof/98.6.44

Fore, A. G., Chapman, B. D., Hawkins, B. P., Hensley, S., Jones, C. E., Michel, T. R., & Muellerschoen, R. J. (2015). UAVSAR polarimetric calibration. *IEEE Transactions on Geoscience and Remote Sensing*, 53(6), 3481–3491. doi: 10.1109/TGRS.2014.2377637

Global Construction Review (2016, September). Ho Chi Minh City to spend $4.4bn to keep its head above water. Retrieved from http://www.globalconstructionreview.com/news/ho-chi-minh-city-spend-44bn-keep-i7ts-he7ad-abo7ve/

Hanssen, R. F. (2001). Radar interferometry: data interpretation and error analysis (Vol. 2). *Springer Science and Business Media*. doi: 10.1007/0-306-47633-9

Hooper, A., Zebker, H., Segall, P., & Kampes, B. (2004). A new method for measuring deformation on volcanoes and other natural terrains using InSAR persistent scatterers. *Geophysical Research Letters*, 31(23). doi: 10.1029/2004GL021737

Ingebritsen, S., Ikehara, M., Galloway, D., & Jones, D. (2000). Delta subsidence in California: the sinking heart of the state (Tech. Rep.). Retrieved from https://pubs.usgs.gov/fs/2000/fs00500/

Jaboyedoff, M., Oppikofer, T., Abellaacute;n, A., Derron, M.-H., Loye, A., Metzger, R., & Pedrazzini, A. (2012). Use of LIDAR in landslide investigations: a review. *Natural Hazards*, 61(1), 5–28. doi: 10.1007/s11069-010-9634-2

Jones, C. E., An, K., Blom, R. G., Kent, J. D., Ivins, E. R., & Bekaert, D. (2016). Anthropogenic

and geologic influences on subsidence in the vicinity of New Orleans, Louisiana. *Journal of Geophysical Research: Solid Earth*, 121(5), 3867–3887. doi: 10.1002/2015JB012636

Jones, C. E., Dudas, J., & Bawden, G. W. (2016). Application of Remote Sensing to Assessment of Water Conveyance Infrastructure Integrity. *Applied Geology in California, Environmental Engineering Geologists*, 26, 253–271.

Kulp, S. A., & Strauss, B. H. (2019). New elevation data triple estimates of global vulnerability to sea-level rise and coastal flooding. *Nature Communications*, 10(1), 1–12. doi: 10.1038/s41467-019-12808-z

Lanari, R., Lundgren, P., Manzo, M., & Casu, F. (2004). Satellite radar interferometry time series analysis of surface deformation for Los Angeles, California. *Geophysical Research Letters*, 31(23). doi: 10.1029/2004GL021294

Lim, M. (2018, March). Seven years after tsunami, Japanese live uneasily with seawalls. Retrieved from https://www.reuters.com/article/us-japan-disaster-seawalls/seven-years-after-tsunami-japanese-live-uneasily-with-seawalls-idUSKCN1GL0DK

Lund, J. R. (2016). California's agricultural and urban water supply reliability and the Sacramento–San Joaquin Delta. *San Francisco Estuary and Watershed Science*, 14(3). doi: 10.15447/sfews.2016v14iss3art6

Luoma, S. N., Dahm, C. N., Healey, M., & Moore, J. N. (2015). Challenges facing the Sacramento–San Joaquin Delta: complex, chaotic, or simply cantankerous? *San Francisco Estuary and Watershed Science*, 13(3). doi: 10.15447/sfews.2015v13iss3art7

Markus, T., Neumann, T., Martino, A., Abdalati, W., Brunt, K., Csatho, B., et al. (2017). The Ice, Cloud, and land Elevation Satellite-2 (ICESat 2): science requirements, concept, and implementation. *Remote Sensing of Environment*, 190, 260–273. doi: 10.1016/j.rse.2016.12.029

McGranahan, G., Balk, D., & Anderson, B. (2007). The rising tide: Assessing the risks of climate change and human settlements in low elevation coastal zones. *Environment and Urbanization*, 19(1), 17–37. doi: 10.1177/0956247807076960

National Academies of Sciences, E., & Medicine. (2018). Thriving on our changing planet: A decadal strategy for earth observation from space. Washington, DC: The National Academies Press. Retrieved from https://www.nap.edu/catalog/24938/thriving-on-our-changing-planet-a-decadal-strategy-for-earth. doi: 10.17226/24938

Özer, I. E., van Leijen, F. J., Jonkman, S. N., & Hanssen, R. F. (2019). Applicability of satellite radar imaging to monitor the conditions of levees. *Journal of Flood Risk Management*, 12(S2), e12509. doi: 10.1111/jfr3.12509

Prokopovich, N. P. (1985). Subsidence of peat in California and Florida. *Bulletin of the Association of Engineering Geologists*, 22(4), 395–420. doi: 10.2113/gseegeosci.xxii.4.395

Reinert, E., Stewart, J. P., Moss, R. E., & Brandenberg, S. J. (2014). Dynamic response of a model levee on Sherman Island peat: A curated data set. *Earthquake Spectra*, 30(2), 639–656. doi: 10.1193/101913EQS274M

Rojstaczer, S., & Deverel, S. J. (1993). Time dependence in atmospheric carbon inputs from drainage of organic soils. *Geophysical Research Letters*, 20(13), 1383–1386. doi: 10.1029/93GL01339

Rosen, P., Hensley, S., Shaffer, S., Edelstein, W., Kim, Y., Kumar, R., et al. (2017). The NASA-ISRO SAR (NISAR) mission dual-band radar instrument preliminary design. *2017 IEEE International Geoscience and Remote Sensing Symposium (IGARSS)*, 3832–3835. doi: 10.1109/IGARSS.2017.8127836

Schmidt, C. W. (2015). Delta subsidence: An imminent threat to coastal populations. *Environmental Health Perspectives*, 123, 204–209. doi: 10.1289/ehp.123-A204

Sehat, S., Vahedifard, F., Aanstoos, J. V., Dabbiru, L., Hasan, K., & Mooney, M. A. (2014). Analysis of the Output from a Radar-Based Levee-Monitoring System Using In Situ Soil Data. *In Geo-congress 2014: Geo-characterization and Modeling for Sustainability* (pp. 943–952). doi: 10.1061/9780784413272.092

Service, R. F. (2007). Environmental restoration. Delta blues, California style. *Science*, 317(5837), 442. doi: 10.1126/science.317.5837.442

Syvitski, J. P., Kettner, A. J., Overeem, I., Hutton, E. W., Hannon, M. T., Brakenridge, G. R., et al. (2009). Sinking deltas due to human activities. *Nature Geoscience*, 2(10), 681. doi: 10.1038/ngeo629

Tebaldi, C., Strauss, B. H., & Zervas, C. E. (2012). Modelling sea level rise impacts on storm surges along US coasts. *Environmental Research Letters*, 7(1), 014032. doi: 10.1088/1748-9326/7/1/014032

Tessler, Z., Vörösmarty, C. J., Grossberg, M., Gladkova, I., Aizenman, H., Syvitski, J., & Foufoula-Georgiou, E. (2015). Profiling risk and sustainability in coastal deltas of the world. *Science*, 349(6248), 638–643. doi: 10.1126/science.aab3574

USACE. (n.d.). National Levee Safety - Levee Situation in the U.S. (Tech. Rep.). Retrieved from https://www.usace.army.mil/National-Levee-Safety/About-Levees/Levee-Situation-in-the-US/

Weir, W. W. (1950). Subsidence of peat lands of the Sacramento-San Joaquin delta, California. *Hilgardia*, 20, 37–56. doi:10.3733/hilg.v20n03p037

The World Bank (2017, September). Project Highlights: Metro Manila Flood Management. Retrieved from https://www.worldbank.org/en/country/philippines/brief/project-highlights-metro-manila-flood-management

Wuebbles, D. J., Fahey, D. W., & Hibbard, K. A. (2017). USGCRP, 2017: Climate Science

Special Report: Fourth National Climate Assessment, Volume I (Vol. 1; Tech. Rep.). Retrieved from https://science2017.globalchange.gov/

Younes, S. A.-M. (2016). Modeling investigation of wet tropospheric delay error and precipitable water vapor content in Egypt. *The Egyptian Journal of Remote Sensing and Space Science*, 19(2), 333–342. doi: 10.1016/j.ejrs.2016.05.002

Zebker, H. A., & Villasenor, J. (1992). Decorrelation in interferometric radar echoes. *IEEE Transactions on Geoscience and Remote Sensing*, 30(5), 950–959. doi: 10.1109/36.175330

CHAPTER THREE

Current-day subsidence within the Sacramento-San Joaquin Delta and its relationship to elevation, soil organic matter and land use practices

Abstract

The Sacramento-San Joaquin Delta is a complex landscape that lies at the confluence of active fault zones, frequent flooding, and critical conveyances. The Delta helps supply part of the water supply for 25 million California residents and contributes billions of dollars to the state's economy from agriculture. However, historical drainage of the land for farming has caused continued subsidence of the Delta islands, and threatens the fragile levee system that protects the region from flooding. For such a study area where field surveys are costly and inefficient, we propose the use of remote sensing technologies using UAVSAR, an airborne radar, to monitor subsidence in the Delta, compared with auxiliary GIS datasets. Over the Delta legal boundary, the high-resolution interferometry map shows a constant value of -1.14 ± 0.23 cm/yr of subsidence for 2009 to 2015, which agrees well with past field studies. What the field studies lack, however, is a continuous map of subsidence across all islands that displays the local-scale complexities for each island. The subsidence map is compared to lidar elevation surveys collected in 2007 and 2017, which lack the continual measurements that the UAVSAR dataset possesses to capture the dynamics of ongoing subsidence across much of the same period. Traditional use of lidar elevation maps are insufficient to monitor dynamic areas such as the Delta, especially with decadal surveys. The elevation change map is used to examine the relationship between subsidence and island characteristics (elevation, soil organic matter, and land cover/land use), analyzed at varying spatial scales. Areas of low elevation generally exhibit more subsidence, as historically observed, but this phenomenon varies across islands and is not

seen in all parts of the Delta. Several islands contained subsidence features which aligned with more organic soils, but most did not. A possible explanation explored herein is the large influence of changing agricultural conditions seen by prominent features in the InSAR map which follow field boundaries. Such comparisons indicate the importance of local-scale studies in the Delta to understand the unique conditions contributing to subsidence on each island.

Introduction

In 1991, the National Research Council estimated that the U.S. annual cost for subsidence related damage and flooding was over $125 million (Galloway et al., 1999). The most common cause of land subsidence is due to aquifer compaction from over-drafting (Ingebritsen et al., 2000). A well-known example of this is seen in the San Joaquin Valley, California where the land surface has sunk up to 9 m in some areas. Other well-known cases of subsidence include aquifer compaction in Mexico City with up to 2 feet of subsidence per year, agricultural drainage in the western Netherlands, and collapse features on the Yucatan Peninsula from rainwater infiltration (Galloway et al., 1999). This is concerning for water resource management since groundwater, which is stored in these aquifers, is being extracted at much faster rates than it is naturally replenished. Furthermore, the size of the aquifer, in terms of how much water volume it can hold, is also decreased due to compaction (Ingebritsen et al., 2000). Other causes of subsidence include mining activities, soil drainage, soil compaction, and soil dissolution (National Research Council, 1991). Land subsidence has been observed in many agricultural and industrial sites around the world (Galloway et al., 2011; Chaussard et al., 2013; Faunt et al., 2016). In drained soils that are primarily composed of organic carbon, subsidence occurs due to the microbial activity of decomposing carbon to carbon dioxide and water (Ingebritsen et al., 2000). In the Sacramento-San Joaquin Delta, it is largely microbial oxidation that drives land subsidence (Deverel et al., 2016). Subsidence quantification is a necessary objective for coastal communities in deltas around the world experiencing relative sea level rise as these lands are the last barrier against flood damage.

History of the Delta

The Sacramento-San Joaquin Delta in northern California is the largest estuary in the western U.S., covering almost 3,000 km^2. The Delta was formed 10,000 years ago from sediment accumulation, which resulted in a complex wetland of about 60 low-lying islands surrounded by water channels (Luoma et al., 2015). Organic peat soils were formed from vegetation decaying over thousands of years (Ingebritsen et al., 2000). Early settlers reclaimed this freshwater marsh during the late 19th and early 20th centuries mainly for agriculture. This took the form of draining the wet soils for more ideal farming conditions, clearing wetland vegetation, and installing earthen levee structures around each island to protect from frequent flooding (Ingebritsen et al., 2000). However, over time these practices have led to land subsidence, largely agreed to be the biggest challenge facing the Delta (Luoma et al., 2015). Subsidence of these peat soils is mainly caused by aerobic microbial oxidation of soil carbon (Deverel et al., 2016). When soil conditions were waterlogged and anaerobic, organic matter accumulated faster than decomposition rates, resulting in organic peat soils. But after drainage to make the land usable for agriculture, aerobic conditions allowed for more rapid carbon loss, in the form of carbon dioxide emitted to the atmosphere (Ingebritsen et al., 2000; Deverel et al., 2014). Subsidence can also be caused by agricultural practices such as historical burning of peat, heavy weight of farming equipment, mining and groundwater withdrawals, and even rodent burrow collapsing (Bates and Lund, 2013; Jones et al., 2016).

The Delta is a complex landscape that lies at the confluence of major fault zones and critical conveyance lines (Figure 1). The almost 1,800 km of aging earthen levees in the Delta are at constant risk of failure and damage. Levee breaks have become commonplace in the last century, with about 160 breaches occurring in the 20th century (Bates and Lund, 2013). Repair

costs for these flooded islands cost between $43 and $240 million and in some cases the islands are even irreparable and must be abandoned (Bates and Lund, 2013). Levee failure is exacerbated by land subsidence, but also by droughts, floods, earthquakes, and rising sea level (Luoma et al., 2015). Threats to the infrastructure include cracking, erosion, sinkholes, seepage, and boils, which can lead to complete failure of the levee. Since the levee system is interconnected in the Delta, one breach can lead to another and greatly disrupt California's water supply if a salinity intrusion were to occur. The Delta pumps water from the northern Sacramento River to Central Valley and southern California, with about 80% of this water for farmers and the rest as part of the water supply for 25 million residents (Ingebritsen et al., 2000; Service, 2007; Luoma et al., 2015).

Today, the Delta not only acts as the hub for a portion of California's water supply, but it is also a large source of economic productivity for the state. Agriculture, being the most dominant, provides $800 million annually and 13,000 jobs within the Delta. Recreation provides $312 million and 3,000 jobs within the Delta and natural gas produces 20% of the state's electricity (Luoma et al., 2015). Outside of the Delta, these activities provide billions of dollars and tens of thousands of more jobs for the state of California. The local ecosystem also faces many challenges with the changing landscape of the Delta. To name a few, dam construction has blocked fish migration and reduced sediment transport, water diversions have resulted in fish entrainment and altered hydrology, and native species have declined from habitat reduction and competition with invasive species (Luoma et al., 2015). Fifty native species in the Delta, including the infamous Delta smelt, have been listed under state and federal endangered species acts (Luoma et al., 2015). Therefore, the management of the Delta is of key interest across environmental, socioeconomic, political, and public safety sectors.

A previous study found that most of the Delta levee system will subside below the current design thresholds in 50 to 100 years, making this a very time sensitive topic (Brooks et al., 2012). Reversal of subsidence can be facilitated by favoring land use practices that implement shallow flooding and increase sediment accumulation (Bates and Lund, 2013). This reversal also naturally occurs in such wetland environments with returning vegetation and protected marshes that allow for natural accretion to occur. (Bates and Lund, 2013). However, Bates and Lund (2013) found that even with improvements in reversal rates, a quarter of the subsiding Delta may still flood in the next 1-2 decades. In another study by Deverel et al. (2014), simulated marsh vertical accretion experiments on some Delta islands indicated that creating impounded marshes could help to restore tidal elevations in 50 to 250 years. Studies have also suggested mineral deposition to slow microbial oxidation, but such practices must be combined with continued investment in levee improvements and emergency planning (Service, 2007; Luoma et al., 2015).

Currently, this complicated system of levees is monitored by the island owners, though the CA Department of Water Resources (DWR) also tracks levee conditions since they administer state funds for repair and maintenance. The DWR relies on field surveys for this maintenance which are costly, infrequently updated, and inefficient. Remote sensing using satellite and airborne instruments of levee conditions in the Delta can offer detailed and quick data collection over the region. This is possible due to the emergence of new instruments such as NASA's Uninhabited Aerial Vehicle Synthetic Aperture Radar (UAVSAR) which possesses the high spatial resolution (1.6 meters) that is necessary for detailed levee monitoring. This would help bolster the DWR's current monitoring programs and emergency response during a major flood or earthquake event.

Radar Interferometry

Since the first instruments in the 1950s, imaging radars and the synthetic aperture radar (SAR) instruments that followed have been monitoring small and large scale surface processes on Earth and throughout our solar system with great accuracy and precision. Interferometric synthetic aperture radar (InSAR) methods involve taking the phase difference either between two SAR images from different measurement times. This can also be referred to as differential InSAR (D-InSAR) or repeat track interferometry. InSAR research allows for high resolution monitoring of surface deformation from earthquakes, glaciology, land subsidence, landslides, and other geophysical processes across large areas that are often inaccessible by field surveys. The advantages with remote sensing instruments also include having frequent and non-invasive measurements, which helps lessen the strain on resources. InSAR has also allowed for centimeter to millimeter level precision in measuring surface displacements over large temporal and spatial scales. Spaceborne SAR instruments have grown in number in recent decades, and can offer data with global coverage, independent of sun illumination and meteorological conditions. Emerging applications of InSAR also point to more direct comparisons with field datasets and informative geographic information systems (GIS) data to explain the intricate features seen in SAR datasets.

Many InSAR studies have shown their utility in measuring land subsidence in dry and urban environments (Galloway et al., 1998; Amelung et al., 1999; Chaussard, 2014). These studies have been limited in agricultural and naturally wet areas due to decorrelation for shorter radar wavelengths. However, provided high coherence, similarity between measurements, differential interferometry can measure surface displacements with millimeter scale accuracy since radar instruments employ centimeter scale wavelengths (Bamler and Hartl, 1998). Coherence limited regions would therefore be better studied using an instrument with longer

wavelength, such as L-band since it is longer than small leaves or vegetation that would cause more decorrelation in shorter wavelengths. Jones et al. (2016) and Sharma et al. (2016) were able to study these types of regions by using UAVSAR's longer wavelength (L-band) data, which is collected at short, regular intervals. Sharma et al. (2016) focused on Sherman Island in the Sacramento-San Joaquin Delta, a prominent island that helps to control the salinity gradient traveling in from the San Francisco Bay. The authors found subsidence rates of 0-5 cm/yr from 2009-2014, and found areas with higher organic soil content on Sherman Island contained higher subsidence rates, and were found to have lower elevation. This could be an indication of ongoing subsidence over longer time periods. The authors were able to make such comparisons by directly visualizing soil and elevation data next to the InSAR data, which will be demonstrated in this study for all major Delta islands.

This study provides individual island comparisons between InSAR measured subsidence, lidar elevation and elevation changes, soil organic matter, and land use practices. Disentangling the different drivers of subsidence with a GIS comparison helps to eliminate features which may not show actual subsidence, but, for example, are more related to agricultural activity. However, real subsidence features which are found can greatly affect the surrounding levee health and future of the island. If increased subsidence causes higher pumping and dewatering costs, the island may be abandoned or different crops may need to be grown. The resolution that UAVSAR offers also allows measurement of movement on the island levees themselves. These results are not included in this study, and readers are directed to the paper that focuses on Delta levee deformation (An et al., 2020, in review).

Materials and Methods

UAVSAR

UAVSAR is an airborne quad-polarized radar instrument from NASA that has been used to measure deformation from earthquakes, volcanoes, subsidence, glacier movement, etc. (Hensley et al., 2012). This instrument flies as a pod attached to a Gulfstream-III aircraft, and is an L-band (23.8 cm wavelength) airborne sensor with high signal-to-noise ratio, repeat flight track accuracy, and P and Ka-band capabilities (Hensley et al., 2011). The instrument operates at an altitude of 12.5 km, with a bandwidth of 80 MHz and a center frequency of 1.2575 GHz. The image swath is 22 km wide, and the incidence angles range from 22°−67°. The instrument spatial resolution is 0.8 m (along flight-line) by 1.7 m (along the line-of-sight (LOS)) (Bekaert et al., 2019). The benefits of radar instruments include their ability to see through smoke, haze, clouds, and that data can be collected during the day or night. This adaptability is especially relevant during disaster events that may include stormy weather inhibiting traditional visual surveys of damage. The UAVSAR system can be deployed after a disaster event to deliver pertinent information to decision makers (Hensley et al., 2012). These capabilities are relevant to disaster and damage assessment studies that can greatly affect public and private decision-making. Providing tangible and useful information to the DWR will help aid their current monitoring efforts, and the millions of residents that depend on the Delta for its protection and sustenance.

UAVSAR has been collecting data over the Delta since 2009, and its high spatial resolution makes the instrument a suitable monitoring tool for the Delta levee system. There is complete spatial coverage over the Delta legal boundary with nine flight lines, each acquiring data between 52 to 60 times from July 2009 to October 2015 for the study period. The average interval between acquisitions for each line was 42 to 45 days (for details see Bekaert et al.,

2019). Although there have been more recent data acquisitions, this data period was chosen due to sufficient data quality that allowed for a continuous time series with fewer long gaps between acquisitions.

GIS Datasets

A collection of GIS (geographic information systems) datasets was used to accompany evaluation of the UAVSAR results. These datasets can be extremely useful in understanding the drivers of subsidence, of which there are many in the Delta (Jones et al., 2016). For example, a correlation with soil type can be used to explain why certain islands exhibit patterns of subsidence or uplift, and past levee break locations can be used to highlight subsiding areas of more concern. Though such correlations require further in situ validation, GIS datasets comparison is a valuable first step in identifying unknown subsidence drivers in complicated coastal landscapes such as the Delta. The GIS datasets for the Delta that are used for comparison in this study are: elevation, percent soil organic matter, land cover, historic levee breaks, past seepage points, and levee vulnerabilities. Areas of lower elevation are expected to display higher subsidence because low elevation in the Delta is an indication of past subsidence. Similarly, more organic soil matter indicates higher compressibility of the soil, and thus, more subsidence. Areas adjacent to past or potential levee breaks also require more attention as these points are already known to be vulnerable.

Median percent soil organic matter data was provided by Deverel and Leighton (2010) and is based on the SSURGO (Soil Survey Geographic Database) from the NRCS (Natural Resources Conservation Service). Crop type information was downloaded from the NASS (National Agricultural Statistics Service) dataset from the USDA (United States Department of Agriculture) for 2015 Cropland Data Layer. This data was generated using field surveys and

satellite imagery to classify 85 categories, and also contains changes from 2009-2015 for users to track land use changes over time. The 2015 data layer is used for this study as the most recent year in the study period. Historical levee breaks and past seepage points were provided by the DWR. Zonal statistics using Esri's ArcMap were performed on the GIS datasets in this study to compare with features seen in the radar interferometry in order to display average subsidence for each class.

Lidar Surveys

Typically, laser elevation (lidar) data are used to generate high precision digital elevation models, e.g., to study forest canopy structure, archaeological sites, and landslides. Lidar is also able to measure elevation change, such as from land subsidence, but measurements are costly and thus infrequent, only measuring the net of all sources of elevation change during the interval between surveys. To measure elevation and elevation change in the Delta, the CA DWR administered decadal lidar surveys in 2007 and 2017, which are included for comparison in this study. Elevation was collected at 0.5-1-meter spacings (vertical datum NAVD88, geoid model Geoid03 Continental US). For the 2007 survey, the vertical accuracy was calculated to be 15 cm at 90% confidence and less than 18.5 cm at 95% confidence (California Department of Water Resources, 2007). For the 2017 survey, the measured vertical accuracy was 10.7 cm at 95% confidence level (California Department of Water Resources, 2017). A differential (Figure 2) was calculated between the lidar surveys as the 2017 elevation minus the 2007 elevation, and divided over 10 years.

Since there are only two data acquisitions, the differential rate should not be considered linear but rather as an indicator of average cumulative change. The lidar differential is compared with the InSAR time series cumulative displacement, which was collected over a shorter time

period, 2009-2015, but with many more frequent measurements. In this sense, the datasets are not directly comparable, but the purpose of comparison is to offer an improved supplement to traditional elevation surveys rather than a validation source.

Extensometer Data

An extensometer instrument is able to detect changes in land surface elevation by measuring the change in thickness of different depths. In situ extensometer data for Sherman Island is provided by Deverel et al. (2016). This dataset contained over 185,000 observations of land surface elevation from August 2011 to February 2017, measured with a linear potentiometer. Land surface elevations were measured relative to the extensometer structure anchored below peat layers (Deverel et al., 2016). On Sherman Island, the extensometer was located next to a drainage pumping station atop 16.9% soil organic matter (Deverel et al., 2016). Changing depth to groundwater levels was also recorded, but not included in this study. In general, groundwater levels rose during the winter from decreased crop evapotranspiration and rainfall recharge, and levels decreased in the spring (Deverel et al., 2016). This dataset can be compared to the seasonality observed with the UAVSAR line-of-sight displacement time series. For Sherman Island, groundwater levels can have as much as two meters of difference between seasons. The land surface elevation time series is compared below with available UAVSAR line-of-sight displacement series for Sherman Island. This comparison acts as a source of ground truth validation, and having a continuous network of extensometers across the Delta is not realistic.

InSAR Methodology

Advanced time-series InSAR methods were used to generate a Delta-wide map of subsidence (Figure 3), the first of its kind using a high spatial resolution such as UAVSAR. The

time series product is used to present the plots of cumulative displacement over time for each acquisition date, and the vertical velocity map is used to visualize the spatial patterns of subsidence. Included below is a summary of how the vertical velocities were generated, with full details in Bekaert et al. (2019).

The cumulative LOS (line-of-sight) displacement time series and uncertainty are calculated from unwrapped interferograms, which show changes between two dates, by using the Small Baseline Subset (SBAS) time-series processing algorithm (Berardino et al., 2002) and the GIAnT toolkit (Agram et al., 2013). To form a single map, the InSAR results are referenced to 24 Global Navigation Satellite System (GNSS) stations in the Delta as a tie-in for the UAVSAR flight swaths. The GNSS products used are provided by the Nevada Geodetic Laboratory and have horizontal rate uncertainties up to 0.3 mm/yr (Blewitt et al., 2013). Broad-scale horizontal movement from nearby faults is also removed from the InSAR rates. For the final combined map, the GNSS rates are used to remove long wavelength artifacts (ramps, tilts), while the InSAR rates constrain local variability. Vertical velocity maps from the different flight lines are combined with a weighted average, allowing areas with overlapping pixels to have lower uncertainty. The corresponding uncertainties for each flight line's velocity map are calculated using a jackknife approach. A full propagation of errors is included, with an RMSE of 7.7 mm/yr between GNSS rates and the vertical velocities. Since the GNSS stations occur mainly outside of the legal Delta, the RMSE may not be reflective of Delta conditions.

Uncertainty

Decorrelation, or loss of coherence, can negatively affect the quality of an interferogram, and is caused when two sets of radar signals, taken at different times over the same area, experience different interactions with the surface. Factors on the ground such as vegetation,

water, wind, soil moisture, etc. can impact radar scattering. The main limitation of InSAR application in agricultural areas is loss of coherence between data acquisitions, which can be caused by vegetation growth, agricultural activity, change in terrain type, and especially occurs in coastal humid regions. Loss of coherence causes higher noise in the interferometric phase signal, leading to errors in the derived change in surface location. This is caused by surface roughness and surface material altering the radar backscatter in a significant way between acquisitions (Zebker & Villasenor, 1992). Agricultural fields that have been watered or plowed is a common loss of coherence for active farmlands. By performing time-series analysis using many acquisitions for low coherence areas, as done for the UAVSAR acquisitions, decorrelation is decreased and the derived phase change reflect more accurately actual surface deformation.

Atmospheric effects from water vapor, pressure, and temperature changes can introduce interferometric phase changes that can be misconstrued as surface deformation. This occurs because atmospheric water vapor scatters and slows the velocity of transmitted radar waves (Woodhouse, 2006). Having multiple images can help to reduce the impact of atmospheric artifacts since these objects will not persist over time, and hence are a random signal while subsidence and many other real surface deformation signals usually exhibit a common trend during the time series. For the InSAR product, atmospheric corrections were also applied using the ERA-Interim global atmospheric model (Doin et al., 2009) using a modified version of the TRAIN toolbox (Bekaert et al., 2015).

Though the InSAR dataset is constrained by the 24 GNSS stations, these are only singular points. And since widespread in situ data on elevation change in the Delta is not feasible, the residuals of two independent datasets, namely the InSAR elevation rate of change map and lidar surveys, are compared. To determine whether the residual of the InSAR and lidar

vertical velocities (v_{InSAR} and v_{LiDAR} , respectively) is larger than their combined uncertainties, the following expression was applied:

$$\left|v_{InSAR} - v_{LiDAR}\right| \leq \sqrt{\sigma_{v_{InSAR}}{}^2 + \sigma_{v_{LiDAR}}{}^2} \quad (1)$$

where $\sigma_{v_{InSAR}}$ is the 1-sigma uncertainty calculated for the InSAR vertical velocities (as stated above) and $\sigma_{v_{LiDAR}}$ is 10.7 mm/yr, which is the 1-sigma uncertainty as calculated from the vertical accuracy reported from the lidar datasets (California Department of Water Resources, 2007; California Department of Water Resources, 2017). If the expression is true, then the InSAR and lidar vertical velocities measured are consistent within both datasets' uncertainties despite the large disagreement shown in some areas. Across the entire Delta legal boundary, where there are both lidar and SAR data, 99.8% of pixels showed agreement (see An et al. (2020) for the visual comparison of these results and Bekaert et al. (2019) for scaling information).

Results

This study reports trends within the legal boundaries of the Delta and separately for selected individual islands in each region (Table 1). The reported subsidence rates show the Delta to be subsiding by -11.9 +/- 4.4 mm/yr on average in 2009-2015, assuming a linear rate, with high variability across islands. This rate does not include the levees, which being engineered structures do not necessarily follow the same trends as the interior of the islands and are the focus of another paper (An et al., 2020). The subsidence rate derived from InSAR agrees well with past field studies (Deverel and Leighton, 2010; Deverel et al., 2016), however these studies lack a continuous map of subsidence that identifies the local-scale complexities evident on each island. In the subsidence rate map, many small subsidence hot spots are evident across the islands, with several that are of high concern due to their proximity to the levee (Figure 3).

These features are investigated alongside informative GIS datasets for each island and Delta-wide.

Across the entire Delta legal boundary (Figure 1), the vertical velocities show different relationships with land cover, elevation, and soil organic matter. For land cover (Figure 4A), the top ten crops grown in the Delta are shown with their average subsidence rate, with negative values denoting subsidence, and with the total land area devoted to each crop indicated. The crop showing the highest rate of subsidence is triticale, a hybrid of wheat and rye, with -17.4 mm/yr of subsidence. Alfalfa has the next highest rate of subsidence with -15.5 mm/yr and covers a much larger portion of the Delta. The most spatially extensive crop, corn, shows an average subsidence rate of -9.73 mm/yr. For elevation (Figure 4B), there are two relationships with subsidence, one at low elevation (-10 to 5 m) and at high elevation (5 to 15 m). For the two groups, subsidence rates increase (vertical velocity is more negative) as the elevation increases, with the low elevation group containing the majority of pixels. For soil organic matter (Figure 4C), the general relationship has the opposite of what is expected, with soils that have a higher percent soil organic matter showing lower rates of subsidence, although, at low percent soil organic matter (0 to 11%), where the majority of pixels is, a slight opposite trend is observed. When comparing the average subsidence rate and elevation for each crop type (Figure 4D), there is a positive relationship where crops with higher average elevation show relatively lower subsidence rates. The order of crops in term of surface area covered is slightly different from the previous figure because the calculation was only performed for the major islands of the study for Figure 4D. The values for elevation and subsidence are more extreme on the right side of the figure, where crops cover less area, but the relationship still holds. These comparisons are further investigated for individual islands below.

Figures 5-19 show profile figures for each island containing: the location of island in Delta, optical imagery from ArcMap basemap with points of interest, subsidence rate map derived from UAVSAR, elevation from the 2007 lidar survey, a lidar differential between the 2007 and 2017 surveys, percent soil organic matter, and land cover. The land cover legend is located on the right side margin, showing only classes covering at least 5 hectares on the island. The islands are discussed by region, beginning with Sherman Island of the western islands. The subsidence rate map for this island is compared with field extensometer data.

Sherman Island

As the westernmost island, Sherman is of critical importance because it helps to regulate the salinity gradient between the San Francisco Bay and the Delta. On the island, there are two historic levee breaks (Figure 5A) that occurred in 1906 at the northern point and 1969 at the southern point. The 1969 levee break coincides with a field test site location that also contains the largest InSAR subsidence signal in the Delta, up to -160.4 mm/yr. This feature has also been compared with GPS station data from the test site location (An et al., 2020). The subsidence feature is located at relatively low elevations, very high percent soil organic matter, and fallow/idle cropland. When compared to the lidar differential, the subsidence feature shows elevation gain between 2007 and 2017 instead of elevation loss. This is likely an effect of ongoing fill material addition by the DWR as this is a known area of subsidence and lidar detects any elevation change, including intentional addition or removal of material. Another large subsidence feature is located to the eastern portion of the island, along the “whale tail”, and matches in shape an area of low elevation, relatively higher soil organic matter, and mixed land cover, though the lidar differential does not show any such feature. The other subsidence features in the center of the island do correlate to low elevation areas, but a correlation is less clear with

regards to percent soil organic matter, land cover, and the lidar differential. The large uplift signals in the center of the island closely follow corn field outlines, and so are at least in part measuring changes in vegetation height and density, measuring changes in crop height, and not elevation change. The large elevation gain features in the lidar differential closely follow waterway outlines for the herbaceous wetlands (Figure 5A and 5D).

For each island, zonal statistics were also calculated for comparison between the InSAR subsidence rates and the GIS datasets. For land cover on Sherman Island (Figure 6A), alfalfa is the most popular crop being grown and has a high rate of subsidence of -15.7 mm/yr, but triticale still has the highest rate at -16.7 mm/yr, as in the Delta-wide analysis, even though it covers a small area. Fallow/idle cropland is the next most common land cover and shows a slightly lower rate of subsidence at -12.2 mm/yr, and corn shows a small positive rate of uplift at 0.2 mm/yr, with the contribution of fields measuring uplift described above. For elevation (Figure 6B), where the majority of pixels lie, between -6 and -2 meters, the subsidence rate increases as elevation decreases. At higher elevations, this relationship is less clear. For soil organic matter (Figure 6C), the average subsidence rate increases as the percent soil organic matter increases, as expected since highly organic soils should be more compressible.

For the Sherman Island extensometer test site (Figure 5A), the LOS cumulative displacement time series from coincident UAVSAR flight lines were compared with the in situ dataset (Figure 6D). The land surface change measured by the extensometer shows gradual elevation loss from 2010-2015, with a steep drop in 2015, followed by seasonal variability until 2017. Over a similar timescale, from 2009-2015, the LOS displacement time series for UAVSAR flights 05519, 15502, and 23518 all show decreasing displacement similar to the extensometer series, with seasonal variability due to changing water levels. The time series for flight line

33502 does not share a decreasing trend, but instead shows high variability and scatter. This may be due to slightly lower coherence at the site for Line 33502, and does not seem to be related to differences in near and far range across the flight tracks.

Twitchell Island

Twitchell Island contains several levee vulnerability points (past and potential damage to the levee) and areas of past seepage (Figure 7A), one of which in the southeast coincides with a subsidence feature seen in the InSAR data. Overall, both the InSAR rate map (Figure 7C) and the lidar differential (Figure 7D) show elevation loss in the western side of the island and elevation gain on the eastern side. The elevation loss seen in the lidar differential looks to follow some perpendicular lines and may be related to the rice cropland in the same area (Figure 7F). The large subsidence features from the InSAR dataset also appear in the same area, but do not follow cropland boundaries. These features may also follow the contours of the soil organic matter map, which also indicate different soil types, although the subsidence occurs in less organic material (Figure 7E).

The crop with the most land area on Twitchell Island is alfalfa, with an average subsidence rate of -15.1 mm/yr (Figure 8A). The crop with the highest subsidence rate is other hay/non-alfalfa at -18.5 mm/yr, though it does not cover a large area. Grassland/pasture and fallow/idle cropland also have relatively high subsidence rates on this island. There is not a clear relationship between elevation and subsidence (Figure 8B), although the two points at lowest elevation show the least average subsidence compared with higher elevations. From 0 to 11% soil organic matter, an increase in subsidence follows an increase in soil organic matter, as expected, but at 17.5% the subsidence rate decreases, possibly indicating that another factor such as agricultural activity may be at play (Figure 8C).

Bradford Island and Webb Tract

Bradford Island and Webb Tract, located to the south of Twitchell Island and east of Sherman Island, also contain several sites of past seepage events and historic levee breaks (Figure 9A). The levee break to the north on Webb Tract shows more stable conditions with subsiding features on either side of the break, indicating a past repair (Figure 9C). The lidar differential shows increases in elevation all along the northern portion of the levee on Webb Tract (Figure 9D). This anticorrelation is likely from added material during repair and is discussed in detail elsewhere (An et al., 2020). In the center of both islands, there are large features of elevation loss seen in the lidar that coincide with dune features, digitized from historic USGS maps (Atwater, 1982), which are also seen in the elevation and soil maps (Figure 9B and 9E) and classified as woody wetlands (Figure 9F).). In the InSAR rate maps, these features have positive rates of elevation change, consistent with little or no subsidence, which is to be expected for dunes, which contain very low soil organic matter. It is unclear whether the depths of measurement between InSAR and lidar may be causing the discrepancy. Two main crops are being grown on the two islands: alfalfa on Bradford Island and corn on Webb Tract. This does not seem to be related to the large subsidence signals seen in the northern portions of both islands, in fact, the islands seem to be subsiding everywhere besides the main dune features.

On Bradford Island, corn has the highest rate of subsidence at -26.9 mm/yr, albeit covering little area, while corn has one of the lowest rates on Webb Tract at -7.11 mm/yr (Figure 10A and 10D) and covers the most area. Unlike previously discussed islands, both Bradford Island and Webb Tract show low subsidence rates for fallow/idle cropland, -5.6 and -3.4 mm/yr respectively, despite being the second most common land cover. Whereas the average subsidence rates for corn differ tremendously, the average subsidence rate for alfalfa is similar across the

islands, at -12.9 mm/yr for Bradford Island and -10 mm/yr on Webb Tract. The herbaceous wetlands along the perimeter of Webb Tract and its water bodies has the highest rate of average subsidence despite covering a small area. For both islands, except the -5 meter class (containing few pixels, Figure 10B), the average subsidence rate is higher at low elevations and gradually decreases at higher elevations. On Bradford Island and Webb Tract, there are higher subsidence rates with higher soil organic matter until above 40%, where the higher soil organic matter classes show less subsidence (Figure 10C and 10F).

Jersey Island and Bethel Tract

Jersey Island and Bethel Tract are located directly south of Bradford Island and Webb Tract. One of the largest signals of subsidence for the Delta is found on Blind Point Peninsula in western Jersey Island with rates up to -59.1 mm/yr (Figure 11C). This peninsula is also located on a different soil type than its surroundings according to the contours of the soil organic matter map (Figure 11E). Bethel Tract does have less organic soil overall, and is subsiding much less than Jersey Island. The large subsidence signals in northern Jersey Island are located on the island's lowest elevation (Figure 11B), though further visual comparisons are difficult. The most common crop being grown on these islands is alfalfa, and Bethel Tract also has a large area of grassland/pasture (Figure 11F). Land cover does have a clear relationship with subsidence rates on these islands. Each island also has a historic levee break, though these sites show relatively stable conditions. The lidar differential shows mostly stable conditions (Figure 11D), with a large elevation gain on Bethel Tract in the southeast harbor and a spot of large elevation loss on Jersey Island that is related to a water body (Figure 11A). There is also elevation gain all along the perimeter of Jersey Island and some parts of Bethel Tract that may be due to past levee repair work.

Due to the lack of visual patterns between subsidence rate and land cover, it is difficult to conclude any relationships from Figures 12A and 12D. The high subsidence rate averages from the top three classes on Jersey Island may be due to their large area coverage (Figure 12A), and the land cover classes for Bethel Tract all show similar values of average uplift (Figure 12D). The relationship with elevation, however, is very similar for both islands (Figures 12B and 12E). The lowest elevation class starts with a slightly higher positive value, but the following classes show a positive linear relationship between increasing elevation and decreasing subsidence. Then at higher elevations, around 2 meters, the subsidence rate does not change as much as the elevation increases. As with previous islands, the subsidence rate increases with increasing percent soil organic matter, but only at low percentages for Jersey Island (Figure 12C). Bethel Tract shows the same relationship mostly consistent at all percentages (Figure 12F).

Venice Island and Empire Tract

There are several historic levee breaks on Venice Island and Empire Tract, all showing more stable rates than their surroundings, likely due to past levee repair work. On Venice Island, there is a large uplift feature on the eastern side of the island that is also located on low elevation and more organic soils (Figures 13B and 13E). On Empire Tract, there is also a large uplift feature in the northwest, which is also seen in the lidar differential, at lower elevation, in a different soil type, and within corn field boundaries. Directly adjacent to this uplift feature is a large subsidence signal in the center of Empire Tract. This subsidence feature is found at lower elevation, higher organic matter, and within alfalfa crop boundaries. The features on these islands contain missing pixels in the subsidence map due to decorrelation, likely from changing cropland conditions.

Holland Tract and Bacon Island

On Holland Tract, the northeastern side of the island is experiencing subsidence in an area that looks to be closely related to lower elevation and the boundaries of higher soil organic material (Figures 14B, 14C, and 14E). The extent of corn fields on this island also closely follows where the subsidence is occurring on this island (Figure 14F). The northernmost point of Holland Tract, containing subsidence up to -49.1 mm/yr, is especially concerning as it surrounds a fairly recent levee break from 1980. The lidar differential does not show similar elevation loss, but instead high elevation gain along the levee, likely due to repair work as in previous islands (Figure 14D). The lidar differential also shows large elevation loss and gain in the southwest, likely due to open water in the wetland environment. On Bacon Island, there are large subsidence features in the northeast and southeast, which are located on more organic soils, and for the northeast feature on lower elevations. These features are not apparent in the lidar differential, which shows elevation loss in field boundaries to the northwest.

For Holland Tract, unlike on previous islands, corn has the highest average rate of subsidence due to the features along the eastern side of the island (Figure 15A). Elevation has a clear relationship with subsidence, with areas of low elevation experiencing higher subsidence (Figure 15B). Soil organic matter also has the expected relationship of more organic soils generally experiencing higher subsidence (Figure 15C), although the trend is not as linear as that in the elevation plot. For Bacon Island, the oats crop has the highest average subsidence rate due to the small field located in the southeast (Figure 15D), but this is likely not representative of the crop since there are more severe subsidence features elsewhere on the island. Interestingly, for elevation, Bacon Island shows an opposite trend as most islands, with lower elevation areas

showing the least amount of subsidence (Figure 15E). The relationship between subsidence and soil organic matter is unclear on this island.

Jones Tract

Jones Tract contains many high subsidence features close to the levee, measuring up to -120.1 mm/yr of subsidence (Figure 16C). These features are once again seen as elevation gain in the lidar differential (Figure 16D), along with some elevation loss in the north in corn fields. There are several historic levee breaks on this tract, two occurring in 1980 and the southernmost occurring in 2004 (Figure 16A). The 2004 Jones Tract failure in the Delta occurred after extensive flooding and cost over $44 million to repair, not including job and crop losses (Mount and Twiss, 2005). The 2004 levee break location is now on more stable ground due to repair work, but is surrounded by subsidence on either side. The lowest elevation on this tract is found in the northwestern portion of the island (Figure 16B), which is also where the largest subsidence features are located. The soil organic matter map depicts historic estuaries running across the island, with zero organic matter (Figure 16E), though evidence of this feature is not seen in the other datasets. Delineations between alfalfa and corn fields are seen in the subsidence map in northern Jones Tract, with more subsidence measured in corn fields. Uplift signals on the western side of tract follow field boundaries closely as well.

Ryer Island and Grand Island

Just east of Ryer Island is a concentration of historic levee breaks occurring on Prospect Island, which has largely been flooded (Figure 17A). The only levee break from this dataset on these two islands is in southern Ryer Island and occurred in 1904. The subsidence features occurring on the islands are mostly inland, and are not in close proximity to these sites. The lidar differential does not show any large changes on these islands other than some small field-related

activity (Figure 17D). On Ryer Island, most subsidence is found in the southern part of the island, where elevations are also lowest and the percent soil organic matter is slightly higher (Figures 17B and 17E). For Grand Island, most of the subsidence features are in the northern portion of the island, where there is a higher concentration of alfalfa fields (Figure 17F). Elevation is lowest in the center of Grand Island (Figure 17B), as well as where there are more organic soils (Figure 17E).

There is not a standalone crop on Ryer Island that shows the highest subsidence rates since the island is well-mixed in crop variety and surface area (Figure 18A). Low elevations do show higher subsidence rates overall on this island (Figure 18B). Though there are only two soil classes on this island, on average there is more subsidence in soils with higher organic matter (Figure 18C). On Grand Island, alfalfa has the highest average rate of subsidence (Figure 18D) due to the fields located in the north, and even in smaller fields in the southern half of the island. The subsidence features on Grand Island match very well spatially with the location of alfalfa fields. For elevation, Grand Island generally holds the same trend as Ryer Island, though there is a slight opposite trend at lower elevations (Figure 18E). And again for soil organic matter, despite the few soil classes available, the island does show more subsidence in more organic soils (Figure 18F).

Canal Ranch Tract, Brack Tract, and Terminous Tract

There are several subsidence features scattered across these tracts in the eastern Delta, but all appear related to agricultural activity based on their rectangular shape and sharp boundaries with neighboring features. The subsidence is more concentrated on the western side of these tracts, where elevation is also lower and the percent soil organic matter is higher (Figures 19B and 19E). The land cover is mixed on the three tracts, though there are more corn fields on the

western side of Terminous Tract (Figure 19F). They do not appear to be related to the subsidence features found on Terminous Tract. The lidar differential does not show much change except for elevation loss on the western sides of Canal Ranch Tract and Brack Tract (Figure 19D), which also is shown in the InSAR subsidence map.

Discussion

The InSAR derived subsidence map (Figure 3) shows many localized subsidence features across the Delta, and it is only with island-scale comparisons with GIS datasets that the causes for these features can be narrowed down. On some islands, land subsidence looks to be closely related to lower elevation and higher soil organic matter, while on other islands neither of these are true or only one factor seems to be related. Individual island activities can greatly impact the results of the subsidence map, with some islands showing clear agricultural field delineations in uplift or subsidence features. Therefore, subsidence in the Delta must be studied on the local, island scale to decipher true land subsidence from expected subsidence caused by human activities such as agriculture. A regional discussion of the results is also included, with the islands corresponding to each region defined in Figure 1 (see supplementary figures for more regional comparisons).

Lidar Comparison

Since the lidar surveys were only collected twice, in 2007 and 2017, the differential is not directly comparable with the InSAR subsidence map, which is based on a cumulative displacement time series product. However the lidar differential is the only Delta-wide dataset measuring elevation change, and can be a helpful reference to the InSAR subsidence results presented in terms of the direction of trends observed and not necessarily the lidar measured magnitude of elevation change. Overall, the average rate of subsidence in the Delta's island

interiors is -11.9 mm/yr from the InSAR vertical velocity map (2009-2015) and the average elevation loss is -0.9 mm/yr from the lidar differential (2007 and 2017).

On many of the islands, the lidar differential showed significant elevation gain while the InSAR map showed subsidence or stable conditions close to the levee. These opposing results are likely due to ongoing levee repair work by the CA DWR, causing the lidar results to only see the net elevation gain while the InSAR technique measures the ongoing subsidence. In fact, at the highest rate of subsidence on Sherman Island, the lidar differential shows elevation gain, as this is a known area of subsidence receiving continual addition of fill material to maintain elevation (Figure 5). For an in-depth exploration of the levee specific results, see An et al. (2020).

Some of the large elevation gain features seen in the lidar differential are related to open water changes, such as in the herbaceous wetlands on Sherman Island (Figure 5) and a harbor in southeastern Bethel Tract (Figure 11). There are also elevation gain features that appear to be related to wetland environments but are not classified as such in the land cover dataset, such as the linear features on eastern Twitchell Island (Figure 7D) and the circular features in northern Bradford Island (Figure 9D) that both match with optical imagery. Historic dune features on Webb Tract also closely outline large elevation gain features (Figure 9D), highlighting the fact that the shape of a feature, not just its elevation change value, can give insight into influencing factors. Examples of elevation loss related to agricultural activity are seen as linear features in the corn and rice fields on Twitchell Island (Figure 7D), corn fields on Bacon Island (Figure 14D), Jones Tract (Figure 16D), and several others. More information about corn farming practices would be beneficial in determining any connections between the crop fields and land subsidence.

Percent Soil Organic Matter Comparison

The map of percent soil organic matter provided by Deverel and Leighton (2010) is the only spatially continuous dataset that models the information for the Sacramento-San Joaquin Delta. In addition to the percentage values of organic matter levels, the dataset also provides soil type boundaries that may indicate different properties, such as texture and drainage efficiency. It is expected for more organic soils to be more compressible and thus experience more land subsidence (Rojstaczer & Deverel, 1995). However, on average in the Delta the opposite is seen (Figure 4C), with more organic soil classes measuring lower subsidence rates. Since the soil dataset only assigns discrete values (the ten classes shown), there is a large disparity between class sizes and the actual detail of soil differences cannot be captured. The spatial uncertainty of this dataset may be contributing to the relationship, or it suggests that other factors such as land use are affecting the vertical velocity measured on certain islands.

For example, on Twitchell Island (Figure 7), Venice Island and Empire Tract (Figure 13), and the three eastern tracts (Figure 19), the InSAR results are likely to be related to land cover changes. On Webb Tract, even though the largest subsidence features do occur in the soil class with the highest organic matter (Figure 9E), the class covers almost the entire island and so the average subsidence value is dampened. On Jersey Island, one of the largest subsidence features in the Delta occurs on Blind Point Peninsula, which contains a medium organic matter soil (Figure 11). But the soil map contours do indicate that this peninsula sits on a different soil type than most of the rest of the island, which may be related to the subsidence found there. On Jones Tract, the large subsidence features are concentrated close to the levees and are likely less related to soil organic matter, which is well mixed on this island (Figure 16).

More concerning subsidence features are found on islands where there seems to be a close relationship between sinking areas and soil organic matter. On Sherman Island, where the highest rate of subsidence occurs exactly coincides with an area of high soil organic matter (Figure 5). Subsidence on Bradford Island (Figure 9) also occurs in a soil class with high organic matter. On Holland Tract, large subsidence features are concentrated on the eastern side of the island, closely following the contours of a high organic matter soil class (Figure 14). Soil organic matter varies with depth, and inorganic material can also be mixed in with organic material in the top two to three centimeters of soil. A peat thickness map can also be useful, though it may not contain a stable reference due to subsidence in the Delta. An ideal dataset for comparison would be a map of the peat/clay border in the Delta since this interface has not changed since peat layers formed over 8,000 years ago.

Elevation Comparison

The Delta islands lie several meters under mean sea level, with individual islands each containing their own elevation gradients and the lowest elevations found in the central islands. If generally the subsidence observed during 2009-2015 is consistent with long-term trends, then areas of low elevation are expected to experience more subsidence because their already low heights were caused by ongoing subsidence. Though this relationship was found on many individual islands, it is not true on average for the Delta as a whole. In Figure 4B, there are two distinct point groups, less than and greater than 5 meters. The low elevation group, where the majority of pixels lie, overall has higher subsidence rates than the higher elevation group. However, for each group the relationship between land subsidence and elevation shows higher subsidence at higher elevation, suggesting that the Delta as a whole does exhibit the expected

relationship between subsidence and elevation, but there are complexities at the local scale. This is confirmed when comparing the DEM with InSAR subsidence map for each island.

The eastern and western islands show a strong relationship between higher subsidence at lower elevations, while the variables seem unrelated in the northern and central islands. The southern islands, covering a large area of the Delta, show a highly variable relationship between elevation and subsidence (see supplementary figures). The only islands for which lower elevations do not show higher subsidence are: Twitchell Island (Figure 7), Venice Island (Figure 13), Bacon Island (Figure 14), Jones Tract (Figure 16), Canal Ranch Tract (Figure 19), and Brack Tract (Figure 19). On Twitchell Island, the subsidence was not concentrated in the center of the island where elevation was lowest, but in the southwestern region, similar to the lidar differential, which is possibly due to agricultural activity (Figure 7). A similar story is found on Venice Island, where not much subsidence at all was measured, but instead large uplift features that seem related to corn fields (Figure 13). On Bacon Island, even though there is a prominent subsidence feature in the lowest part of the island, overall the pattern did not hold true (Figure 14). The major subsidence occurring on Jones Tract is related to the levees, and does not follow the elevation gradient on the island (Figure 16). In the eastern Delta, on Canal Ranch and Bract Tracts, the subsidence features closely followed crop field boundaries and are likely related to farming activities (Figure 19). Where low elevation does measure higher land subsidence and the feature does not seem to be related in shape or location to cropland, are the areas more likely to be experiencing actual land subsidence on already subsided land. Areas such as northern Webb Tract (Figure 9), northern Holland Tract (Figure 14), areas close to the levee on Jones Tract (Figure 16), and southern Ryer Island (Figure 17) are locations of concern that require field observations for possible threats to the levee.

Land Cover Comparison

Crop type can greatly influence the subsidence of agricultural fields, and also act as a proxy for other important variables (e.g. elevation). In Figure 4, crops which were grown at lower elevations in general displayed higher subsidence rate. Cultivation and grazing schedules of different crop types can cause misleading results in the InSAR subsidence map, as seen by the uplifting corn fields on Sherman Island (Figure 5). Agriculture plays a large role in the Delta's economy, with the crops holding the largest surface area being corn and alfalfa (Figure 4A). Though alfalfa covers less area than corn, the average subsidence rate for alfalfa is -15.5 mm/yr and -9.7 mm/yr for corn. Alfalfa is not the most dominant crop in the northern, eastern, and central regions but still measures higher subsidence than corn. An example of alfalfa field boundaries matching subsidence features are found on Empire Tract (Figure 13) and Bacon Island (Figure 14). These features are likely not measuring true subsidence, but farming activity, since they closely follow field boundaries. Watering of fields and increases in crop cover can affect the height changes measured by InSAR. Similarly, several islands show large uplift features related to corn field boundaries: on Sherman Island (Figure 5), Venice Island and Empire Tract (Figure 13), Jones Tract (Figure 16), and Terminous Tract (Figure 19). Alfalfa crops are harvested between April and September while corn is harvested between September and November (Delta Crops Calendar, 2015). The opposing growing seasons of these active fields may have contributed to some of these large apparent subsidence and uplift signals in the Delta.

Land cover also has a close relationship with elevation, suggesting that certain crops may be more suitable at different elevation levels (Figure 4D). Crops grown at lower elevation such as barley/corn, cotton, herbs, oat/corn, and pumpkins have relatively higher subsidence rates than

other crops. Similarly, crops grown at higher elevations such as cantaloupes, onions, peaches, herbs, and pecans show more positive uplift rates on average. More information on how different crops in the Delta are cultivated, including their growing season, preferred soil type, and ideal elevation level could help limit further subsidence on already sinking areas. For example, if an area is already experiencing subsidence, and may be on more organic soil and/or lower elevation, only certain types of crops could be grown there. Choosing a crop that does not require intense dewatering, for instance, could help prevent further subsidence. Or it is possible that no farming activity would be suitable on very compressible, low elevations that are sinking further.

Conclusions

Typically, due to the constant drainage of agricultural soils, subsidence and thick peat soils tend to be concentrated near the center of many islands. This did not seem to be the case for most islands, at least for the most rapid observed subsidence, since the subsidence hot spots occurred more often close to the levee. However, this observation could be skewed by the addition of fill material near levees, which causes compression of peat soils below for these hot spots. Elevation seemed to have a strong relationship with subsidence in general. Since low elevation can be proxy for previous subsidence, if these areas continue to subside, the elevation will lower even further than current levels. For many islands, the soil organic matter outlines also matched fairly well with large subsidence signals. This indicates more compressible soils that may be more prone to subsidence, and that soil type boundaries, not just organic matter content, may also be a determining factor for subsidence. However, many islands did not show more subsidence in more compressible soils, so there appear to be other factors at play, such as land cover and land use. It was visually evident that some apparent subsidence and uplift features followed closely the shape and size of agricultural fields, and that on average certain crops grow

at lower elevations with lower average subsidence values. Further investigation into how different crops impact subsidence through different agricultural practices may be helpful in explaining more subsidence features.

UAVSAR is an advantageous instrument to study the Delta due to very high-resolution instrument that can penetrate vegetation, not be inhibited by stormy weather, and data coverage over the Delta. The resolution of this dataset allows the capability to identify features on individual islands, of which a representative set from each part of the Delta is shown, and to compare patterns of subsidence with auxiliary datasets in GIS. Comparisons with historic levee breaks and seepage points with proximity to levees also help to prioritize certain subsidence features as more concerning than others. Being able to identify subsidence features occurring at specific locations on particular islands in the Delta can help aid the DWR in their ongoing monitoring efforts. In addition, such applications of UAVSAR help to show how satellite data from emerging space sensors such as NISAR, for which UAVSAR is the prototype, and Sentinel-1 can be applied for regional studies. UAVSAR applications can be designed for emergency response situations after a flood event or earthquake to allow resources, as in the Sacramento-San Joaquin Delta, to focus on areas most likely damaged.

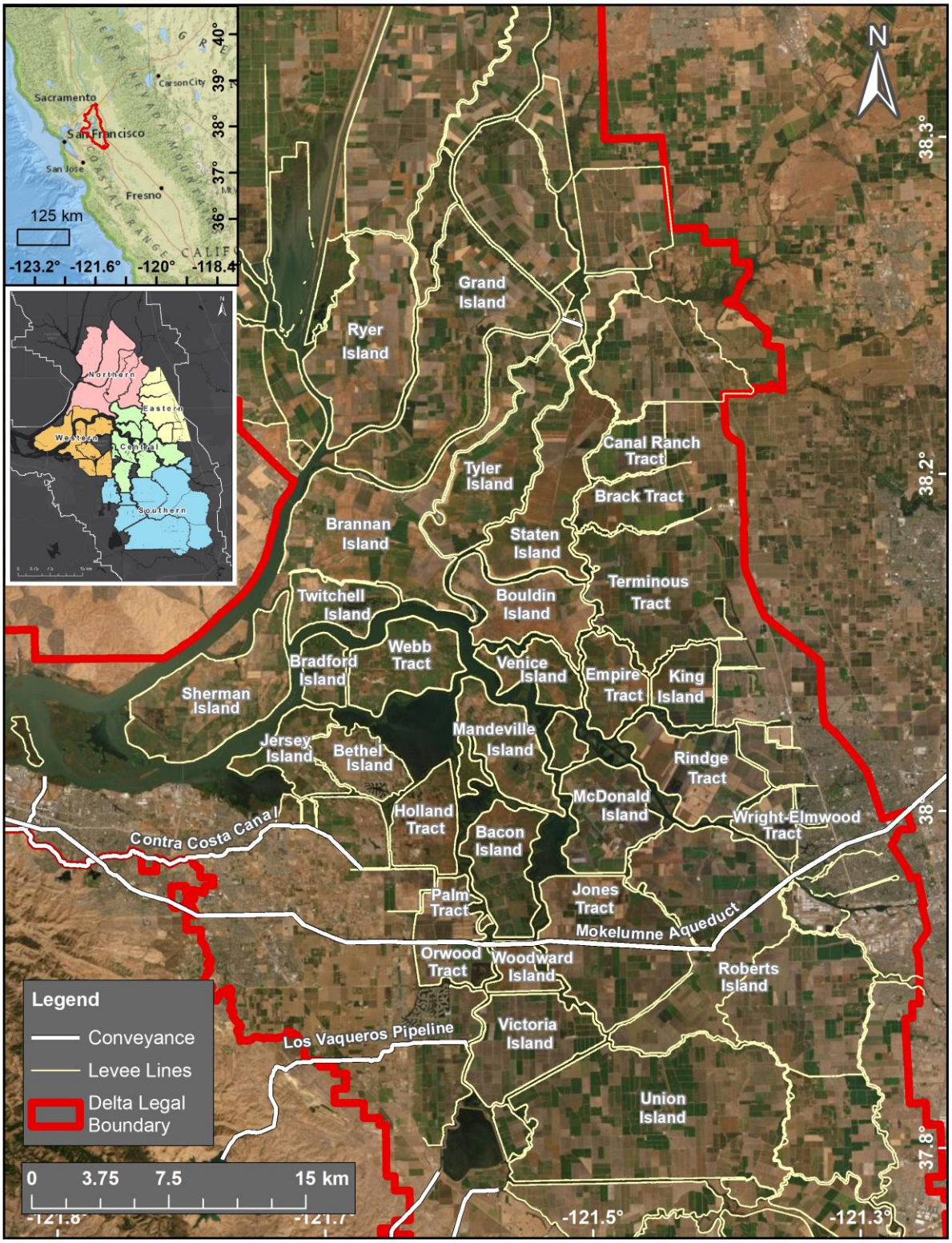

Figure 1: Study area of Sacramento-San Joaquin Delta with inset showing nearby fault lines (green) and major conveyance lines (red). The legal Delta boundary is shown (red) and levee lines (yellow) outline each island.

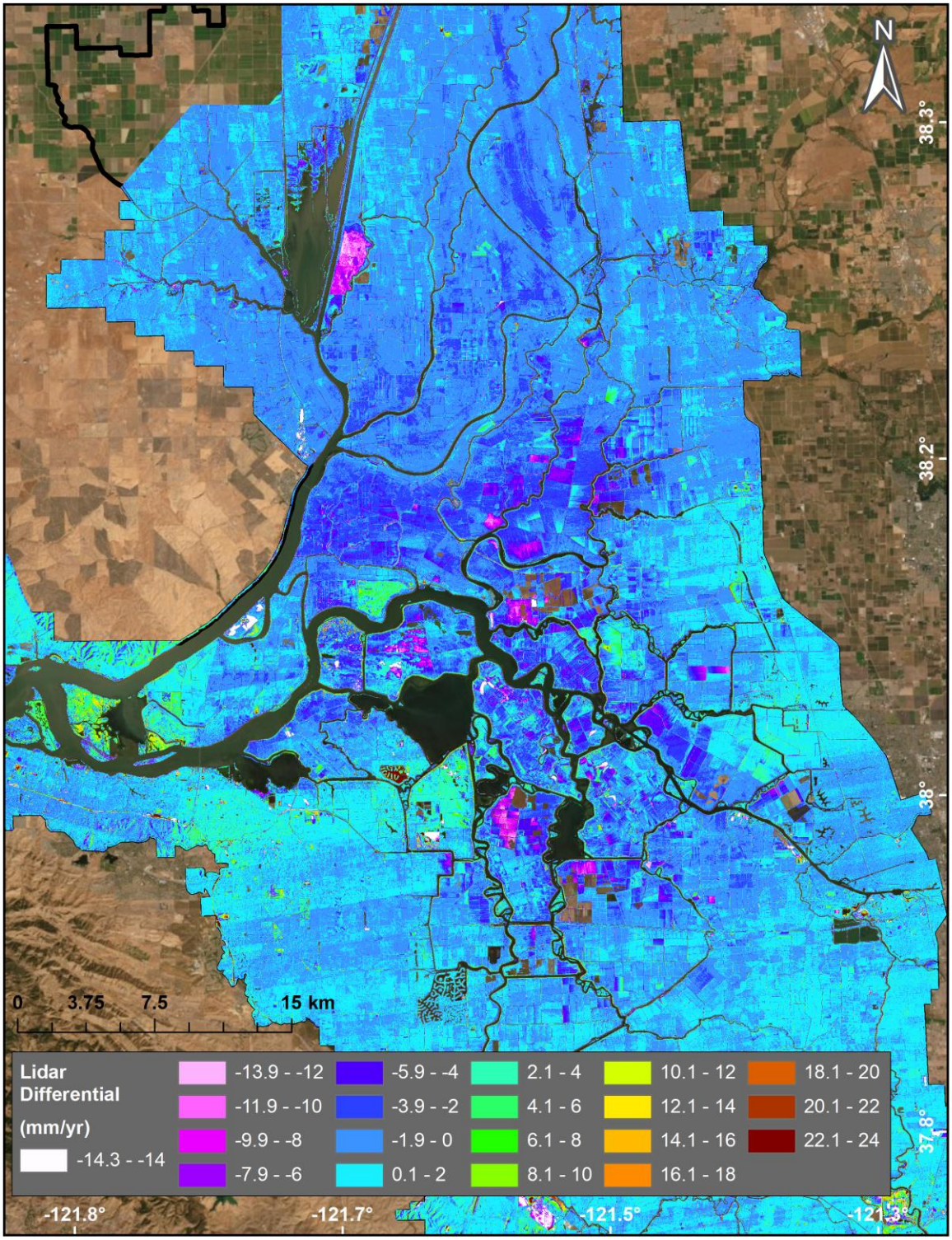

Figure 2: Lidar differential between the 2007 and 2017 elevation surveys collected by the California Department of Water Resources. Elevation change is shown in millimeters per year, with red areas showing an elevation increase from 2007 to 2017 and pink areas showing an elevation decrease.

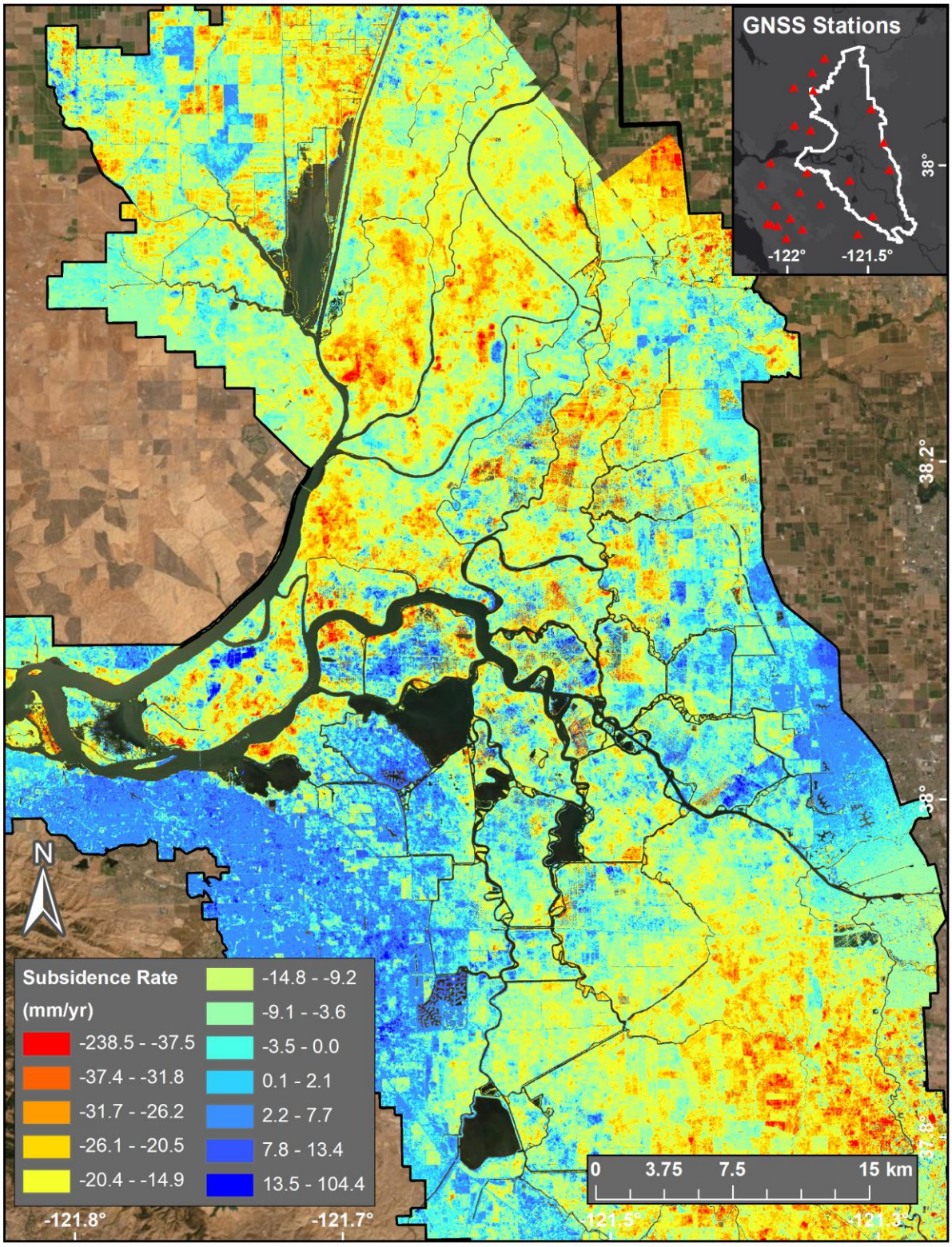

Figure 3: Vertical velocity rates for the Delta from UAVSAR for 2009-2015 in millimeters per year, with orange/red areas showing the highest subsidence and blue areas showing the least.

Table 1: A summary table of the average subsidence rate in millimeters per year, derived from the InSAR rate map, for each region and individual island. Levee areas are not included in this calculation. Islands marked with an asterisk are not included in this study, but figures for which can be found in the appendix material.

Average Subsidence Rate (mm/yr)	Central	Eastern	Western	Northern	Southern
	-7.6	-7.9	-7.9	-15.8	-13.7
Bacon Island	-5.4				
Bethel Tract			2.3		
Bishop Tract*		-0.5			
Bouldin Island*	-11.4				
Brack Tract		-11.7			
Bradford Island			-11.6		
Brannan Island*				-15.4	
Canal Ranch Tract		-16.4			
Empire Tract	-9.0				
Grand Island				-16.0	
Holland Tract			-2.3		
Hotchkiss Tract*			-0.9		
Jersey Island			-11.5		
Jones Tract					-9.0
King Island*		-2.4			
Mandeville Island*	-8.5				
McDonald Tract*	-10.1				
Orwood Tract*					-2.2
Palm Tract*					-3.7
Rindge Tract*	-2.6				
Rio Blanco Tract*		-4.9			
Roberts Island*					-16.3
Ryer Island				-19.9	
Sherman Island			-12.4		
Shin Kee Tract*		-3.1			
Staten Island*				-16.4	
Terminous Tract		-8.4			
Twitchell Island			-12.8		
Tyler Island*				-9.3	
Union Island*					-15.6
Venice Island	-6.8				
Victoria Island*					-11.5
Webb Tract			-6.5		
Woodward Island*					-4.6

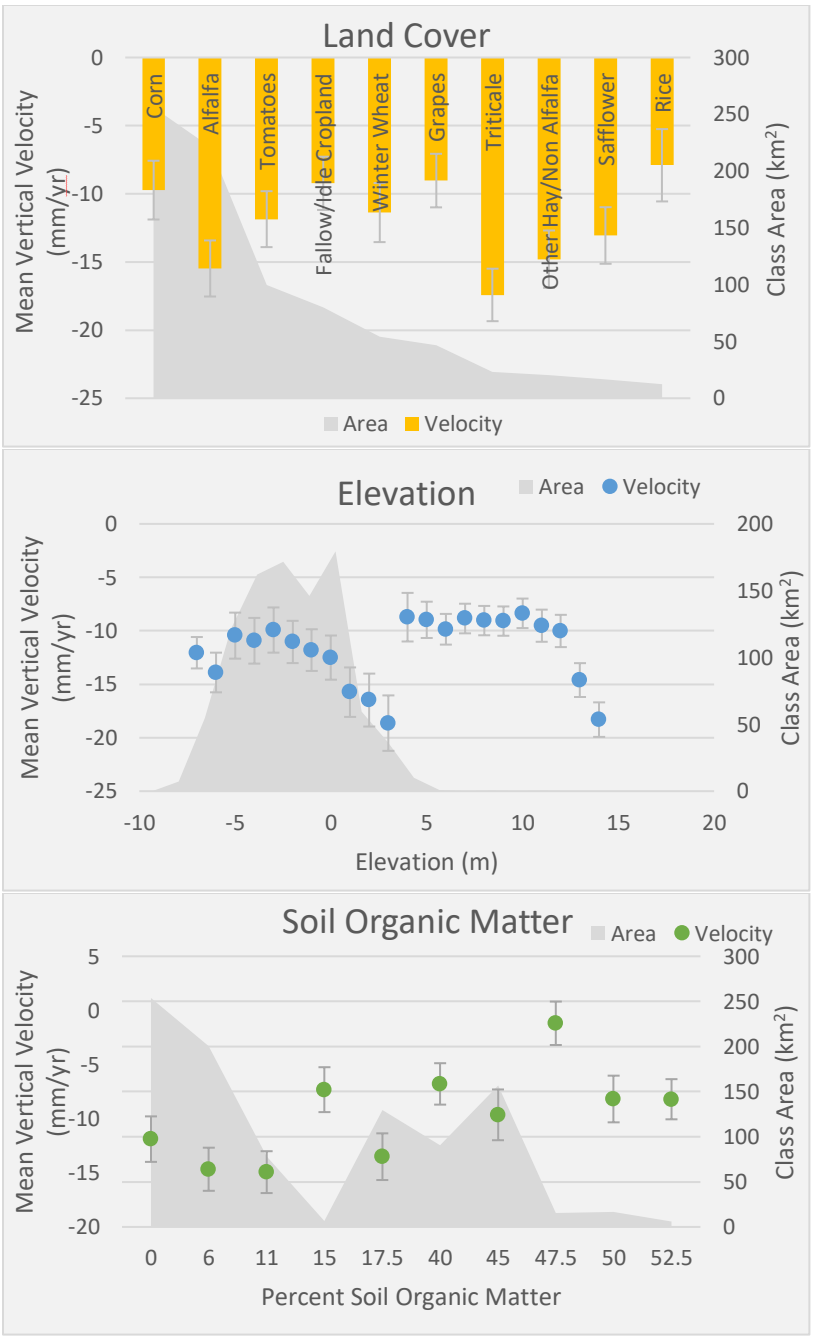
Land Cover
Mean Vertical Velocity (mm/yr)
Class Area (km²)
Corn
Alfalfa
Tomatoes
Fallow/Idle Cropland
Winter Wheat
Grapes
Triticale
Other Hay/Non Alfalfa
Safflower
Rice
Area
Velocity
Elevation
Elevation (m)
Soil Organic Matter
Percent Soil Organic Matter

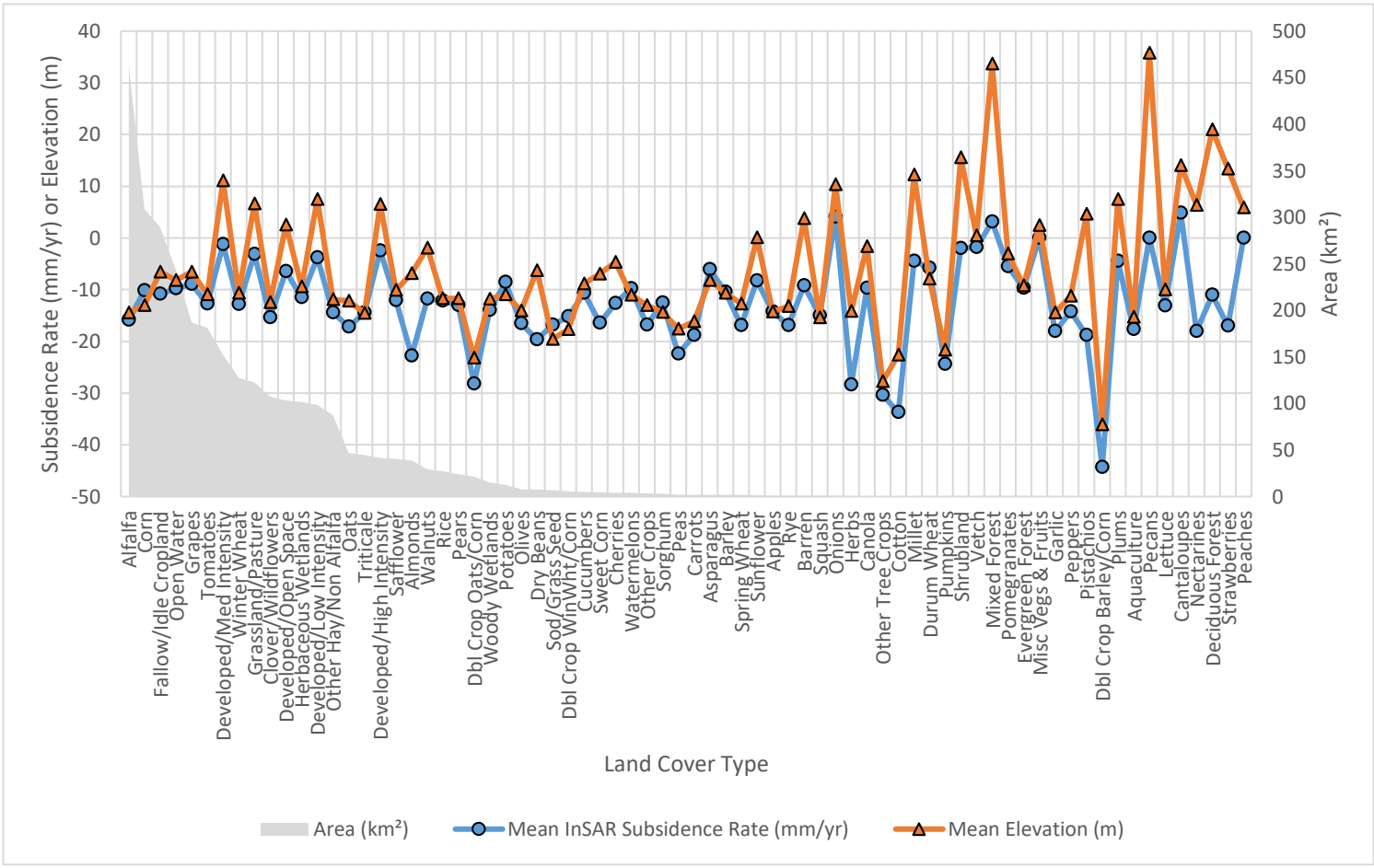

Figure 4: (A) Mean subsidence rates for the top ten crops across the Delta. (B) Mean subsidence rates for each elevation class across the Delta. (C) Mean subsidence rates for each soil organic matter class across the Delta. (D) The average subsidence rate (blue) and elevation (orange) are shown for each crop type. Crops are listed in order of decreasing area, from left to right.

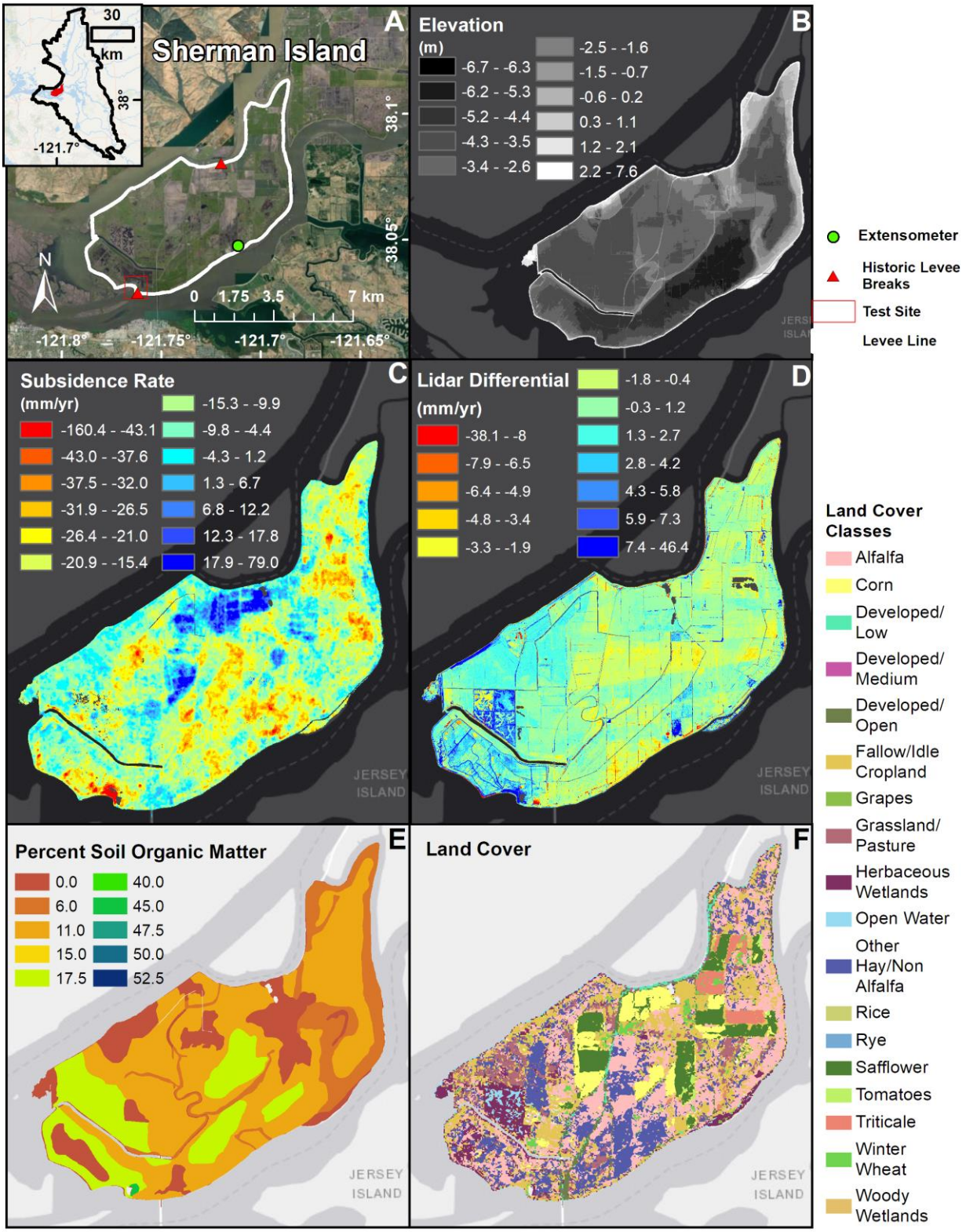

Figure 5: A profile figure for Sherman Island showing: (A) location of island in Delta and optical imagery from ArcMap basemap with points of interest, (B) elevation in meters, (C)

InSAR derived subsidence rate in mm/yr for 2009-2015, (D) lidar differential in mm/yr for 2007 and 2017, (E) percent soil organic matter, and (F) land cover (legend only shows classes with at least 5 hectares).

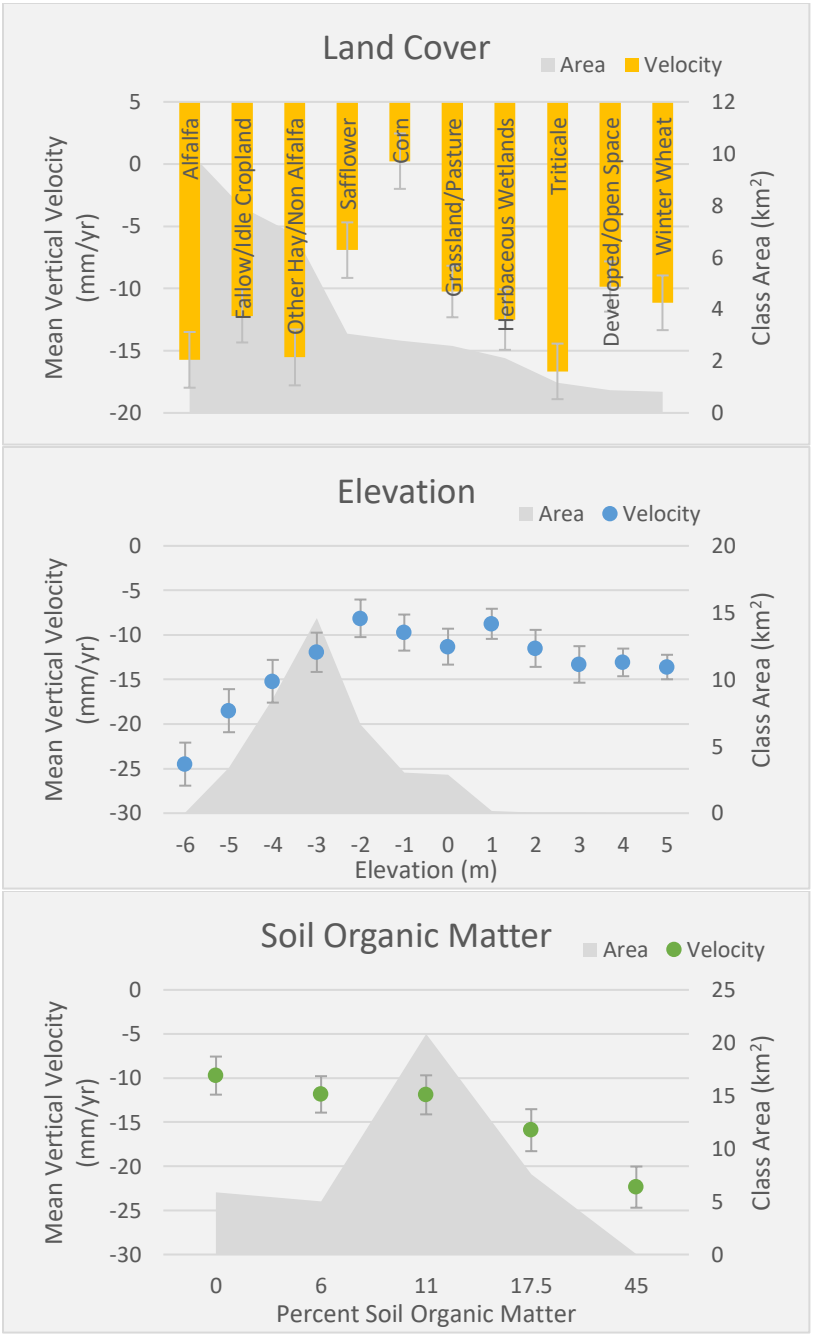

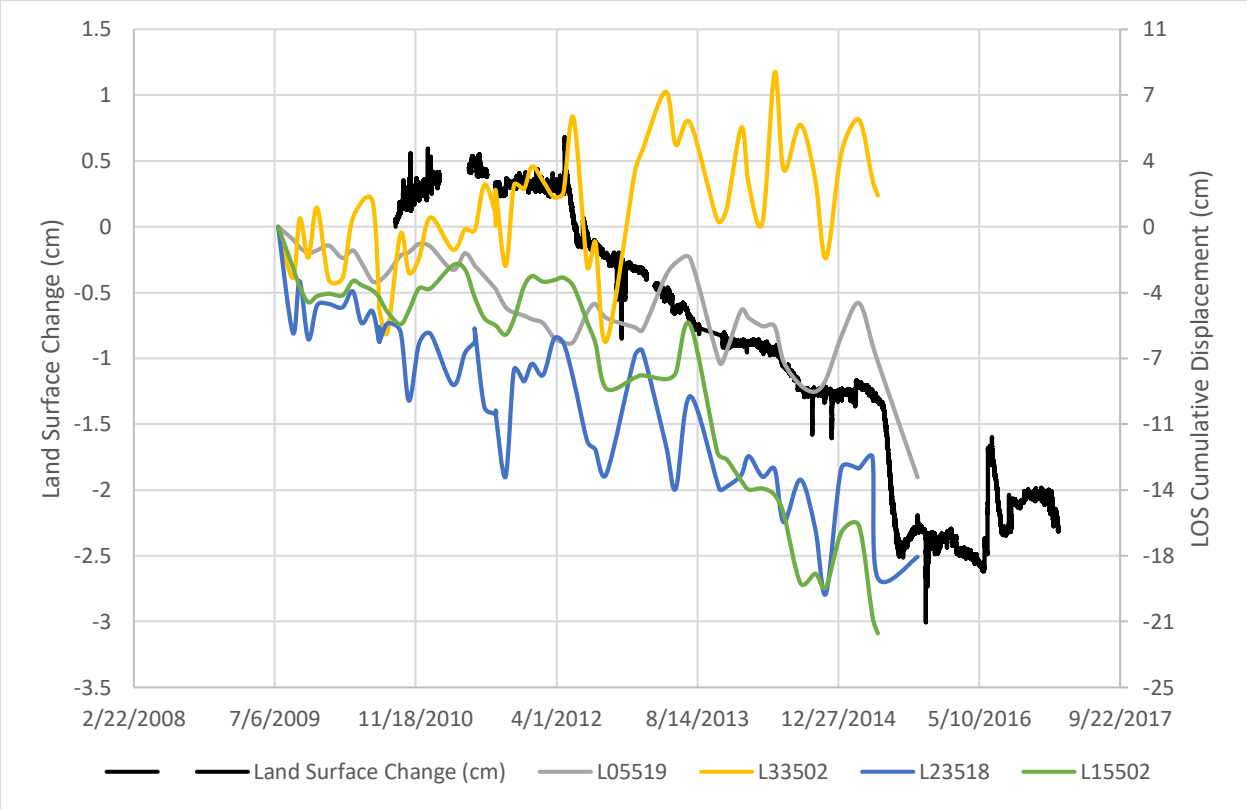

Figure 6: (A) Mean vertical velocity for top ten land cover classes, (B) elevation classes, and (C) soil organic matter classes in Sherman Island. The area of each class is shown in the dark grey background. (D) Land surface change time series from extensometer data (black) plotted alongside line-of-sight displacement time series derived from UAVSAR (multi-color).

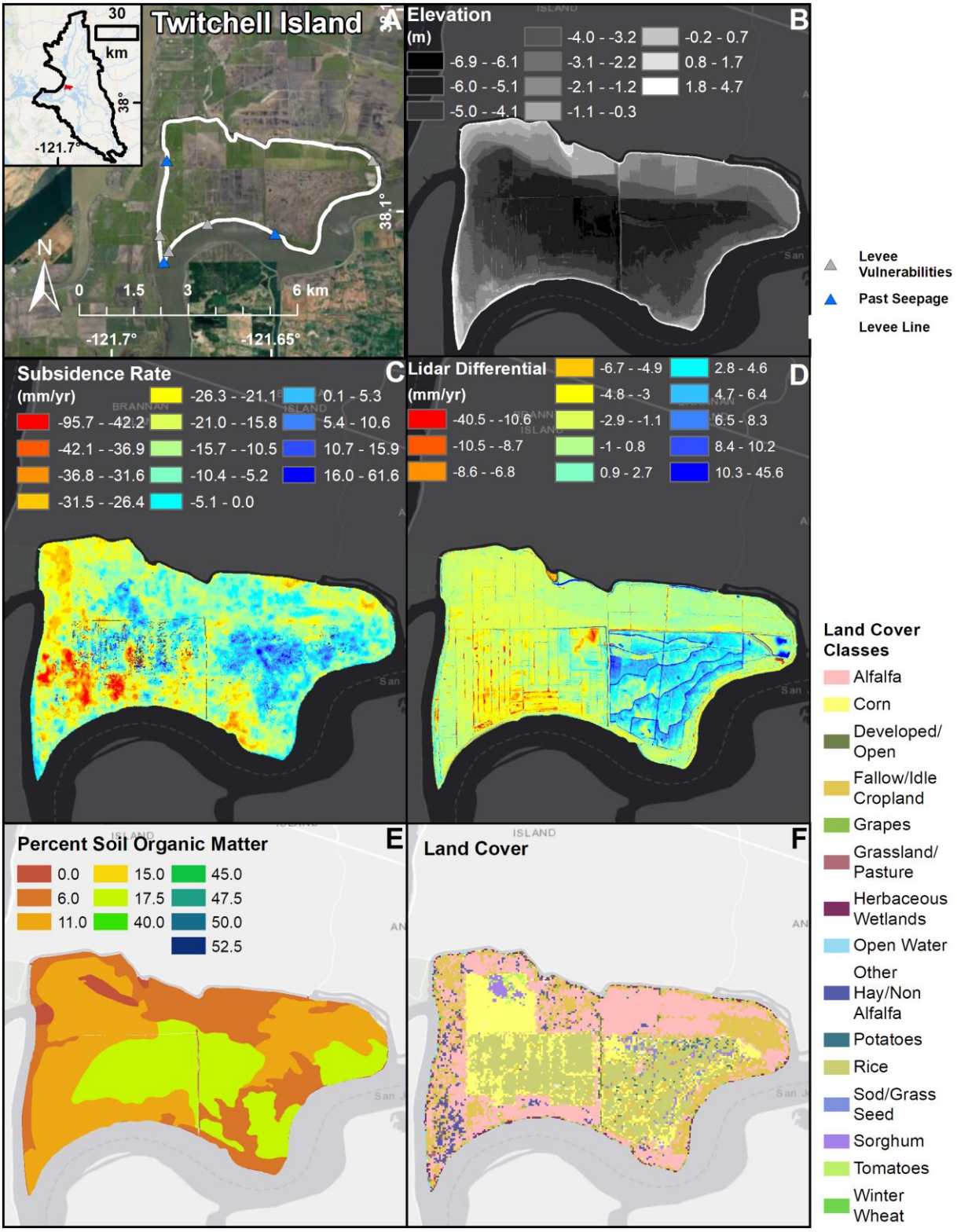

Figure 7: A profile figure for Twitchell Island showing: (A) location of island in Delta and optical imagery from ArcMap basemap with points of interest, (B) elevation in meters, (C)

InSAR derived subsidence rate in mm/yr for 2009-2015, (D) lidar differential in mm/yr for 2007 and 2017, (E) percent soil organic matter, and (F) land cover (legend only shows classes with at least 5 hectares).

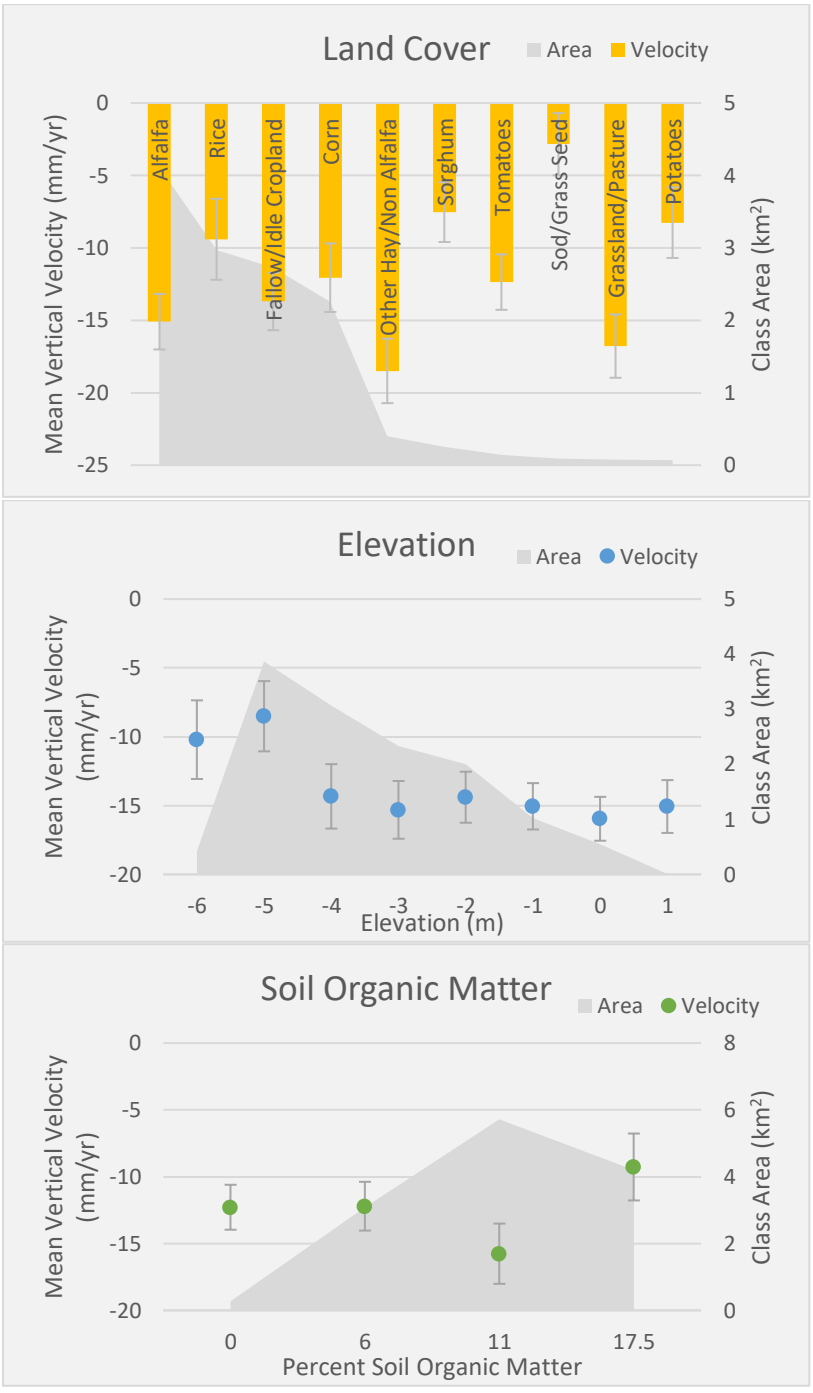

Figure 8: (A) Mean vertical velocity for top ten land cover classes, (B) elevation classes, and (C) soil organic matter classes in Twitchell Island. The area of each class is shown in the dark grey background.

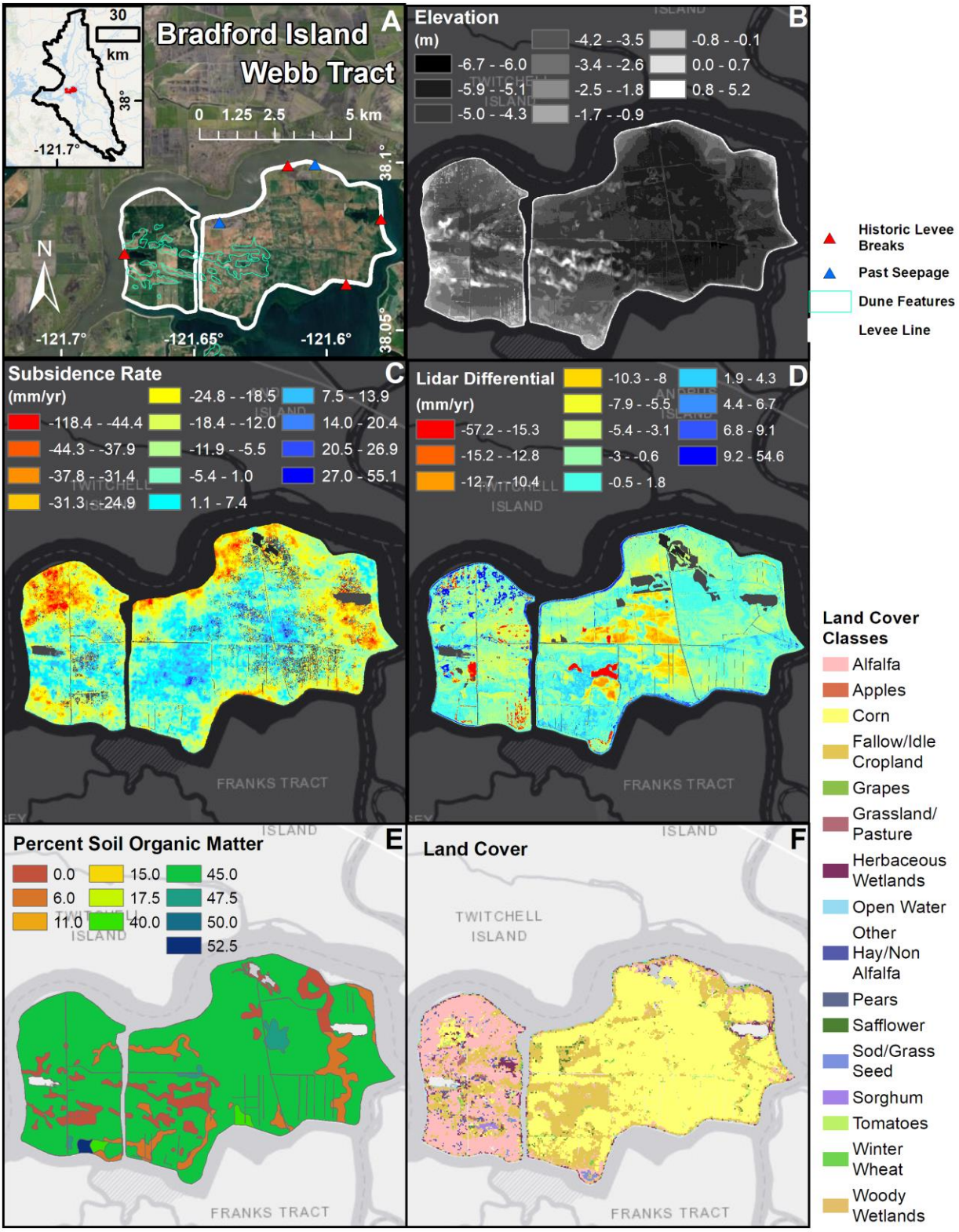

Figure 9: A profile figure for Bradford Island and Webb Tract showing: (A) location of islands in Delta and optical imagery from ArcMap basemap with points of interest, (B) elevation in

meters, (C) InSAR derived subsidence rate in mm/yr for 2009-2015, (D) lidar differential in mm/yr for 2007 and 2017, (E) percent soil organic matter, and (F) land cover (legend only shows classes with at least 5 hectares).

Bradford Island:

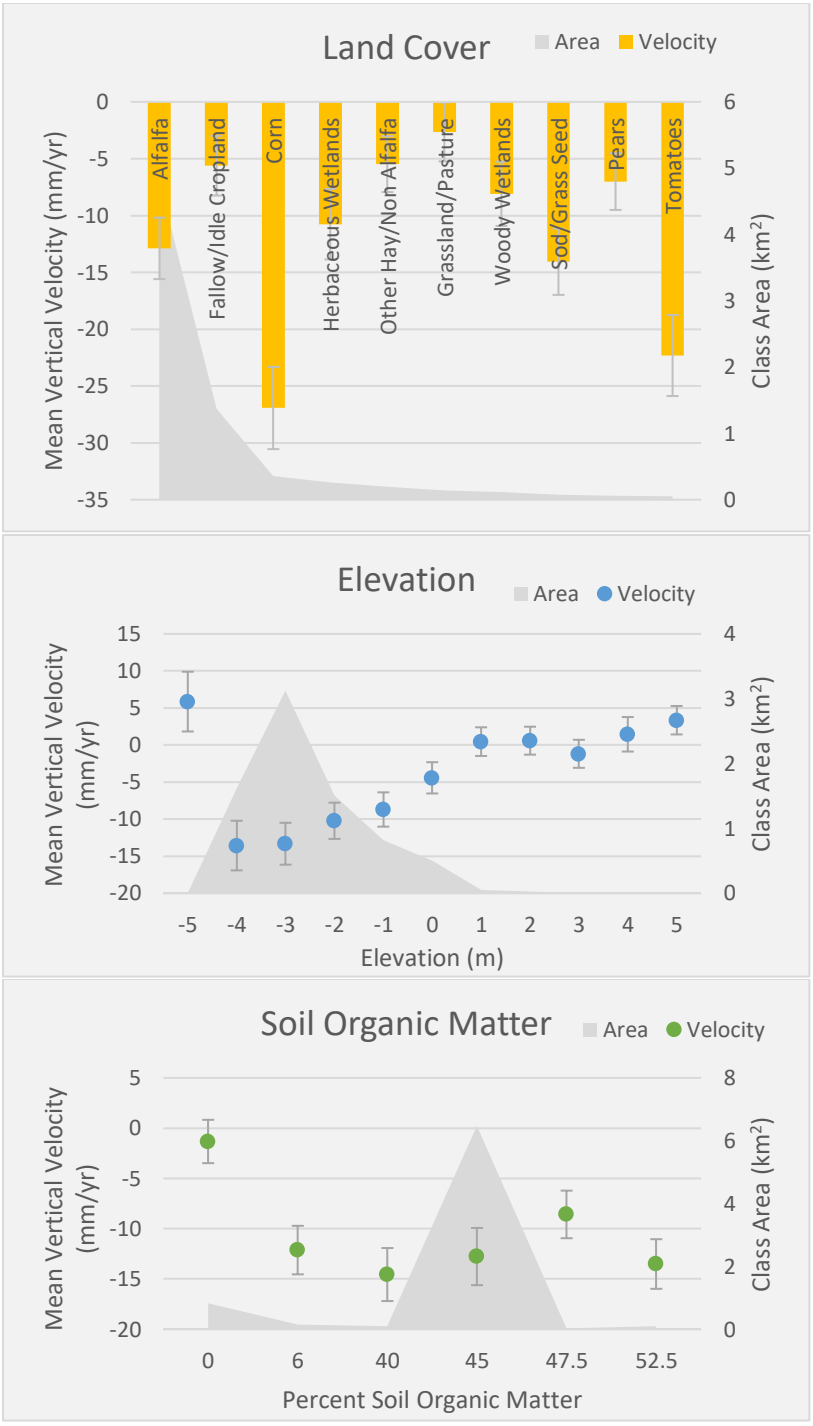

Webb Tract:

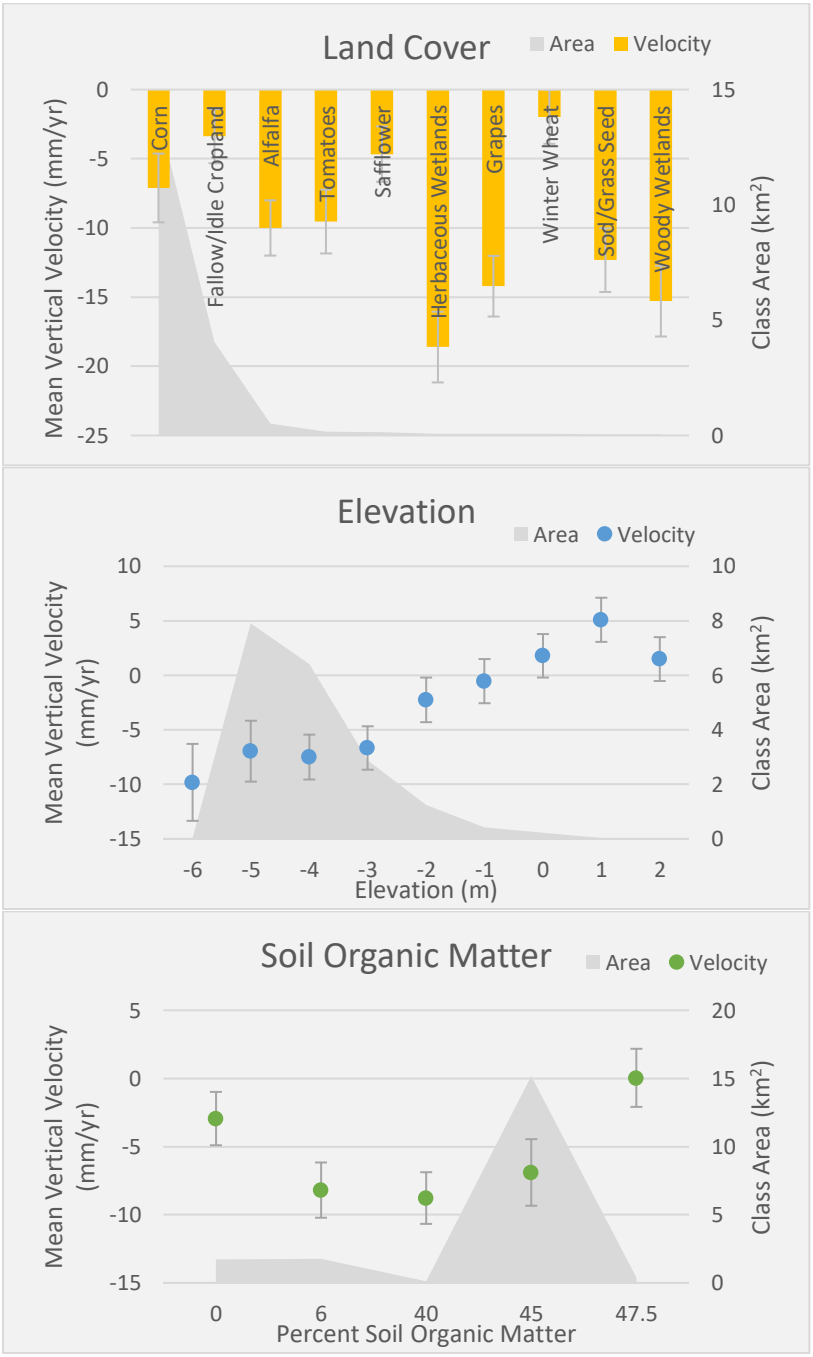

Figure 10: (A) Mean vertical velocity for top ten land cover classes, (B) elevation classes, and (C) soil organic matter classes in Bradford Island. (D) Mean vertical velocity for top ten land cover classes, (E) elevation classes, and (F) soil organic matter classes in Webb Tract. The area of each class is shown in the dark grey background.

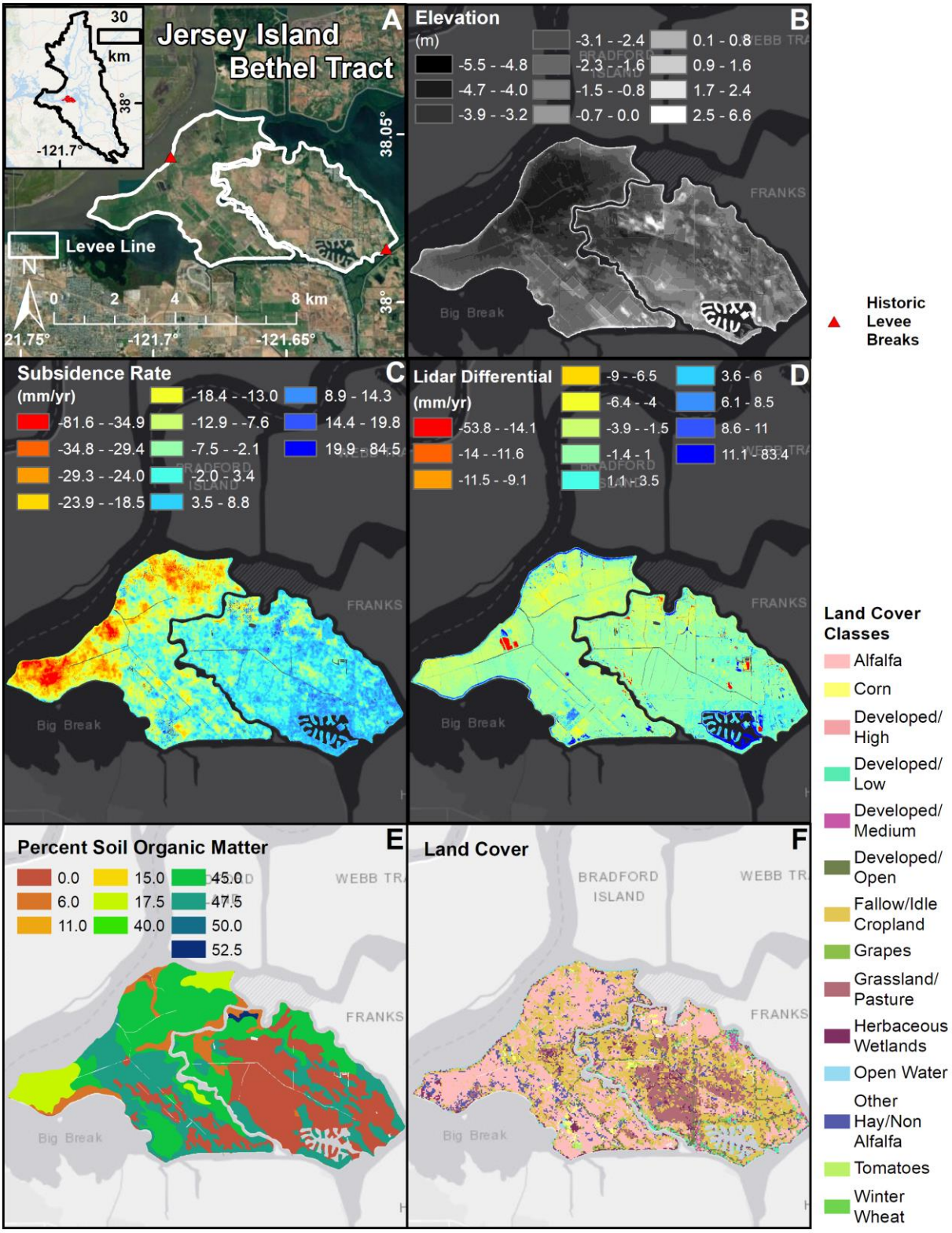

Figure 11: A profile figure for Jersey Island and Bethel Tract showing: (A) location of islands in Delta and optical imagery from ArcMap basemap with points of interest, (B) elevation in meters,

(C) InSAR derived subsidence rate in mm/yr for 2009-2015, (D) lidar differential in mm/yr for 2007 and 2017, (E) percent soil organic matter, and (F) land cover (legend only shows classes with at least 5 hectares).

Jersey Island:

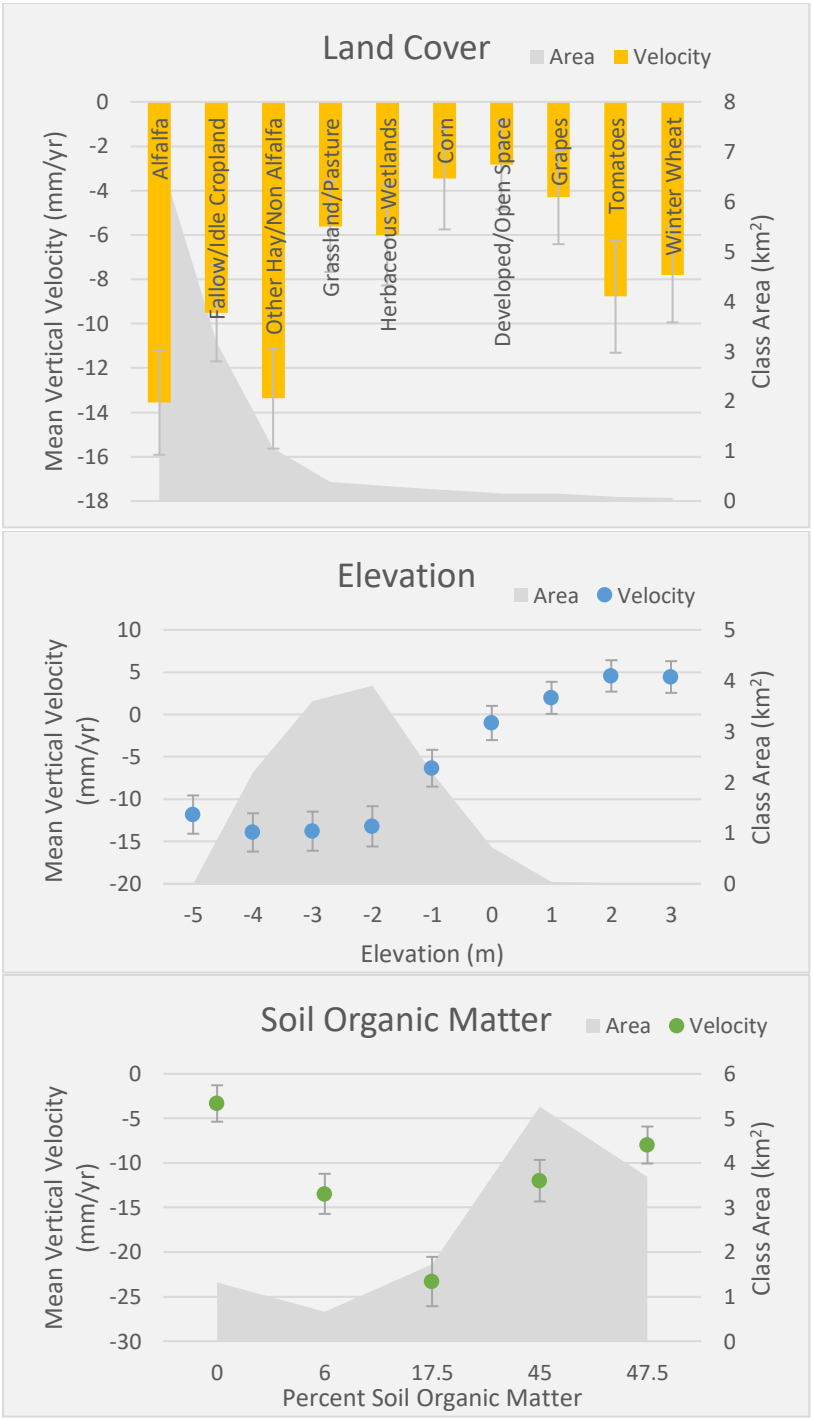

Bethel Tract:

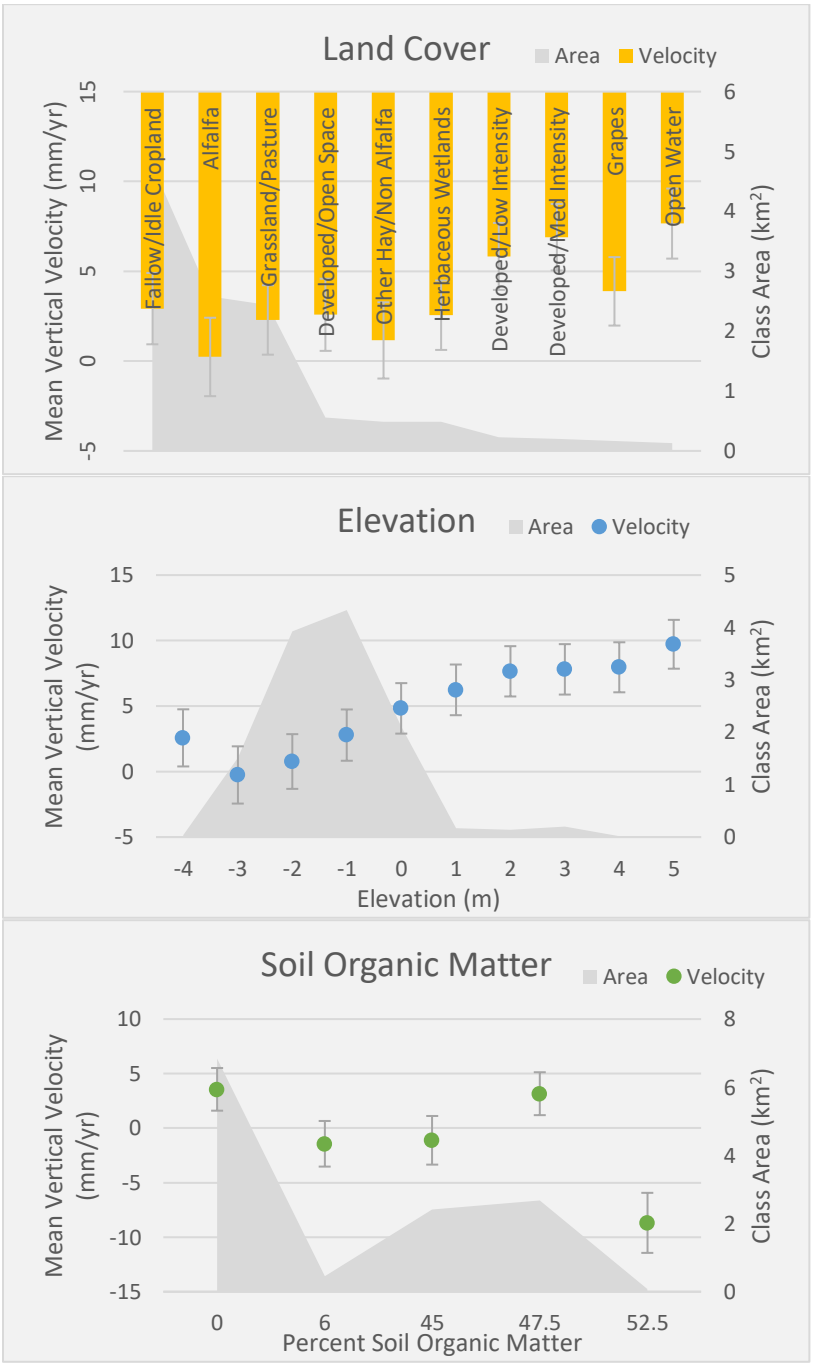

Figure 12: (A) Mean vertical velocity for top ten land cover classes, (B) elevation classes, and (C) soil organic matter classes in Jersey Island. (D) Mean vertical velocity for top ten land cover classes, (E) elevation classes, and (F) soil organic matter classes in Bethel Tract. The area of each class is shown in the dark grey background.

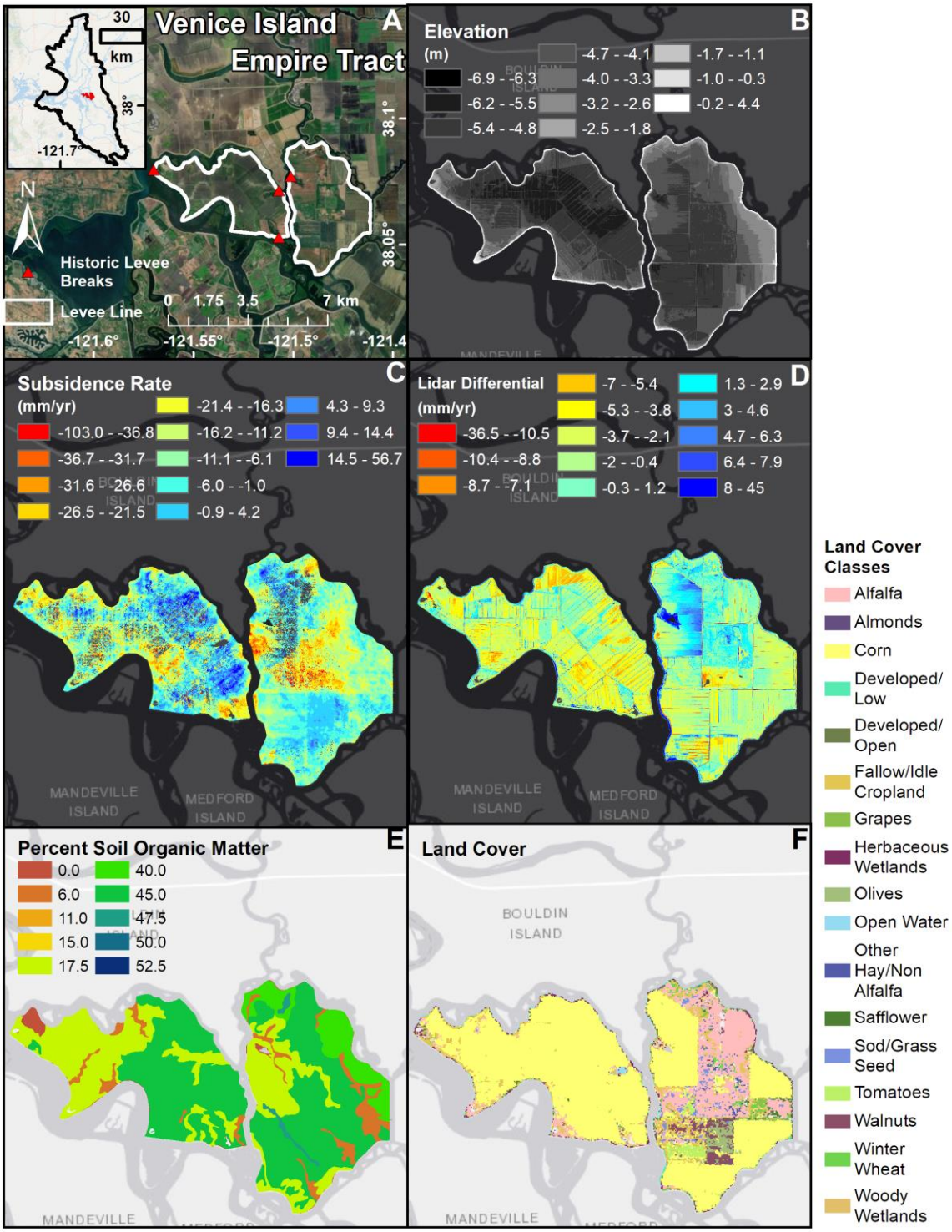

Figure 13: A profile figure for Venice Island and Empire Tract showing: (A) location of islands in Delta and optical imagery from ArcMap basemap with points of interest, (B) elevation in meters, (C) InSAR derived subsidence rate in mm/yr for 2009-2015, (D) lidar differential in mm/yr for 2007 and 2017, (E) percent soil organic matter, and (F) land cover (legend only shows classes with at least 5 hectares).

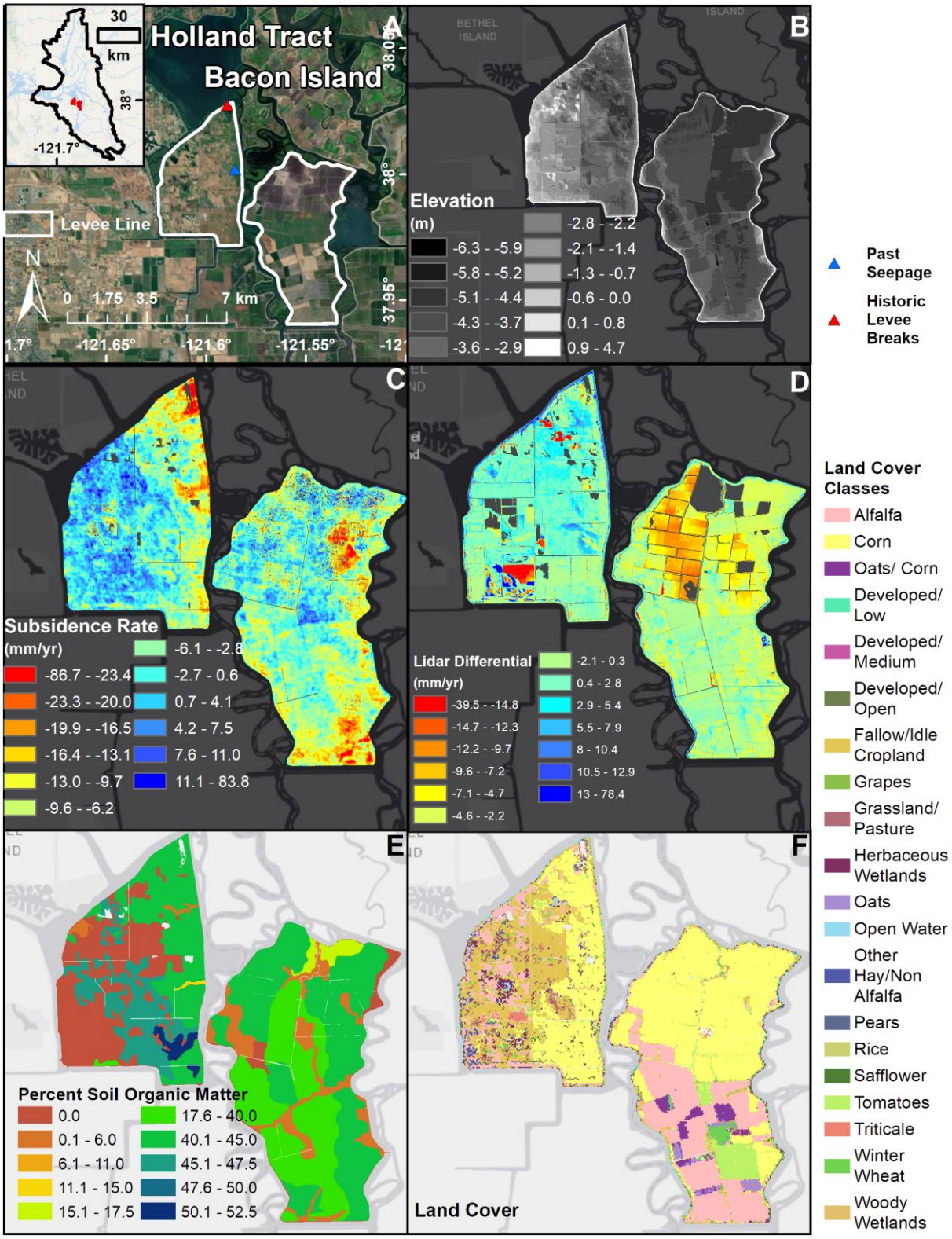

Figure 14: A profile figure for Holland Tract and Bacon Island showing: (A) location of islands in Delta and optical imagery from ArcMap basemap with points of interest, (B) elevation in

meters, (C) InSAR derived subsidence rate in mm/yr for 2009-2015, (D) lidar differential in mm/yr for 2007 and 2017, (E) percent soil organic matter, and (F) land cover (legend only shows classes with at least 5 hectares).

Holland Tract:

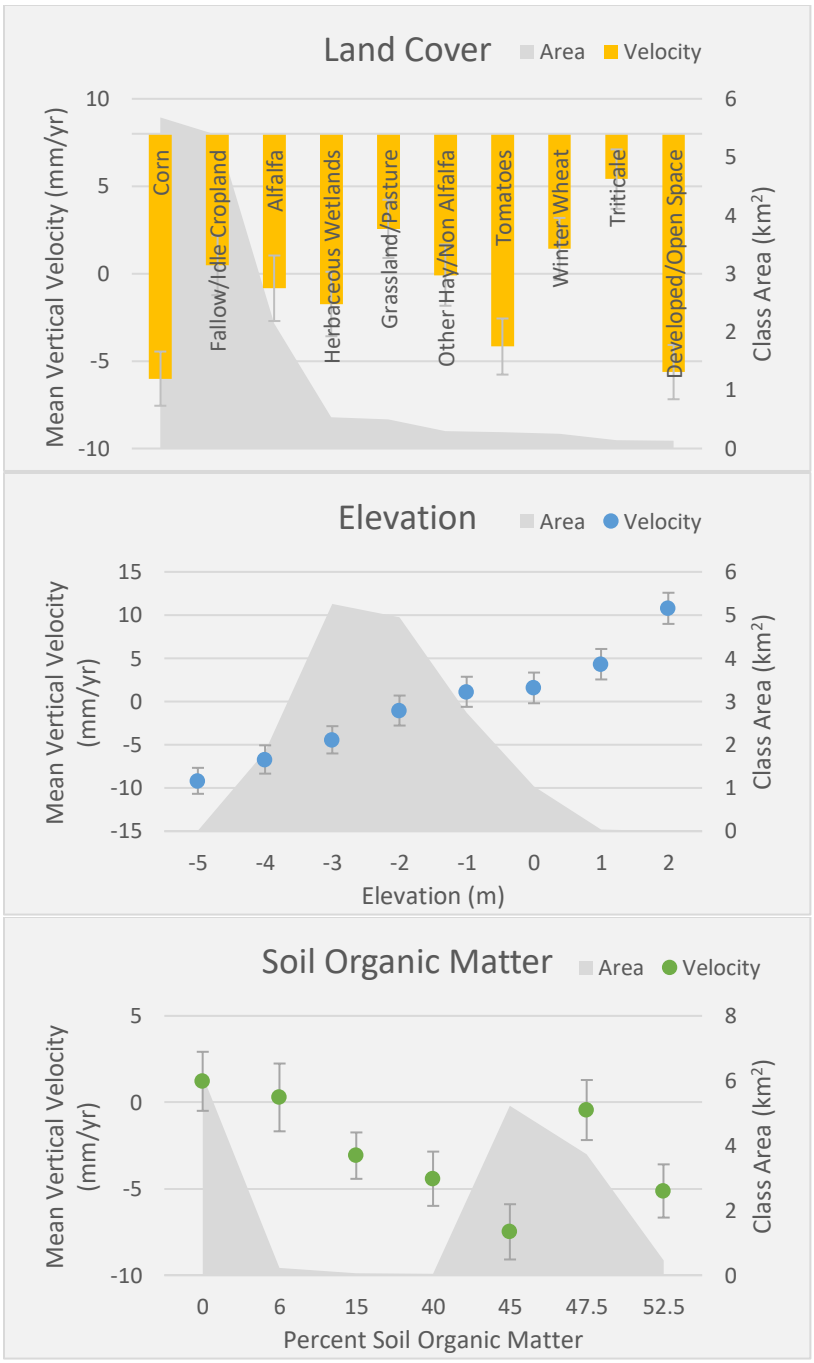

Bacon Island:

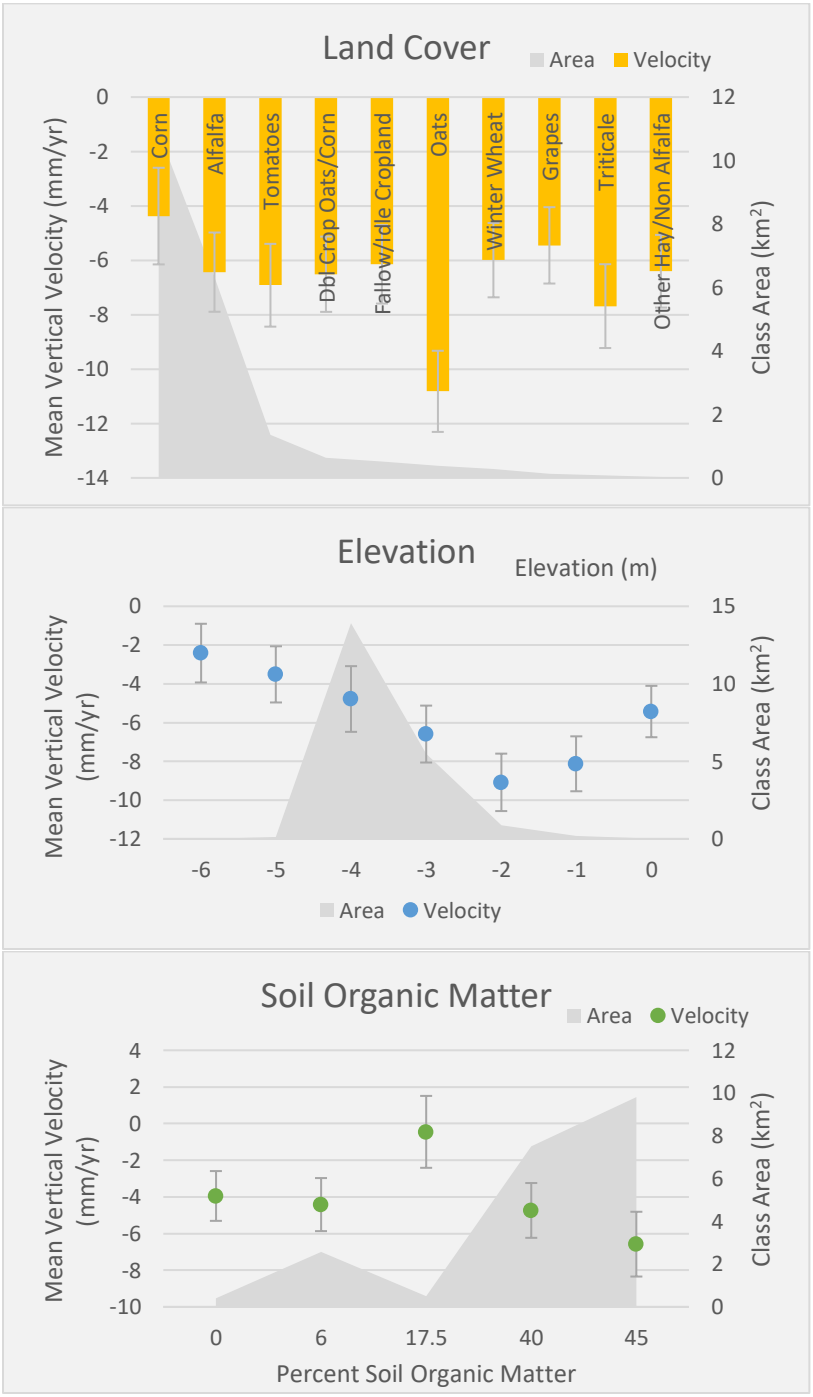

Figure 15: (A) Mean vertical velocity for top ten land cover classes, (B) elevation classes, and (C) soil organic matter classes in Holland Tract. (D) Mean vertical velocity for top ten land cover classes, (E) elevation classes, and (F) soil organic matter classes in Bacon Island. The area of each class is shown in the dark grey background.

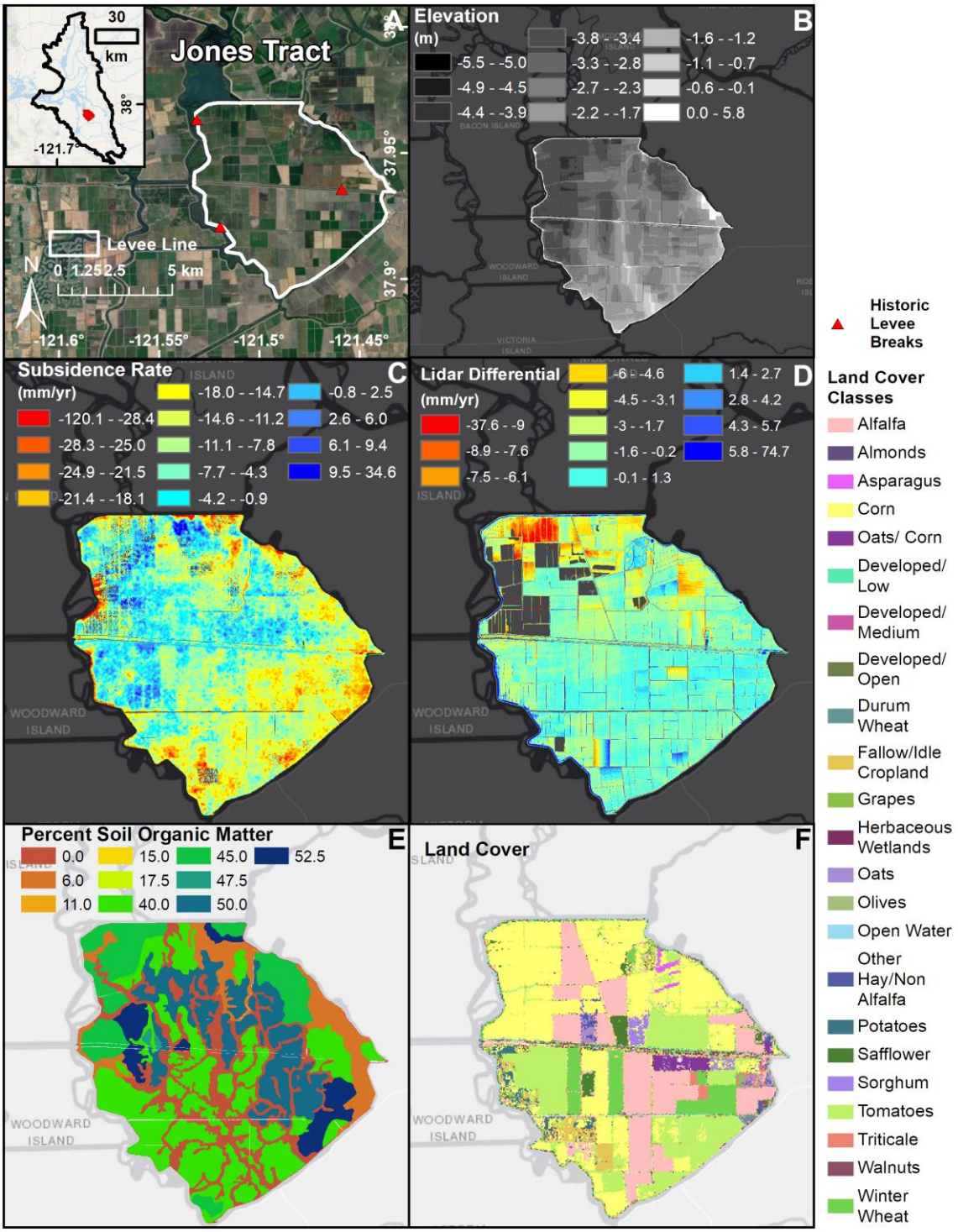

Figure 16: A profile figure for Jones Tract showing: (A) location of island in Delta and optical imagery from ArcMap basemap with points of interest, (B) elevation in meters, (C) InSAR derived subsidence rate in mm/yr for 2009-2015, (D) lidar differential in mm/yr for 2007 and 2017, (E) percent soil organic matter, and (F) land cover (legend only shows classes with at least 5 hectares).

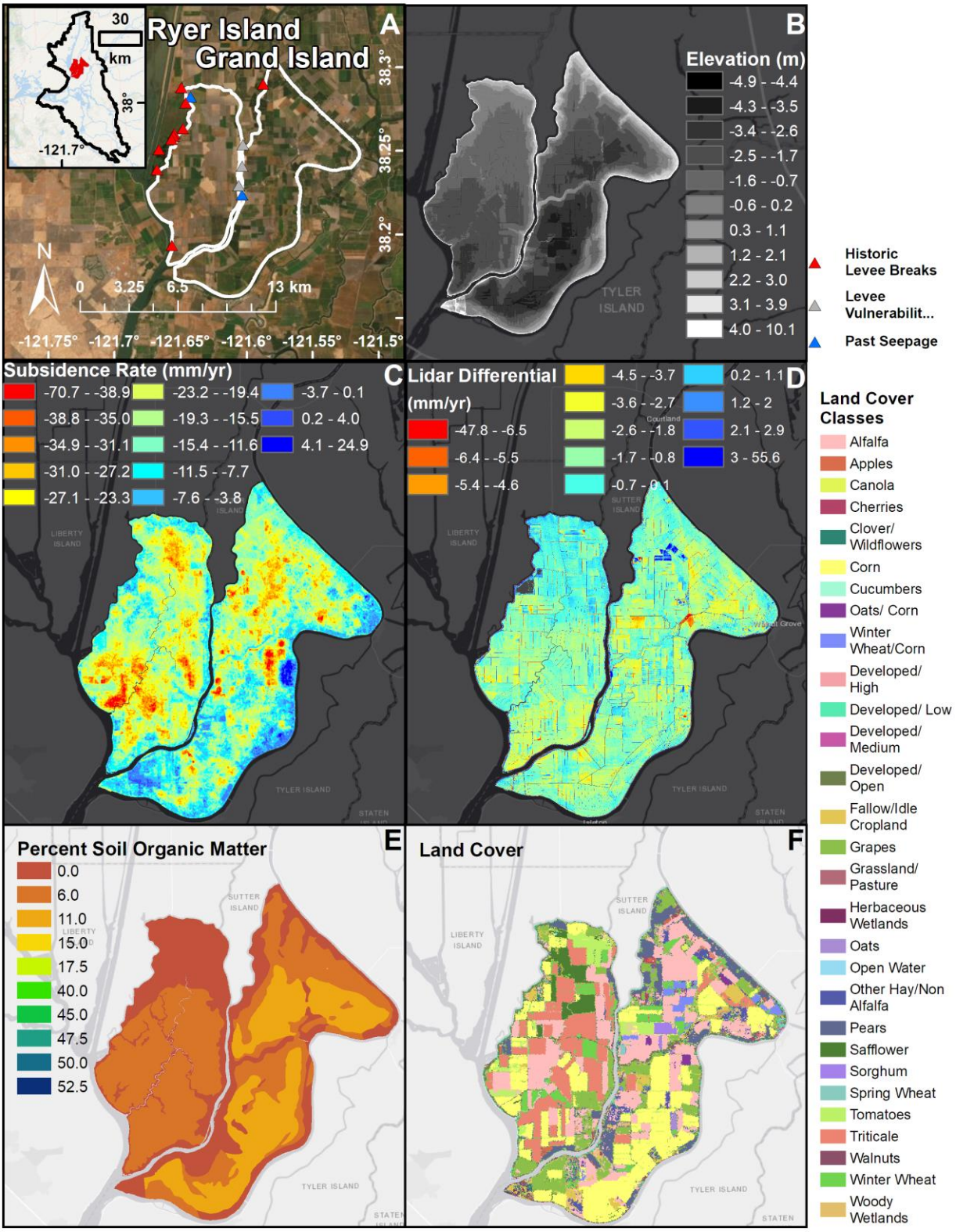

Figure 17: A profile figure for Ryer Island and Grand Island showing: (A) location of islands in Delta and optical imagery from ArcMap basemap with points of interest, (B) elevation in meters,

(C) InSAR derived subsidence rate in mm/yr for 2009-2015, (D) lidar differential in mm/yr for 2007 and 2017, (E) percent soil organic matter, and (F) land cover (legend only shows classes with at least 5 hectares).

Ryer Island:

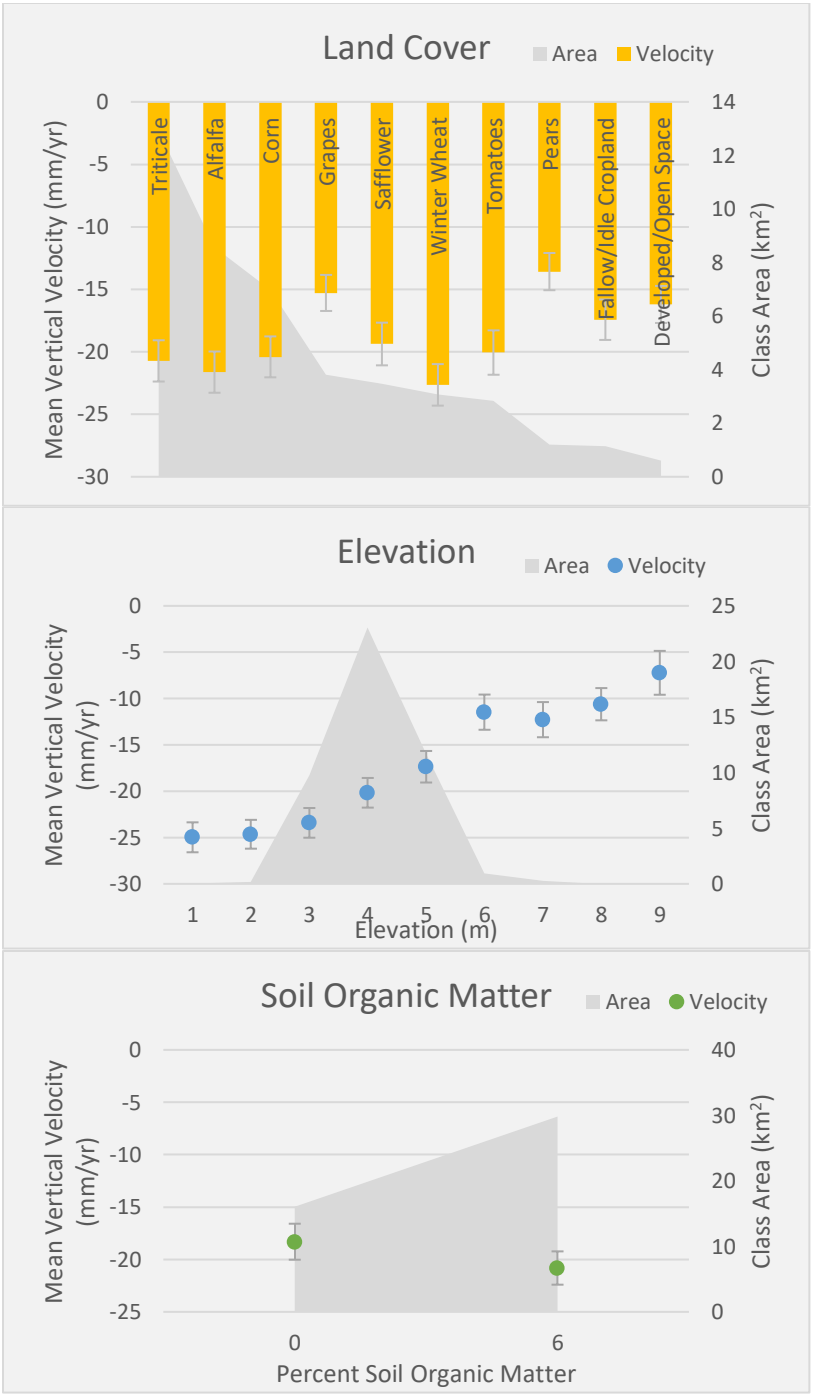

Grand Island:

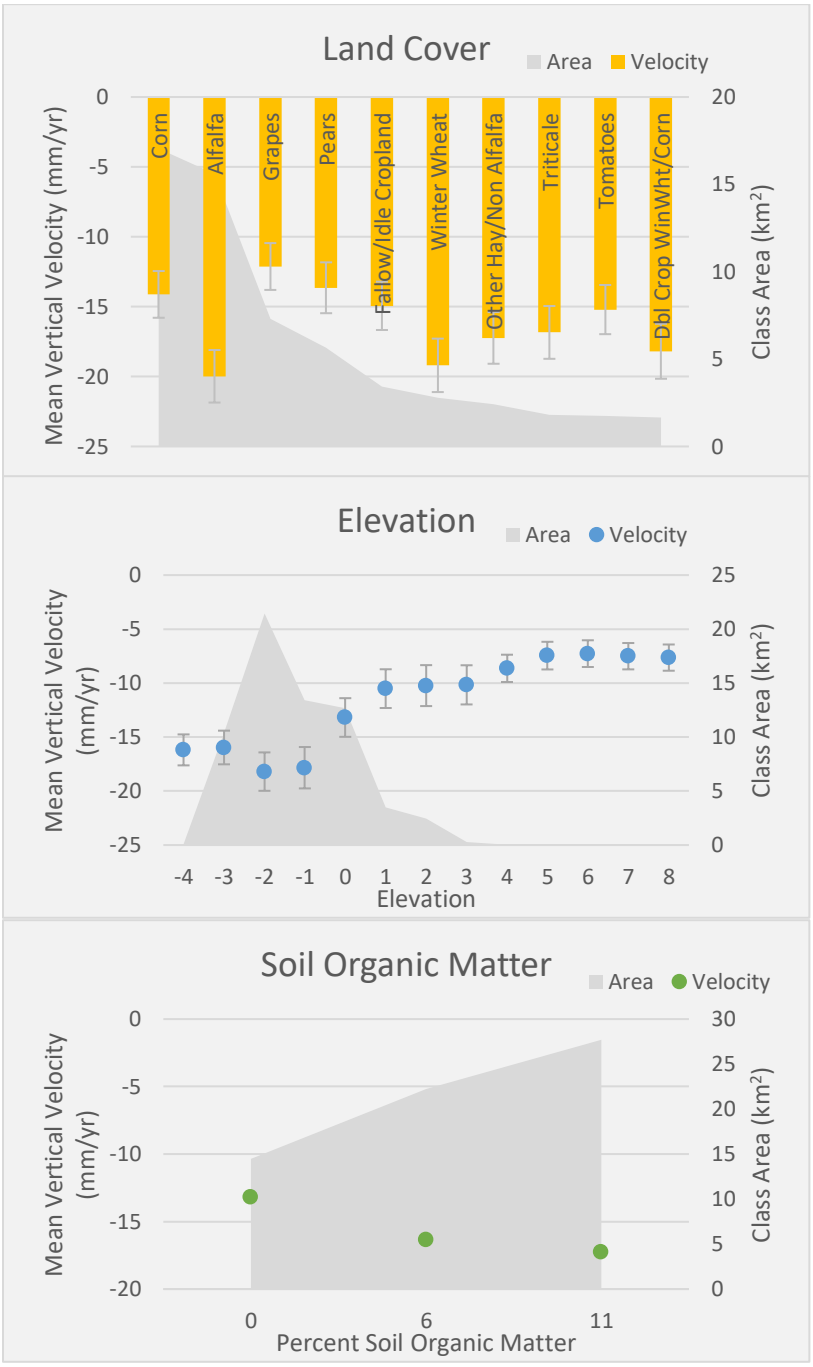

Figure 18: (A) Mean vertical velocity for top ten land cover classes, (B) elevation classes, and (C) soil organic matter classes in Ryer Island. (D) Mean vertical velocity for top ten land cover classes, (E) elevation classes, and (F) soil organic matter classes in Grand Island. The area of each class is shown in the dark grey background.

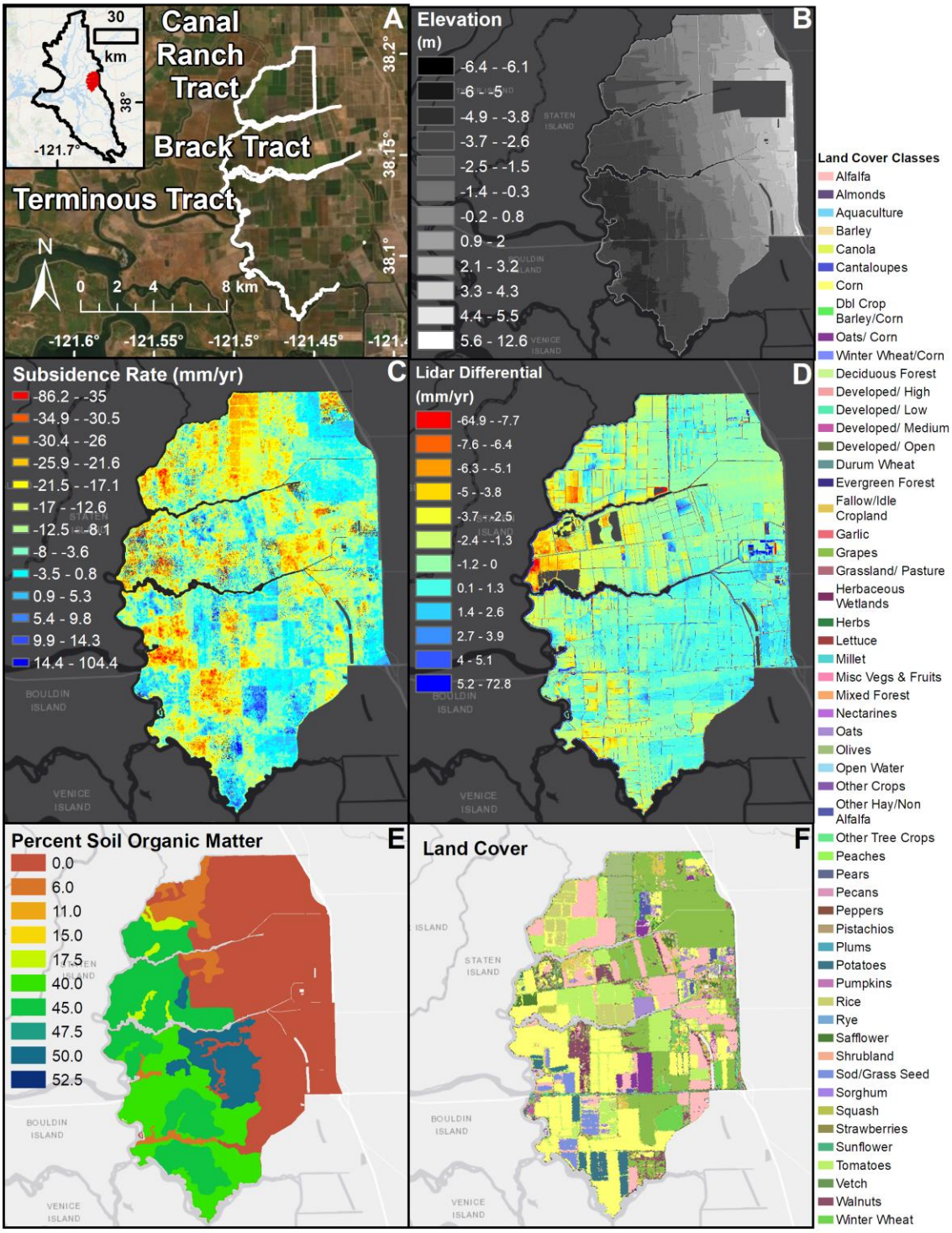

Figure 19: A profile figure for Canal Ranch Tract, Brack Tract, and Terminous Tract showing: (A) location of islands in Delta and optical imagery from ArcMap basemap with points of interest, (B) elevation in meters, (C) InSAR derived subsidence rate in mm/yr for 2009-2015, (D) lidar differential in mm/yr for 2007 and 2017, (E) percent soil organic matter, and (F) land cover (legend only shows classes with at least 5 hectares).

Supplementary Figures

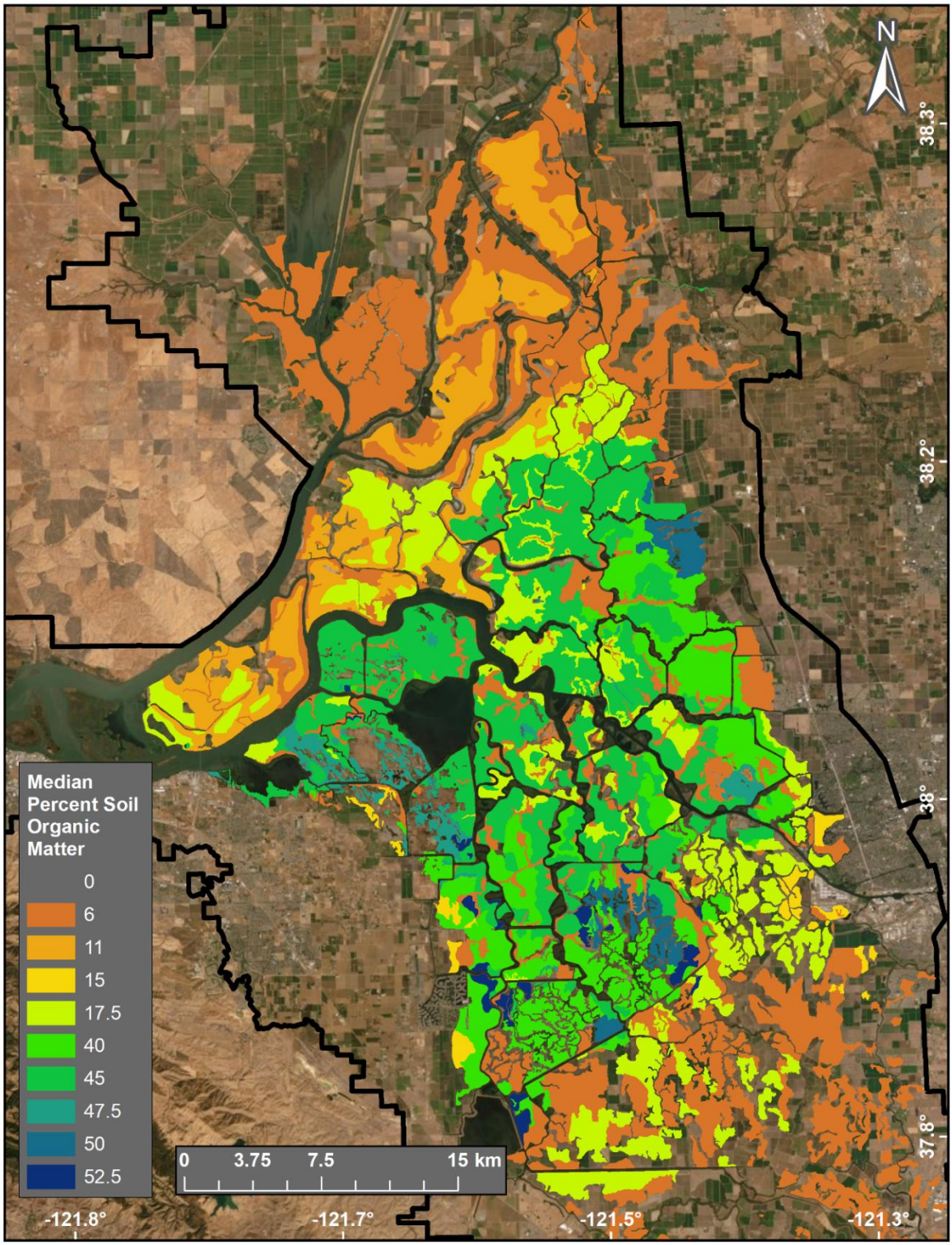

Figure S1: Median percent soil organic matter data provided by Deverel and Leighton (2010), based on SSURGO (Soil Survey Geographic Database) from the NRCS (Natural Resources Conservation Service).

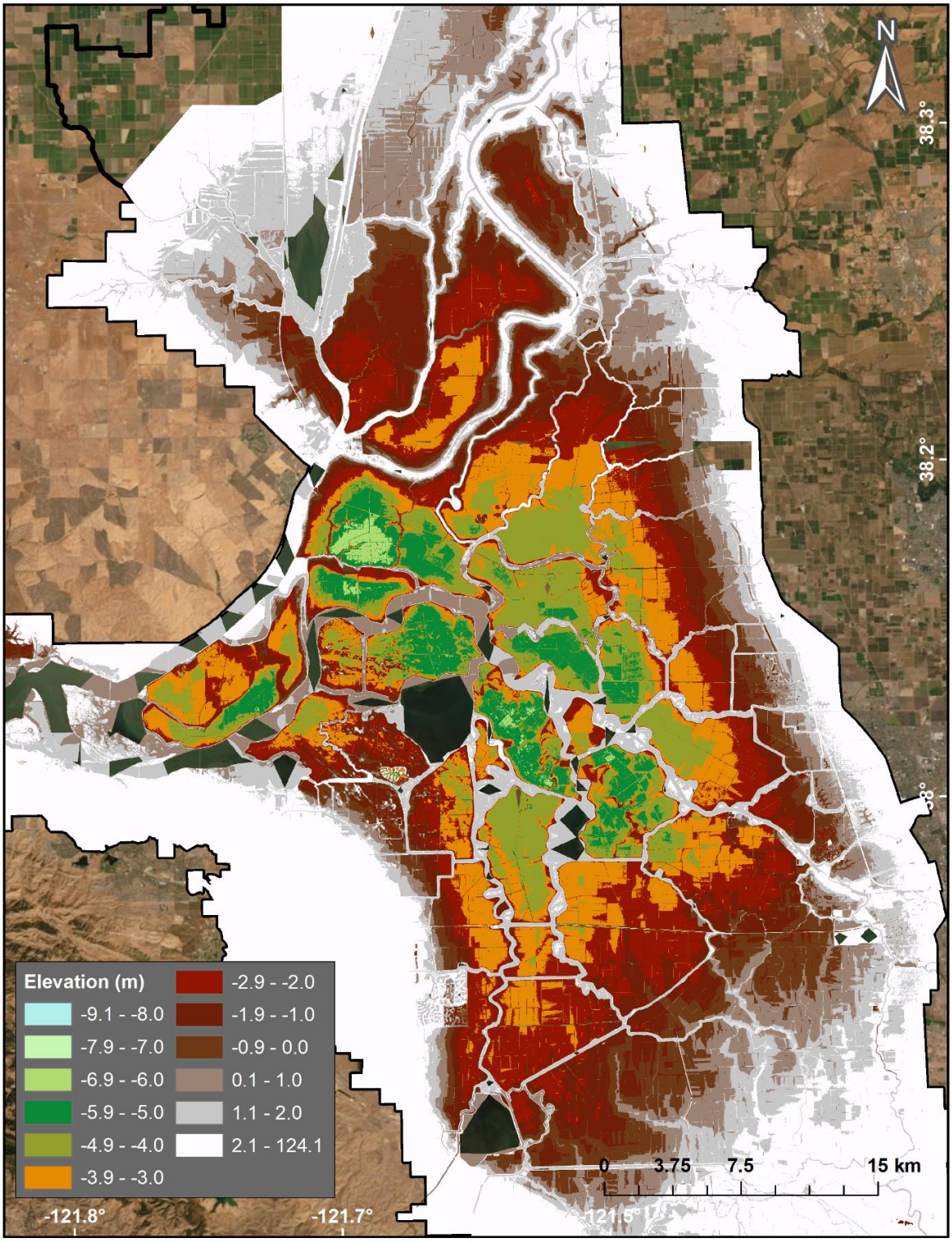

Figure S2: Lidar DEM showing elevation in meters from a land-use survey conducted by DWR in 2007. Elevation was collected in at 1-meter spacings using vertical datum NAVD88, geoid model Geoid03 Continental US, and ellipsoid GRS-80.

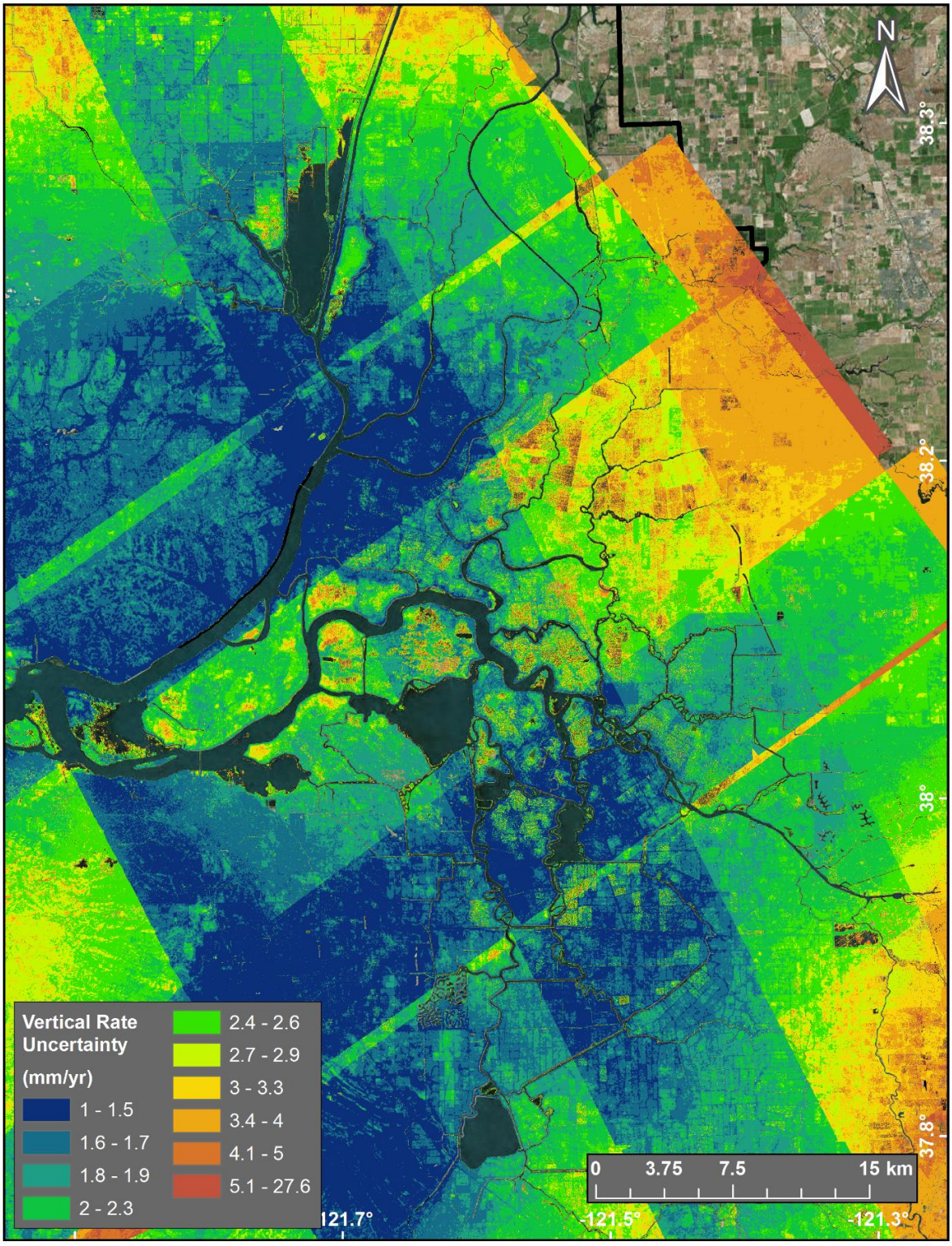

Figure S3: The uncertainty values for the vertical velocity rates in millimeters per year, with blue/green areas showing the least uncertainty.

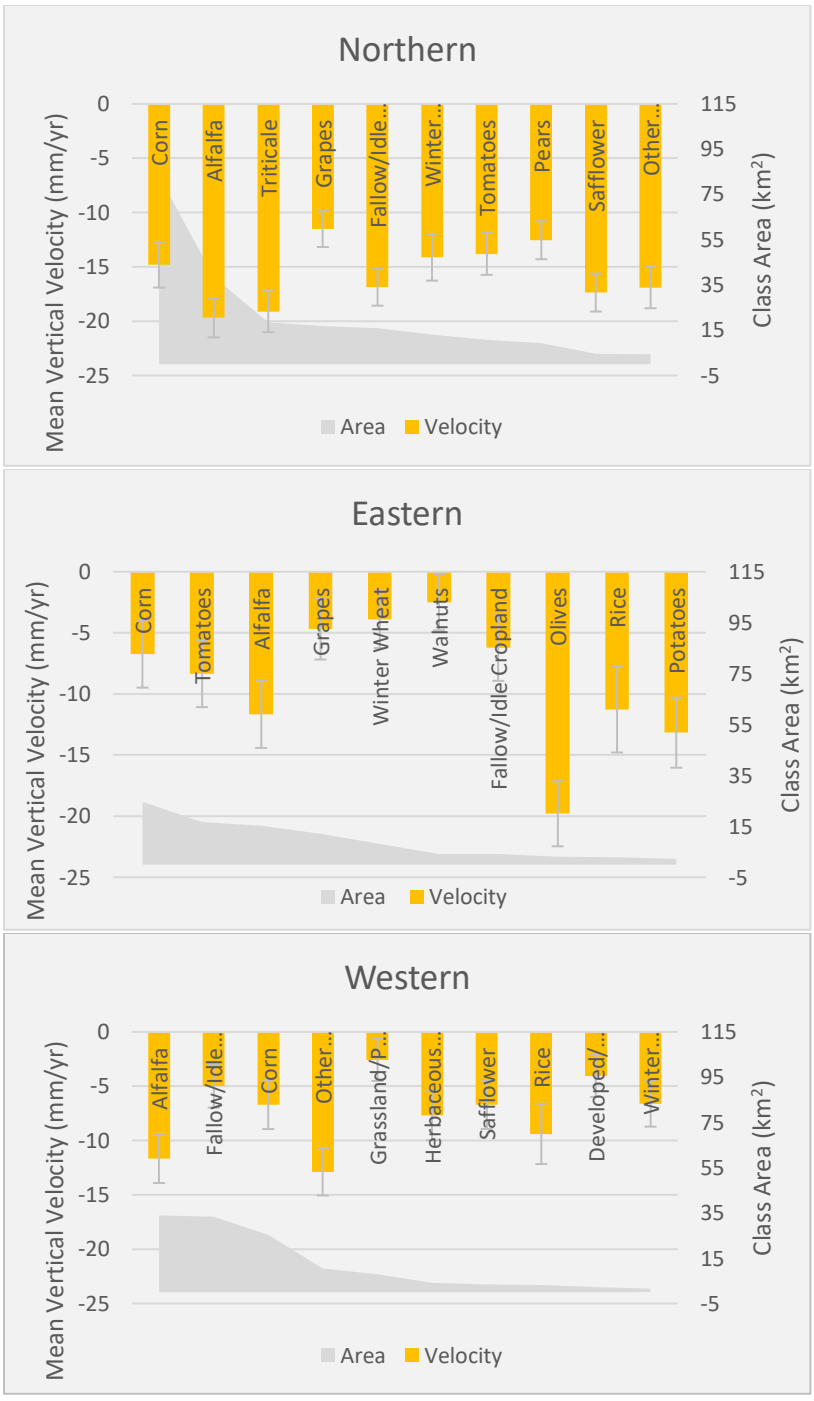
Northern
Mean Vertical Velocity (mm/yr)
0
-5
-10
-15
-20
-25
Class Area (km²)
115
95
75
55
35
15
-5
Corn
Alfalfa
Triticale
Grapes
Fallow/Idle...
Winter...
Tomatoes
Pears
Safflower
Other...
Area
Velocity
Eastern
Mean Vertical Velocity (mm/yr)
Class Area (km²)
Corn
Tomatoes
Alfalfa
Grapes
Winter Wheat
Walnuts
Fallow/Idle Cropland
Olives
Rice
Potatoes
Area
Velocity
Western
Mean Vertical Velocity (mm/yr)
Class Area (km²)
Alfalfa
Fallow/Idle...
Corn
Other...
Grassland/P...
Herbaceous...
Safflower
Rice
Developed/...
Winter...
Area
Velocity

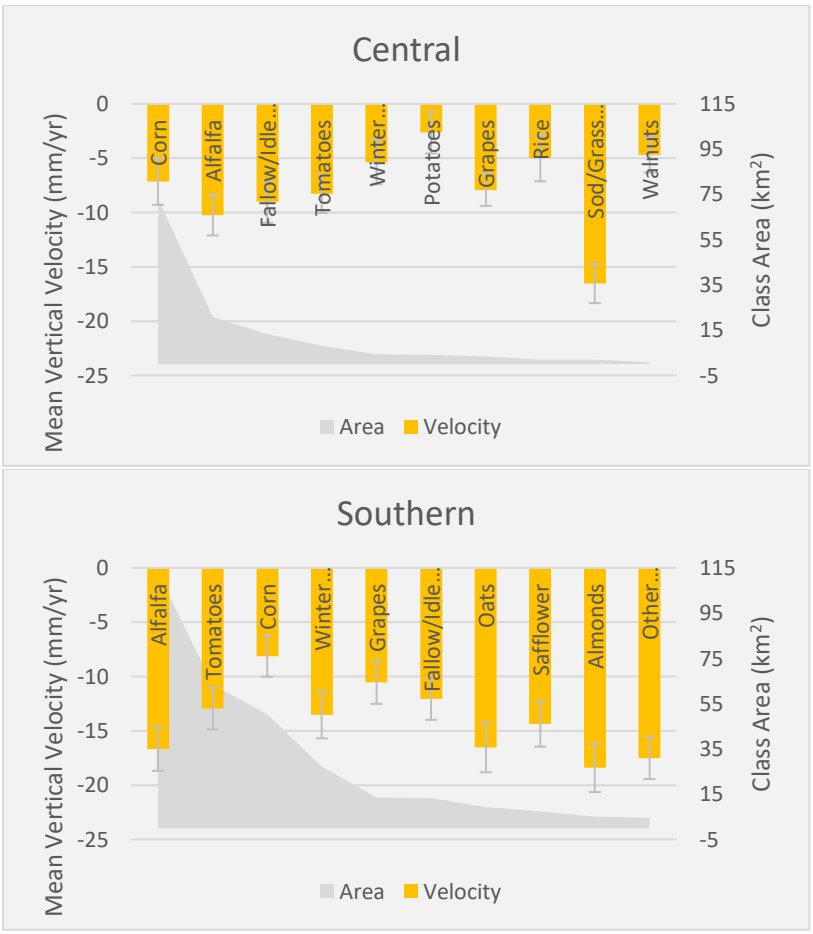

Figure S4: (A) Mean vertical velocity for the top ten land cover classes in the northern, (B) eastern, (C) western, (D) central, and (E) southern Delta. The area of each class is shown in the dark grey background.

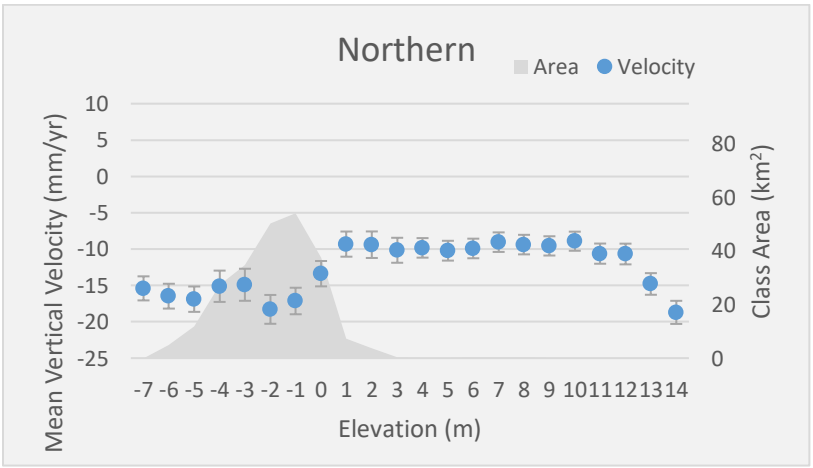

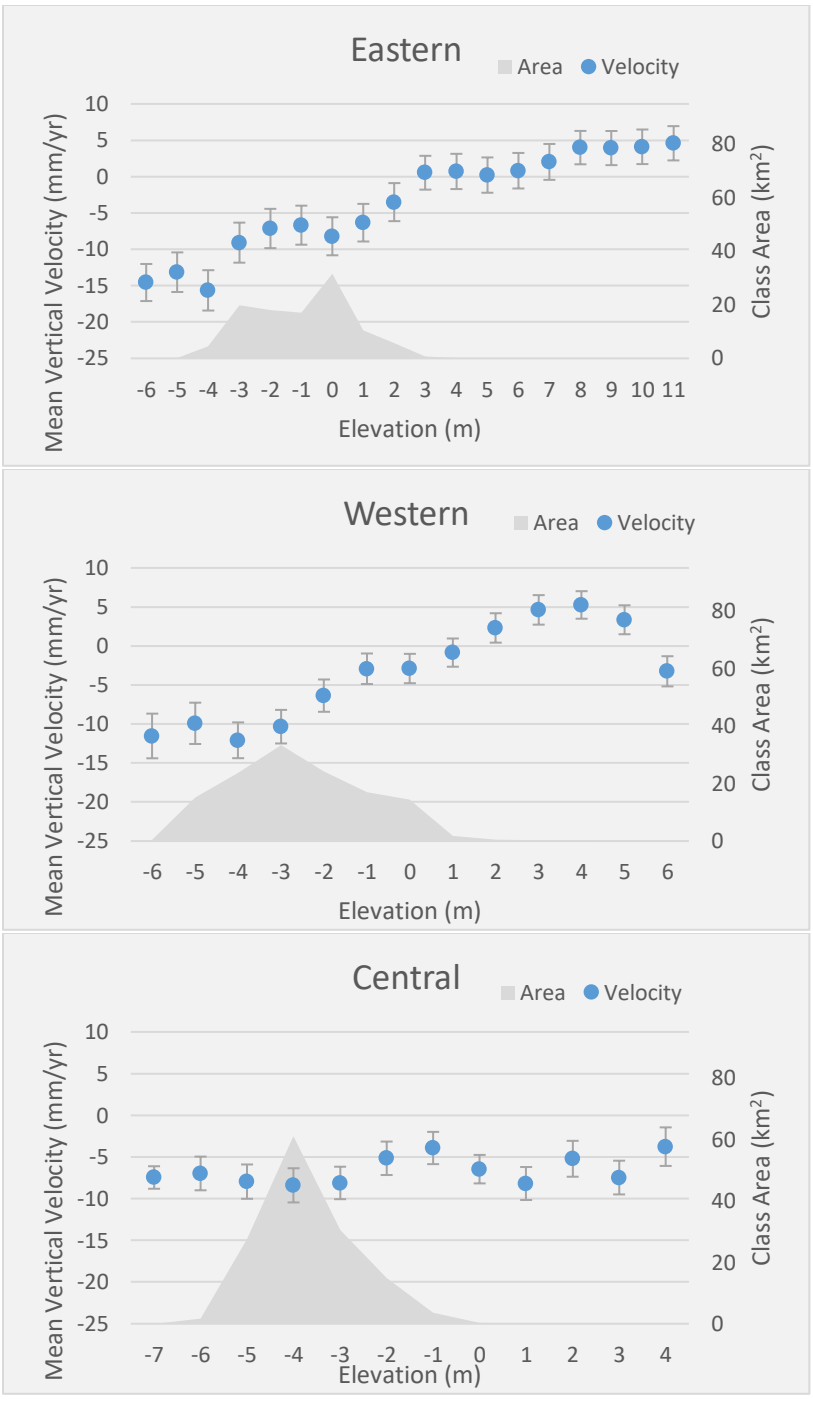
Eastern
Area
Velocity
Mean Vertical Velocity (mm/yr)
Class Area (km²)
Elevation (m)
Western
Area
Velocity
Mean Vertical Velocity (mm/yr)
Class Area (km²)
Elevation (m)
Central
Area
Velocity
Mean Vertical Velocity (mm/yr)
Class Area (km²)
Elevation (m)

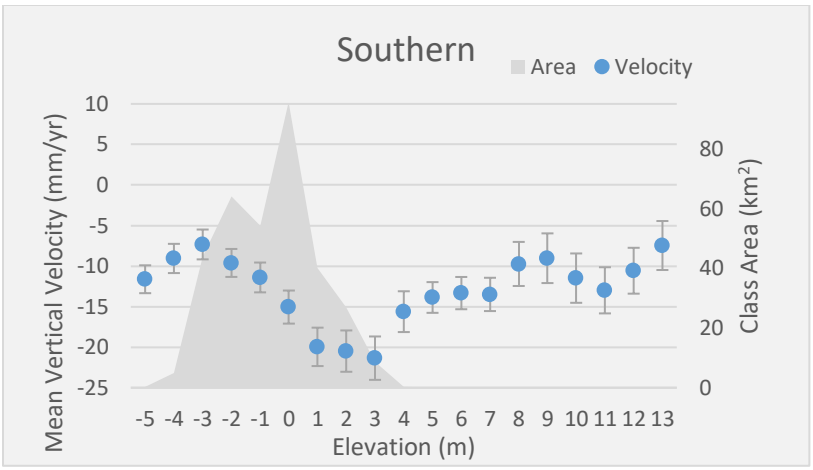

Figure S5: (A) Mean vertical velocity for elevation classes in the northern, (B) eastern, (C) western, (D) central, and (E) southern Delta. The area of each class is shown in the dark grey background.

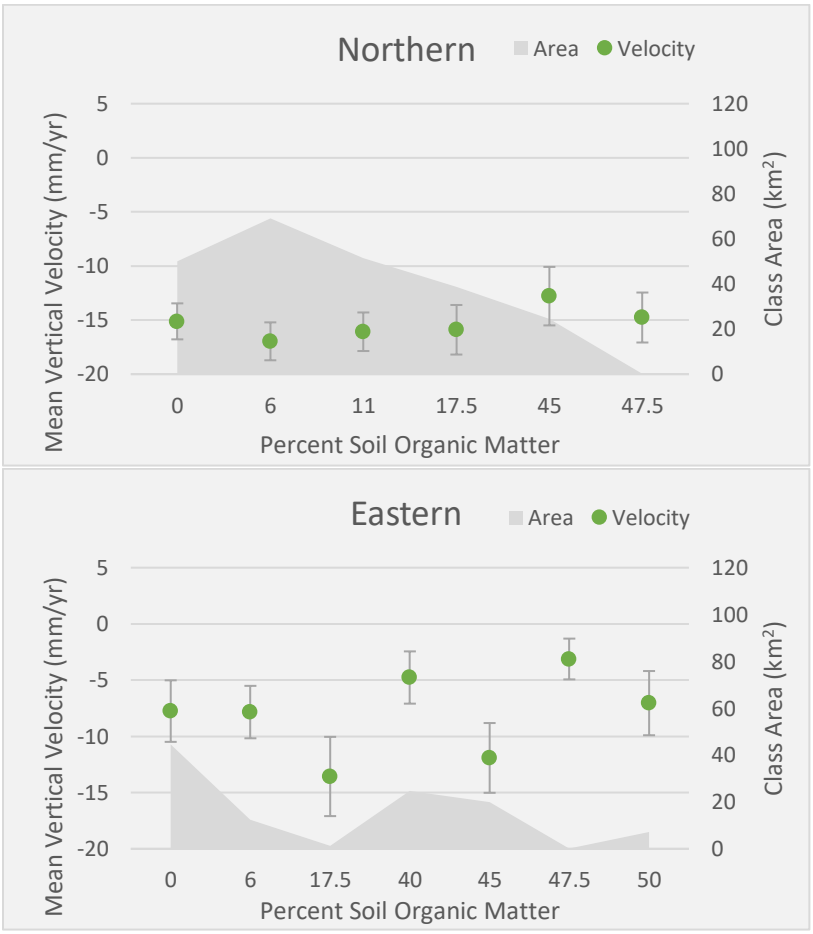

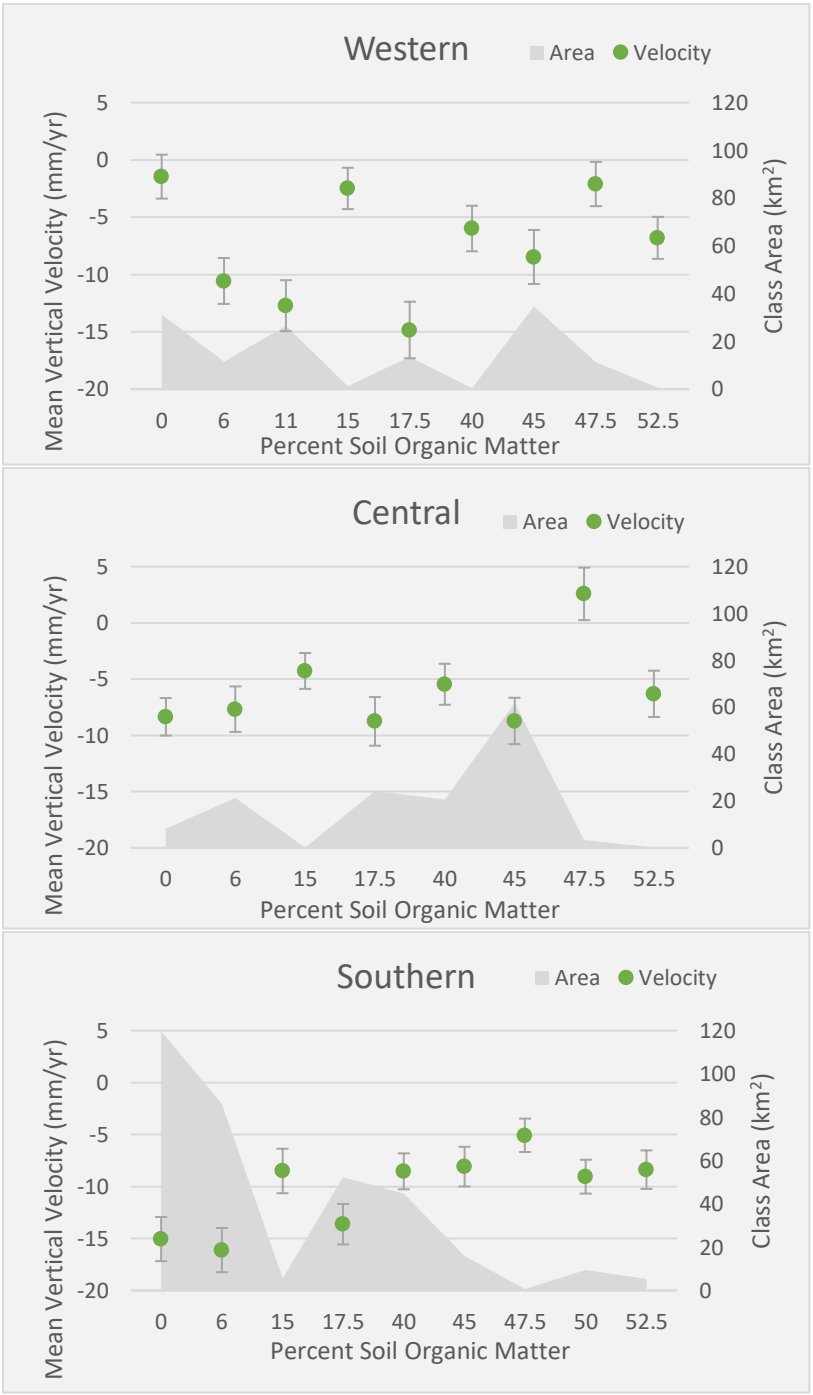

Figure S6: (A) Mean vertical velocity for soil organic matter classes in the northern, (B) eastern, (C) western, (D) central, and (E) southern Delta. The area of each class is shown in the dark grey background.

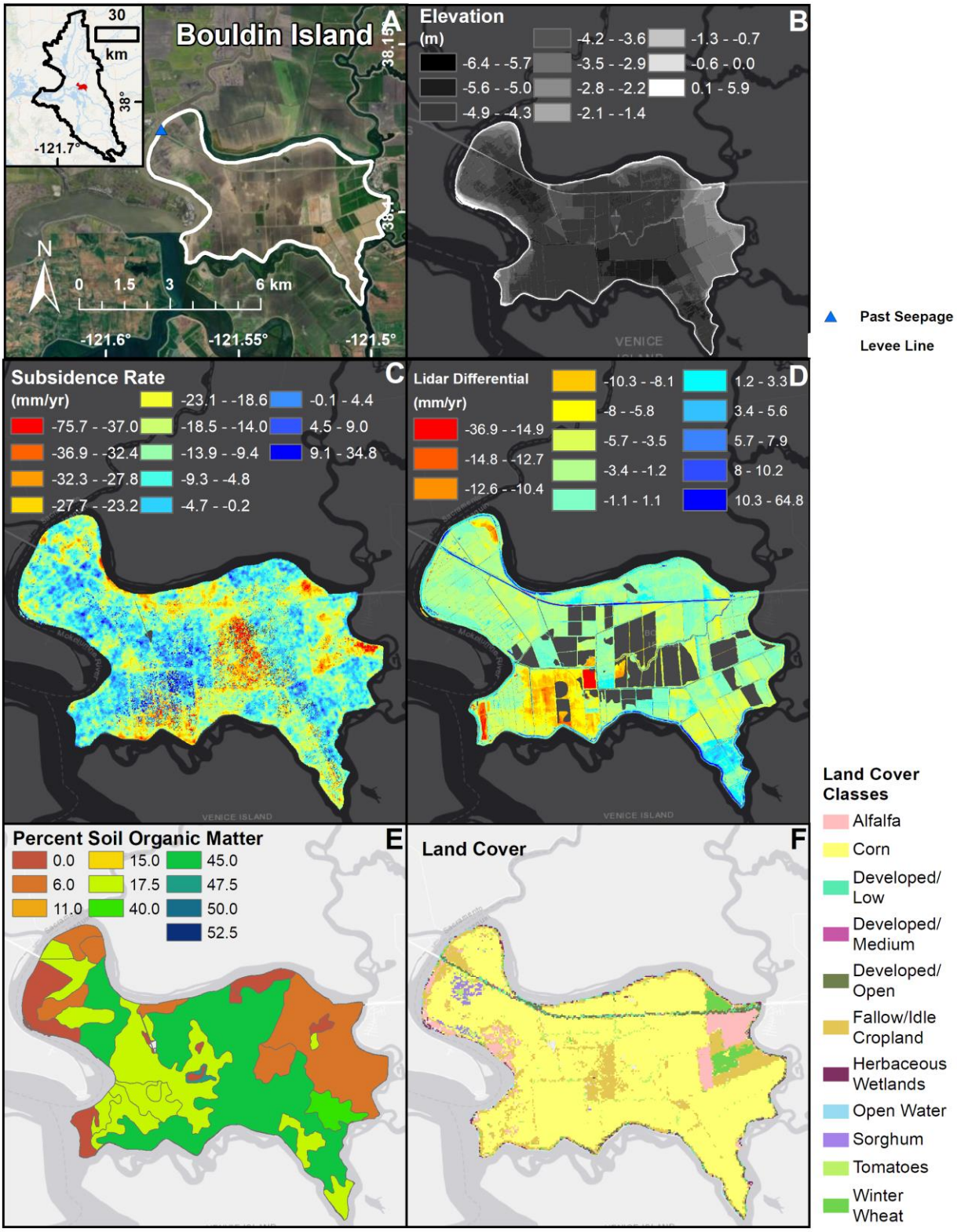

Figure S7: A profile figure for Bouldin Island showing: (A) location of island in Delta and optical imagery from ArcMap basemap with points of interest, (B) elevation in meters, (C)

InSAR derived subsidence rate in mm/yr for 2009-2015, (D) lidar differential in mm/yr for 2007 and 2017, (E) percent soil organic matter, and (F) land cover (legend only shows classes with at least 5 hectares).

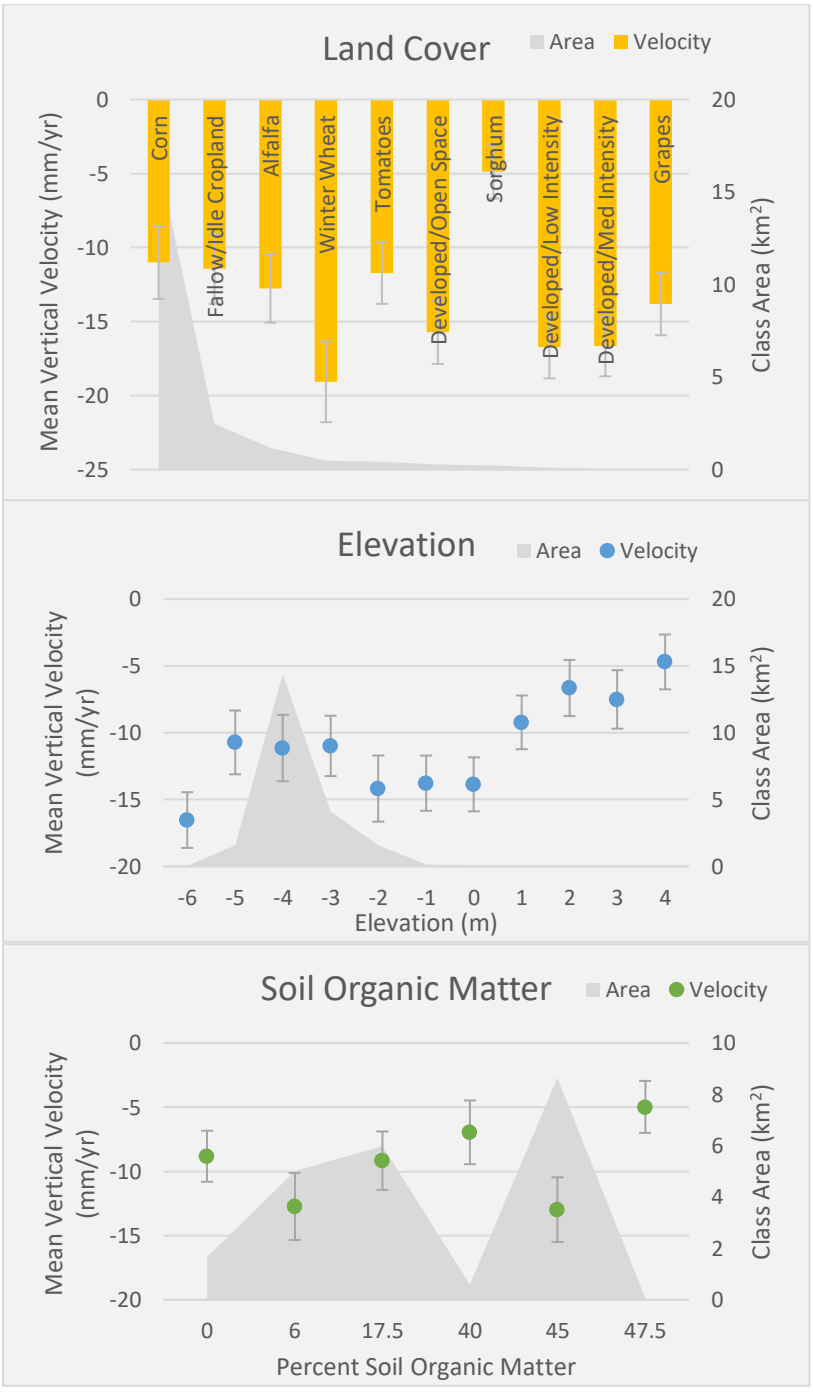

Figure S8: (A) Mean vertical velocity for top ten land cover classes, (B) elevation classes, and (C) soil organic matter classes in Bouldin Island. The area of each class is shown in the dark grey background.

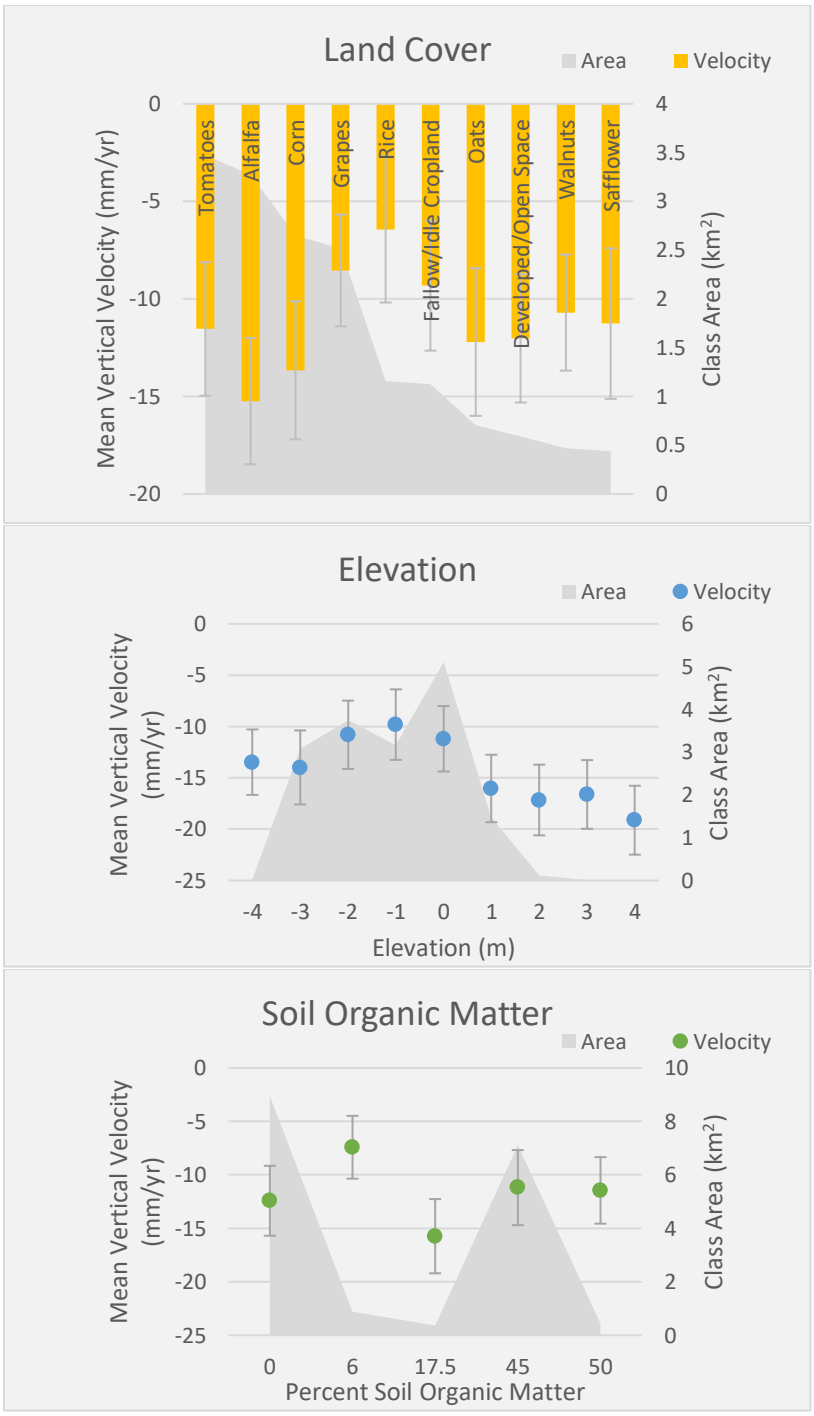

Figure S9: (A) Mean vertical velocity for top ten land cover classes, (B) elevation classes, and (C) soil organic matter classes in Brack Tract. The area of each class is shown in the dark grey background.

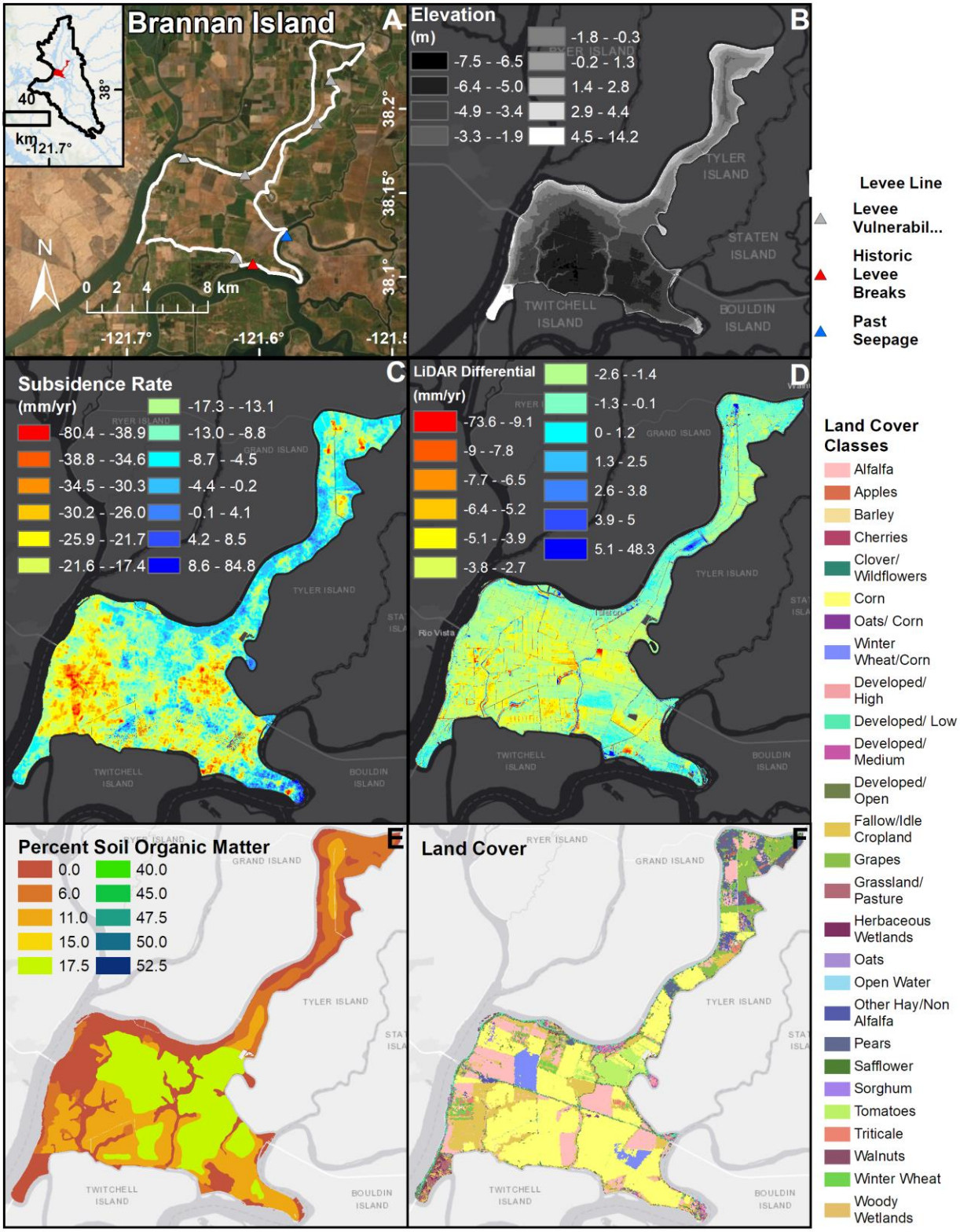

Figure S10: A profile figure for Brannan Island showing: (A) location of island in Delta and optical imagery from ArcMap basemap with points of interest, (B) elevation in meters, (C)

InSAR derived subsidence rate in mm/yr for 2009-2015, (D) lidar differential in mm/yr for 2007 and 2017, (E) percent soil organic matter, and (F) land cover (legend only shows classes with at least 5 hectares).

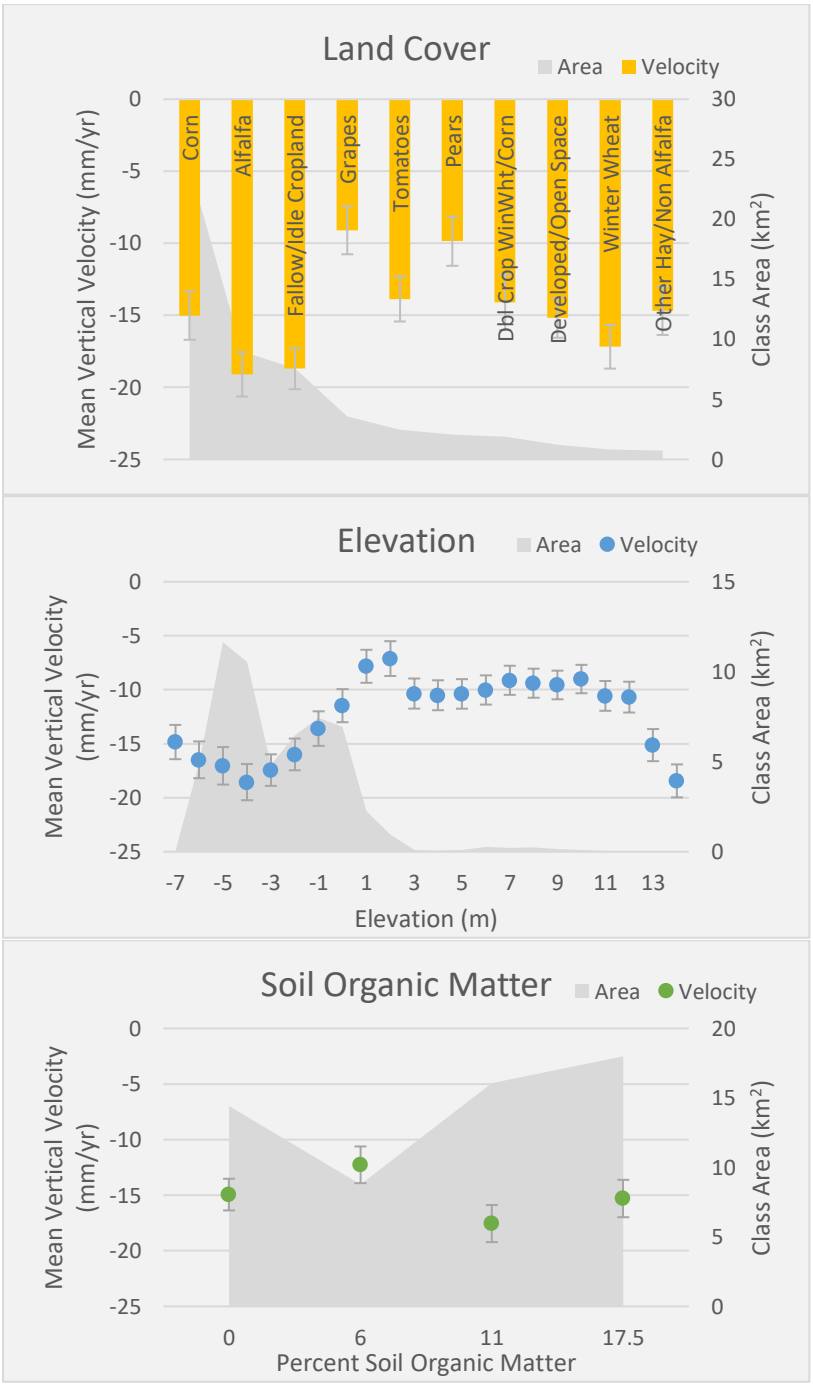

Figure S11: (A) Mean vertical velocity for top ten land cover classes, (B) elevation classes, and (C) soil organic matter classes in Brannan Island. The area of each class is shown in the dark grey background.

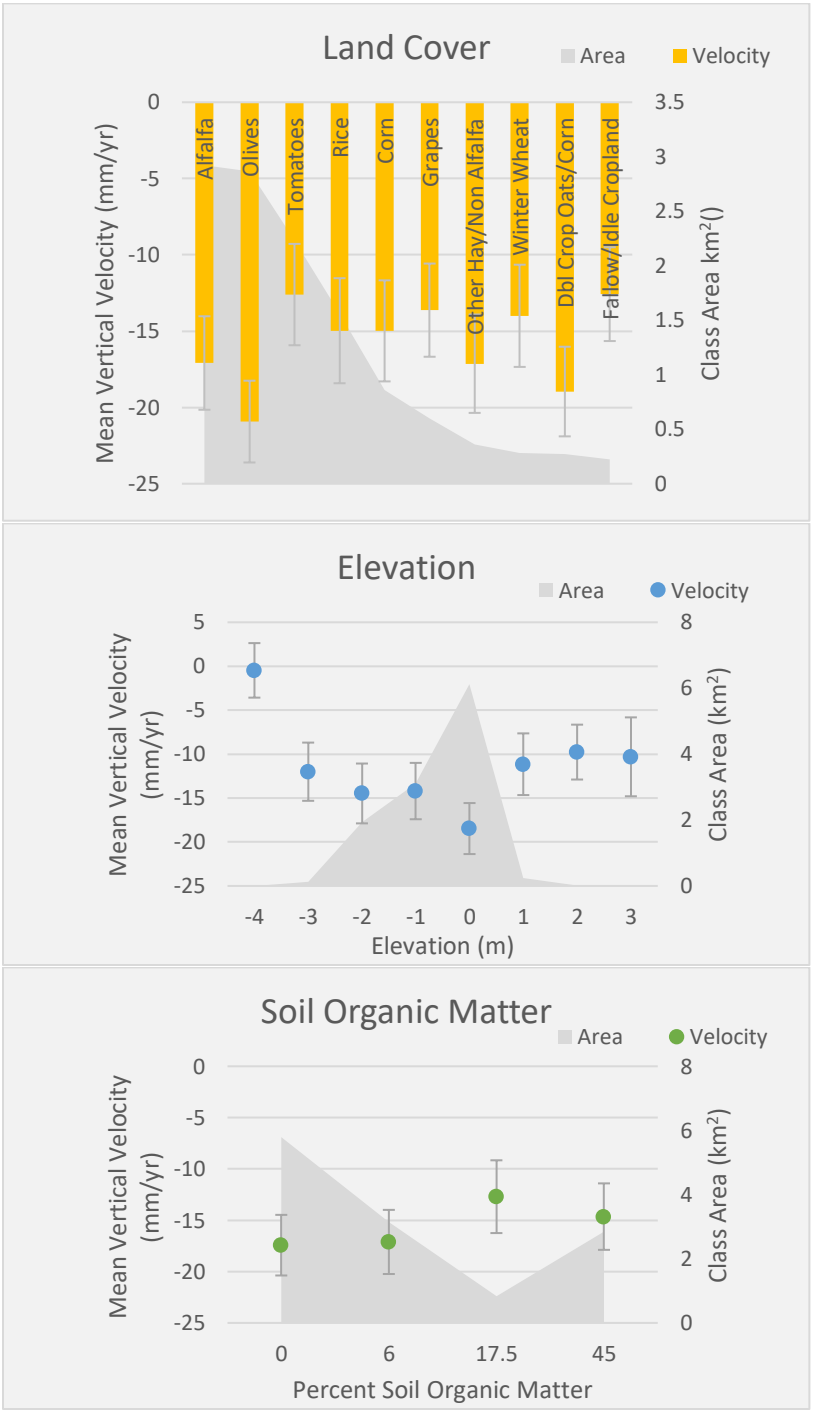

Figure S12: (A) Mean vertical velocity for top ten land cover classes, (B) elevation classes, and (C) soil organic matter classes in Canal Ranch Tract. The area of each class is shown in the dark grey background.

Empire Tract:

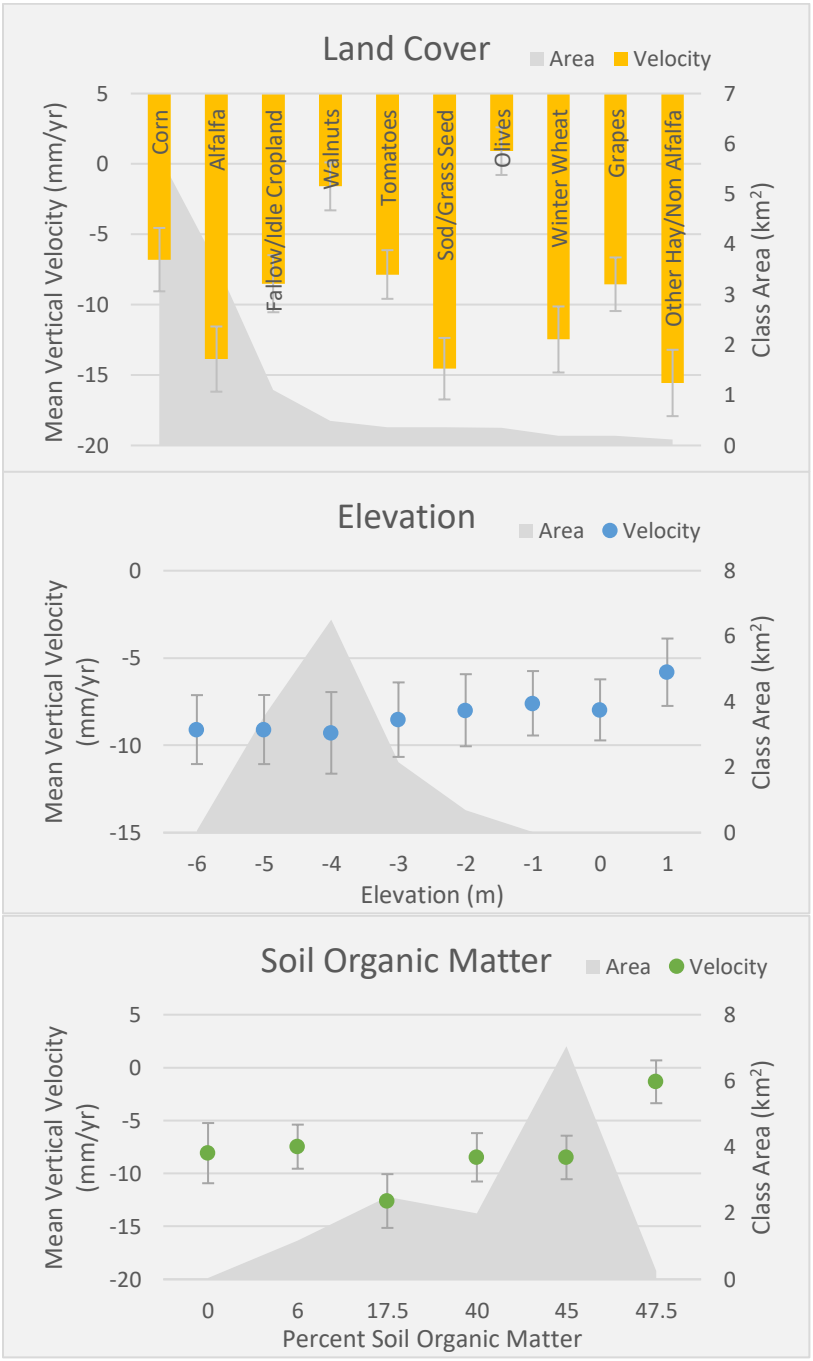

Figure S13: (A) Mean vertical velocity for top ten land cover classes, (B) elevation classes, and (C) soil organic matter classes in Empire Tract. The area of each class is shown in the dark grey background.

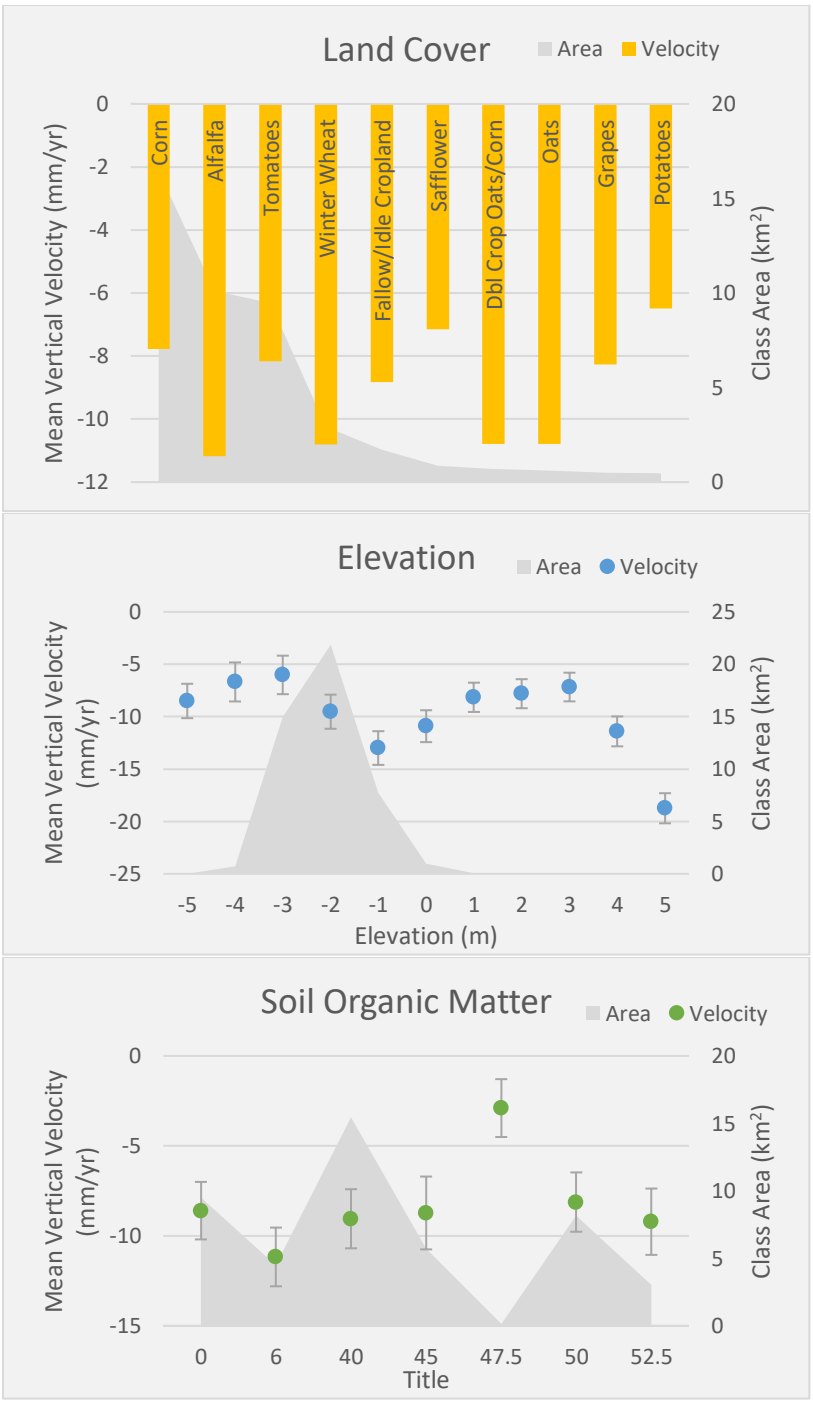

Figure S14: (A) Mean vertical velocity for top ten land cover classes, (B) elevation classes, and (C) soil organic matter classes in Jones Tract. The area of each class is shown in the dark grey background.

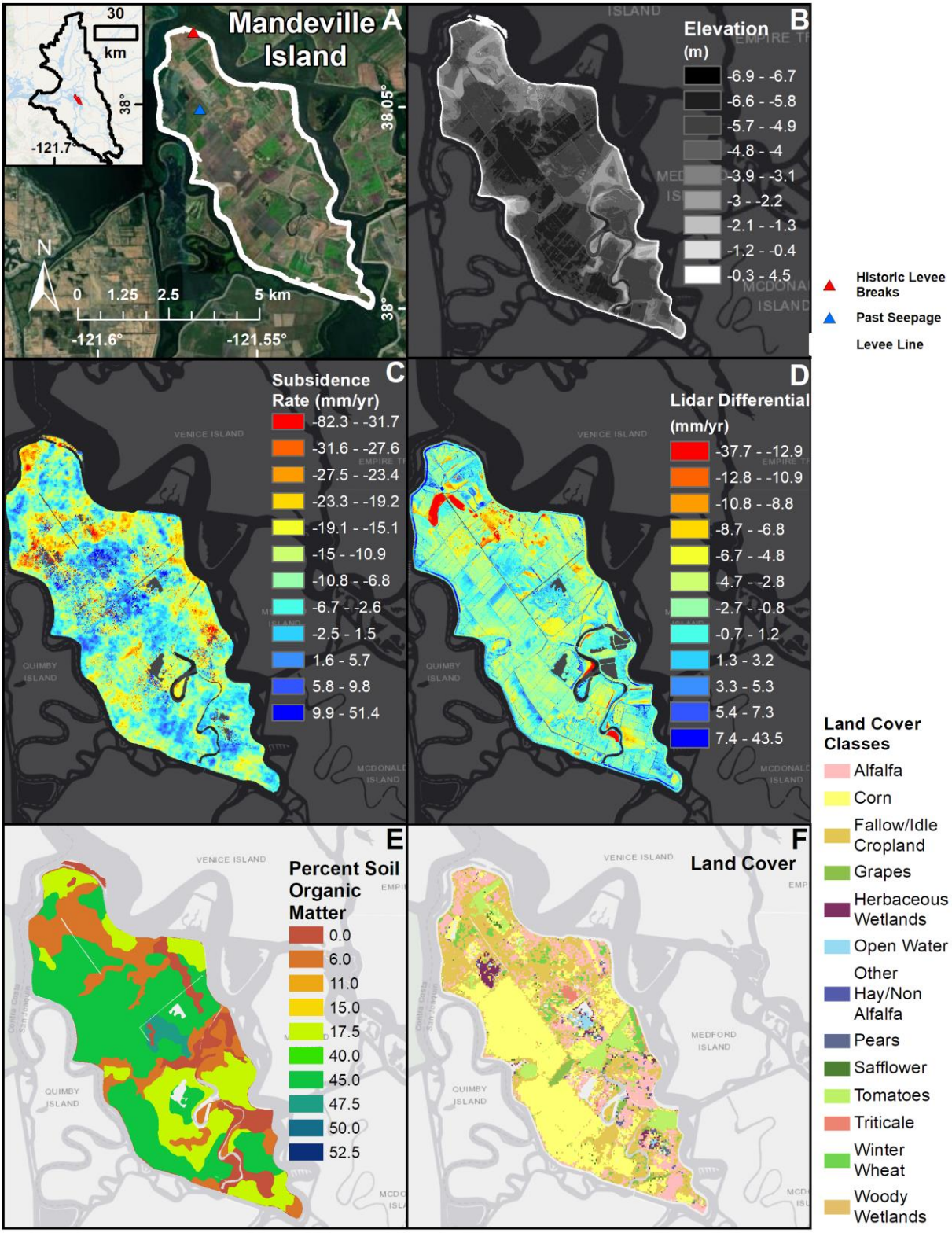

Figure S15: A profile figure for Mandeville Island showing: (A) location of island in Delta and optical imagery from ArcMap basemap with points of interest, (B) elevation in meters, (C)

InSAR derived subsidence rate in mm/yr for 2009-2015, (D) lidar differential in mm/yr for 2007 and 2017, (E) percent soil organic matter, and (F) land cover (legend only shows classes with at least 5 hectares).

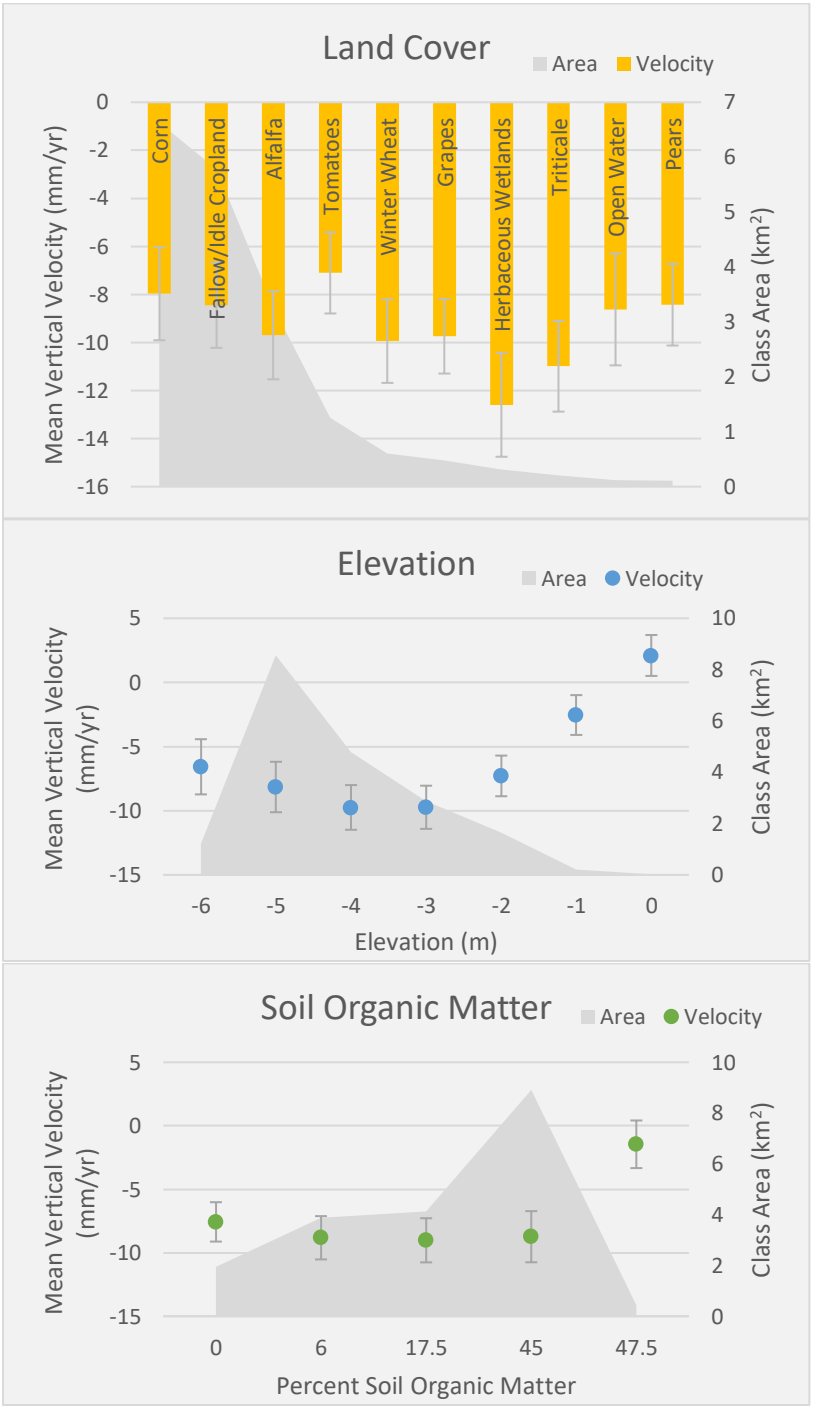

Figure S16: (A) Mean vertical velocity for top ten land cover classes, (B) elevation classes, and (C) soil organic matter classes in Mandeville Island. The area of each class is shown in the dark grey background.

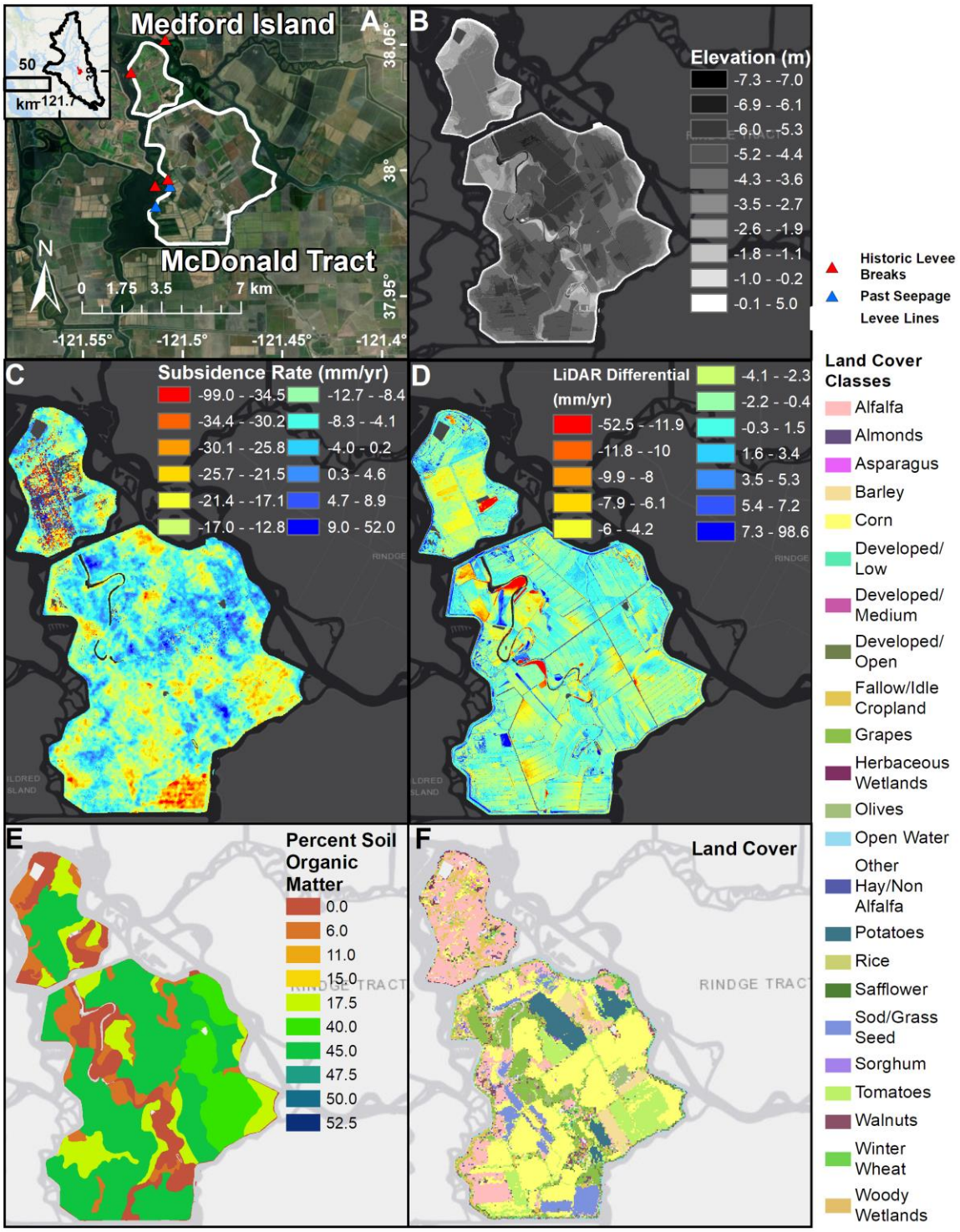

Figure S17: A profile figure for McDonald Tract showing: (A) location of island in Delta and optical imagery from ArcMap basemap with points of interest, (B) elevation in meters, (C) InSAR derived subsidence rate in mm/yr for 2009-2015, (D) lidar differential in mm/yr for 2007 and 2017, (E) percent soil organic matter, and (F) land cover (legend only shows classes with at least 5 hectares).

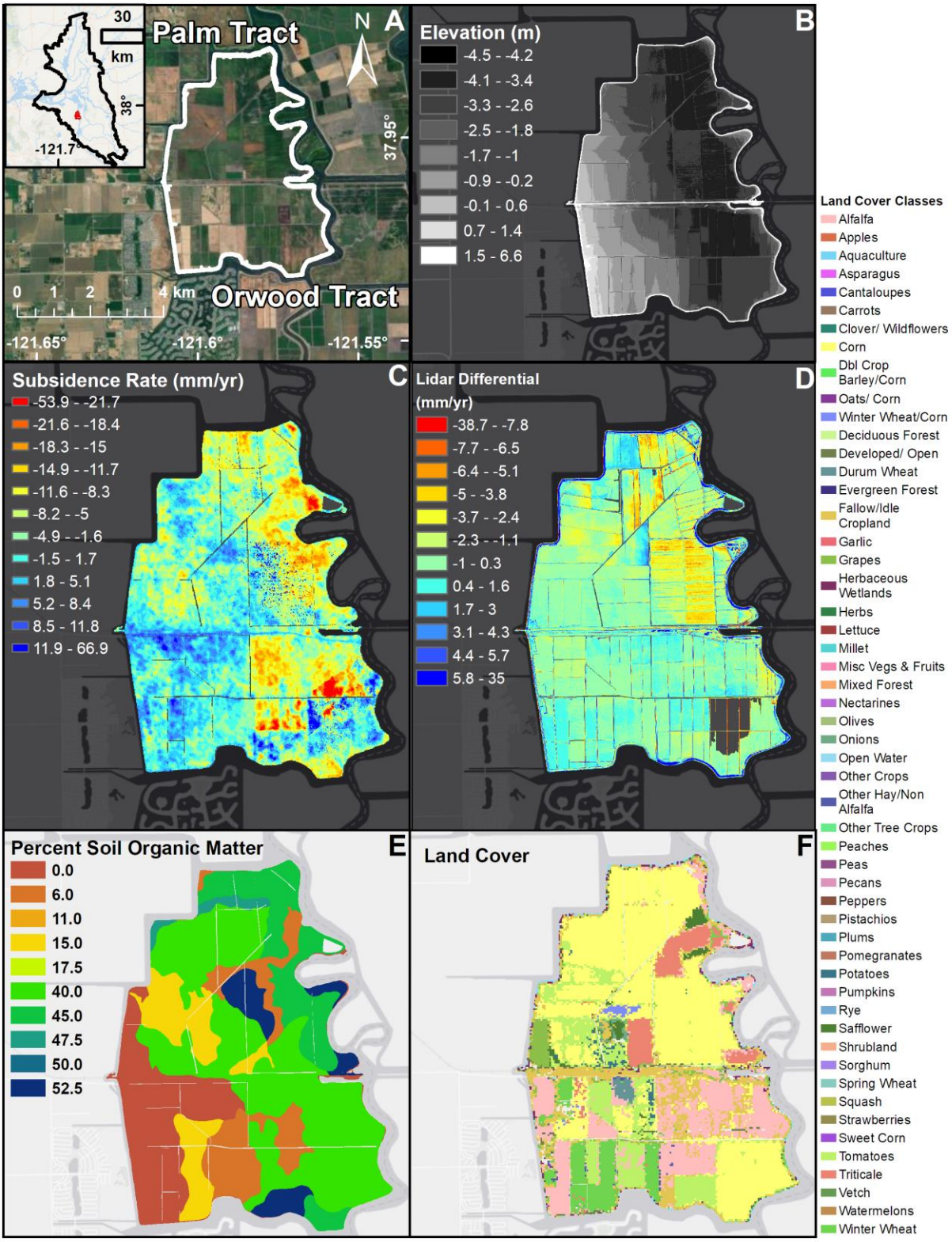

Figure S18: A profile figure for Palm Tract and Orwood Tract showing: (A) location of islands in Delta and optical imagery from ArcMap basemap with points of interest, (B) elevation in

meters, (C) InSAR derived subsidence rate in mm/yr for 2009-2015, (D) lidar differential in mm/yr for 2007 and 2017, (E) percent soil organic matter, and (F) land cover (legend only shows classes with at least 5 hectares).

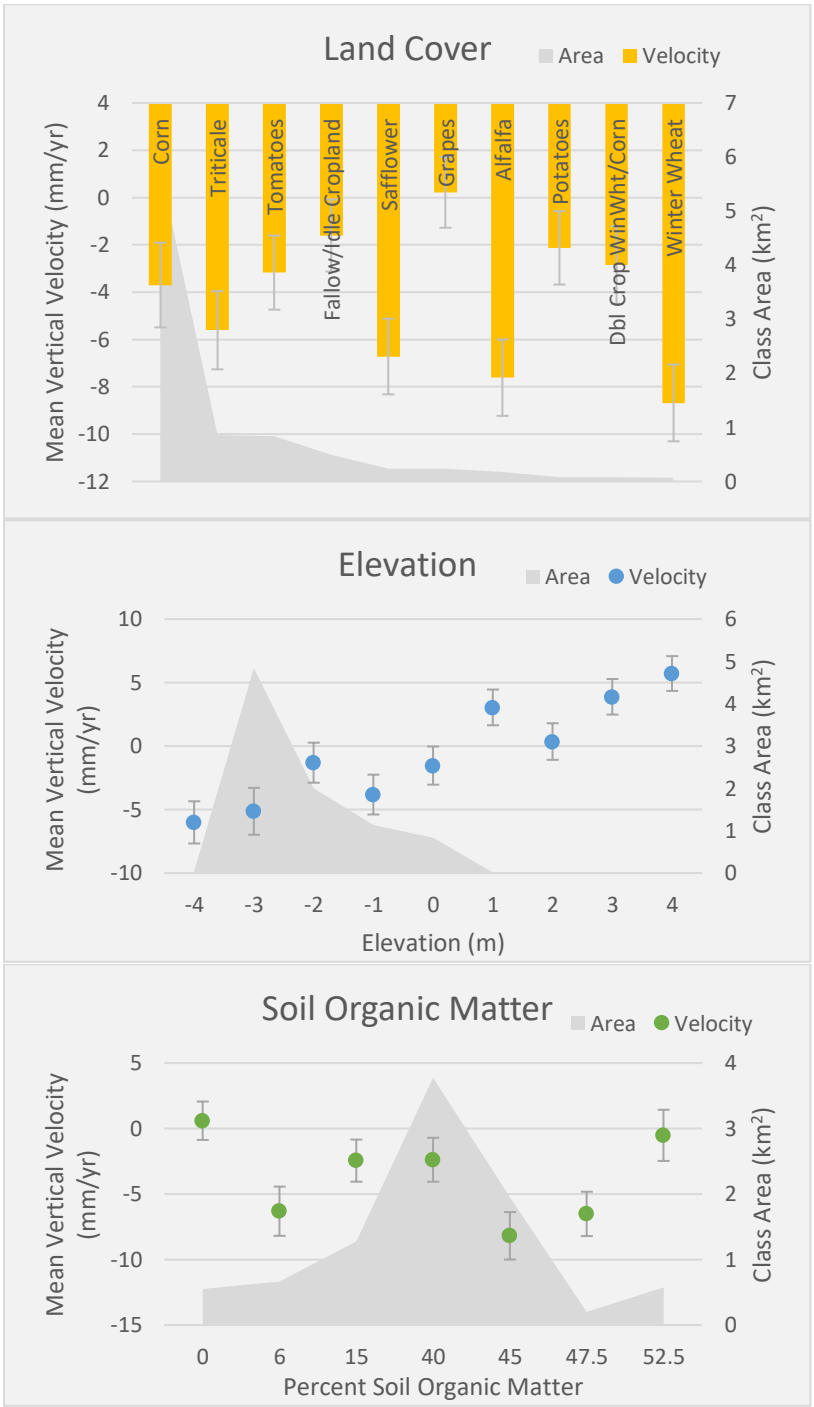

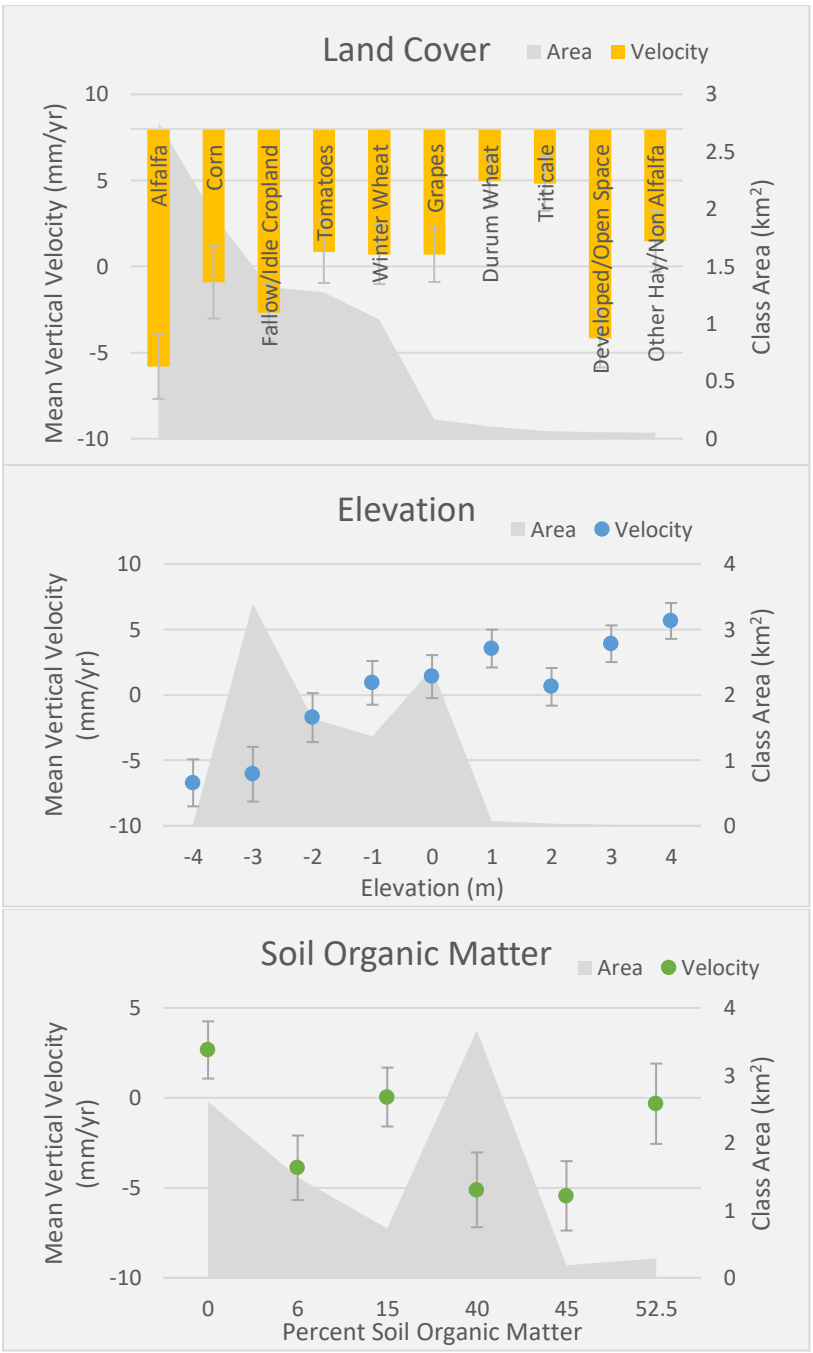

Figure S19: (A) Mean vertical velocity for top ten land cover classes, (B) elevation classes, and (C) soil organic matter classes in Palm Tract. (D) Mean vertical velocity for top ten land cover classes, (E) elevation classes, and (F) soil organic matter classes in Orwood Tract. The area of each class is shown in the dark grey background.

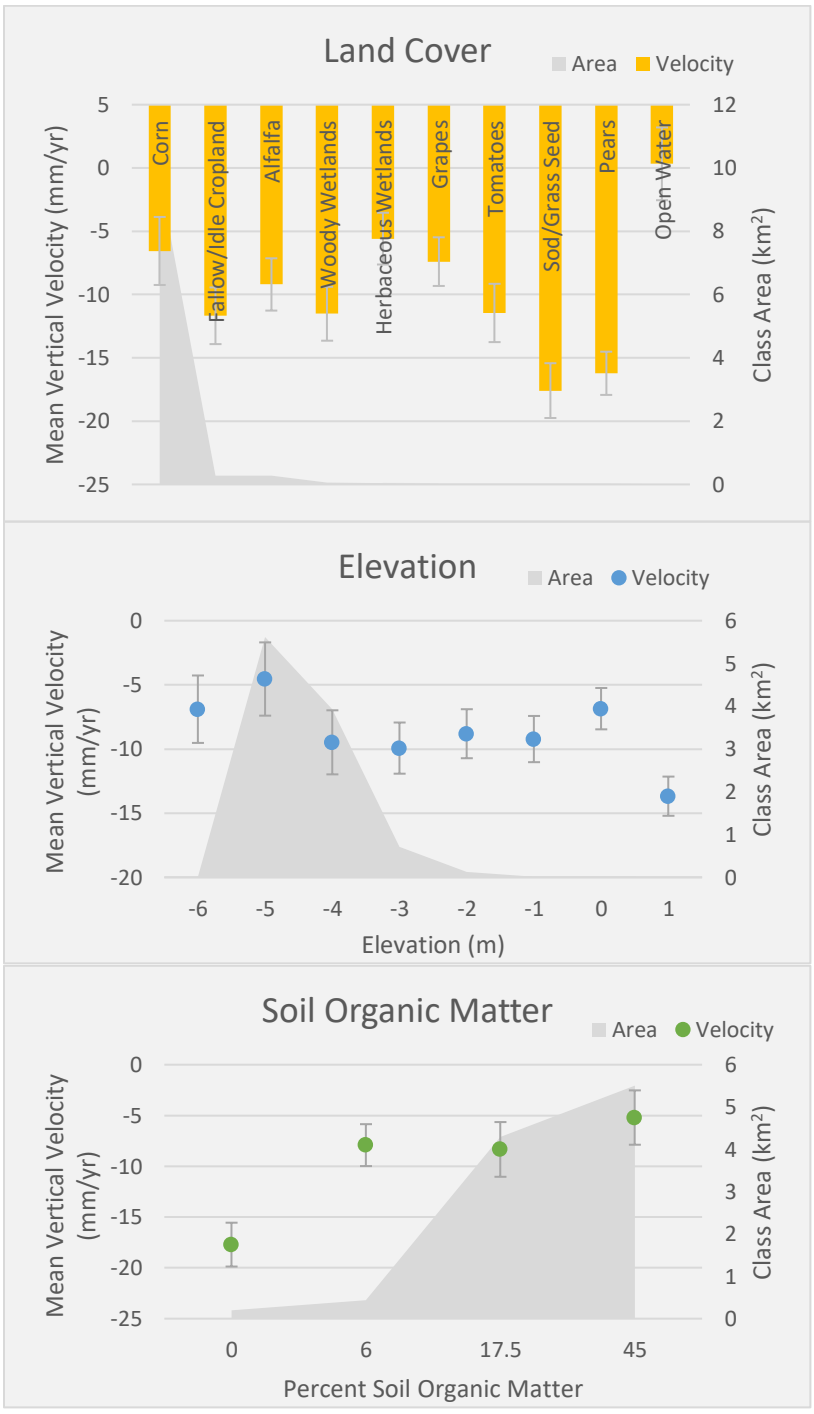

Figure S20: (A) Mean vertical velocity for top ten land cover classes, (B) elevation classes, and (C) soil organic matter classes in Venice Island. The area of each class is shown in the dark grey background.

References

Agram, P., Jolivet, R., Riel, B., Lin, Y., Simons, M., Hetland, E., et al. (2013). New radar interferometric time series analysis toolbox released. *Eos, Transactions American Geophysical Union*, 94(7), 69–70. doi: 10.1002/2013EO070001

Amelung, F., Galloway, D. L., Bell, J. W., Zebker, H. A., & Laczniak, R. J. (1999). Sensing the ups and downs of Las Vegas: InSAR reveals structural control of land subsidence and aquifer-system deformation. *Geology*, 27(6), 483–486. doi: 10.1130/0091-7613(1999)027<0483:STUADO>2.3.CO;2

An, K., Jones, C., Bekaert, D., & Bennett, V. (2020). Radar interferometry offers new monitoring approach for critical flood control infrastructure. In review.

Atwater, B. F. (1982). *Geologic maps of the Sacramento-San Joaquin Delta, California* (No. 1401). US Government Printing Office.

Bamler, R., & Hartl, P. (1998). Synthetic aperture radar interferometry. *Inverse problems*, *14*(4), R1.

Bates, M. E., & Lund, J. R. (2013). Delta subsidence reversal, levee failure, and aquatic habitat—a cautionary tale. *San Francisco Estuary and Watershed Science*, 11(1). doi: 10.15447/sfews.2013v11iss1art1

Bekaert, D., Walters, R., Wright, T., Hooper, A., & Parker, D. (2015). Statistical comparison of InSAR tropospheric correction techniques. *Remote Sensing of Environment*, 170, 40–47. doi: 10.1016/j.rse.2015.08.035

Bekaert, D. P., Jones, C. E., An, K., & Huang, M.-H. (2019). Exploiting UAVSAR for a comprehensive analysis of subsidence in the Sacramento Delta. *Remote Sensing of Environment*, 220, 124–134. doi: 10.1016/j.rse.2018.10.023

Berardino, P., Fornaro, G., Lanari, R., & Sansosti, E. (2002). A new algorithm for surface deformation monitoring based on small baseline differential SAR interferograms. *IEEE Transactions on Geoscience and Remote Sensing*, 40(11), 2375–2383. doi: 10.1109/TGRS.2002.803792

Blewitt, G., Kreemer, C., Hammond, W. C., & Goldfarb, J. M. (2013). Terrestrial reference frame NA12 for crustal deformation studies in North America. *Journal of Geodynamics*, 72, 11–24. doi: 10.1016/j.jog.2013.08.004

Brooks, B. A, Bawden, G., Manjunath, D., Werner, C., Knowles, N., Foster, J., et al. (2012). Contemporaneous Subsidence and Levee Overtopping Potential, Sacramento-San Joaquin Delta, California. San Francisco Estuary and Watershed Science, 10(1). Retrieved from https://escholarship.org/uc/item/15g1b9tm

California Department of Water Resources, Delta-Suisun Marsh office (2007). 2007 Sacramento

San Joaquin Delta LiDAR Acquisition. Retrieved from http://gisarchive.cnra.ca.gov/iso/ImageryBaseMapsLandCover/LIDAR/DeltaLIDAR2007/

California Department of Water Resources, Delta-Suisun Marsh office (2017). 2017 Sacramento San Joaquin Delta LiDAR Acquisition. Retrieved from http://gisarchive.cnra.ca.gov/iso/ImageryBaseMapsLandCover/LIDAR/DeltaLIDAR2017/

Chaussard, E., Amelung, F., Abidin, H., & Hong, S. H. (2013). Sinking cities in Indonesia: ALOS PALSAR detects rapid subsidence due to groundwater and gas extraction. *Remote sensing of environment*, *128*, 150-161.

Chaussard, E., Wdowinski, S., Cabral-Cano, E., & Amelung, F. (2014). Land subsidence in central Mexico detected by ALOS InSAR time-series. *Remote Sensing of Environment*, 140, 94–106. doi: 10.1016/j.rse.2013.08.038

University of California Agriculture and Natural Resources. (2015, accessed 2020, May 1) Delta Crops Calendar. (2015) Available from https://ucanr.edu/sites/deltacrops/files/225792.pdf

Deverel, S. J., & Leighton, D. A. (2010). Historic, recent, and future subsidence, Sacramento-San Joaquin Delta, California, USA. *San Francisco Estuary and Watershed Science*, *8*(2).

Deverel, S. J., Ingrum, T., Lucero, C., & Drexler, J. Z. (2014). Impounded marshes on subsided islands: simulated vertical accretion, processes, and effects, Sacramento-San Joaquin Delta, CA USA. *San Francisco Estuary and Watershed Science*, *12*(2).

Deverel, S. J., Ingrum, T., & Leighton, D. (2016). Present-day oxidative subsidence of organic soils and mitigation in the Sacramento-San Joaquin Delta, California, USA. *Hydrogeology Journal*, 24(3), 569–586. doi: 10.1007/s10040-016-1391-1

Doin, M.-P., Lasserre, C., Peltzer, G., Cavali´e, O., & Doubre, C. (2009). Corrections of stratified tropospheric delays in SAR interferometry: Validation with global atmospheric models. *Journal of Applied Geophysics*, 69(1), 35–50. doi: 10.1016/j.jappgeo.2009.03.010

Faunt, C. C., Sneed, M., Traum, J., & Brandt, J. T. (2016). Water availability and land subsidence in the Central Valley, California, USA. *Hydrogeology Journal*, *24*(3), 675-684.

Galloway, D. L., Hudnut, K. W., Ingebritsen, S. E., Phillips, S. P., Peltzer, G., Rogez, F., & Rosen, P. A. (1998). Detection of aquifer system compaction and land subsidence using interferometric synthetic aperture radar, Antelope Valley, Mojave Desert, California. *Water Resources Research*, *34*(10), 2573-2585.

Galloway, D. L., Jones, D. R., & Ingebritsen, S. E. (1999). *Land subsidence in the United States* (Vol. 1182). US Geological Survey.

Galloway, D. L., & Burbey, T. J. (2011). Regional land subsidence accompanying groundwater extraction. *Hydrogeology Journal*, *19*(8), 1459-1486.

Hensley, S., Michel, T., Van Zyl, J., Muellerschoen, R., Chapman, B., Oveisgharan, S., ... & Mladenova, I. (2011, July). Effect of soil moisture on polarimetric-interferometric repeat pass observations by UAVSAR during 2010 Canadian soil moisture campaign. In *2011 IEEE International Geoscience and Remote Sensing Symposium* (pp. 1063-1066). IEEE.

Hensley, S., Jones, C., & Lou, Y. (2012, July). Prospects for operational use of airborne polarimetric SAR for disaster response and management. In *2012 IEEE International Geoscience and Remote Sensing Symposium* (pp. 103-106). IEEE.

Holzer, T. L. (1991). *Mitigating losses from land subsidence in the United States*. National Academies. https://doi.org/10.17226/1796.

Ingebritsen, S., Ikehara, M., Galloway, D., & Jones, D. (2000). Delta subsidence in California: the sinking heart of the state (Tech. Rep.). Retrieved from https://pubs.usgs.gov/fs/2000/fs00500/

Jones, C. E., Dudas, J., & Bawden, G. W. (2016). Application of Remote Sensing to Assessment of Water Conveyance Infrastructure Integrity. *Applied Geology in California, Environmental Engineering Geologists*, 26, 253–271.

Luoma, S. N., Dahm, C. N., Healey, M., & Moore, J. N. (2015). Challenges facing the

Sacramento–San Joaquin Delta: complex, chaotic, or simply cantankerous? *San Francisco Estuary and Watershed Science*, 13(3). doi: 10.15447/sfews.2015v13iss3art7

Natural Resources Conservation Service, Soil Survey Staff, United States Department of Agriculture (2015), Web Soil Survey, Available online at http://websoilsurvey.nrcs.usda.gov/.

Rojstaczer, S., & Deverel, S. J. (1995). Land subsidence in drained histosols and highly organic mineral soils of California. *Soil Science Society of America Journal*, *59*(4), 1162-1167.

Service, R. F. (2007). Environmental restoration. Delta blues, California style. *Science*, 317(5837), 442. doi: 10.1126/science.317.5837.442

Sharma, P., Jones, C. E., Dudas, J., Bawden, G. W., & Deverel, S. (2016). Monitoring of subsidence with UAVSAR on Sherman Island in California's Sacramento–San Joaquin Delta. *Remote sensing of environment*, *181*, 218-236.

Woodhouse, I. H. (2005). *Introduction to microwave remote sensing*. CRC press.

Zebker, H. A., & Villasenor, J. (1992). Decorrelation in interferometric radar echoes. *IEEE Transactions on Geoscience and Remote Sensing*, 30(5), 950–959. doi: 10.1109/36.175330

CHAPTER FOUR

Using PolSAR indices and decomposition products to identify increased soil moisture for levee seepage detection of California water conveyance systems

Abstract

Levee seep detection with microwave radar is dependent upon the presence of vegetation, dielectric properties of the surface, and geometry of the objects measured. Seeps occur when water pipes through or beneath the levee structure, and can range from small areas of increased soil moisture to large ponded water on the surface. Levee seeps can lead to sand boils and eventually levee failure if not properly maintained. The optical imagery and polarimetric radar products compared in this study show that seep detection is successful for certain environmental conditions. The California Aqueduct is chosen as a dry testbed environment to investigate polarimetric seep signatures, and the procedure is then applied to Twitchell Island in the Sacramento-San Joaquin Delta. Both conveyance systems provide critical water supplies to southern California and are vulnerable to seepage. The seep examples presented in this study cover this range and each contain different polarimetric signatures. Large seeps can also occur during intense floods, which usually accompany stormy weather. Optical imagery and a derived water index dataset show many unusable acquisitions due to cloud cover. Therefore, seep detection cannot solely rely on optical imagery and can be used in conjunction with polarimetric radar datasets. Single polarization, polarization ratios, and decomposition products are compared with each other for five seep examples in the California Aqueduct and five examples of small seeps on Twitchell Island in the Sacramento Delta. The VV/HH ratio is effective at monitoring large seeps especially in drier environments, but small seep features are difficult to differentiate

in wetter environments such as the Delta. For a large flood event, seepage features will be much larger and more easily detectable by polarimetric radar.

Introduction

Levee seeps occur when water pipes through or beneath the levee structure, and can range from small areas of increased soil moisture to large ponded water on the surface. Levee seeps can lead to sand boils and eventually levee failure if not properly maintained. These features are especially common in consistently wet environments such as the Sacramento Delta, but can also occur for water conveyance structures in dry conditions, like the California Aqueduct in the San Joaquin Valley, California. Levee seeps can range in size and characteristics may vary in its shape, soil moisture, presence of standing water, and source of water, for example from shallow groundwater, overtopping, high tide levels, etc. Levee seeps usually result in a small area of increased soil moisture, which can be highlighted using polarimetric radar imagery. Levee seep monitoring only requires the presence of increased soil moisture, and not necessarily its volumetric soil water content.

Soil moisture, the amount of water that is stored between particles in the soil, plays a critical role in hydrology, biogeochemistry, water resource management, flood control, agriculture, early indications of drought, and more (Robock et al., 2000). Soil moisture acts as the interface between our land surface and atmospheric processes, and is dependent on a multitude of factors including evapotranspiration, precipitation, land use, topography, and soil type (Robock et al., 2000). Though soil moisture can be measured on a point-by-point basis, the variability that exists spatially and temporally makes field measurements extremely inefficient. By implementing microwave technology, satellites and airborne instruments can measure soil moisture based on the dielectric properties of liquid water and dry soil (Engman and Chauhan,

1995). Remote sensing offers a measurement solution that is spatially both continuous and extensive, and potentially can be applied on a regional and global scale.

Soil moisture has traditionally been measured in the field using different point based sensors (Vereecken et al., 2013). Time domain reflectometry (TDR) probes use the dielectric permittivity of the soil, which is closely related to soil moisture content, for field measurements, however, these probe networks are limited by cable length for local studies (Vereecken et al., 2013). A less expensive alternative to TDR are capacitance sensors, which again measure the permittivity of the soil but by measuring the charge time from a starting voltage to an applied capacitor voltage (Vereecken et al., 2013). The time domain transmission (TDT) sensor measures the velocity of an electromagnetic wave propagating along a closed transmission line (Vereecken et al., 2013). These TDT sensors operate at higher frequencies than most capacitance sensors and offer better measurement quality (Vereecken et al., 2013). Wireless soil moisture sensor networks can also be used, which contain hundreds of soil moisture sensors (capacitance and TDT sensors) that connect to a main server wirelessly (Vereecken et al., 2013). These networks can be combined with other sensors to create a continuous spatial and temporal network for applications such as irrigation management.

Hydrogeophysical instruments such as ground penetrating radar (GPR) are non-invasive methods of monitoring soil moisture (Vereecken et al., 2013). GPRs use a transmitting and receiving antenna in the same manner as TDR probes. Deeper penetration depths can be achieved by using a surface GPR antenna rather than off-ground GPR, which penetrate shallower depths and are more sensitive to surface roughness. An electromagnetic induction (EMI) system generates magnetic fields by inducing electromagnetic currents that contain information about the conductivity and soil properties (Vereecken et al., 2013). Electrical resistivity tomography

(ERT) is another non-invasive method that uses a set of electrodes to measure the electrical conductivity of a surface.

Remote sensing can vastly improve upon the spatial density of *in situ* soil moisture measurements, and is accomplished by both passive and active microwave technologies. Soil moisture can be detected with a passive sensor, where a radiometer measures the emission intensity from the Earth's surface, based on surface temperature and emissivity, however this relationship does not apply in the presence of vegetation since additional absorption and scattering occurs in the canopy (Vereecken et al., 2014). The soil emissivity is related to the reflectivity, which relates to the dielectric properties of the soil. These relationships are complicated due to factors such as surface roughness and the presence of vegetation, which are discussed below. Soil moisture can also be measured with an active sensor, where the radar backscatter can be directly related to soil moisture, given some ground truth data. An increase in soil moisture causes an increase in the dielectric constant, which increases backscatter to the instrument (Ulaby et al., 1996). Change detection methods using either passive or active microwave sensors are also possible, and can reduce the effects of soil texture and vegetation, which should not change between acquisitions taken frequently (Ulaby et al., 1996). Active radar remote sensing, which typically offers much higher spatial resolutions than passive sensors, is capable of producing products of only a few meters resolution (depending on the incidence angle, antenna size, etc.). Radar remote sensing measures the backscattering coefficient, which depends on the dielectric properties of the soil. Discussed below, active remote sensing of soil moisture can be difficult to interpret since soil moisture, surface roughness, and vegetation can all affect the backscatter coefficient. Using datasets with different collecting frequencies and penetration depths may be a possible method of differentiation.

Polarimetric Synthetic Aperture Radar (PolSAR)

The polarization of an electromagnetic wave describes the direction of the waves' electric field, for example being transmitted and received by synthetic aperture radar (SAR) instruments (van Zyl et al., 1987). PolSAR, or polarimetric SAR, can allow for separation of scattering mechanisms, which can indicate different surface properties. Different objects on the surface, water, buildings, vegetation, etc., react differently to the polarized waves, and therefore can offer useful identification from their scattering properties. For a horizontally polarized wave, the electric field is parallel to the Earth's surface, and for vertically polarized waves, the field is orthogonal to the surface (van Zyl et al., 1987). Knowing the polarimetric information of an object allows for scientists to deduce some knowledge of the physical properties of that object. This is especially pertinent in remote sensing applications where the study area is inaccessible, has a variety of land cover types, or field surveys are expensive. Modern polarimeters are typically fully polarized, meaning they transmit and receive waves in multiple polarizations. This is implemented to capture the full amount of information available from polarimetry. For linearly polarized systems, the nomenclature for these polarizations is: VV, HH, VH, and HV. H denotes horizontal polarization and V represents vertically polarized waves. The first letter signifies the transmitted wave while the second letter denotes the received wave. For a monostatic radar, which has the same antenna for sending and receiving radar pulses, HV and VH are assumed to be equivalent after instrument calibration since radar scattering is reciprocal (Ulaby et al., 1996; Barrett et al., 2009).

PolSAR also has great potential to be combined with traditional interferometric (InSAR) applications. In the past, missions did not possess sufficient downlink bandwidth to transmit and store data from all these polarizations, but newer instruments such as UAVSAR, used in this

study, is airborne and can store fully polarized data onboard. The returned data from polarimetric radars is the scattering matrix and the polarization phase difference. The scattering matrix is converted to the scattering coefficient during processing, which is a unit-less intensity measured by the imaging system (Ulaby et al., 1996). Therefore, there is a scattering coefficient value collected for each HH, VV, and HV polarization (for fully polarized instruments). The magnitude of the backscattering coefficient is dependent on the dielectric constant of the surface, which is dependent on the soil moisture, and also the surface roughness (Ulaby et al., 1996). The dielectric constant of vegetation can also be a contributing factor to the backscatter, with multiple scattering mechanisms between the soil surface and vegetation that may disrupt soil moisture studies. The penetration depth of L-band radars such as UAVSAR, is detecting soil moisture up to 5 cm depth (Ulaby et al., 1996). The phase difference can help to highlight surface differences in an image that can be useful for land cover classification. The co-polarized phase difference, $\Phi_{HH}^{0} - \Phi_{VV}^{0}$, has usually been more effective at classification than the cross-polarized phase difference, $\Phi_{HV}^{0} - \Phi_{VV}^{0}$ (Ulaby et al., 1996). This is due to the fact that for most surfaces not heavily vegetated (e.g., forested), the signal-to-noise ratios are higher for the HH and VV returns (Jones, 2016). The VV polarization is especially sensitive to changes in soil moisture because it has larger returns with the presence of water (Jones, 2016).

Soil is made up of soil particles, air, bound water, and free water (Barrett et al., 2009). When the moisture content of the soil increases, there is more free water, which has a strong effect on the dielectric constant (Barrett et al., 2009). An increase in soil moisture will cause an increase in the dielectric constant, which will increase the intensity of the backscattering coefficient (Barrett et al., 2012). Coherence measured from interferogram products can also be used as an indicator of soil moisture change. While temporal decorrelation is a source of error for

topographic products, the change in coherence can be a helpful indicator of soil moisture change (Barrett et al., 2009). Low coherence values coupled with high radar backscatter may suggest that an abrupt change has occurred in surface roughness, for example, from farming activity (Barrett et al., 2012). High coherence values with a large backscatter change may indicate moisture content change. Significant moisture changes can lead to decorrelation, as shown in laboratory experiments (Barrett et al., 2012).

The application of radar remote sensing to soil moisture retrieval is based on the backscattering coefficient (σ^0), expressed in decibels (dB), which is derived from the scattering matrix containing all polarizations. The backscattering coefficient is the fraction of backscattered energy compared to energy of the incident field (Barrett et al., 2009). The intensity of this value is based on the target's physical characteristics, polarization, and the incidence angle of the instrument (Barrett et al., 2009). As the incidence angle increases, more energy is scattered back towards the instrument with increasing surface roughness (Ulaby et al., 1996; Barrett et al., 2009). Holah et al. (2005) found that incidence angles between 20° and 37° were best suited to measure soil moisture.

The backscattering coefficient is more sensitive to surface roughness than moisture content (Oh, 2004). Very rough surfaces do not show much difference between σ^0_{HH} and σ^0_{VV}, while smooth surfaces will have a value between 0 and 1 for the $\sigma^0_{HH}/\sigma^0_{VV}$ ratio (Oh et al., 1992). Therefore, the copolarized ratio is not appropriate for very rough surfaces. Incidence angle can also play a role in the copolarized ratio, where $\sigma^0_{HH}/\sigma^0_{VV}$ approaches 1 for very rough surfaces and is independent of incidence angle, while smooth surfaces have lower ratio values as the incidence angle increases (Oh et al., 1992). Based on data using a laser profiler and dielectric probes for L, C, and X-bands, the magnitude (absolute value) of the copolarized ratio ($\sigma^0_{HH}/\sigma^0_{VV}$)

is larger for wet surfaces than dry surfaces (Oh et al., 1992). The cross-polarized ratio has been experimentally shown to have a large dependence on roughness conditions, and a weak relationship to moisture content (Oh et al., 1992). Many studies are in agreement that the VV polarization is most sensitive to soil moisture, with HH and then HV being the least sensitive (Barrett et al., 2009).

Polarimetry has been used to study scattering from vegetation canopies, 3-D imaging of canopies, forest canopy heights, and soil moisture estimates (Cloude, 2010). In order to retrieve volumetric soil moisture content and surface height, a past study by Oh (2004) presented a semi-empirical polarimetric backscattering model for bare soil surfaces in South Korea. Oh showed through theoretical scattering models that the backscattering coefficients from radar measurements are more sensitive to surface roughness than soil moisture (Oh, 2004). This is realistic due to the known discrepancies that can occur with microwave radar over topography, as discussed earlier. Oh has developed inversion techniques, the co-polarization ratio and cross-polarization ratio, from which the dielectric constant can be retrieved to highlight areas of increased soil moisture. Recent studies using these techniques have demonstrated the capability of PolSAR in identifying levee seepage locations (Hensley et al., 2011; Jones et al., 2012; Sehat et al., 2014). These demonstrations did not quantify soil moisture, but relied on contrast to tell a seep from adjacent drier land.

Earthen levees are flood protection infrastructure found in different coastal regions of the world, and monitoring of their health is critical for public safety and emergency response. InSAR and PolSAR have a variety of applications and can be difficult to interpret for novices in terms of data products and processing, but are powerful in terms of their ability to discern objects of different characteristics. The future developments of combining the high spatial resolution and

accuracy of InSAR with the descriptive capabilities of PolSAR preview an all-encompassing remote sensing tool for studying critical flood infrastructure.

Challenges of Measuring Soil Moisture with Remote Sensing

Though passive microwave sensors tend to have a higher temporal repeat time to their measurements, their spatial resolution tends to decrease as a result (tens of kilometers). This can be overcome in the field by hosting several mobile installations or disaggregation methods to interpolate the data (Fang and Lakshmi, 2013). However, since most land processes studies require observations at the kilometer to sub-kilometer scale (and even smaller scales for conveyance studies described below), methods concerning active sensors will be discussed, though many drawbacks will apply to both active and passive microwave instruments.

The measurement of soil moisture can be affected by a variety of factors from soil texture, measurement depth, surface roughness, vegetation, and incidence angle and frequency of the instrument (Barrett et al., 2012; Engman and Chauhan, 1995; Ulaby et al., 1996). Soil texture can affect soil moisture measurements because the dielectric properties of the soil change based on the varying amounts of sand, silt, and clay. This effect is usually small relative to other soil properties discussed below, and are usually neglected. The penetration depth of the radar is dependent on the frequency of the instrument, but is understood to only measure a couple centimeters of soil at the surface. Soil moisture also has a depth profile, therefore, penetration depth is not necessarily equal to the depth of soil being measured by the radar (Ulaby et al., 1996). The penetration depth also reaches a maximum value, and so change detection studies are less sensitive for higher soil moisture levels (Jones, 2016). L-band (1-3 GHz) instruments are capable of higher penetration depths and are generally best suited to measure soil moisture because of their longer wavelength (Jones, 2016). These radar pulses are able to better penetrate

vegetation and receive pulses that are more directly reflected from the soil surface rather than indirect backscattering from vegetation, which occurs more often at shorter wavelengths.

Depolarization occurs over areas with increased surface roughness, such as from terrain, or from volume scattering, such as over a vegetation canopy or during wet weather conditions (Woodhouse, 2006). Surface roughness, which can also be affected by wavelength, can increase the surface emissivity, which decreases its sensitivity to soil moisture (Engman and Chauhan, 1995). The effects of surface roughness are especially important for radars since these effects can be equal or even greater than the effects of soil moisture on the backscatter. Since in reality, soil surfaces are not perfectly smooth, the backscatter travels in many directions. The surface roughness can be represented by the standard deviation of surface heights. However, this effect can be isolated by using multipolarized radar data as co-polarized (HH/VV) and cross-polarized (HV/VV) ratios to classify the image. Multiple polarizations can be used to classify a surface with variable terrain and vegetation (Engman and Chauhan, 1995).

The presence of vegetation plays an especially large role in microwave measurements due to its ability to attenuate the signal and add its own emission to the microwave signal (Barrett et al., 2012). The backscatter measured from a canopy can be from the plants themselves, the actual soil surface, or a combination of the two, called multiple scattering (Ulaby et al., 1996). The influence of vegetation is the main source of decorrelation over any soil moisture changes. As mentioned, this is not as large a signal for instruments with longer wavelengths that are able to better penetrate the vegetation (Barrett et al., 2012). Effects of vegetation are also dependent on the polarization of the instrument because vertically polarized data exhibit greater attenuation since vegetative structures tend to be vertical. Ground truth studies have shown that the radar backscatter response is primarily a result of the top 2-3 cm of

the soil layer, and that a longer wavelength like L-band may penetrate even deeper into the soil for a dry surface (Oh, 2004). Long wavelength instruments are necessary to retrieve soil moisture beneath vegetation canopies since the dielectric permittivity of the plant affects the backscattering coefficient (Vereecken et al., 2014). Even the surface area of leaves from different plant species has an effect on backscatter, with broader leaves increasing backscatter return and narrow leaves, such as barley, decreasing backscatter (Barrett et al., 2012). Especially in lower wavelengths such as C-band, vegetation changes account for the primary source of decorrelation, masking any soil moisture changes (Barrett et al., 2012). In agricultural fields, the radar backscatter is affected by plant cover, water content, and even crop residue (Merzouki et al., 2010).

Such signal complication demonstrates the need for further knowledge of the study site, including but not limited to, elevation, soil type, land cover, vegetation type, etc. These types of datasets can easily be integrated with a GIS database that allows for a direct comparison of, for example, a digital elevation model (DEM) overlain on a SAR interferogram (change detection image). However, the benefit of remote sensing is to gain information about a study site that are difficult to access or expensive to conduct field surveys. The tradeoff of high spatial resolution offered by active microwave sensors (versus passive) is their increased sensitivity to factors such as surface roughness and vegetation. One can also investigate the coherence product for more information. Low coherence coupled with high backscatter intensity can indicate a sudden surface change, such as harvesting and other farming activities. High coherence and high backscatter intensity can signify actual soil moisture change.

California Conveyance Systems

The CA Aqueduct is chosen as a testbed environment due to the naturally dry conditions in the San Joaquin Valley, allowing any leakage feature to be visually prominent in the PolSAR data. The aqueduct is an artificial river and concrete channel that is shaped like an inverted trapezoid, with a bottom width of 3-25 m and depth of 9 m (Water Education Foundation). This conveyance system transports water from the Delta to farmers in the San Joaquin Valley and also to southern California residents as part of the State Water Project. The San Joaquin Valley has experienced notable land subsidence since the mid-1920s due to excessive groundwater withdrawal, threatening the structural integrity of the aqueduct (Poland et al., 1972). Early detection of leaks helps agencies to administer repairs in a timely manner before excess potable water is loss, and prevent structural damage. The CA Aqueduct testbed proves a proof of concept that a leak or seep is detectable with PolSAR data. Five seep examples along the aqueduct and five examples on Twitchell Island in the Delta are investigated in this study alongside various PolSAR products. This study uses polarimetric data products from UAVSAR to highlight areas of increased soil moisture in order to identify possible levee seepages that threaten the integrity of the flood infrastructure in the Delta.

Levee systems throughout the country play a crucial role in flood protection for citizens, infrastructure, and agricultural land that is vital to the livelihood of these regions. The Sacramento-San Joaquin Delta (Delta) in northern California is the largest estuary in the western U.S. (over 2500 km^2) and contains over 1,500 km of centuries-old earthen levees that protect the 65 islands surrounded by levees in the area from flooding, due to subsidence over the past 150 years (Service, 2007). These waterways also supply irrigation water for about 1 million hectares of agricultural land, and serve as a main water supply for 23 million California residents. Many

of these islands are 3-7 meters below sea level, and the levees that surround them are only 1 foot above the 100-year flood elevation, sitting atop compressible peat and organic clay soils (Ingebritsen et al., 2000). Levee damage can be attributed to a variety of factors, including: floods, subsidence due to groundwater withdrawal and mining, seismic events, and even rodent burrowing (Jones et al., 2016). Threats to the infrastructure include cracking, erosion, sinkholes, boils and the focus of this study: seepage and subsidence. Seepage occurs when there is water movement below the structure, which can weaken the levee and develop into a boil, leading to complete failure of the levee.

Currently, this complicated system of levees is monitored by the island owners, though the CA Department of Water Resources (DWR) also tracks levee conditions since they administer state funds for repair and maintenance. The DWR relies on field surveys for this maintenance which are both costly and inefficient. Remote sensing of levee conditions in the Delta can offer detailed and quick data collection over the region that would help bolster the DWR's current monitoring programs and emergency response during a flood or earthquake event. This is due to the emergence of new instruments such as UAVSAR, which possesses the high spatial resolution (1.6 meters) that is necessary for detailed levee monitoring. For this study, this dataset is applied to the California Aqueduct, a 640 km (400 mi) long conveyance system in central California, as a testbed for polarimetric radar seep detection.

Materials and Methods

UAVSAR

UAVSAR is an airborne polarimetric radar instrument from NASA that has been used to measure deformation from earthquakes, volcanoes, subsidence, glacier movement, etc. (Hensley et al., 2012). This instrument flies as a pod attached to a Gulfstream-III aircraft, and is an L-band

(23.8 cm wavelength) airborne sensor with high signal-to-noise ratio, repeat flight track accuracy, high range resolution (1.67 m), and P and Ka-band capabilities (Hensley et al., 2011). The benefits of radar instruments include their ability to see through smoke, haze, clouds, and that data can be collected during the day or night. This adaptability is especially relevant during disaster events that inhibit traditional visual surveys of damage. UAVSAR has been collecting data over the Delta since 2009 for ~7 week intervals. Its high spatial resolution makes the instrument the best monitoring tool for the Delta levee system, given the combination of long wavelength (L-band) and high spatial resolution, subject to regular imaging which ended in 2018.

A previous study found that most of the Delta levee system will subside below the current design thresholds in 50 to 100 years, making monitoring improvements especially time sensitive (Brooks et al., 2012). The UAVSAR system can be deployed within hours of a disaster event and deliver information to decision makers within an hour of data collection (Hensley et al., 2012). These capabilities are relevant to disaster and damage assessment studies that can profoundly affect public and private decision-making. For example, the 2004 Jones Tract failure in the Delta occurred after extensive flooding and cost over $44 million to repair, not including job and crop losses (Mount and Twiss, 2005). Providing tangible and useful tools to the DWR will help aid their current monitoring efforts, and the millions of residents that depend on the Delta for its protection and sustenance.

The UAVSAR polarimetric datasets are hosted on the UAVSAR JPL website, and are available for download for 2010-2018 for the CA Aqueduct and 2009-2018 for the Delta. There are three flight lines over the aqueduct and nine flight lines over the Delta study region. Each collection date contains: an annotation file containing metadata, and orthorectified products

(which already contain geographic projections) for different polarizations. This study utilizes the full polarization products to generate the co- and cross-polarization ratios and polarimetric decomposition products.

NDWI

The Normalized Difference Water Index (NDWI) was proposed by Gao (1996) to detect liquid water in vegetation. This index is analogous to the widely used Normalized Difference Vegetation Index (NDVI), which utilizes the red and near-infrared channels of the electromagnetic spectrum to detect vegetation. NDWI, on the other hand, uses the near-infrared (0.86 μm) and shortwave infrared (1.24 μm) channels to highlight wet vegetation, and is calculated as follows:

$$NDWI = \frac{NIR - SWIR}{NIR + SWIR}$$

NDWI measures the amount of water in vegetation that has interacted with solar radiation, but has also been shown to be sensitive to water present in bare soils, but like NDVI is still susceptible to soil reflectance (Gao, 1996). *In situ* measurements also concluded that NDWI values are mostly negative for wet and dry bare soils (with wet soils have slightly more positive values) because the reflectance for these surfaces in the shortwave infrared is greater than at the near-infrared band (Gao, 1996). Using laboratory measurements, NDWI was also found to be less sensitive to atmospheric scattering effects than NDVI (Gao, 1996).

A NDWI dataset is included in this study as a simple comparison of soil moisture content to the PolSAR datasets. NDWI is an intuitive product that can easily be implemented into a leak/seep detection system for response agencies to review. RGB composites of the corresponding Landsat data were not effective at seep visualization with its 30-meter resolution. However, the same resolution for its NDWI product with a smaller range of values does allow

for detection of seep features. The dataset acts as an independent confirmation of increased soil moisture, but cannot be used on its own to identify small-scale leaks and seeps due to the typical spatial resolutions offered by these products. For this study, the Landsat 5 and 8 Tier 1 8-Day NDWI Composite products were collected as GeoTIFF images for the two study areas for 2009-2018. The Landsat RGB surface reflectance images did not have sufficient spatial resolution to differentiate any features in the study areas, but the NDWI products, being on a -1 to 1 scale, still allowed for modest feature identification at 30 meters resolution.

Additional NDWI algorithms exist, including a version from McFeeters (1996) utilizing the green band and near-infrared band, and a more recent modified NDWI index using the green and middle-infrared bands (Xu, 2006). The McFeeters index is capable of maximizing the reflectance of water, but has been found to produce results of mixed water and built-up land noise as false positives. Xu's modified NDWI (MNDWI) reduces this effect from built-up land by utilizing the middle-infrared band, which has higher reflectance than the green band, assigning built-up land areas with negative values instead. Both of these NDWI algorithms may be more efficient at detecting standing water features when compared to Gao's version of NDWI, which highlights water content in vegetation. As seen by this study, seeps have varied characteristics of the presence of standing water and vegetation, so a future analysis comparing all different NDWI algorithms may help highlight seeps of varying standing water and vegetation content. For this study, the Gao (1996) algorithm is used, and it is noted that standing water features are still detectable in the seeps chosen for this study.

GIS Datasets

GIS (geographic information systems) datasets are included in this study's visualization and analysis. The California Department of Water Resources (CA DWR) provided the majority

of the GIS layers through personal communication. For the CA Aqueduct, point KMZ files contained 57 past seep repairs and 65 potential seep locations along the structure. For the Delta, 131 past seepage locations were provided, about 30 of which were collected through personal communication with the DWR and various texts. It is worthy to note that these datasets contained minimal metadata about the nature of the seep and most entries did not include any specific dates. The aqueduct seep repair comments only list the repaired date, ranging from 1985 to 2018, with the majority of points having been repaired before 2000. The aqueduct potential seep comments consist of one line describing the condition of the location, but only a handful contain date information. The Delta seep points from the DWR only labeled the seep as either Serious or Critical, and did not contain any date information.

A conveyance line GIS shapefile was provided by the DWR for the CA Aqueduct which runs through the San Joaquin Valley. Similarly, they also provided a levee anatomy polygon shapefile for the Delta, which can allow identification of the various levee parts known to managers in the area. The landside versus waterside levee areas, levee crown, ramp, tow berm and ditch areas can be used to describe the nature of a seep and help to classify its severity based on the area of the levee it encompasses. Analyzing data in the Delta also requires the use of a surface water mask since the area is composed of small islands surrounded by waterways. The most detailed water mask was created by merging the water classes in two separate datasets, a DWR land cover raster and the TIGER LINE surface water dataset.

Manual Seep Detection

The UAVSAR products are available for public download via the UAVSAR website and Alaska Satellite Facility (ASF). Due to the bulk of data storage required for this study (terabyte-level), the UAVSAR datasets were downloaded and stored via a remote Linux server. A

download script generated by ASF Vertex tool calls the ASF web API and downloads all available PolSAR products from a given flight line. A python script was written by the UAVSAR team to extract the ZIP files that were downloaded, converting each polarization product to decibels and generating ENVI header files for readability in ArcGIS. The VV and HV ratios are also computed at this step by differencing VV and HH, and HV and HH, respectively. Since decibels occur on a logarithmic scale, the difference between these products is equivalent to their ratio. The UAVSAR products denote four characters for the polarization since these are cross product datasets. The copolarization phase is calculated as the angle of the complex value of the HHVV product. The angle indicates the difference in phase between HH and VV polarizations.

For both study areas, each of the seep repair and potential seep locations were manually inspected for evidence of increased soil moisture. Each location was brought into Google Earth Pro and inspected by combing through the available historical optical imagery for observable seep features. The same process was applied to the PolSAR datasets, focusing first on the single HH and VV polarization products for ease of interpretation. Any distinguishable seep-like features coincident with the DWR point datasets were noted. These features would match in shape and size to damp areas observed in the optical imagery and are seen as highly contrasted in the single polarization imagery. This manual process was necessary to identify a primary collection of confirmed seep features in the PolSAR data that could be verified by optical imagery and DWR field observations. The collection can then be used to help guide an automated detection system for future development. A few of the locations from this collection are previewed in this study.

In addition to the single polarization products and polarization ratios computed, a simple decomposition was performed on the single polarization products. Hundreds of decomposition techniques exist, but one of the most basic algorithms was used for this study, the H-A-Alpha decomposition. This method produces three products, entropy (H), anisotropy (A), and the mean alpha angle. These products provide insight into the types of scattering mechanisms which characterize a seep feature, and how those mechanisms may change as the seep grows or may be present before the seep occurs.

The decomposition was applied using the European Space Agency's PolSARPro program, which required the full polarization product as input. The algorithm quantifies the different scattering mechanisms by first converting the scattering matrix into a 3x3 coherency matrix (T3), defined as follows (Cloude and Pottier, 1996):

$$\langle |T| \rangle = \frac{1}{2} \begin{bmatrix} \left\langle |S_{HH} + S_{VV}|^2 \right\rangle & \left\langle (S_{HH} + S_{VV})(S_{HH} - S_{VV})^* \right\rangle & \left\langle 2S^*_{HV}(S_{HH} + S_{VV}) \right\rangle \\ \left\langle (S_{HH} - S_{VV})(S_{HH} + S_{VV})^* \right\rangle & \left\langle |S_{HH} - S_{VV}|^2 \right\rangle & \left\langle 2S^*_{HV}(S_{HH} - S_{VV}) \right\rangle \\ \left\langle 2S_{HV}(S_{HH} + S_{VV})^* \right\rangle & \left\langle 2S_{HV}(S_{HH} - S_{VV})^* \right\rangle & \left\langle 4|S_{HV}|^2 \right\rangle \end{bmatrix}$$

The * symbol denotes conjugation while the brackets indicate an average. The coherency matrix is modeled as a sum of the three main scattering mechanisms: surface scattering, dihedral scattering, and volume scattering. These nine elements are calculated for each pixel of each image, and then the eigenvectors and eigenvalues are calculated from the T3 matrix. The eigenvectors differentiate the scattering types while the eigenvalues relay information about the intensity of scattering (Alberga, 2007). The H-A-Alpha decomposition parameters are defined as a function of these eigenvectors and eigenvalues.

Entropy, whose values range from 0 to 1, is a measure of the randomness of the scattering medium (Alberga, 2007). Entropy values near zero indicate that the coherency matrix only has one non-zero eigenvalue (Alberga, 2007). Entropy is near zero for isotropic surfaces that contain low roughness such as oceans, where the primary scattering mechanism is surface scattering (Marapareddy et al., 2016). Larger values of entropy indicate multiple scattering mechanisms at play, such as for vegetation. A medium entropy value suggests that there is more than one scattering mechanism at play, but doesn't indicate how many there are. Anisotropy, which ranges from 0 to 1, provides information on the importance of the secondary scattering mechanism, and is derived from the eigenvalues (Alberga, 2007). A high anisotropy value close to 1 suggests that there are two dominant scattering mechanisms and a less important third mechanism. A low anisotropy value close to 0 suggests that there is one dominant scattering mechanism and two secondary mechanisms (Marapareddy et al., 2016).

The alpha angle contains information about the type of scattering that is dominant and unlike entropy and anisotropy, is derived from the eigenvectors. The mean alpha angle contains values ranging from 0 to 90 degrees, where 0 degrees denotes surface scattering, 45 degrees shows volume scattering, and 90 degrees shows double-bounce scattering. Surface scattering can occur over open water bodies, volume scattering is common within vegetation canopies, and double-bounce can be found in urban areas from scattering between the ground and building walls.

Google Earth Engine

In the interest of future automated seep detection workflows, the Landsat NDWI products were downloaded via Google Earth Engine. The products were masked spatially and temporally using a Google Colaboratory (Colab) Notebook, which are Jupyter notebooks hosted in the cloud

and easily integrated with Google Drive. The Colab script created an Image Collection of the intended Landsat NDWI product, filters the desired time period, filters the bounds with a polygon shapefile mask, and selects the appropriate bands. It then iterates over this collection list and extracts each image's date, batch exporting the images to a Google Drive folder with each image labeled with its acquisition date. The images can then be downloaded locally from the Google Drive output folder. Jupyter-style notebooks can easily be distributed to response agencies and are interactive, intuitive methods of sharing projects such as a seep detection workflow. This integration is beyond the scope of this study but will be its intended conclusion.

GIS Preparation

All analysis and figures were generated using Esri's ArcMap 10.6 program to be compatible with future emergency response and monitoring initiatives. The PolSAR and NDWI datasets were prepared for GIS readability and displayed alongside relevant GIS datasets. To easily scroll through each dataset chronologically, each of the PolSAR datasets (HH and VV single polarizations, VV and HV ratios, copolarization phase, H-A-Alpha decomposition) and NDWI dataset were converted to mosaic datasets in ArcMap. The Time Slider capability in ArcMap allows for the user to scroll chronologically through each dataset. Each figure included in this study was manually exported in this manner due to the limitations of exporting each frame of a Time Slider video – not every image would have been included.

Results

California Aqueduct

Five past seep locations were chosen along the California Aqueduct and are presented here alongside Google Earth historical imagery, NDWI images, and PolSAR datasets. The figures for Seeps 1-3 are included as Figures 1-12. The first three seep examples are located in

the northern section of the aqueduct (Figure 1A), and are clustered close together. Seeps 4 and 5 are located further south. Seeps 2 and 3 are located on the same agricultural field, and Seep 1 is on a separate field slightly north of the other seeps (Figure 1B). For all examples, the seep will be denoted by a star symbol and the aqueduct line will be shown as a black line. The DWR comments for these seeps are as follows:

#1 is directly across from the 300-ft long sheet pile wall we installed to cut off seepage along the east bank at MP 88.96. This is definitely an area that I would expect to exhibit higher than normal subsurface moisture conditions. In fact, 6/28/11 aerial photo in Google Earth suggests the presence of a shallow water bearing geologic feature (former streambed perhaps) running directly through our leak site.

#2 is also interesting as it is immediately west of the spoil pile we used as a borrow source in 2012 to construct the seepage berm at MP88.96. You can see the recent ground disturbance there in the 8/27/12 Google Earth photo. There are several green spots in the fields on the east side of this location in the 8/31/09 photo (below) that are similar to the emergent vegetation east of MP88.96 in the same photo. (The vegetation is probably our best indicator of shallow seepage…)

#3 is on the west side of an area (MP89.5) that has had a couple of repairs. In the photos you can see a small berm that was constructed within the last 5-7 years on the east side of the bend. On the west side you can also see about 80 feet of new concrete panels that placed around the same time. I also see a couple of small dimples in the concrete liner that suggest differential

settlement in line with your pin. These dimples are where we have seen a lot of seepage as cracks form in the liner.

The Google Earth imagery shows the seasonal changes of agriculture throughout the years, and the fields that the seeps are located on look much drier after 2006, possibly due to the ongoing drought in the region. Seep 1 starts to appear close to the aqueduct on 04/24/2010, starts to grow on 07/07/2010, and reaches its maximum size on 06/18/2011 where the feature can be seen traversing the field (Figure 2B). On these dates, the water in the aqueduct also appears to have high flow, which may have caused these seeps to occur. On 04/12/2015 and 09/20/2018, the rectangular scar left by the seep is apparent, and this shape is also seen in the PoLSAR data, discussed below (Figures 2B and 2C). Seeps 2 and 3 are not as large as Seep 1, but the locations do contain darker wet soils close to the aqueduct on the same aforementioned dates. On both of the 2009 images, Seep 2 shows a dark line close to the aqueduct and also a feature directly across the aqueduct on the adjacent field (Figure 2A). This feature is reminiscent of a seep as it travels from the aqueduct across the field. In fact there is a similar feature for Seep 1 in its adjacent field on 08/31/2009 that is likely related to that seep.

The NDWI legend and all subsequent legends are shared in Figure 3, where each colorbar displays high values as orange-red (wetter) and low values as blue-pink-white (drier). In 2013, the NDWI images show dry conditions, with a blue circle feature between Seep 1 and 2 that corresponds to the scour pond-like feature seen in Figure 2 (Figure 4A). An outline of the field containing Seep 1 is slightly wetter than its surroundings. In 2014, a couple of dates in January and February are obscured by cloud cover. On 03/06/2014 the first appearance of the three seeps can be seen on wetter surfaces, and Seep 1 reappears in August-October 2014 (Figure 4B and 4C). All seeps show much wetter conditions in February and March of 2015, with the entire field

containing Seeps 2 and 3 having high NDWI values (Figure 4C). Seep 1 is faintly seen through the rest of 2015, and the entire area appears wet again in January to March 2016. A similar pattern is seen the next year, with a prominent rectangular feature showing up on 04/15/2017 (Figure 4F). Spring 2018 does not look as wet as previous years, but Seep 1 remains prominent (Figure 4G).

For the HH and VV single polarization datasets, higher values indicate higher radar backscatter return in the specified polarization. The entire HH image scene brightness changes between two extremes throughout the time period, for example the backscatter is much greater on 05/29/2013 (orange-red) than on 07/19/2013 (blue-purple) (Figure 5A). The water in the aqueduct itself also shifts between these values. The crop lines are apparent in the HH polarization for both fields of interest, especially in 2013 and 2014 (Figure 5A). Seep 1 first appears on 10/06/2014 and persists until the end of 2015 (Figure 5A). It doesn't return until October and November 2017, and isn't seen in the remaining time period (Figure 5B). Small features appear near Seeps 2 and 3 on 10/24/2016 and 02/05/2017. The VV single polarization images, on the other hand, stay within the same value range over time (Figure 6). A small feature persists across the aqueduct from Seep 3 on the adjacent field. The formation of all three seeps is first seen on 10/06/2014, and grows until 03/10/2015 (Figure 6A). Seep 1 returns in late 2016, but Seep 2 and 3 are hard to differentiate from field activity (Figure 6B).

The HV and VV ratios highlight areas more sensitive to vegetation and soil moisture, respectively. Seep 1 first appears in the HV/HH ratio images on 10/06/2014 until the end of 2015, but Seeps 2 and 3 are not as apparent (Figure 7A). The seeps do not reappear in the rest of the time period, and only seasonal changes on the field-scale are seen. The aqueduct water also is not as distinguishable as in previous datasets. In the VV/HH ratio data, on the other hand, the

aqueduct water can be seen prominently at times with high values (e.g., 06/16/2014) (Figure 8A). Here, the two fields of focus are not delineated clearly as for the HV ratio. Seeps 1-3 first appear on 10/06/2014 until 03/10/2015 (Figure 8A). The copolarization phase is presented in radians, indicating the phase shift between HH and VV. The scene is quite similar throughout time, with some noise appearing at Seep 1 on 11/13/2014 and 01/07/2015.

The H-A-Alpha decomposition results are presented next, with entropy containing values from 0 to 1, where larger values indicate multiple scattering mechanisms present. The two fields that the seeps are located on generally have very low entropy values (Figure 10). The entropy value at Seep 1 increases starting from 10/06/2014 to 01/07/2015, and decreases again thereafter (Figure 10A). Low entropy features are seen near Seeps 2 and 3 on 02/19/2016. The seeps are not seen in the remaining dates, but the fields shift in entropy values. Anisotropy also contains values from 0 to 1, where a high value suggests there is more than one dominant scattering mechanism. On the aforementioned dates where Seep 1 is noticeable, the anisotropy value is slightly lower than its surroundings (Figure 11A). The changes mainly occur at the field-level, with a very high increase in anisotropy for the field containing Seeps 2 and 3 in late 2017 to 2018 (Figure 11B). The mean alpha angle ranges from 0 to 90 degrees, characterizing the type of scattering present. The two fields containing the seeps generally have very low alpha angles following field boundaries. Seep 1 appears on 10/06/2014 with 30-35 degrees and increases to 45 degrees by 01/07/2015 (Figure 12A). High alpha angles are also seen at Seep 1 on 04/03/2017.

The figures for Seep 4 are included as Figures 13-24. Seep 4 is located about 75 kilometers south of Seeps 1-3 (Figure 1A). Seep 4 is located close to the aqueduct, in a position that may be receiving water from multiple sources, as described by the DWR:

#4 – That whole area looks damp in the recent and historical photos. I notice an unlined irrigation ditch at the toe of our embankment leading south to a turnout. That would be a prime source from shallow groundwater. It may be difficult to determine if the source is the ditch, the Aqueduct, or both.

In the Google Earth imagery, Seep 4 makes its first appearance in 05/24/2009, when the aqueduct water appears to be at high levels (Figure 14A). The seep signature is prominent by 04/05/2014 and continues to grow even larger over the next few images, keeping confined to a triangular boundary (Figure 14B). In 2017-2018, a white deposit can be seen around the seep, which may indicate that water is evaporating and leaving behind some mineral deposit, such as a salt pan. This feature appears to contain much more water than previous seep examples, and contains unique layers within the seep itself.

Seep 4 can first be seen on 03/30/2014, and similar to the Google Earth imagery, begins as a small feature close to the aqueduct that begins to grow southward (Figure 16C). The feature continues to grow, and increases starkly in size by 09/2014 (Figure 16D). The feature itself is wetter in the center, which may not be apparent in optical imagery alone. The seep reaches a maximum size in 2015, and then begins to shrink in early 2016 before growing again to its maximum by fall 2016. After this, the feature remains at a smaller size close to the aqueduct, and a separate feature that is not as wet begins to form (e.g., in 01/25/2017). In April and May 2017, the seep feature shows its highest NDWI values, but then begins to shrink before returning in March 2018 (Figures 16M and 16N). The feature alternates as two separate features and one whole shape in 2018, reaching peak size before shrinking again by the end of the year (Figures 16O and 16P).

The HH polarization images begin to show wet conditions near Seep 4 in 10/31/2013, and the feature continues to grow throughout time (Figure 17A). The shape of this feature is only similar to the feature closest to the aqueduct see in the NDWI imagery, and not the full triangular shape. The HH images also differentiate between these two features, although due to the overall scene brightness shifts, the feature size is difficult to track visually. The VV polarization images have a more consistent scene brightness, and Seep 4 can first be seen on 04/02/2014 (Figure 18A). The seep then shrinks and reappears on 10/06/2014, shrinks again, and reappears slightly lower and as a different shape on 03/10/2015. The seep continues to grow until 04/10/2017, around when the southern feature begins to take shape (Figure 18B). Then on 07/20/2018, the northern feature reappears again, and shrinks until the end of the time period.

The consistent features of Seep 4 seen in the HH and VV polarizations are mostly absent from the HV/HH ratio (Figure 19). Only in 2016-2017 is some semblance of the northern feature seen with higher HV values, and in August and October 2018 the southern feature is apparent as well. In the VV/HH ratio imagery, however, the seep is prominently observed, starting on 04/02/2014 (Figure 20A). The seep follows a similar timeline as described in the VV single polarization dataset above, but the VV/HH ratio results show the seep as a larger feature with higher intensity. The triangular field shape is seen in the copolarization phase dataset, but it is not apparent whether these phase shifts are related to the seep or the field activity (Figure 21).

Seep 4 can be observed in the entropy dataset as well, and begins in 2014 with low values, with slight increases in entropy and a changing shape over the time period (Figure 22). Not much difference is seen in the anisotropy results for Seep 4; the area cannot visually be differentiated from the surrounding fields (Figure 23). The seep consistently approached high

alpha angles, at 50 to 60 degrees on 10/06/2014 when it first appeared (Figure 24A). Like the previous datasets, the alpha angle images show the feature changing in size over time.

The figures for Seep 5, the final California Aqueduct example, is shown in Figures 25-36. Seep 5 is located slightly south of Seep 4, and is described as follows by the DWR:
#5 –I see some ponds on the farmer's property, what is likely a water line crossing over the Aqueduct, a recent liner repair adjacent to the location you identified, and a darker (damp) area in the 4/13/13 aerial photo. The apparent damp area and the liner repair suggest to me that this could be Aqueduct water.

In the Google Earth imagery, Seep 5 can be seen as early as 06/03/2003 as greener vegetation close to the aqueduct (Figure 26A). The area is seen as more damp and darker than the surroundings throughout the time period, though may not be visible by 06/30/2018 (Figure 26C). On 05/02/2015 and 05/01/2017, the seep area again shows an increase in green vegetation that differs from the bare surroundings, which may have been caused by wetter conditions (Figure 26B). The aqueduct does not appear to have high water levels in any of the images captured for this location. In the NDWI imagery, a small seep feature is seen starting on 10/08/2013 (Figure 28B). This feature stays about the same size and disappears by 2014, not to be confused with the adjacent feature of the farmer's ponds. Some linear features occur north-south in February to March 2015 that look similar to that seen in the Google Earth imagery on 05/02/2015. The feature reappears in February 2016 when the entire field is wet, and is most well seen on 03/21/2016 and 03/29/2016 (Figure 28I). The seep disappears before reappearing in December 2016, reaching maximum size around April 2017 (Figure 28K and 28L). Again the feature shrinks and is not seen for the rest of the time period. The end of the time period in

November to December 2018, the field that the seep is located on has very low NDWI values, indicating dry conditions (Figure 28P).

Seep 5 first appears in the HH single polarization images on 10/31/2013 as a small feature close to the aqueduct (Figure 29A). The feature persists over time, and the field in which it is contained is especially wet on 02/05/2017 (Figure 29B), reminiscent of the Google Earth image on 06/03/2003. The seep is most prominent around this date, February to April 2017, and diminishes in intensity until the end of the time period (Figure 29B). The UAVSAR line over this area is missing data on 10/07/2015, and so this panel remains blank. Interestingly, the VV single polarization consistently observes a small circular feature with high values near the center of the scene, and is co-located with a similar feature seen in the Google Earth imagery on 04/13/2013 (Figure 26B) and 06/30/2018 (Figure 26C). This feature appears to be of similar intensity as the farmer's ponds. The original seep feature closest to the aqueduct is still seen in the VV images, but at smaller values.

The same small circular feature in the center of the scene is observed in the HV/HH ratio images (Figure 31) at high values. The farmer's ponds for this dataset also are highly distinguishable, but at very low values. The seep feature close to the aqueduct is not apparent in the HV/HH ratio images. For the VV ratio, the small circular feature is not seen at all and the aqueduct-adjacent feature is only seen on 02/05/2017 at high values (Figure 32B). The copolarization results are very noisy, with high phase difference between HH and VV seen near the seep close to the aqueduct, though the seep feature itself is not clearly outlined. Similar to the VV/HH ratio results, the entropy images only prominently show the seep closest to the aqueduct on 02/05/2017 (Figure 34B) as having lower entropy values, closer to zero. The entropy changes in the scene are mostly attributed to agricultural activity. For anisotropy, no discernable changes

are seen either, except for higher values (closer to 1) on 02/05/2017 for the field that contains the seep (Figure 36B). For the mean alpha angle, no seep feature is displayed and the only outstanding features are the farmer's ponds which have very high alpha angles. The agricultural fields also show changing alpha angles over time.

Sacramento Delta – Twitchell Island

A similar procedure is applied to five seep examples on Twitchell Island in the Delta, a much wetter environment. All five locations are located on the southern side of the island and confirmed as past seepage by the DWR. These seep examples are much smaller in extent than those of the CA Aqueduct. For these examples, only the Google Earth imagery, NDWI, and VV/HH ratio products are presented in the interest of space. The VV/HH ratio results are presented for all available UAVSAR flight tracks over the area. Based on the findings from the CA Aqueduct, the VV/HH ratio showed the best ability to differentiate between seeps and their surroundings.

The first three seeps are located on Chevron Point on Twitchell Island close to the levee (Figure 37B). Seeps 1 and 2 are labeled as past seepage sites and "critical", and Seep 3 was confirmed from personal communication with the DWR. The western side of this area contains a consistent damp area (north-south feature, slightly inland) that persists throughout the Google Earth imagery (Figure 38). The land cover classification in this area is mixed; there is fallow/idle cropland but also alfalfa crop designation. This area may be continuously flooded. The seep areas begin to appear wet starting on 05/16/2002, with an isolated seep feature seen by Seep 2 on 09/30/2002 (Figure 38A). This area near Seep 2 continues to show much greener vegetation than its surroundings, suggesting more moist conditions. A small green patch can also be seen near Seep 3 on 05/31/2007 (Figure 38B). The entire eastern side of Chevron Point is green on

08/31/2008, and the area near Seep 2 remains green until 04/24/2010 where strong seep-like features are seen (Figure 38C). The area near Seep 1 begins to look damp on 05/11/2011 during high tide (Figure 38D). The seep near Seep 2 continues to the end of the time period, with the entire area showing green vegetation during the spring months (e.g., 04/05/2014 and 03/11/2017).

Every spring, the NDWI imagery shows much wetter conditions at Chevron Point (Figure 40). These wet features are not isolated on the levee, but occur for the general area. In 2010, this wet area contains a gap of drier conditions where Seep 1 is located, though the feature is still wetter than previous acquisitions (Figure 40A). It is unclear what caused the east-west feature shown on 05/25/2010 (Figure 40B). A consistent L-shaped feature that is drier than the surroundings is found at Seep 1 throughout the time period, a location at which the Google Earth imagery shows roads leading to a structure. The western strip feature that looked wet in the Google Earth imagery is also seen as a similar shape and slightly wetter than its surroundings in the NDWI images. The feature shows its driest state in early 2018, despite wetter hotspots nearby (Figure 40J). The tip of Chevron Point near Seep 3 remains dry over time (e.g., Summer 2016) (Figure 40H).

For Line 05519, the VV/HH ratio results show high values along the western levee stretch, starting on 07/17/2009 and reappearing in late 2010-early 2011 and 07/18/2012 (Figure 41). The feature is not seen again until the end of the time period. The aforementioned inland feature is also seen, but at very low ratio values, starting on 05/10/2010, reappearing on 05/12/2011 and May 2015. High ratio values are observed near Seep 2 on 08/10/2010 and again on 10/04/2015 and 03/23/2016. This stretch of levee also has high ratio values at the end of the time period, but is indistinguishable from the rest of the scene. In contrast, for Line 15502, this

eastern feature is easily differentiated from the surroundings, seen first on 07/18/2009 (Figure 42A). The feature shows the highest ratio values on 05/12/2011 and 07/18/2012, similar dates to the western feature in Line 05519. This eastern levee feature is seen at similar times of the year: May-June 2011, March 2012, May-July 2012, July-October 2013, June 2014, June 2016, and July 2018. Line 33502 contains similar results for both the inland eastern feature and the western levee feature (Figure 43). The tip of Chevron Point appears to be more connected to the eastern levee subsidence feature. (e.g., 08/10/2010). There is also a large high-value feature close to Seep 1 on 03/23/2016 (Figure 43D). For Line 23518, high ratio values are also seen on the western side of Chevron Point, and the feature seen on 12/07/2016 is especially concentrated near Seep 1 (Figure 44D).

Seep 4 is also located on the southern side of Twitchell Island, but further east of Seeps 1-3 (Figure 45). The optical and polarimetric results for this area are included in Figures 46-52. It is unclear when this seep first appears in the Google Earth imagery due to the low spatial resolution (Figure 46). The area does look damp beginning on 05/16/2002 and 06/16/2002, but is not as obvious as on 03/04/2011 when water is seen traveling across the road. The vegetated portions of this area look dark and damp from September 2009 leading up to 03/04/2011 (Figure 46C and 46D). These areas continue to look damp, and the seep can be seen on the road again from 07/01/2012 to a larger spread on 09/01/2012 and 01/26/2013. (Figure 46E and 46F) The same seep signature then reoccurs for an even larger area on 03/11/2017 (Figure 46G). After this event, a smaller seep can be seen in the center of the image on the road, on 08/31/2017 and again on 06/20/2019 (Figure 46G).

For reference, the levee line displayed in Figure 48 is located slightly south of the road on which Seep 4 is seen in the Google Earth imagery. The damp and dark vegetation features are

not clearly outlined in the NDWI imagery. Instead large features of dry and wet conditions are seen (e.g., 05/09/2011 versus 07/12/2011). The NDWI product is missing the dates of the 2012-2013 progression of Seep 4 displayed by the Google Earth imagery described above (Figure 48C). Only Landsat 5 and 8 are included in this study due to the striping issues that exist in Landsat 7, which would have covered this time period. The seep signature seen in the Google Earth imagery in 2017 is not seen in the NDWI, although conditions are wetter during this time. Only large-scale features are discernable in the NDWI images.

In contrast, small-scale features can be differentiated in the UAVSAR VV/HH ratio results (Figure 49). For Line 05519, the first acquisition date (07/17/2009) shows a high value feature parallel to the levee (Figure 49A). Although this feature does not occur exactly on the road as seen in the Google Earth imagery, it does indicate wetter conditions in the approximate area. Spring 2011, spring 2012, early 2013-2017, and late 2018 show the highest values of VV/HH ratio for Seep 4. A small scale feature with low ratio values also persists throughout the dataset, located close to where the seep was seen on the road (e.g., 04/27/2015). In Line 15502, higher values are seen in the area overall, starting on 10/03/2009 (Figure 50A). Large VV/HH ratio values are still seen in the spring, but at higher intensity and more concentrated close to the levee. Lower values are seen overall for Line 33502, especially close to the levee (Figure 51). As in other lines, 2012-2013 shows larger values for VV/HH ratio (Figure 51B and 51C), and spring months in other years. The small features close to the road are not apparent in this line. Line 23518 shows similar results (Figure 52), but does show a small low ratio value feature close to the road on 04/23/2013 and 03/23/2016.

Seep 5 is located close to Seep 4 on Twitchell Island but further east (Figure 54) and the results are shown in Figures 54-61. Like Seep 4, the spatial resolution of many Google Earth

images is inadequate for these small seep areas in the Delta (Figure 54). The area first appears damp on 09/30/2002 and greener vegetation is noticeable closer to the levee on 05/31/2007 (Figure 54A and 54B). Vegetation response to a seep is especially apparent on 09/23/2009, where greener areas outline where the seep has traveled from the levee towards inland areas (Figure 54C). An active seep is observed on 03/04/2011 on the road between the previously greener areas of vegetation (Figure 54D). The effects of this seep is again seen by greener vegetation on 05/19/2012 and onward. The seep is seen again traveling across the road on 04/05/2014, growing over time and reaching its largest span by 03/11/2017 (Figure 54G). By the last frame in 2019, there is no visual evidence of the seep or changes in vegetation.

The road on which Seep 5 is observed in the Google Earth imagery follows the contours of the levee line in the subsequent figures, and is located slightly north of the line. In general, the NDWI results show dry conditions in the winter and wetter conditions in the spring and summer (Figure 56). Consistently wet conditions are observed in 2015-2017, near the peak of the active seep observed in the Google Earth images (Figure 56F). On the day that the largest area of the seep was observed, 03/11/2017, there is no Landsat acquisition date available and the two closest dates are obscured by weather. No small-scale seep feature is seen in this dataset.

For Line 05519, the VV/HH ratio results for Seep 5 show high values in the scene every spring, especially around March (Figure 57). These seasonal features are generally large, which denies the ability to identify small-scale features as seen in the Google Earth imagery. Only a few examples of small-scale seep-like features are observed, e.g., on 05/29/2013 on the levee border, and a low value feature on the road on 11/25/2013 (Figure 57C). These dates are consistent with active seep formation in the optical imagery. Similar to Seep 4, Line 15502 for Seep 5 shows higher VV/HH ratio values on the levee itself, e.g., 03/04/2010 (Figure 58A). The

high value scenes generally also occur in the spring time, but is less consistent than in Line 05519. No small features are seen in this line, though some features occur close to the road and are similar in size (e.g., 05/16/2015 and 06/14/2016) (Figure 58D). An additional line, 15503, is available for this area (Figure 59). The VV/HH ratio for this line does not show high intensity as in previous flight tracks, though spring months (March) do show higher values. There are many small individual features for this track, but cannot be differentiated from each other. For Line 33502, the months with the highest intensity values are: March 2012, January 2013, and January 2014 (Figure 60B and 60C). These dates correspond with when the active seep was observed in the Google Earth imagery. Lastly, for Line 23518, the highest intensity images again occur on March 2012, January 2013, and January 2014 (Figure 61), as seen in Line 33502. A small feature of lower intensity persists from 05/29/2013 to 01/16/2014 (Figure 61C), which may be seep related. A higher intensity version of a similar feature is seen on 04/27/2015 (Figure 61D).

Discussion

California Aqueduct

The overall efficacy of each parameter used to study the CA Aqueduct seep examples are summarized in Table 1, and discussed further below.

Parameter	Seep 1 (medium)	Seep 2 (small)	Seep 3 (small)	Seep 4 (large)	Seep 5 (medium)
Google Earth Imagery	Well detected	Somewhat detected	Somewhat detected	Very well detected	Well detected
NDWI	Well detected	Somewhat detected	Somewhat detected	Very well detected	Somewhat detected
HH	Somewhat detected	Somewhat detected	Somewhat detected	Well detected	Well detected
VV	Somewhat detected	Somewhat detected	Somewhat detected	Well detected	Well detected
HV/HH Ratio	Somewhat detected	Poorly detected	Poorly detected	Somewhat detected	Not detected
VV/HH Ratio	Well detected	Well detected	Well detected	Very well detected	Somewhat detected
Copolarization Phase	Poorly detected	Not detected	Not detected	Somewhat detected	Somewhat detected
Entropy	Somewhat detected	Poorly detected	Poorly detected	Well detected	Poorly detected
Anisotropy	Not detected	Not detected	Not detected	Poorly detected	Not detected
Alpha Angle	Well detected	Somewhat detected	Somewhat detected	Well detected	Poorly detected

Table 1: Summary table for each parameter used to characterize the seep examples for the California Aqueduct. Qualitative ratings range from: Not detected, Poorly detected, Somewhat detected, Well detected, to Very well detected. Size of each seep is also noted.

Both the Google Earth and NDWI imagery are susceptible to cloud cover and weather conditions prohibiting data collection. For the five seep examples along the CA Aqueduct, there was a sufficient amount of data available to track the seeps' progression through time for this study, but for providing information during an extreme weather event, these optical datasets cannot reliably be used as the primary indication of conditions on the ground. Google Earth imagery is able to track seep changes very well for large and medium seeps, Seeps 1, 4, and 5 (Table 1). The size of these features contributes directly to their visibility in the optical imagery. Similarly, NDWI is well detected for the largest seep (Seep 4) and one of the medium-sized seeps, Seep 1 (Table 1). The NDWI dataset is in agreement with the PolSAR data on the average

time that the three seeps first appeared, March – October 2014 for NDWI and October 2014 for the PolSAR data. Since the seeps can reoccur and disappear over time, the low temporal resolution of UAVSAR may be the reason for the time lag. Seeps 2 and 3 cannot be discerned from the Google Earth imagery or the NDWI images due to their small size, although the general region does appear wetter for these seeps in certain months. Seep 4 is an example of a significant feature that is capable of being detected with optical imagery. This feature is also more complex than Seeps 1-3 since Seep 4 contains 2 features within and appears geologically more involved in the optical imagery. The NDWI dataset shows high efficacy in monitoring capabilities for a seep of this size in this study area. Seep 5 is only somewhat detected with NDWI despite its medium size, likely due to the different nature of the seep. Seep 5 does not appear to contain standing water like Seep 4 or a distinctive boundary such as the rectangular shape that Seep 1 takes in optical and PolSAR imagery. When Seep 5 reached maximum size in the NDWI imagery is around the same time as the seep area showed much greener vegetation in the Google Earth imagery, indicating wetter conditions. Both datasets show dry conditions in 2018. Spring 2017, where the seep is at maximum size, is also a similar time to the date (02/05/2017) in the PolSAR data for which the seep most consistently appears.

Single HH polarization only somewhat detects Seeps 1-3 and better detects Seep 4 and 5 (Table 1), with a similar pattern for the single VV polarization dataset. However, Seep 1 is slightly more detectable in the single polarization data than Seeps 2 and 3 despite having the same ranking. Seep 4 is observable in the HH polarization, but is difficult to track. The HH single polarization shows constant scene brightness shifts in overall values, which complicates visual tracking of the seep features. The VV polarization and VV/HH ratio products are most effective at differentiating the seep from the surroundings and showing the progression of the

feature over time. The VV single polarization is more sensitive to surface roughness, and has more consistent scene brightness over time for all seep examples. Seep 4, the largest seep example, is easily identified with the HH and VV imagery, and Seep 5 also shows good contrast from the surroundings. For Seep 5, the VV single polarization data introduced a small circular feature that was not observed in the NDWI data and was only faintly visible in the Google Earth imagery. This feature may be more related to land surface change since VV polarization is more sensitive to this. Single polarization images, especially VV, are simple datasets that can more easily identify large seeps in a dry environment.

The HV/HH ratio is more sensitive to changes in vertical vegetation and the features follow field boundaries closely. Seeps are very poorly detected using the HV/HH ratio, with Seep 5 not being detected at all (Table 1). The largest seep (Seep 4) and Seep 1 are only somewhat detected, and are not very discernable from the surroundings. The HV/HH ratio is more effective at identifying vegetated fields, as is its more common usage. On the other hand, the VV/HH ratio reduces the effects of surface roughness and highlights wet soils, which is apparent as the aqueduct and seep features have much higher VV/HH values than their surroundings. The VV/HH ratio is very effective at detecting the seeps from the California Aqueduct, with the best detection made for Seep 4. Unlike previous seeps where the VV/HH ratio displayed the seep most prominently, Seep 5 does not appear at all in the VV/HH ratio imagery except on 02/05/2017. The circular feature also does not appear in the VV ratio, which supports the fact that the feature may be related to surface roughness. In fact, the farmer's ponds are more consistently apparent throughout these datasets, and are similar to Seep 4, which may have contained standing water. Large seep features are best detected in both optical and polarimetric datasets, especially the VV/HH ratio. The copolarization phase is very poorly

detected across all seeps, and is not detected at all for the smallest two examples, Seeps 2 and 3 (Table 1). The copolarization phase indicates that HH and VV are out of phase mostly for the agricultural fields in each seep's scene.

For the H-A-Alpha decomposition results, the entropy images showed that entropy increases as the seeps grow. This suggests that as the soil gets wetter, more scattering mechanisms are taking place. Entropy is only well detected for Seep 4, and poorly detected for the other seep examples (Table 1). Similar to Seeps 1-3, the entropy values for Seep 4 slightly increase as the seep grows and more scattering mechanisms are taking place. The anisotropy changes were not significant for the seeps, but mostly occurred at the field-level. Like entropy, anisotropy differences are negligible for the seeps. For Seep 1, the anisotropy decreased in value during the seep's formation, indicating that there is likely only one dominant scattering mechanism. Anisotropy was not detected for the majority of seep examples, and only poorly detected for Seep 4. Seep 4's lack of distinction in the anisotropy images also suggests that only one dominant scattering mechanism is present. The alpha angle was moderately effective at detecting seep features, and the rankings range across the seeps, which does not seem size-dependent (Table 1). The change in alpha angle during Seep 1's peak formation shows the scattering type shifting from surface to volume scattering. These results contribute to characterizing a shallow seep feature in this study area. For Seep 4, the high alpha angles during seep formation suggest a mixture of volume and double-bounce scattering occurring. These values are higher than those of Seeps 1-3, which again indicates a different seep characterization for Seep 4. This feature may contain more standing water, contains two separate features, and possibly different soil types. The H-A-Alpha decomposition results did not include Seep 5 at all, which suggests that the seep is unlike previous seeps, and may not be detectable with

polarimetric imagery though it is visible in optical imagery. The depth of this seep may be shallower and the moisture content may be less than that of previous seeps, especially as the ponds in the scene looked similar to Seep 4's polarimetric signatures. Therefore, not only does the size of a seep greatly affect its detection capabilities in both optical and polarimetric radar data, but the characteristics of the seep, such as depth and material, also contribute to its polarimetric signatures.

Sacramento Delta - Twitchell Island

The small seep examples for Twitchell Island most closely resembled the results for Seeps 2 and 3 of the California Aqueduct, the smallest seeps (Table 1). The NDWI results for Twitchell Island displayed the seasonal conditions of Chevron Point, with wetter surface returning each spring. The VV/HH ratio showed a similar pattern, where the eastern seep feature reoccurred in the spring/summer. The full NDWI dataset shows that seep detection in the Delta is much more challenging than in the San Joaquin Valley, perhaps because the seep features are much smaller. The wet and dry features shown in the NDWI imagery do not seem to follow any clear boundaries, as they did for the examples in the California Aqueduct. On Twitchell Island, the surrounding ground is less dry, vegetation has more variability, and seep features are smaller. In addition, there are more dates with unusable optical imagery due to cloud cover and weather conditions. Spring 2017 was an especially wet year for the Delta, and this is seen by the maximum seep signature seen in the Google Earth imagery on 03/11/2017. However, the PolSAR results only show the seasonal wet conditions and 2017 was not an outstanding year in the VV/HH ratio imagery. The UAVSAR results also include a high level of noise, with many small features scattered across the scene. If not for previous knowledge of the seep locations and Google Earth imagery, it would be difficult to differentiate the seep features from others. The

small feature that did appear in a few of the UAVSAR lines had low ratio values, which may characterize a wet road surface instead of a wet soil surface that was seen in the CA Aqueduct examples. However, these features did not look unique from the other features in the scene and further investigation of the other PolSAR datasets is required.

Even though the active state of the seep can be observed by optical data alone, the passive sensors are still sensitive to weather conditions, as seen by the loss of data in the NDWI imagery at the peak seep date in March 2017. Therefore, for any given storm, optical imagery alone is insufficient as a seep monitoring tool due to cloud cover that will likely occur. Regardless, the active state of Seep 5 was successfully captured in the Google Earth imagery in 2011 and 2014-2017. Similar dates, especially in the spring months, observed high intensity values of the VV/HH ratio for the seep location. The results for most flight lines contained many small features and so the seep was difficult to differentiate, except for the few examples that were mentioned. These examples had much lower values of the VV/HH ratio instead, and were found on dates between the high intensity conditions. Cathleen Jones (NASA JPL) also provided field photos of Seep 5 from June 2014 (Figure 62), and the signatures follow what was observed in the Google Earth imagery, where the seep traveled through vegetation and across the road. Though the seep examples in the Delta were not as well detected as those in the San Joaquin Valley, the VV/HH ratio and optical imagery were able to identify broad wet/dry regions on matching dates. During intense flooding, larger seeps will form and can potentially be better detectable with PoLSAR data, even for wet regions.

Conclusions

Levee seep detection of increased soil moisture using microwave radar is dependent upon the presence of vegetation, dielectric properties of the surface, and geometry of the objects

measured. For levee seep detection, soil moisture does not need to be measured quantitatively, and only a binary decision needs to be made whether a seep exists or not. This is performed visually for this study based on relative values of how much a seep is contrasted with its surroundings. The optical imagery and polarimetric radar products compared in this study show that seep detection is successful for certain environmental conditions.

For the California Aqueduct, the Google Earth imagery and NDWI products were very effective at detecting seep features, especially for the larger size examples. The datasets were able to track seep characteristics and size over time, with frequent acquisitions. However, both optical datasets suffer from data availability due to cloud cover interference. During stormy conditions when seep tracking is especially important, responders cannot solely rely on optical imagery. HH polarization showed large scene brightness shifts, but still shows the ability for seep tracking. The VV single polarization is more sensitive to surface roughness, and is also able to track seeps effectively, especially for Seep 4 for the California Aqueduct. Both HH and VV single polarization were somewhat effective at seep identification, especially for larger seeps. The HV/HH ratio is most sensitive to vegetation changes, and was not able to detect seep features effectively, showing changes in agriculture instead. The VV ratio, on the other hand, was able to reduce effects of surface roughness and highlight seep features prominently, even smaller seeps. The VV/HH ratio is chosen to study seeps in the Delta as the most effective PolSAR product. The copolarization phase did not provide much information for the aqueduct seeps, but did display noisy areas where HH and VV were out of phase, especially for agricultural fields.

For the polarimetric decomposition products, entropy was able to show that as a seep grows, more scattering mechanisms begin to take place and the entropy value increases over

time. Entropy was only effective at differentiating larger seep examples. The anisotropy product did not show most seeps clearly, suggesting that only one dominant scattering type was present. The mean alpha angle showed a variety of values for the aqueduct seeps, showing all scattering types. This indicates that the seeps studied are characterized by different scattering mechanisms, especially apparent for Seep 5 (CA Aqueduct), which unlike the previous seeps, was not identified in any of the H-A-Alpha decomposition results. The alpha angle is also a simplistic mean which weighs the probability of the 3 mechanisms, and possibly averages out other non-dominant mechanisms. An investigation into the individual eigenvectors contributing to the alpha angle. Seeps may range from small areas of increased soil moisture to large ponded water on the surface (e.g., Seep 4 for the CA Aqueduct), and each contain different polarimetric seep signatures.

The Twitchell Island PolSAR results were visually much noisier than those of the California Aqueduct, likely due to wetter conditions overall. No discernable field boundaries could be seen in either the NDWI or VV/HH ratio imagery for Twitchell Island. Although the Google Earth imagery was effective at tracking active seeps over time, with many images showing the seep traveling over roads and increases in green vegetation nearby, optical imagery is insufficient for seep tracking during emergencies resulting from high river discharge. Seeps most commonly occur during large floods (high tide conditions), which usually accompany stormy weather. As seen by the many missing acquisitions for the NDWI product, cloud cover obscures data collection for optical sensors. Relying solely on optical imagery for seep detection during a storm may not result in successful seep detection. The VV/HH ratio product shows general agreement temporally for higher ratio values occurring during wetter months, but is unable to differentiate very small seep features. Seeps 1-3 show isolated levee stretches of high

ratio values, but Seeps 4 and 5 are surrounded by too many similar small features to be identifiable. A more detailed comparison of the full range of PolSAR products as performed for the CA Aqueduct is to be applied to the Twitchell Island seeps for further characterization of these small-scale seeps. For a large flood event, seepage features will be much larger and easily detectable by PolSAR, which is especially compatible with UAVSAR's emergency response capabilities.

Current monitoring efforts by the CA DWR rely on field surveys driving around the different islands to locate any signs of damage or seepage from the levee system. Using radar remote sensing data can offer instant snapshots of the entire Delta to help focus monitoring efforts. The Sacramento-San Joaquin Delta is a dynamic landscape with spatially heterogeneous soil composition that requires high resolution and continuous monitoring to identify the mechanisms driving levee seepage and subsidence. A previous study found that most of the Delta levee system will subside below the current design thresholds in 50 to 100 years, making this a very time sensitive topic (Brooks et al., 2012). Since the Delta protects valuable water supplies and is vulnerable to disaster events, improving emergency response for the region is critical for the well-being of California residents, and similar methodologies could be applied for other levee systems. This study shows the level of detail, both spatially and temporally, that UAVSAR can offer in locating potential seepage locations. This study supports the effort for more continuous high resolution, long wavelength radar acquisitions to monitor levee systems such as the Delta.

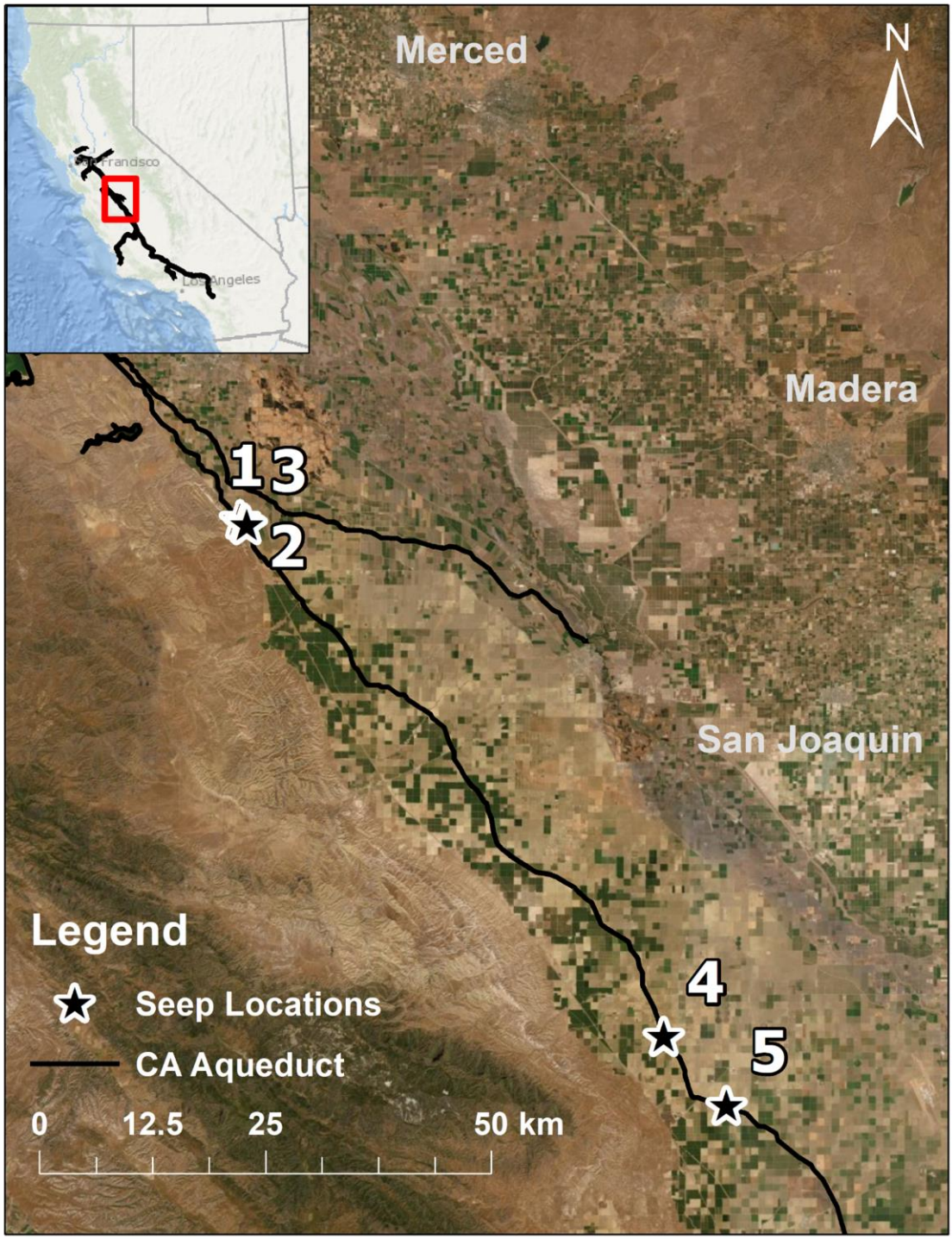

Figure 1A: Study area overview of seep examples along the California Aqueduct.

Figure 1B: Study area overview for Seeps 1-3 along the California Aqueduct.

Figure 2A: Seeps 1, 2, and 3 – Google Earth Imagery

Figure 2B: Seeps 1, 2, and 3 – Google Earth Imagery

Figure 2C: Seeps 1, 2, and 3 – Google Earth Imagery

Figure 3: Legends for NDWI and PolSAR data products.

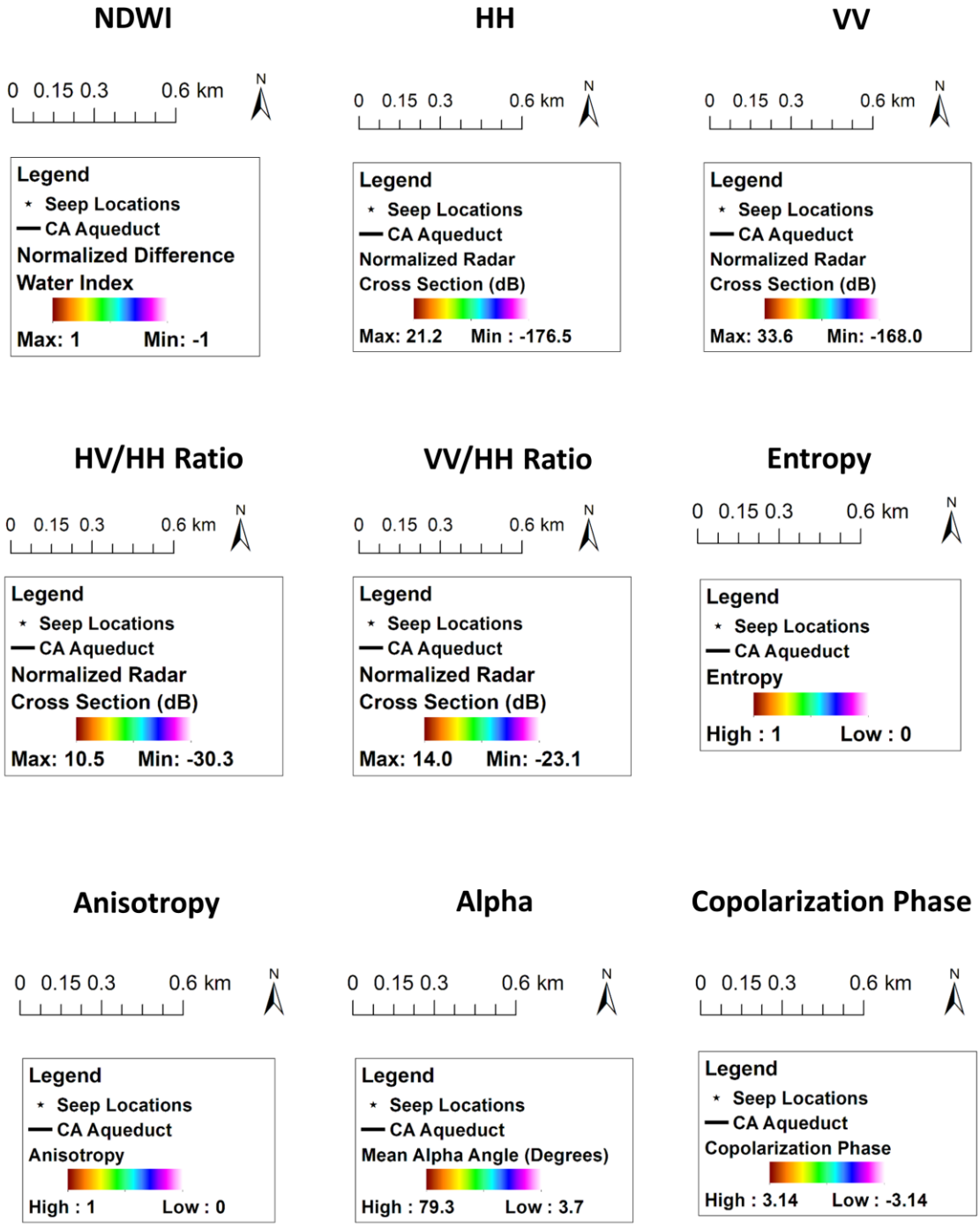

Figure 4A: Seeps 1, 2, and 3 – NDWI

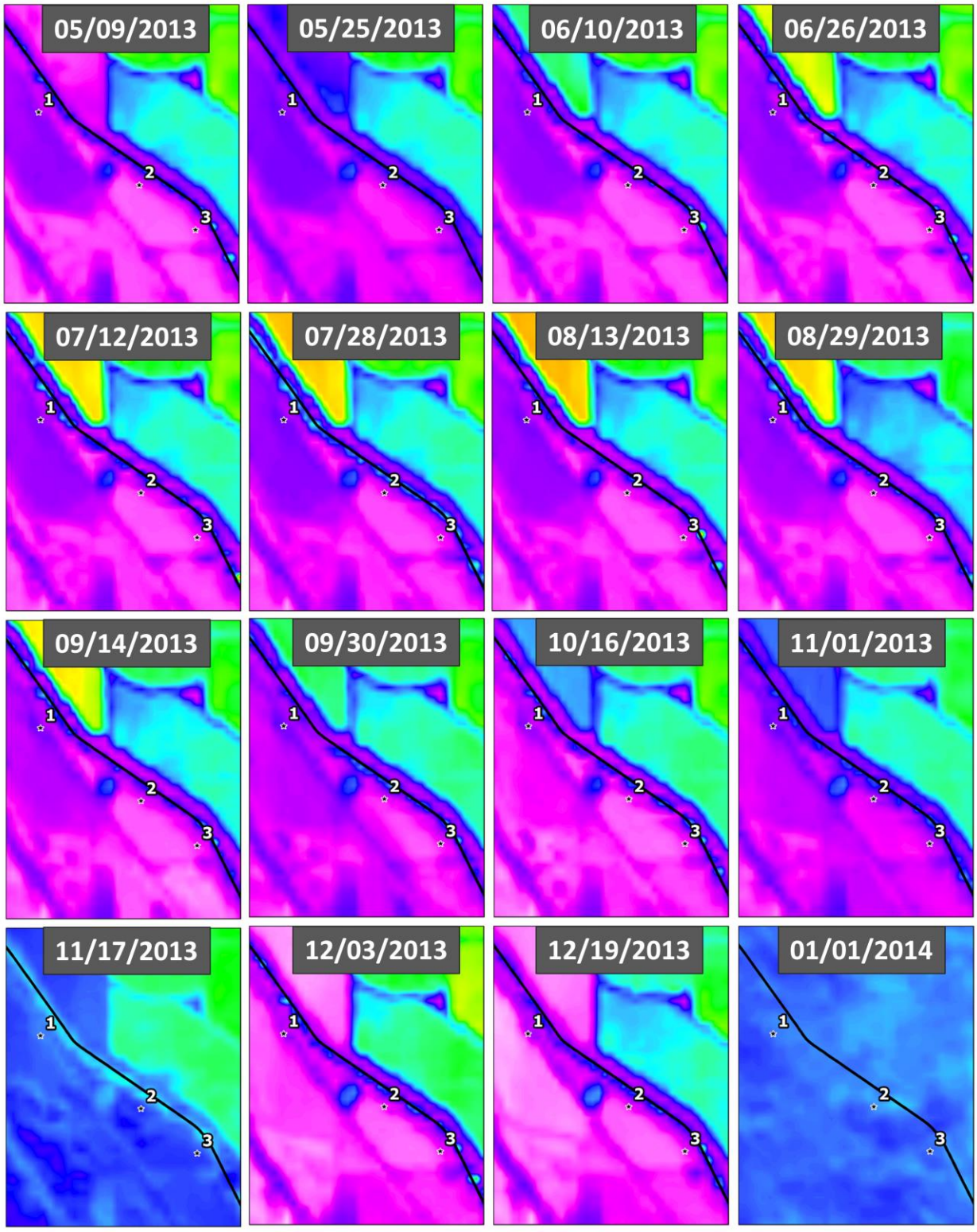

Figure 4B: Seeps 1, 2, and 3 – NDWI

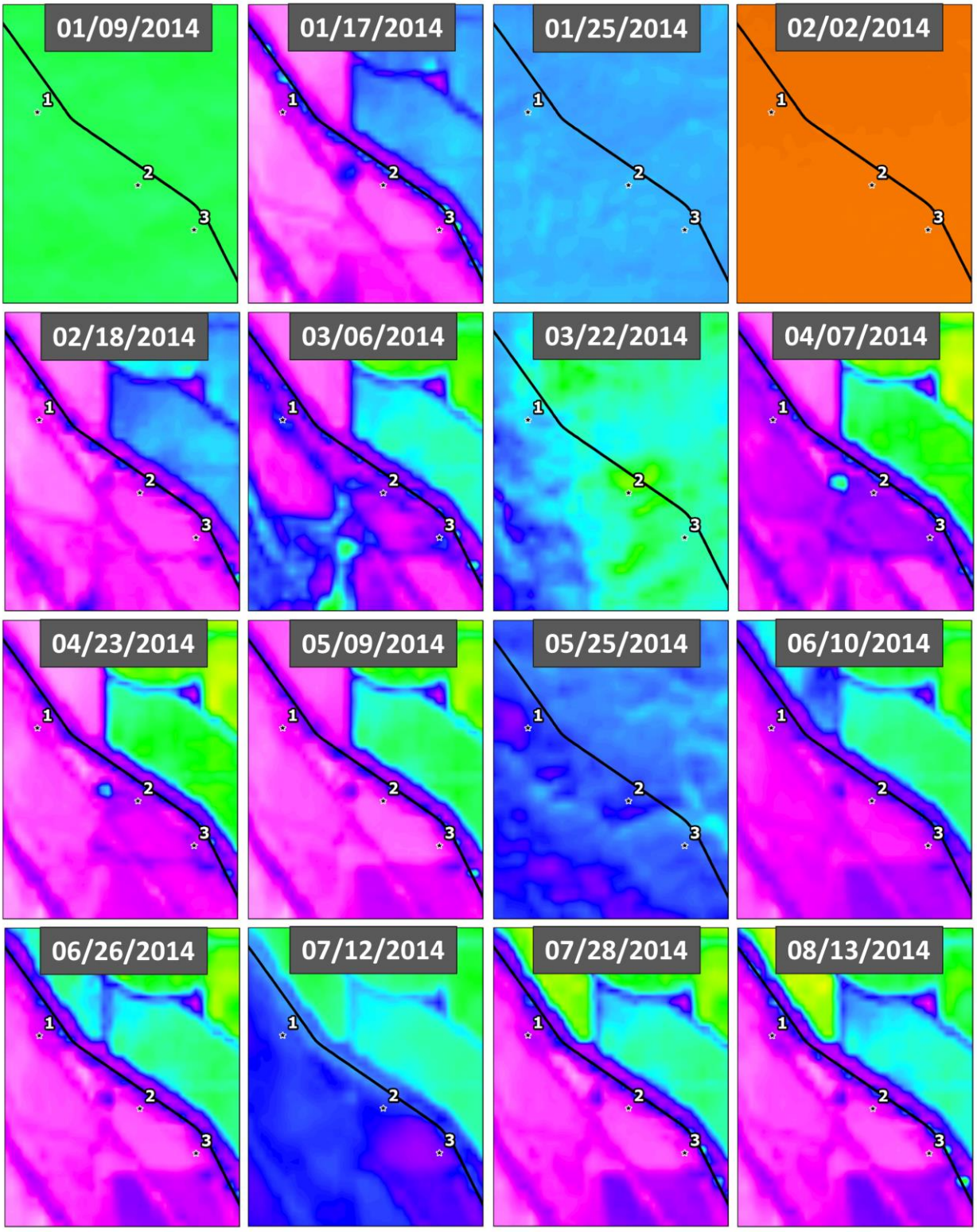

Figure 4C: Seeps 1, 2, and 3 – NDWI

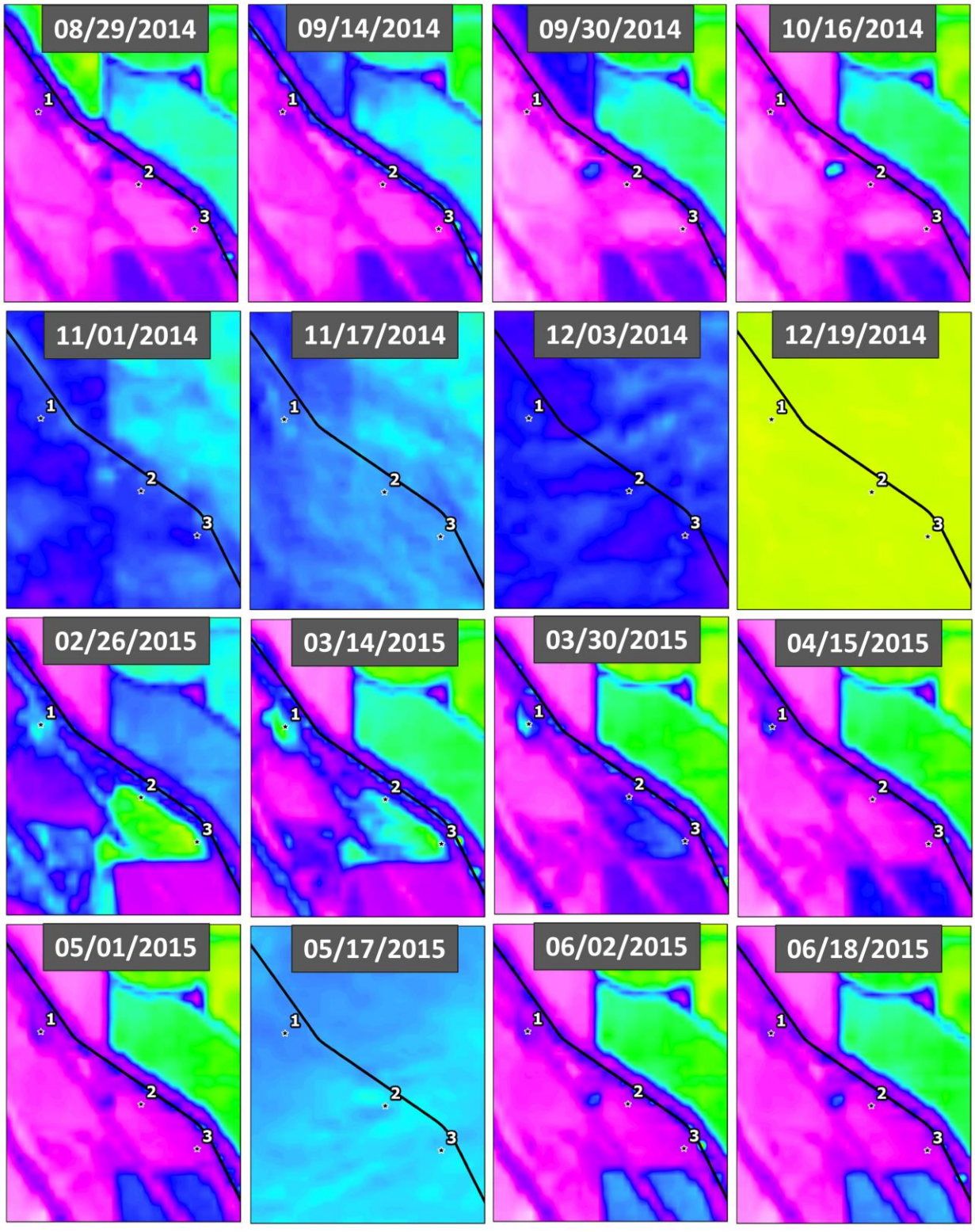

Figure 4D: Seeps 1, 2, and 3 – NDWI

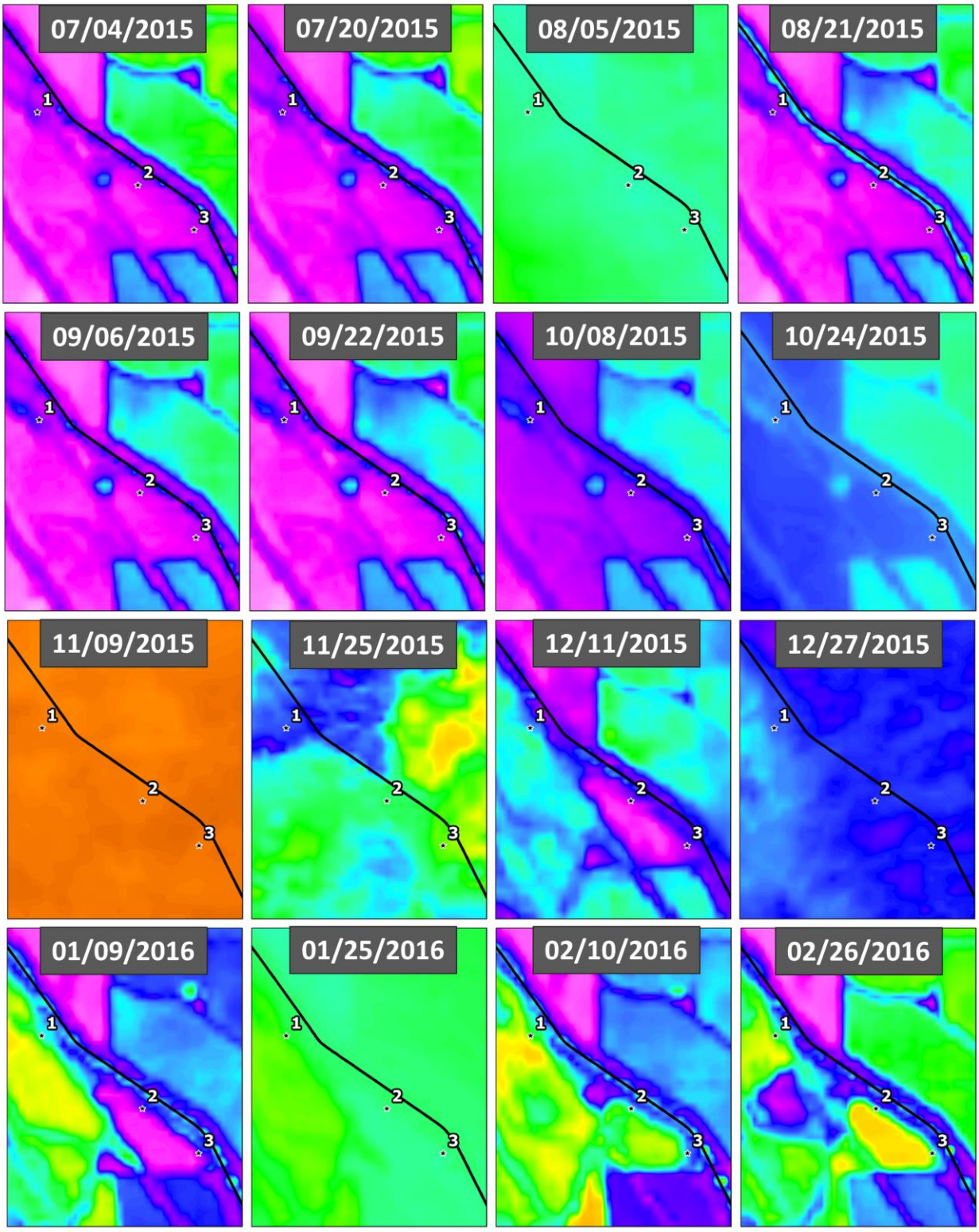

Figure 4E: Seeps 1, 2, and 3 – NDWI

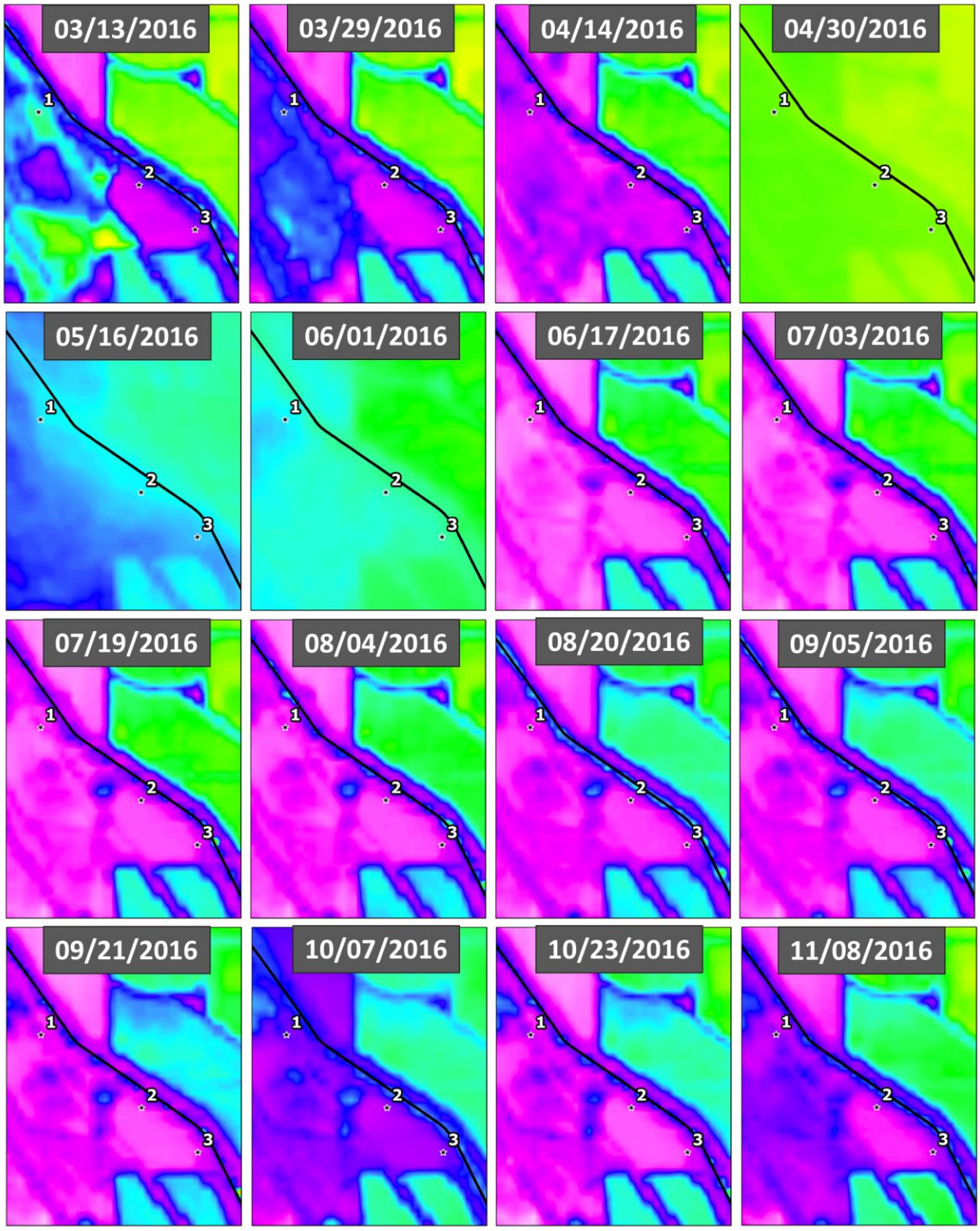

Figure 4F: Seeps 1, 2, and 3 – NDWI

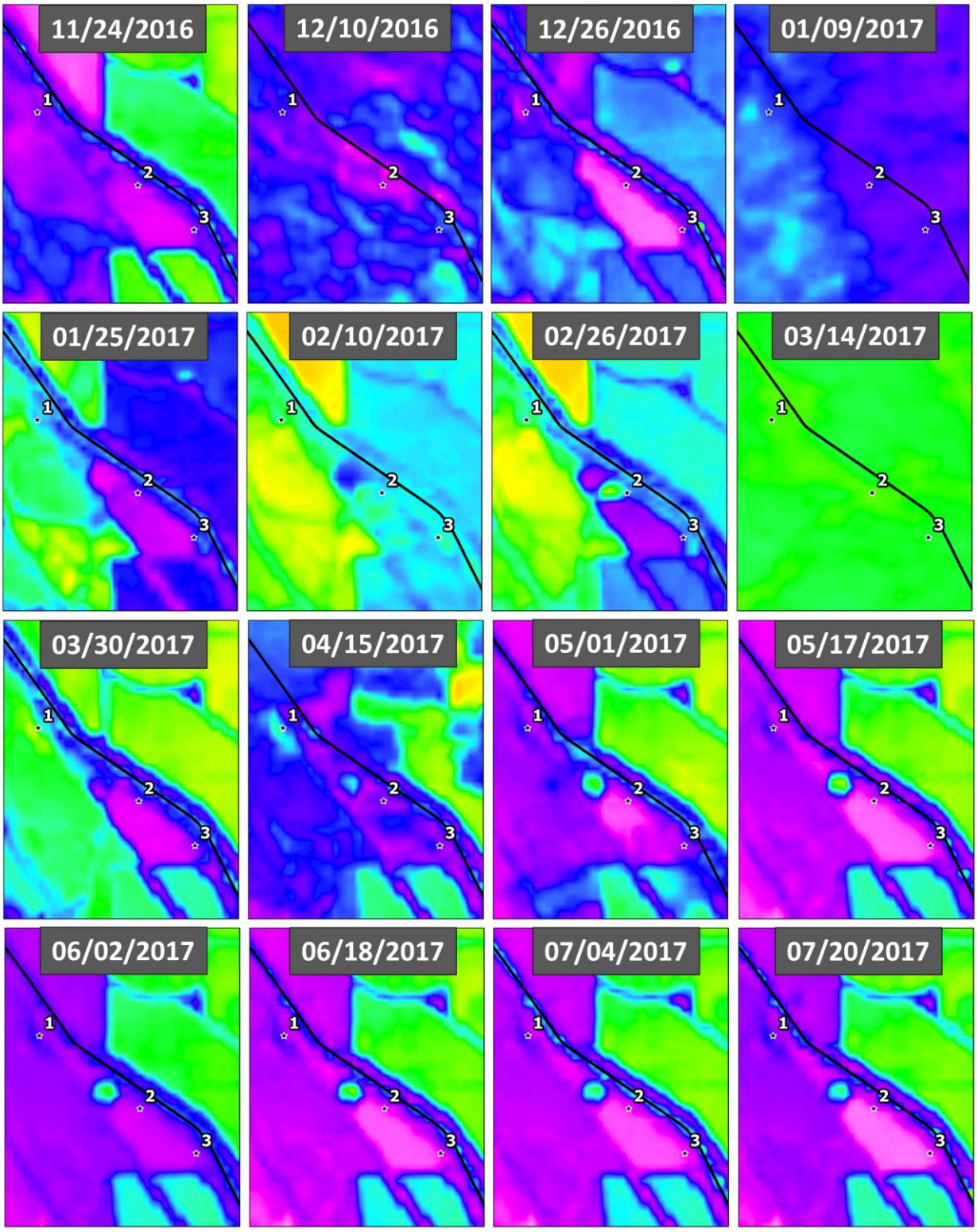

Figure 4G: Seeps 1, 2, and 3 – NDWI

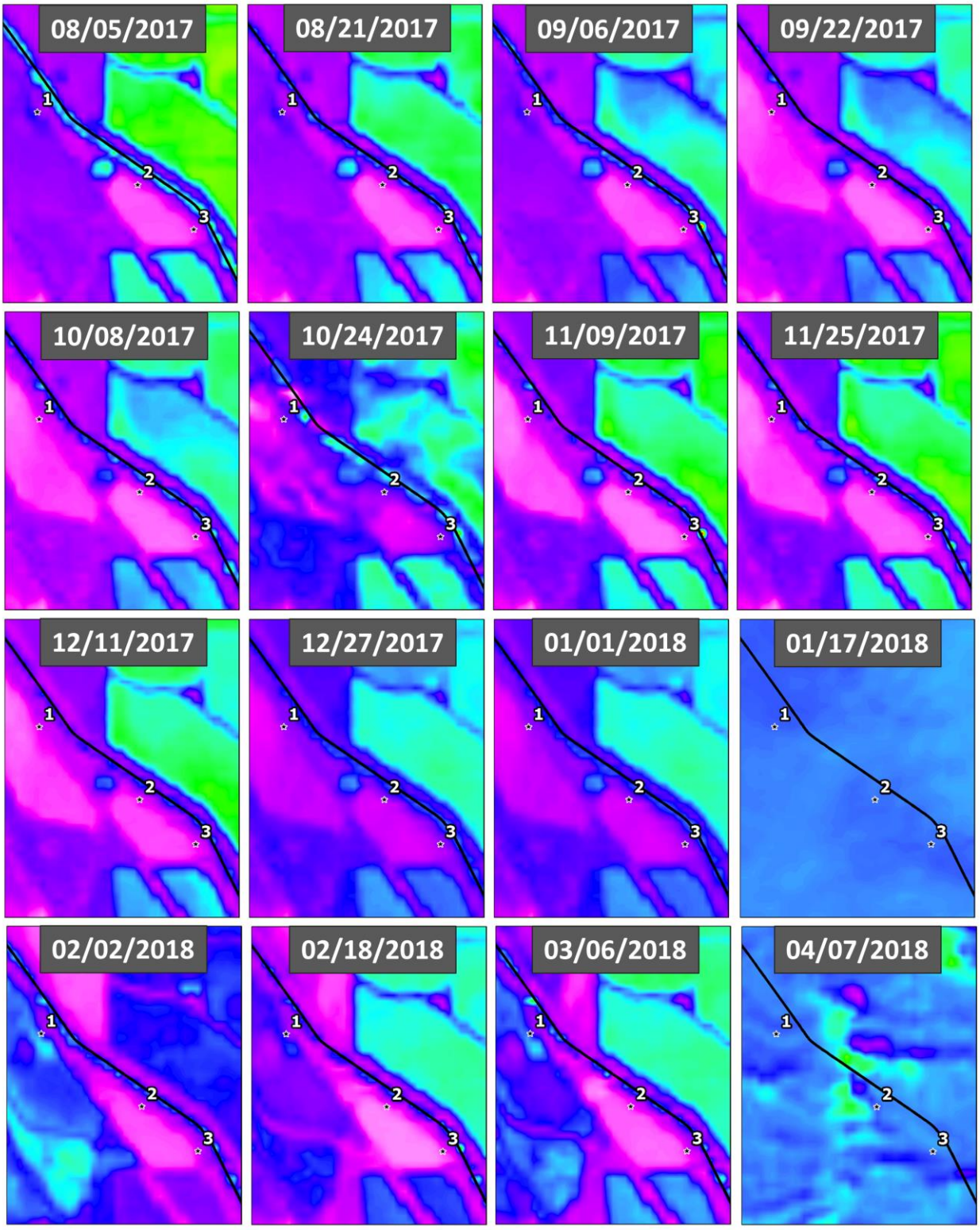

Figure 4H: Seeps 1, 2, and 3 – NDWI

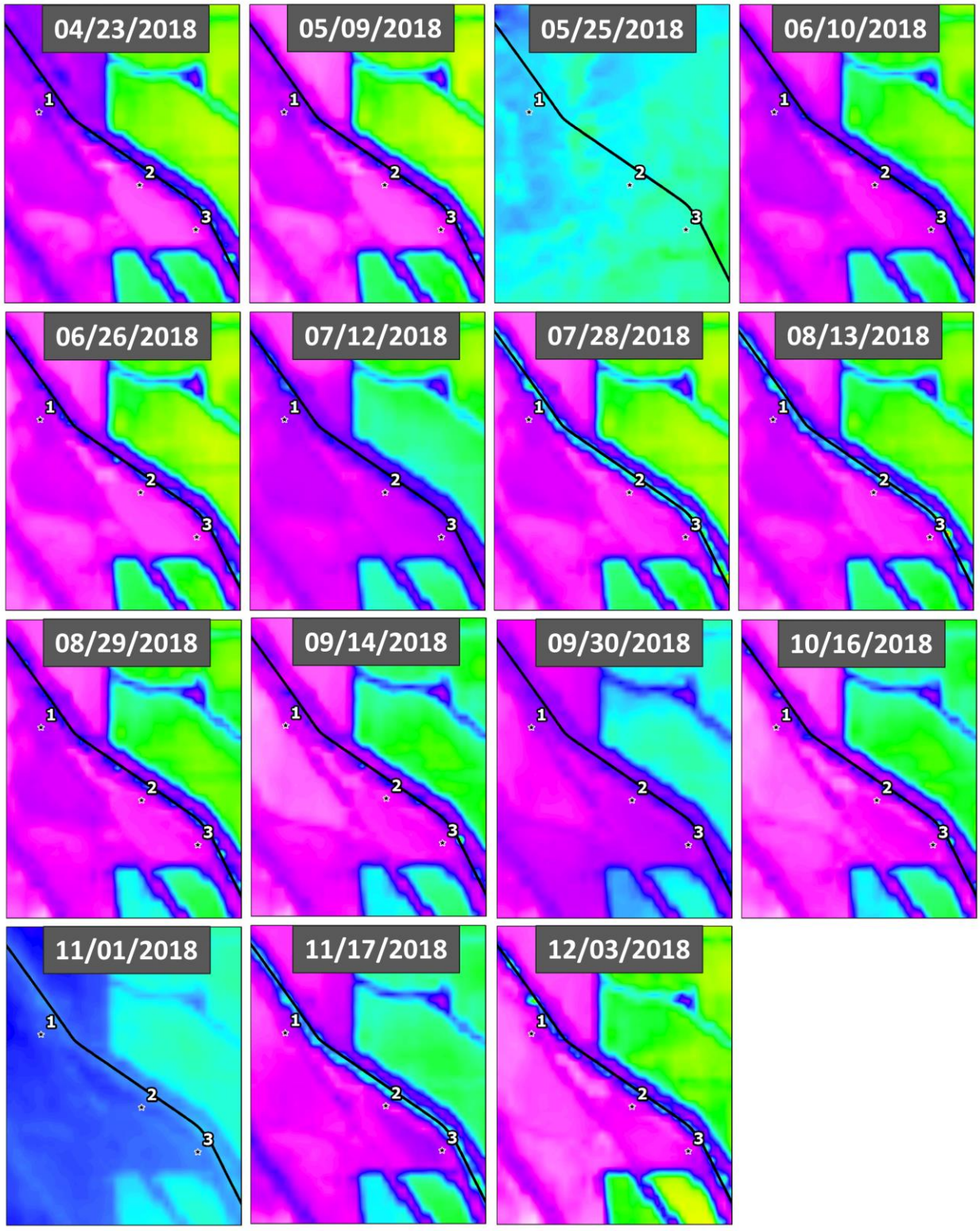

Figure 5A: Seeps 1, 2, and 3 – HH Single Polarization

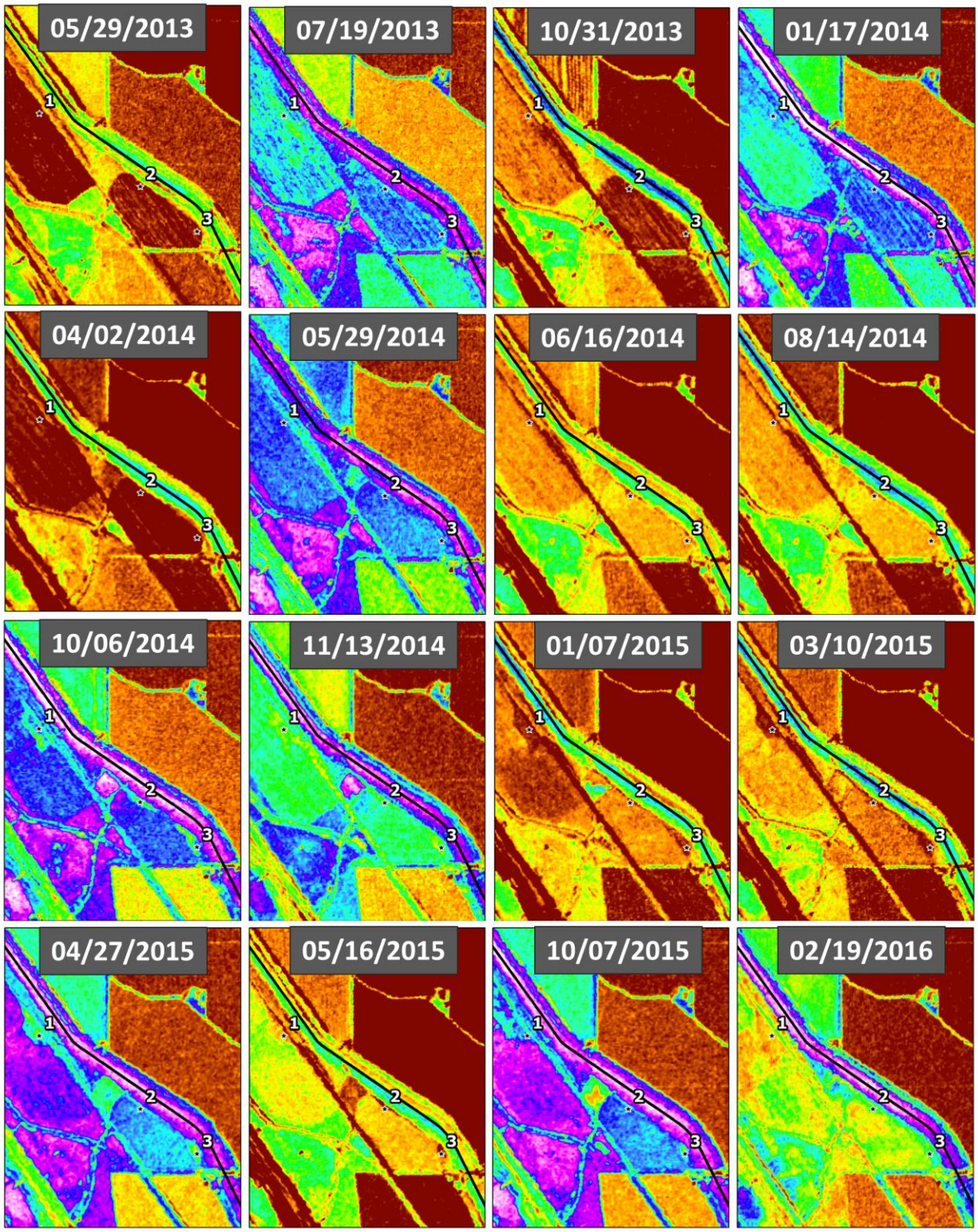

Figure 5B: Seeps 1, 2, and 3 – HH Single Polarization

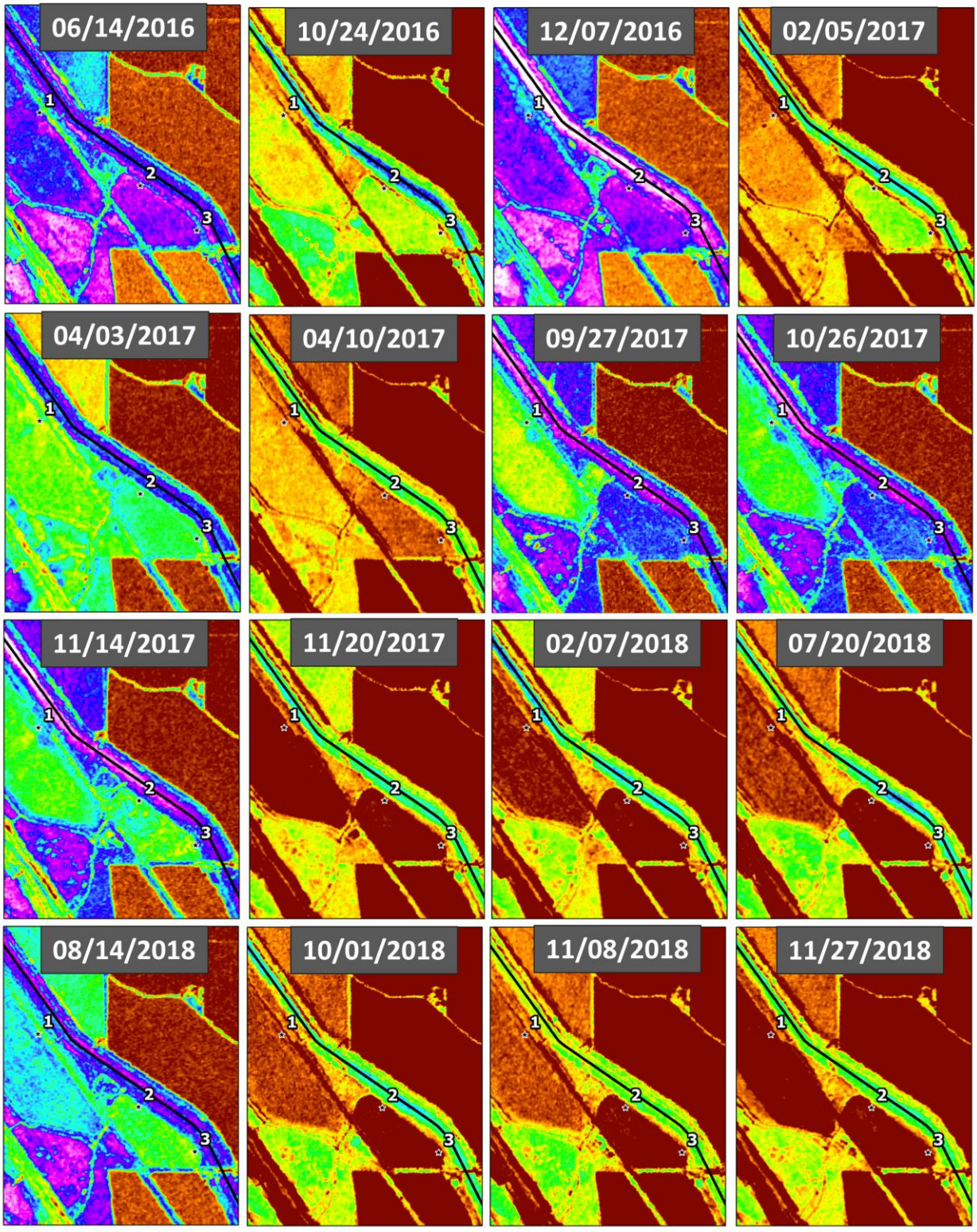

Figure 6A: Seeps 1, 2, and 3 – VV Single Polarization

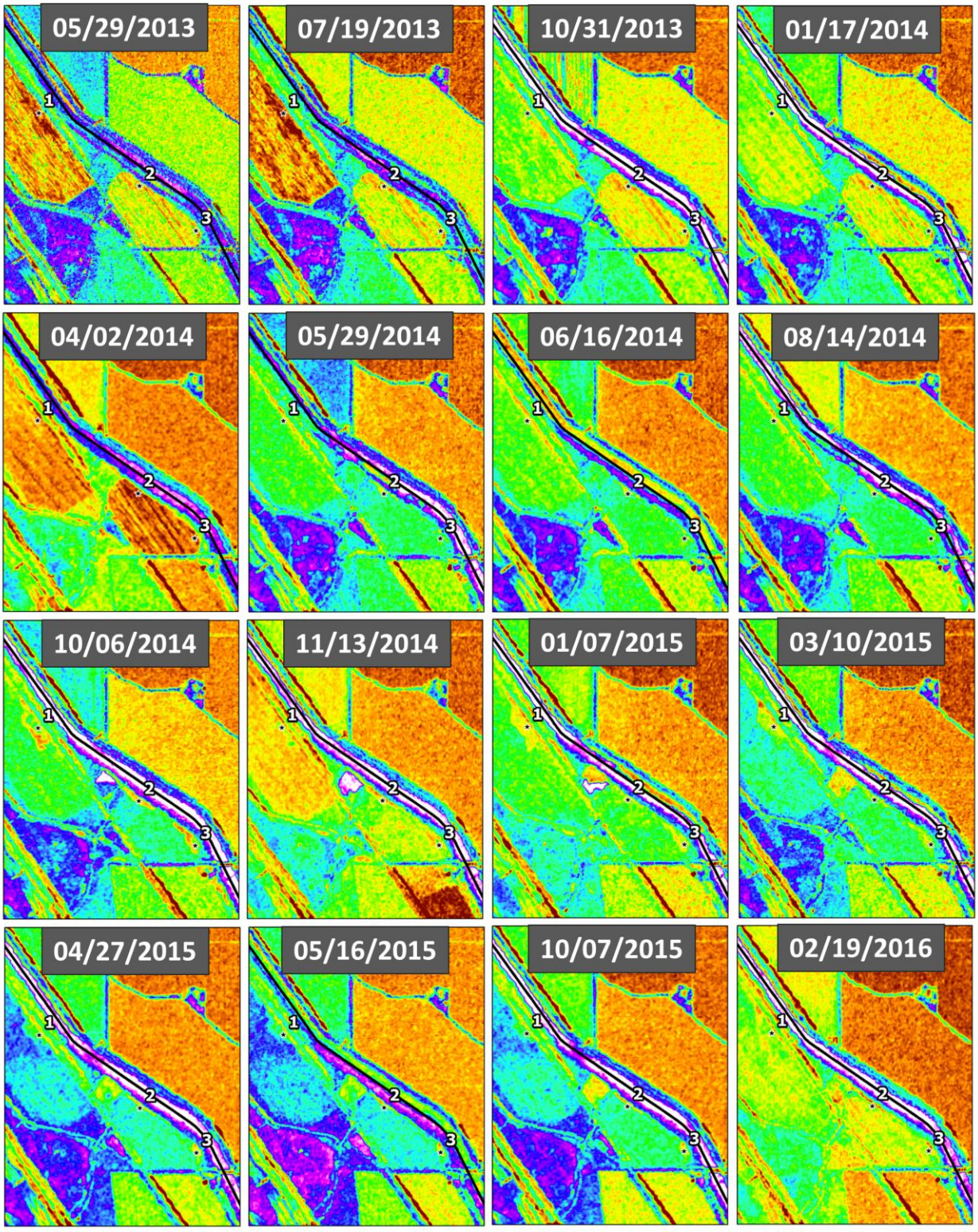

Figure 6B: Seeps 1, 2, and 3 – VV Single Polarization

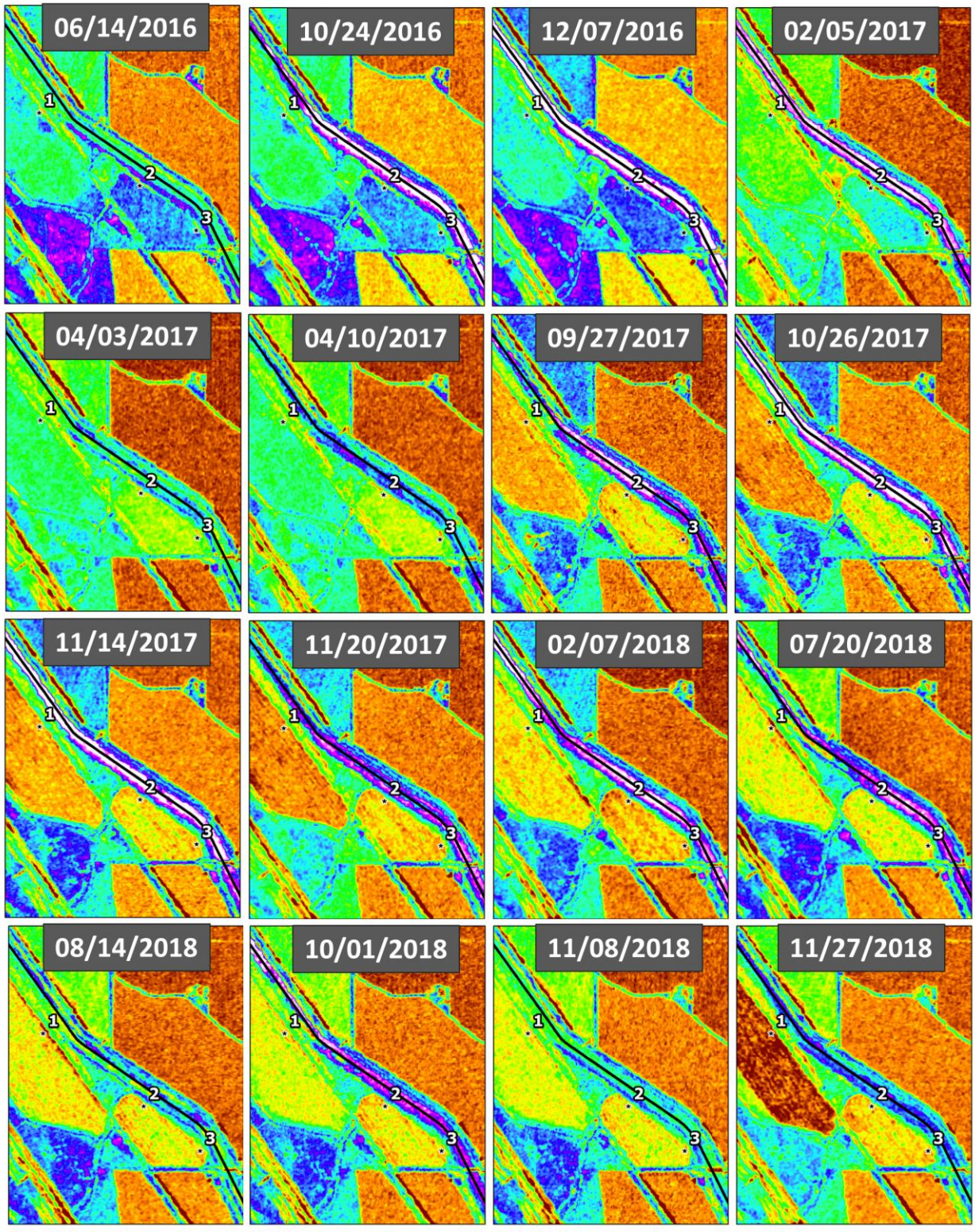

Figure 7A: Seeps 1, 2, and 3 – HV/HH Ratio

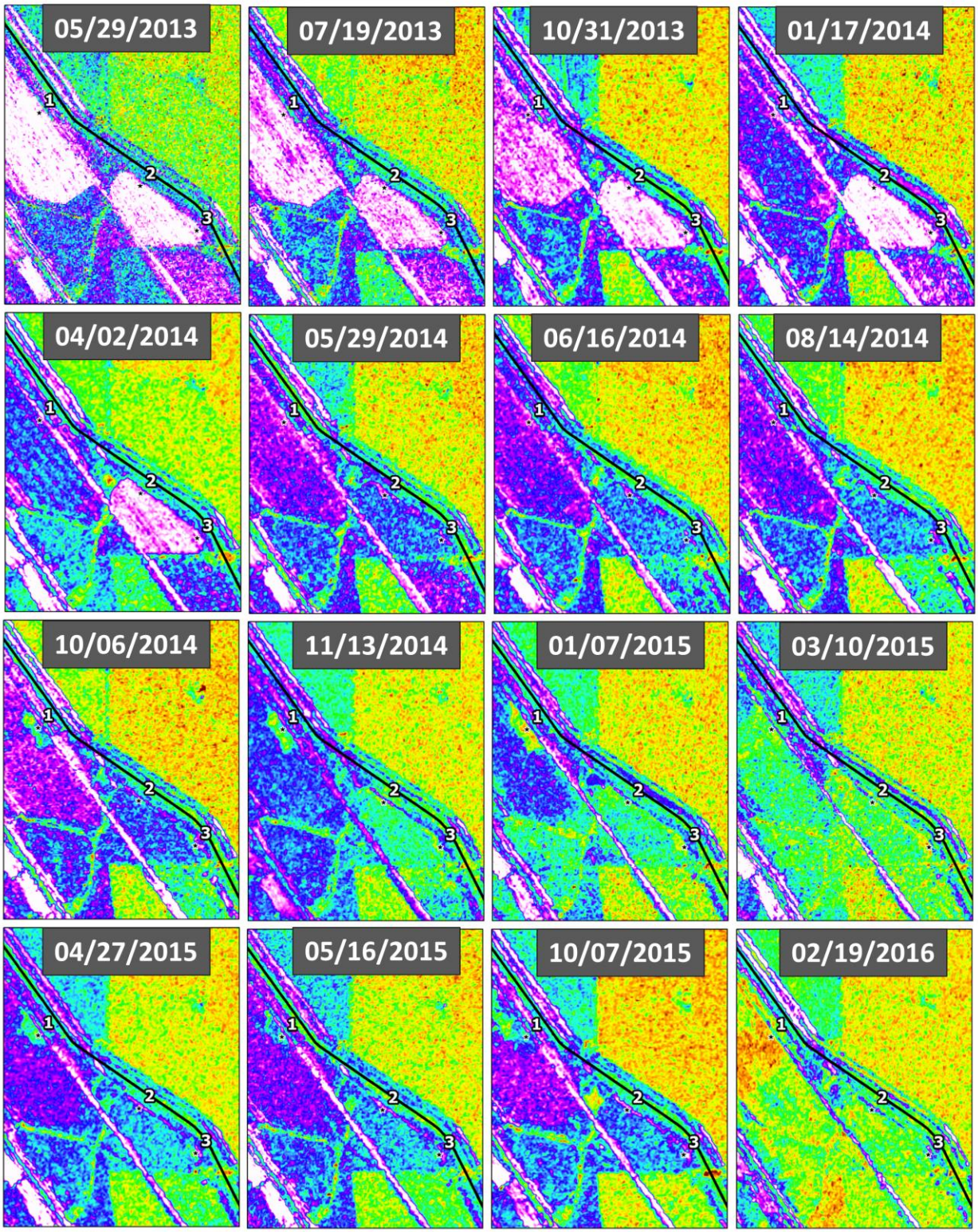

Figure 7B: Seeps 1, 2, and 3 – HV/HH Ratio

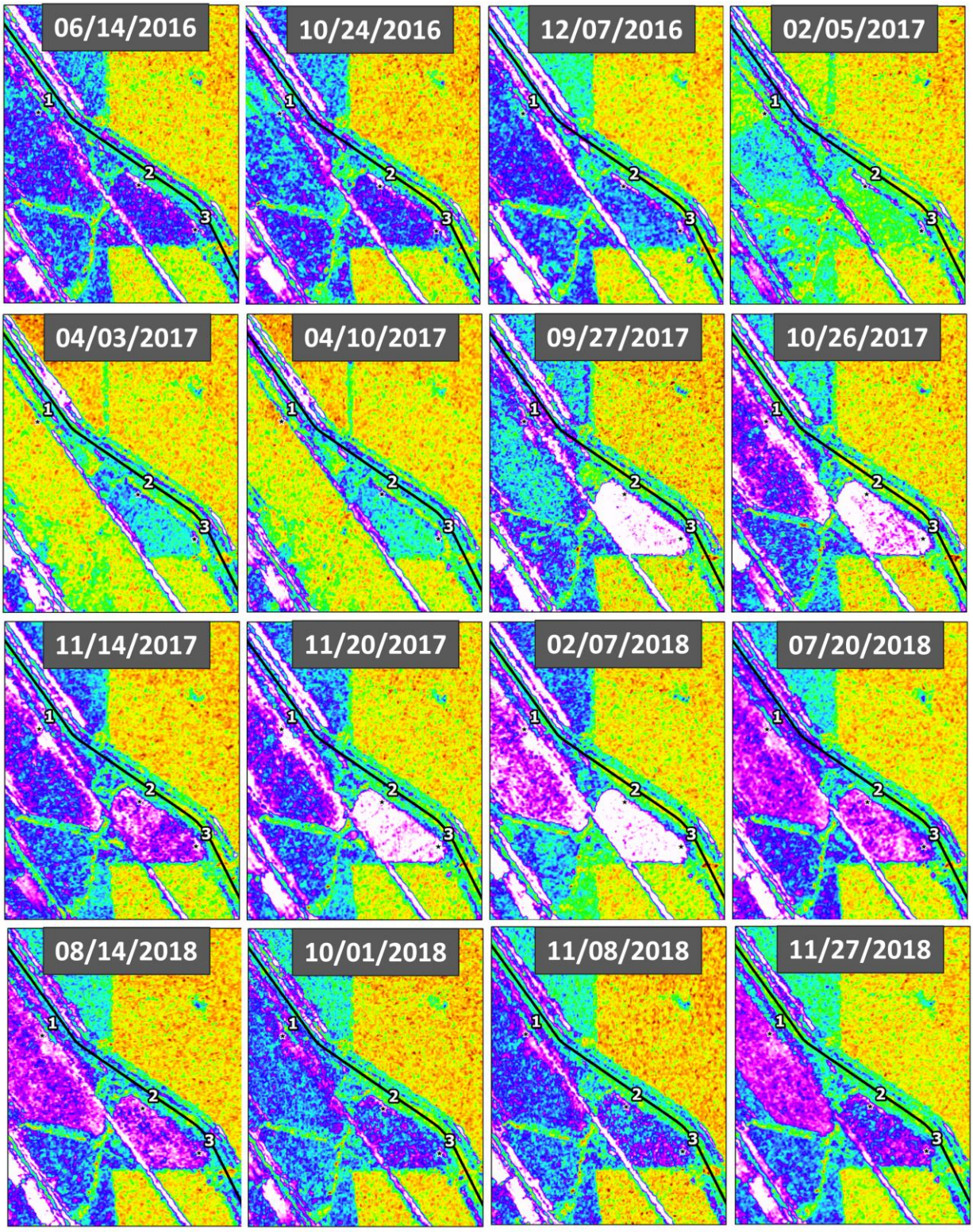

Figure 8A: Seeps 1, 2, and 3 – VV/HH Ratio

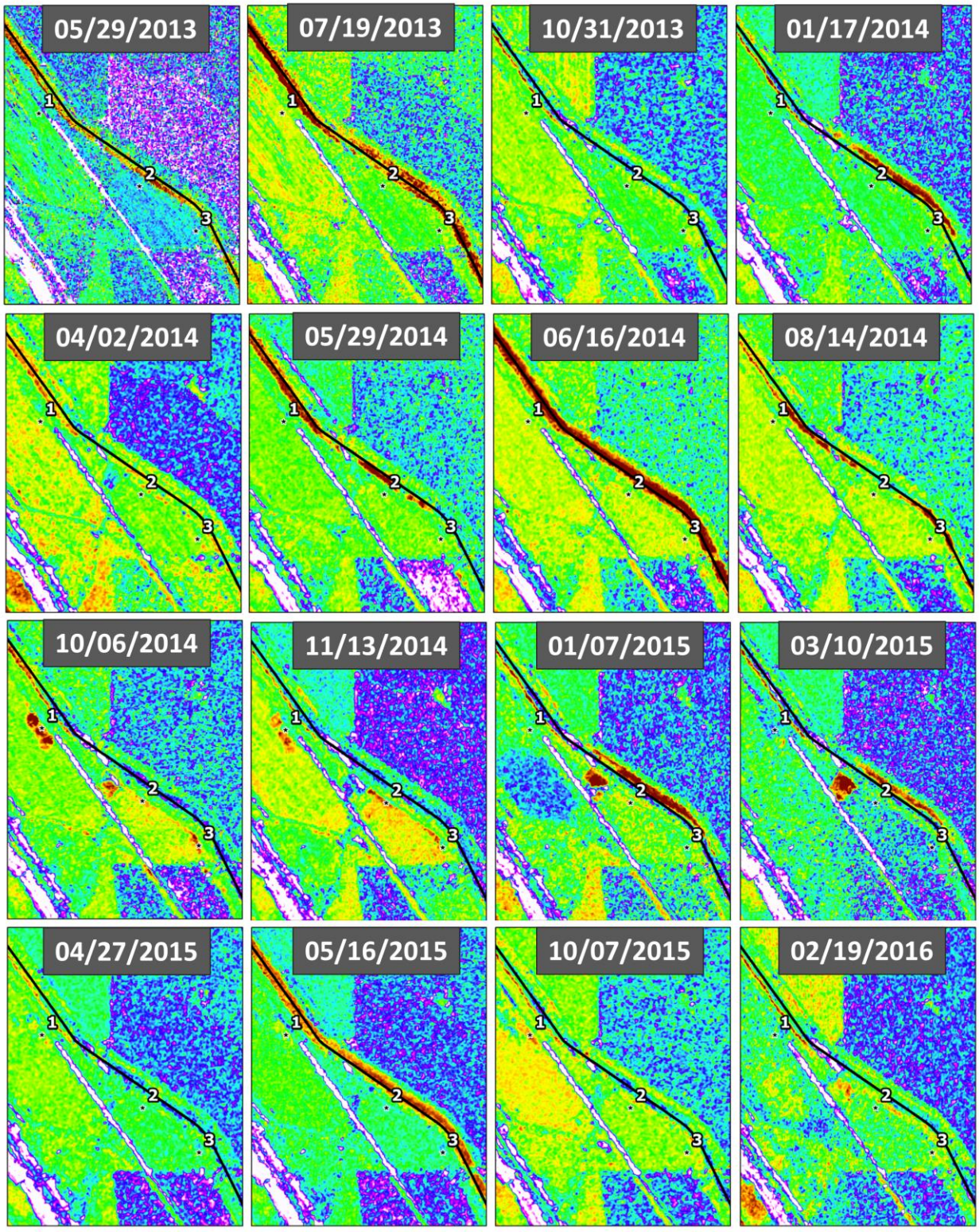

Figure 8B: Seeps 1, 2, and 3 – VV/HH Ratio

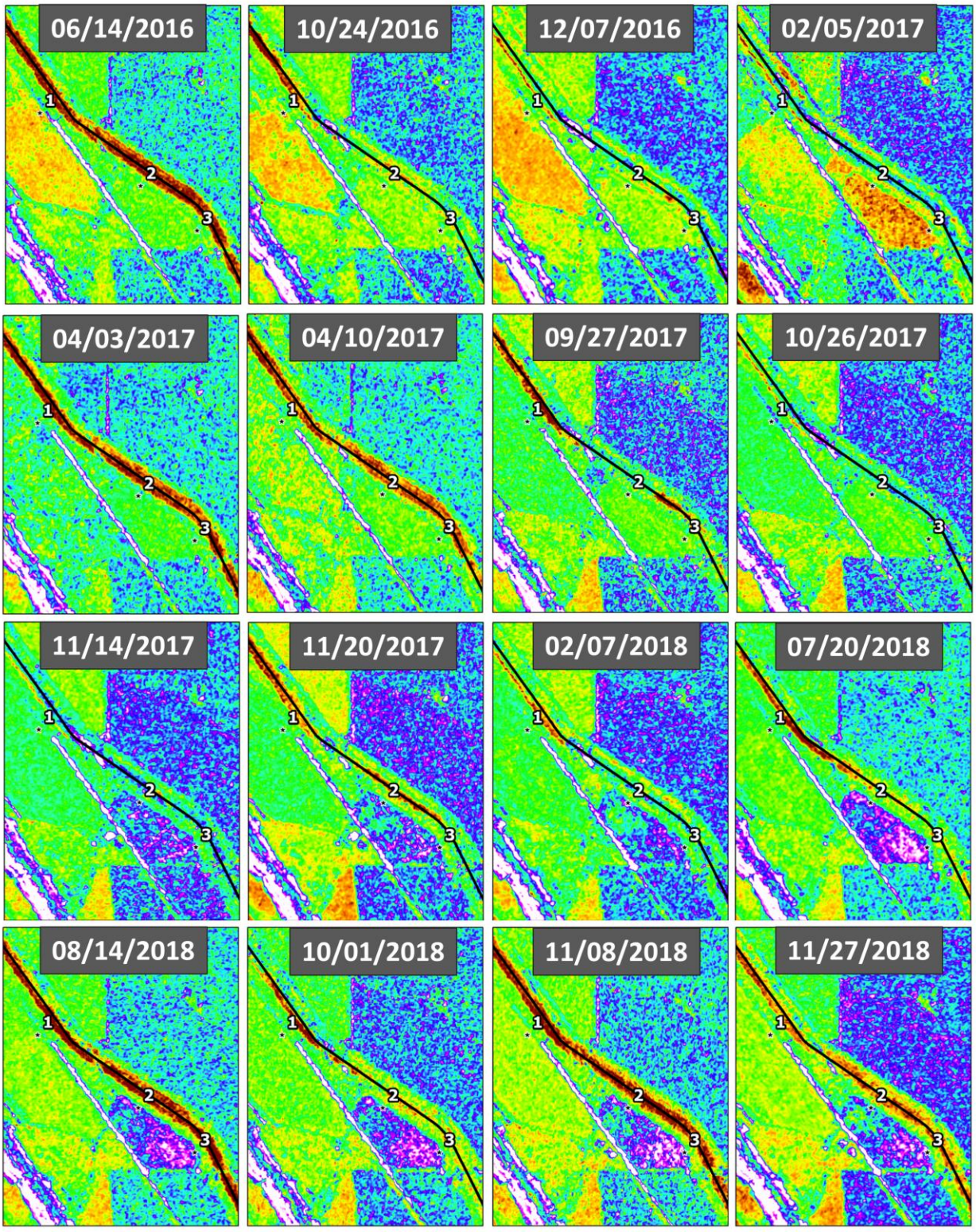

Figure 9A: Seeps 1, 2, and 3 – Copolarization Phase

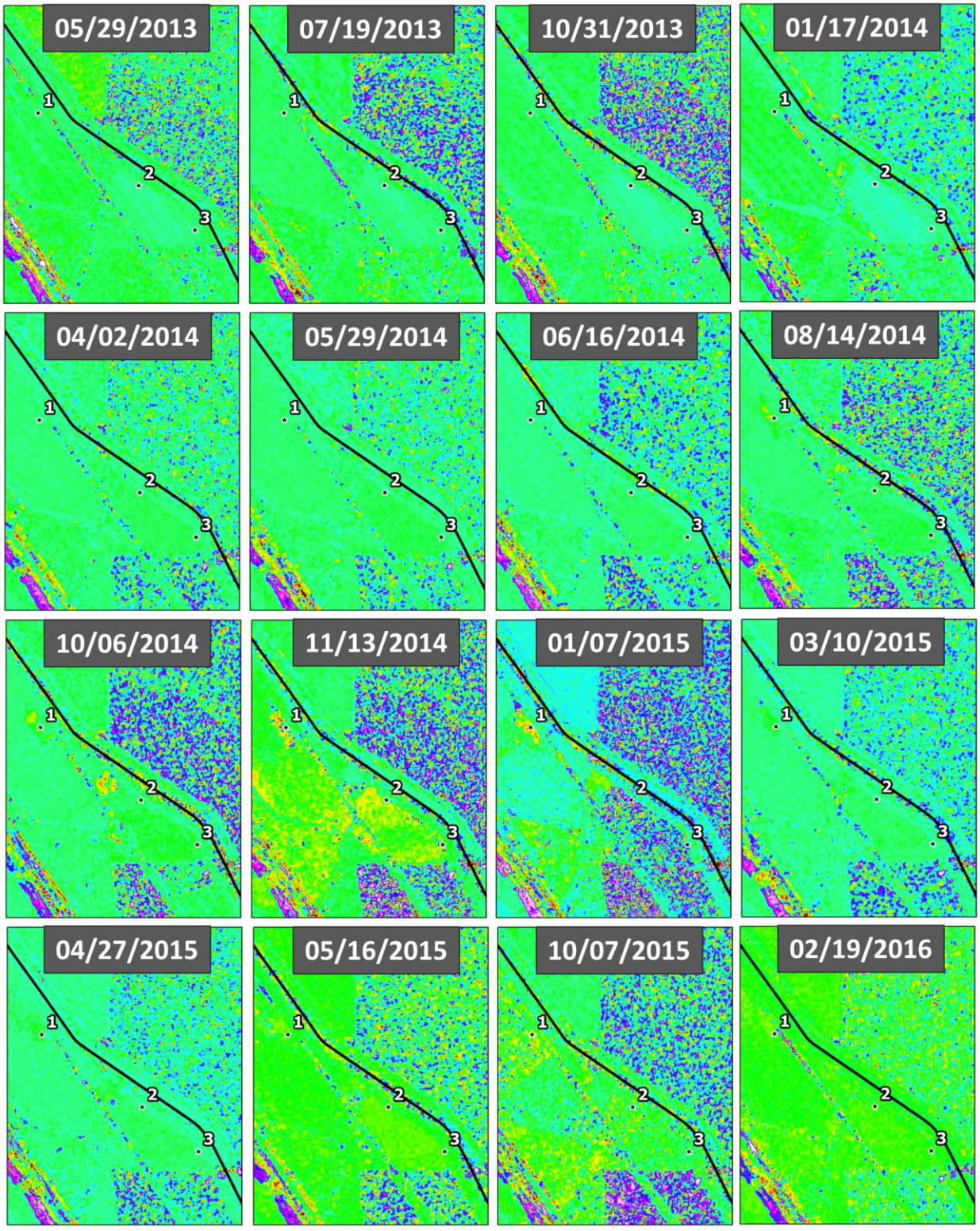

Figure 9B: Seeps 1, 2, and 3 – Copolarization Phase

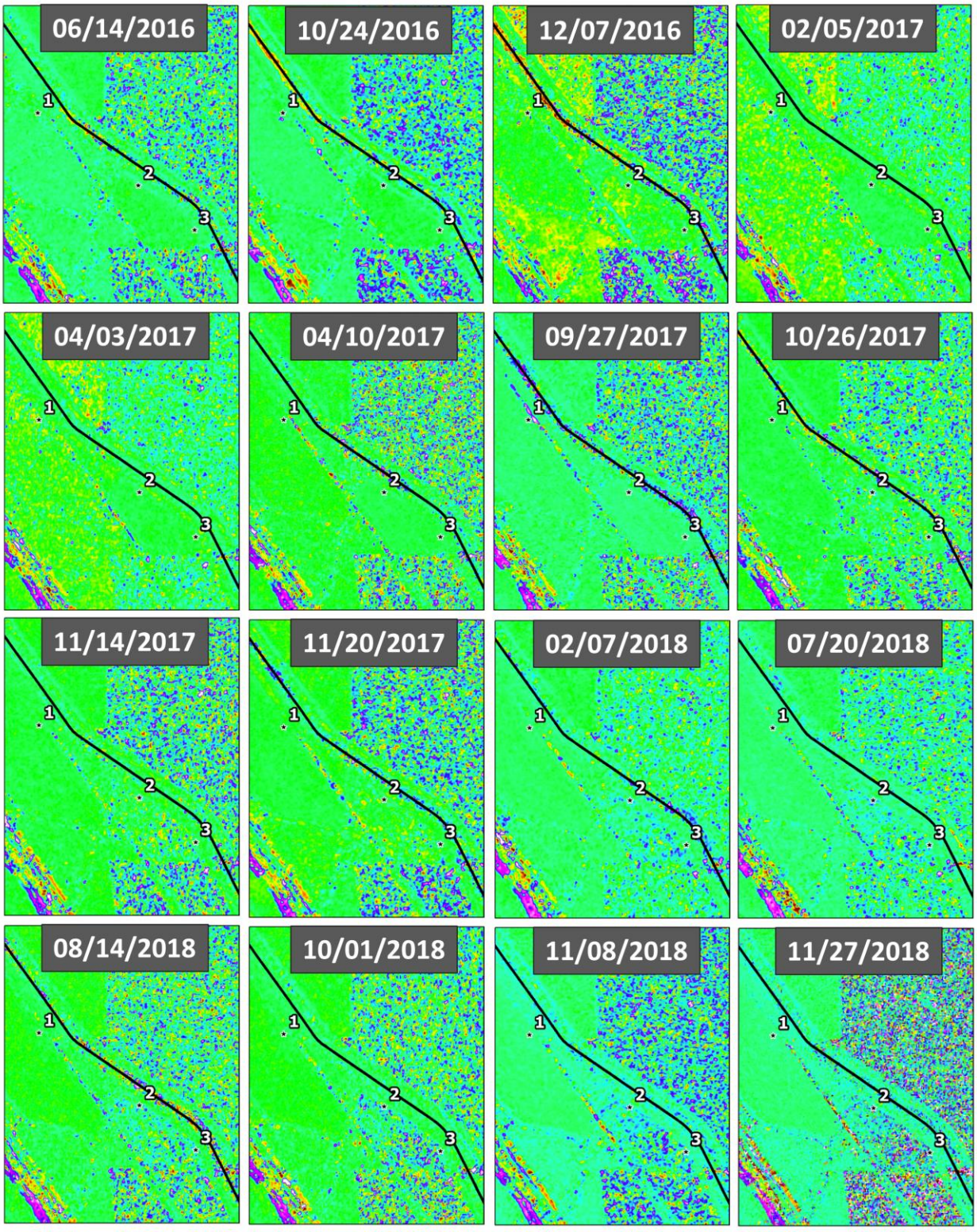

Figure 10A: Seeps 1, 2, and 3 – Entropy

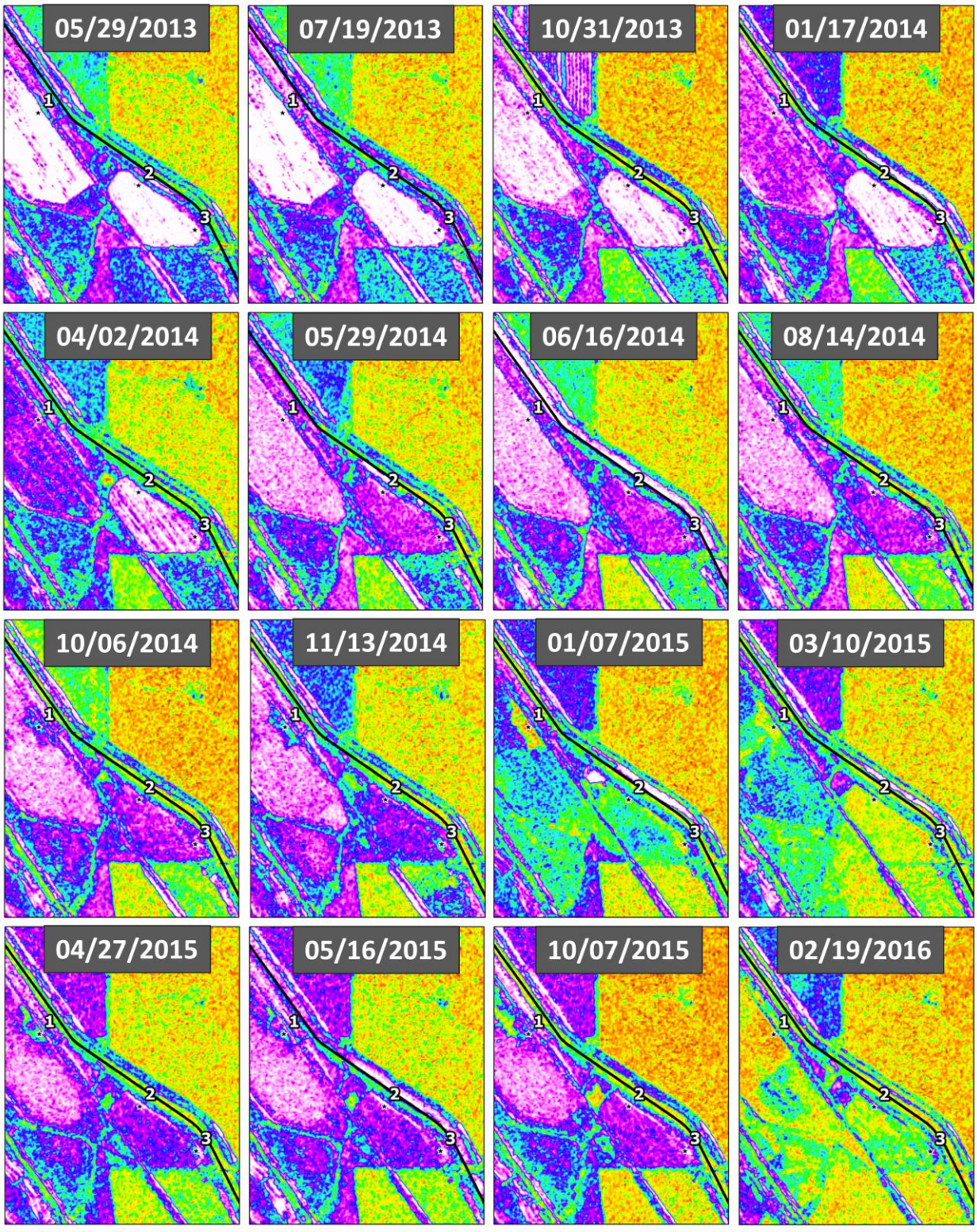

Figure 10B: Seeps 1, 2, and 3 – Entropy

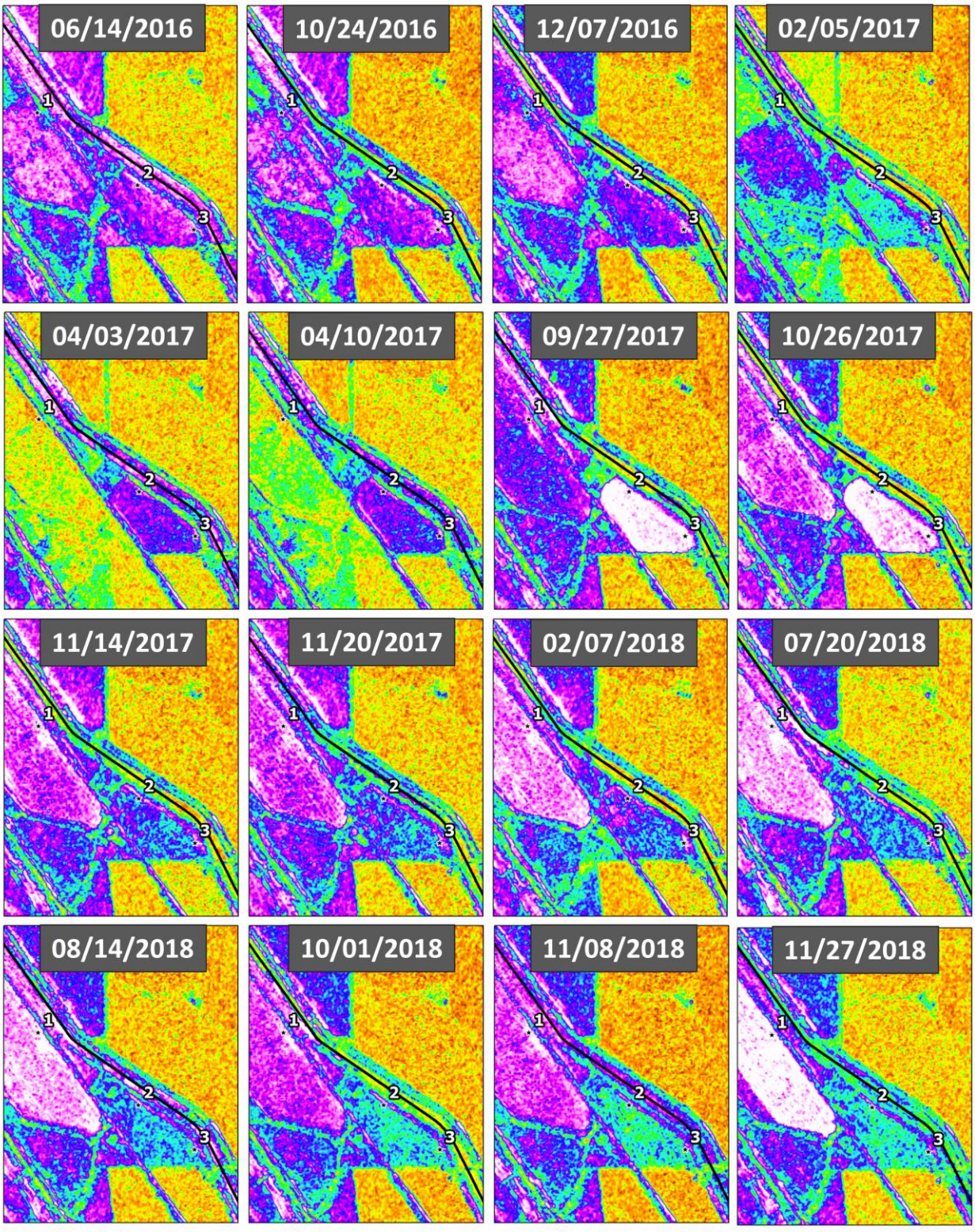

Figure 11A: Seeps 1, 2, and 3 – Anisotropy

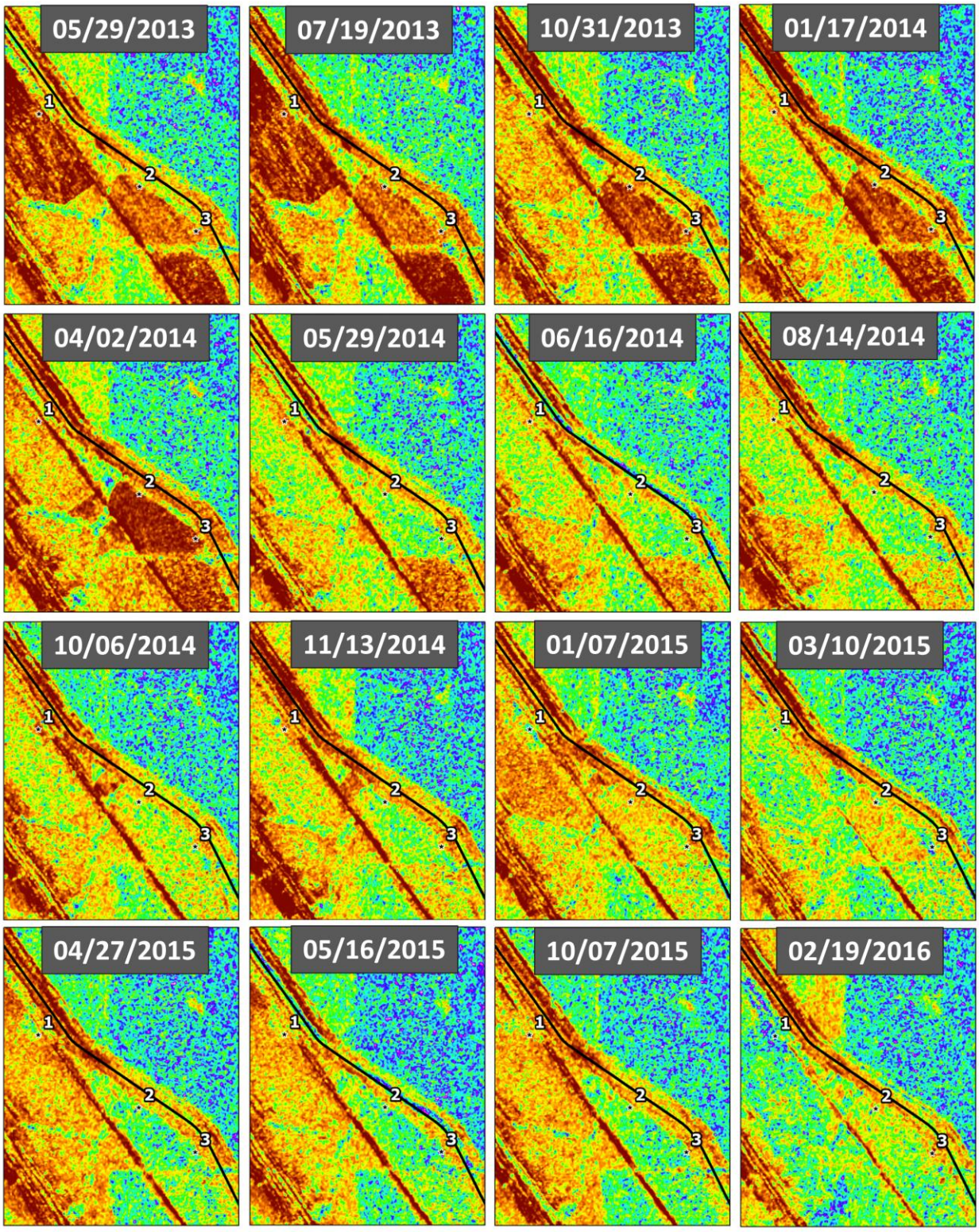

Figure 11B: Seeps 1, 2, and 3 – Anisotropy

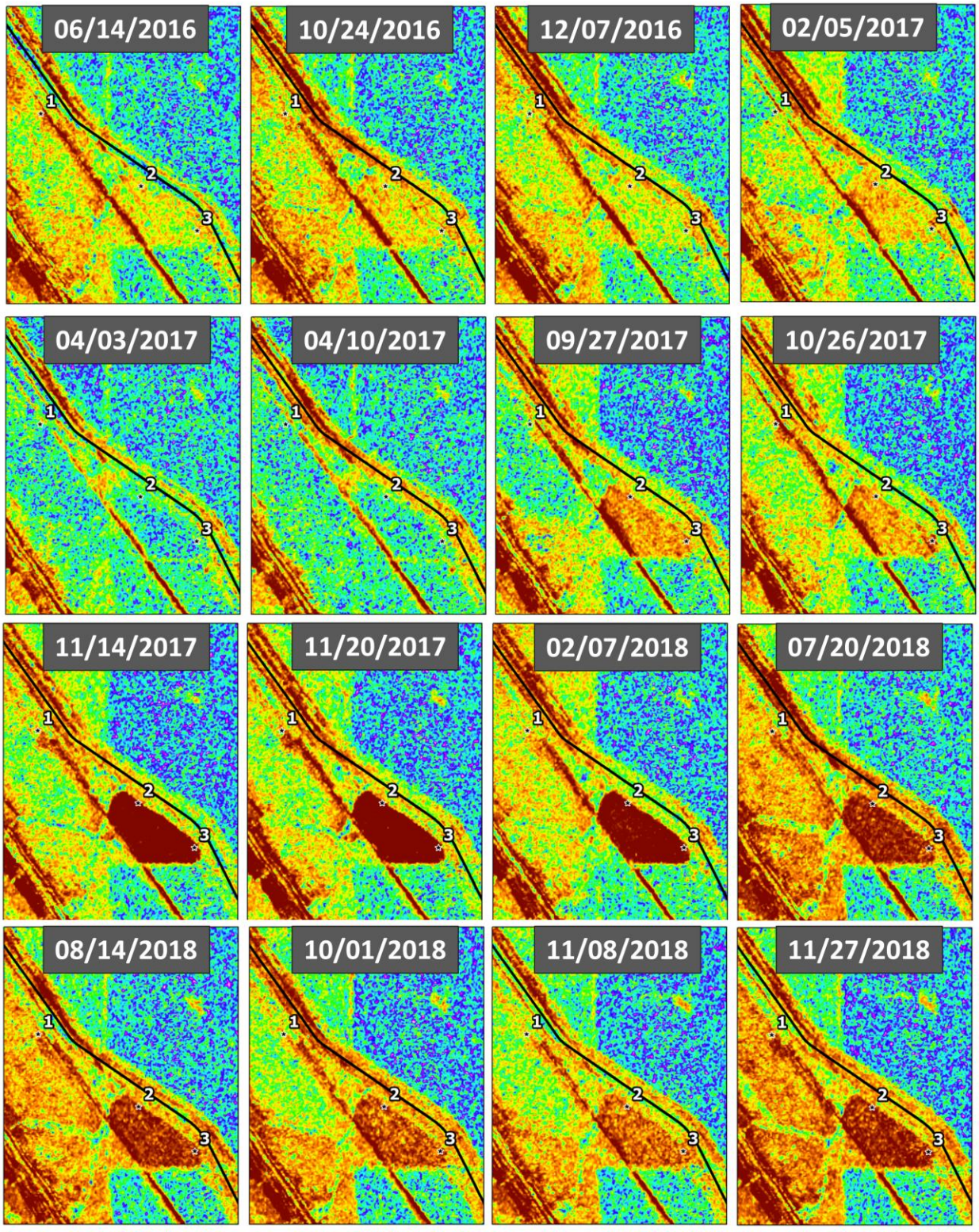

Figure 12A: Seeps 1, 2, and 3 – Mean Alpha Angle

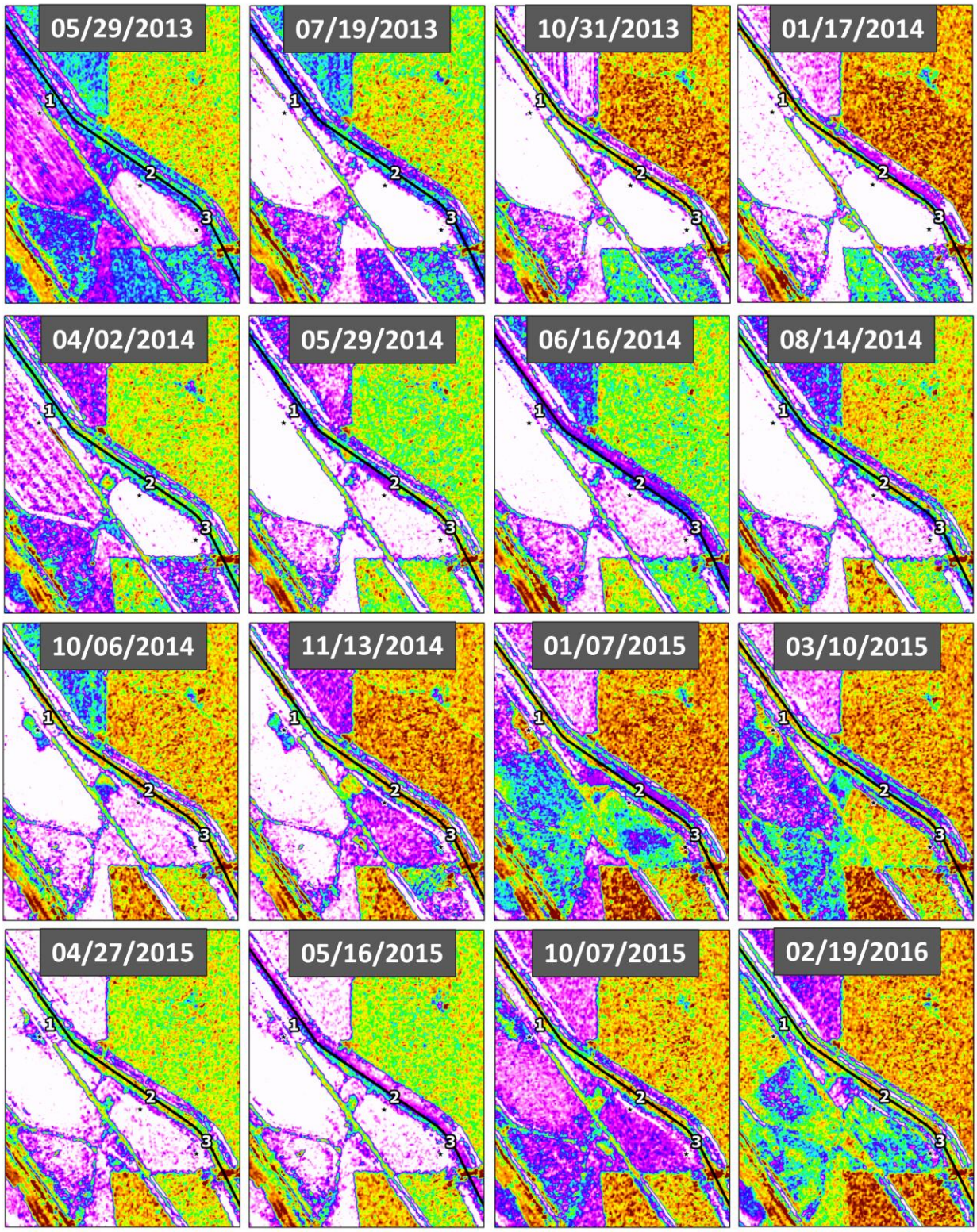

Figure 12B: Seeps 1, 2, and 3 – Mean Alpha Angle

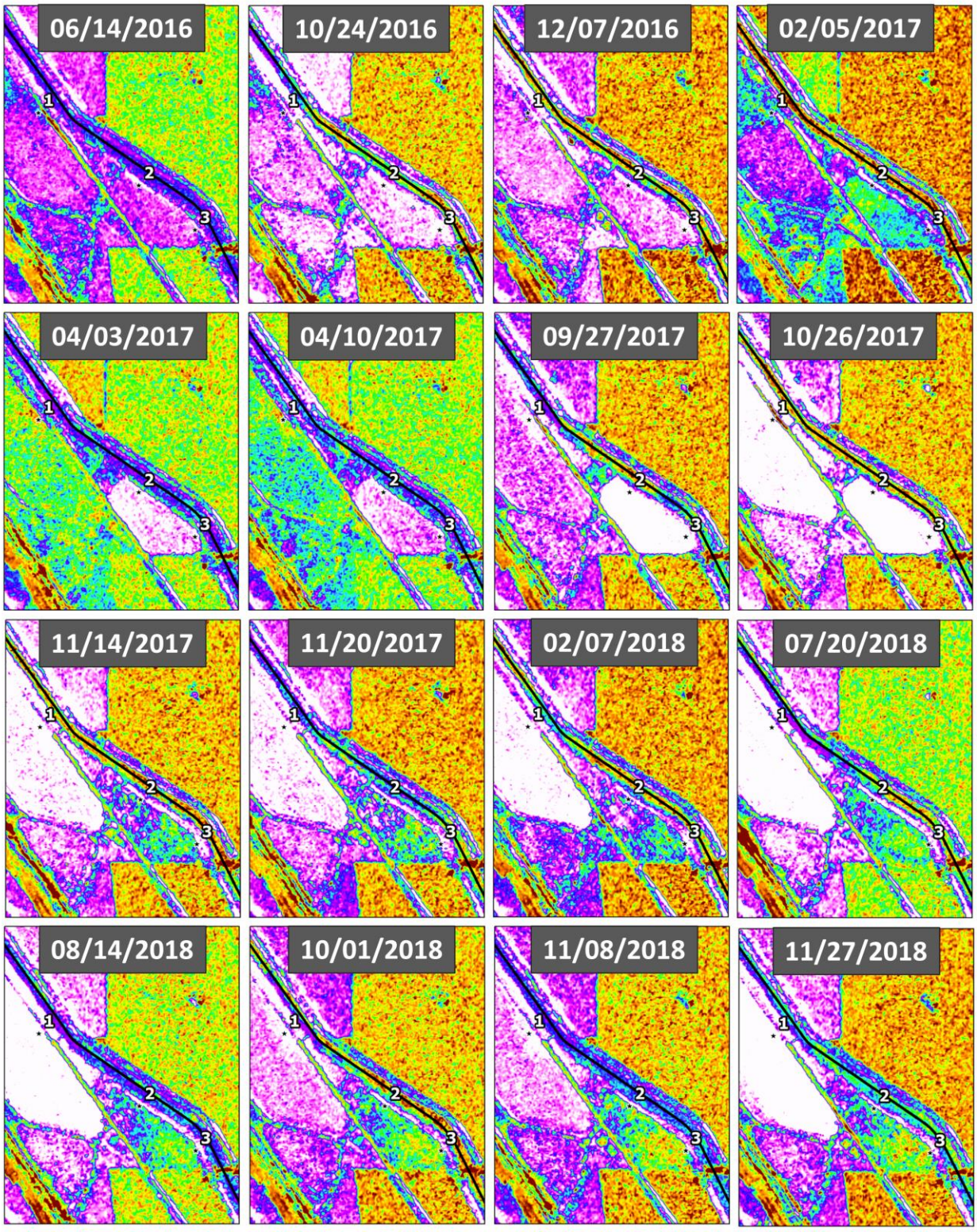

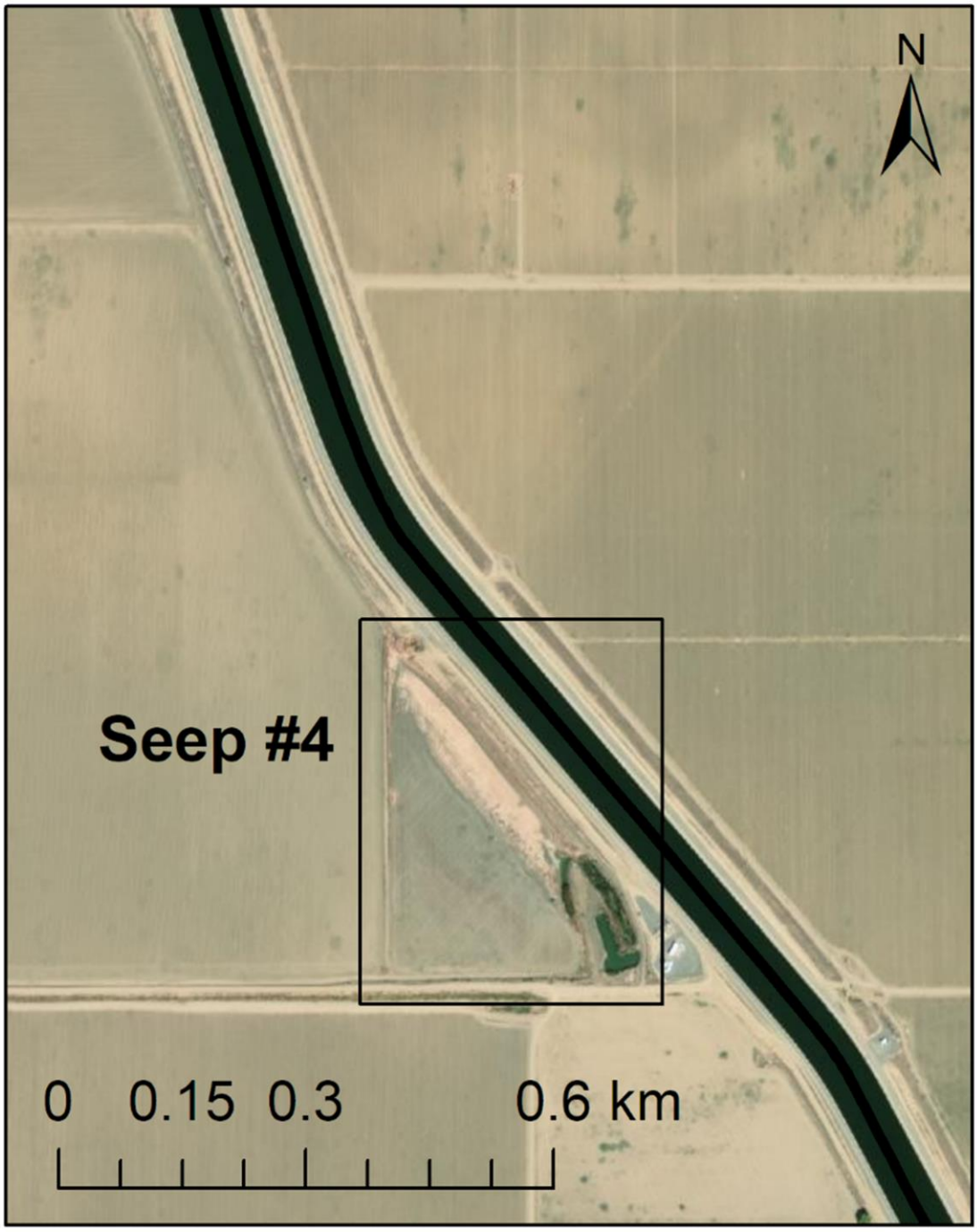

Figure 13: Study area overview for Seep 4 along the California Aqueduct.

Figure 14A: Seep 4 – Google Earth Imagery

Figure 14B: Seep 4– Google Earth Imagery

Figure 14C: Seep 4– Google Earth Imagery

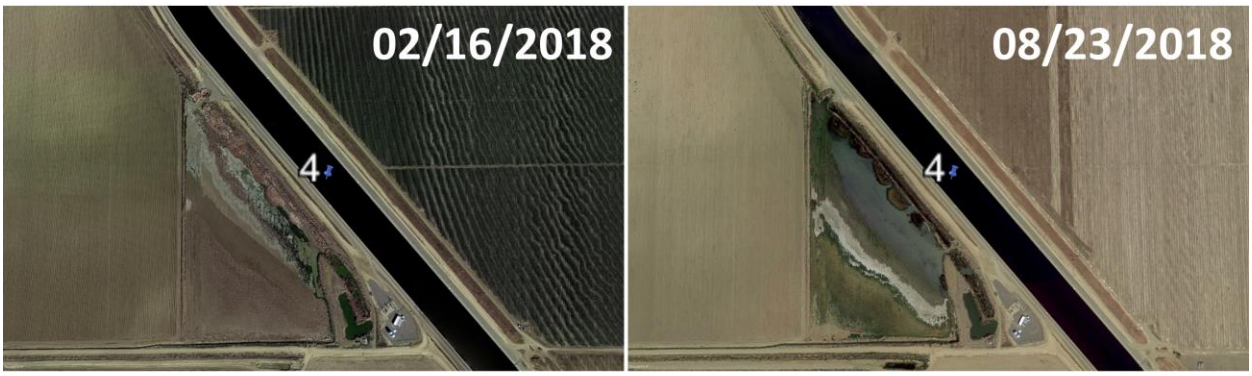

Figure 15: Legends for NDWI and PolSAR data products.

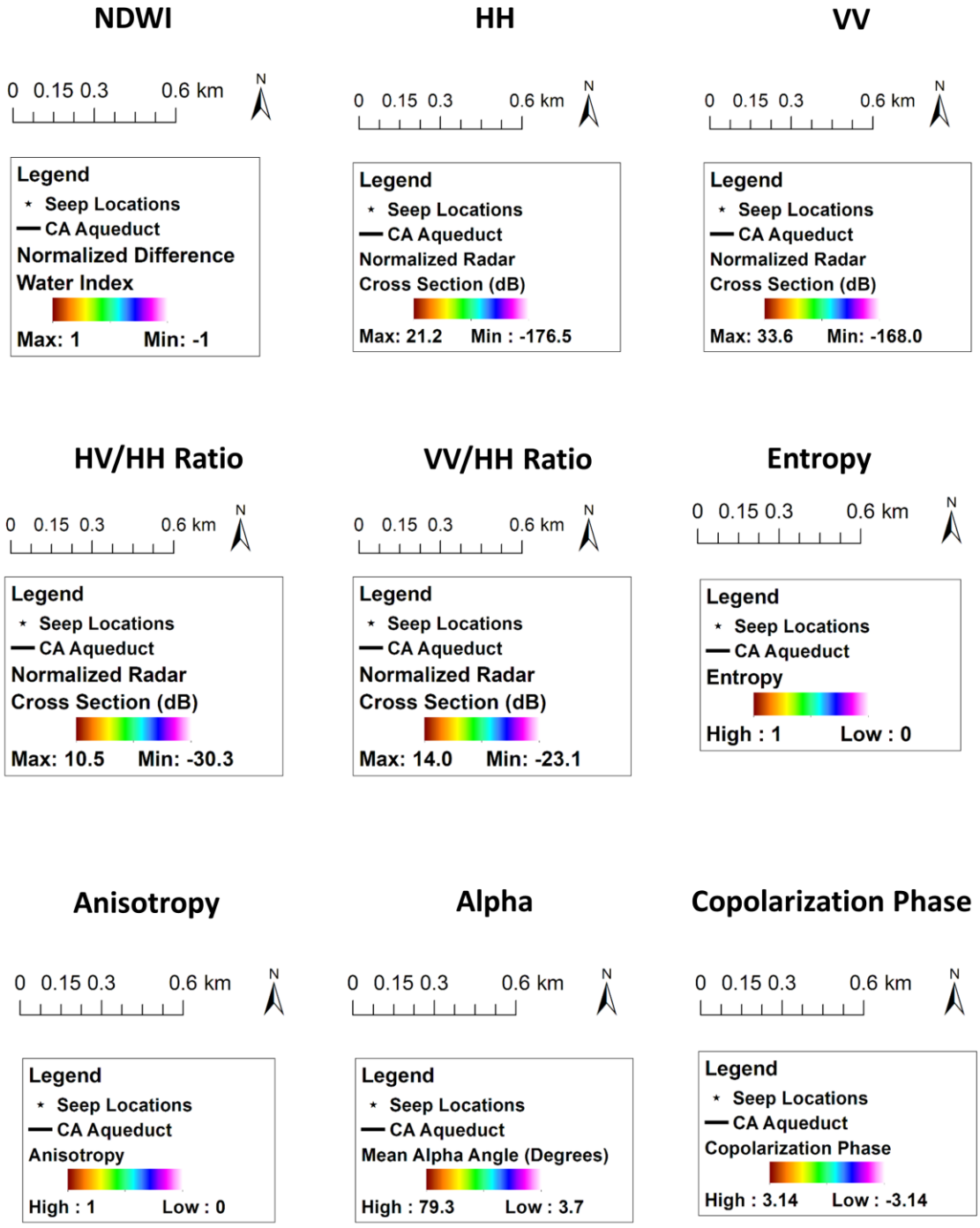

Figure 16A: Seep 4– NDWI

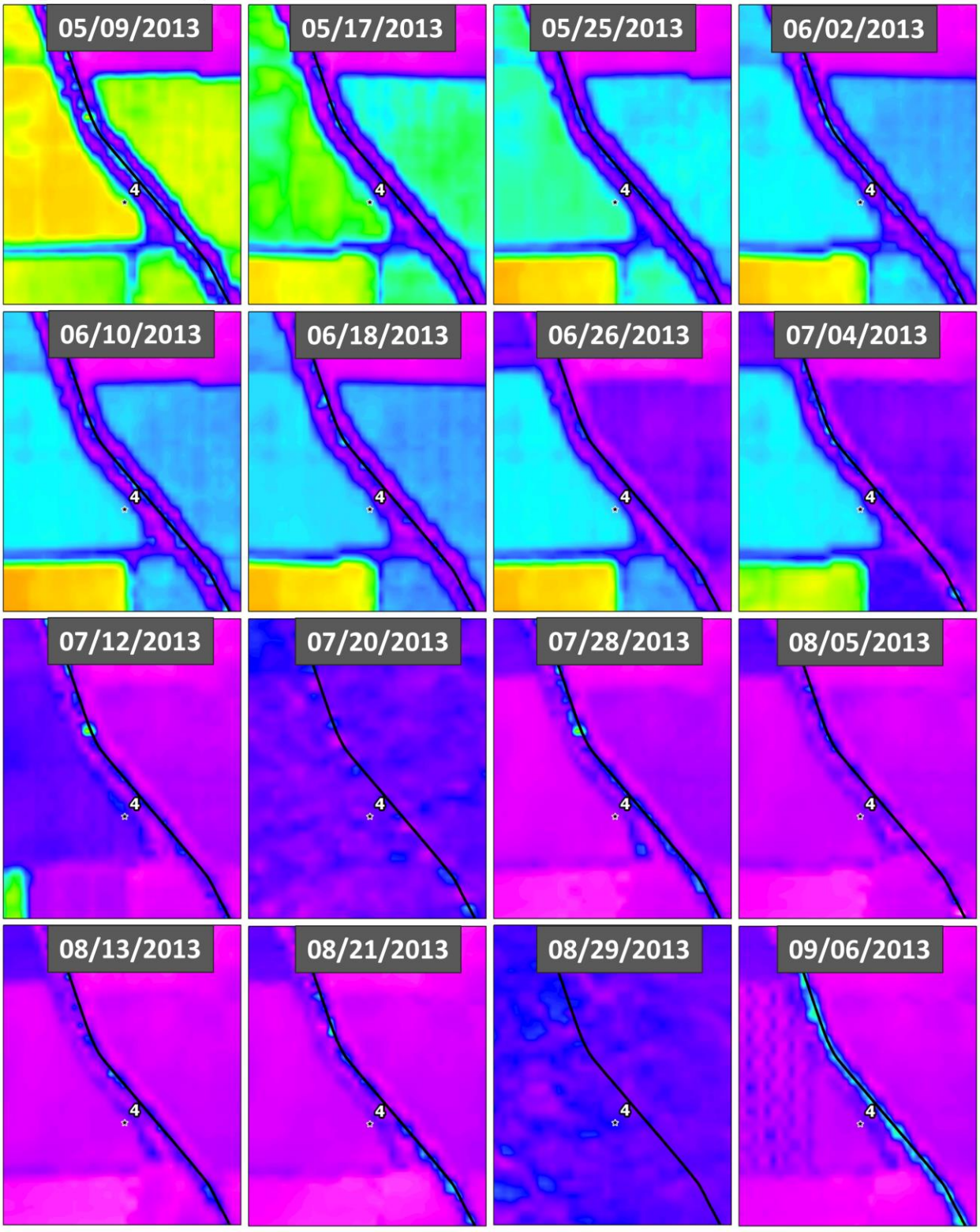

Figure 16B: Seep 4– NDWI

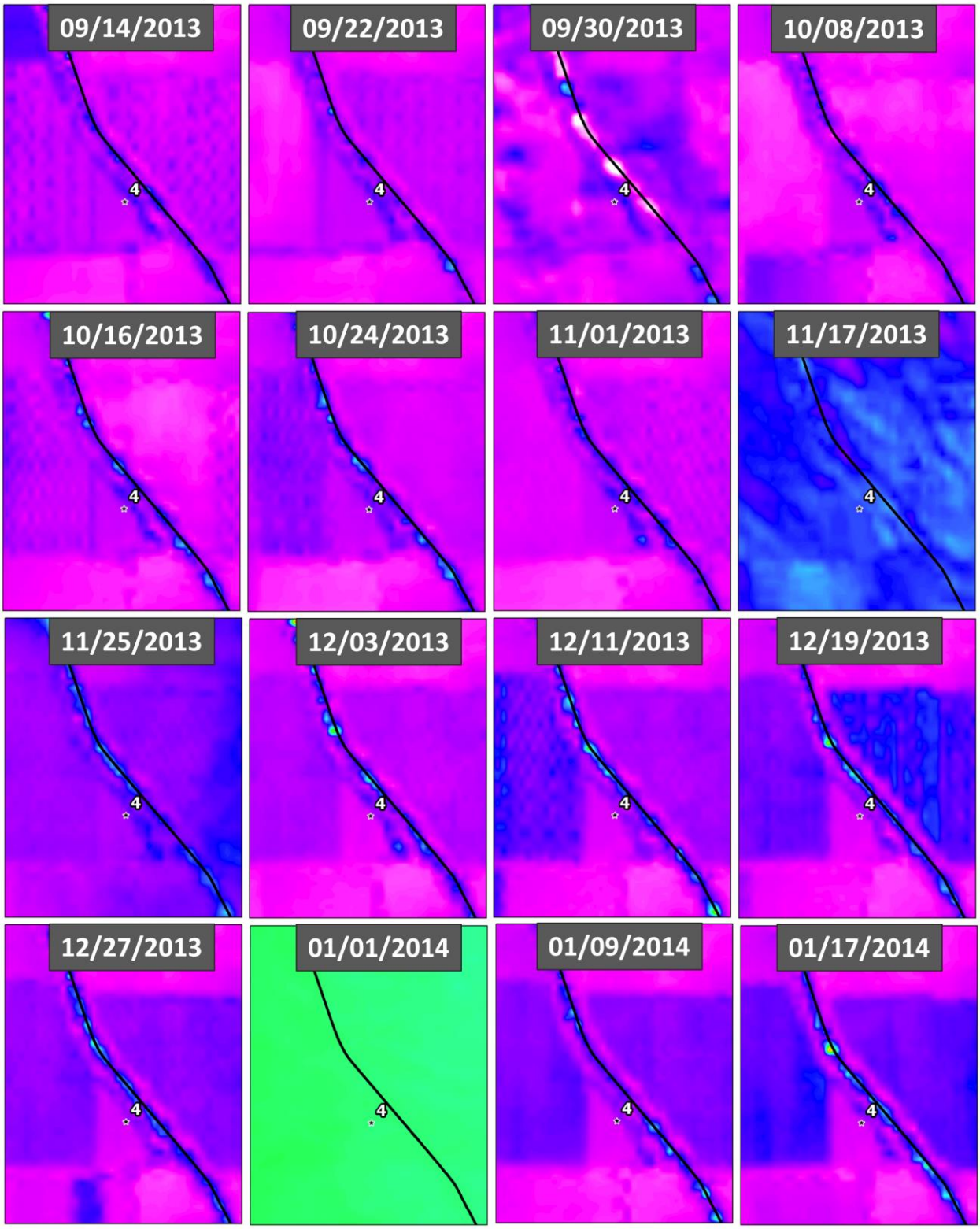

Figure 16C: Seep 4– NDWI

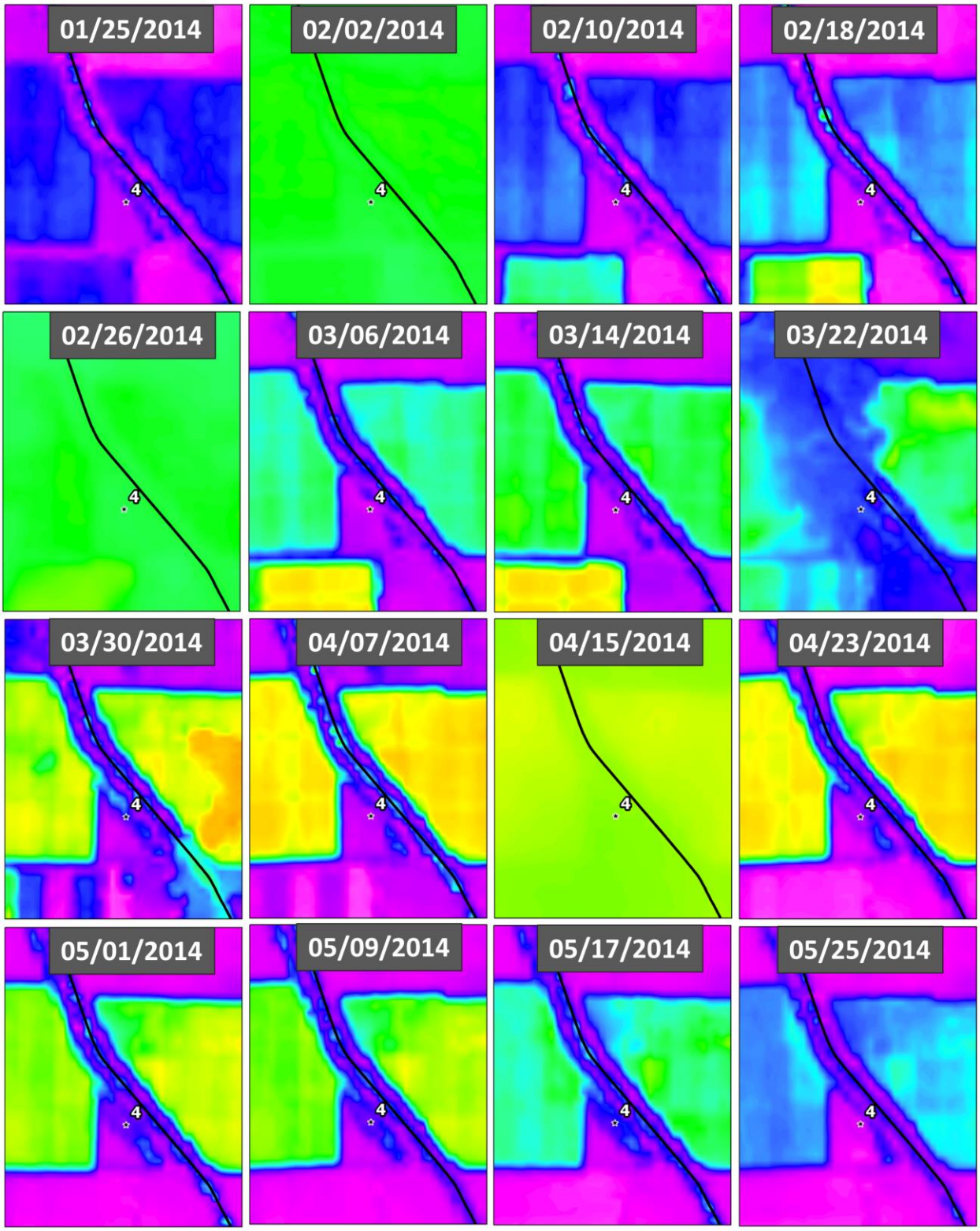

Figure 16D: Seep 4– NDWI

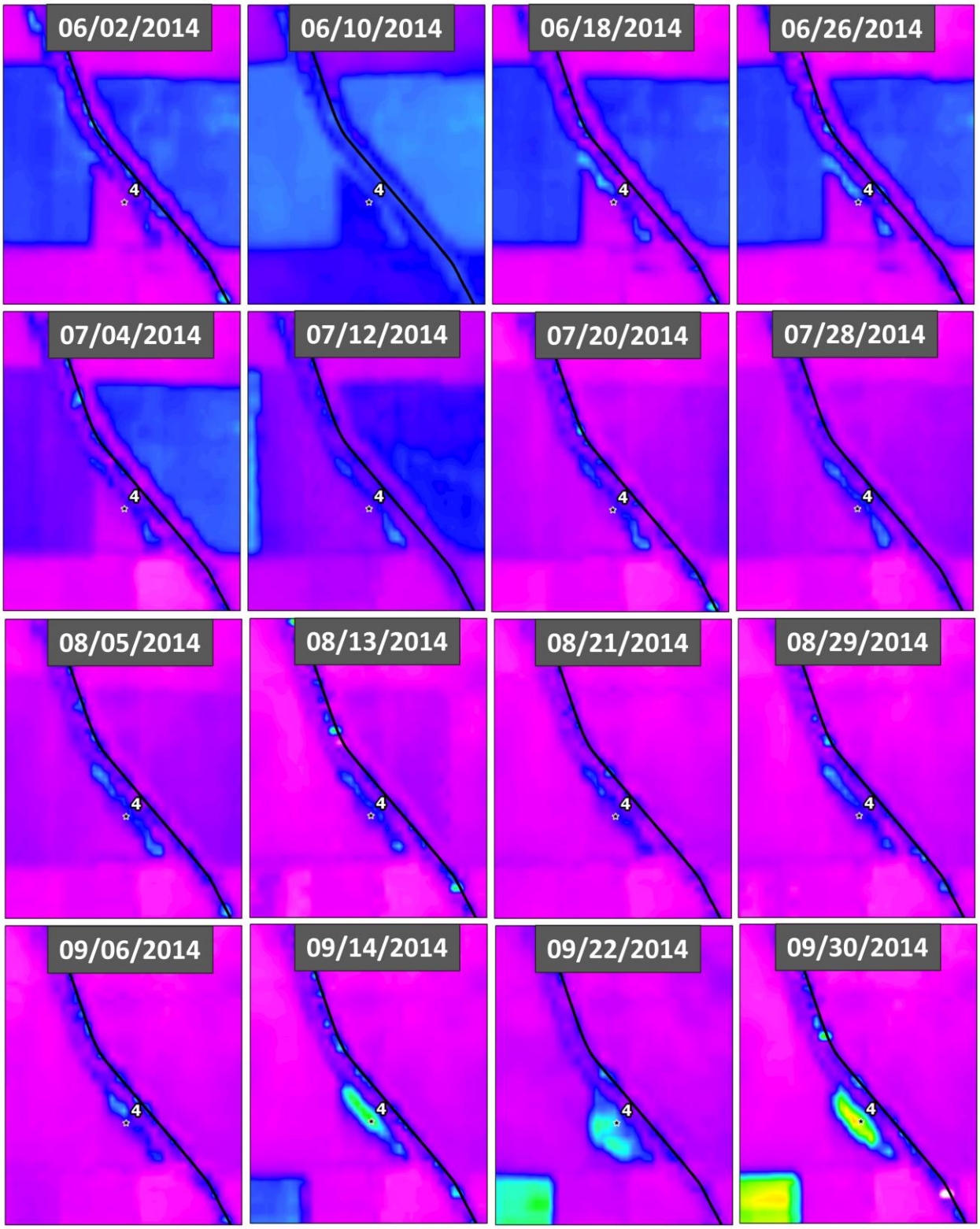

Figure 16E: Seep 4– NDWI

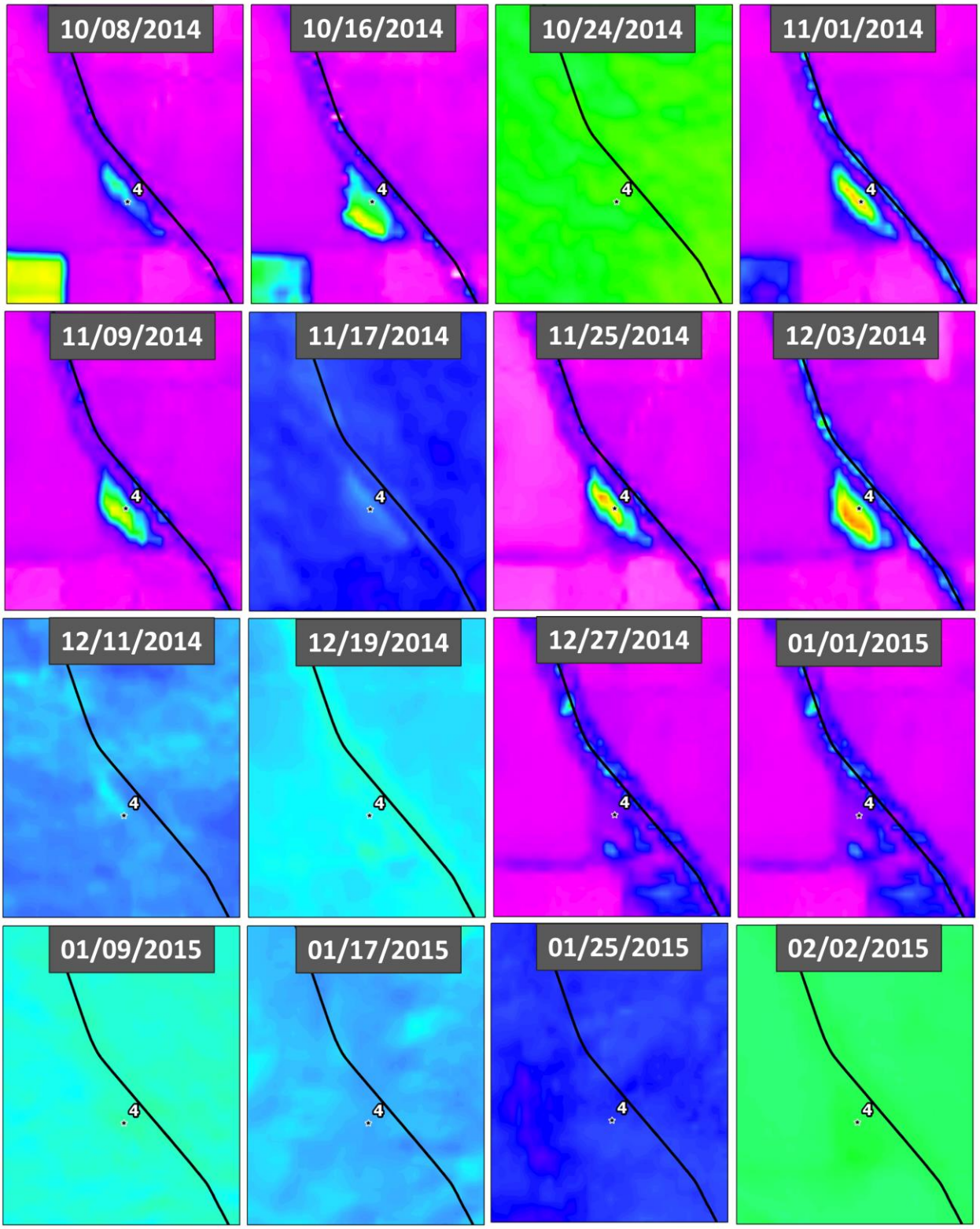

Figure 16F: Seep 4– NDWI

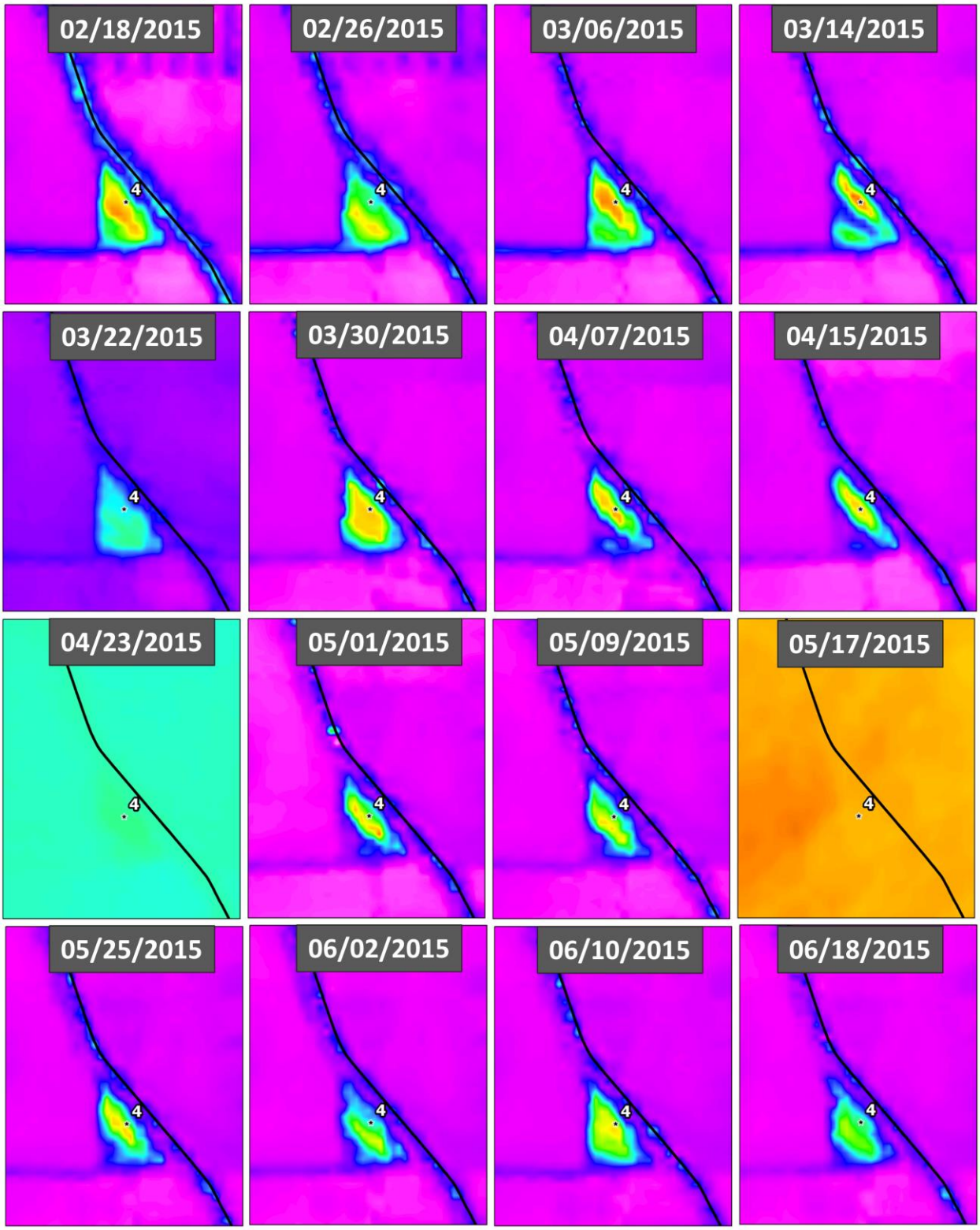

Figure 16G: Seep 4– NDWI

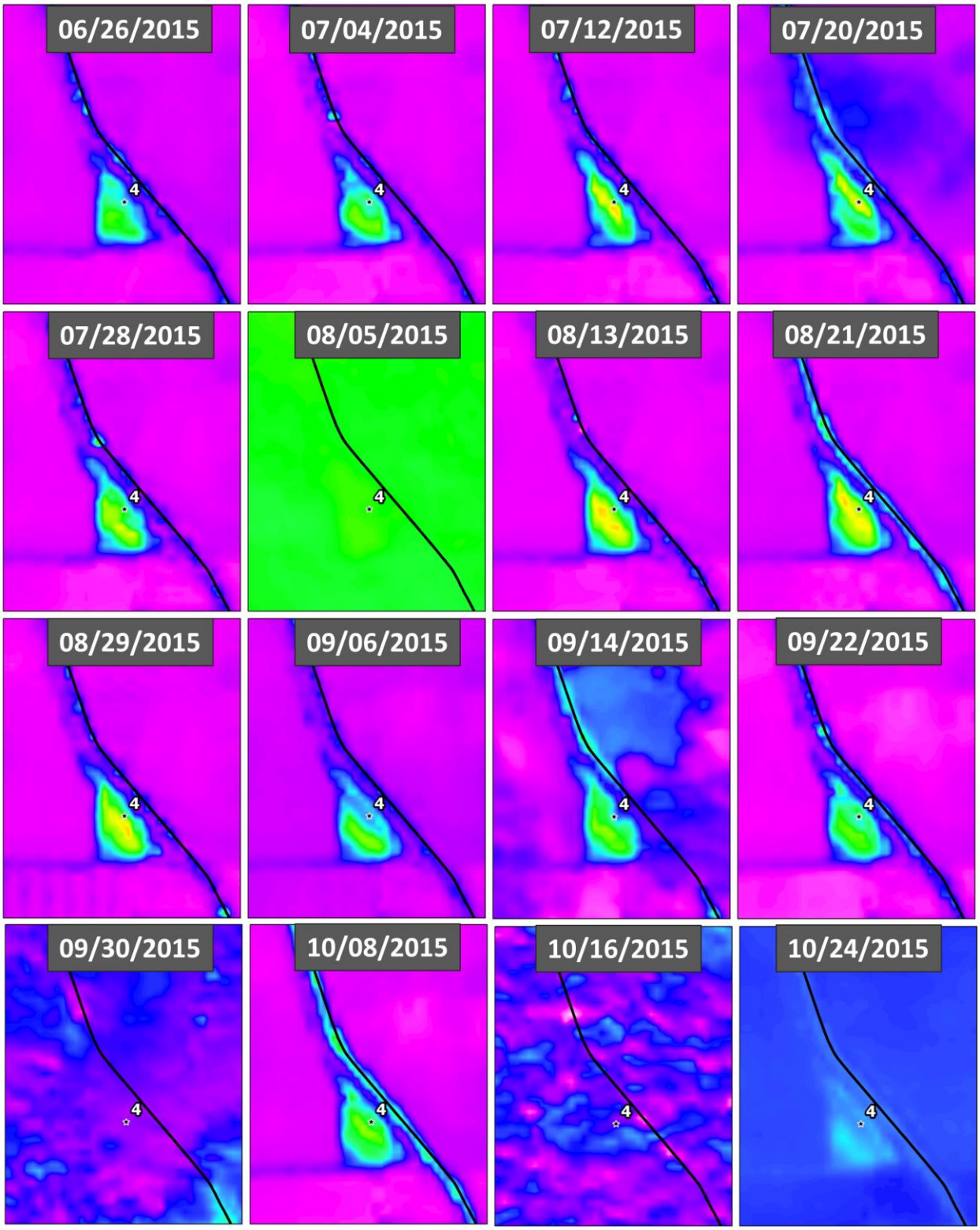

Figure 16H: Seep 4– NDWI

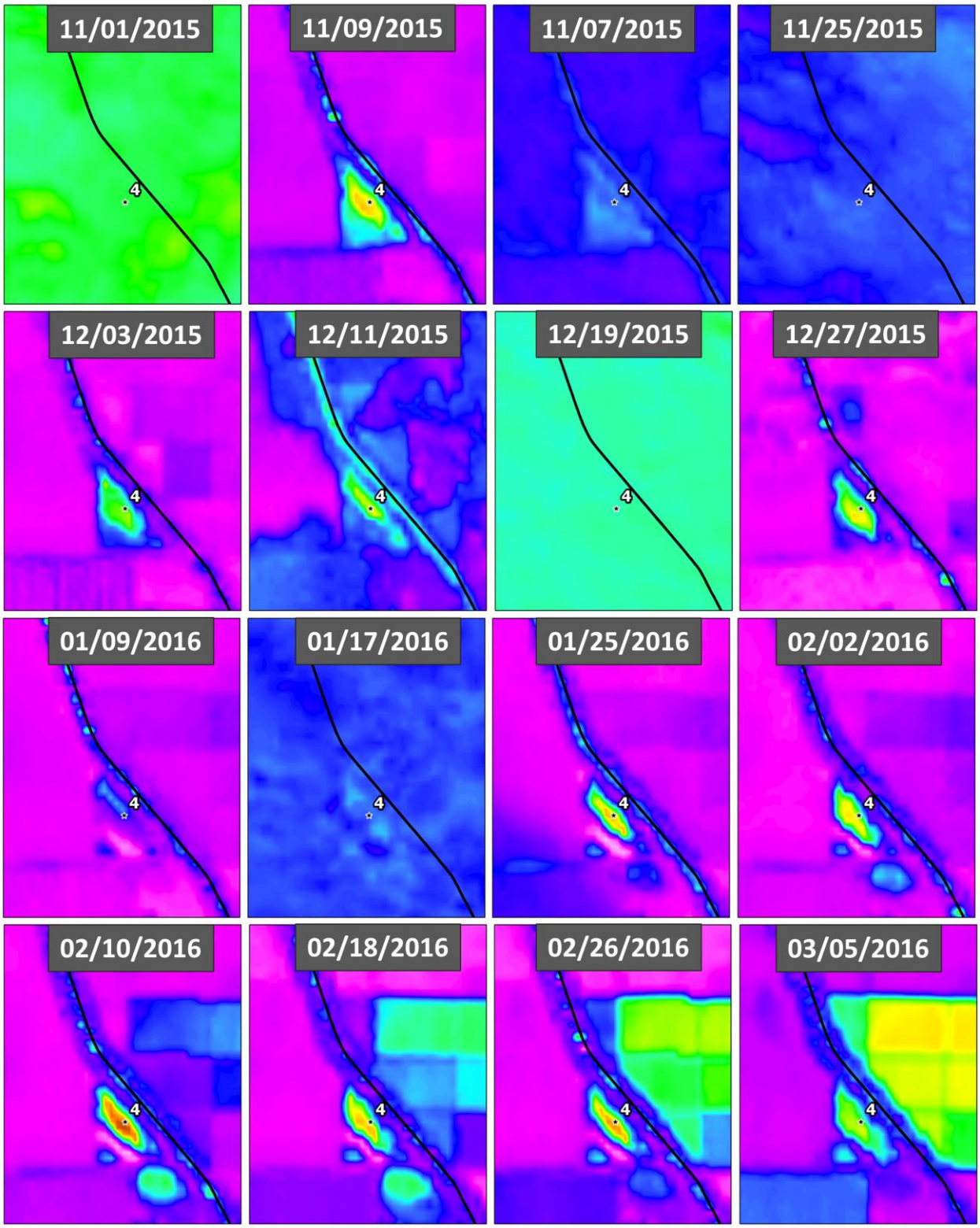

Figure 16l: Seep 4– NDWI

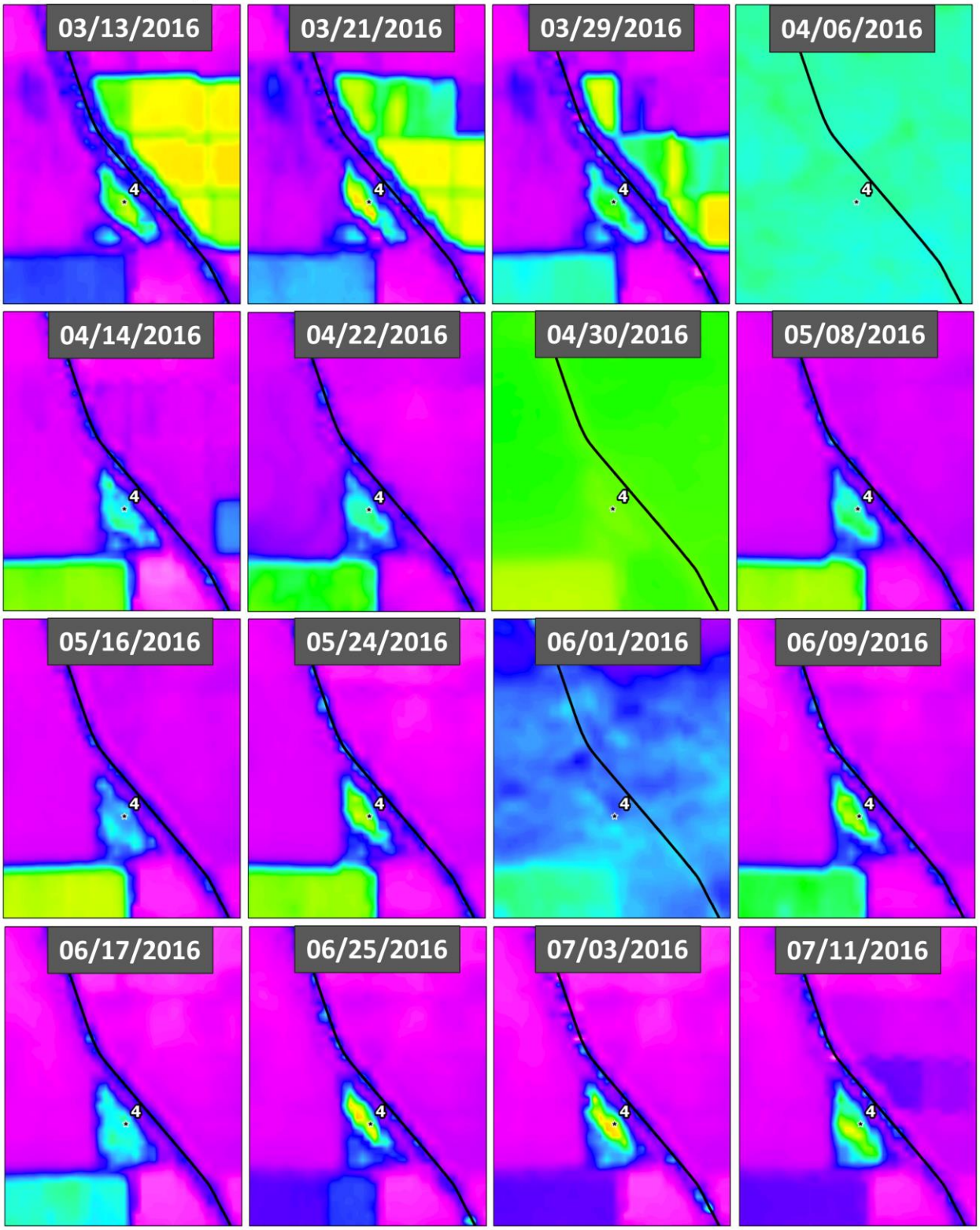

Figure 16J: Seep 4– NDWI

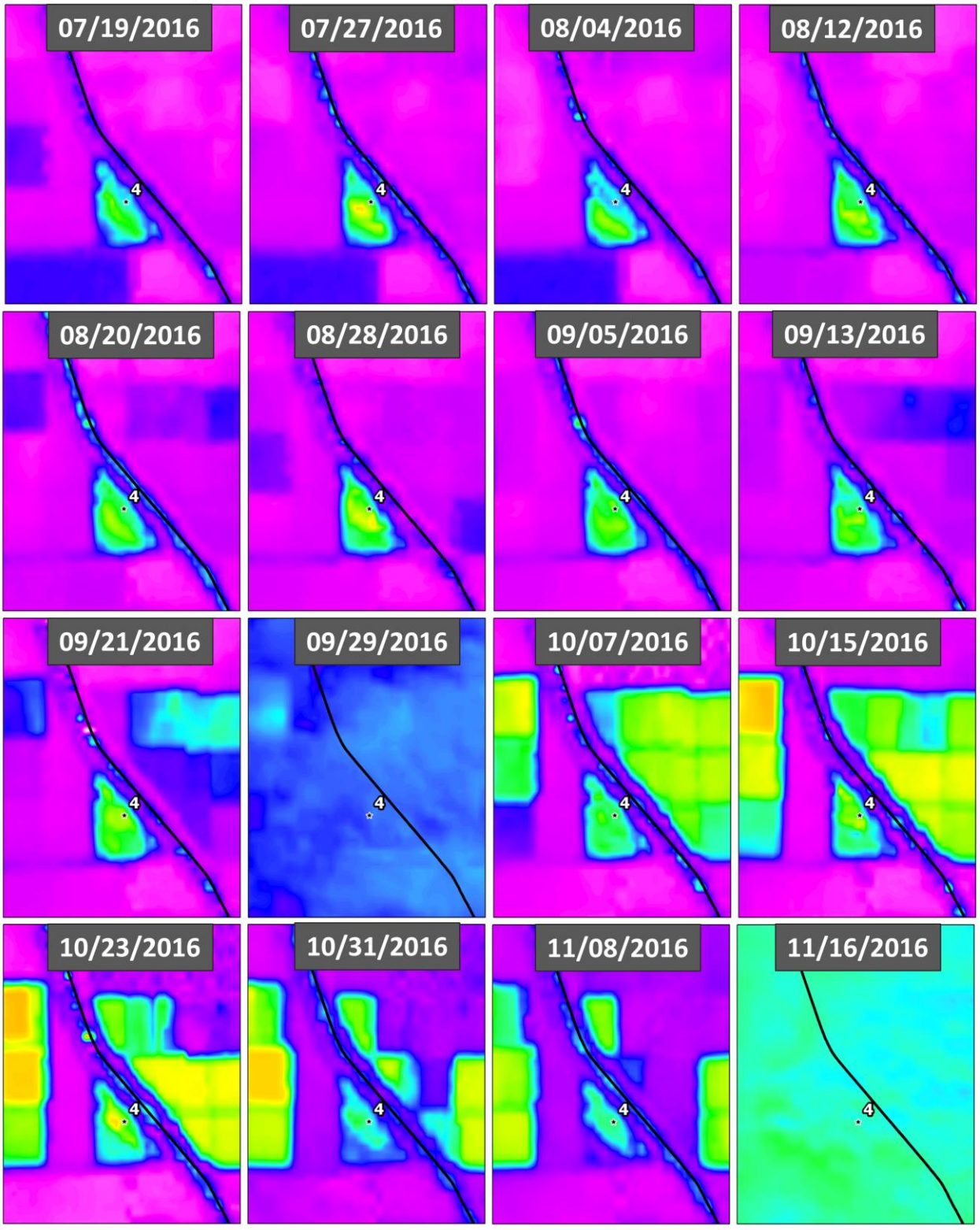

Figure 16K: Seep 4– NDWI

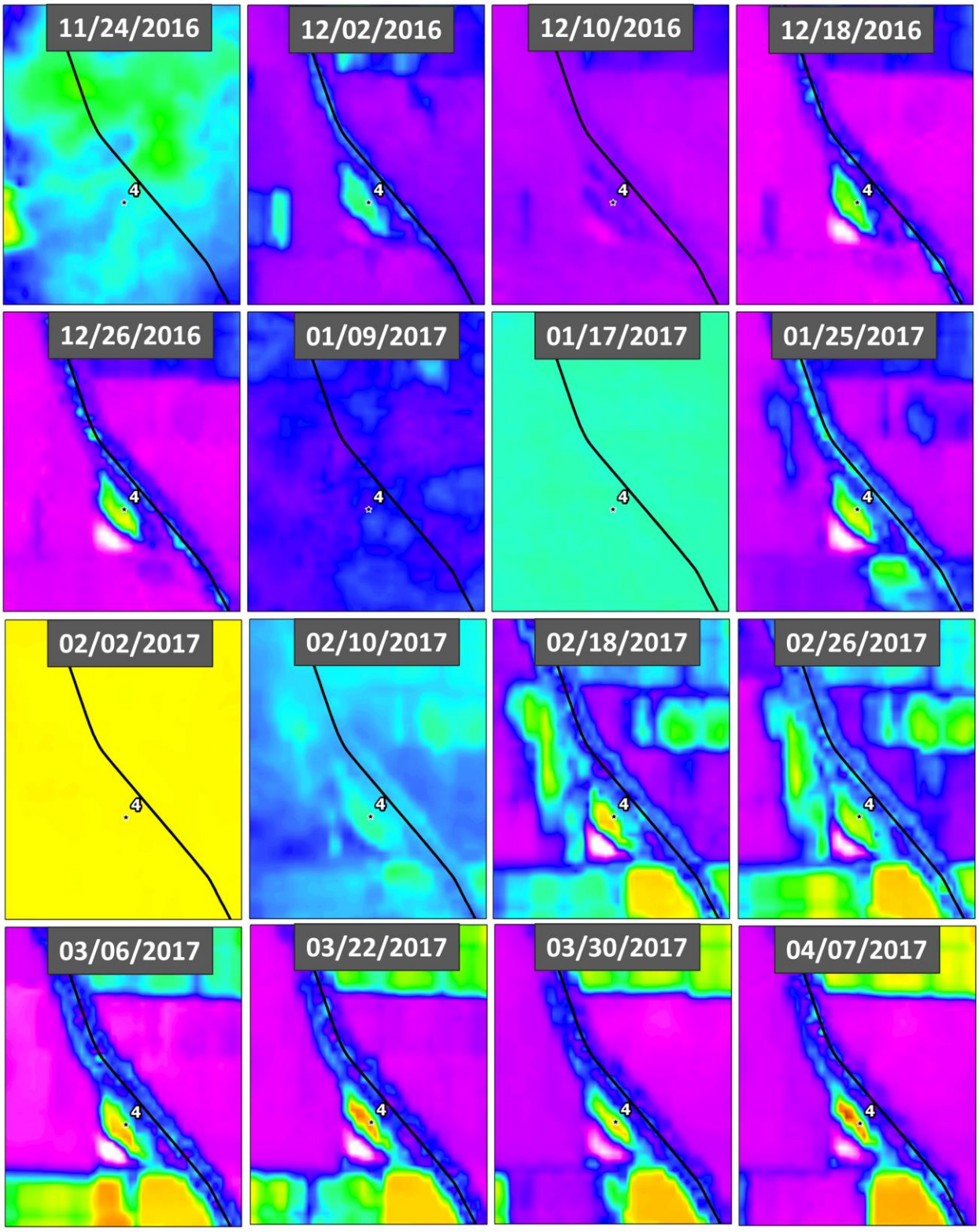

Figure 16L: Seep 4– NDWI

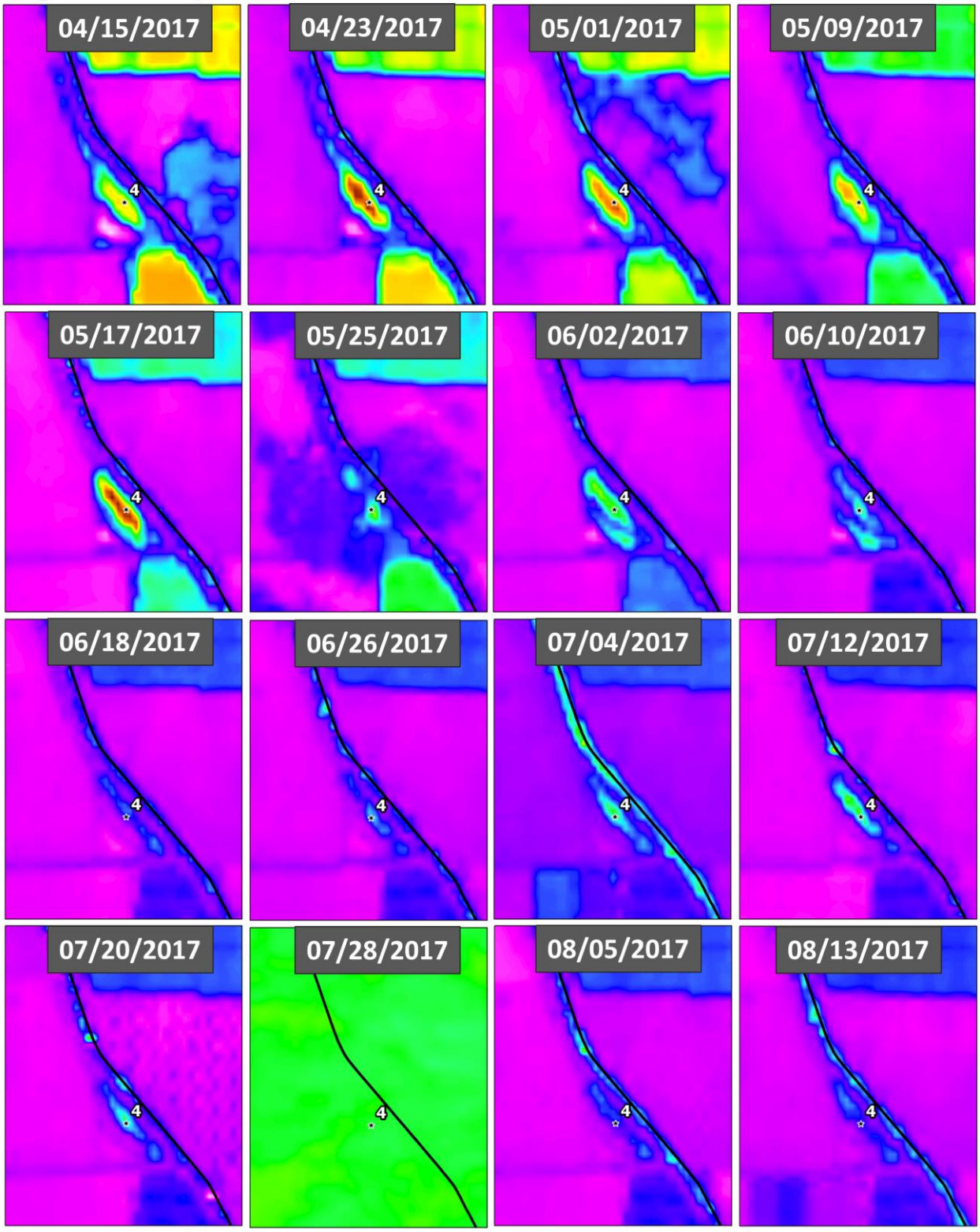

Figure 16M: Seep 4– NDWI

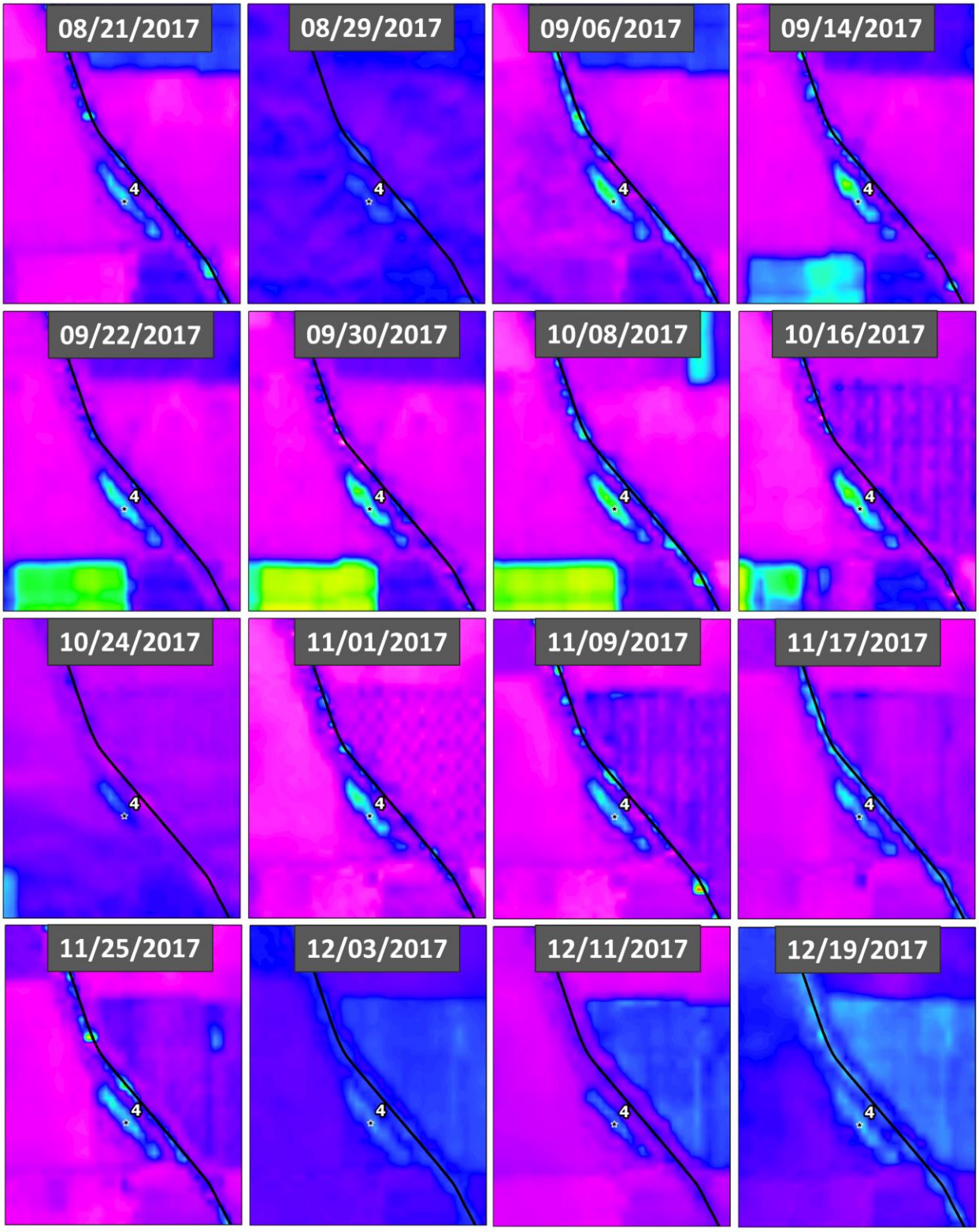

Figure 16N: Seep 4– NDWI

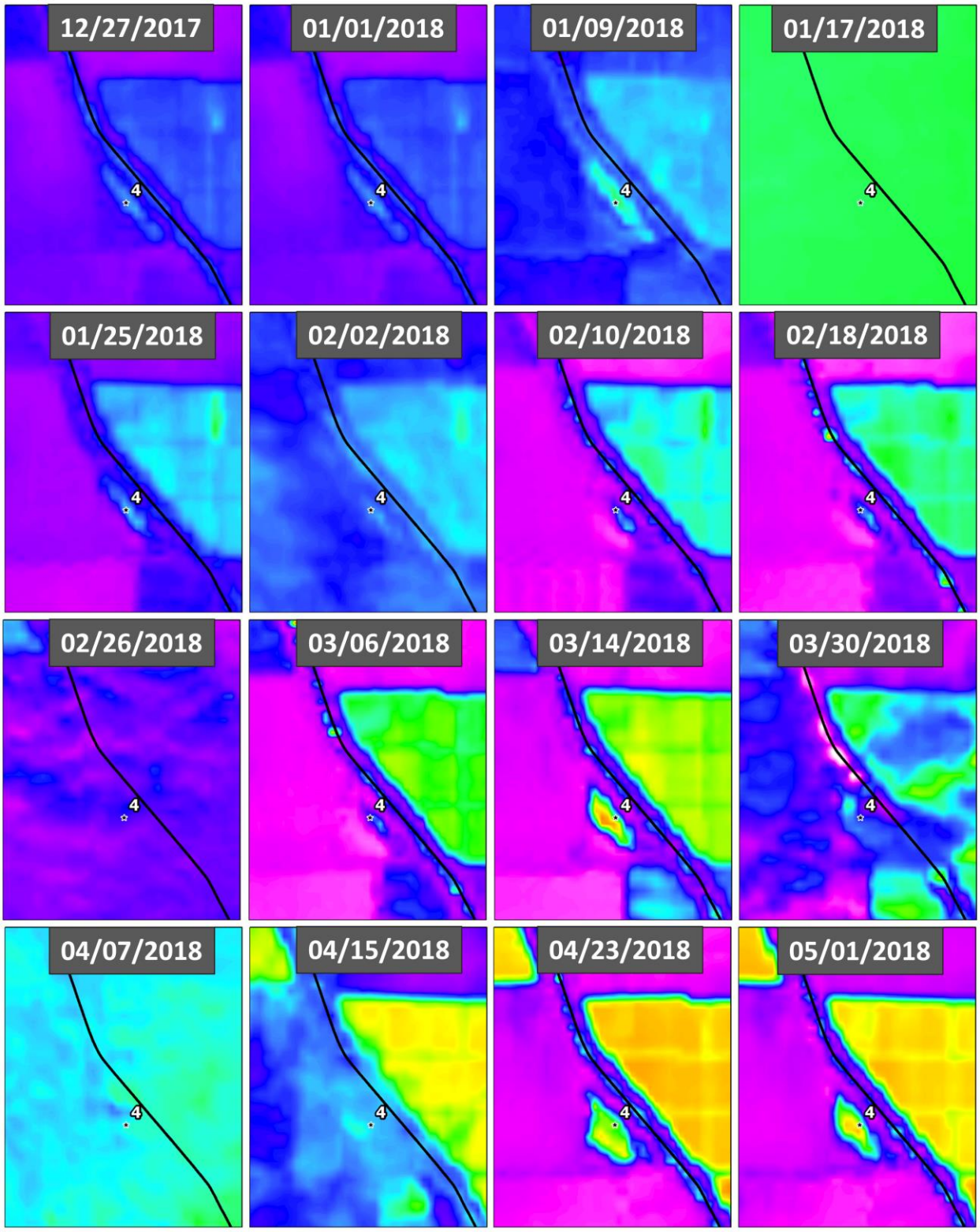

Figure 16O: Seep 4– NDWI

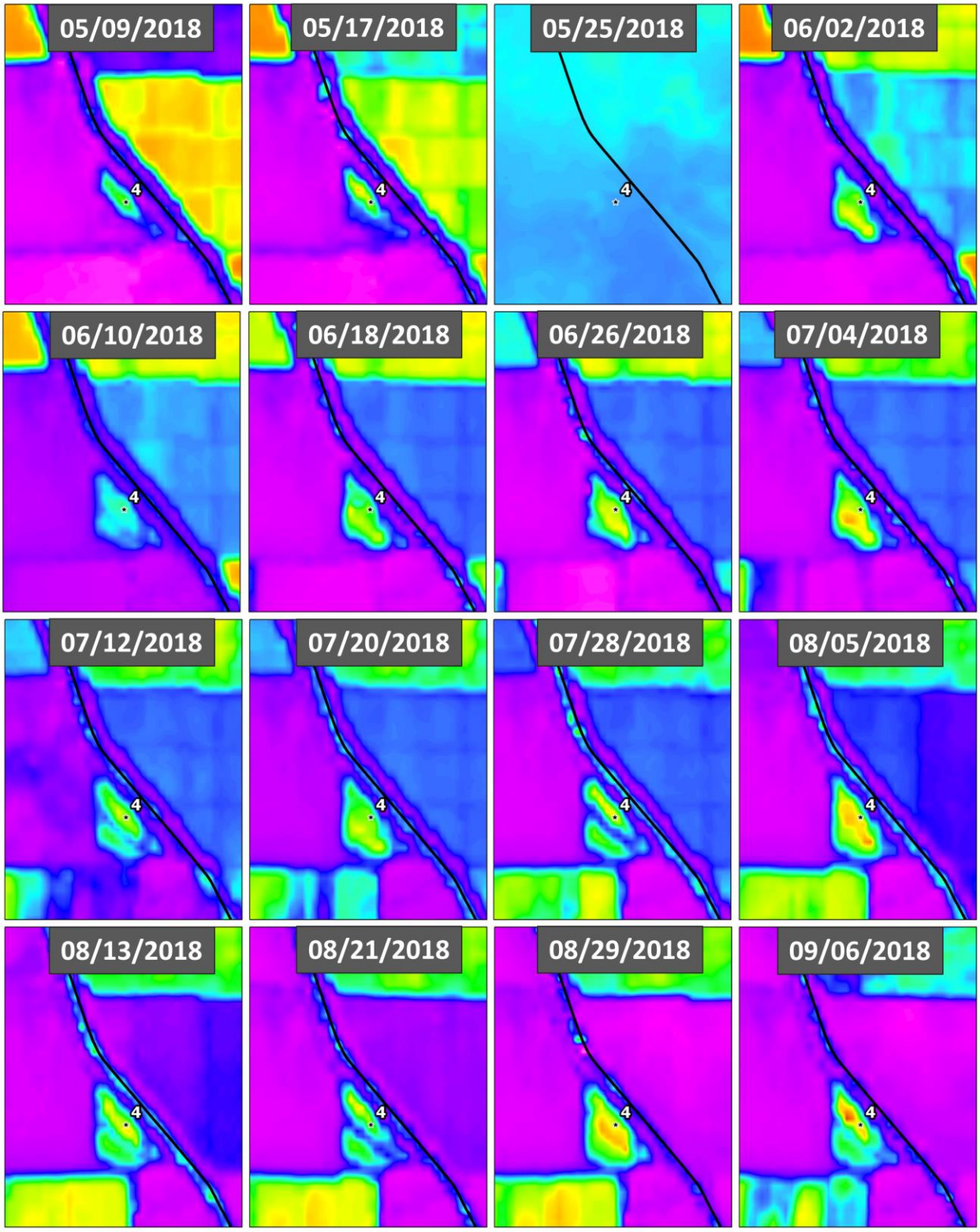

Figure 16P: Seep 4– NDWI

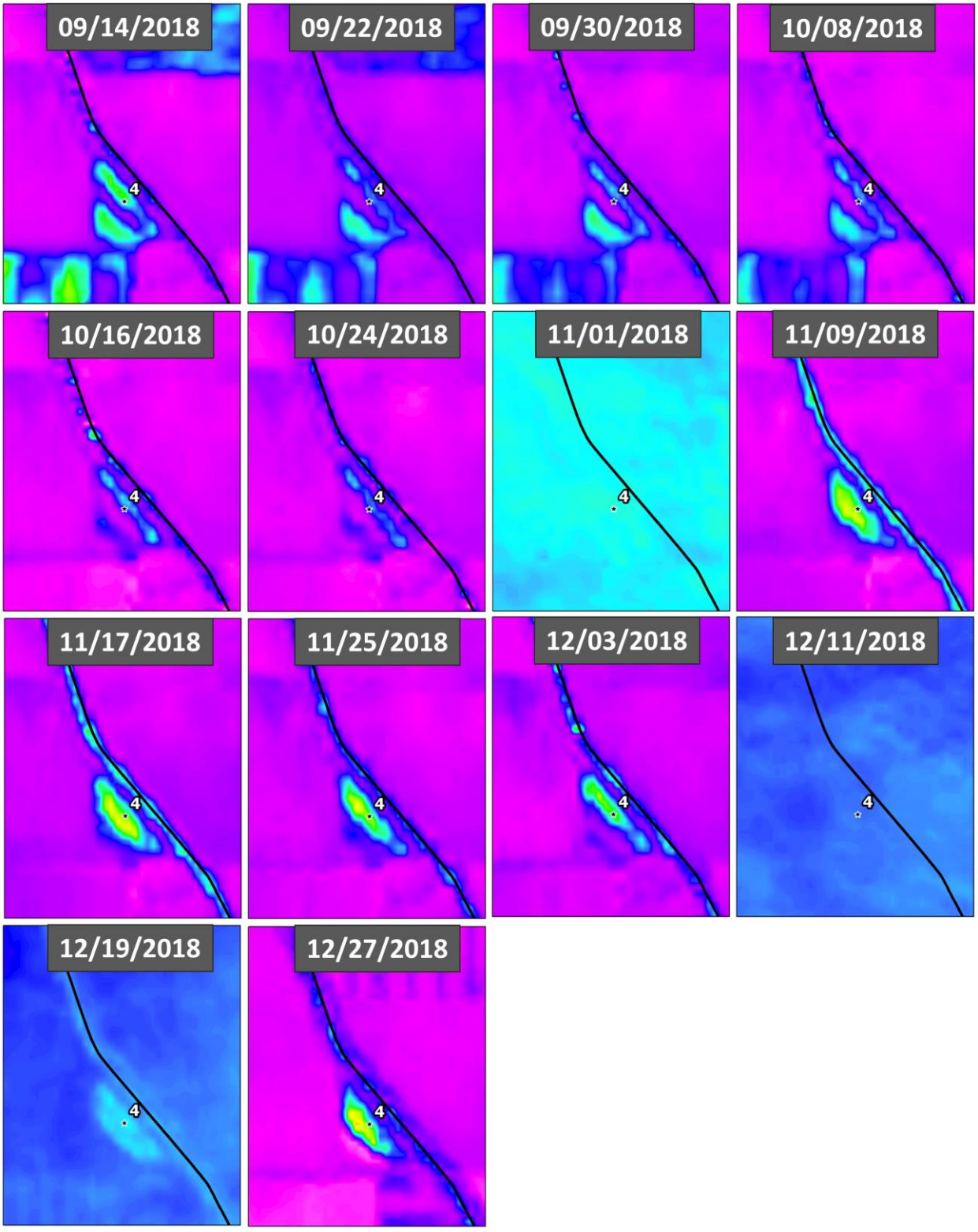

Figure 17A: Seep 4 – HH Single Polarization

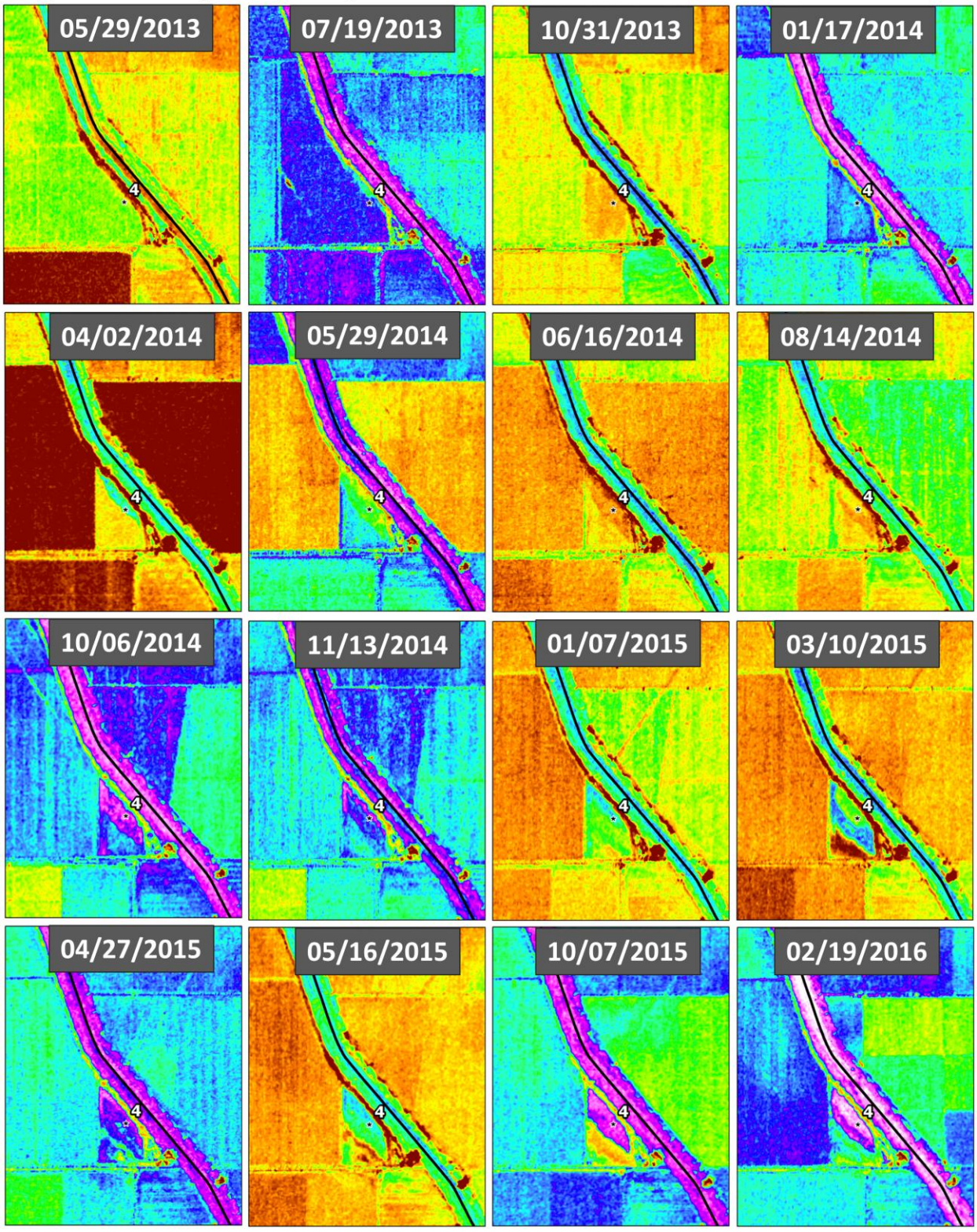

Figure 17B: Seep 4 – HH Single Polarization

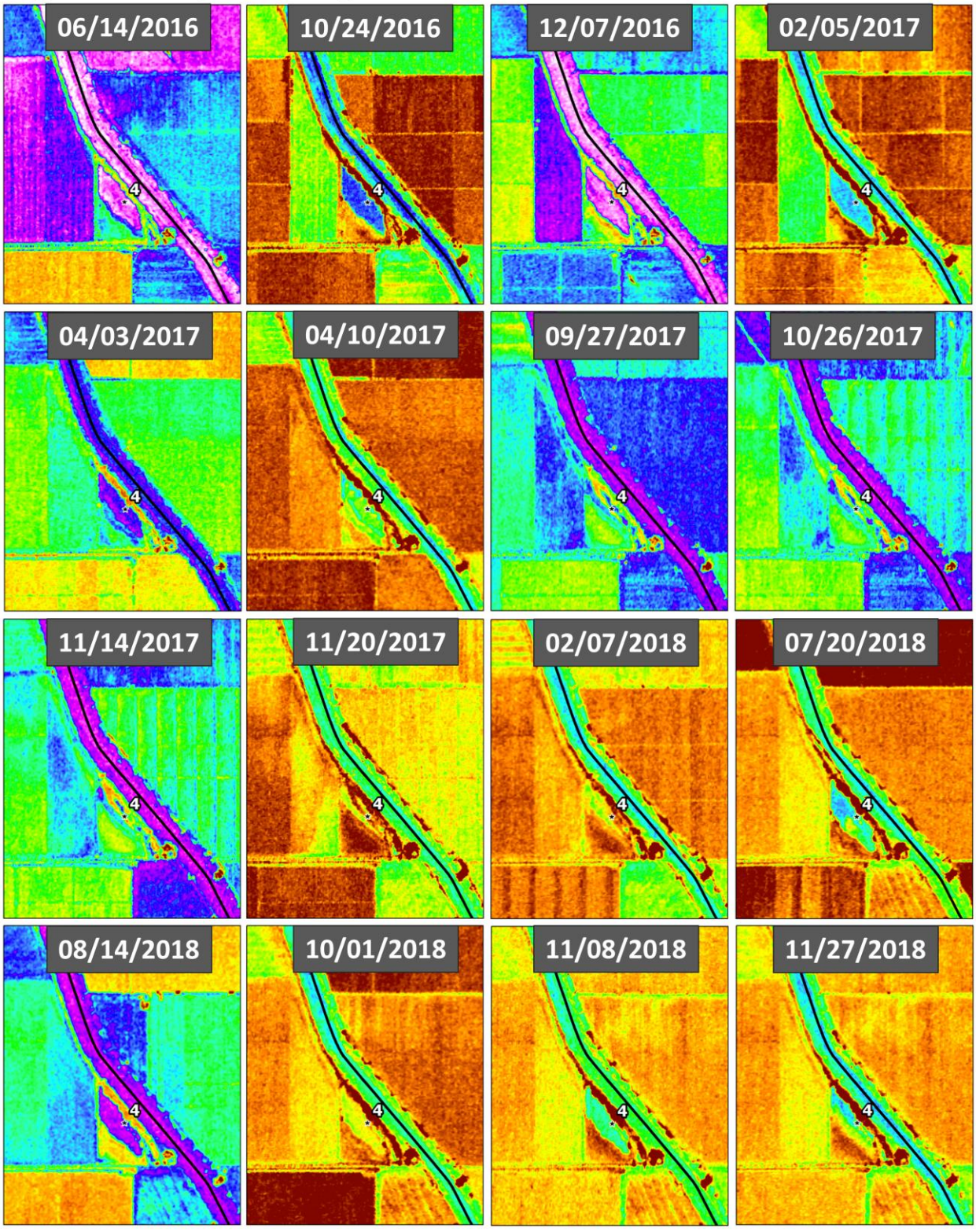

Figure 18A: Seep 4 – VV Single Polarization

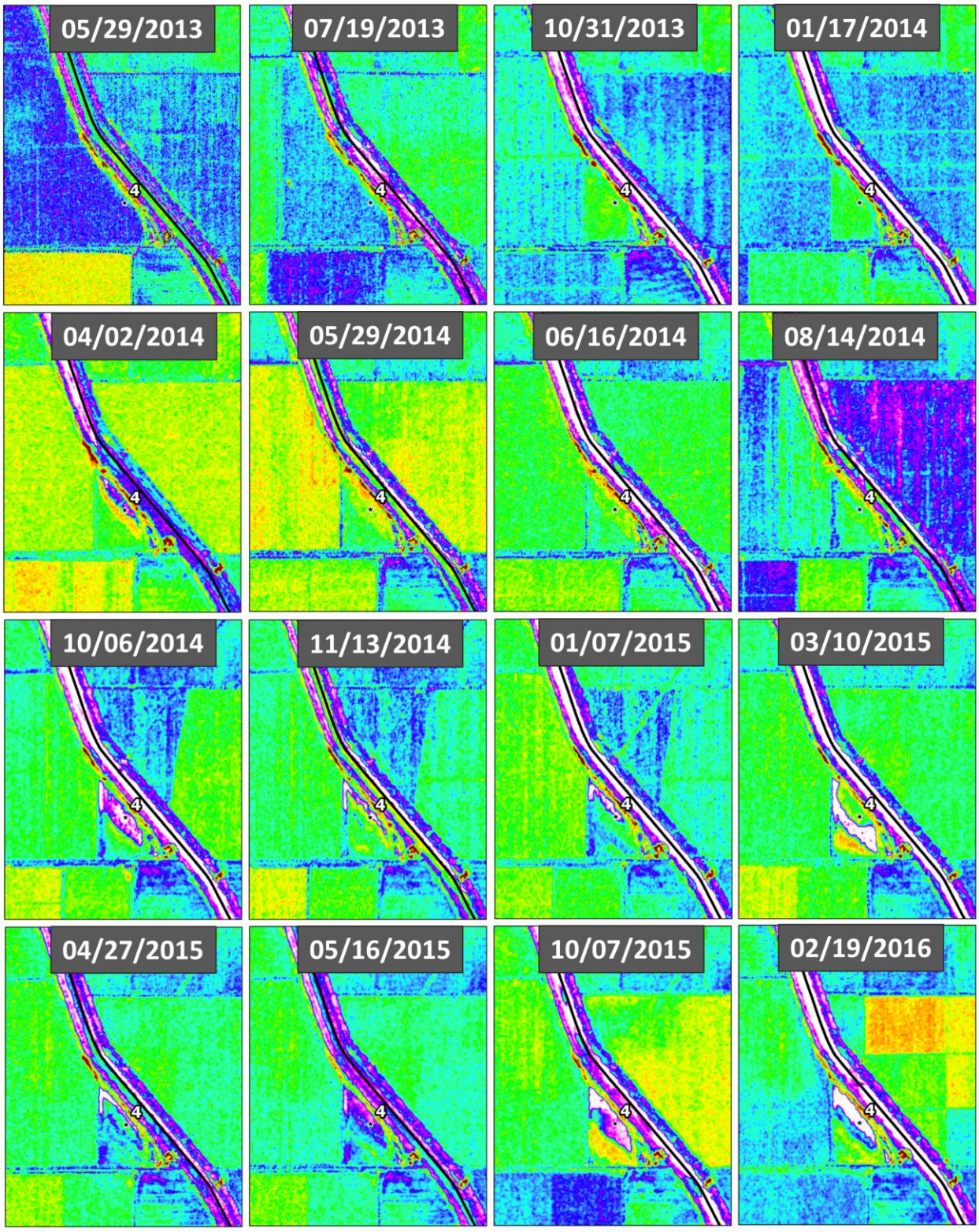

Figure 18B: Seep 4 – VV Single Polarization

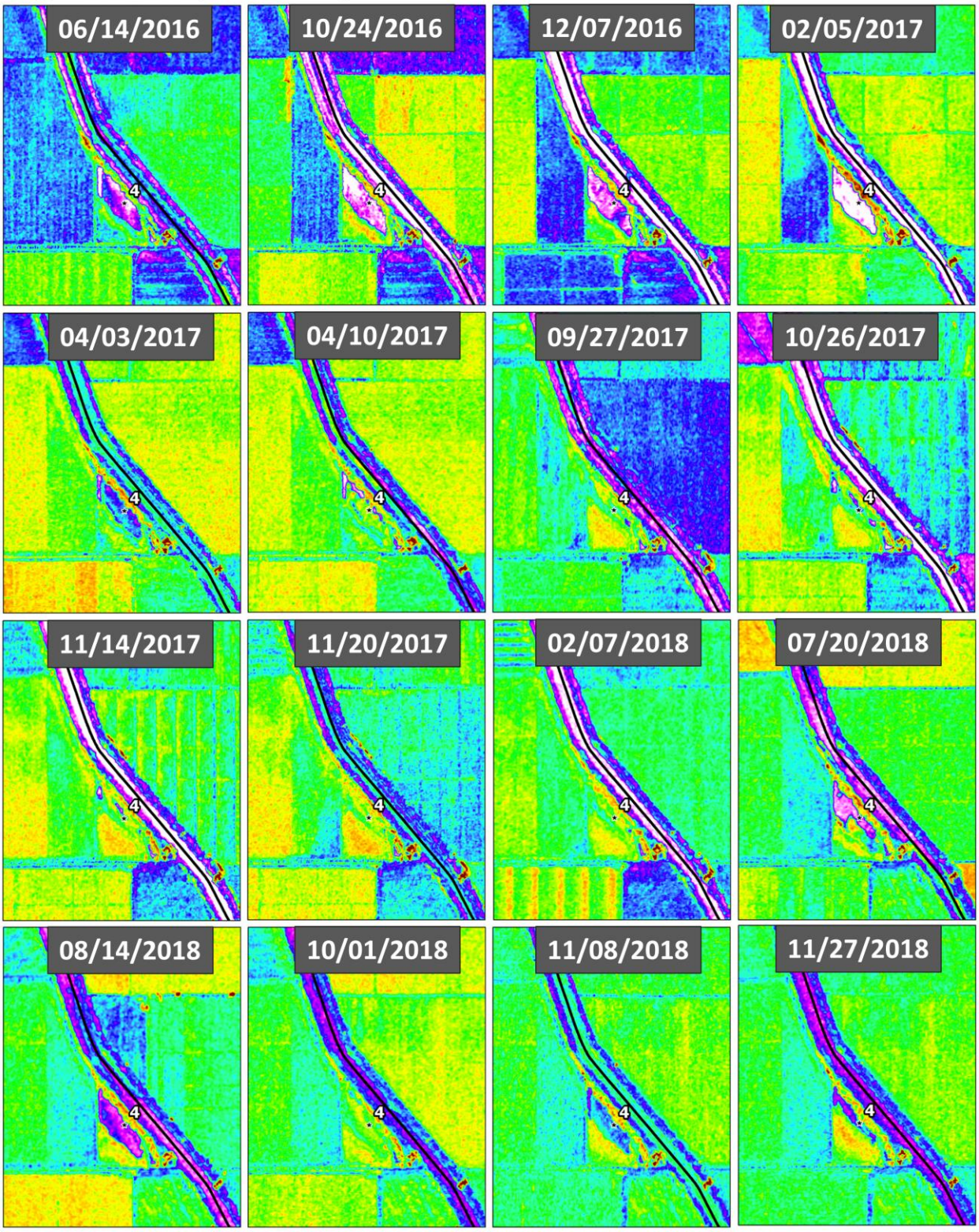

Figure 19A: Seep 4 – HV/HH Ratio

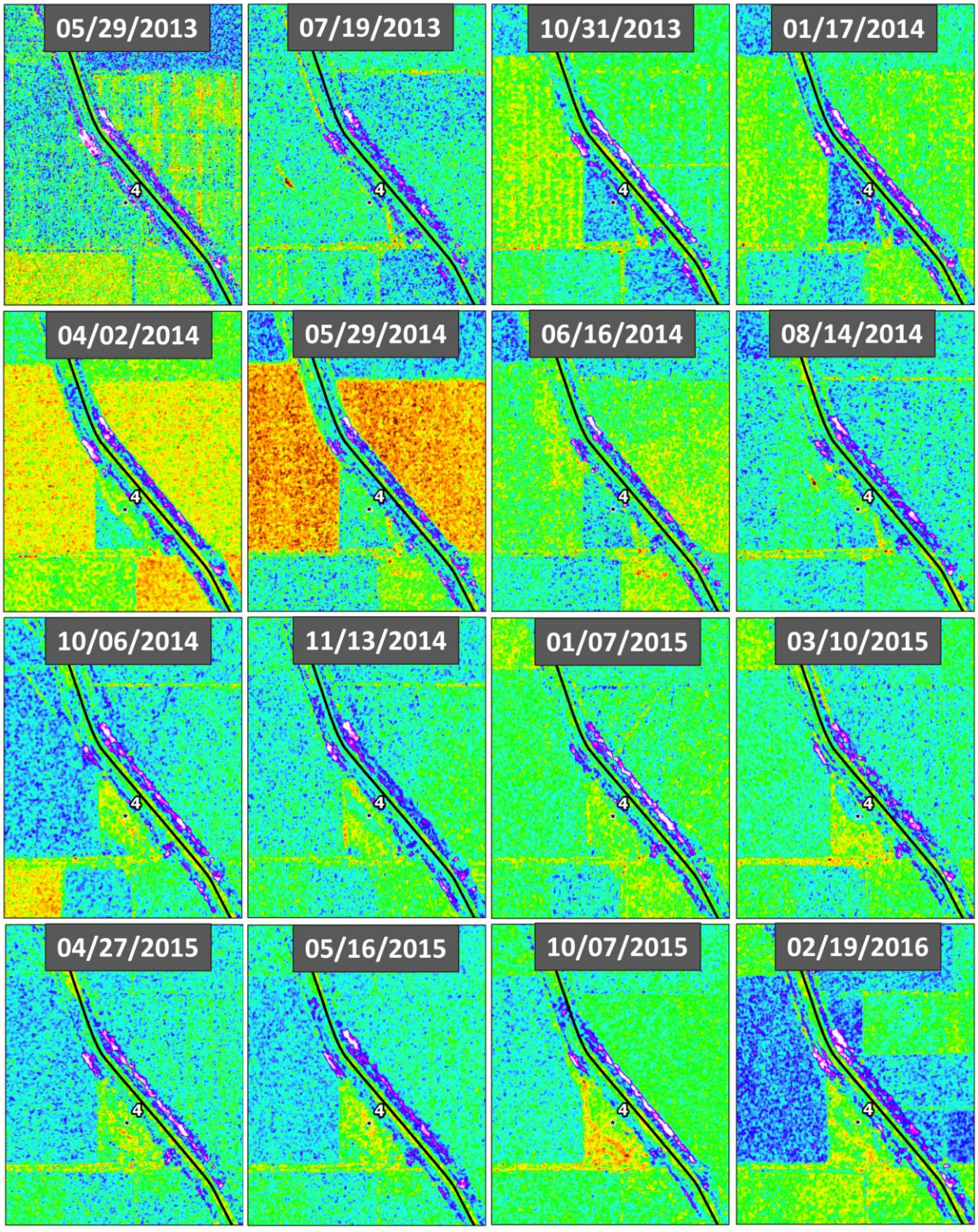

Figure 19B: Seep 4 – HV/HH Ratio

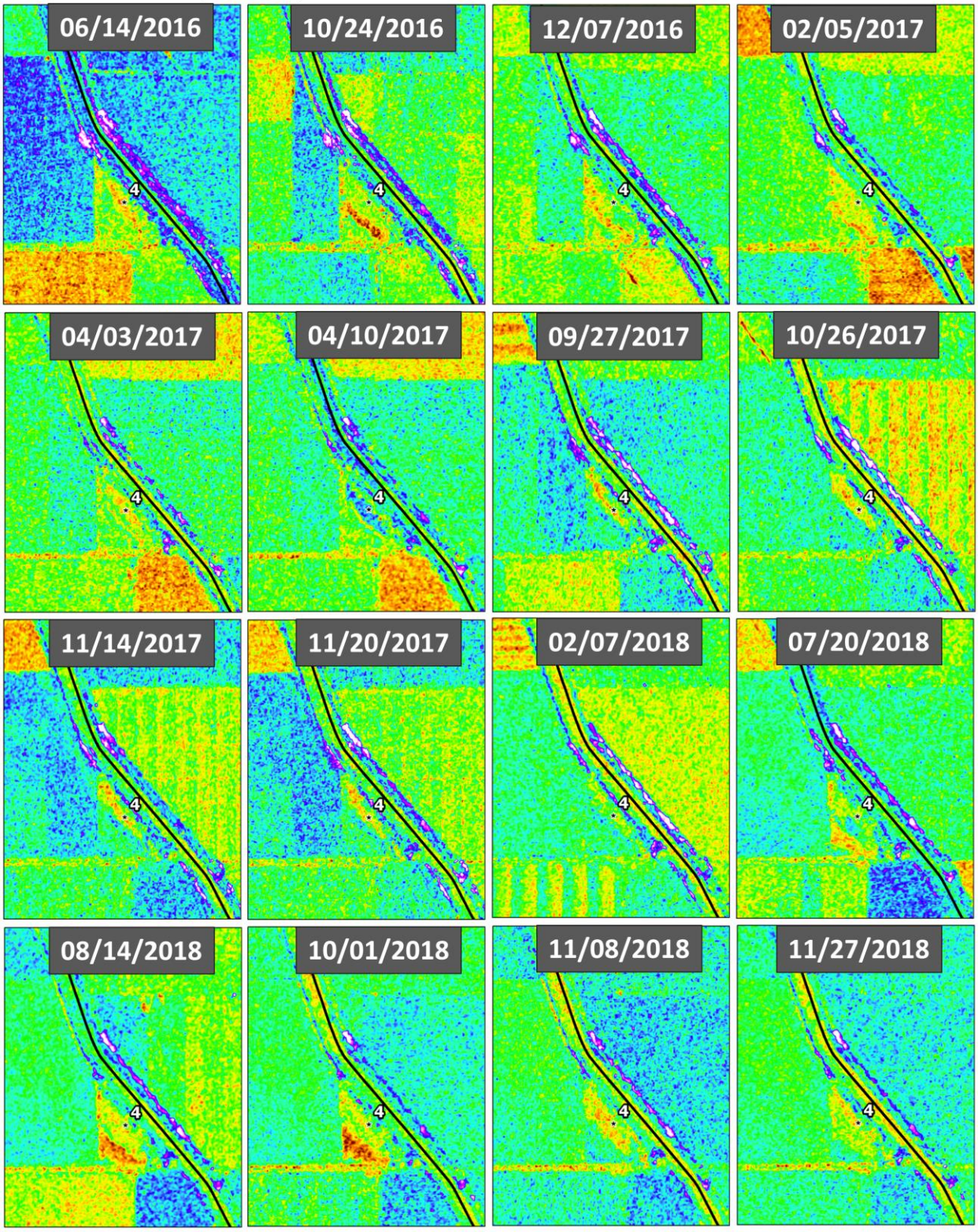

Figure 20A: Seep 4 – VV/HH Ratio

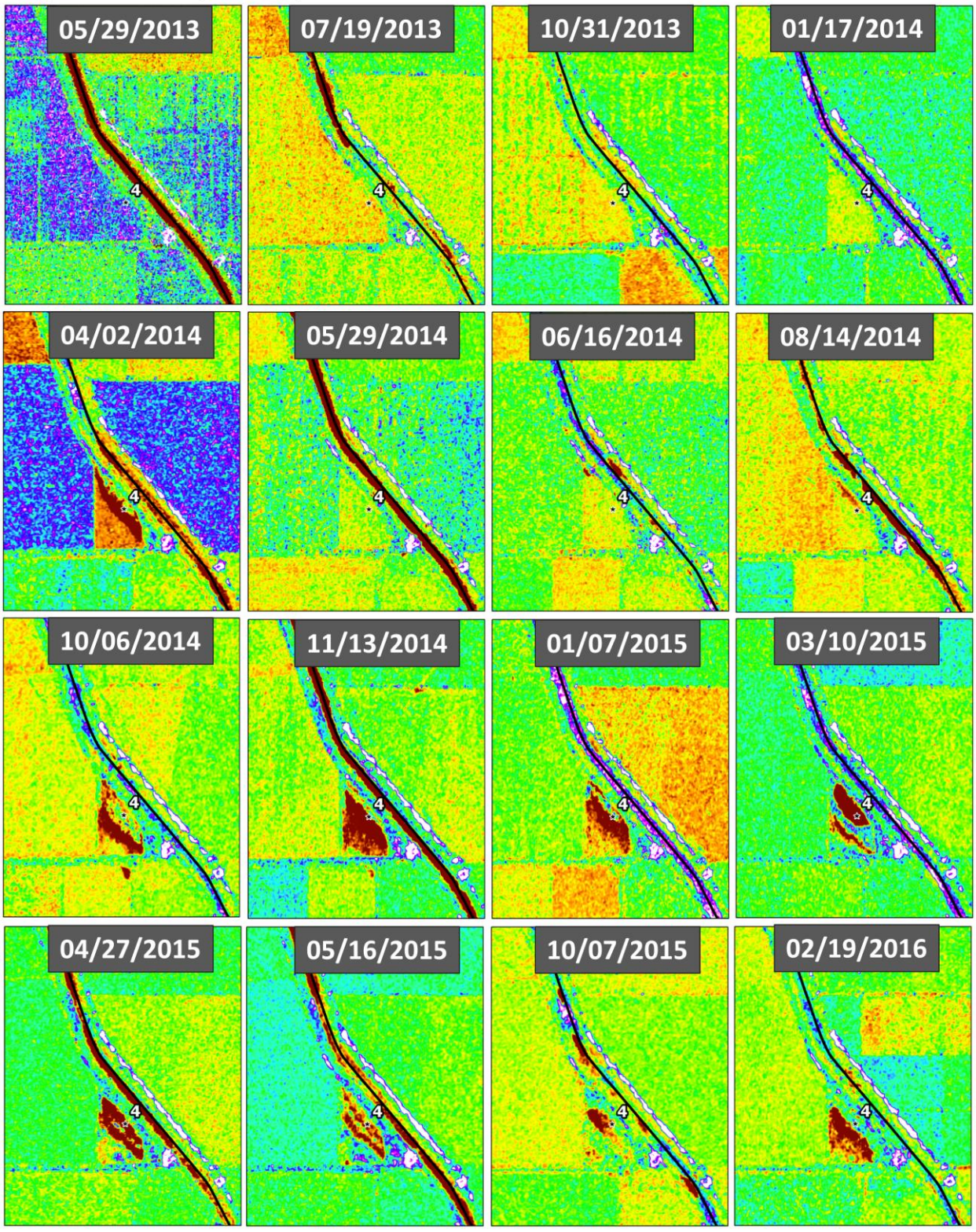

Figure 20B: Seep 4 – VV/HH Ratio

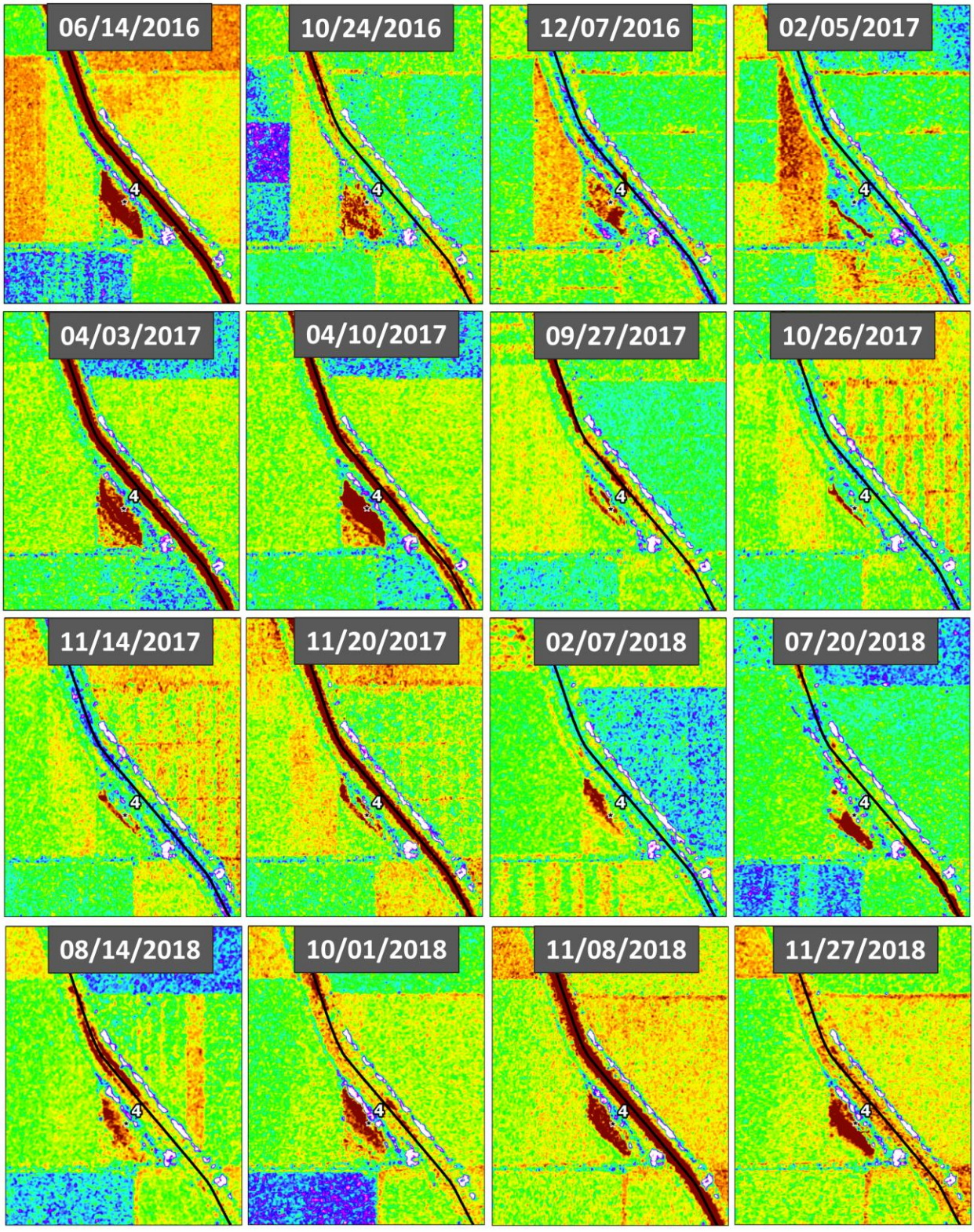

Figure 21A: Seep 4 – Copolarization Phase

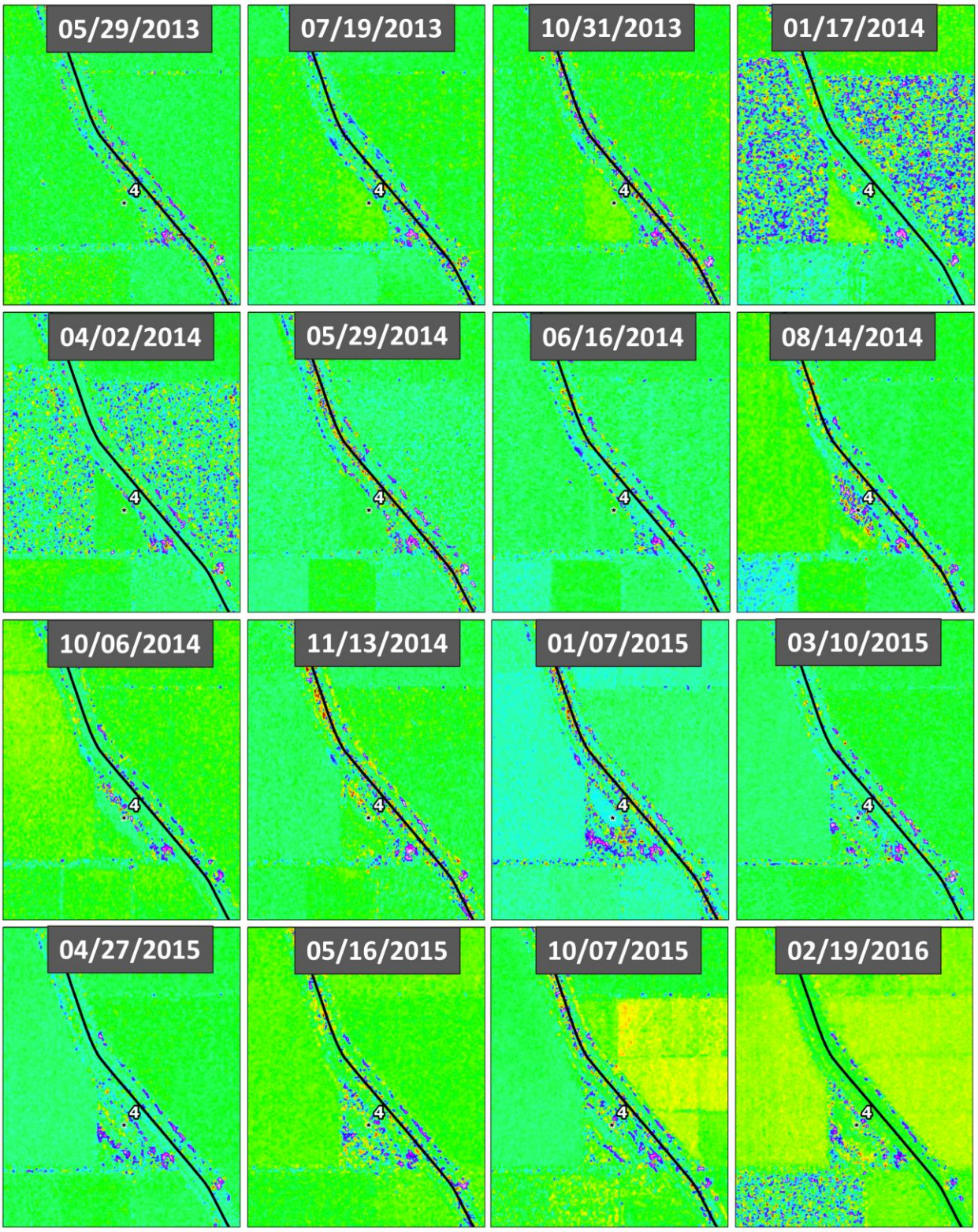

Figure 21B: Seep 4 – Copolarization Phase

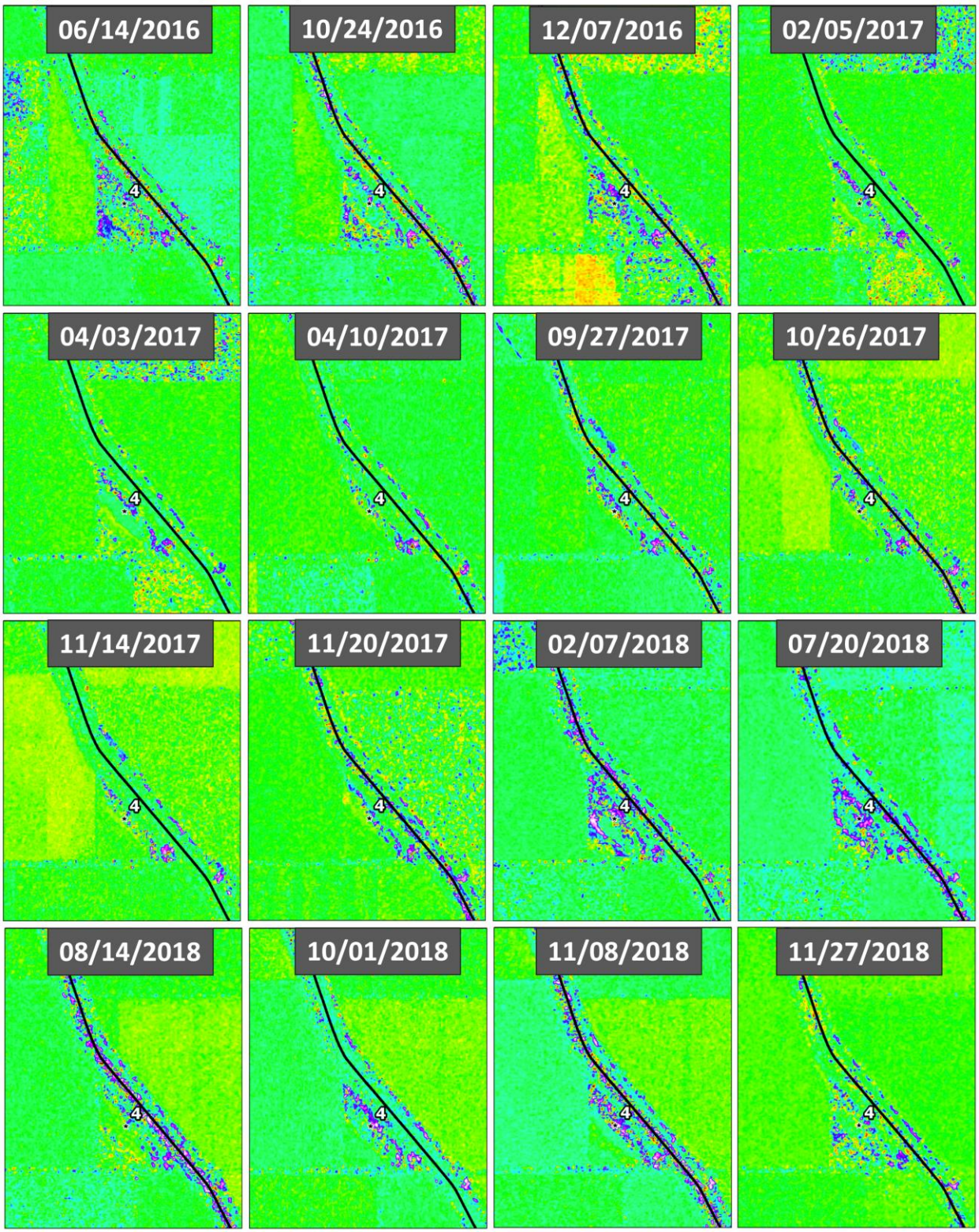

Figure 22A: Seep 4 – Entropy

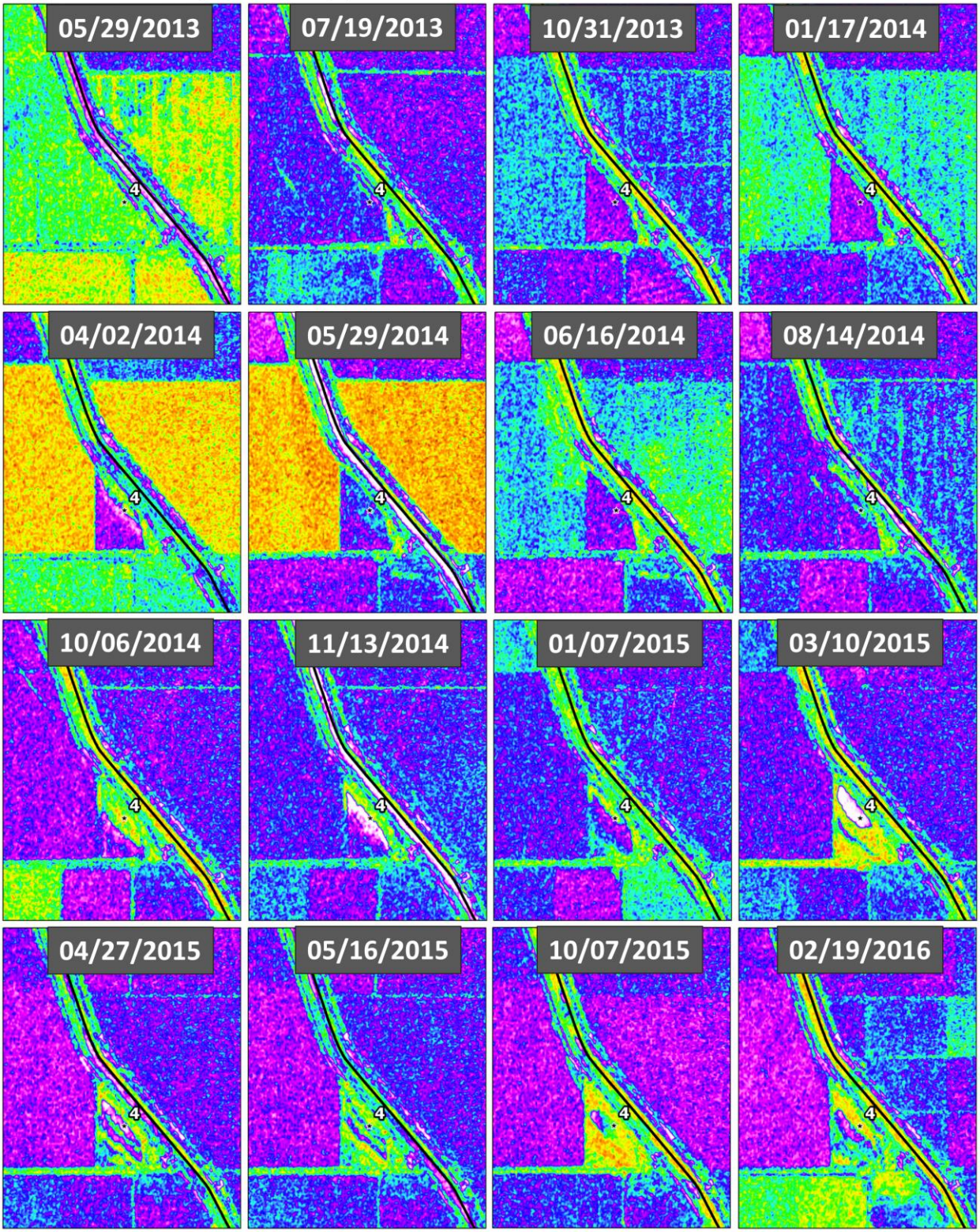

Figure 22B: Seep 4 – Entropy

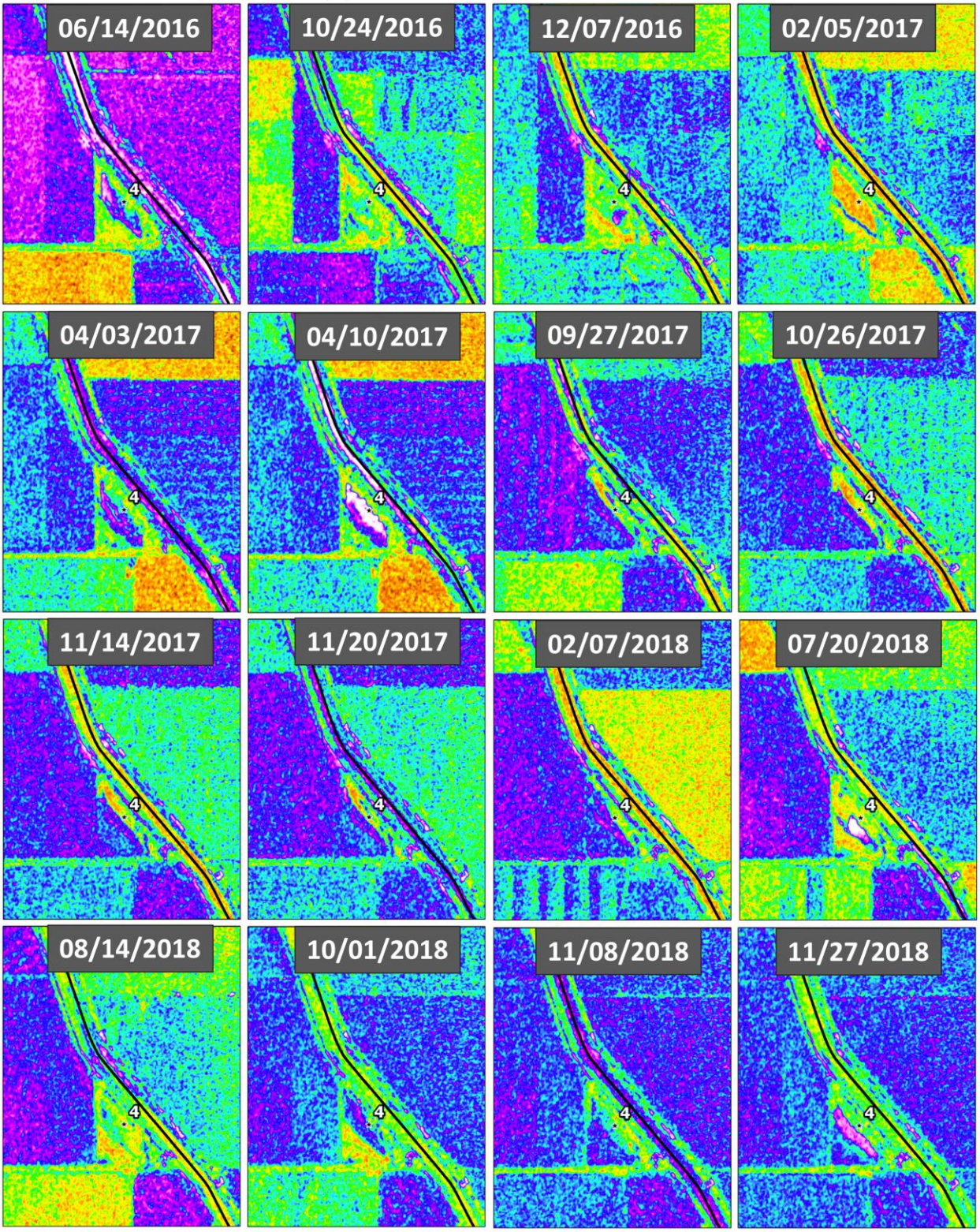

Figure 23A: Seep 4 – Anisotropy

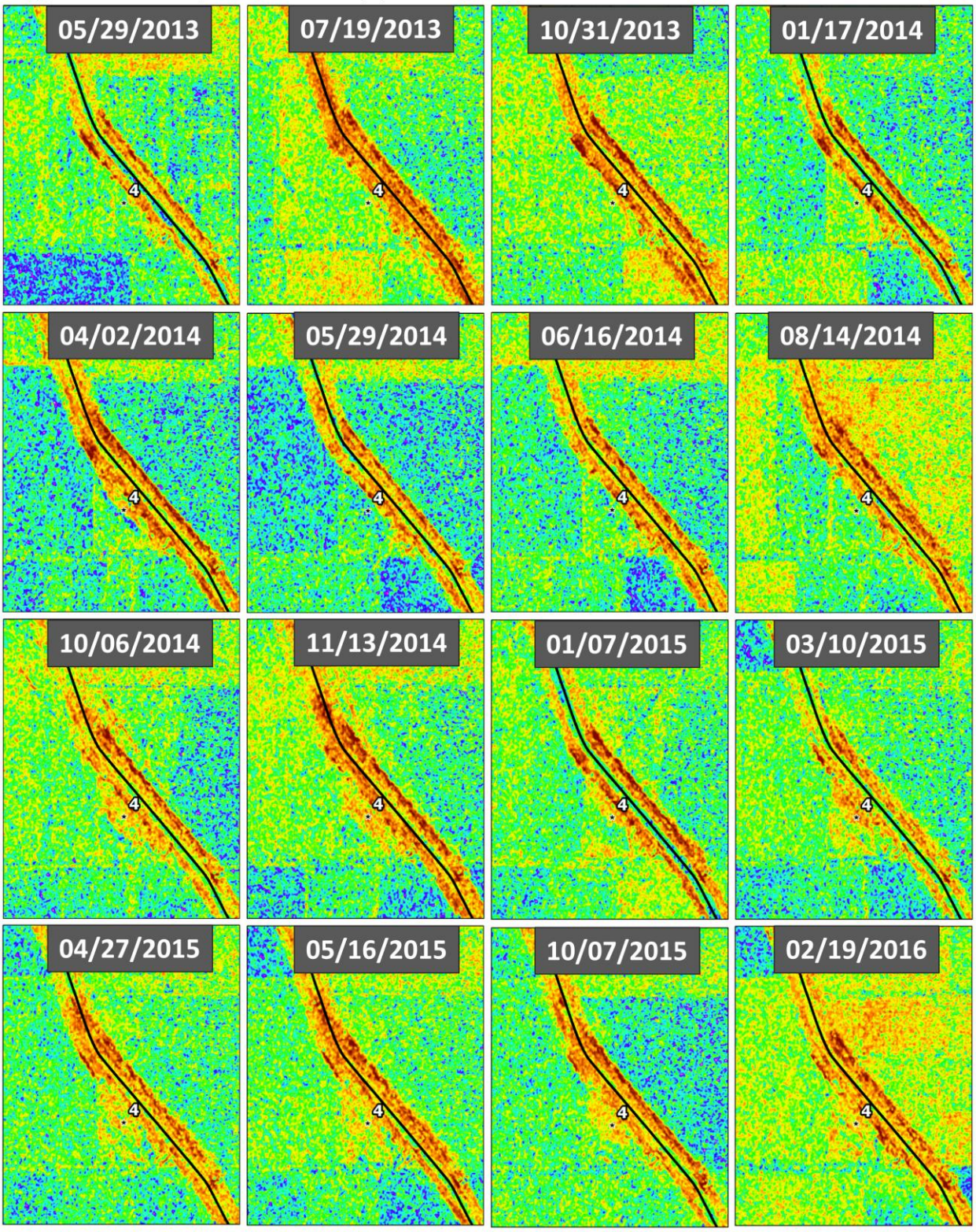

Figure 23B: Seep 4 – Anisotropy

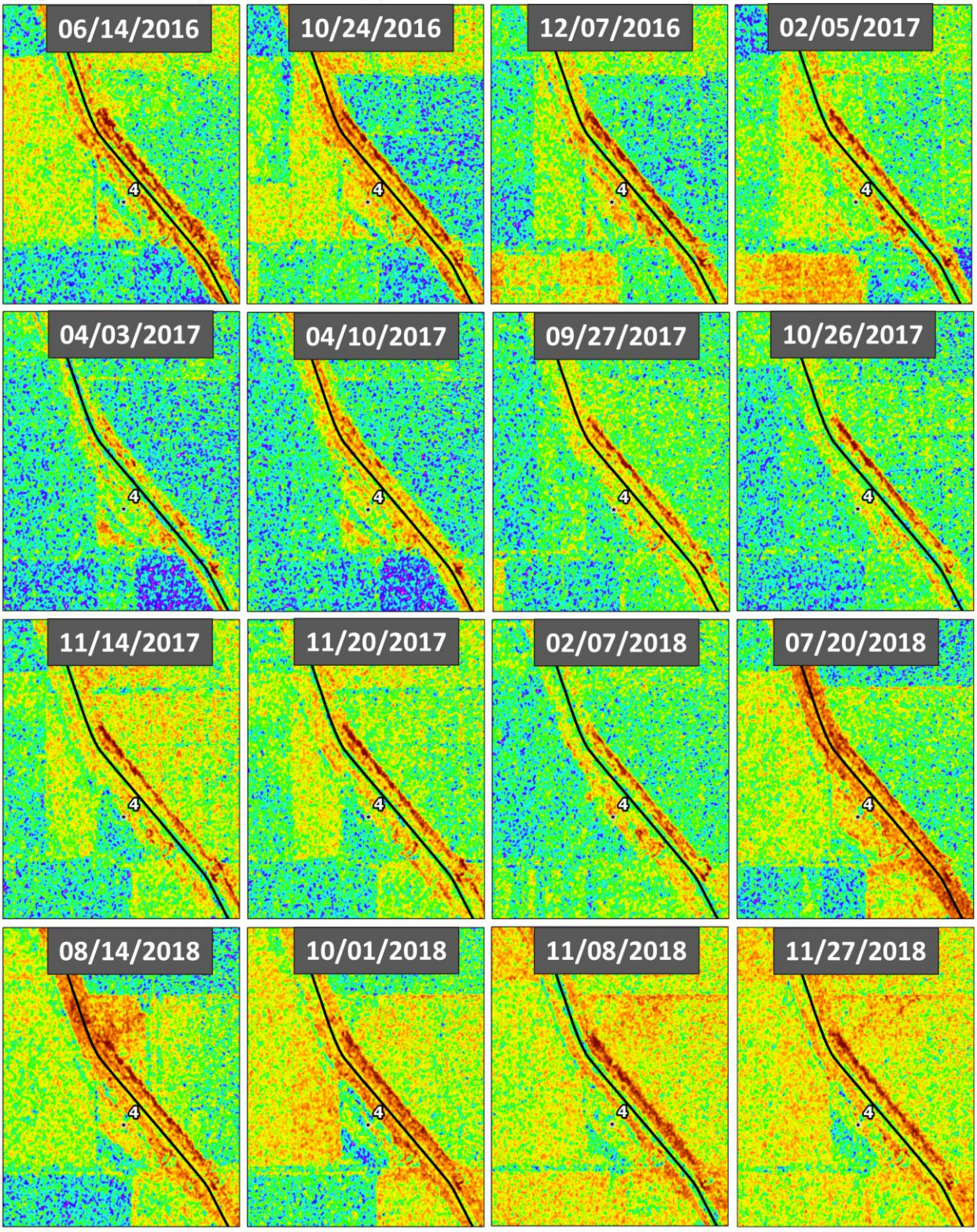

Figure 24A: Seep 4 – Mean Alpha Angle

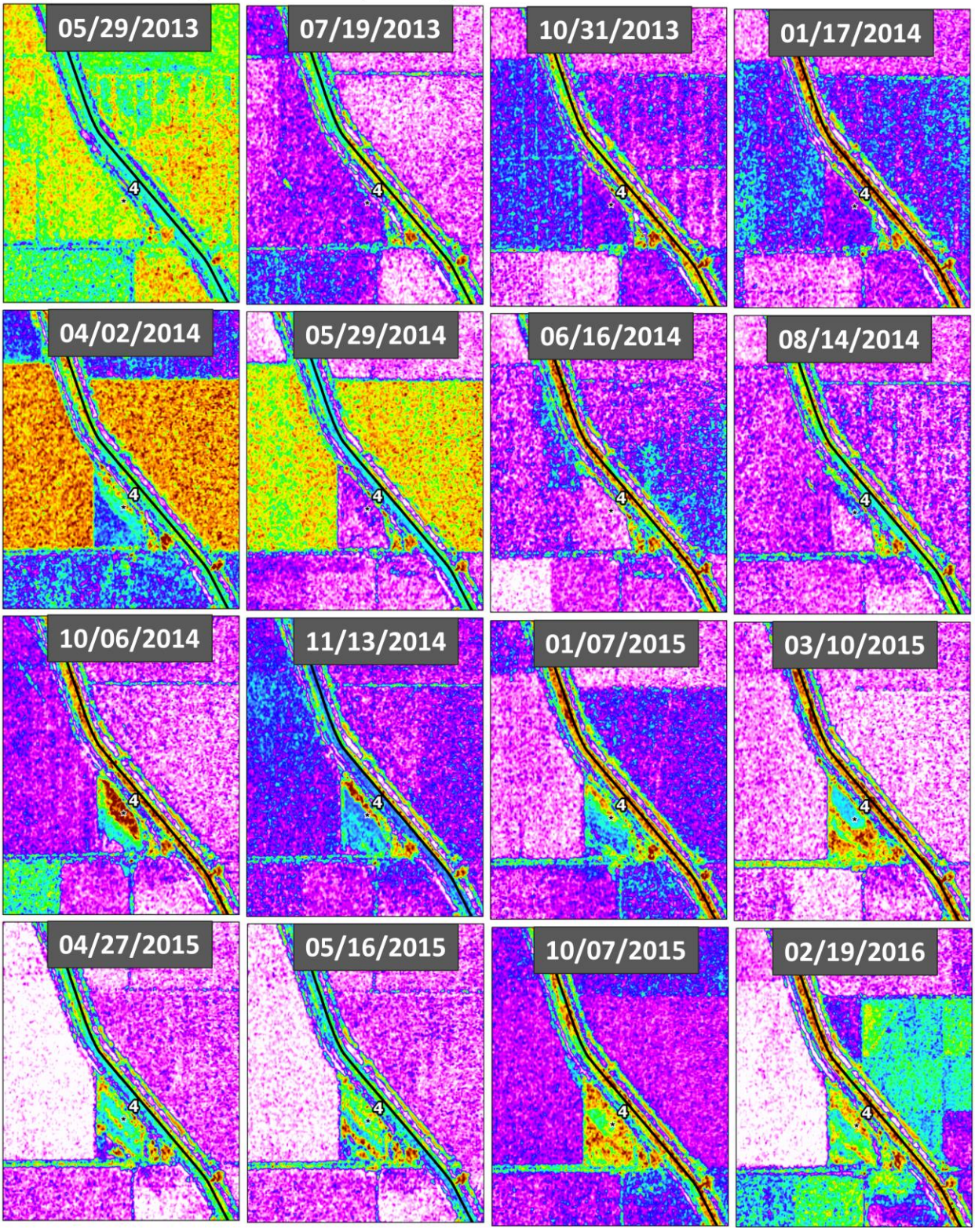

Figure 24B: Seep 4 – Mean Alpha Angle

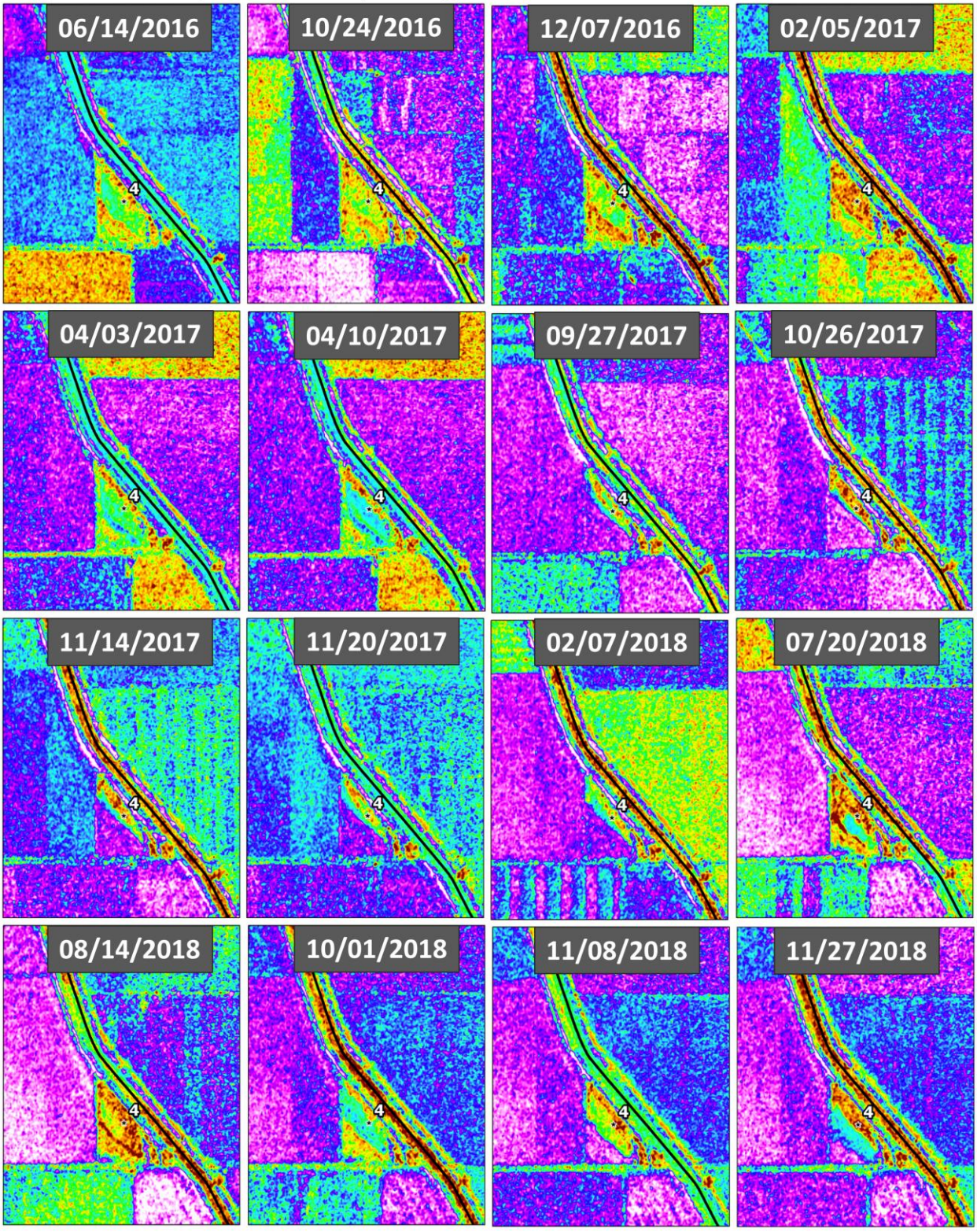

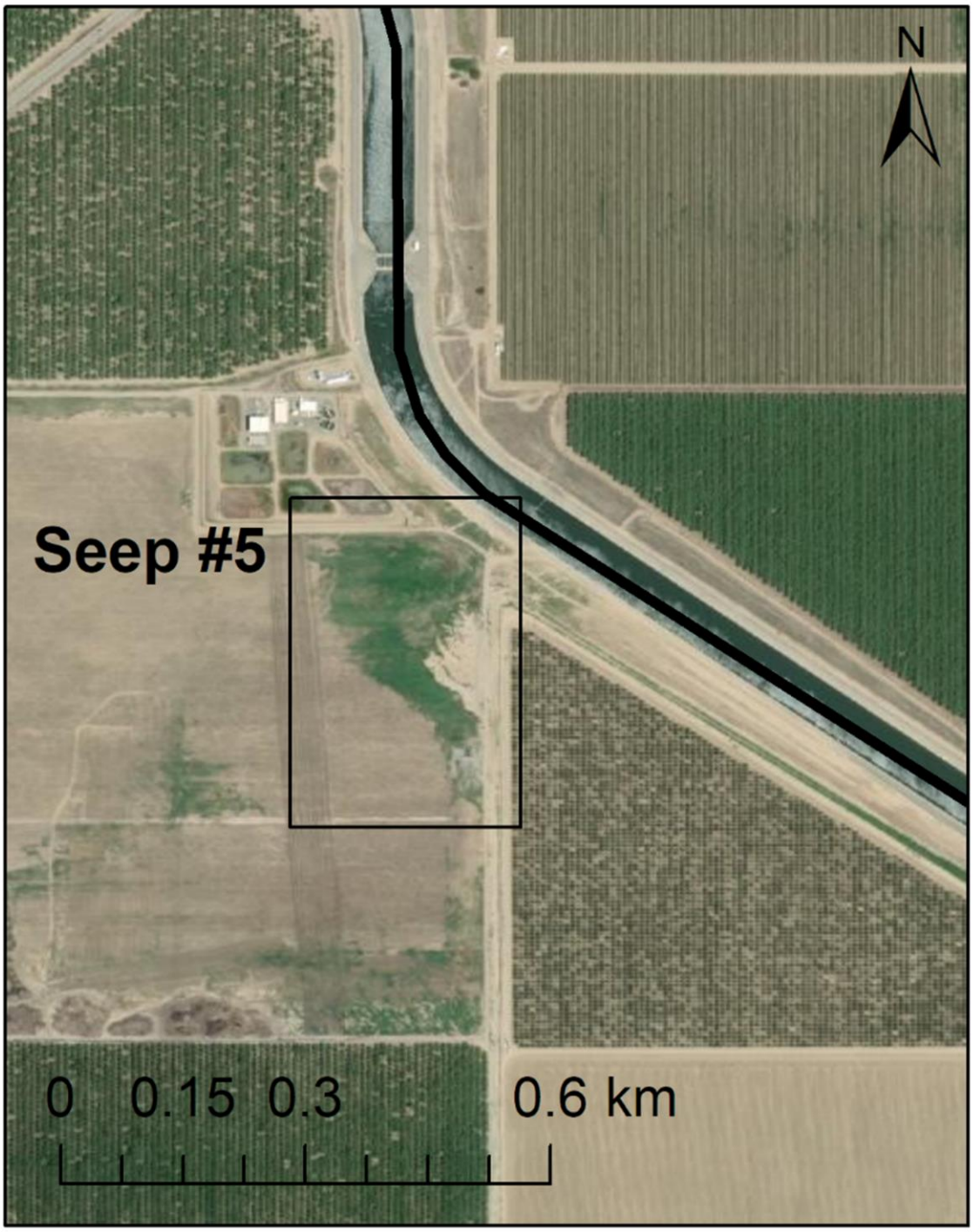

Figure 25: Study area overview for Seep 5 along the California Aqueduct.

Figure 26A: Seep 5 – Google Earth Imagery

Figure 26B: Seep 5– Google Earth Imagery

Figure 26C: Seep 5– Google Earth Imagery

Figure 27: Legends for NDWI and PolSAR data products.

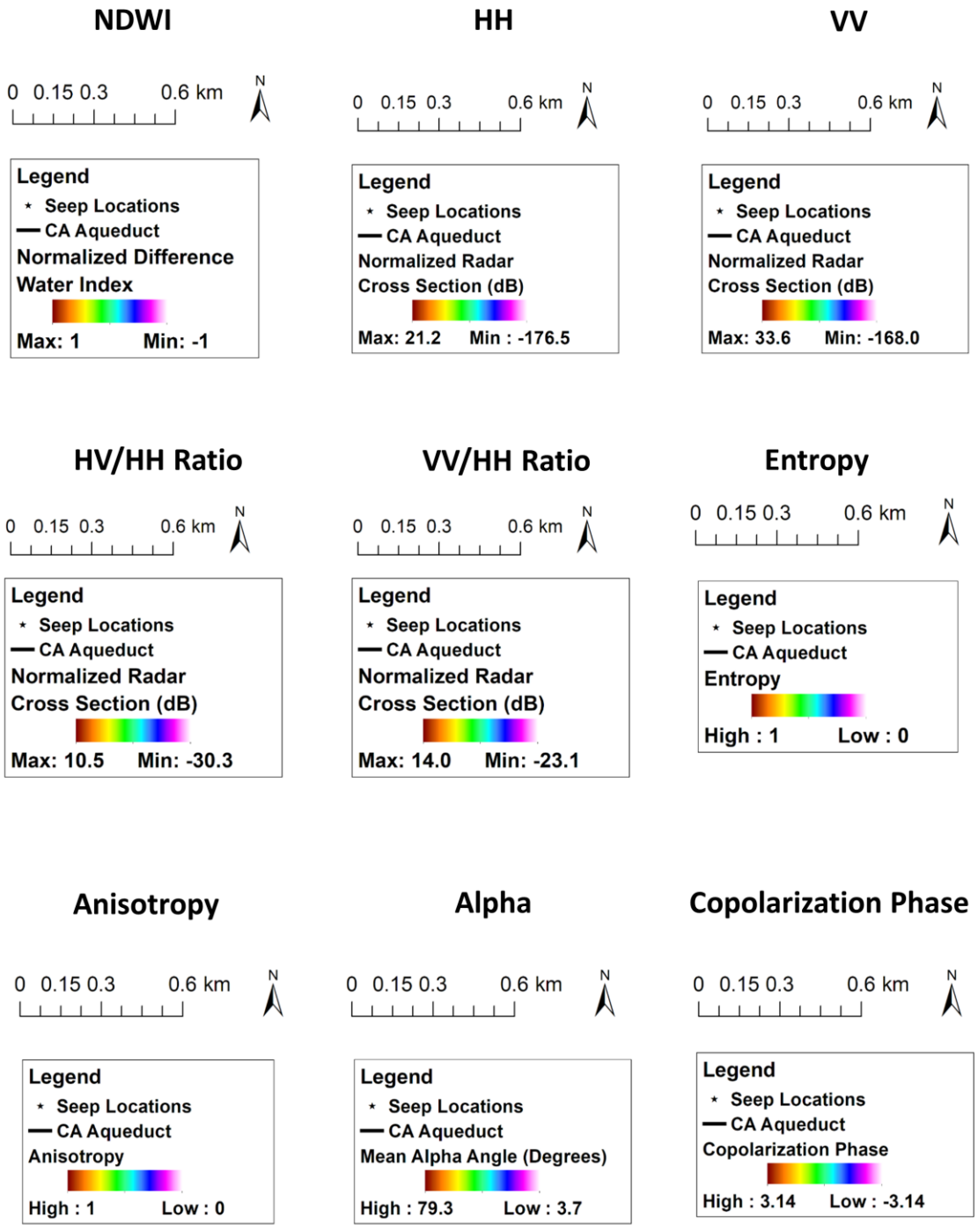

Figure 28A: Seep 5– NDWI

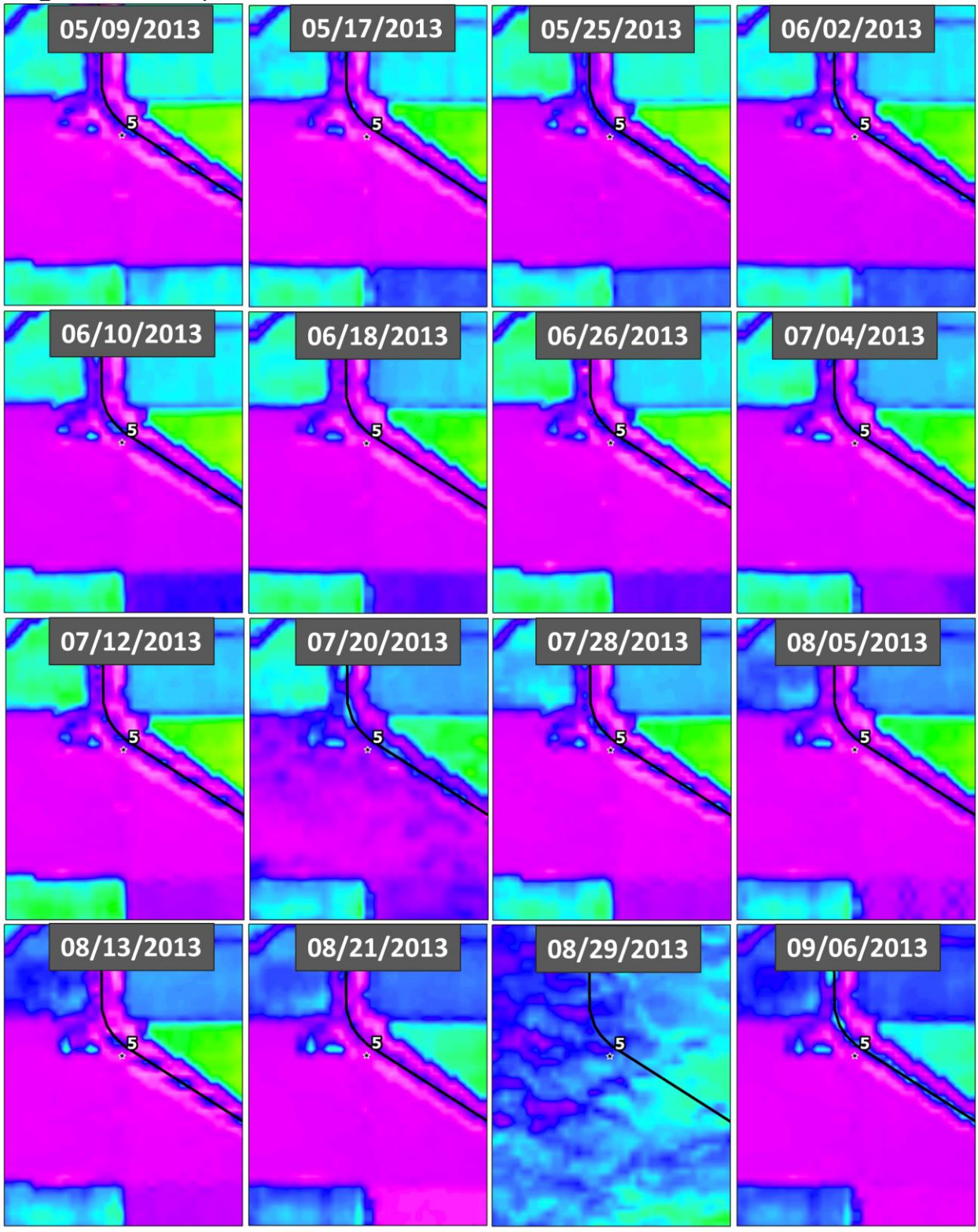

Figure 28B: Seep 5– NDWI

Figure 28C: Seep 5– NDWI

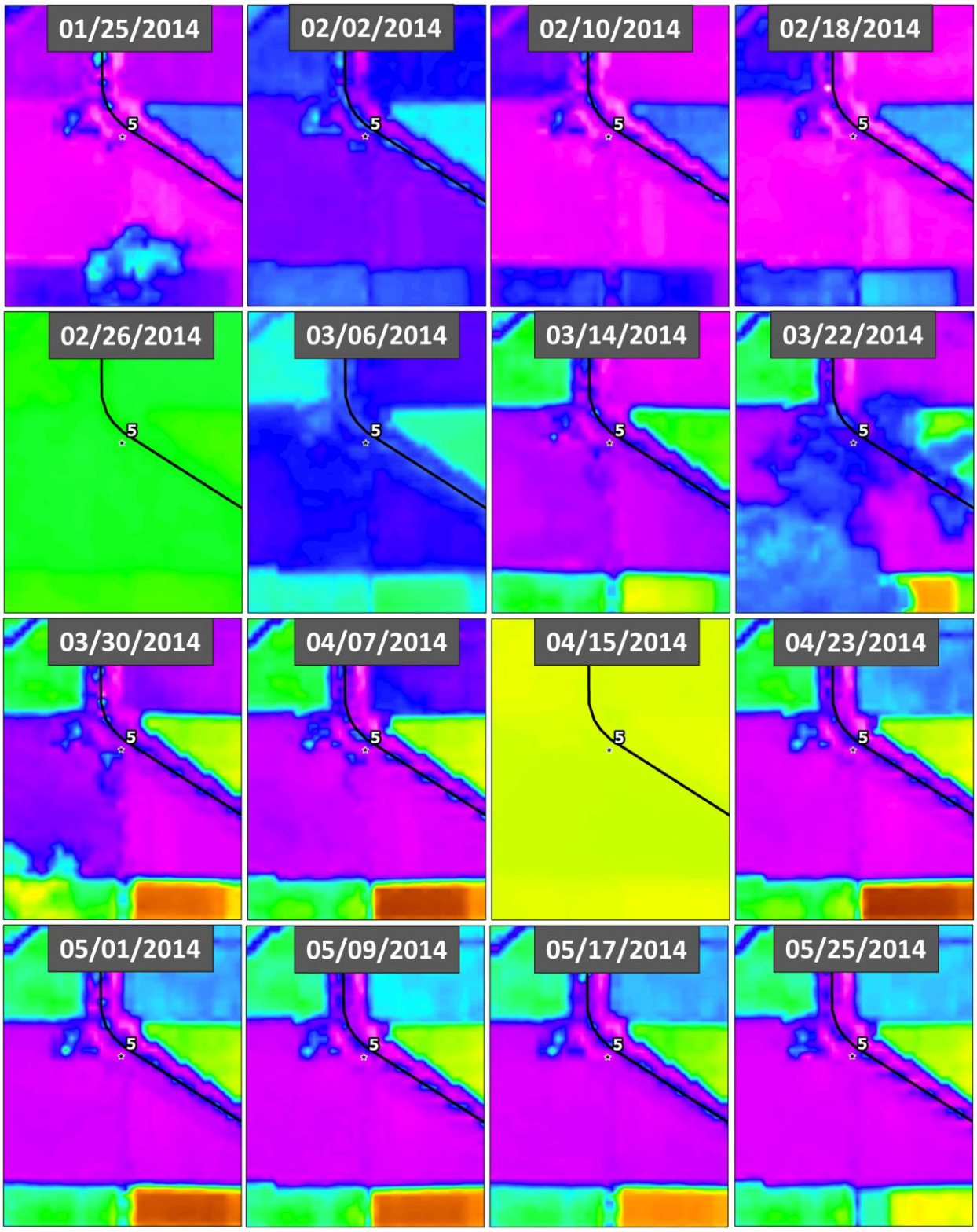

Figure 28D: Seep 5– NDWI

Figure 28E: Seep 5– NDWI

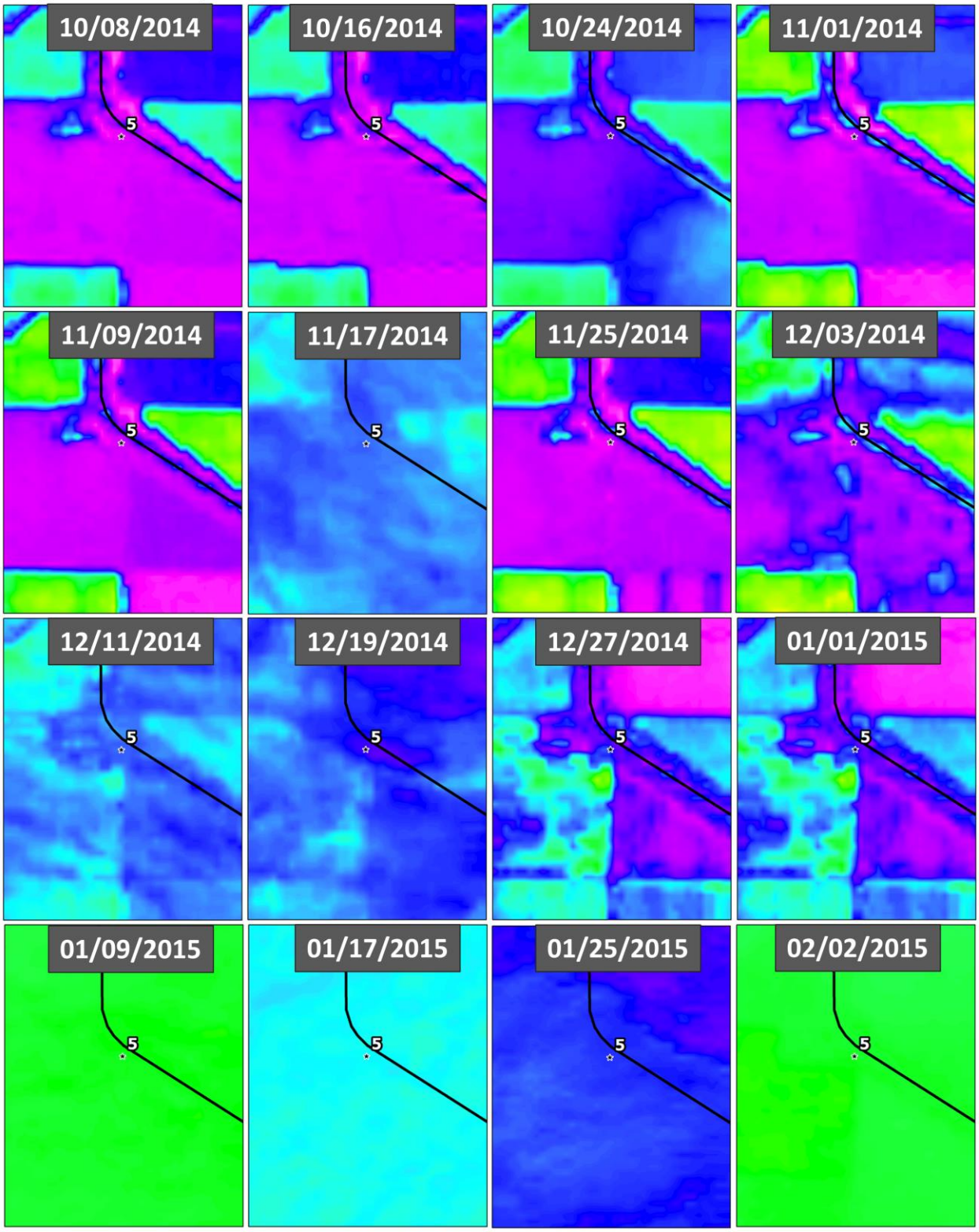

Figure 28F: Seep 5– NDWI

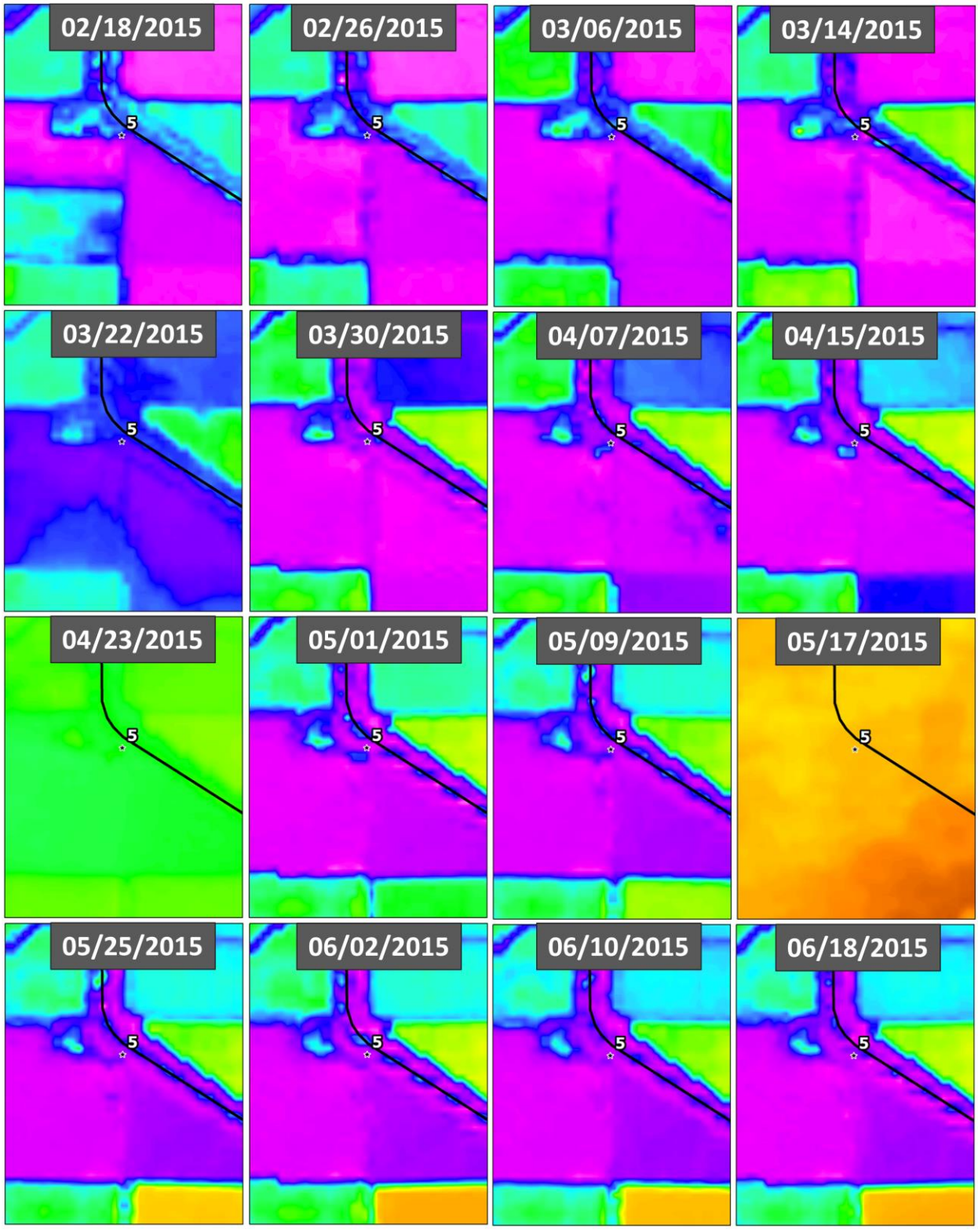

Figure 28G: Seep 5– NDWI

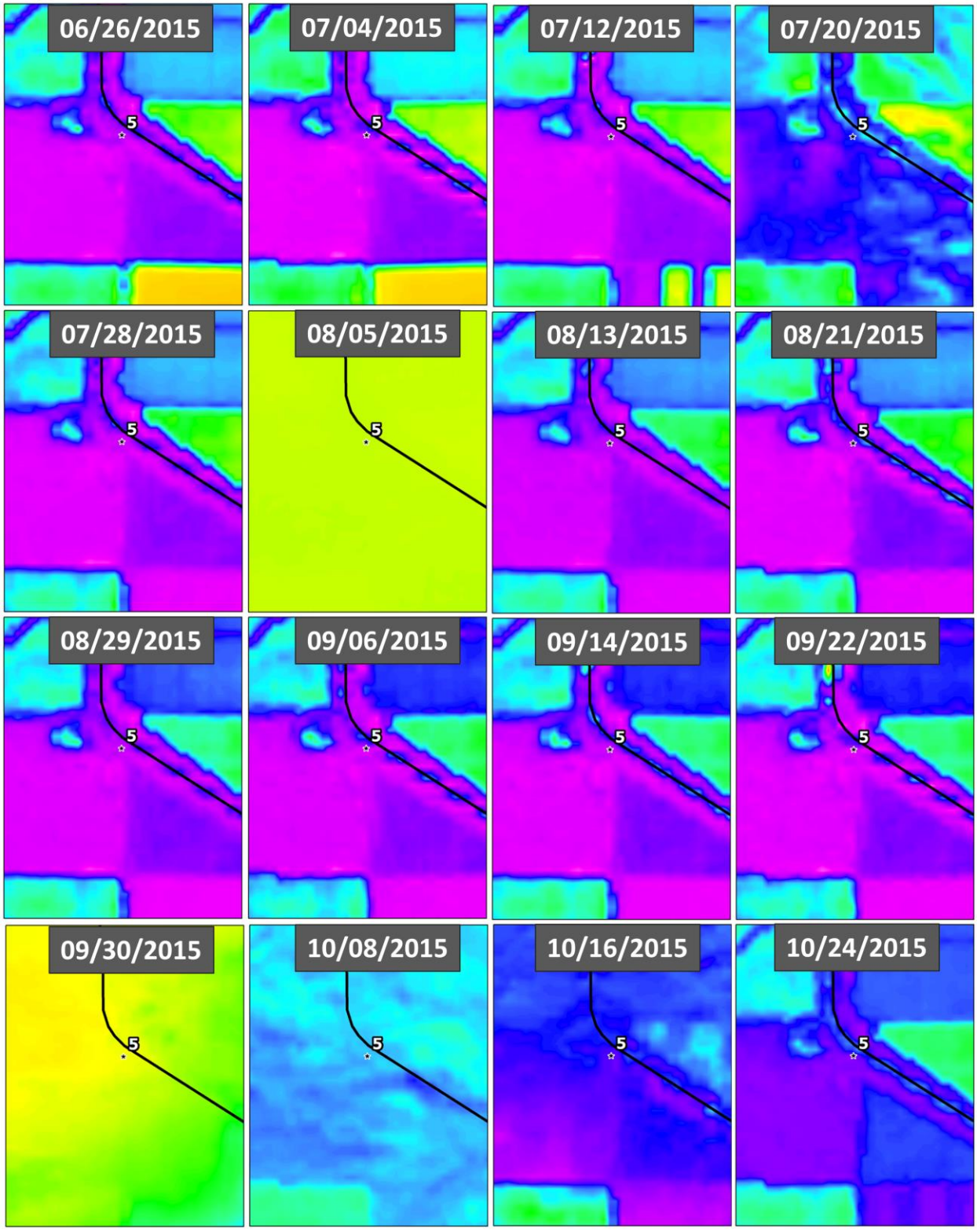

Figure 28H: Seep 5– NDWI

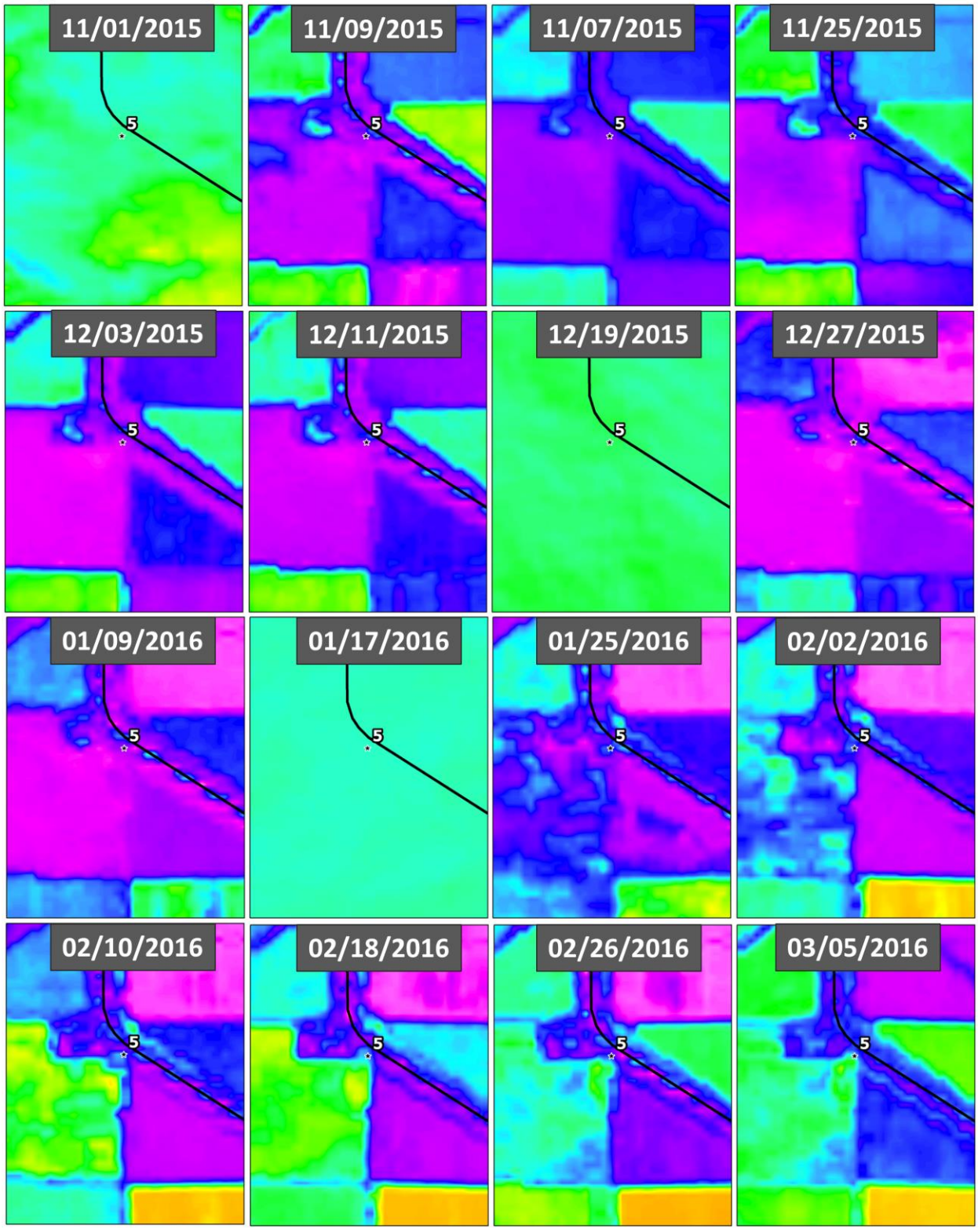

Figure 28I: Seep 5– NDWI

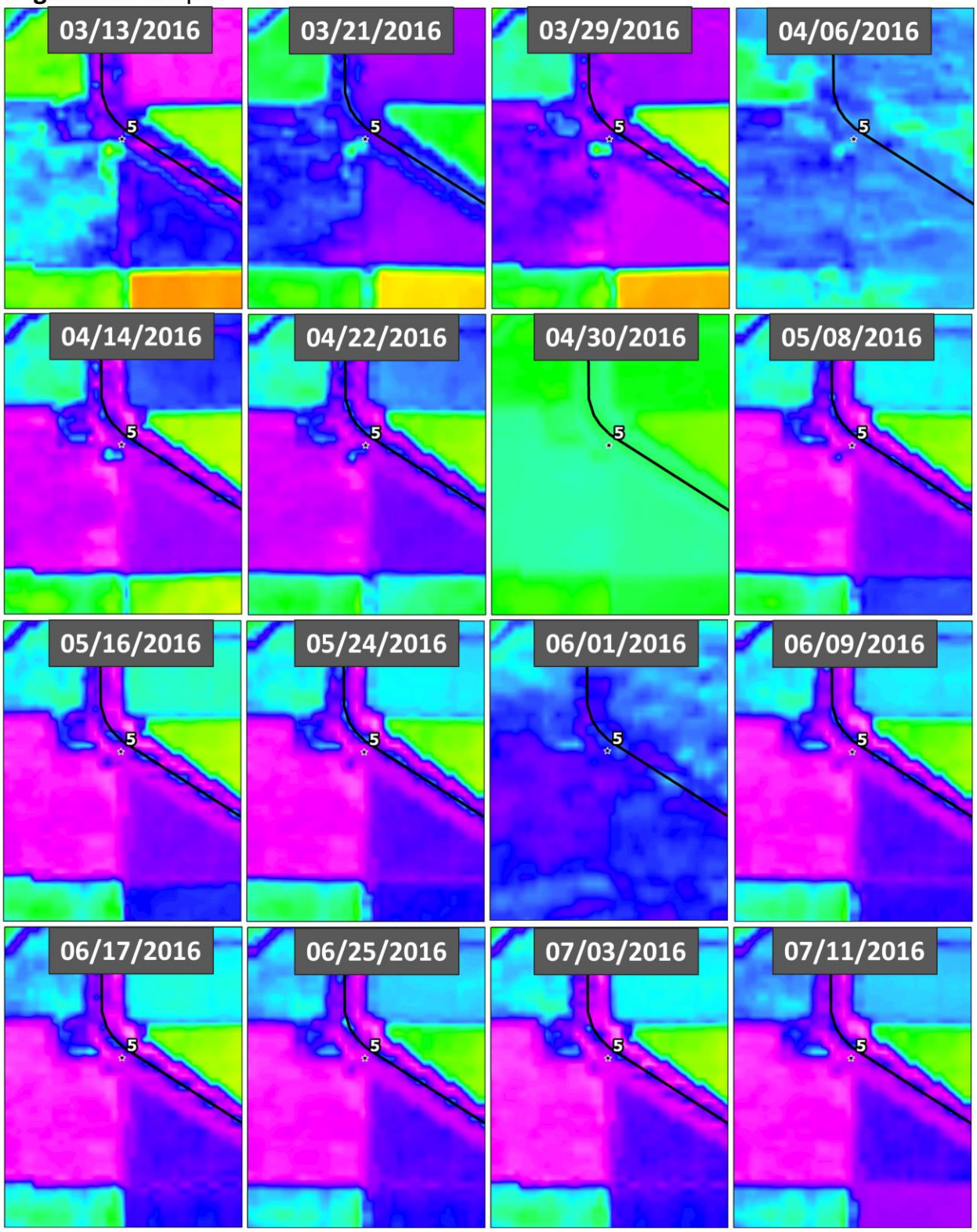

Figure 28J: Seep 5– NDWI

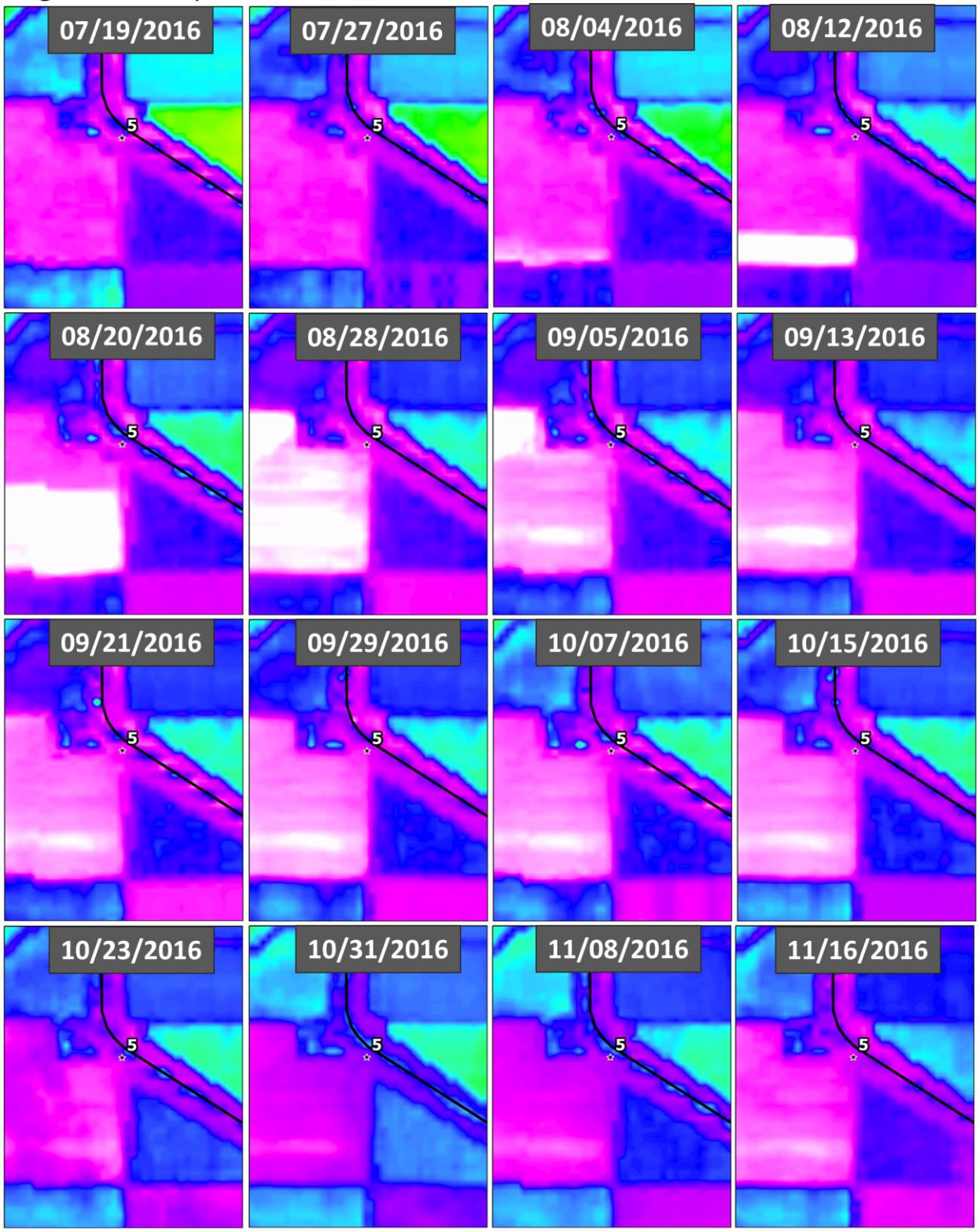

Figure 28K: Seep 5– NDWI

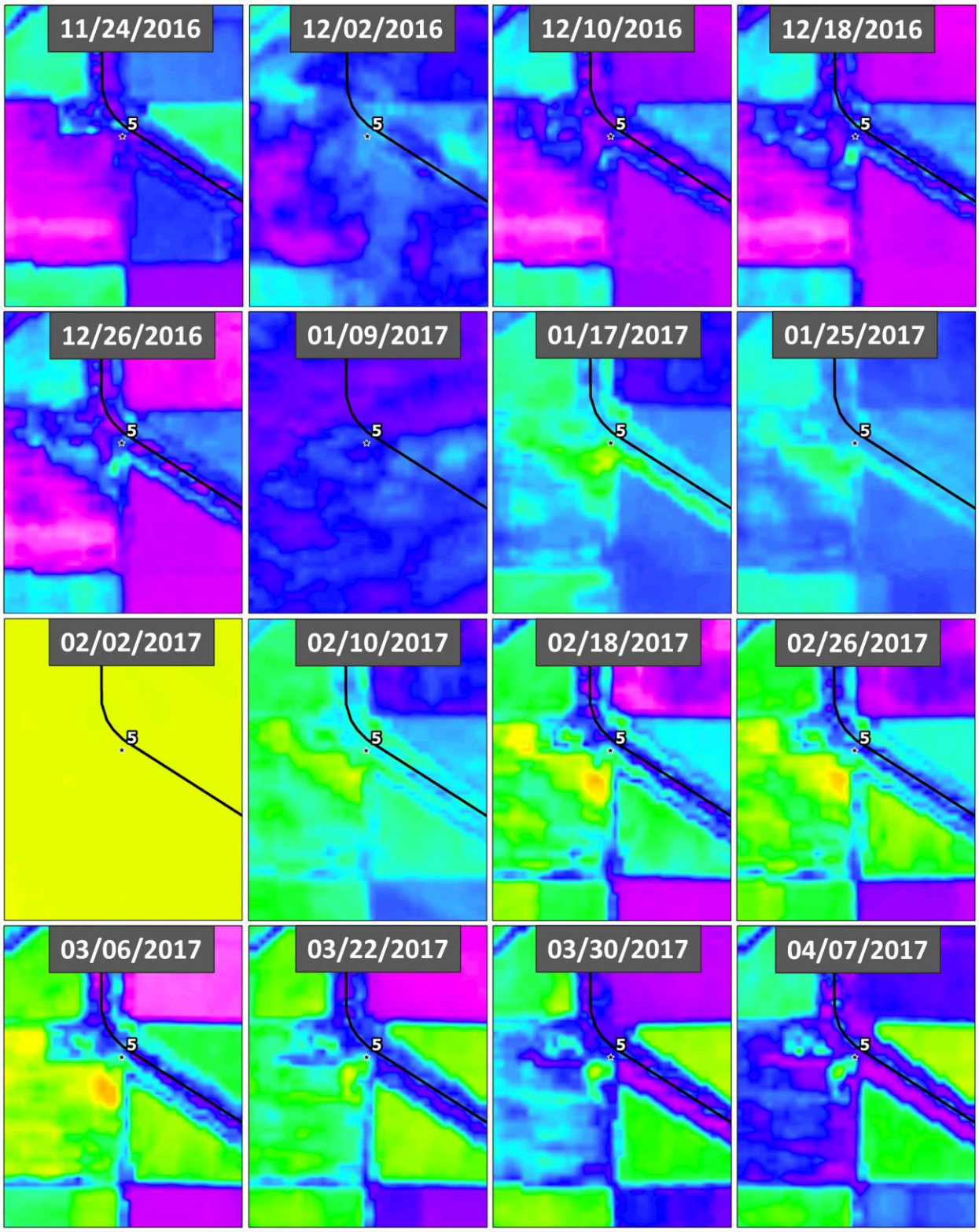

Figure 28L: Seep 5– NDWI

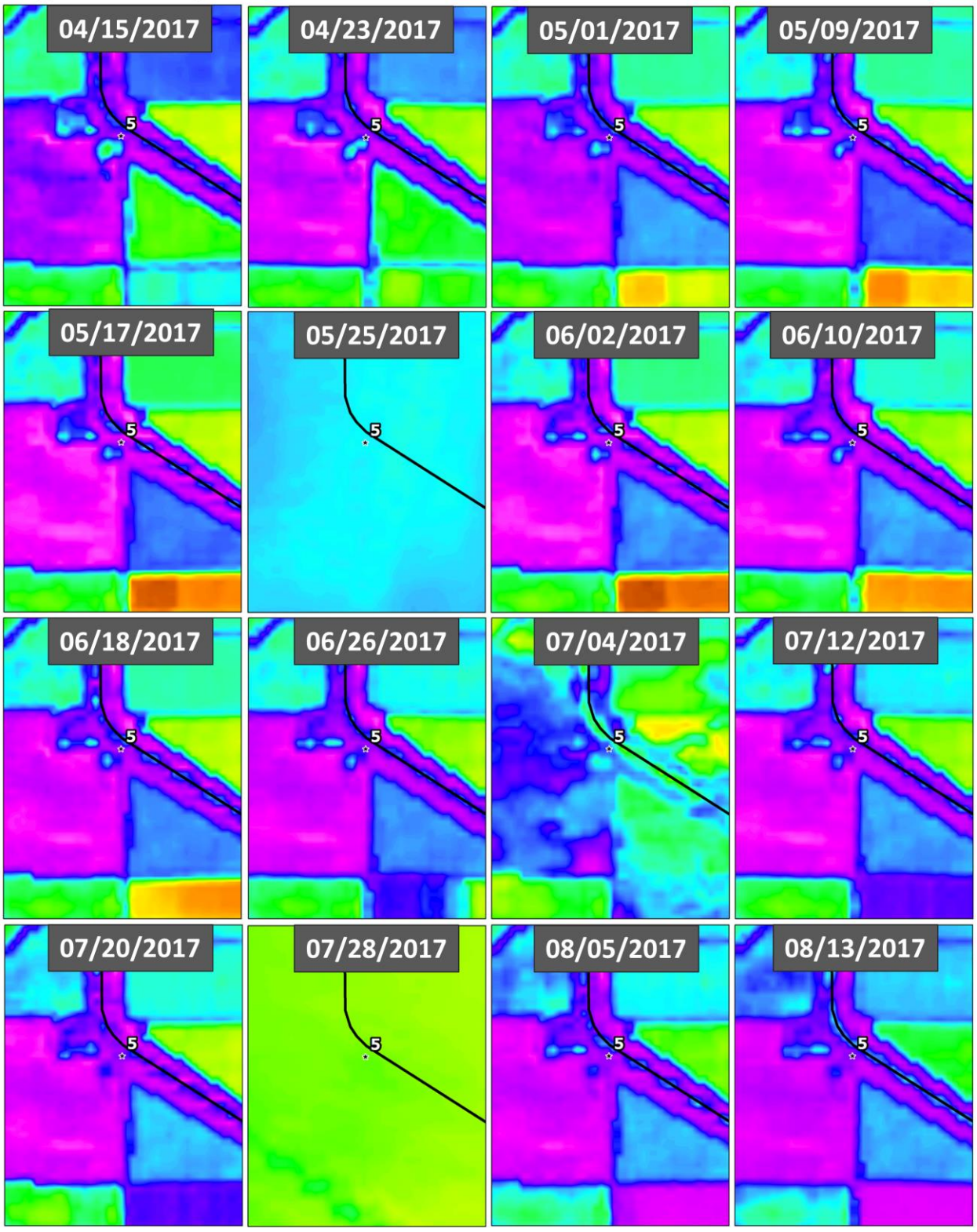

Figure 28M: Seep 5– NDWI

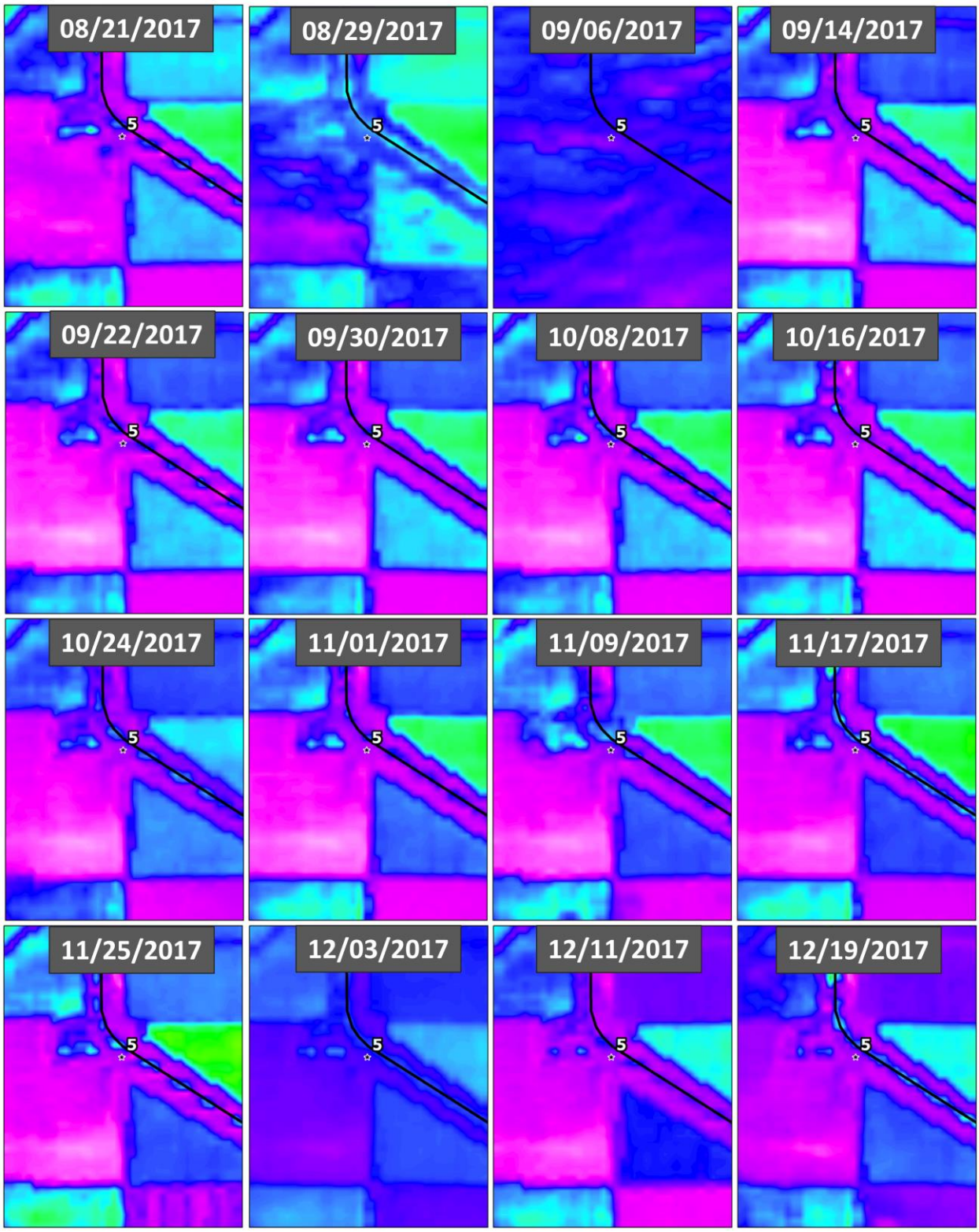

Figure 28N: Seep 5– NDWI

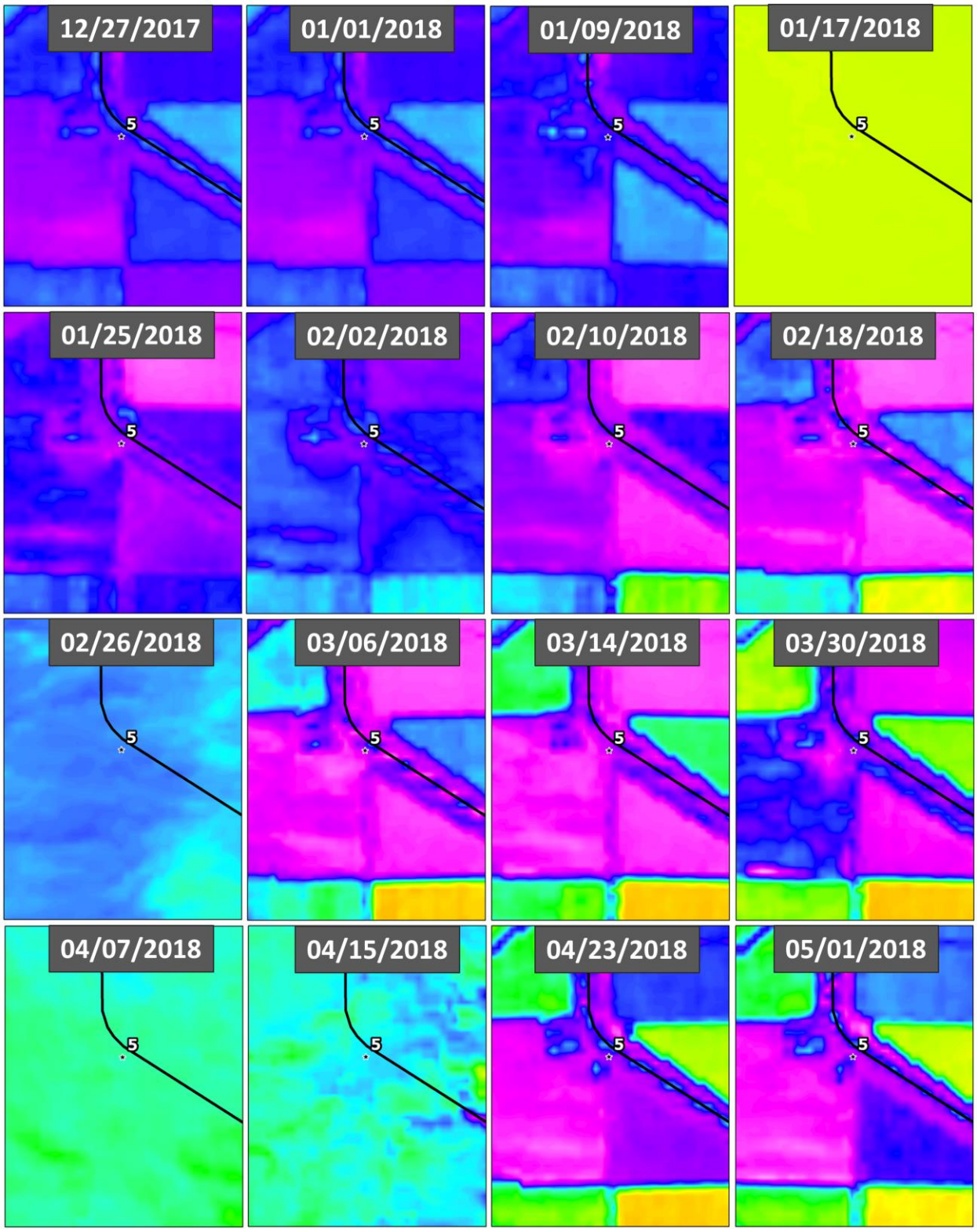

Figure 28O: Seep 5– NDWI

Figure 28P: Seep 5– NDWI

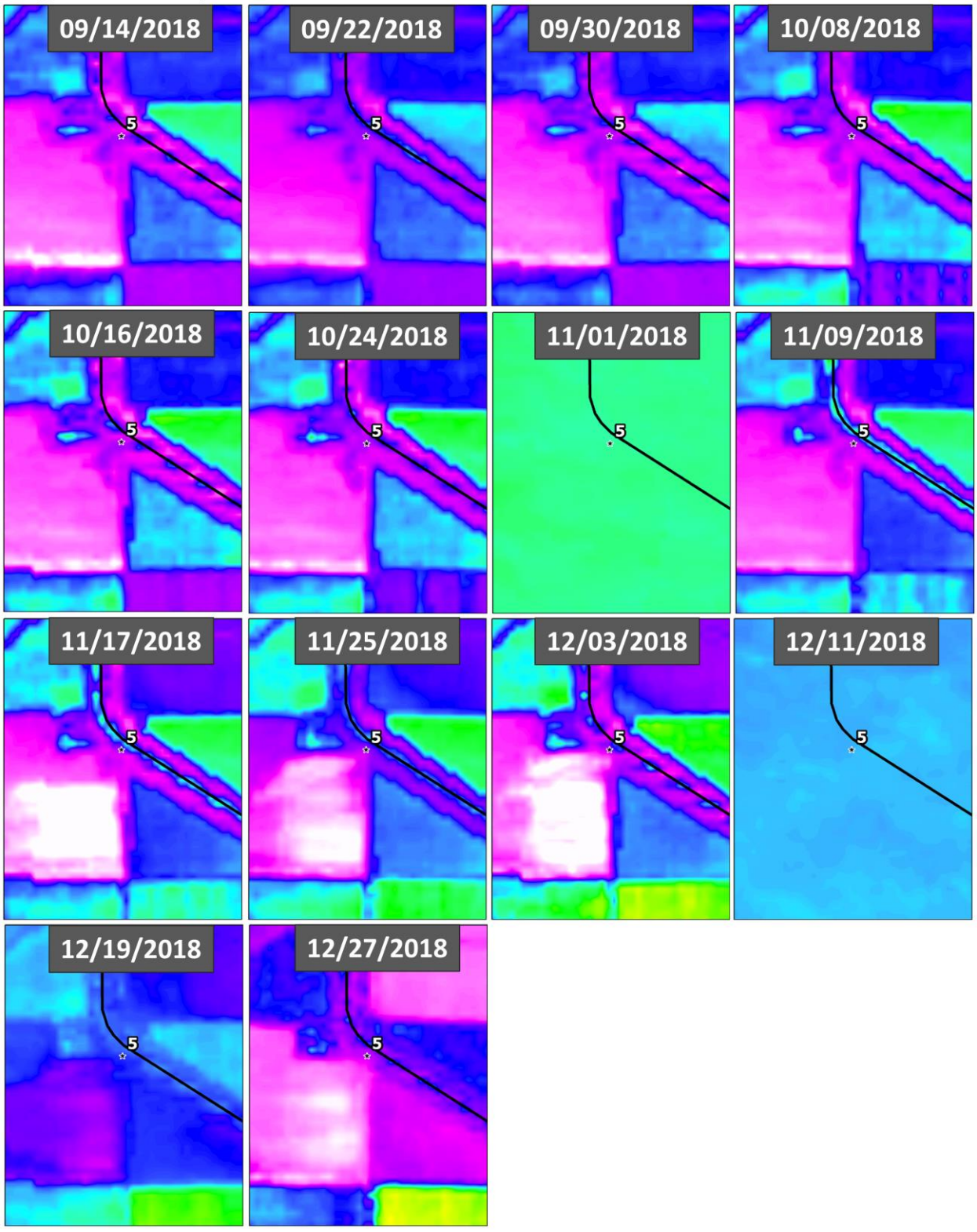

Figure 29A: Seep 5 – HH Single Polarization

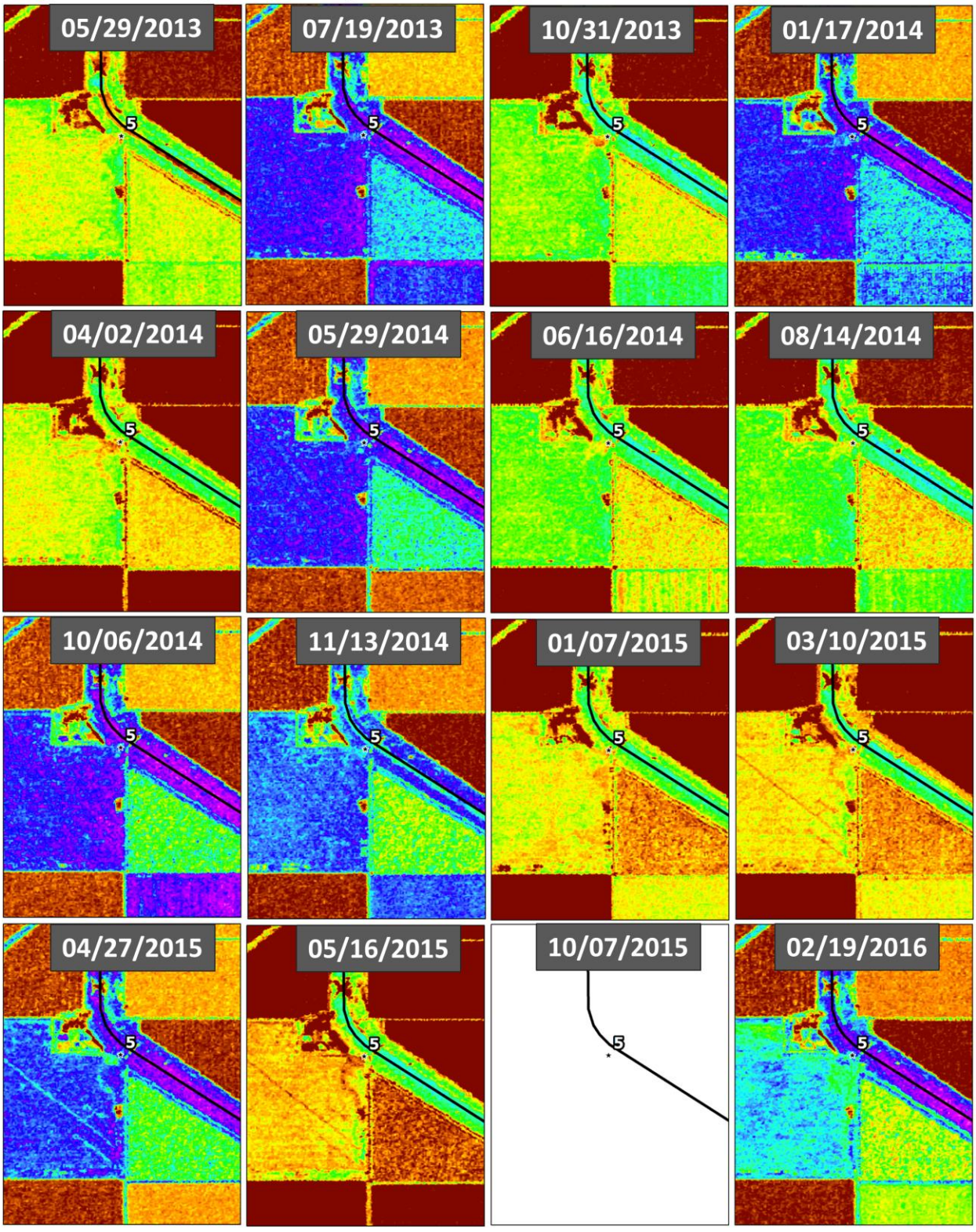

Figure 29B: Seep 5 – HH Single Polarization

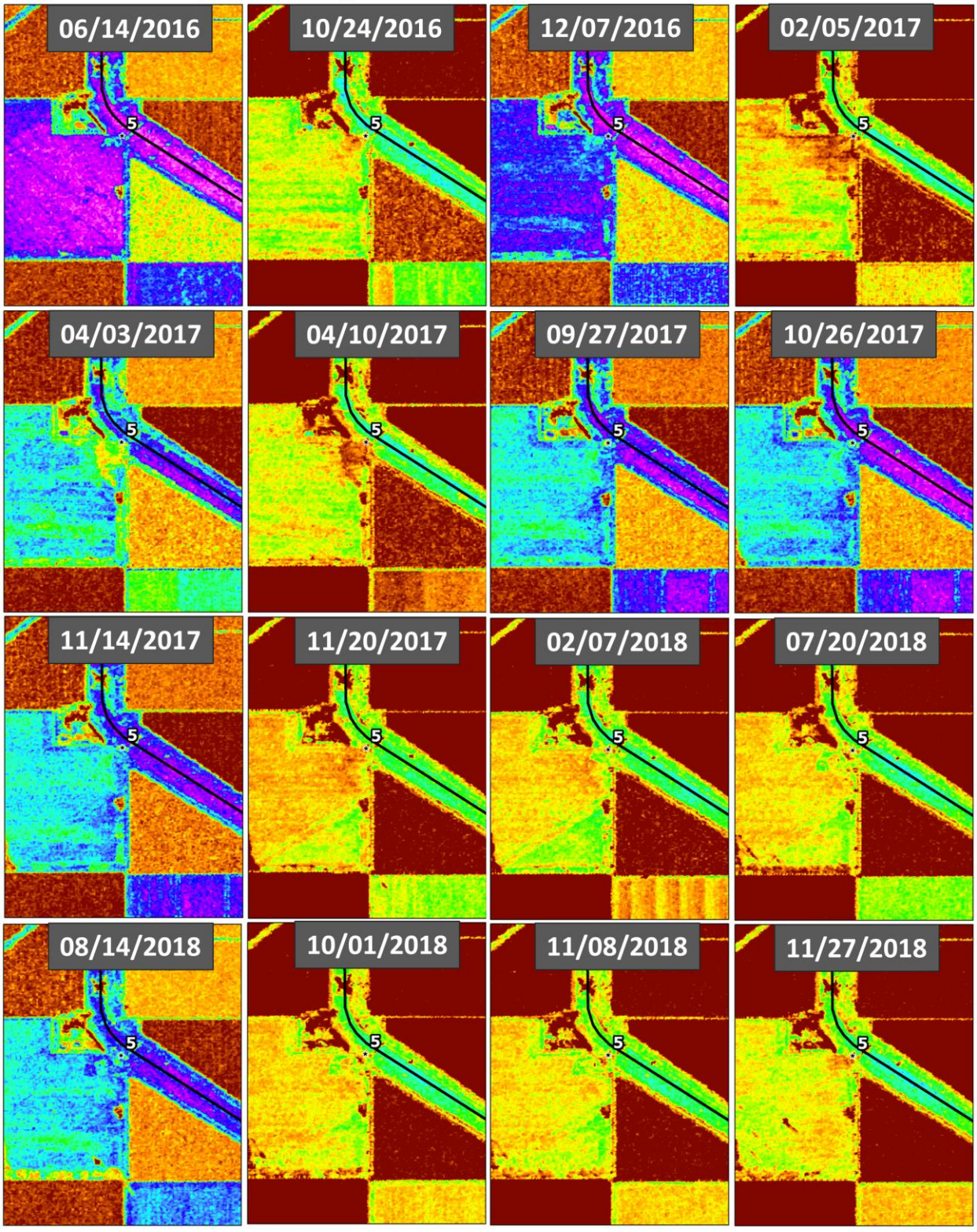

Figure 30A: Seep 5 – VV Single Polarization

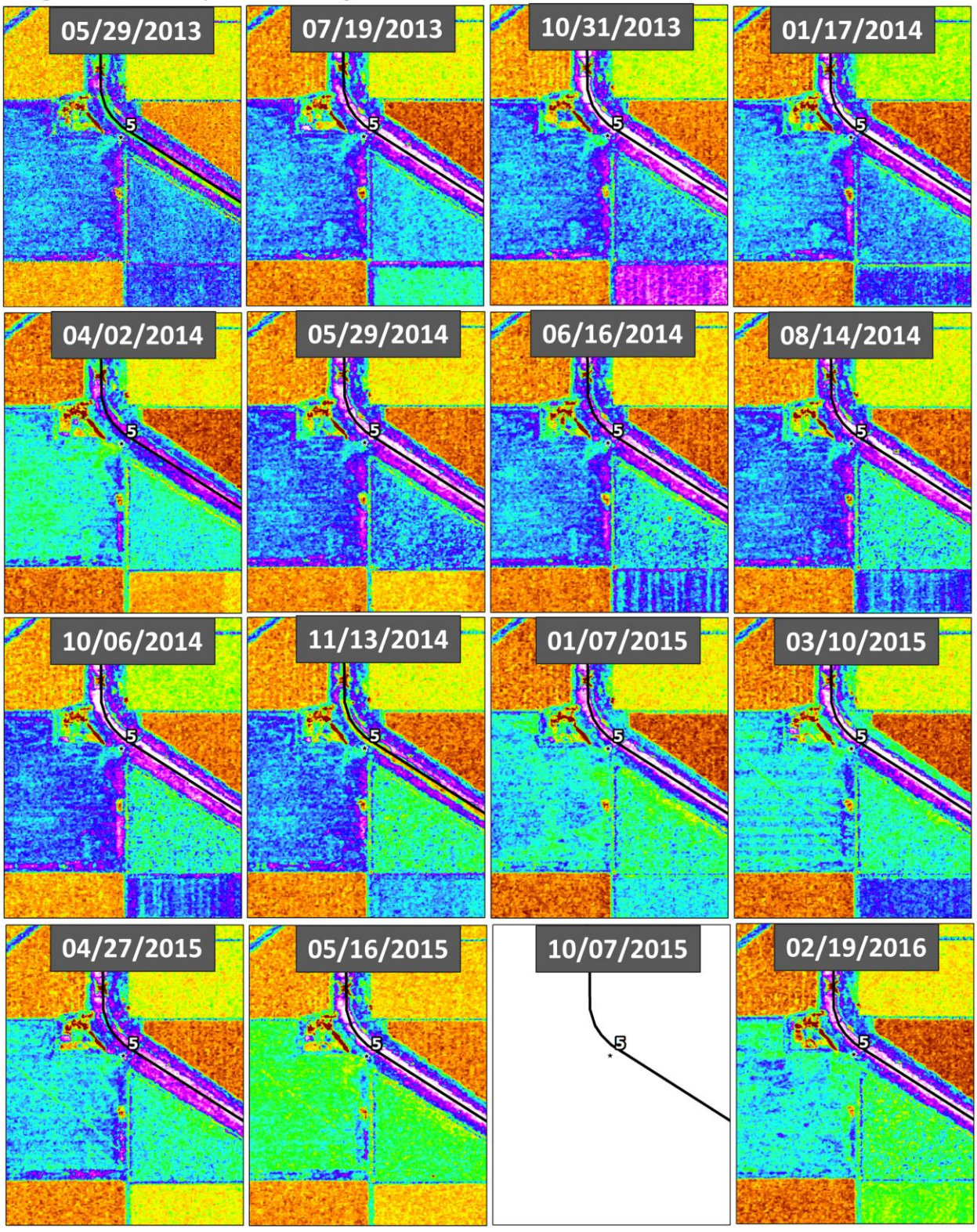

Figure 30B: Seep 5 – VV Single Polarization

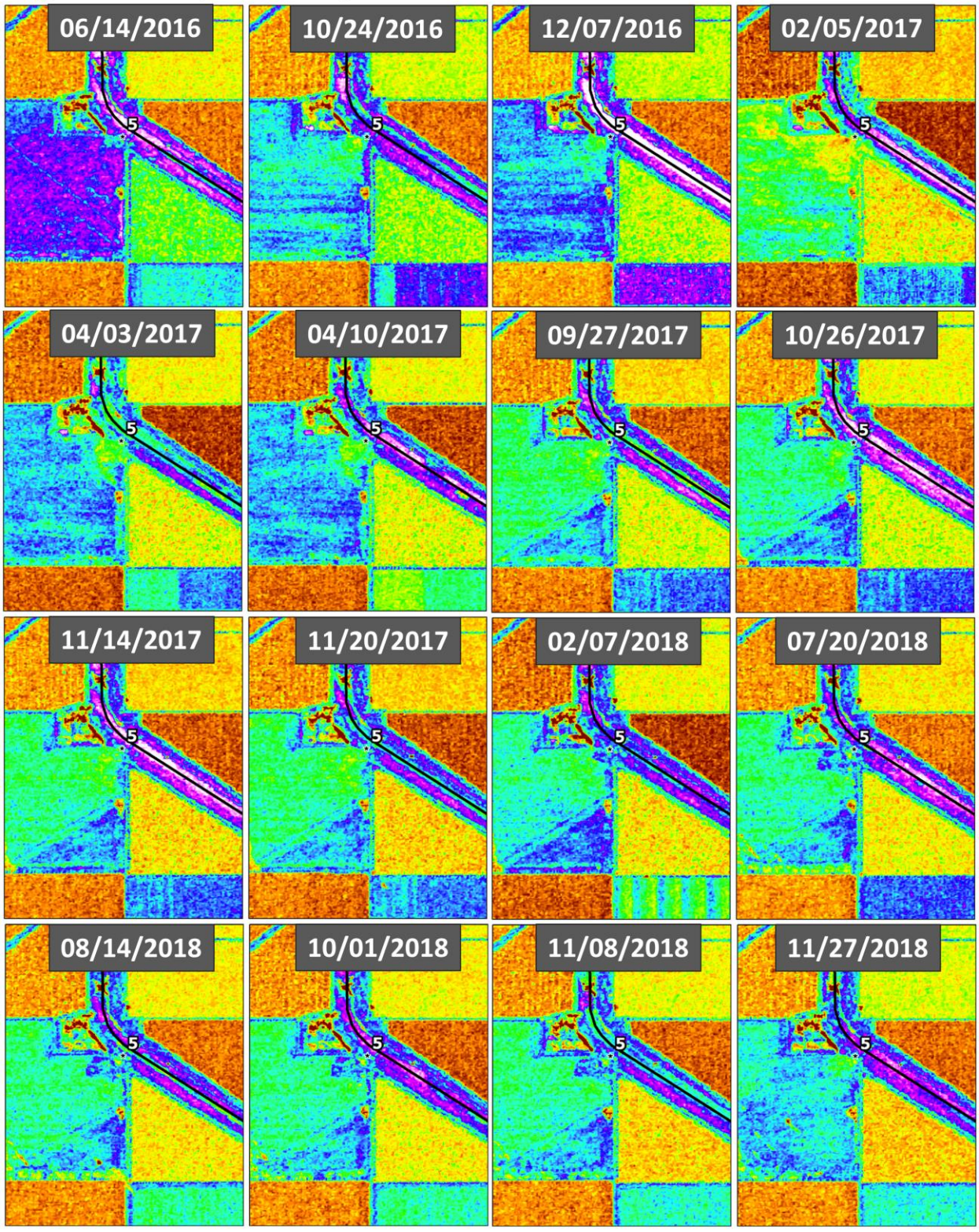

Figure 31A: Seep 5 – HV/HH Ratio

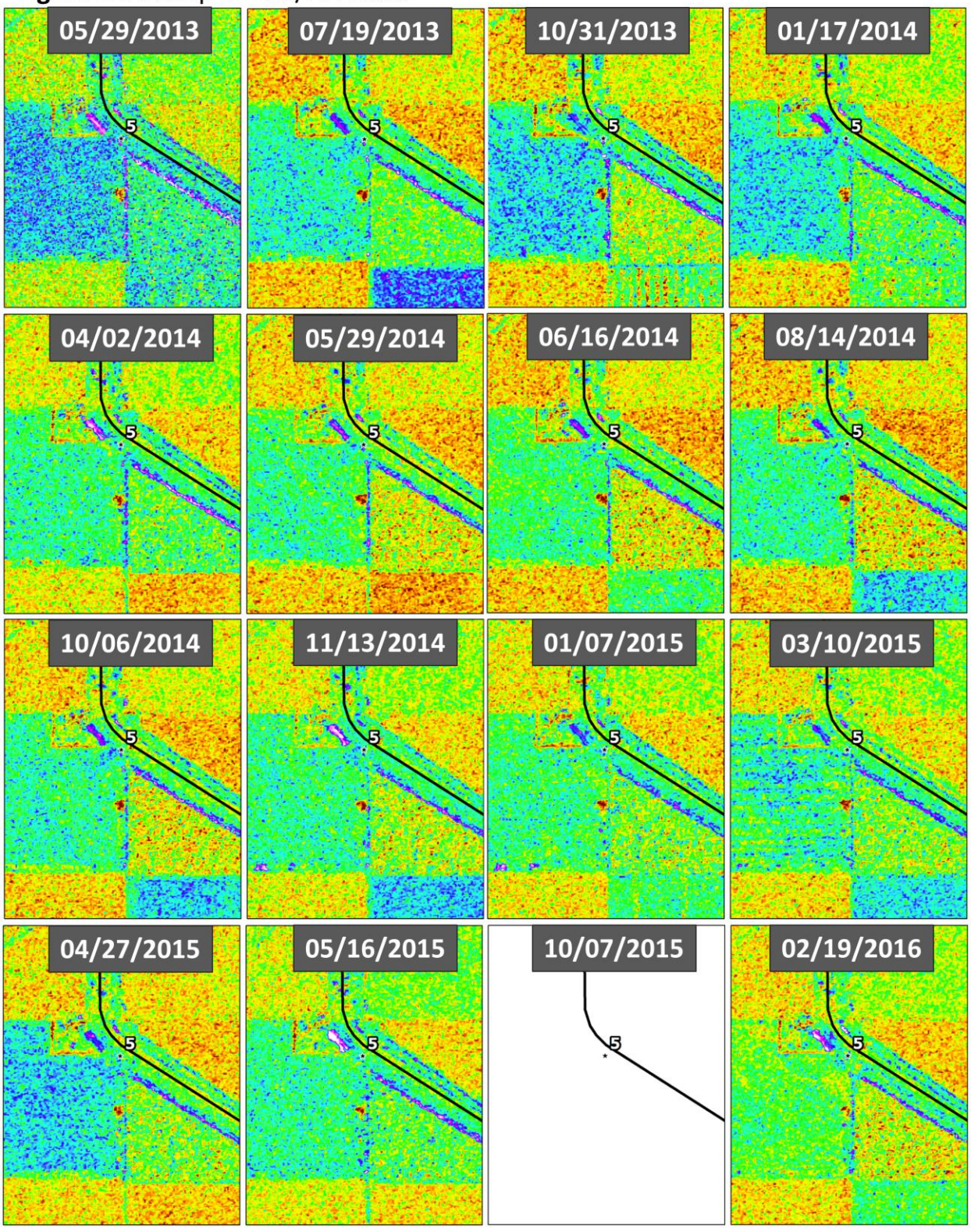

Figure 31B: Seep 5 – HV/HH Ratio

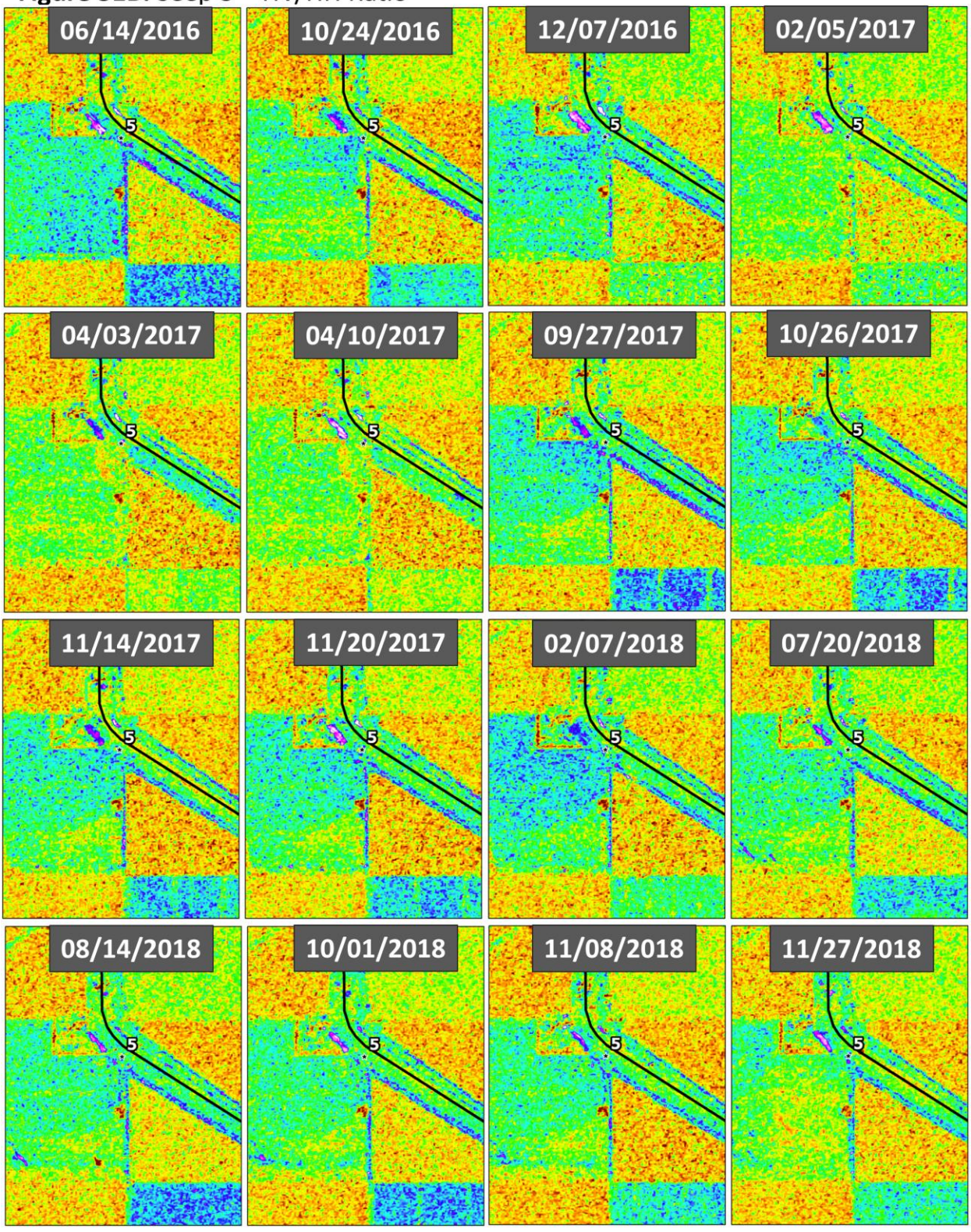

Figure 32A: Seep 4 – VV/HH Ratio

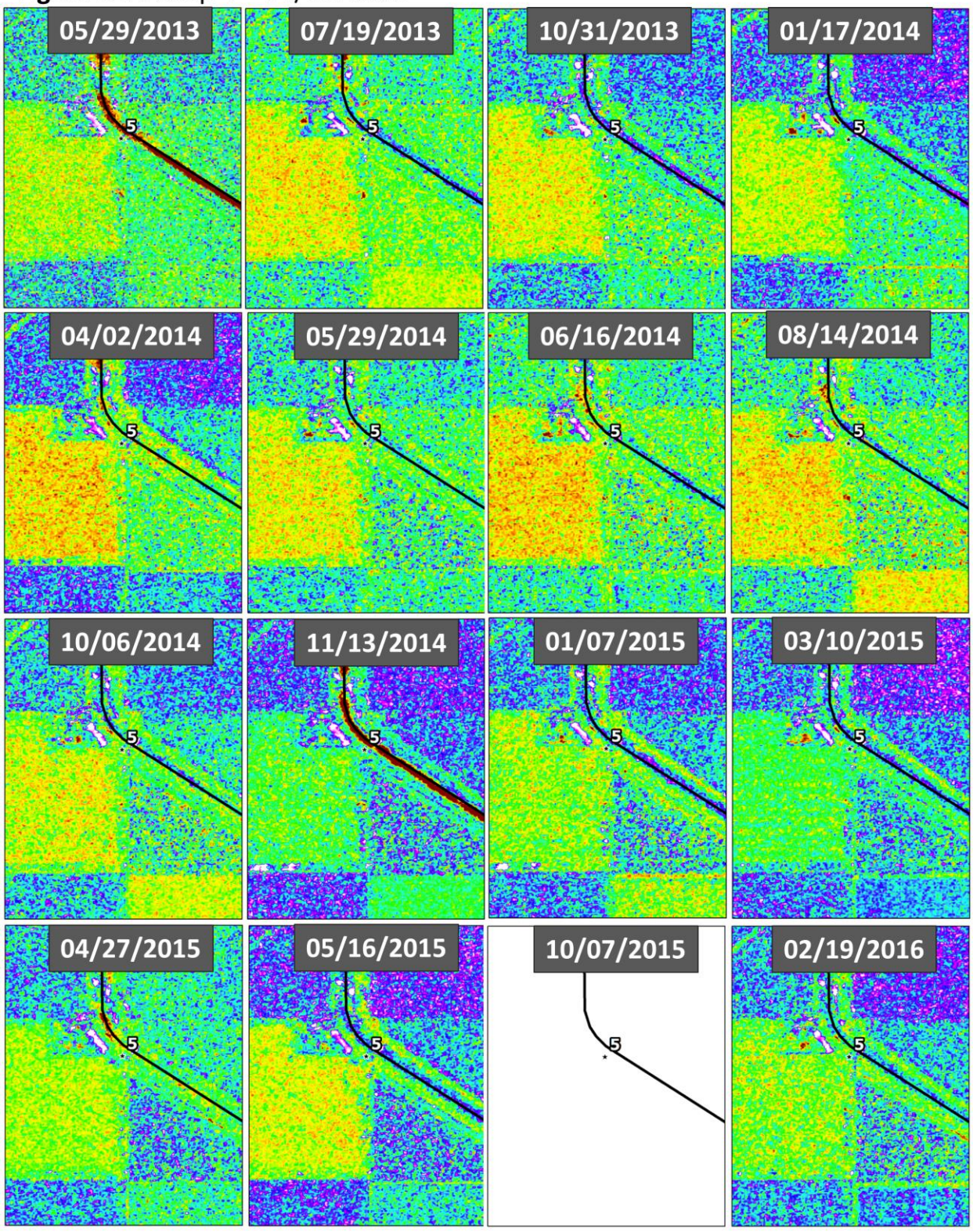

Figure 32B: Seep 4 – VV/HH Ratio

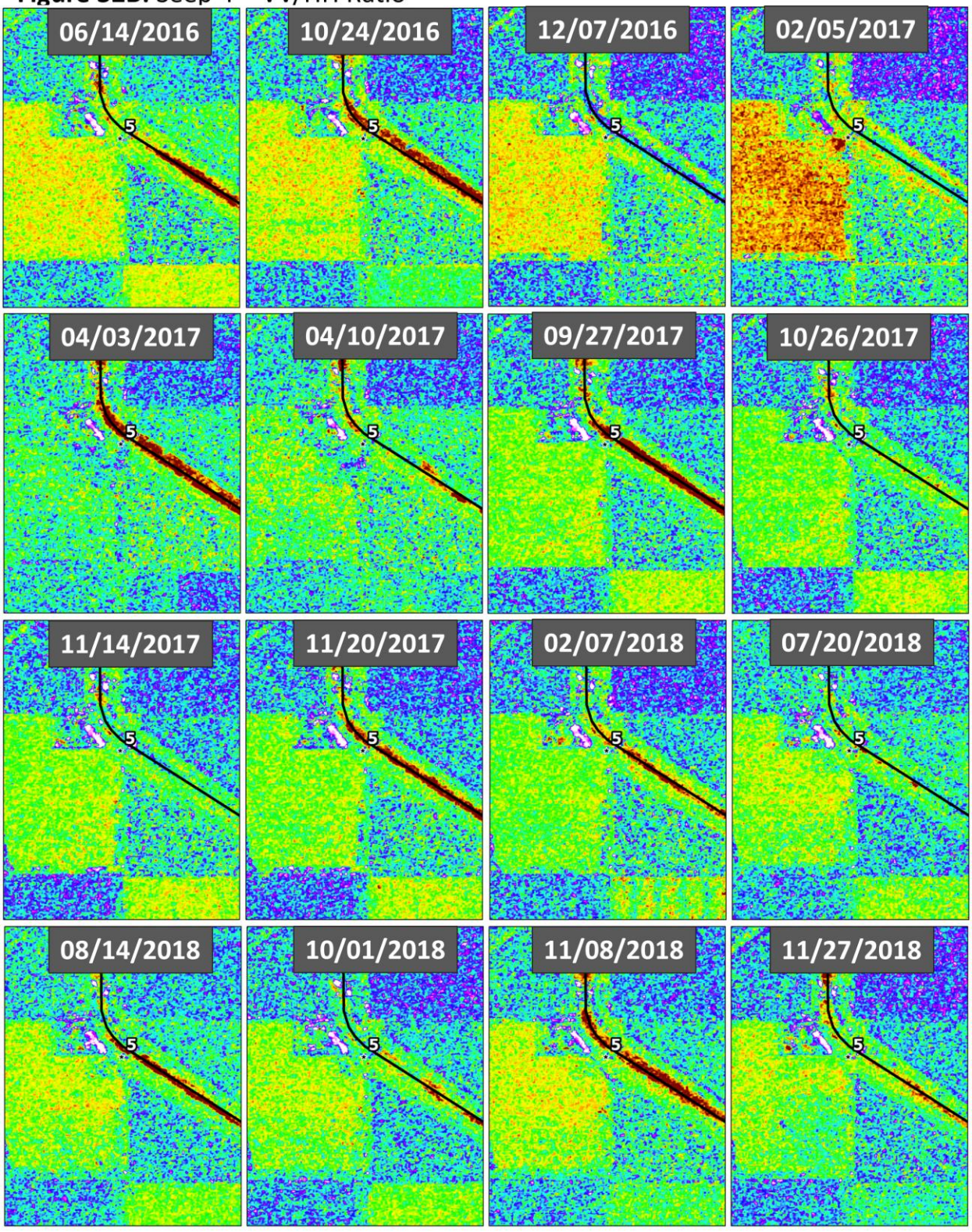

Figure 33A: Seep 5 – Copolarization Phase

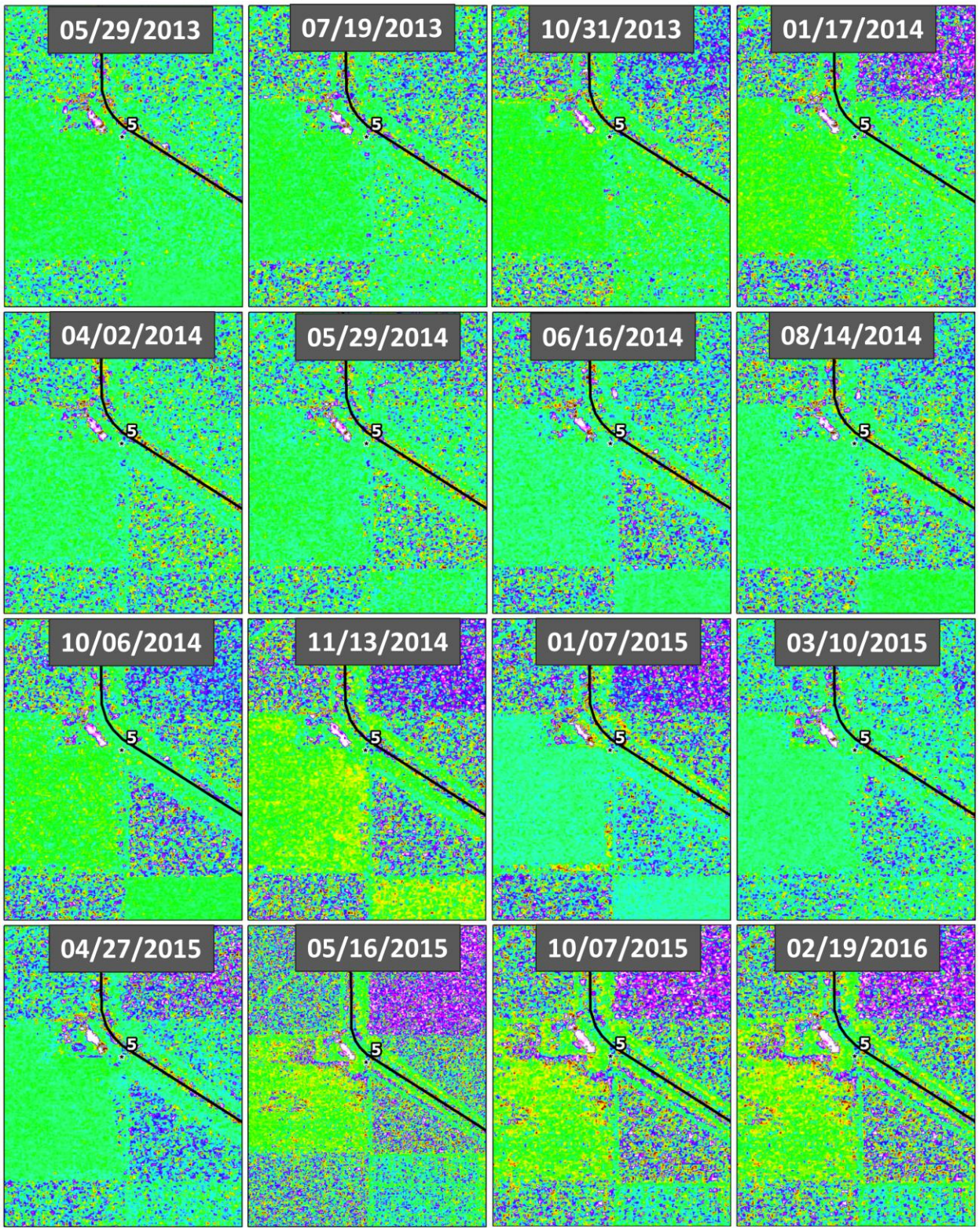

Figure 33B: Seep 5 – Copolarization Phase

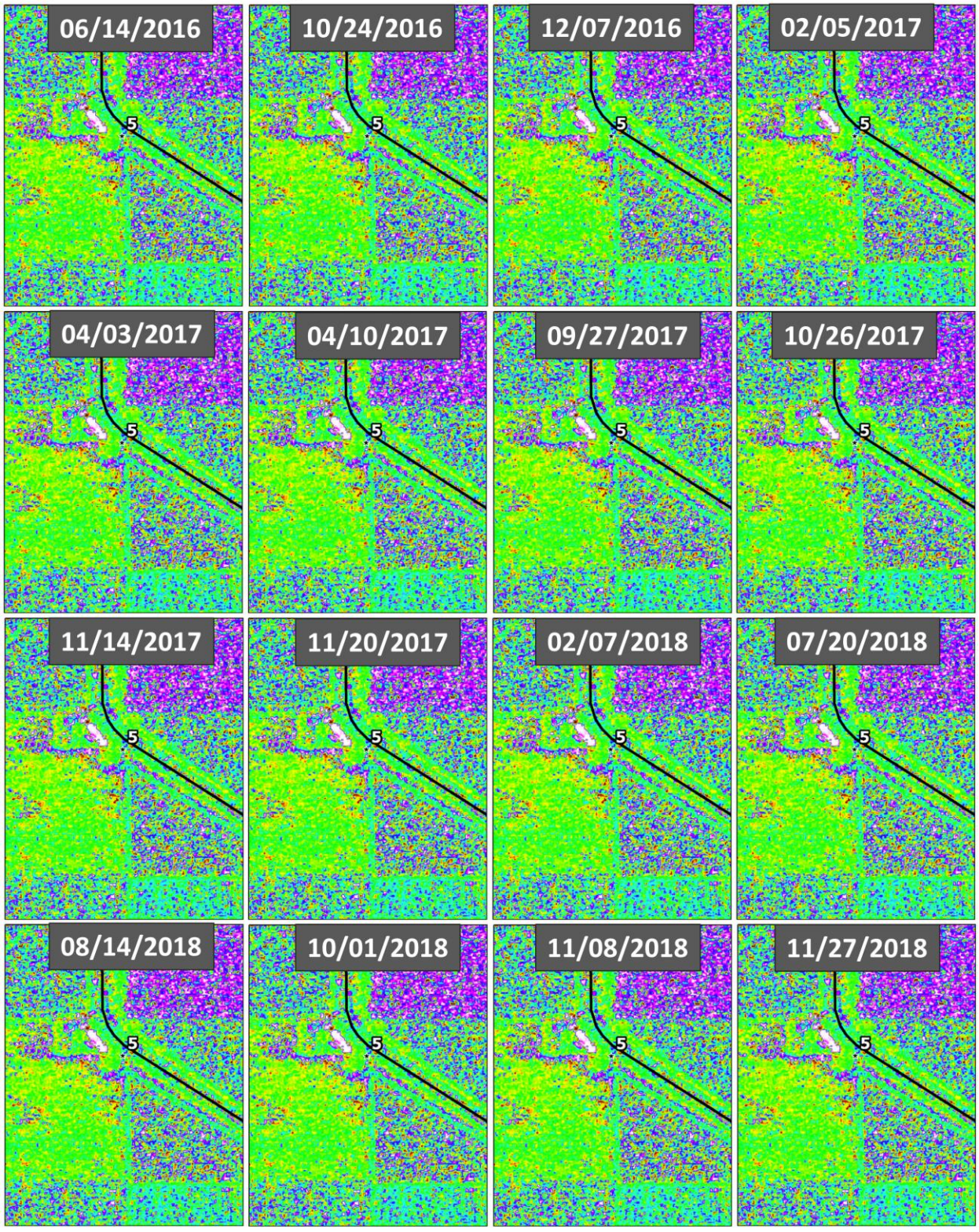

Figure 34A: Seep 5 – Entropy

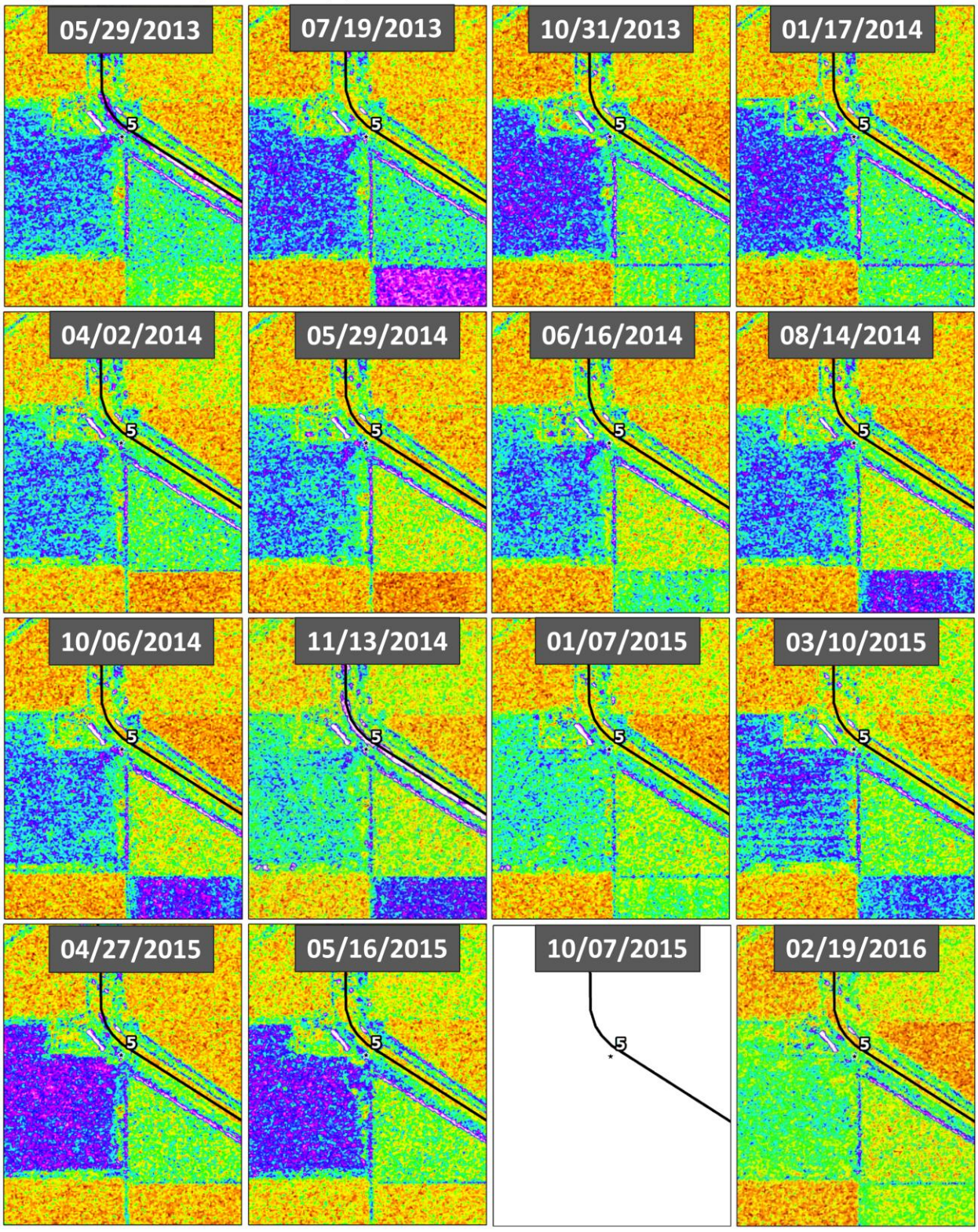

Figure 34B: Seep 5 – Entropy

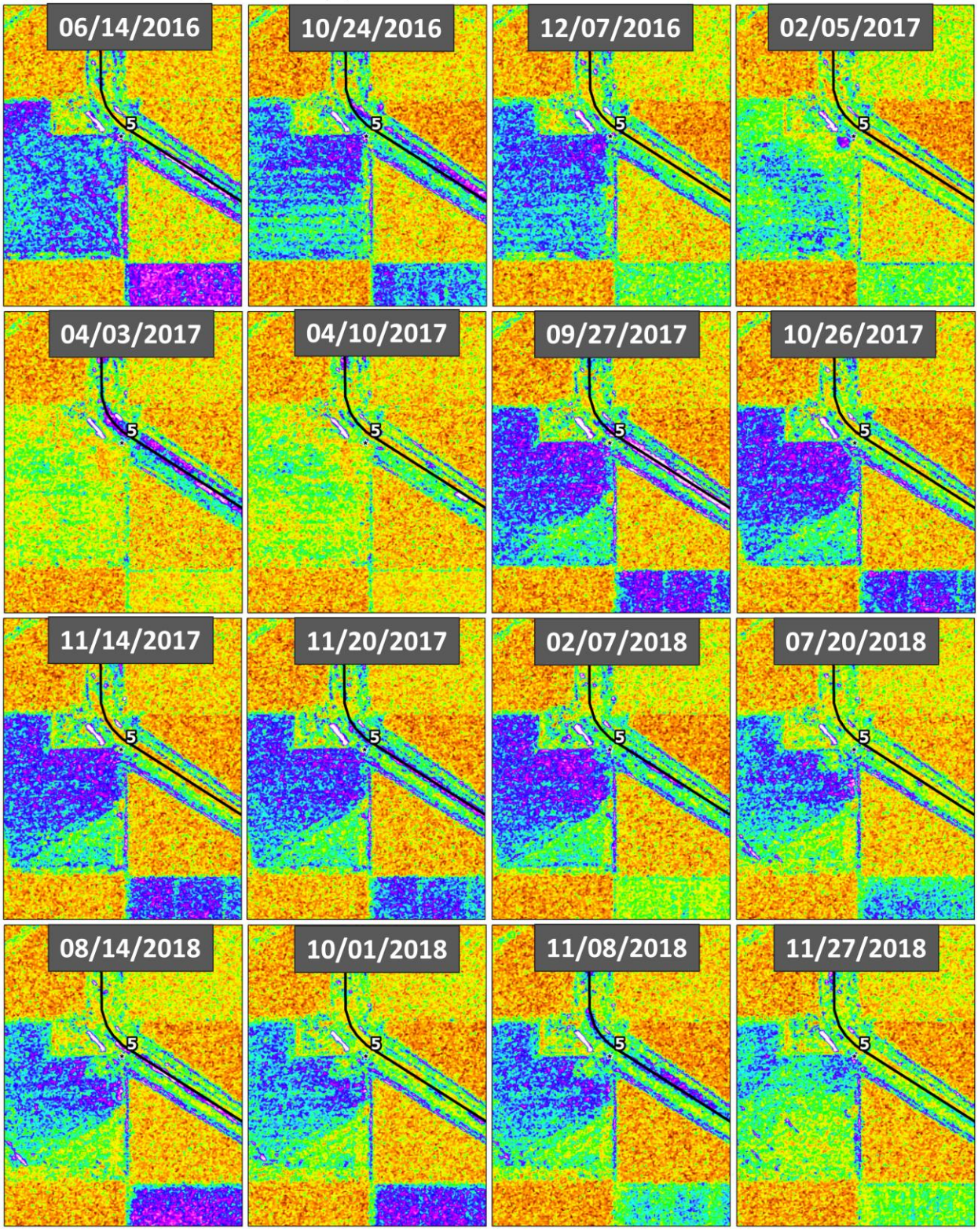

Figure 35A: Seep 5 – Anisotropy

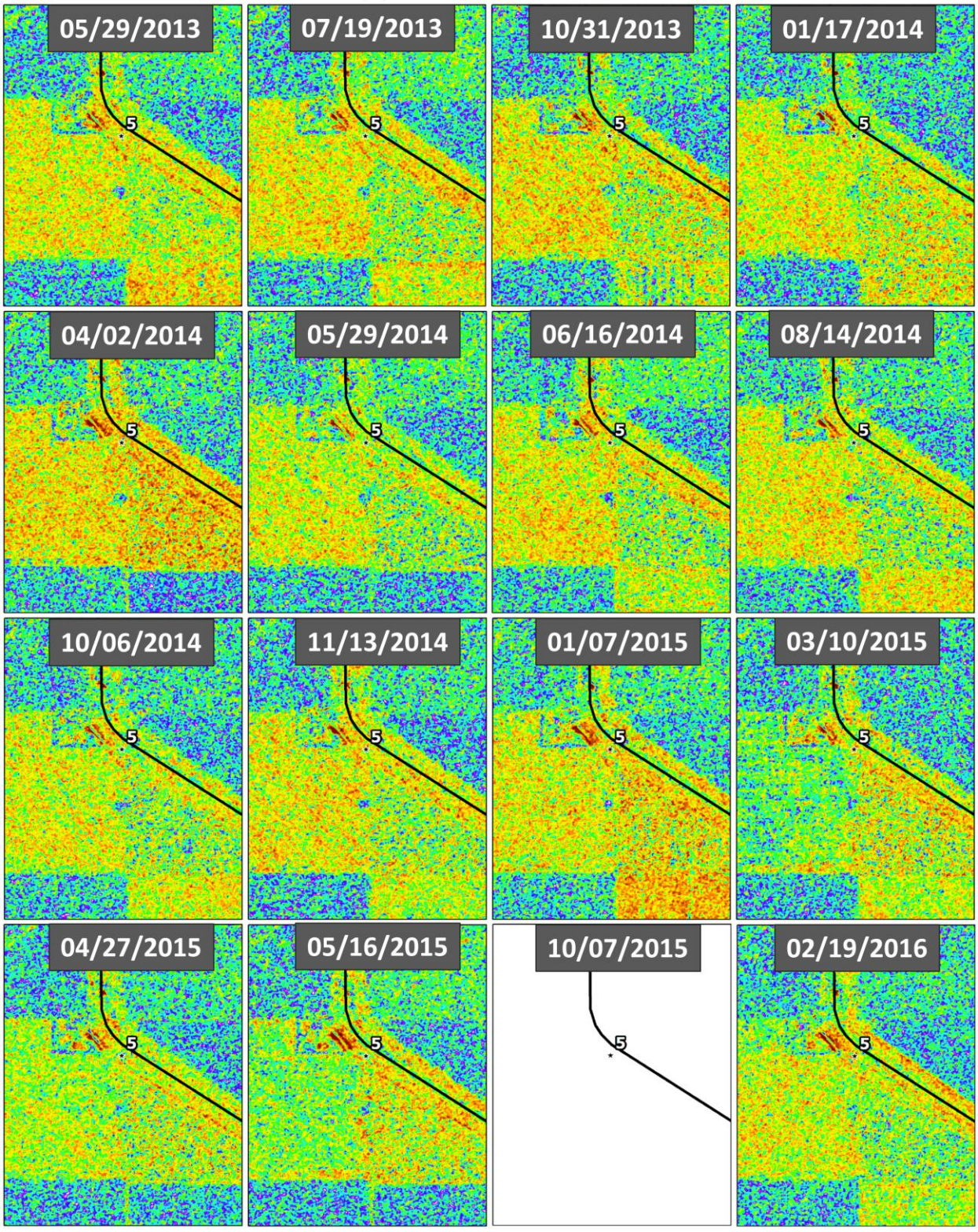

Figure 35B: Seep 5 – Anisotropy

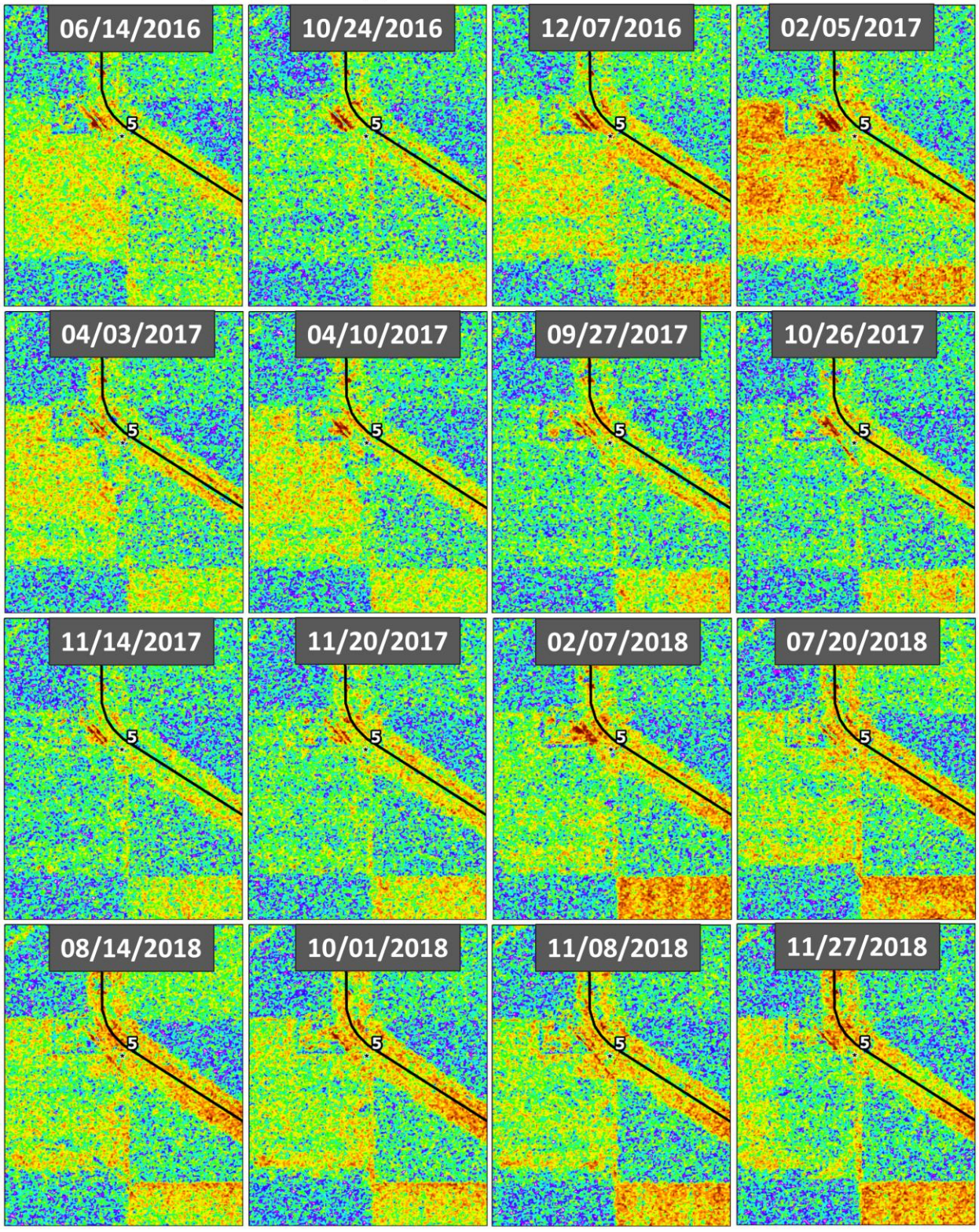

Figure 36A: Seep 5 – Mean Alpha Angle

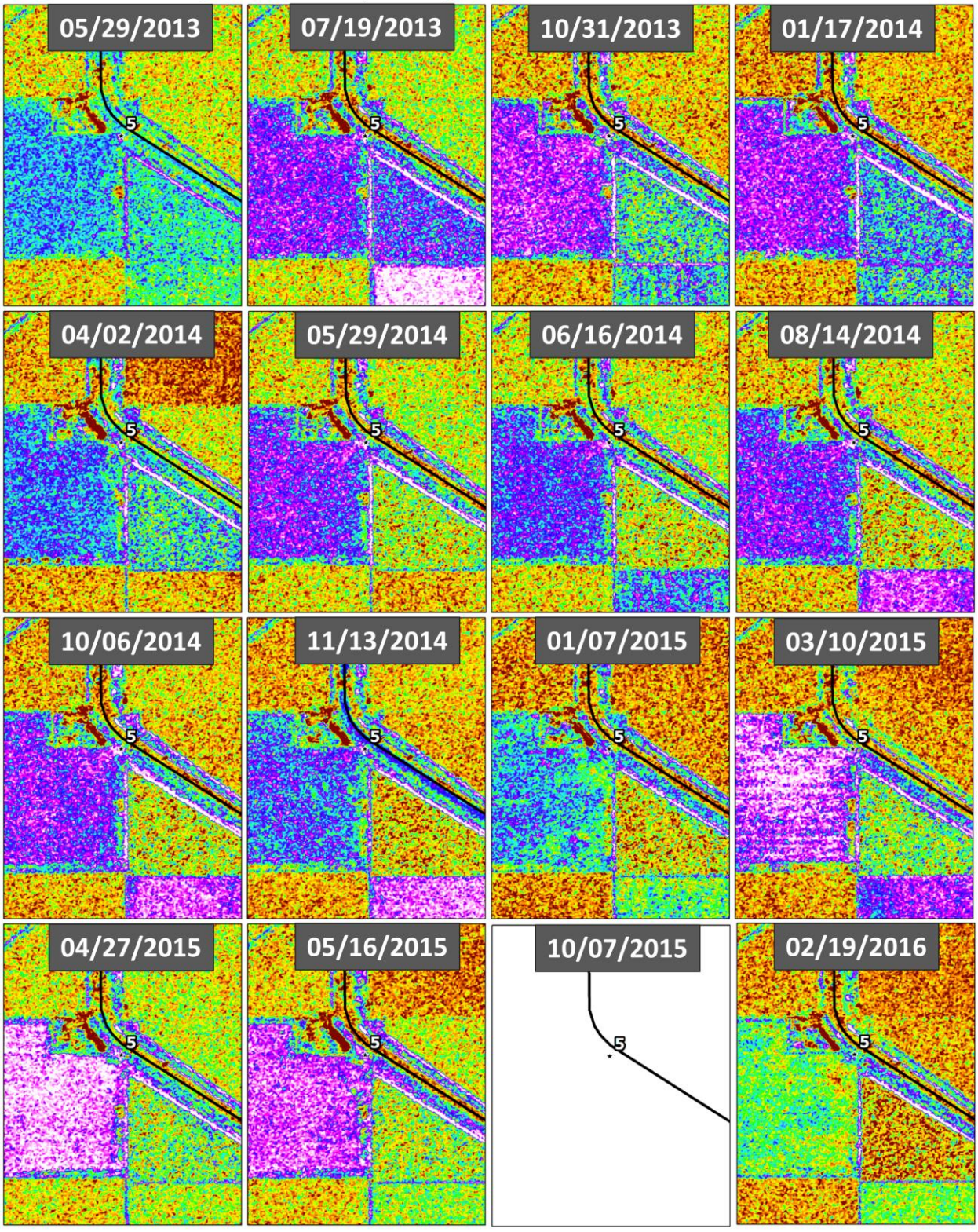

Figure 36B: Seep 5 – Mean Alpha Angle

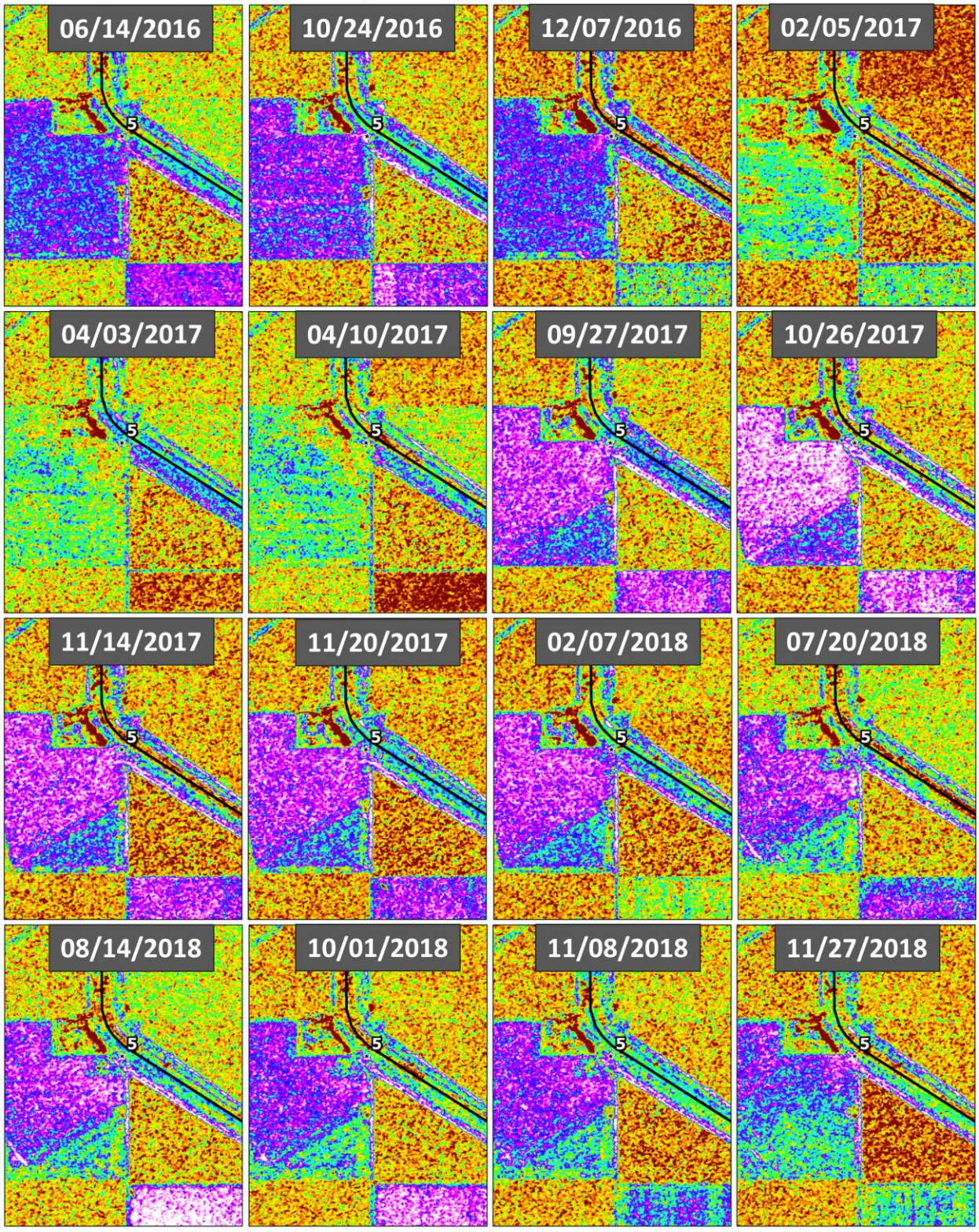

Figure 37A: Study area overview of Delta seep examples on Twitchell Island.

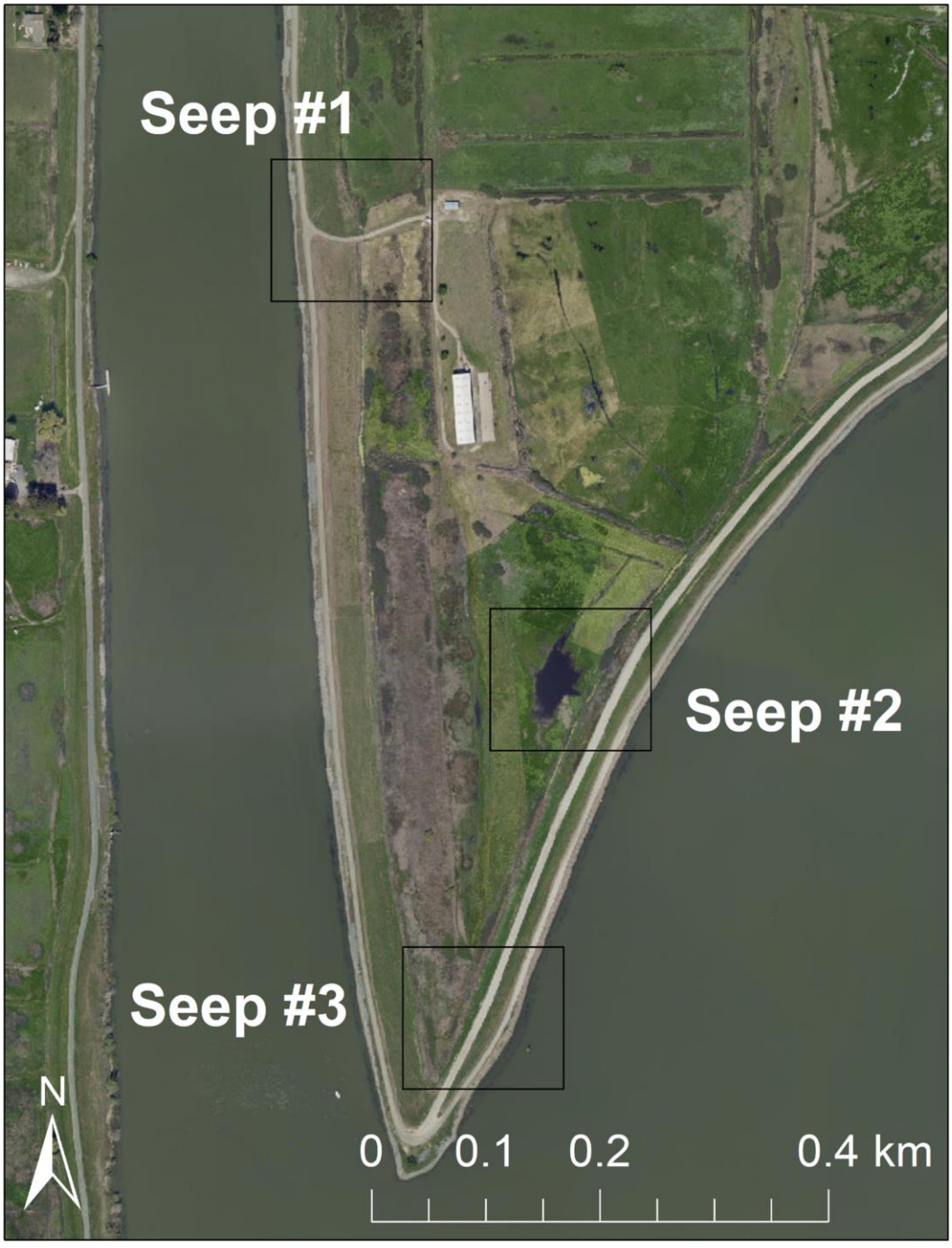

Figure 37B: Study area overview for Seeps 1-3 on Twitchell Island.

Figure 38A: Seeps 1-3 – Google Earth Imagery

Figure 38B: Seeps 1-3 – Google Earth Imagery

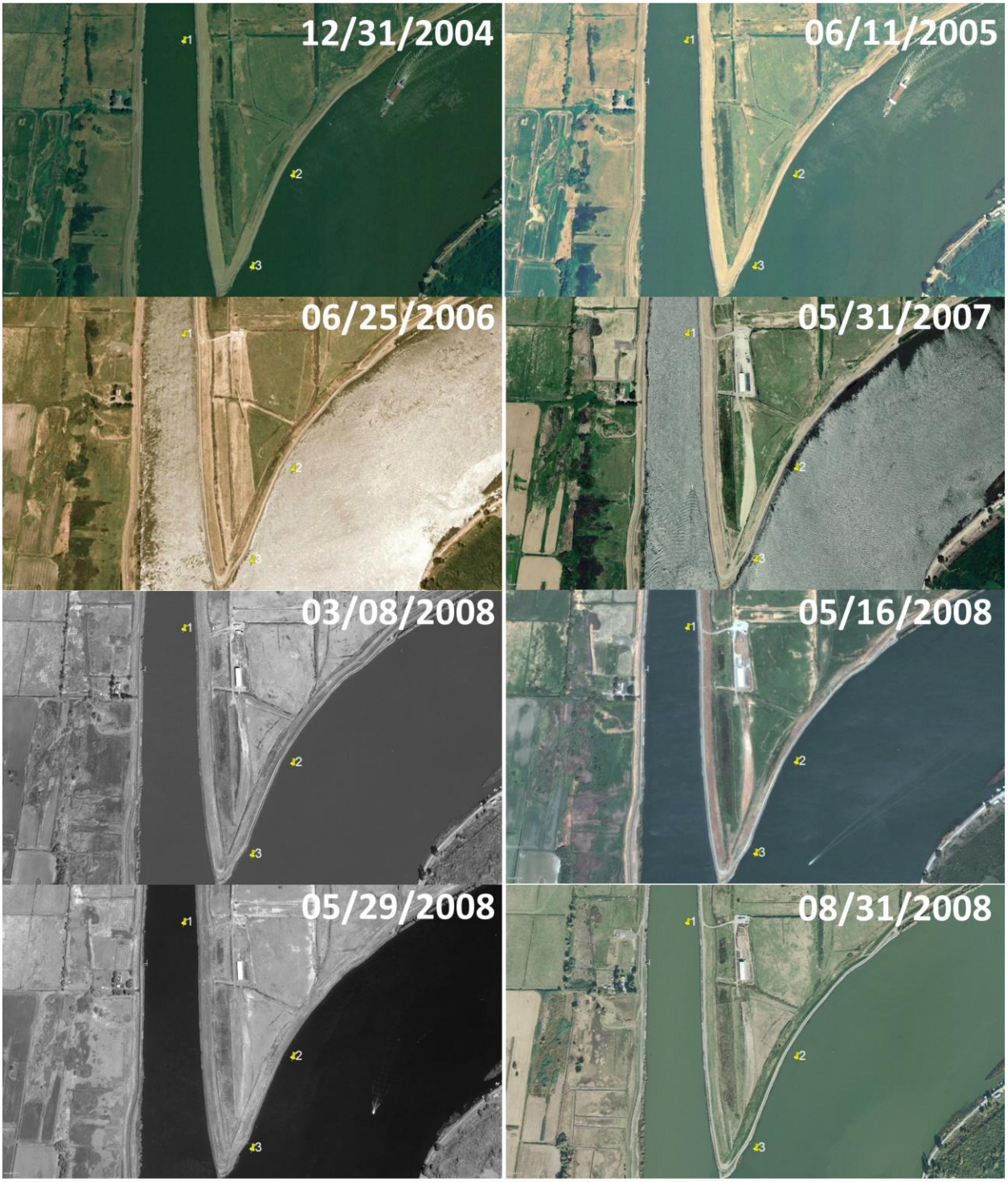

Figure 38C: Seeps 1-3 – Google Earth Imagery

Figure 38D: Seeps 1-3 – Google Earth Imagery

Figure 38E: Seeps 1-3 – Google Earth Imagery

Figure 38F: Seeps 1-3 – Google Earth Imagery

Figure 38G: Seeps 1-3 – Google Earth Imagery

Figure 39: Legends for NDWI and PolSAR data products.

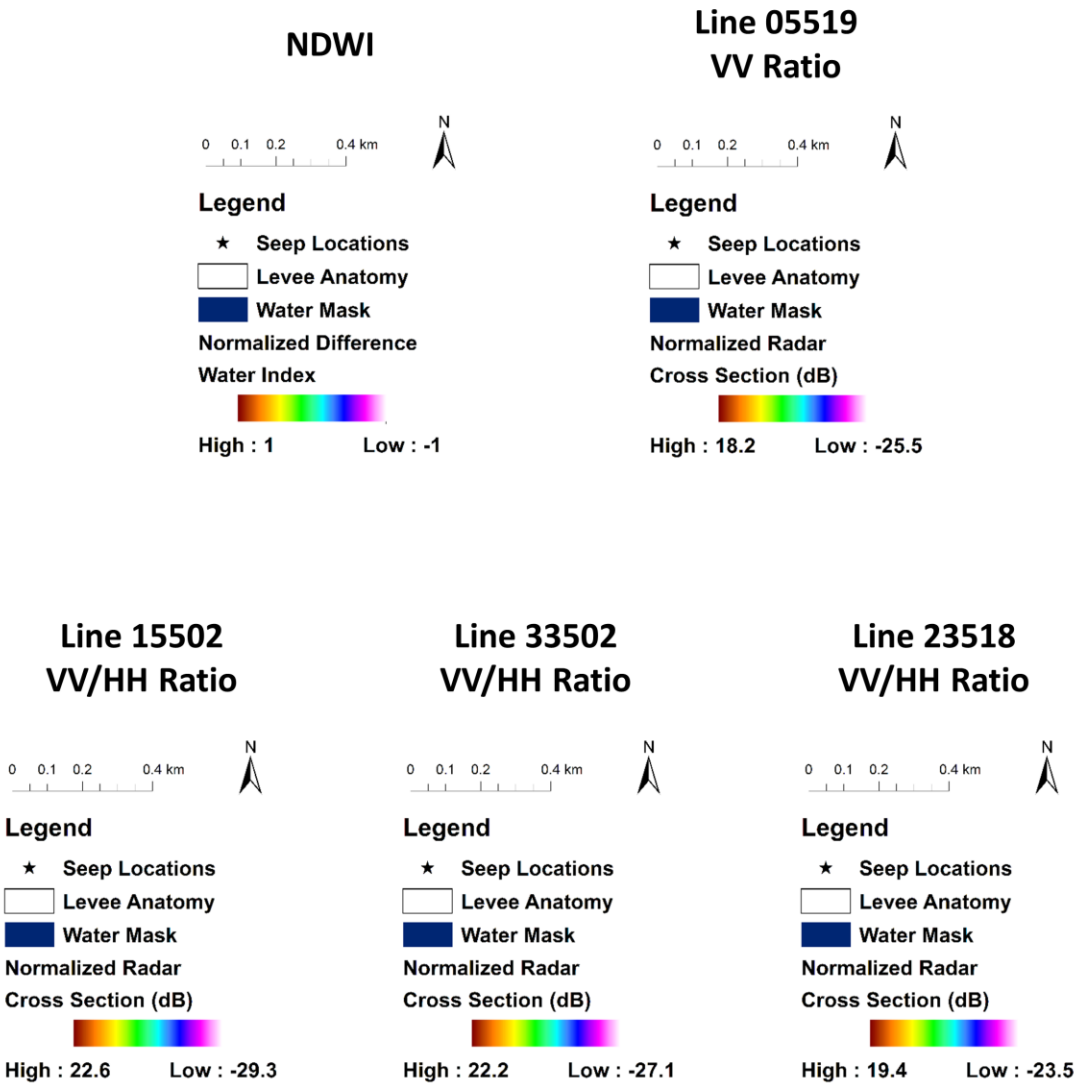

Figure 40A: Seeps 1-3 – NDWI

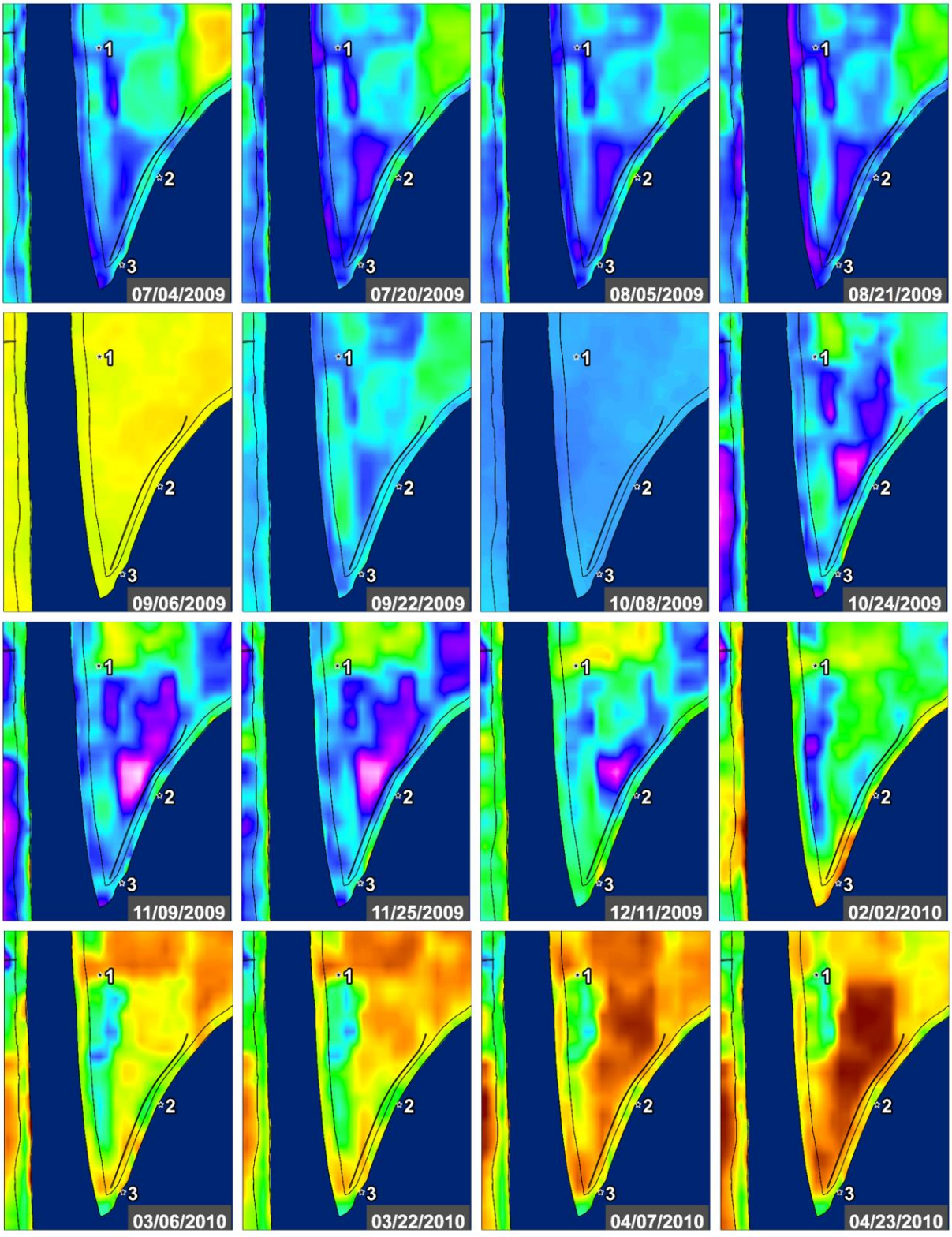

Figure 40B: Seeps 1-3 – NDWI

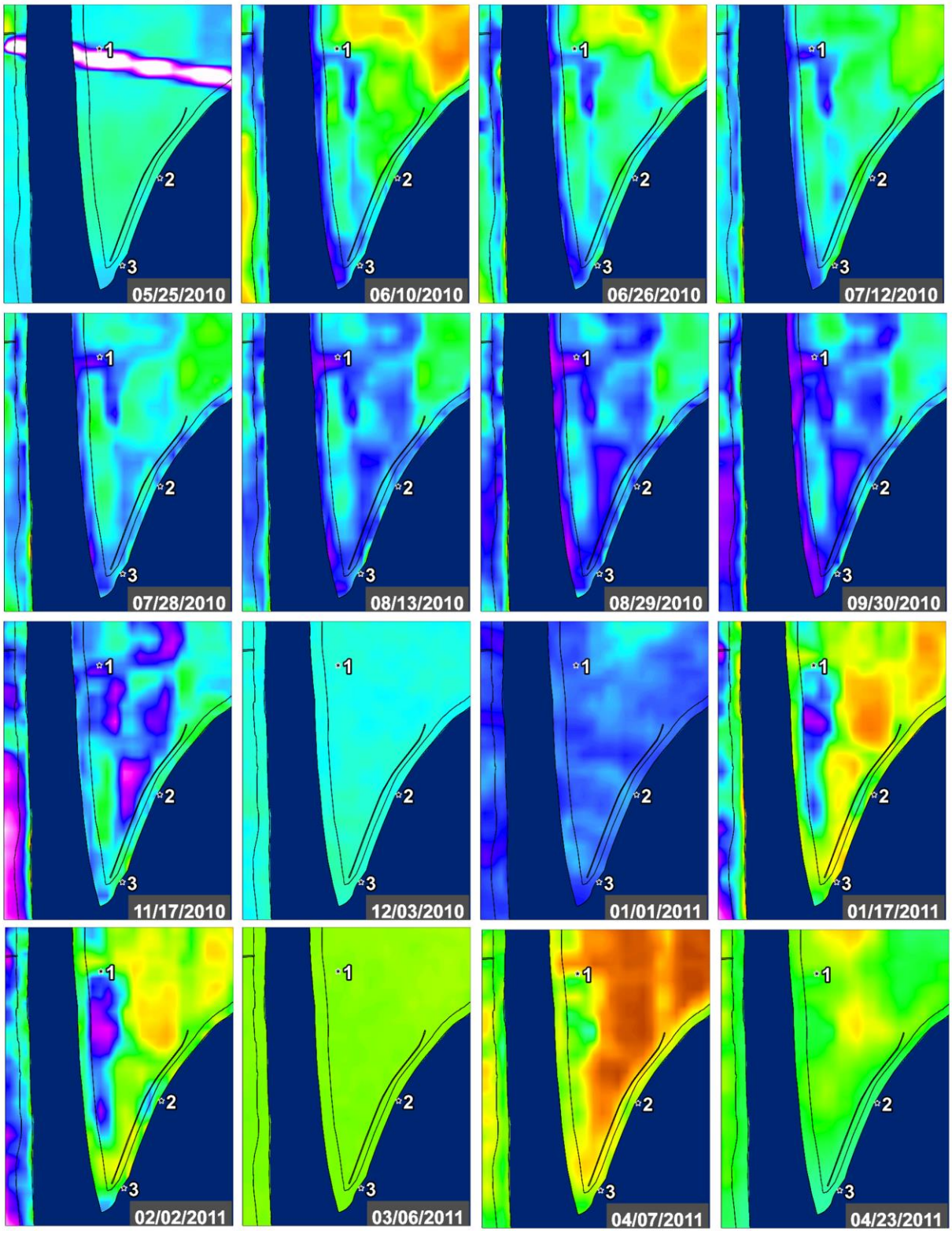

Figure 40C: Seeps 1-3 – NDWI

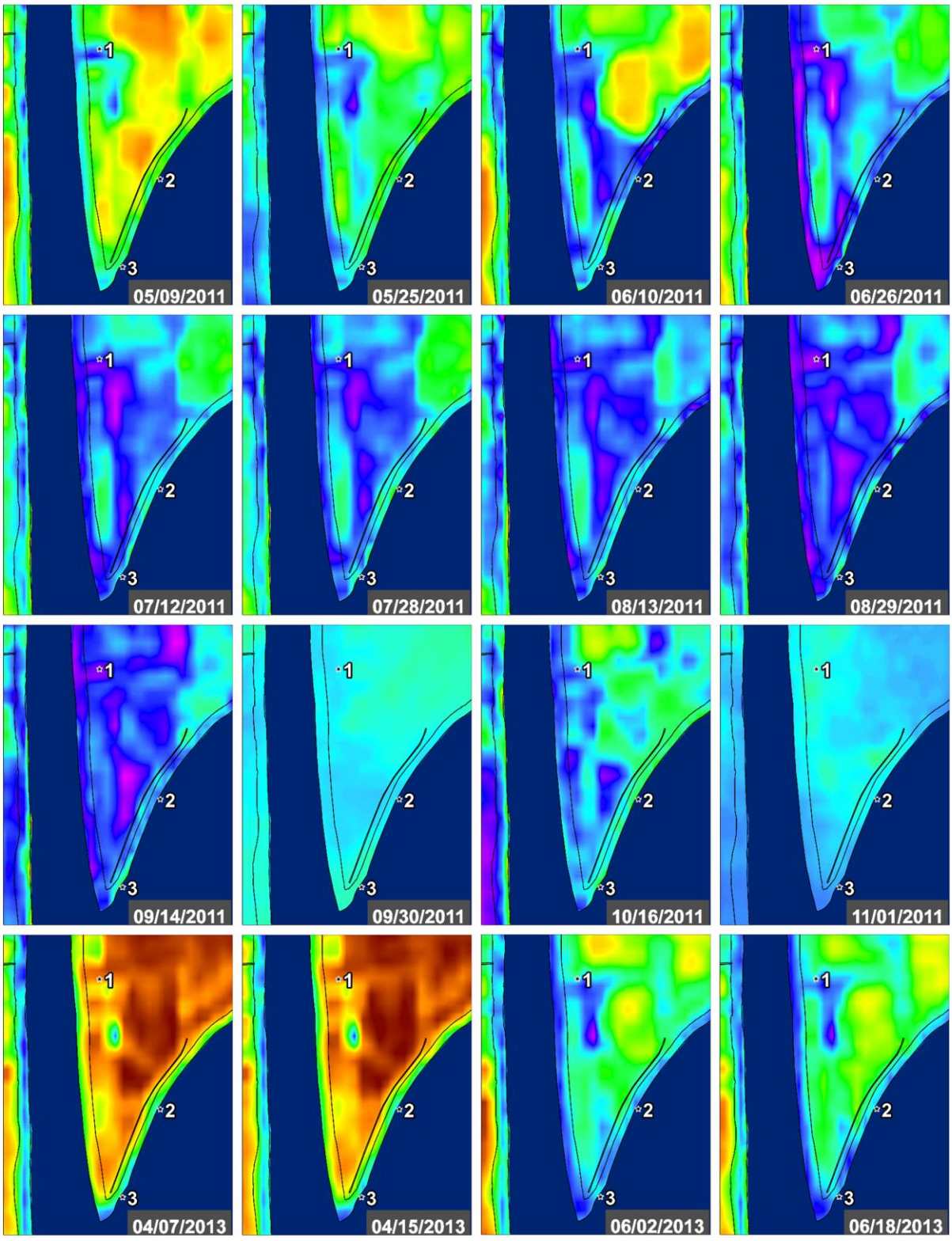

Figure 40D: Seeps 1-3 – NDWI

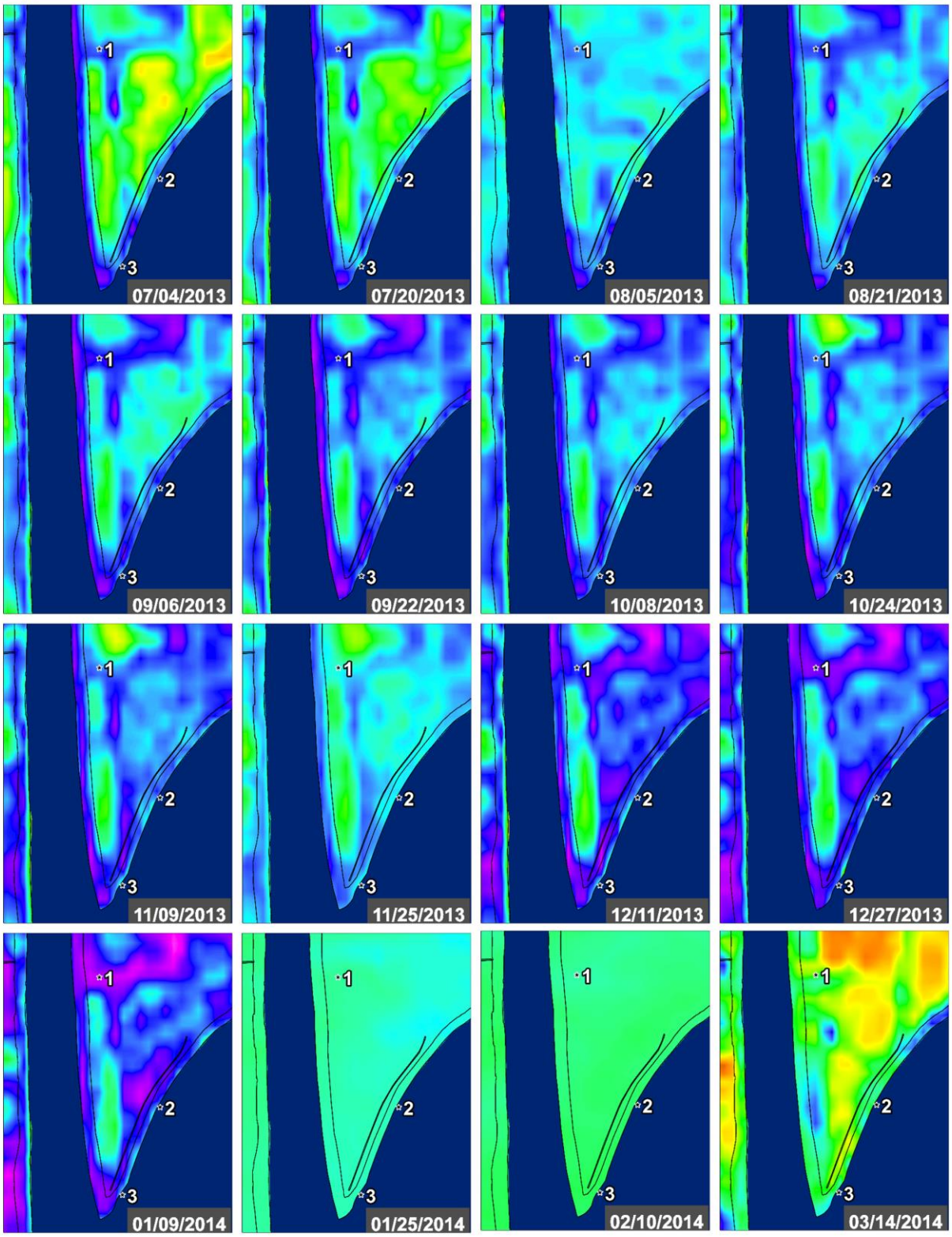

Figure 40E: Seeps 1-3 – NDWI

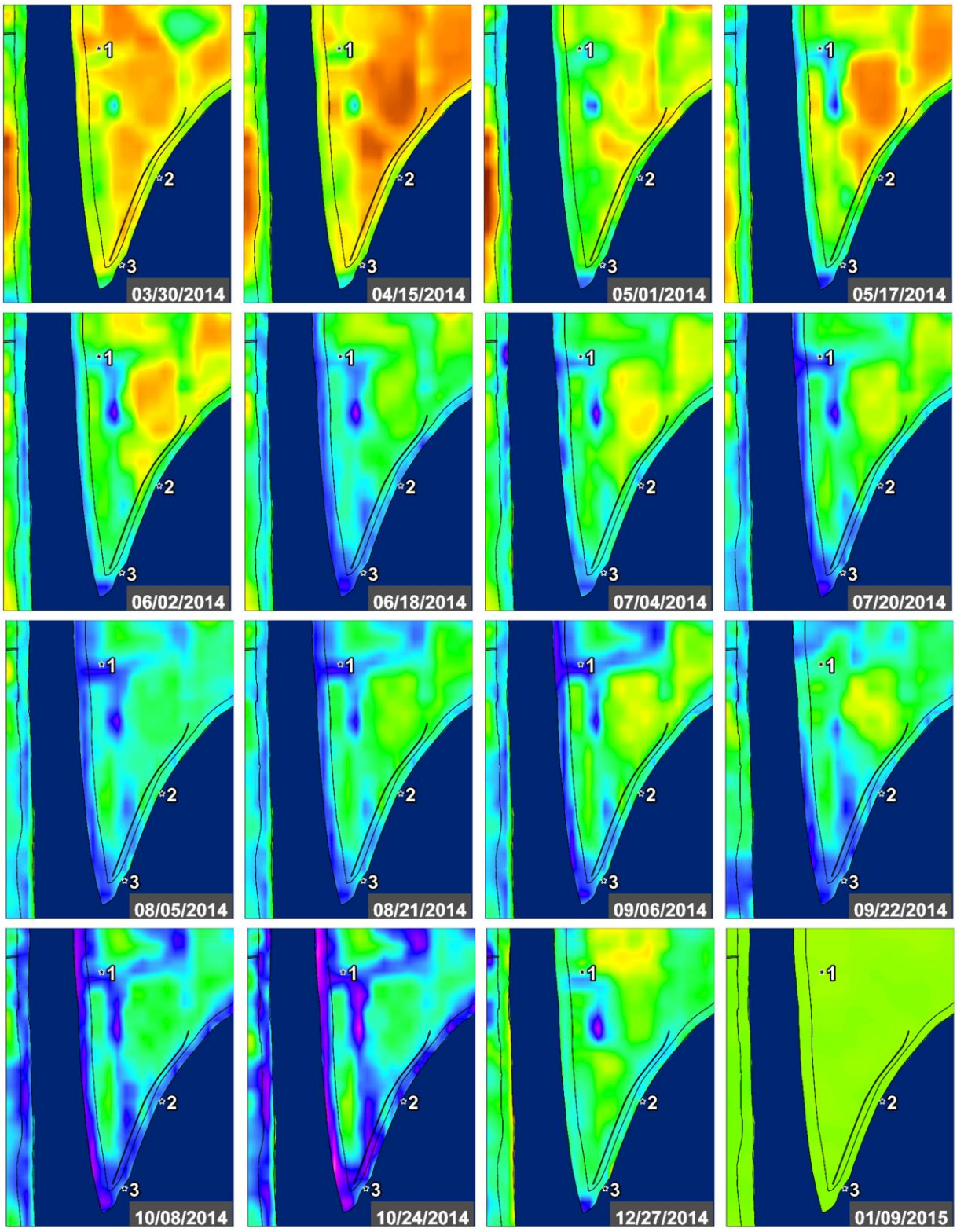

Figure 40F: Seeps 1-3 – NDWI

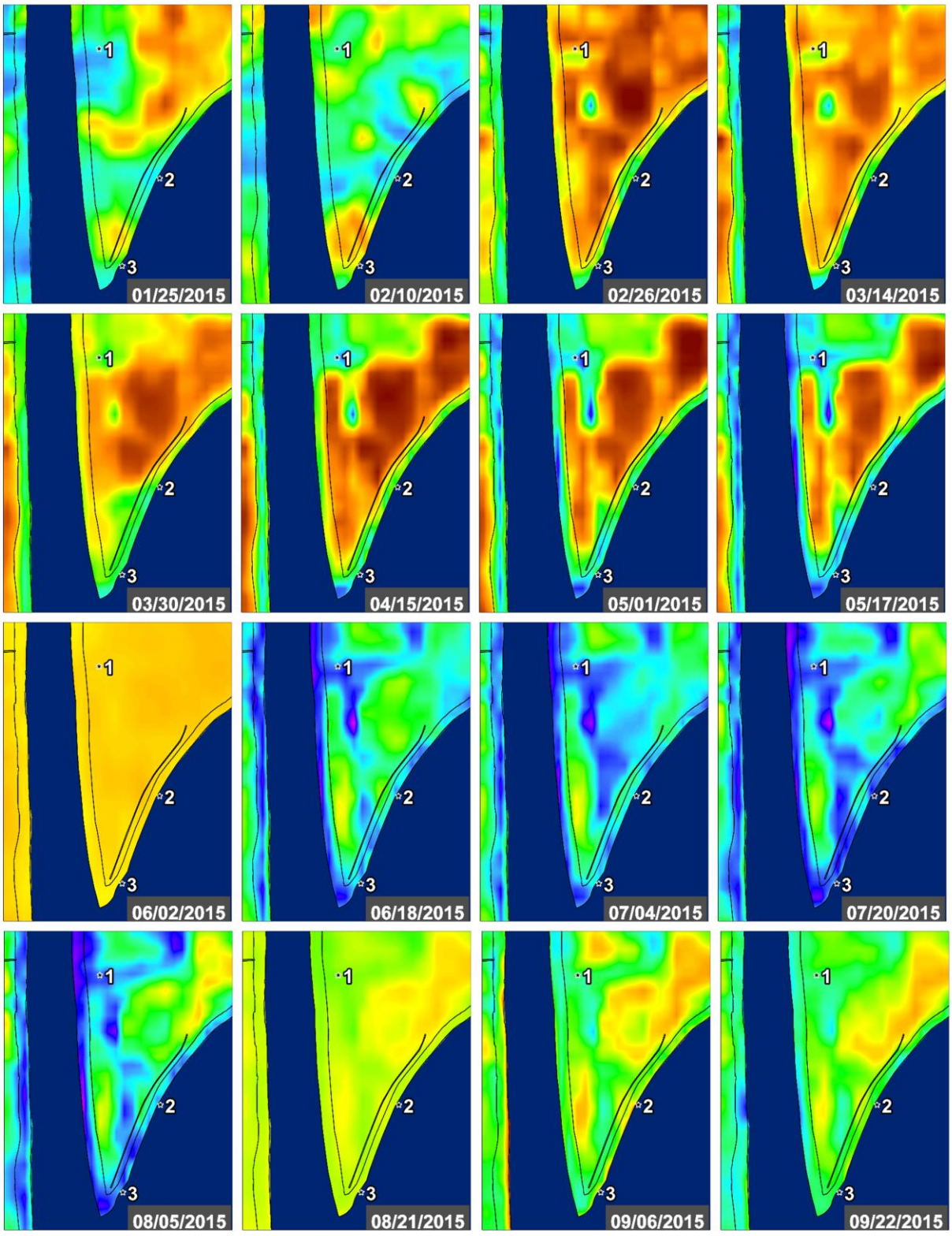

Figure 40G: Seeps 1-3 – NDWI

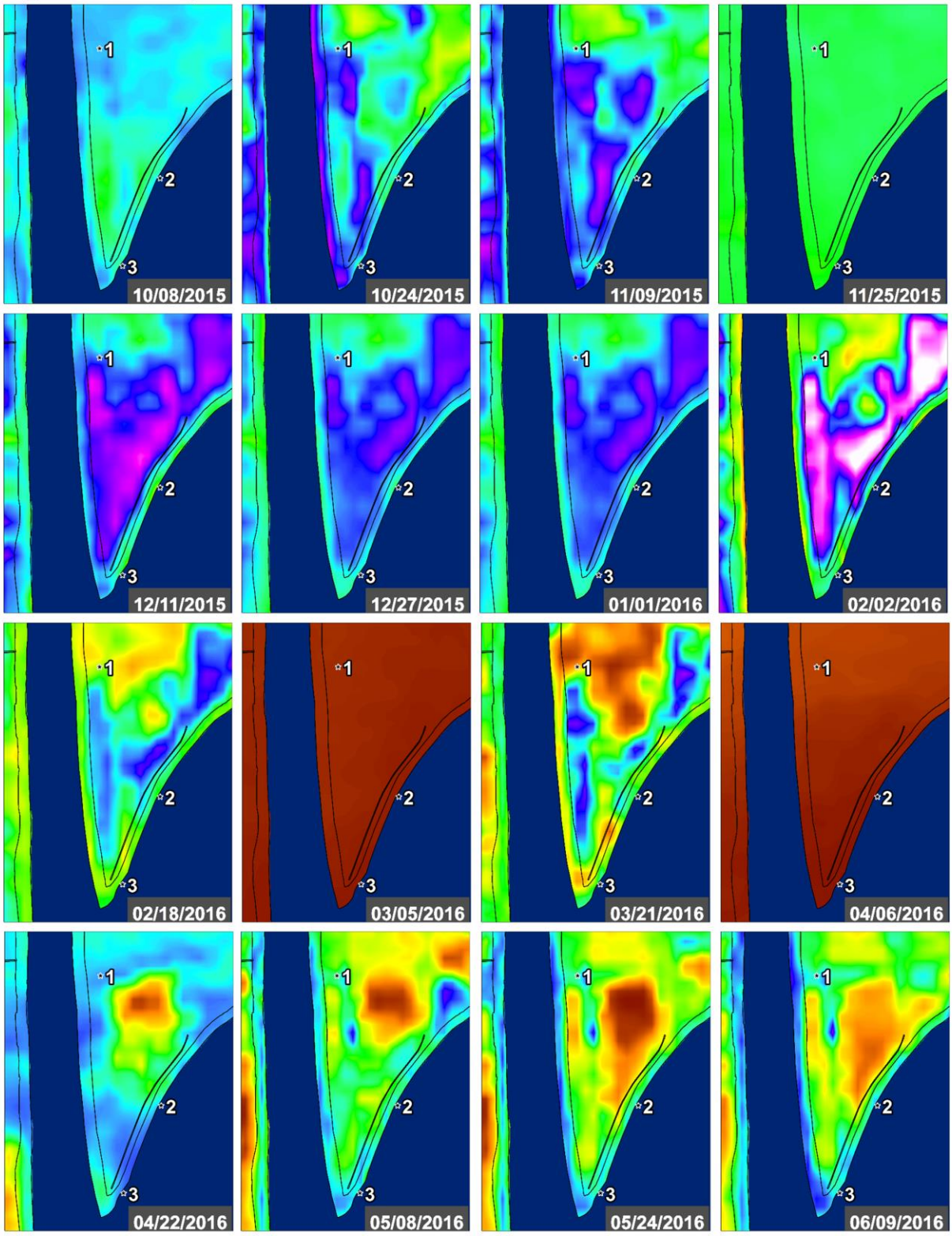

Figure 40H: Seeps 1-3 – NDWI

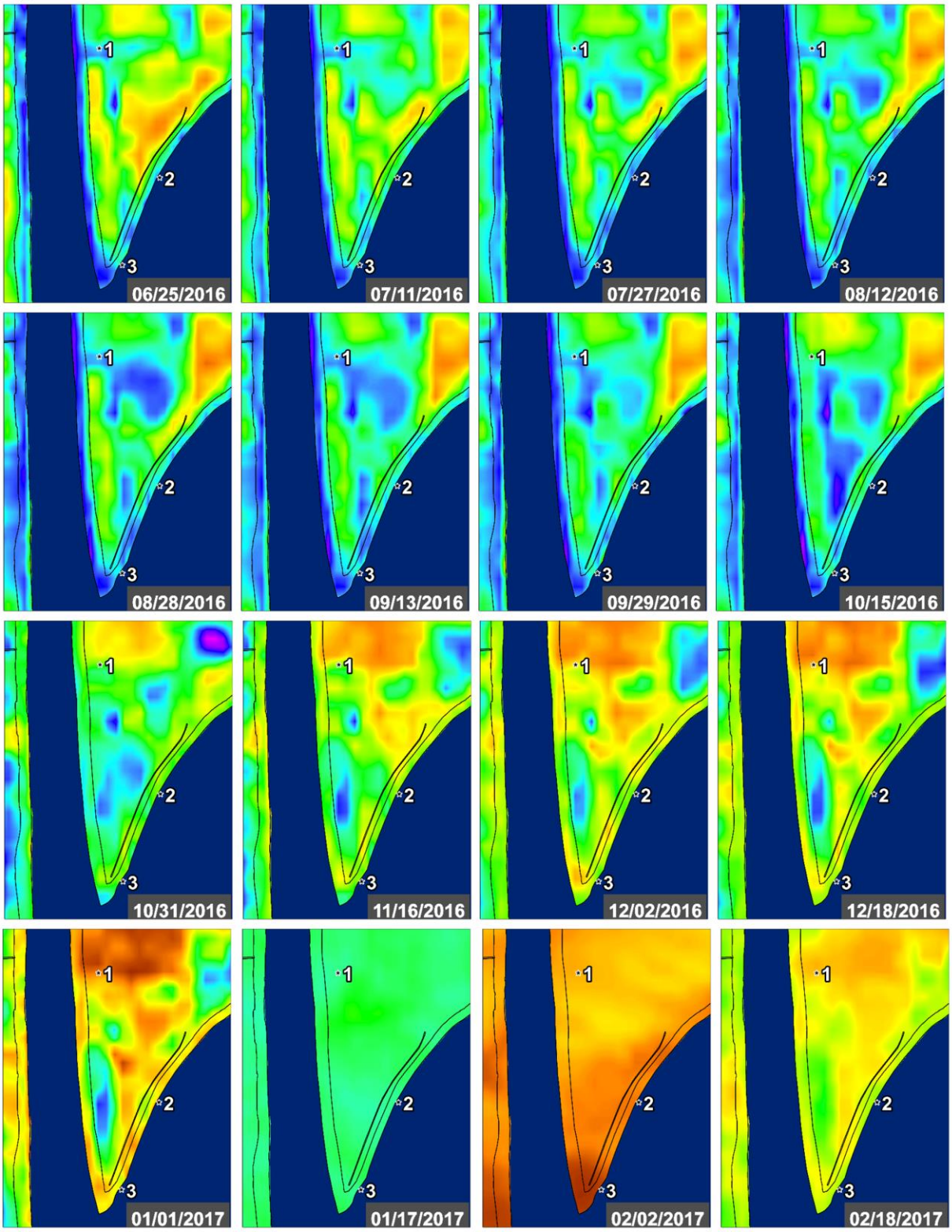

Figure 40I: Seeps 1-3 – NDWI

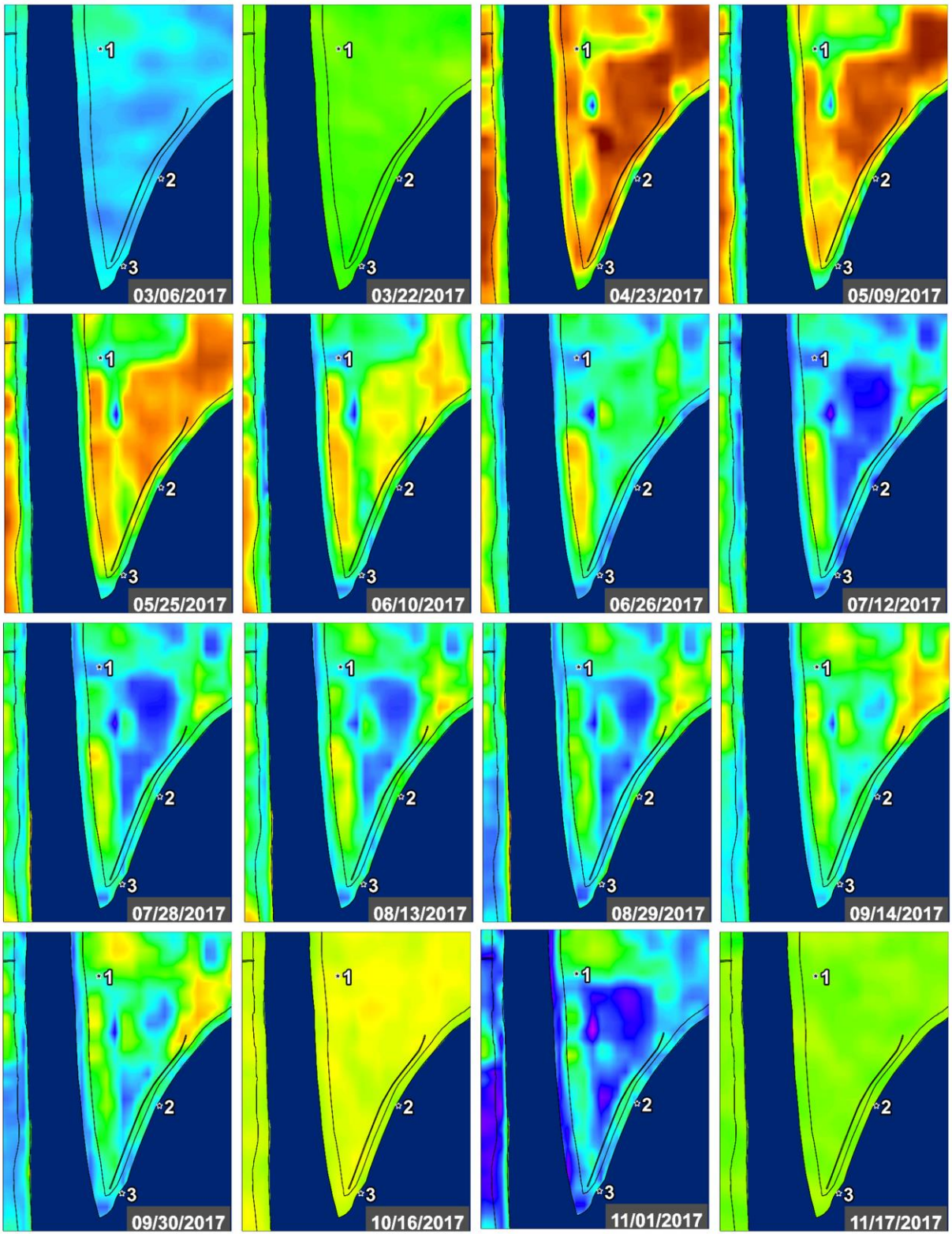

Figure 40J: Seeps 1-3 – NDWI

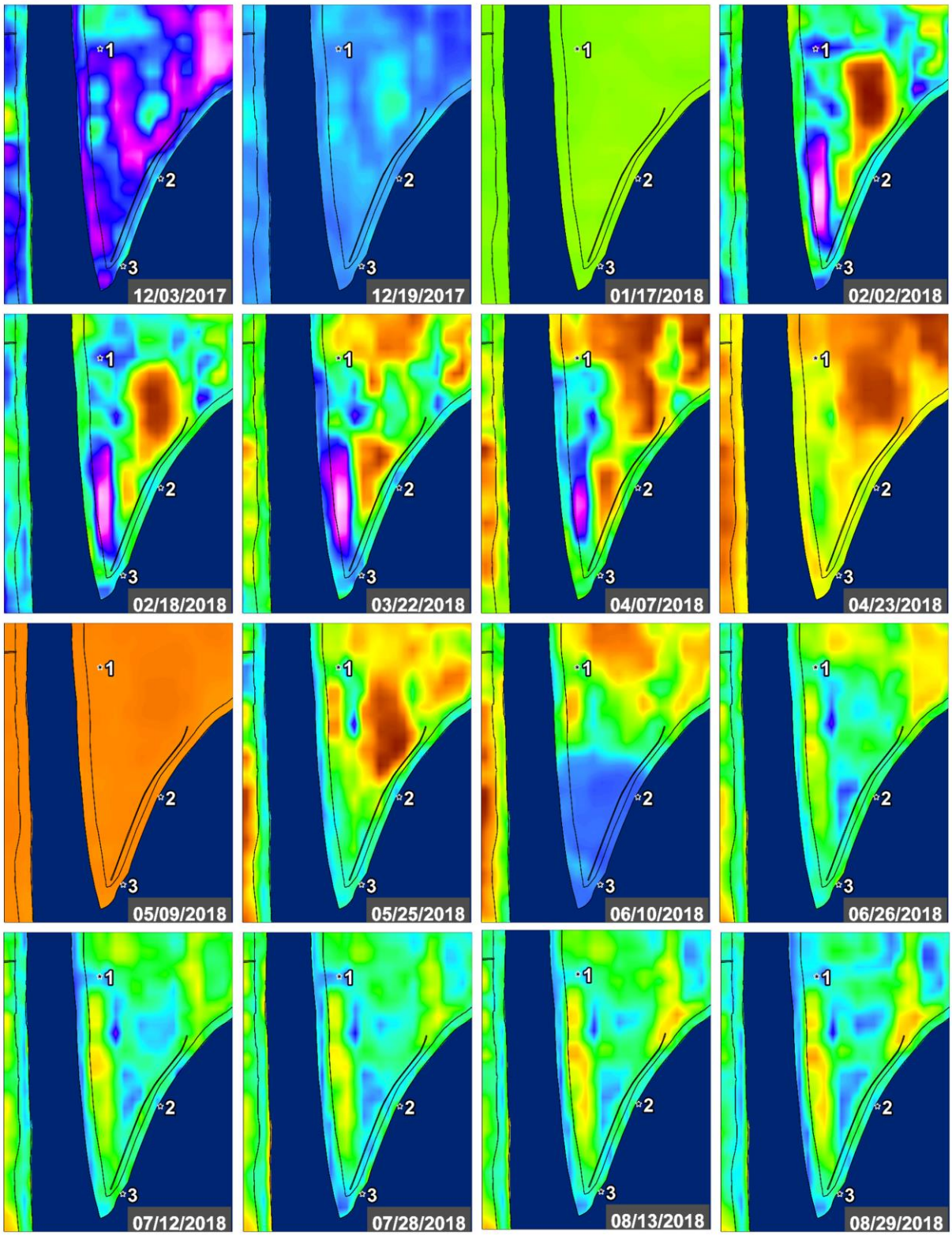

Figure 40K: Seeps 1-3 – NDWI

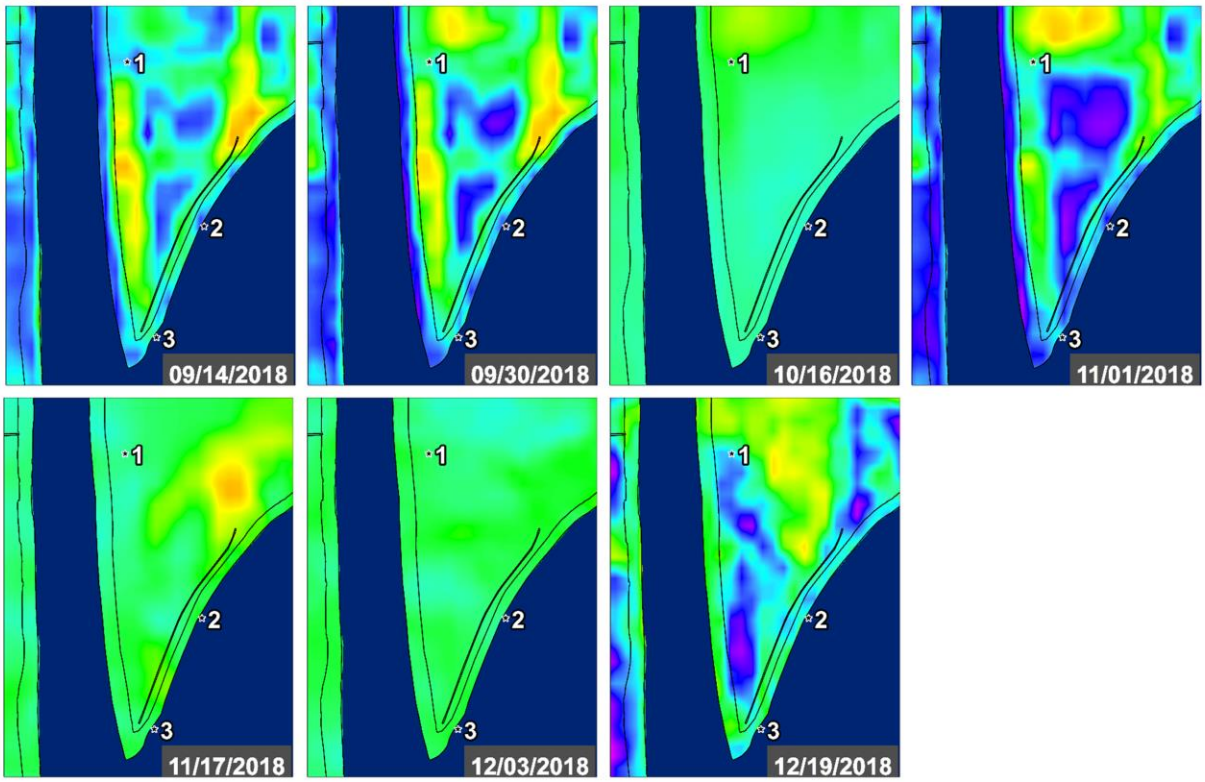

Figure 41A: Seeps 1-3 – VV/HH Ratio – Line 05519

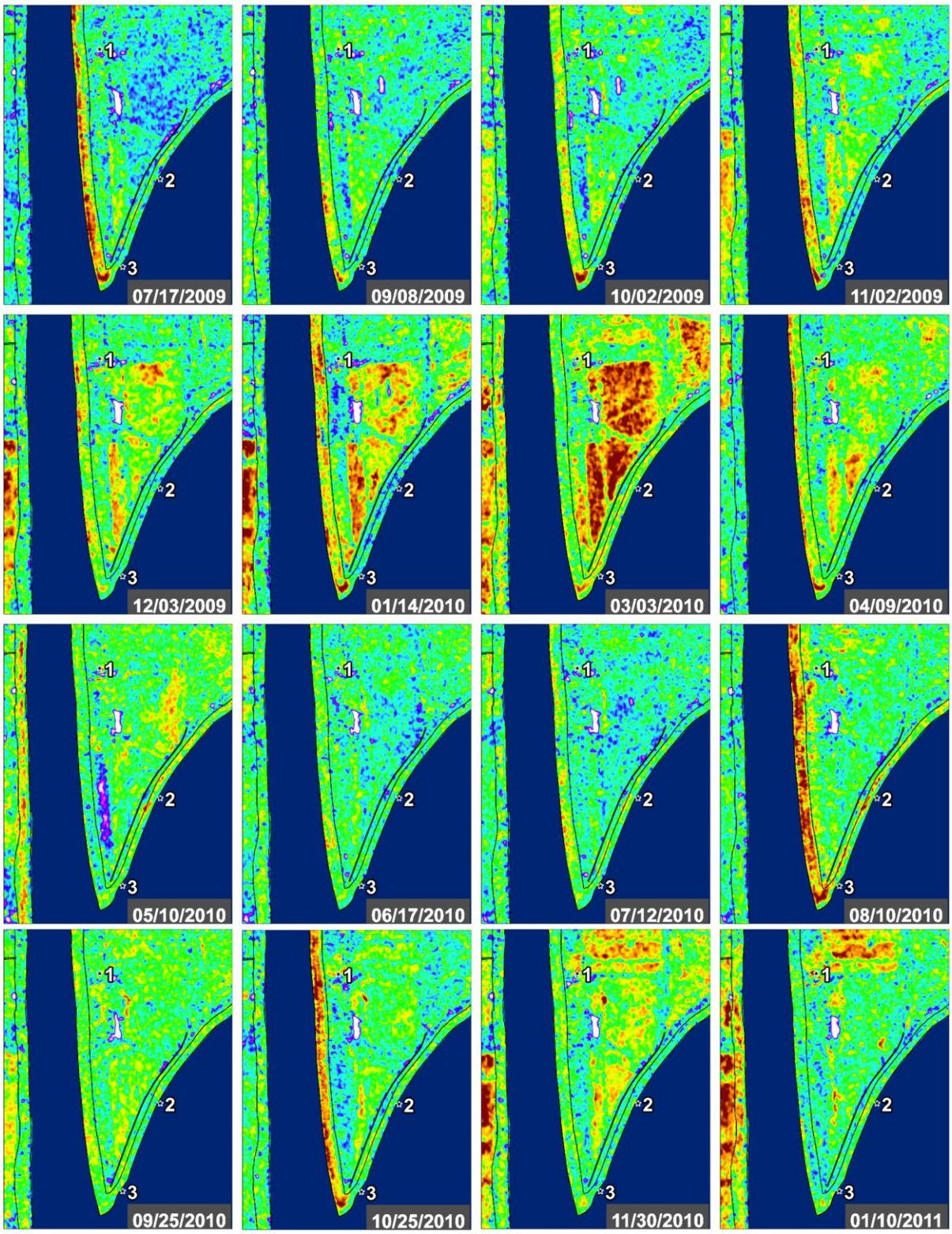

Figure 41B: Seeps 1-3 – VV/HH Ratio – Line 05519

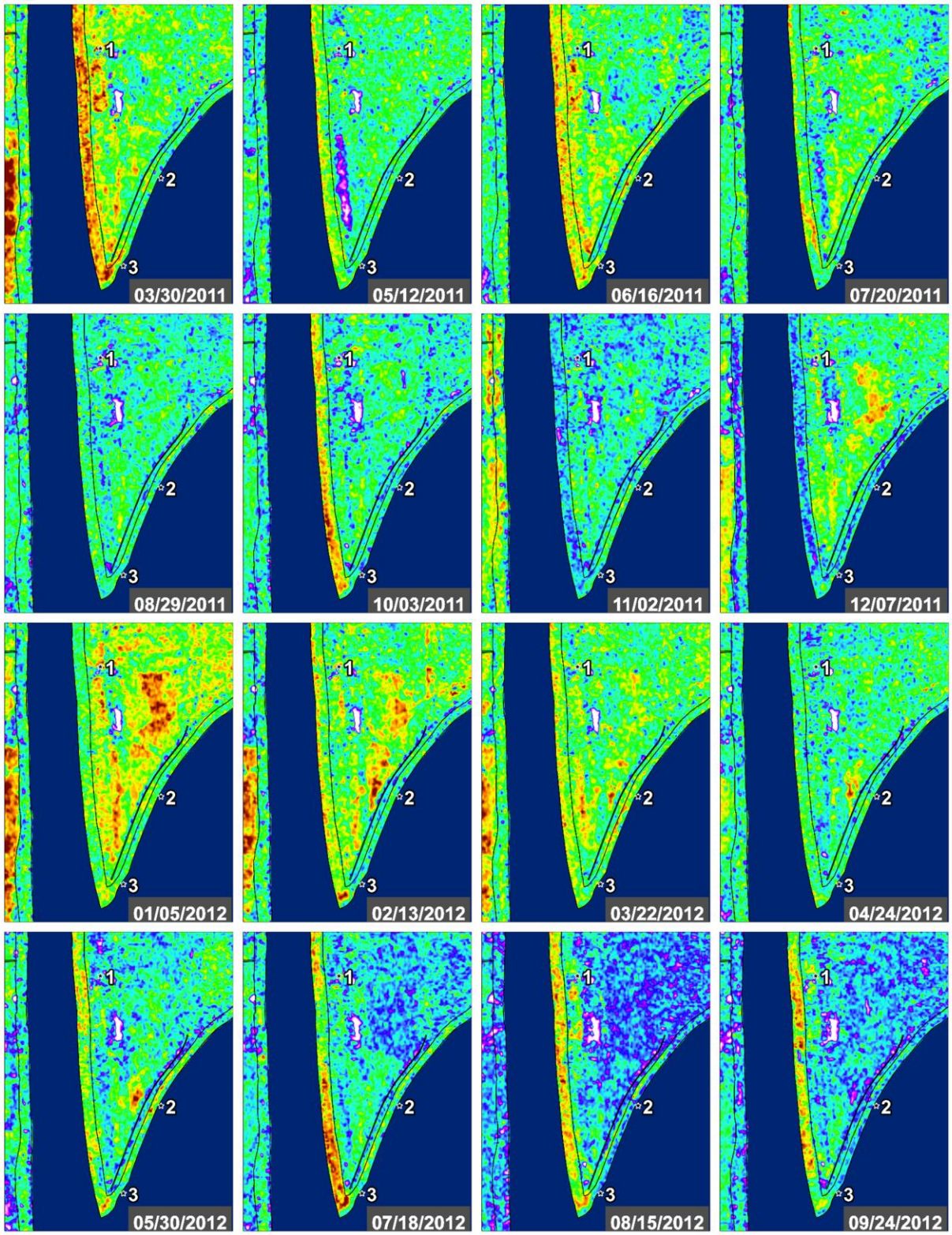

Figure 41C: Seeps 1-3 – VV/HH Ratio – Line 05519

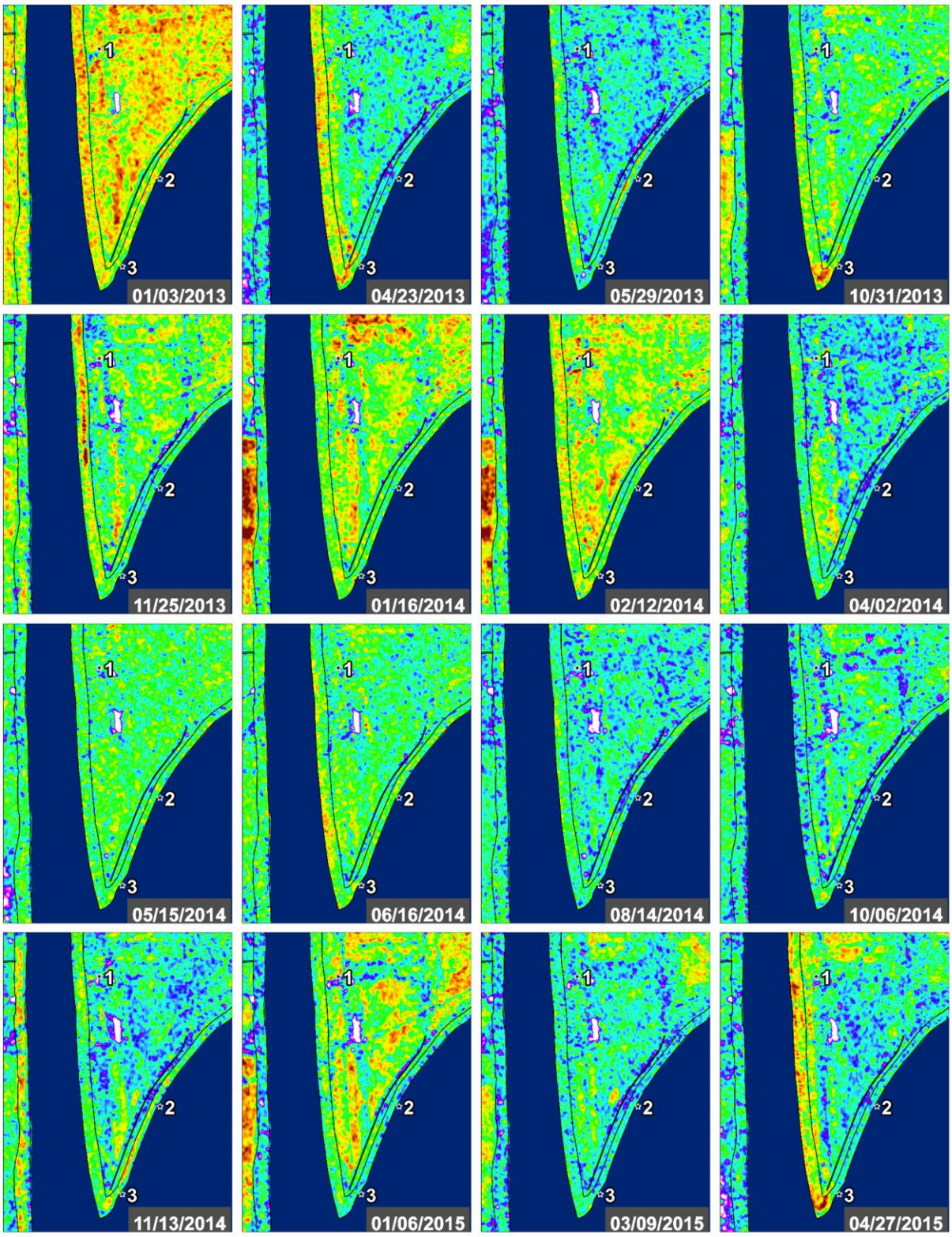

Figure 41D: Seeps 1-3 – VV/HH Ratio – Line 05519

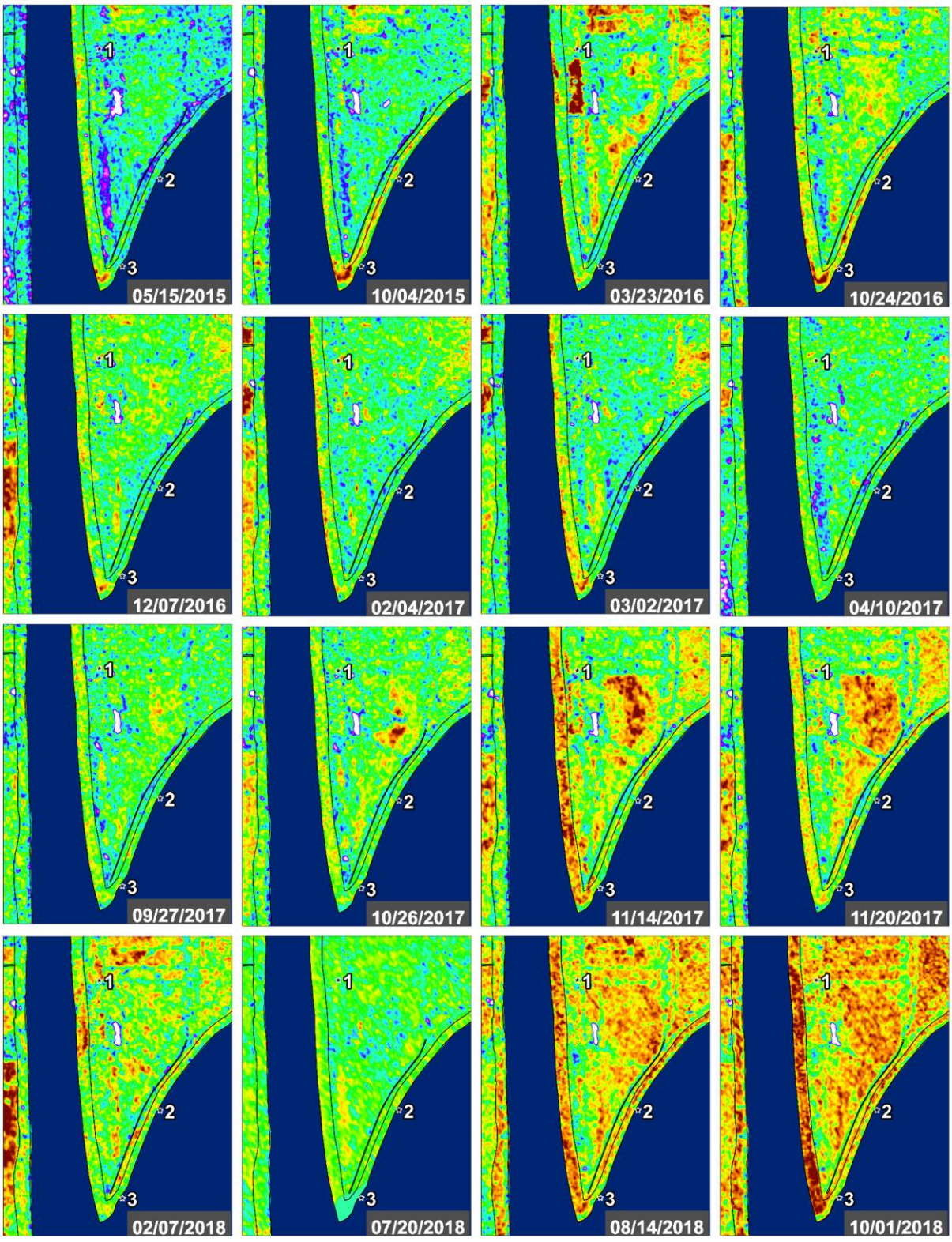

Figure 41E: Seeps 1-3 – VV/HH Ratio – Line 05519

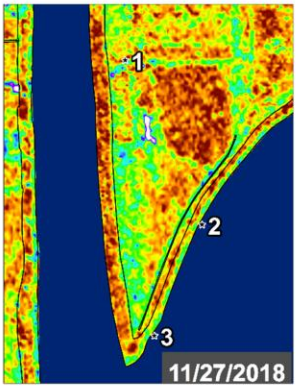

Figure 42A: Seeps 1-3 – VV/HH Ratio – Line 15502

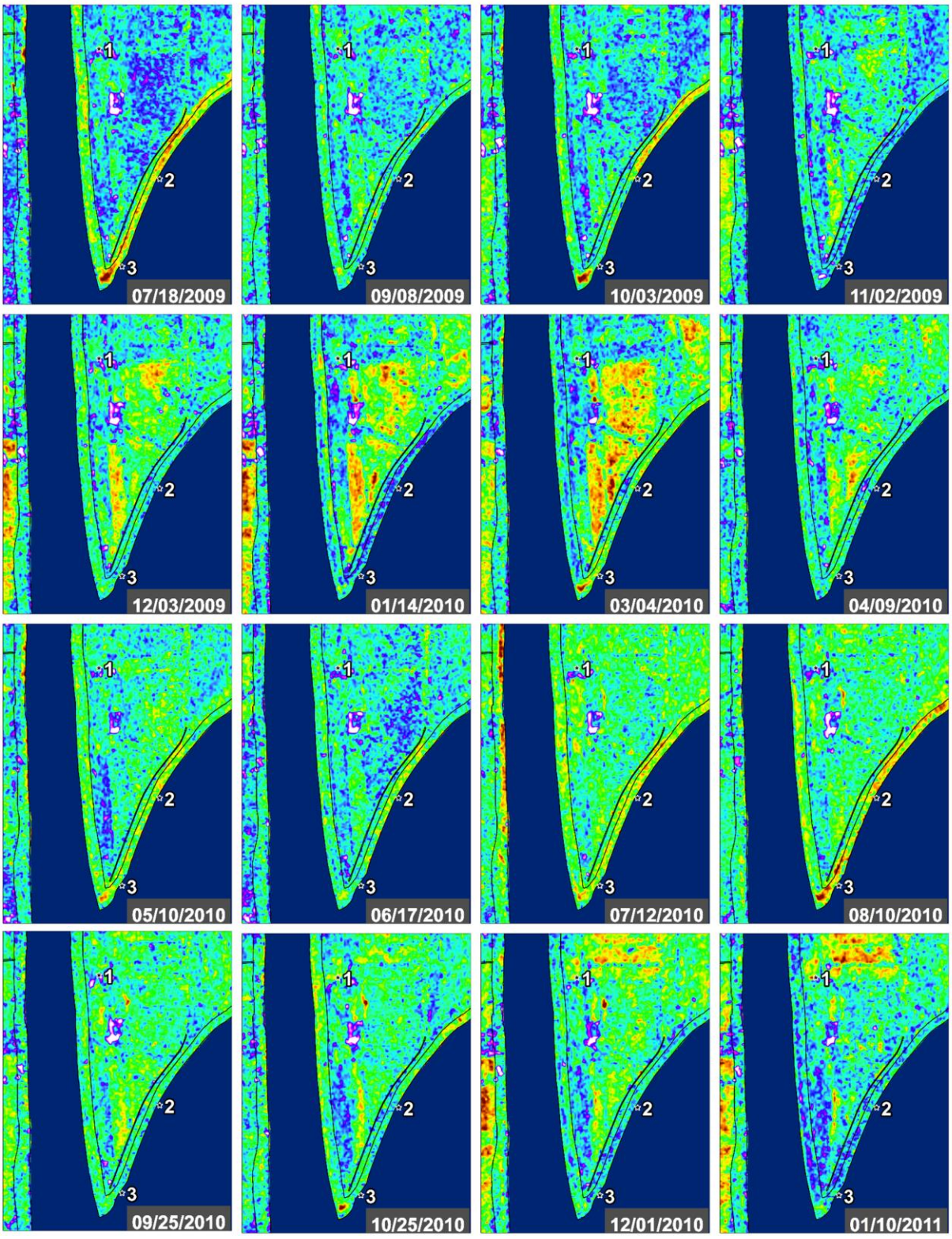

Figure 42B: Seeps 1-3 – VV/HH Ratio – Line 15502

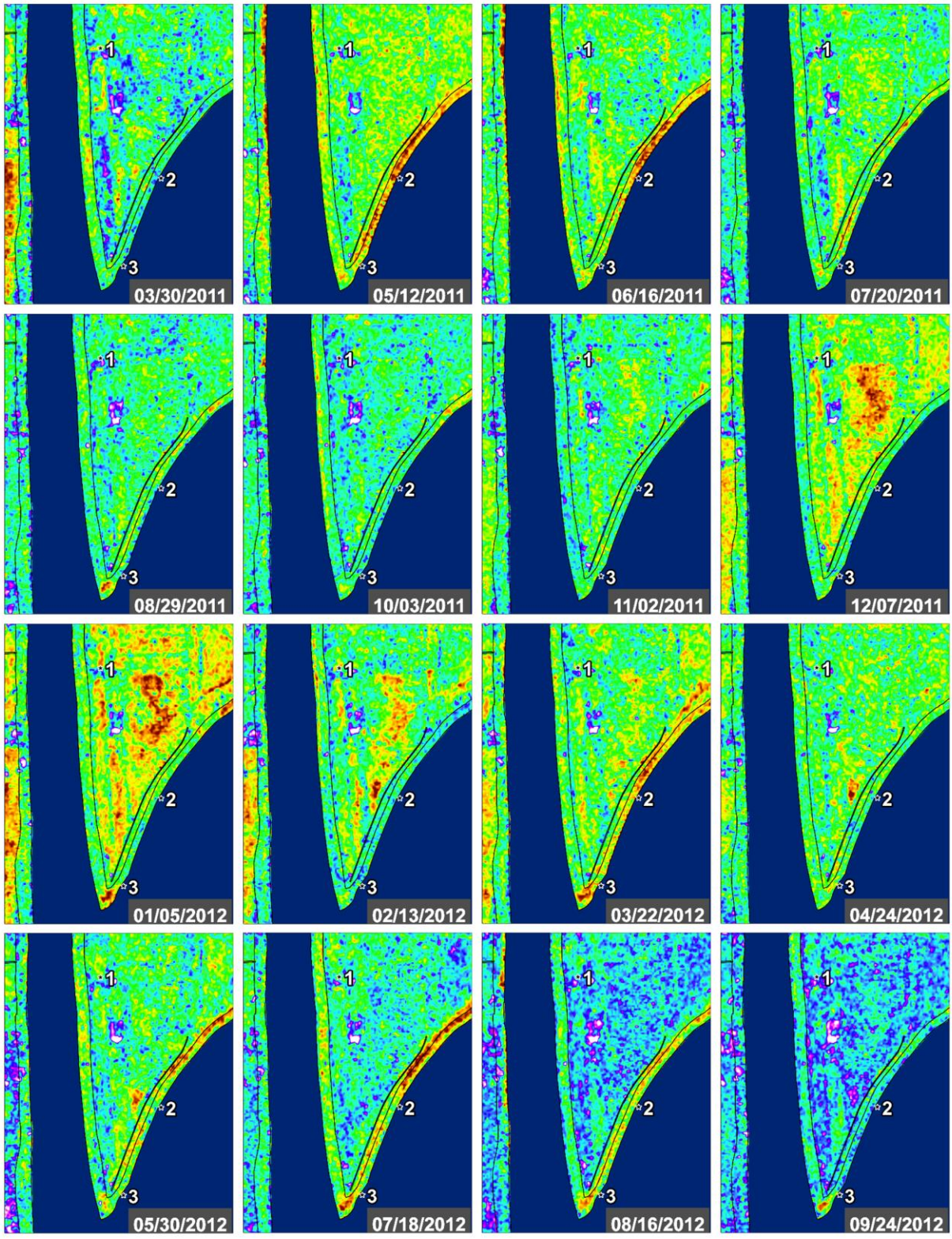

Figure 42C: Seeps 1-3 – VV/HH Ratio – Line 15502

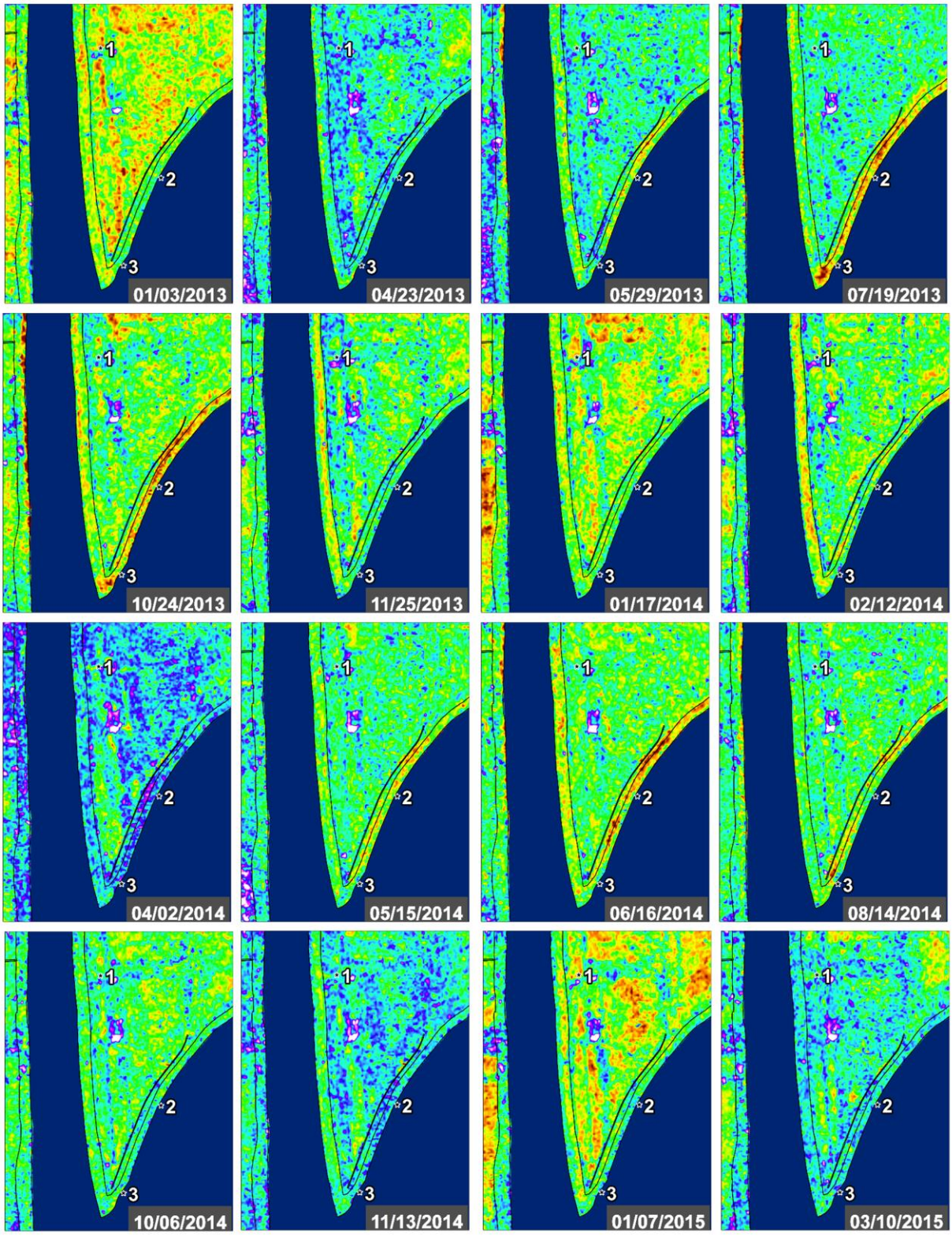

Figure 42D: Seeps 1-3 – VV/HH Ratio – Line 15502

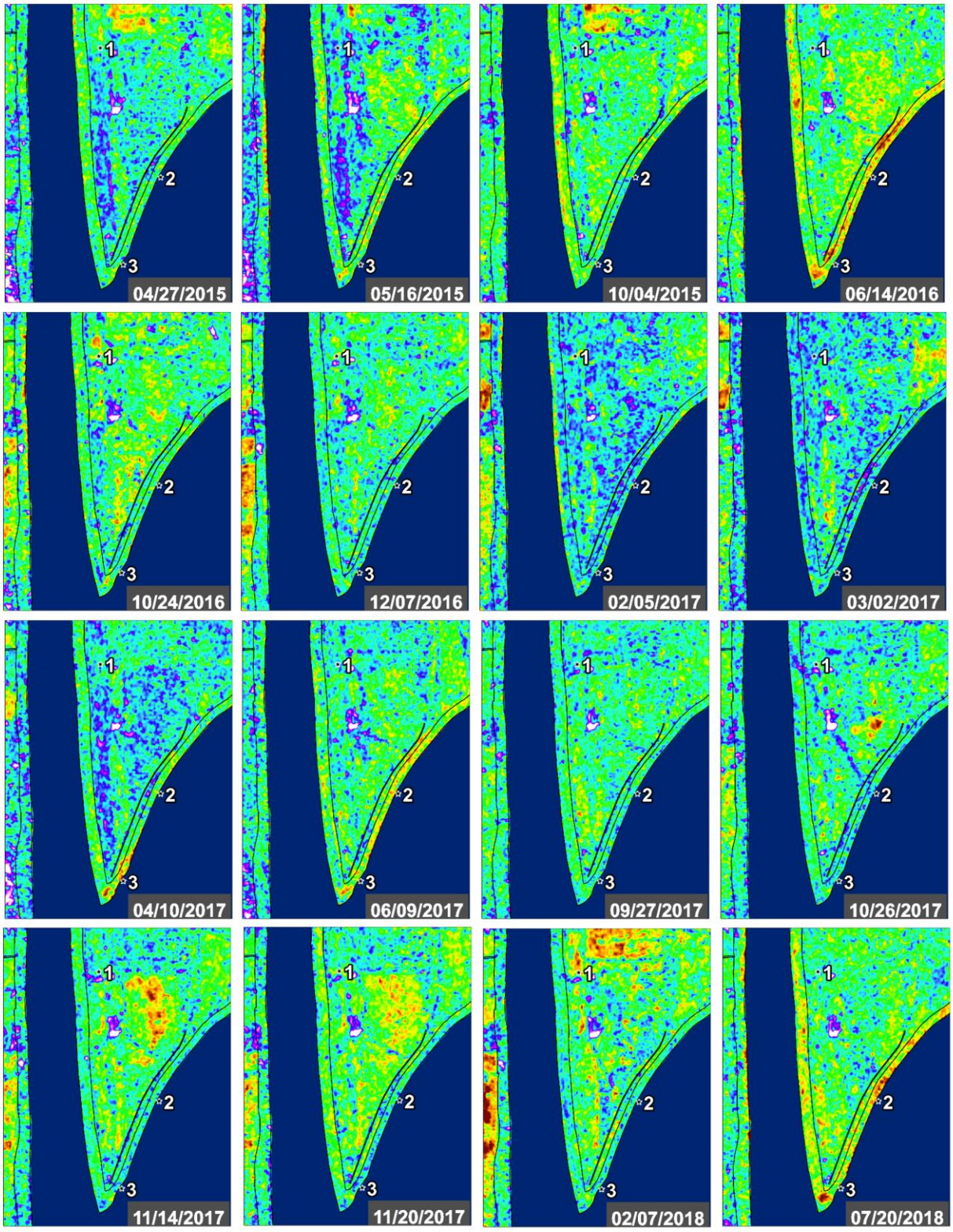

Figure 42E: Seeps 1-3 – VV/HH Ratio – Line 15502

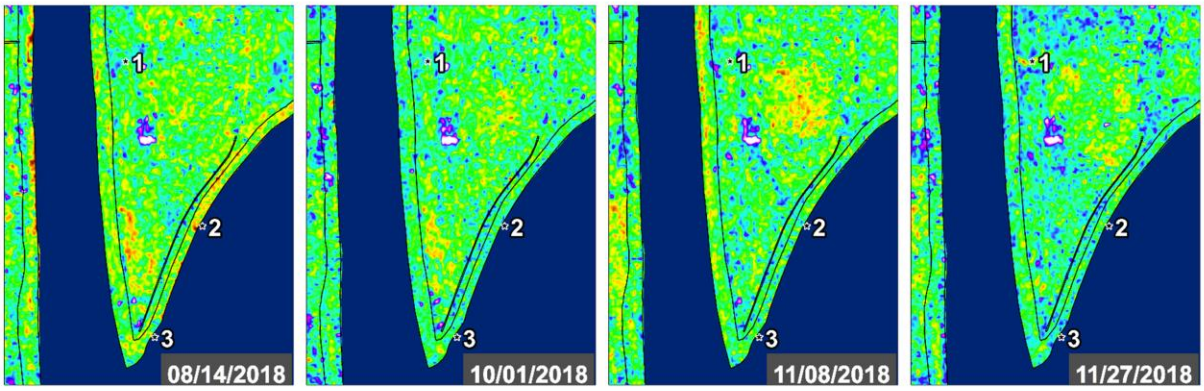

Figure 43A: Seeps 1-3 – VV/HH Ratio – Line 33502

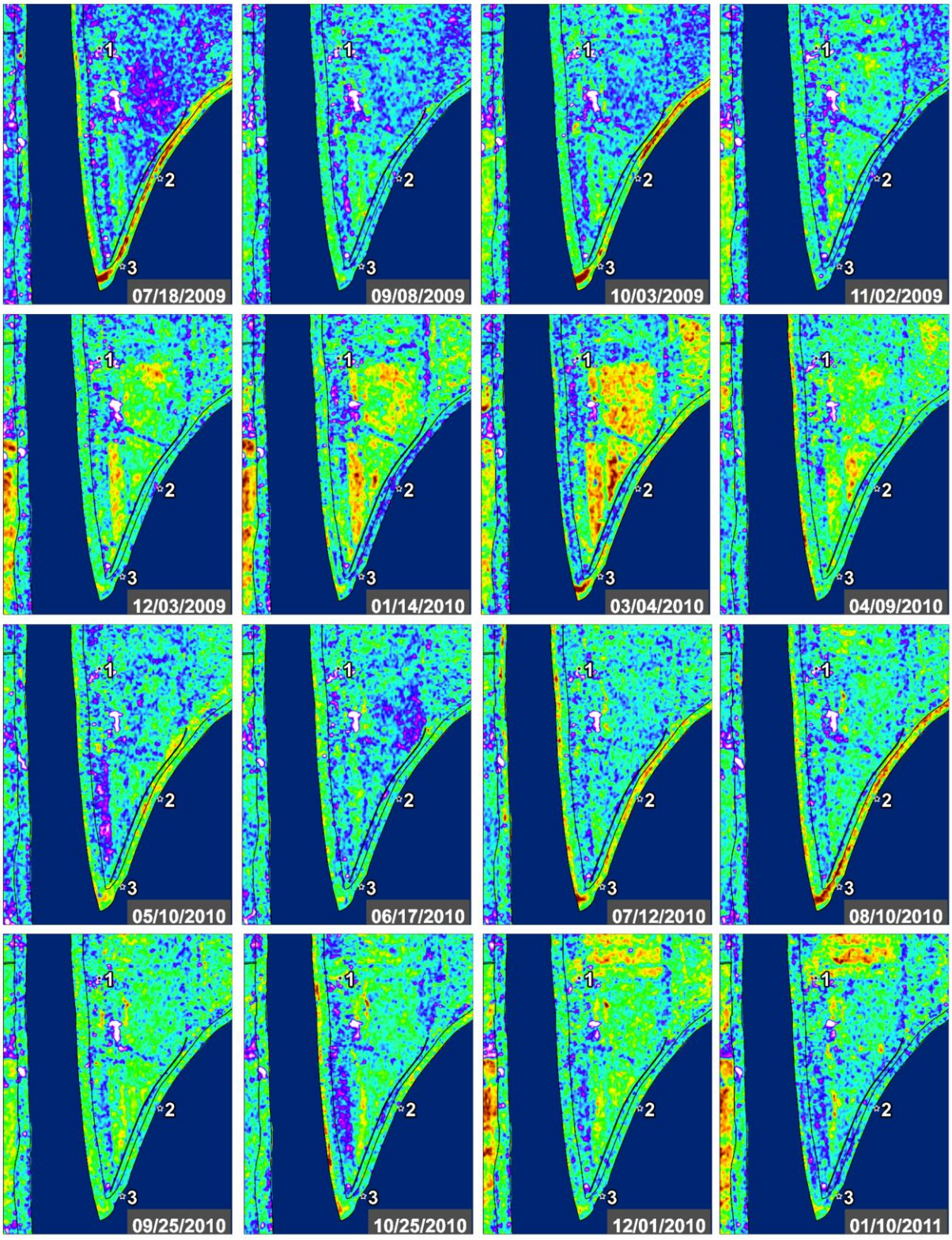

Figure 43B: Seeps 1-3 – VV/HH Ratio – Line 33502

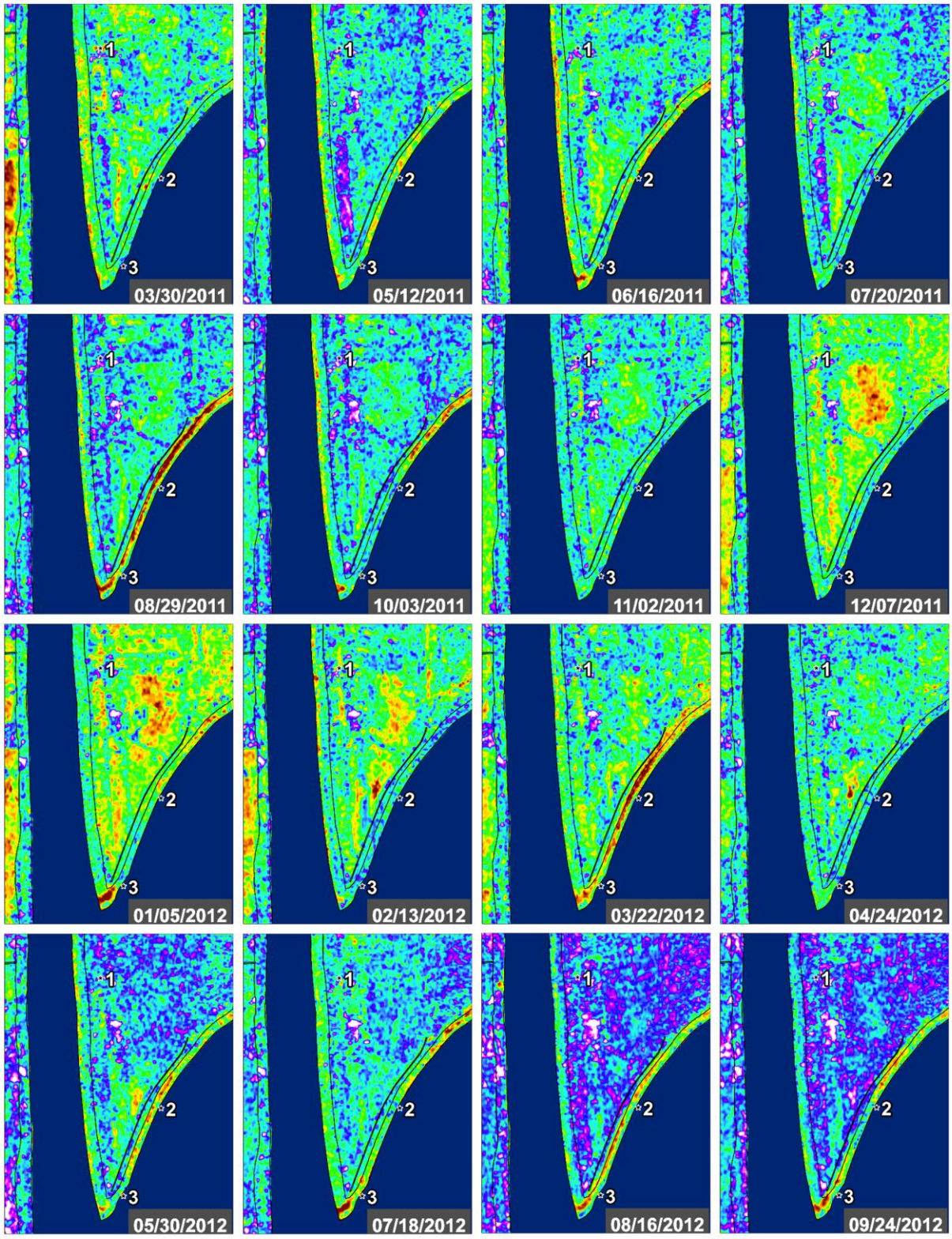

Figure 43C: Seeps 1-3 – VV/HH Ratio – Line 33502

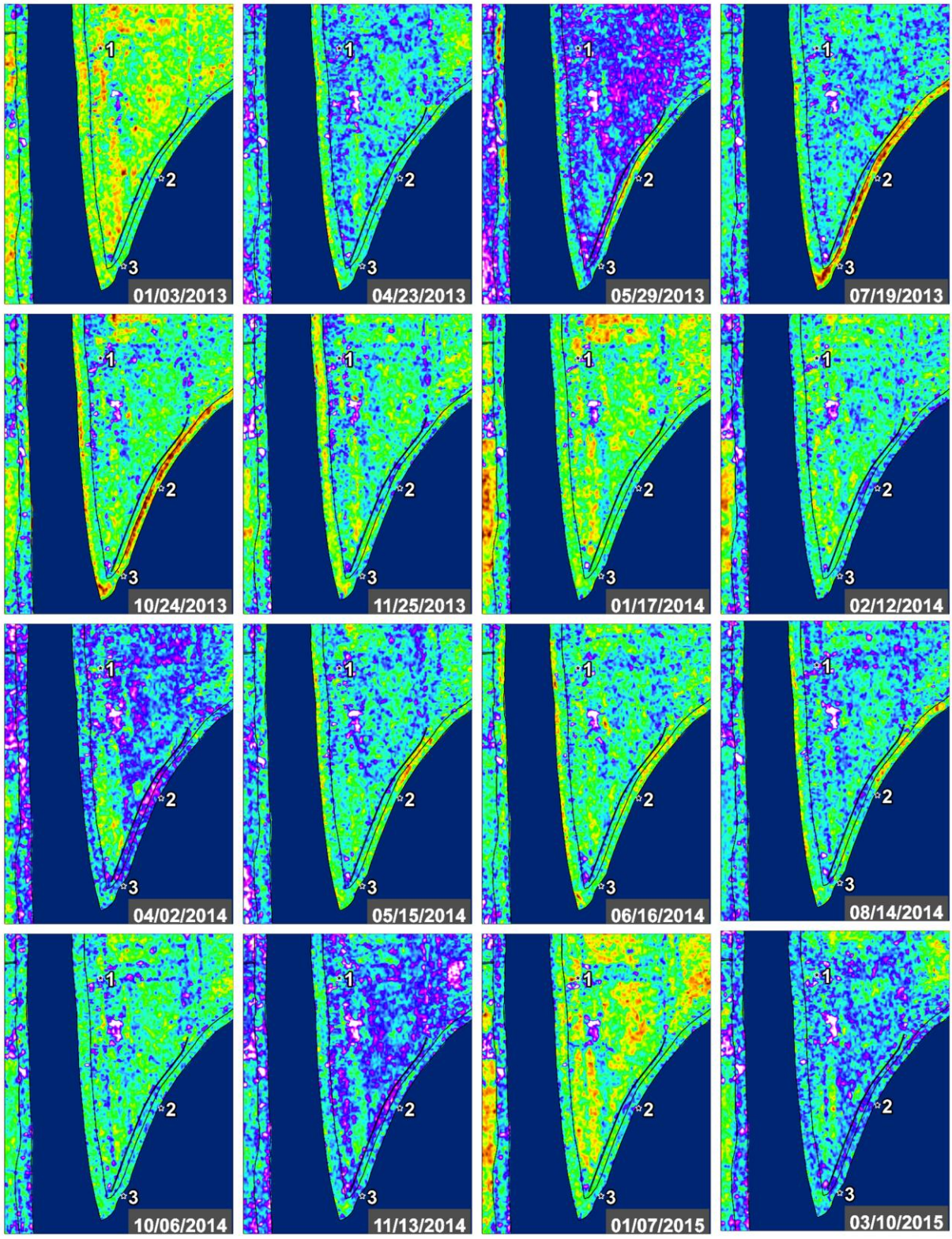

Figure 43D: Seeps 1-3 – VV/HH Ratio – Line 33502

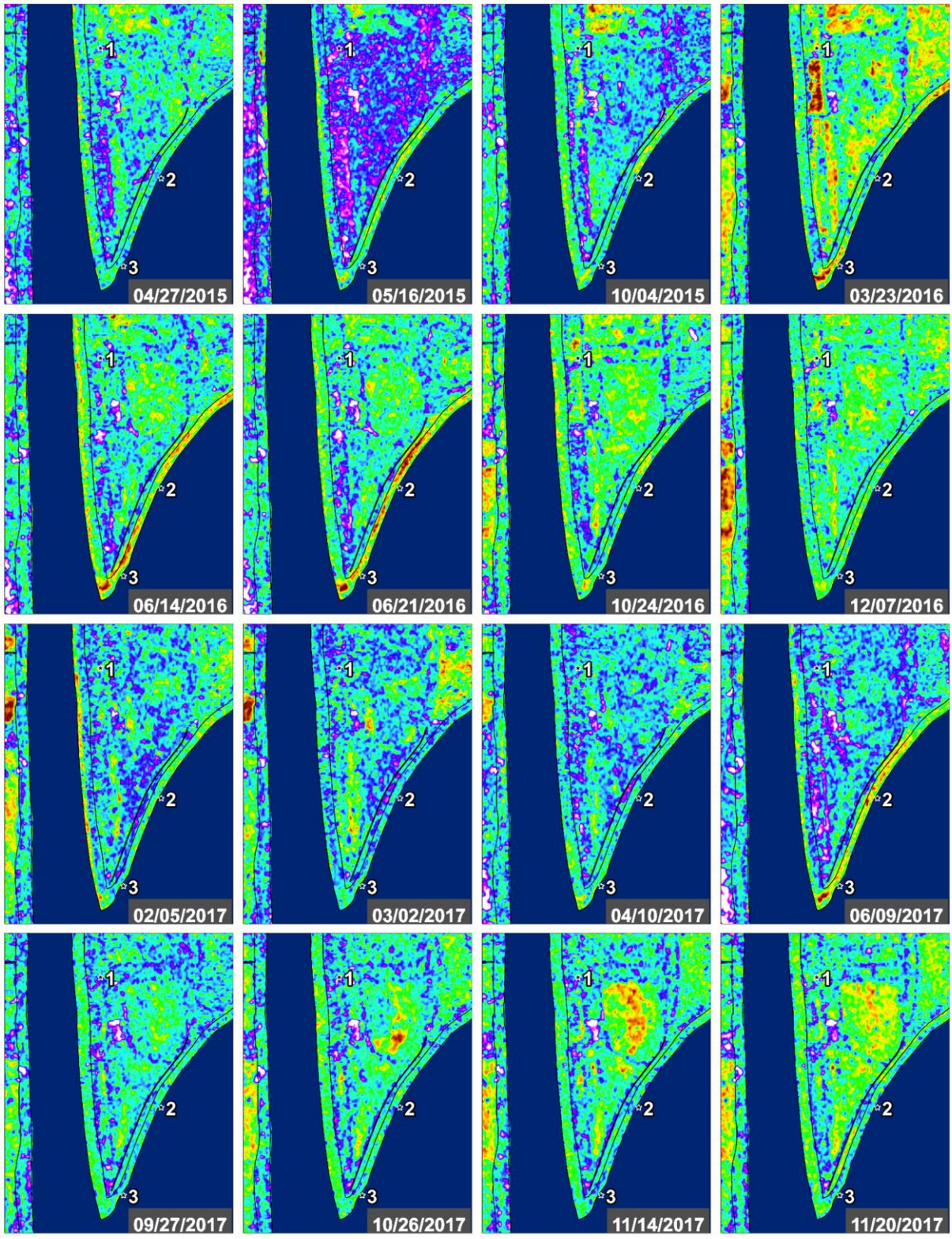

Figure 43E: Seeps 1-3 – VV/HH Ratio – Line 33502

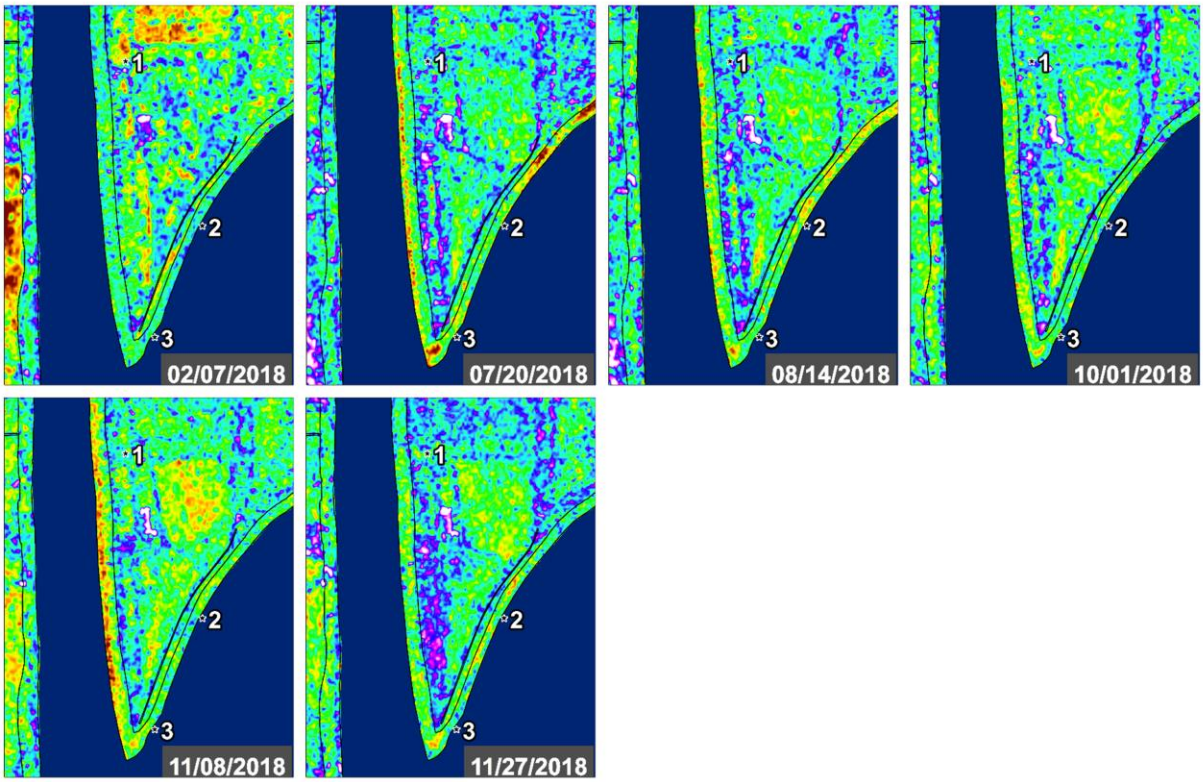

Figure 44A: Seeps 1-3 – VV/HH Ratio – Line 23518

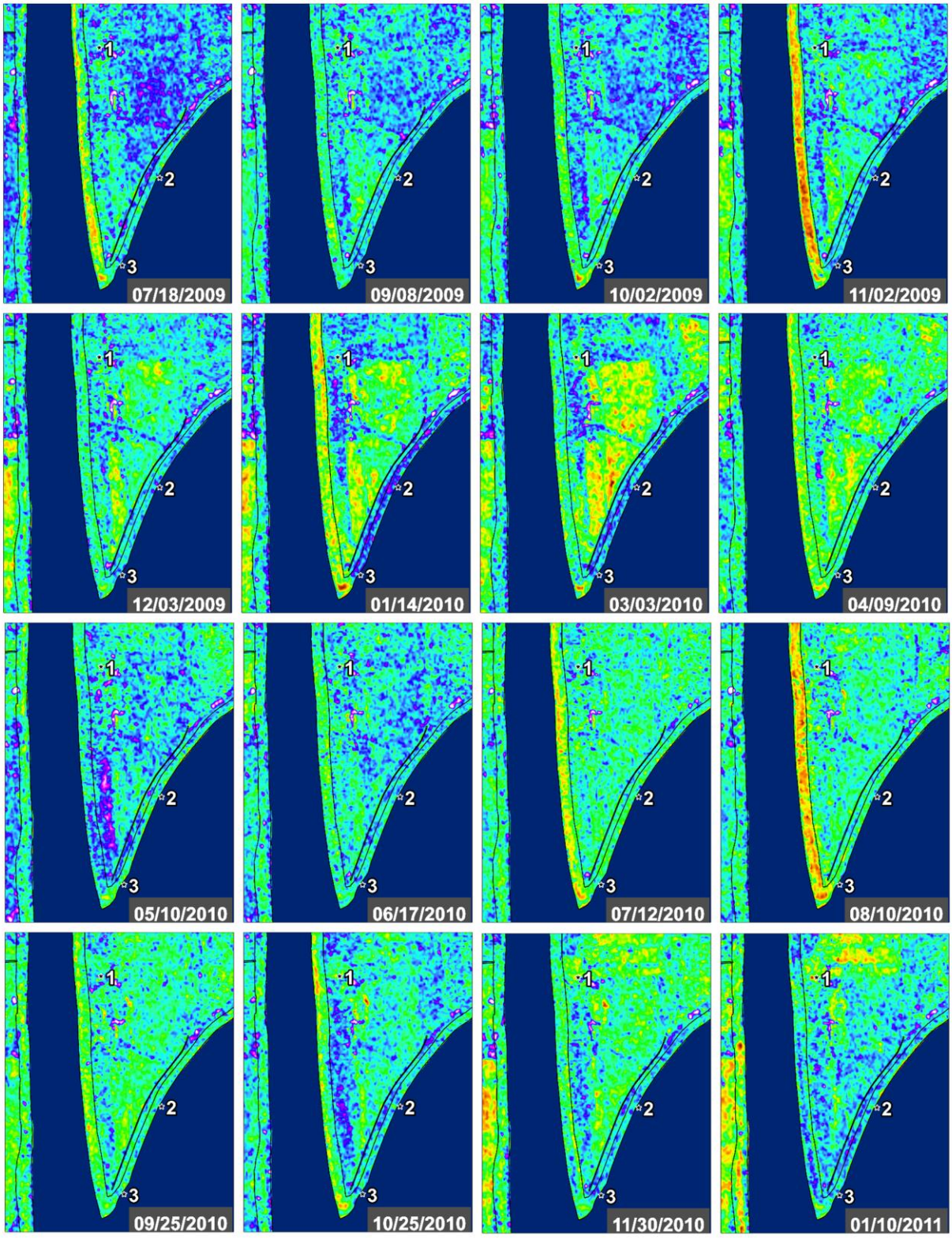

Figure 44B: Seeps 1-3 – VV/HH Ratio – Line 23518

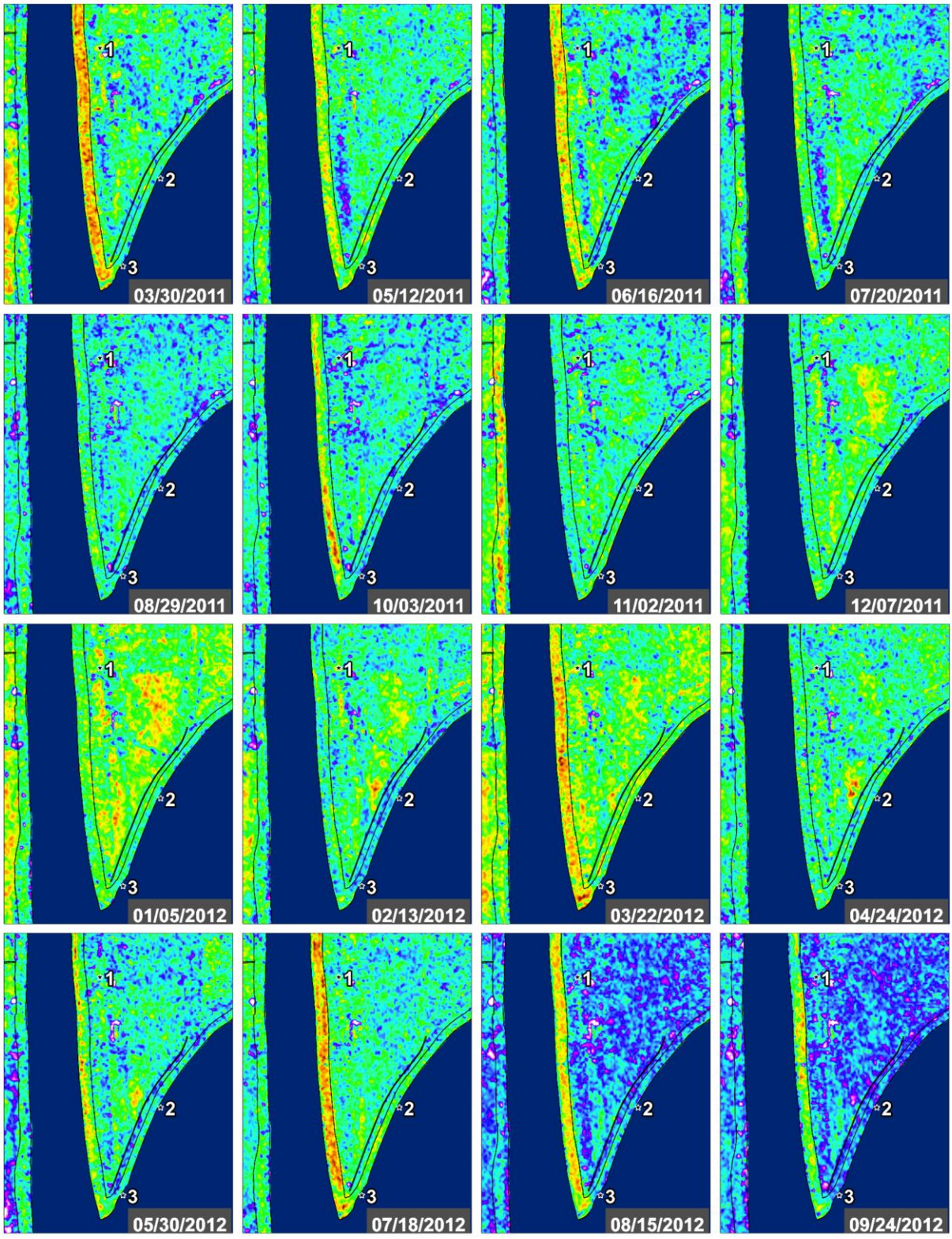

Figure 44C: Seeps 1-3 – VV/HH Ratio – Line 23518

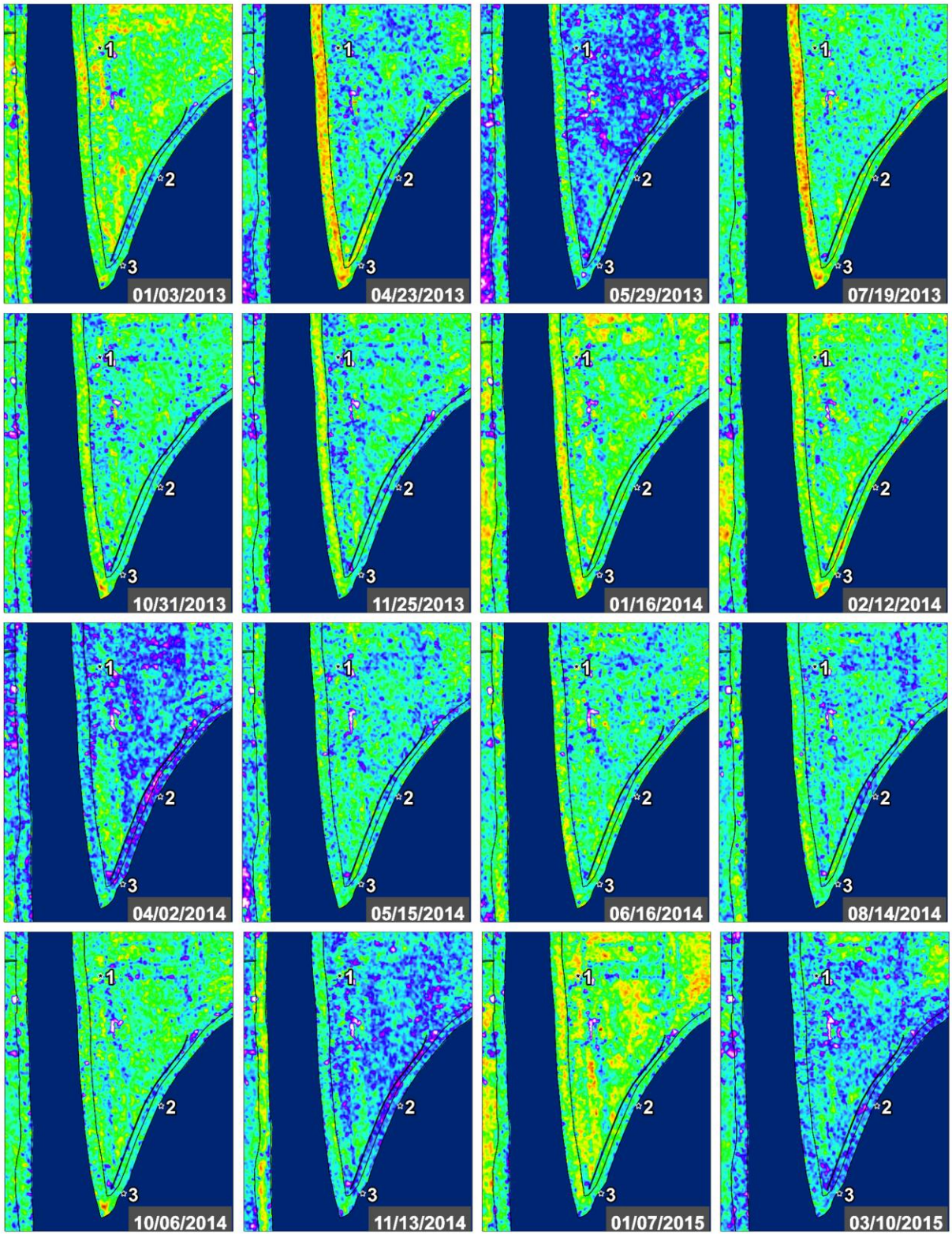

Figure 44D: Seeps 1-3 – VV/HH Ratio – Line 23518

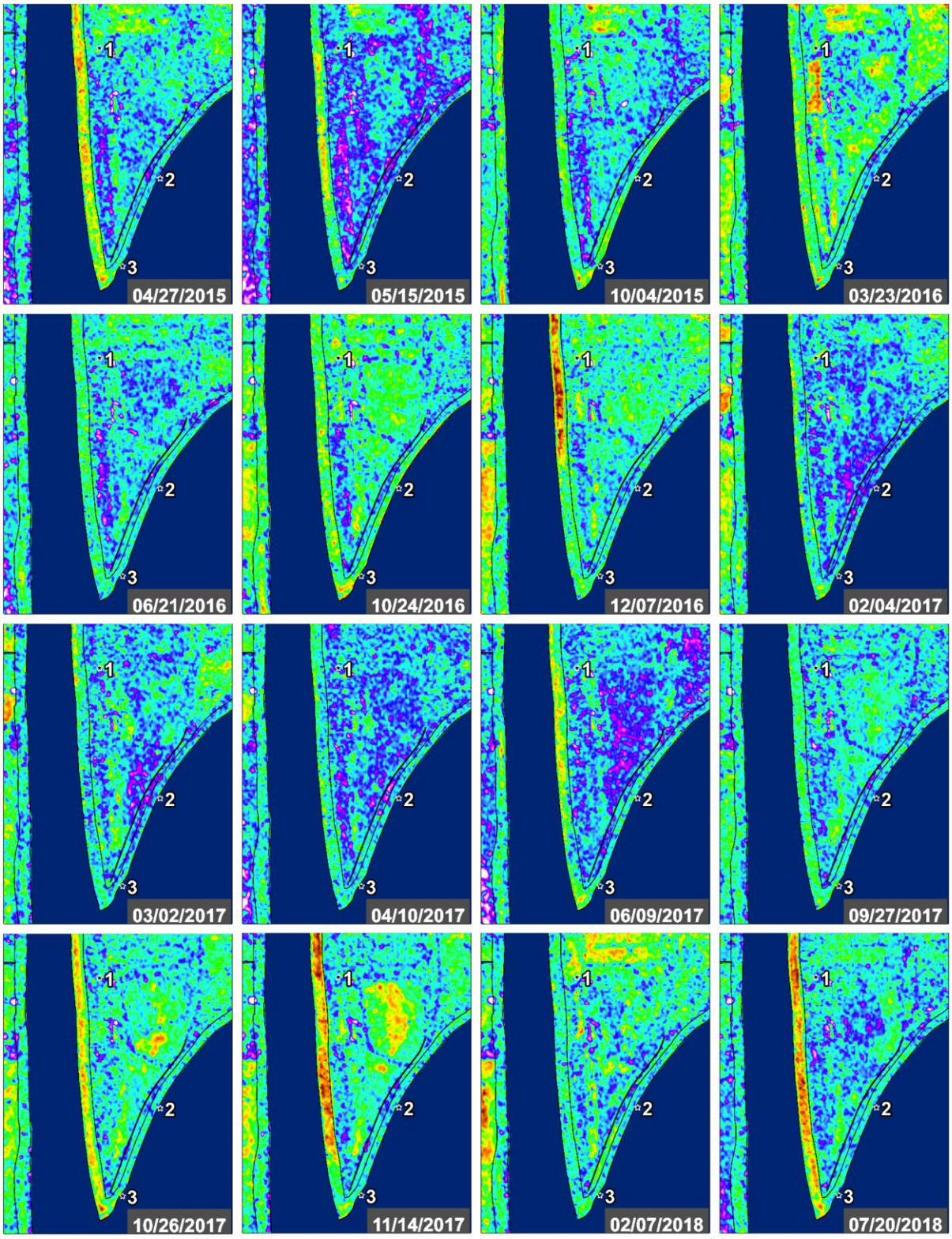

Figure 44E: Seeps 1-3 – VV/HH Ratio – Line 23518

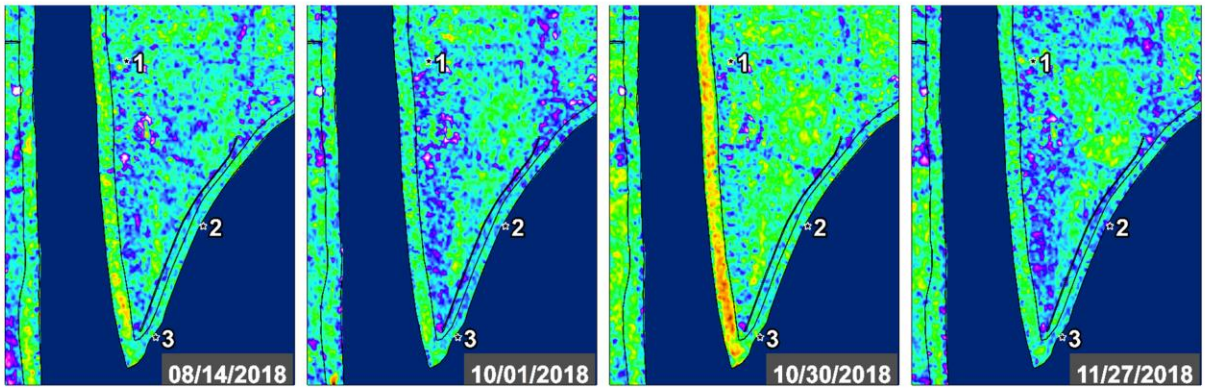

Figure 45: Study area overview for Seep 4 on Twitchell Island.

Figure 46A: Seep 4– Google Earth Imagery

Figure 46B: Seep 4– Google Earth Imagery

Figure 46C: Seep 4– Google Earth Imagery

Figure 46D: Seep 4– Google Earth Imagery

Figure 46E: Seep 4– Google Earth Imagery

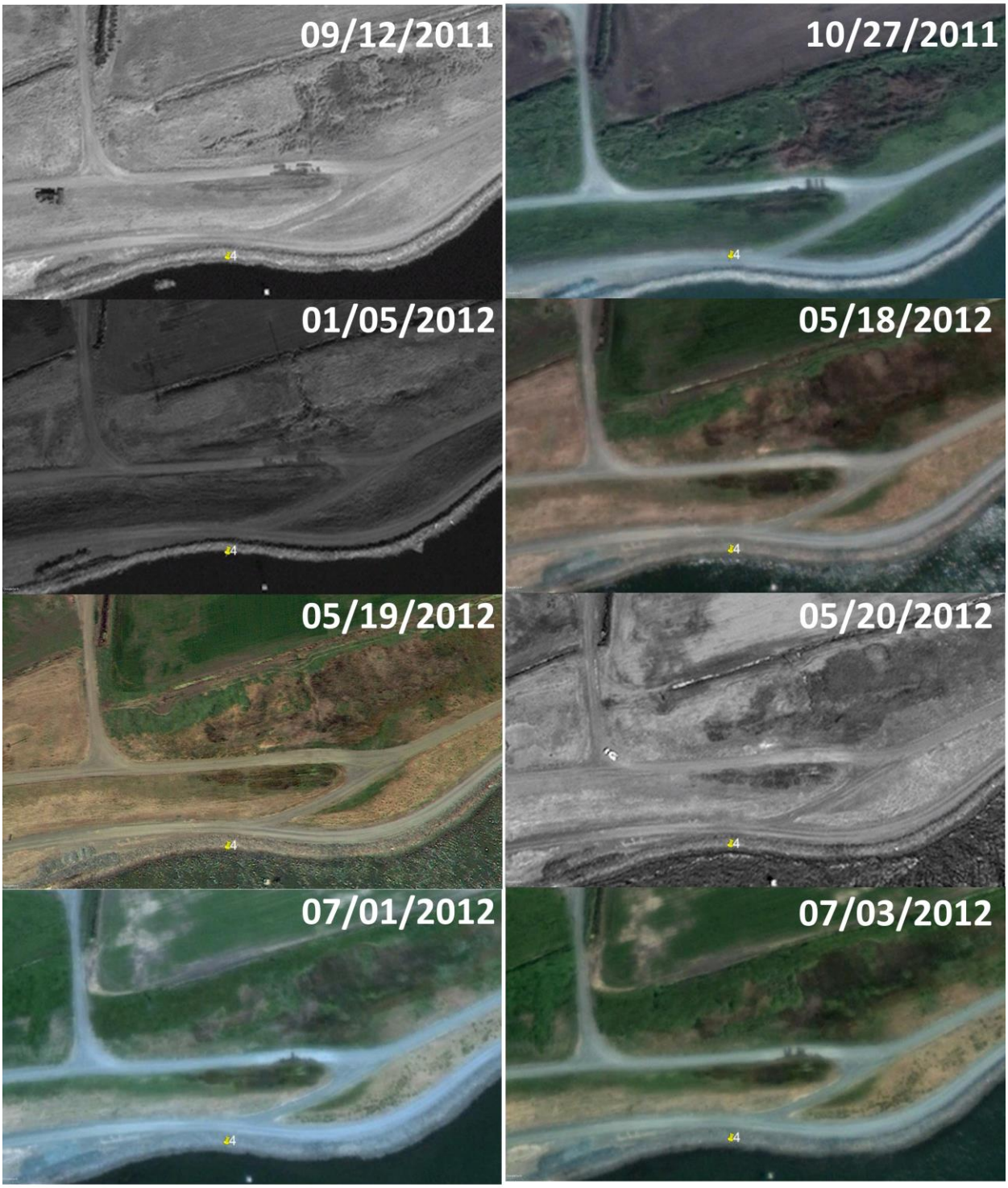

Figure 46F: Seep 4– Google Earth Imagery

Figure 46G: Seep 4– Google Earth Imagery

Figure 47: Legends for NDWI and PolSAR data products.

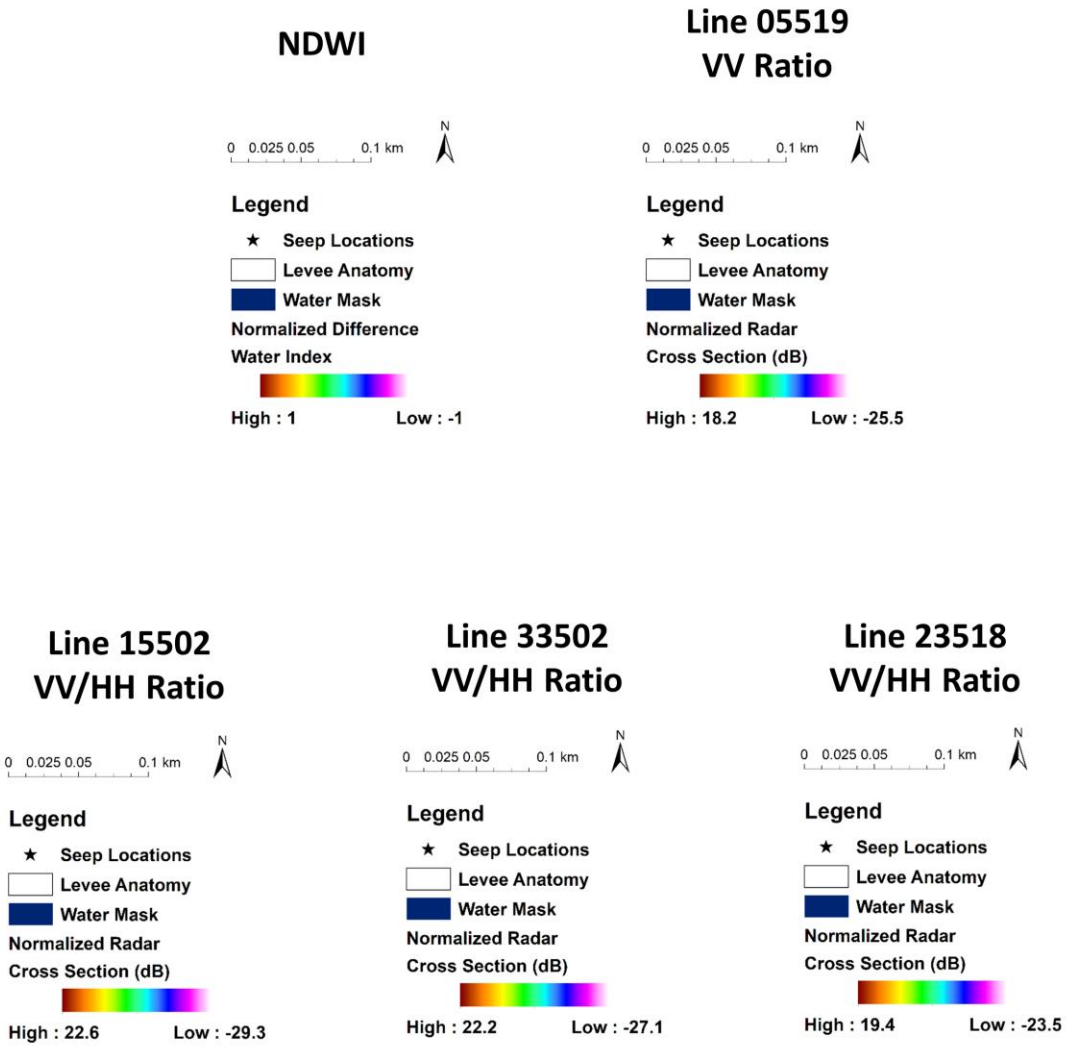

Figure 48A: Seep 4 – NDWI

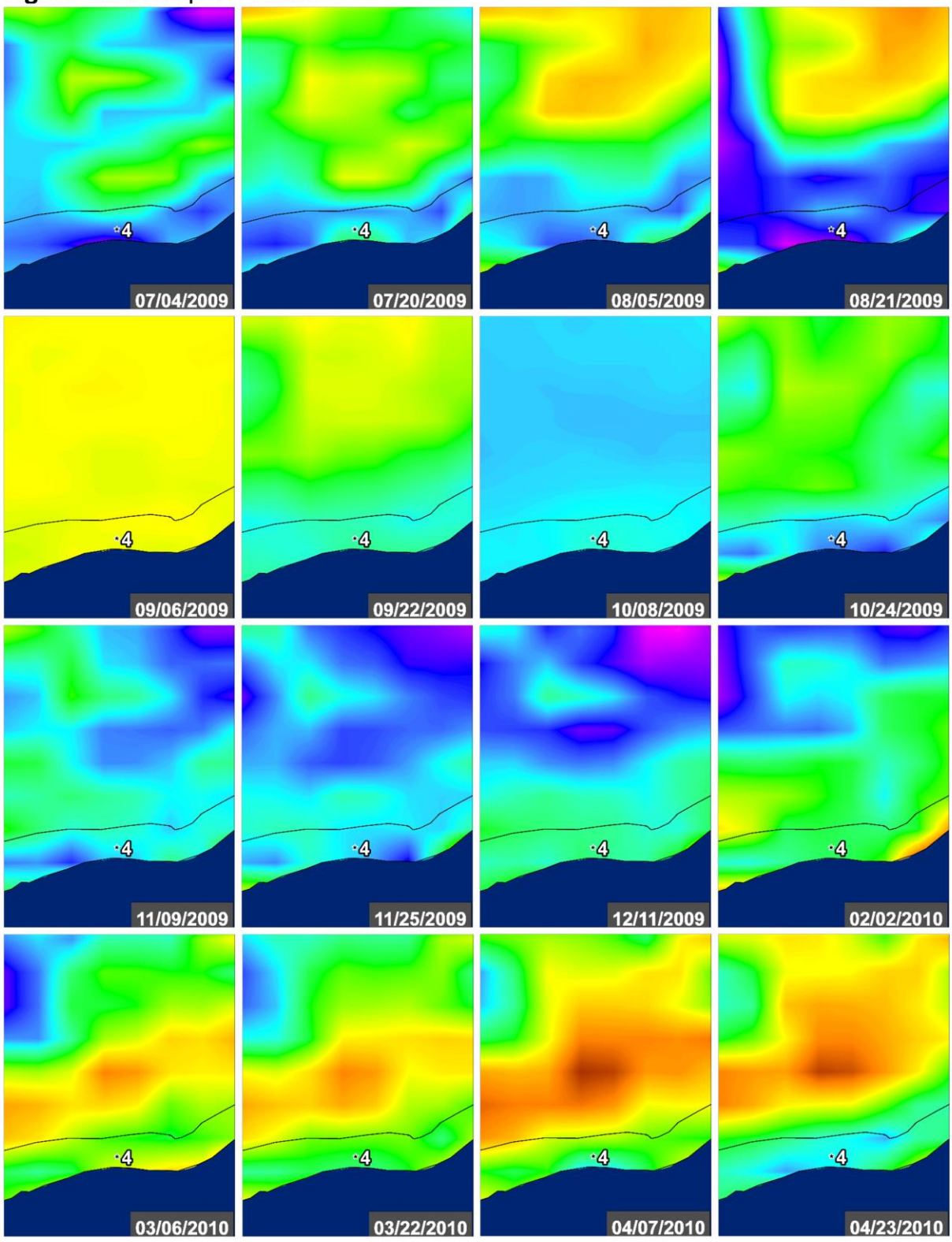

Figure 48B: Seep 4 – NDWI

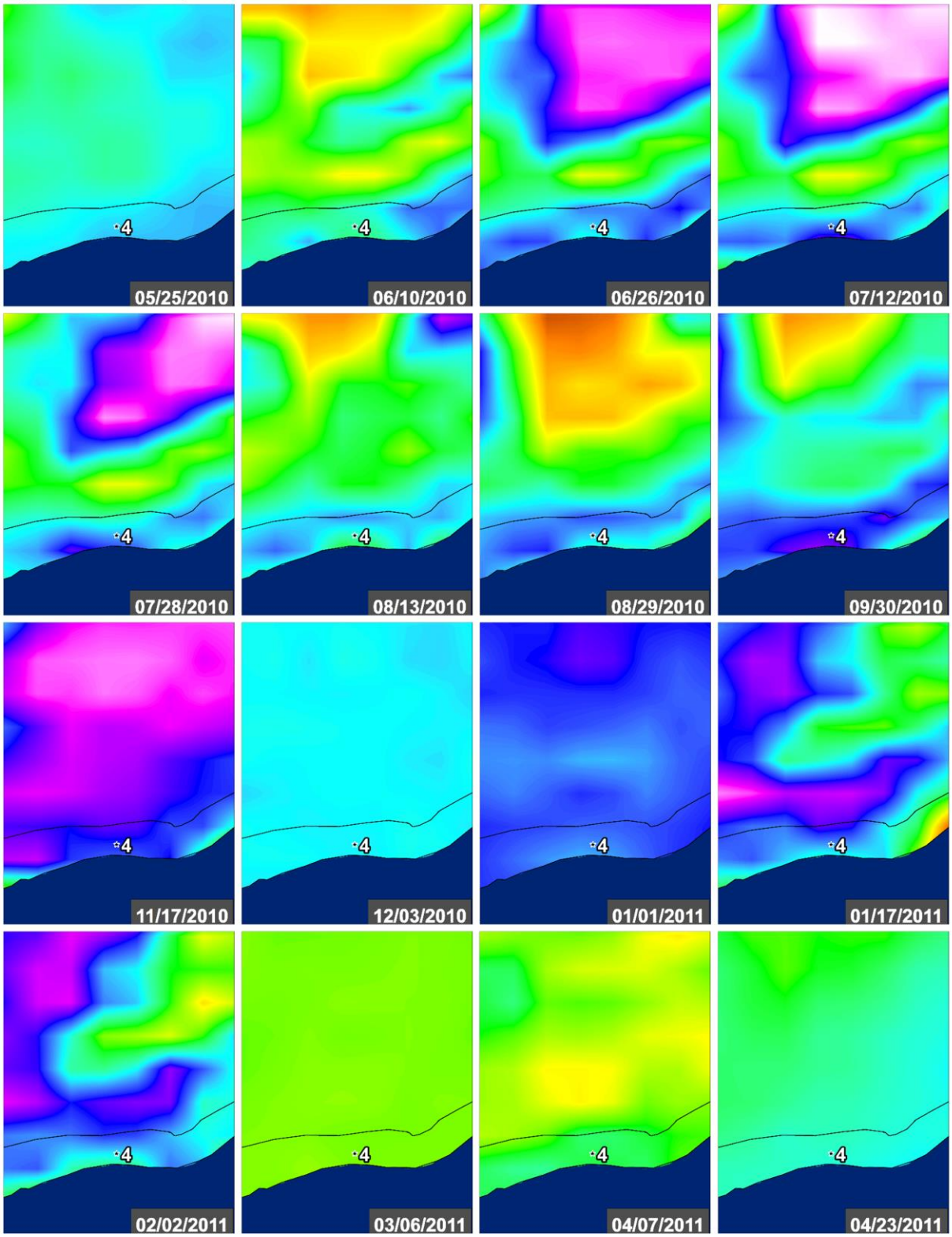

Figure 48C: Seep 4 – NDWI

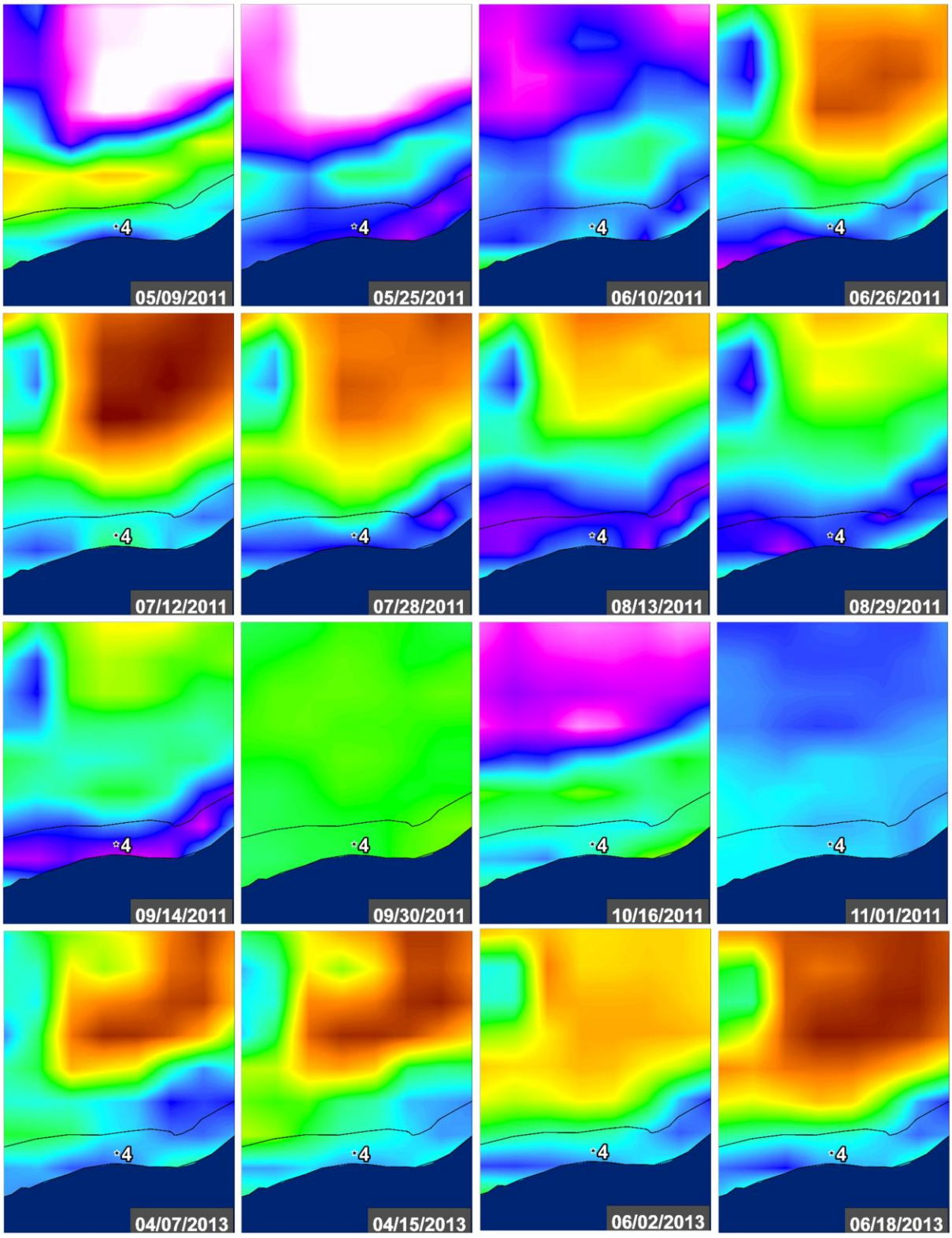

Figure 48D: Seep 4 – NDWI

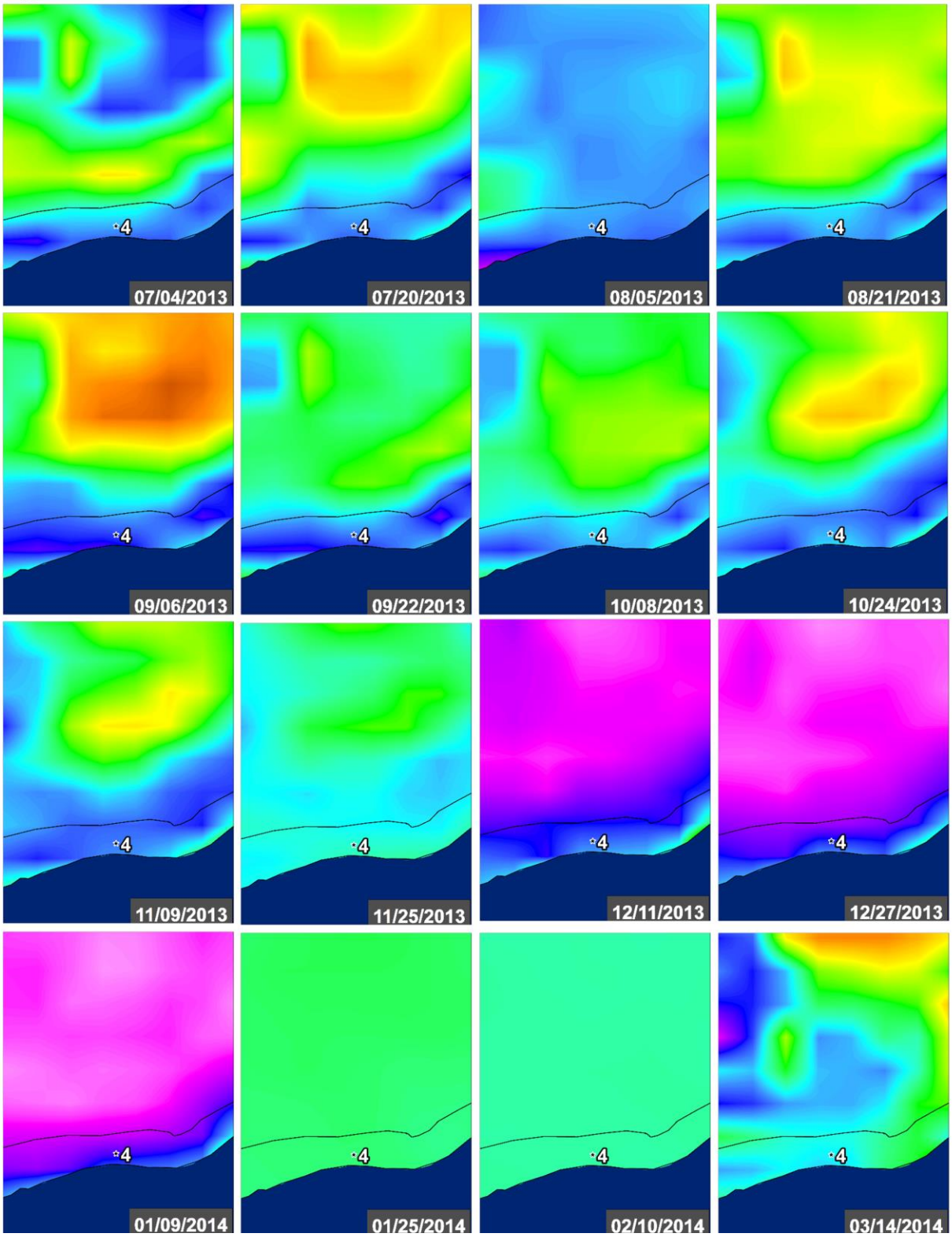

Figure 48E: Seep 4 – NDWI

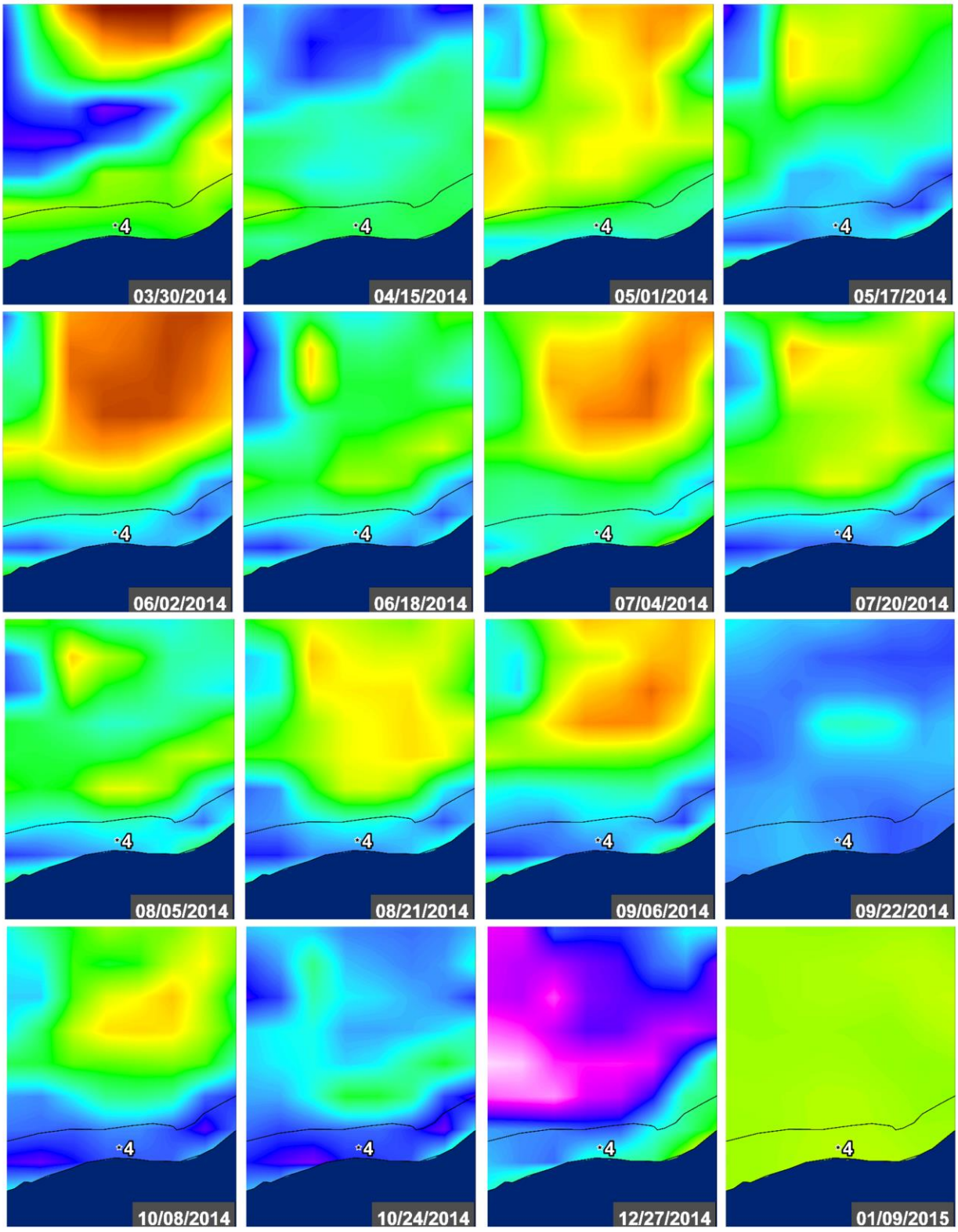

Figure 48F: Seep 4 – NDWI

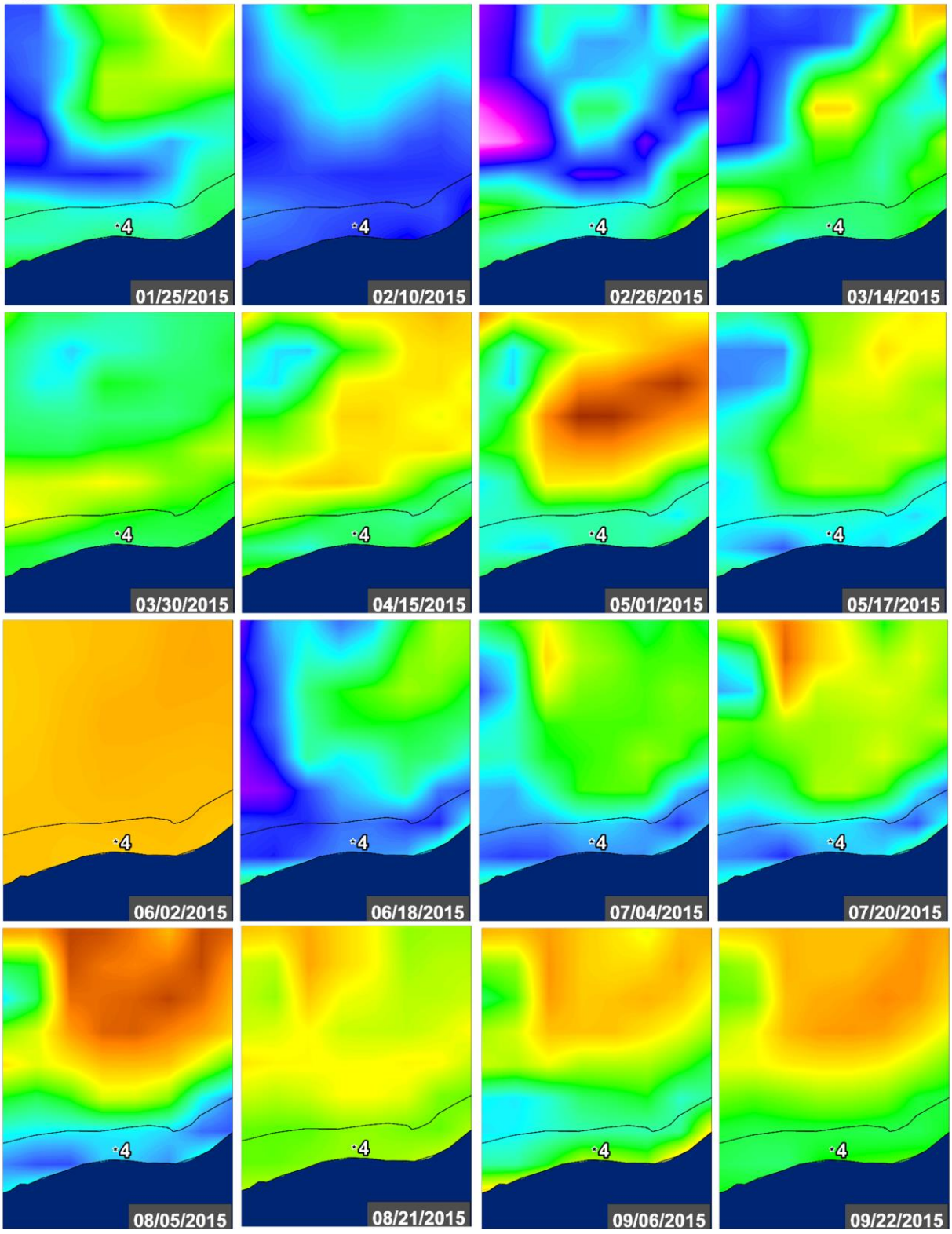

Figure 48G: Seep 4 – NDWI

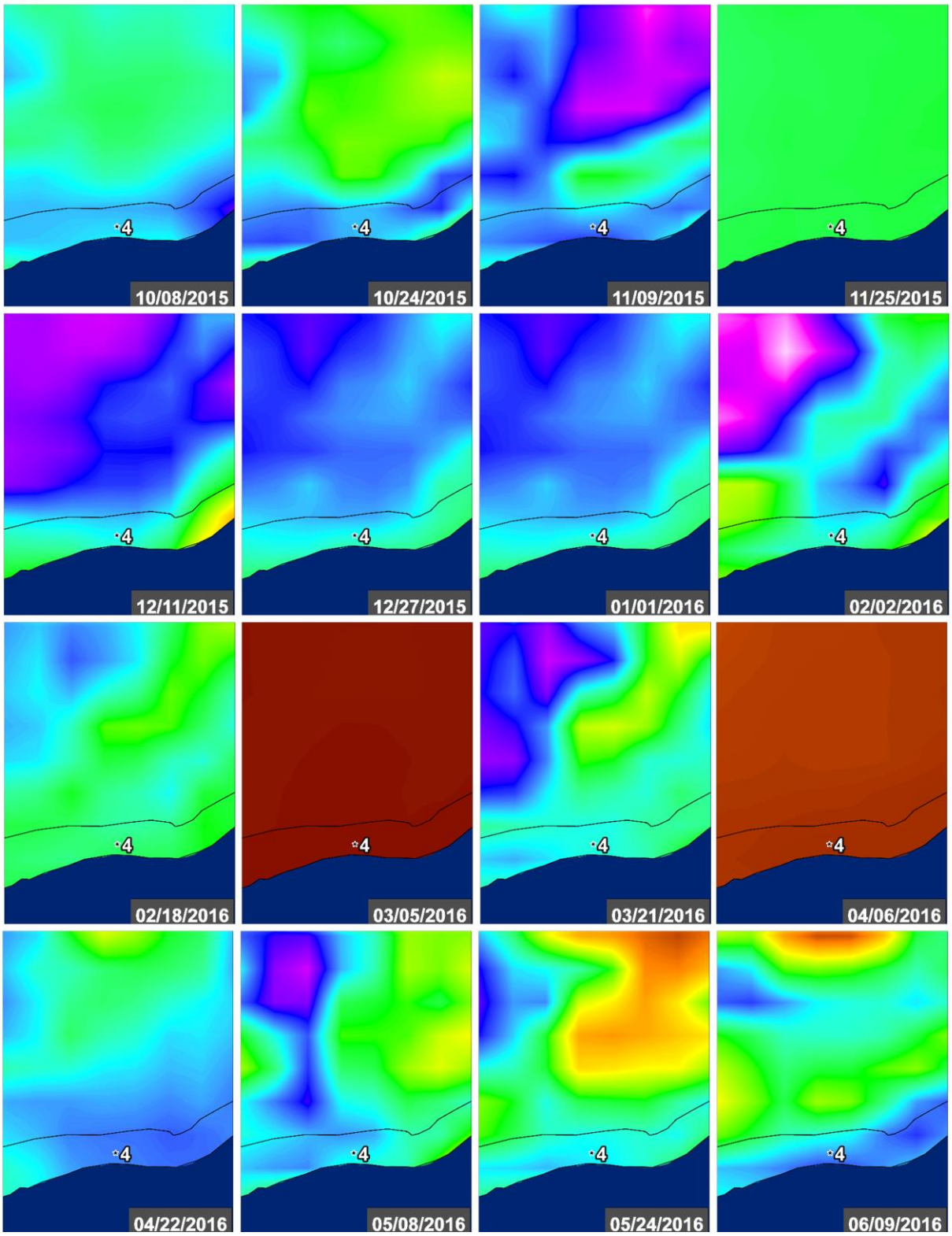

Figure 48H: Seep 4 – NDWI

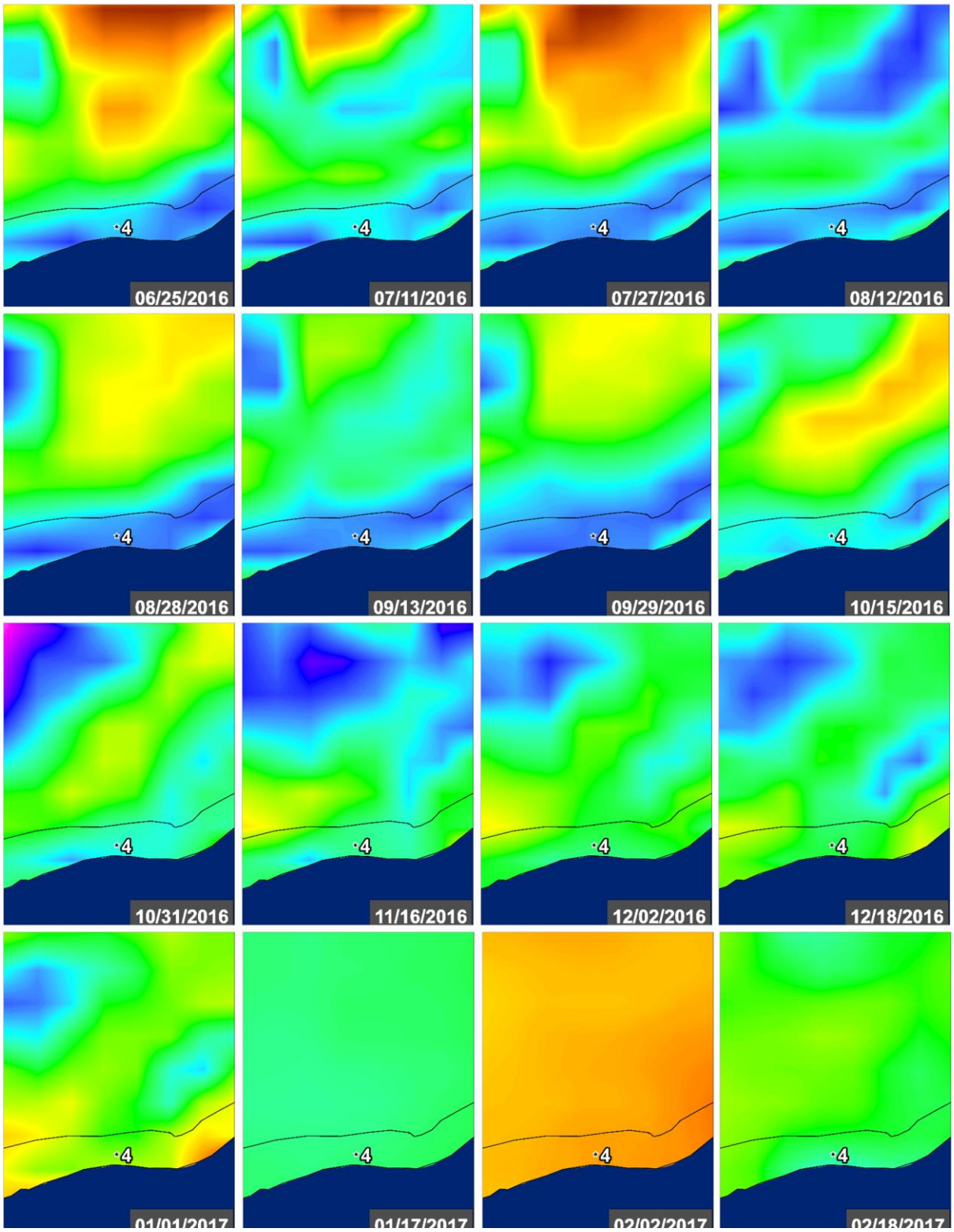

Figure 48I: Seep 4 – NDWI

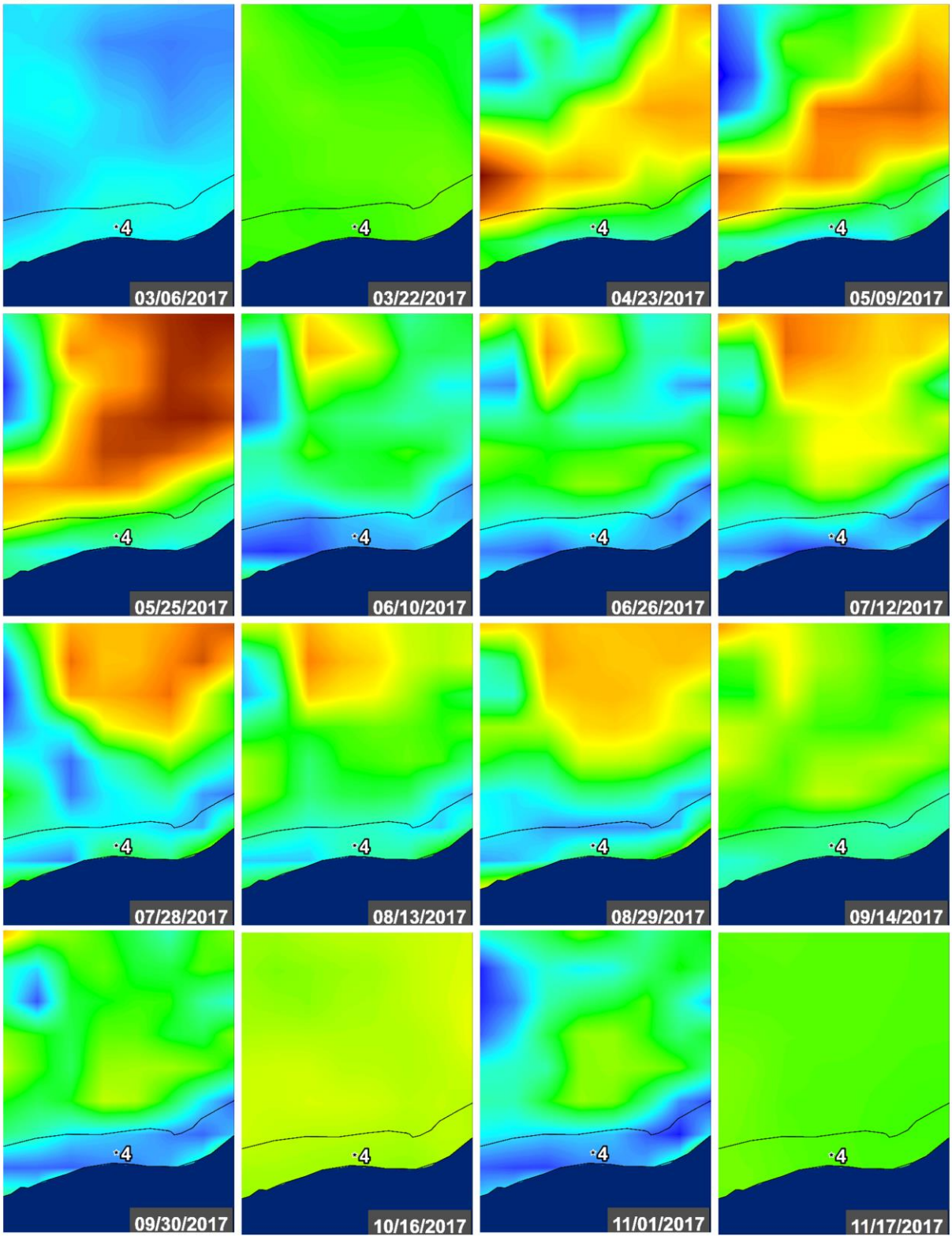

Figure 48J: Seep 4 – NDWI

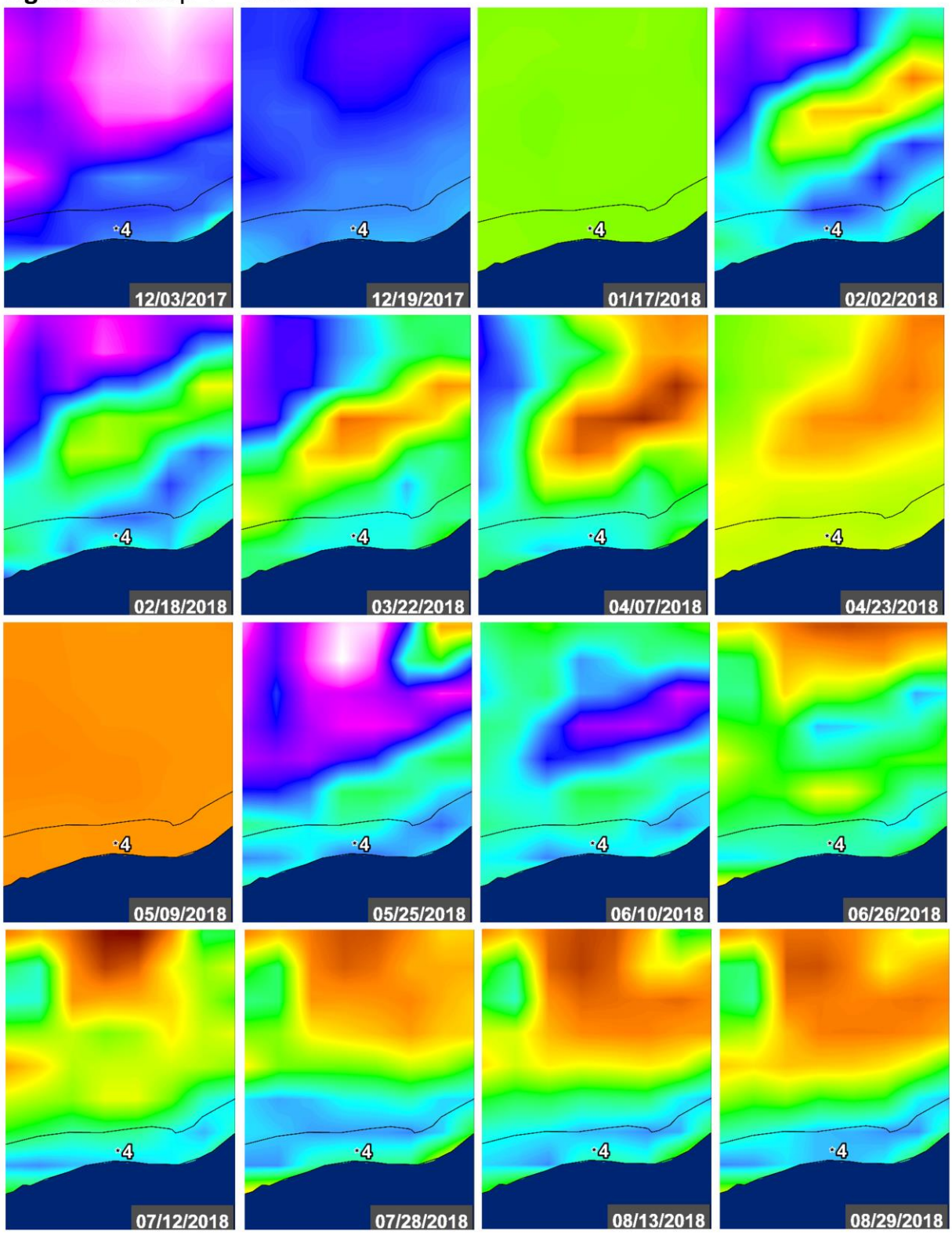

Figure 48K: Seep 4 – NDWI

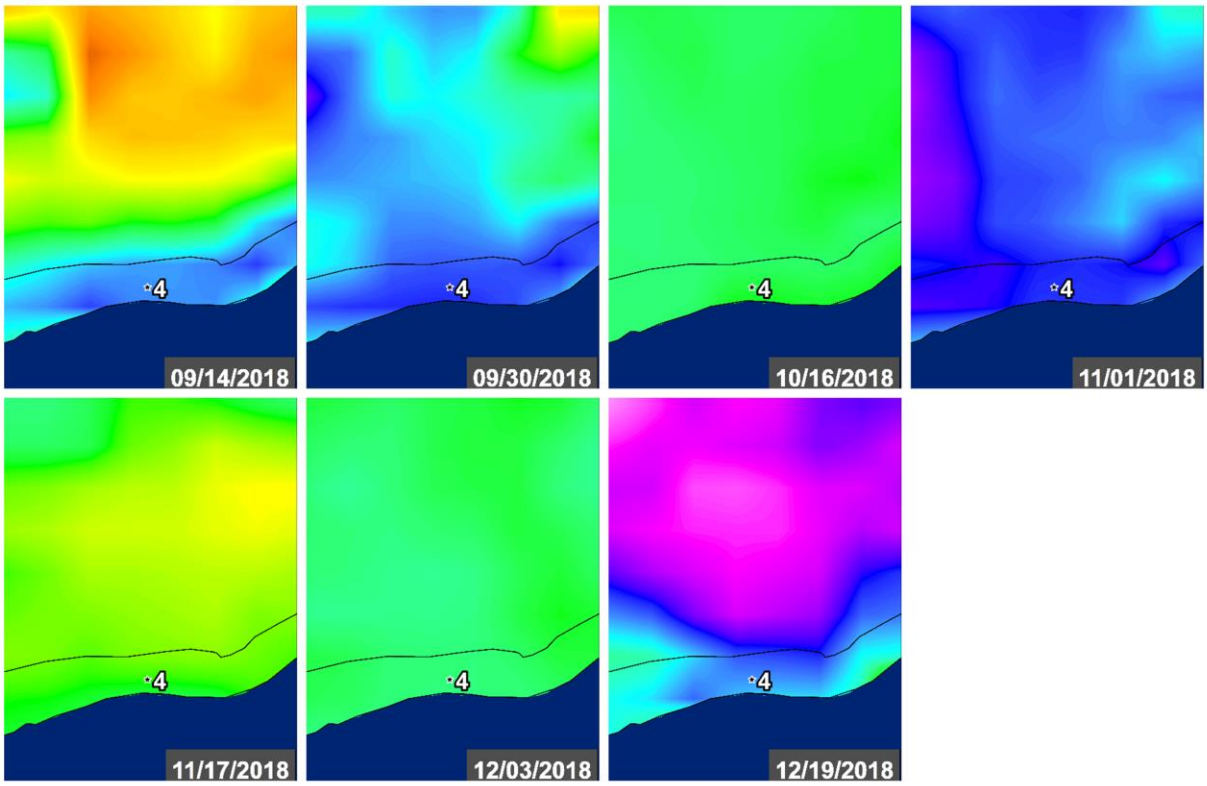

Figure 49A: Seep 4 – VV/HH Ratio – Line 05519

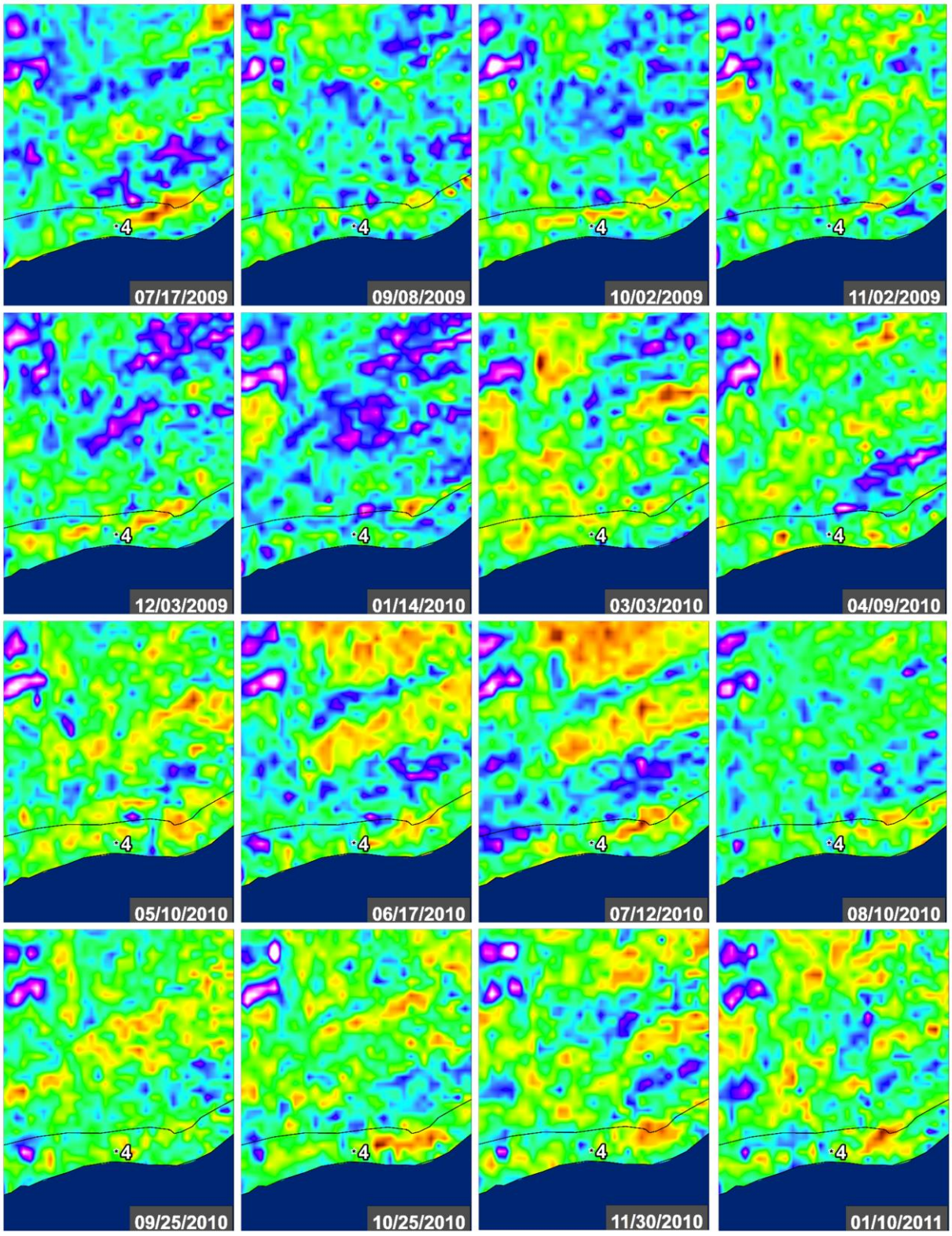

Figure 49B: Seep 4 – VV/HH Ratio – Line 05519

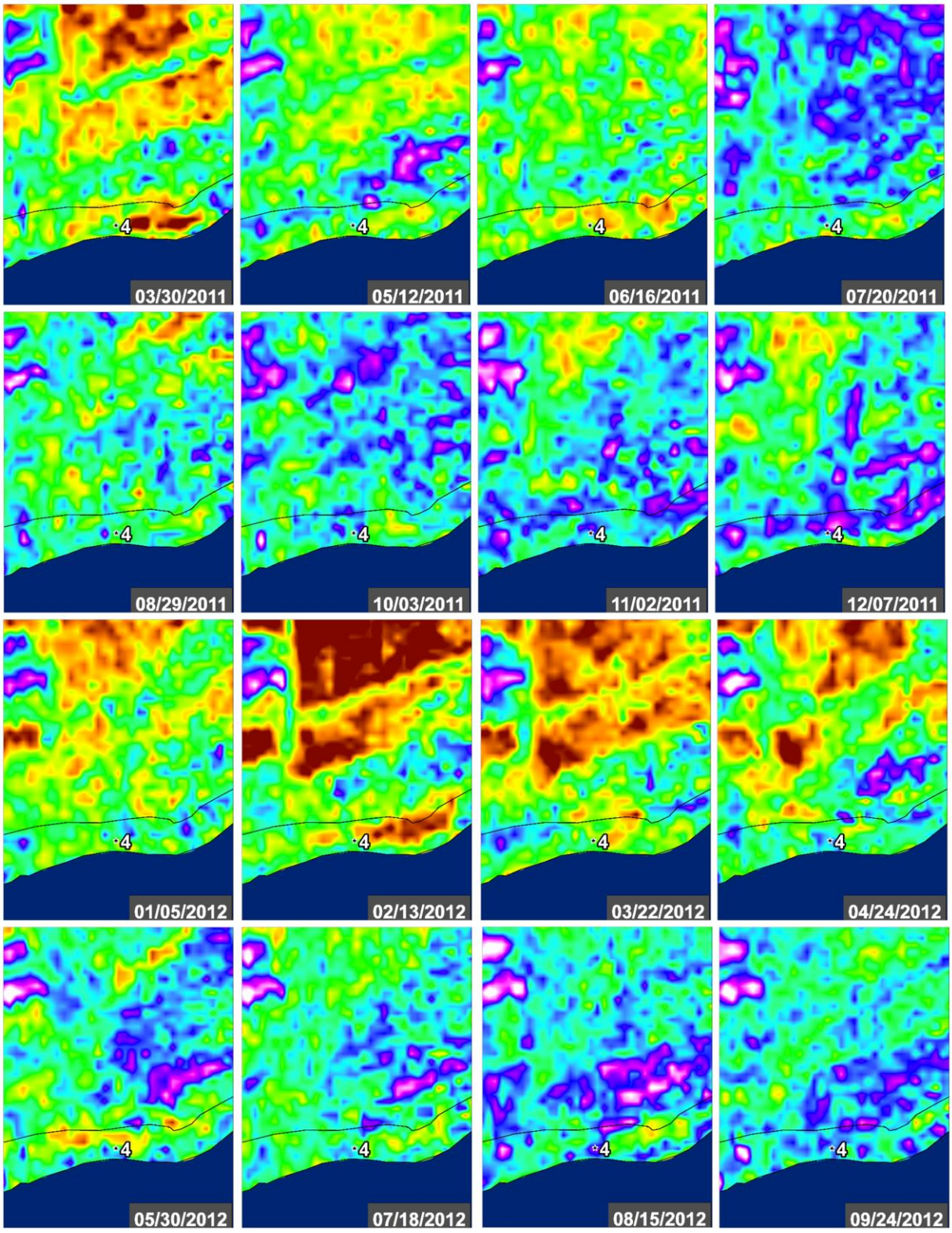

Figure 49C: Seep 4 – VV/HH Ratio – Line 05519

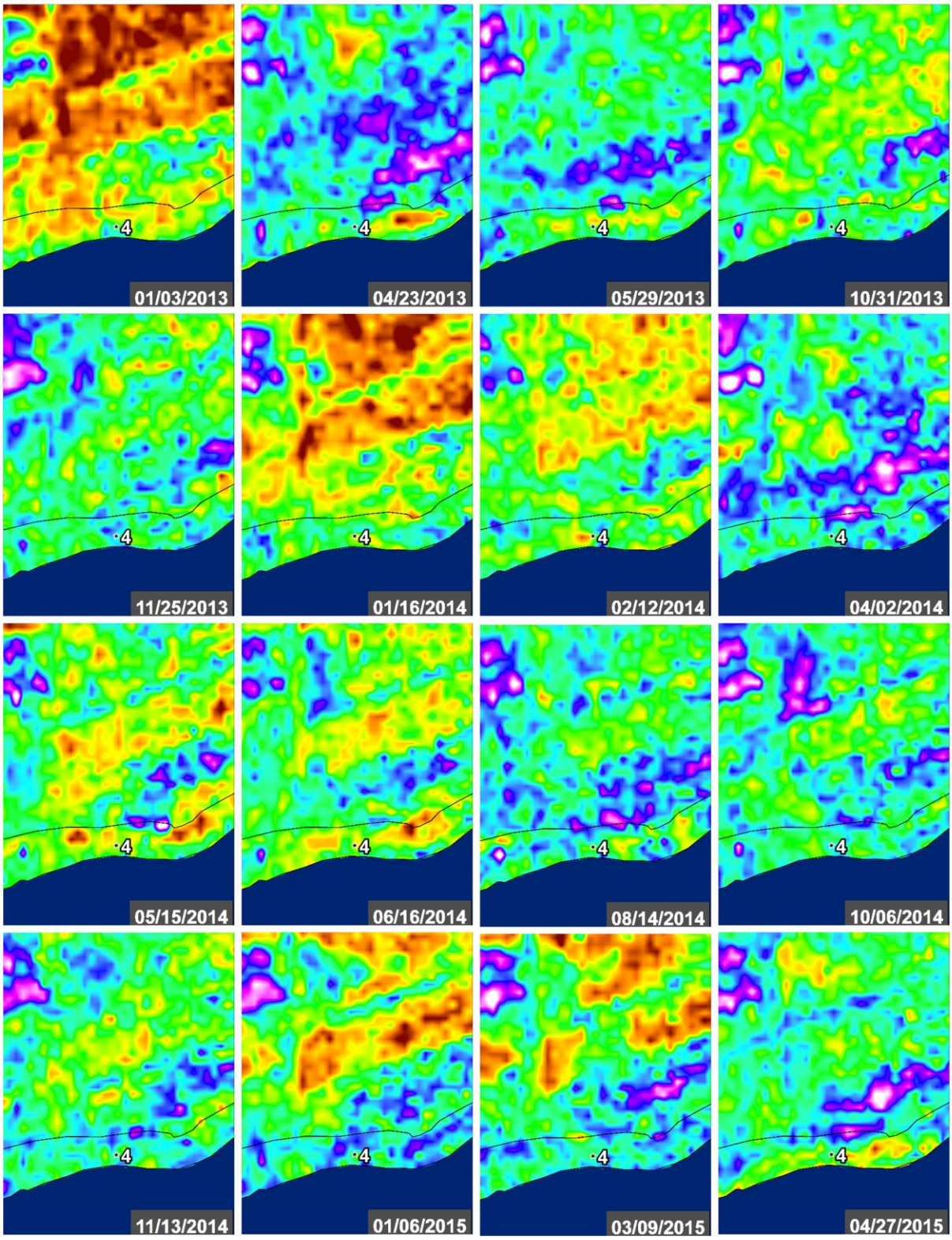

Figure 49D: Seep 4 – VV/HH Ratio – Line 05519

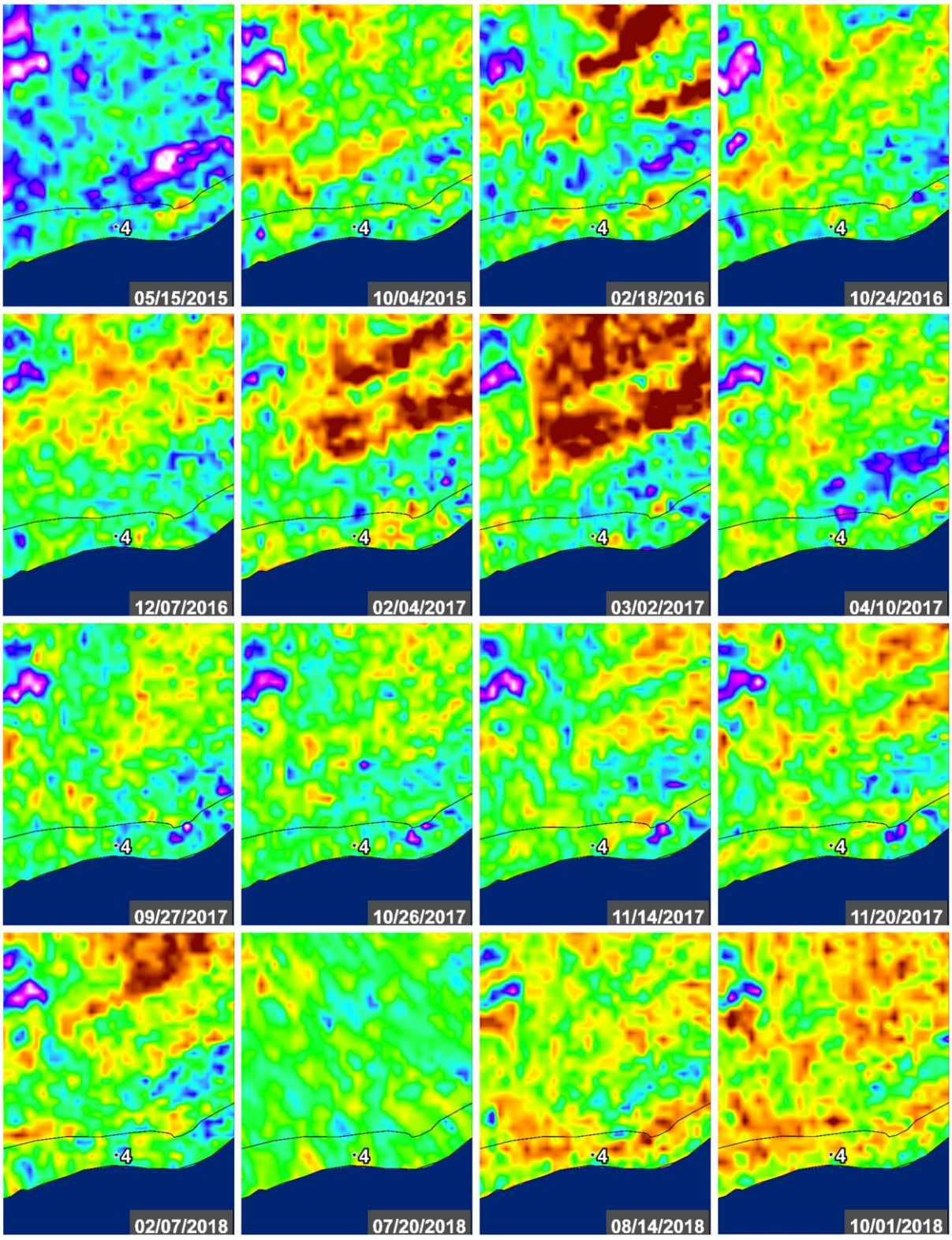

Figure 49E: Seep 4 – VV/HH Ratio – Line 05519

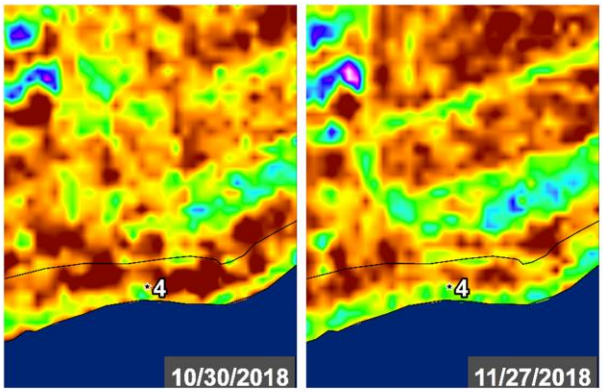

Figure 50A: Seep 4 – VV/HH Ratio – Line 15502

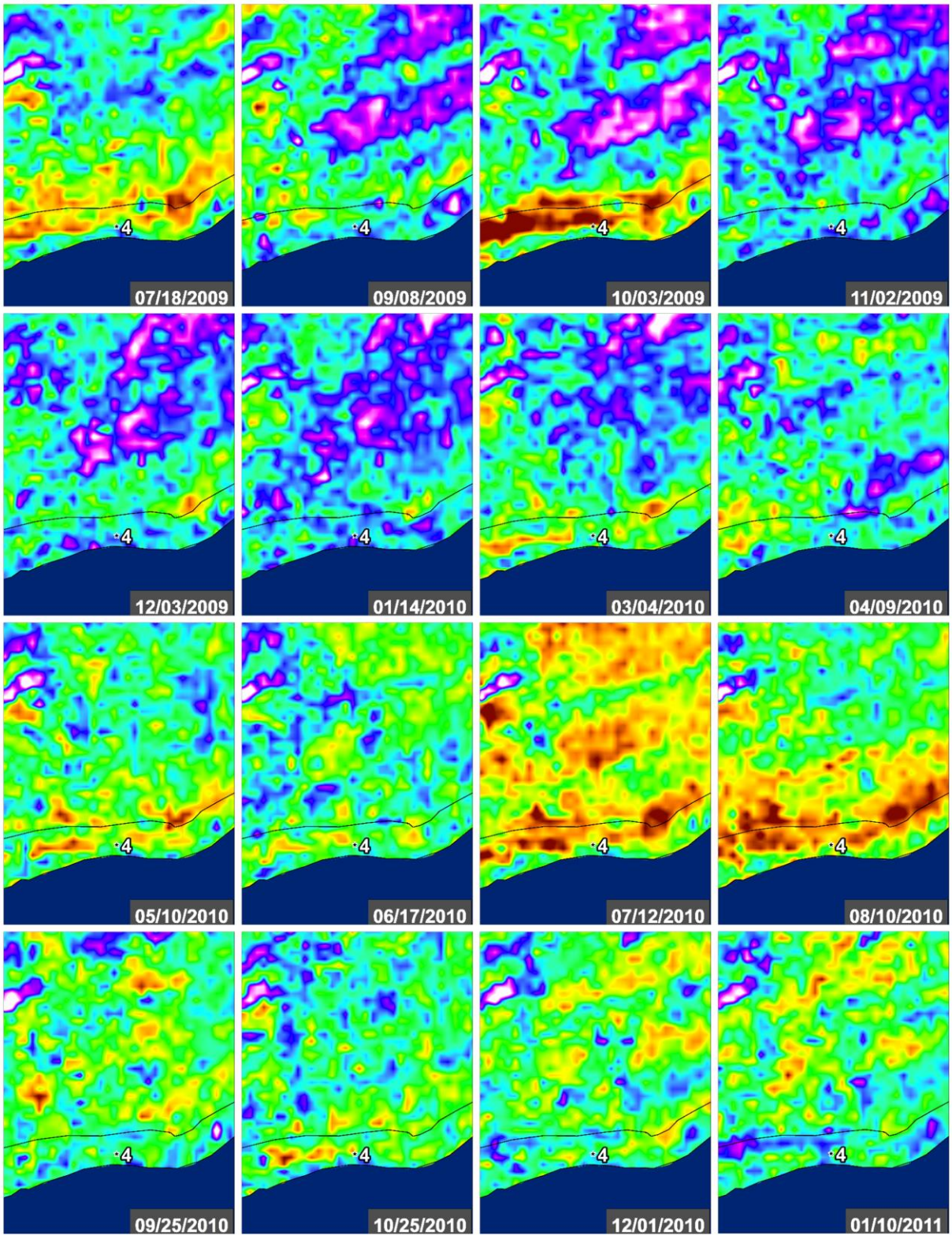

Figure 50B: Seep 4 – VV/HH Ratio – Line 15502

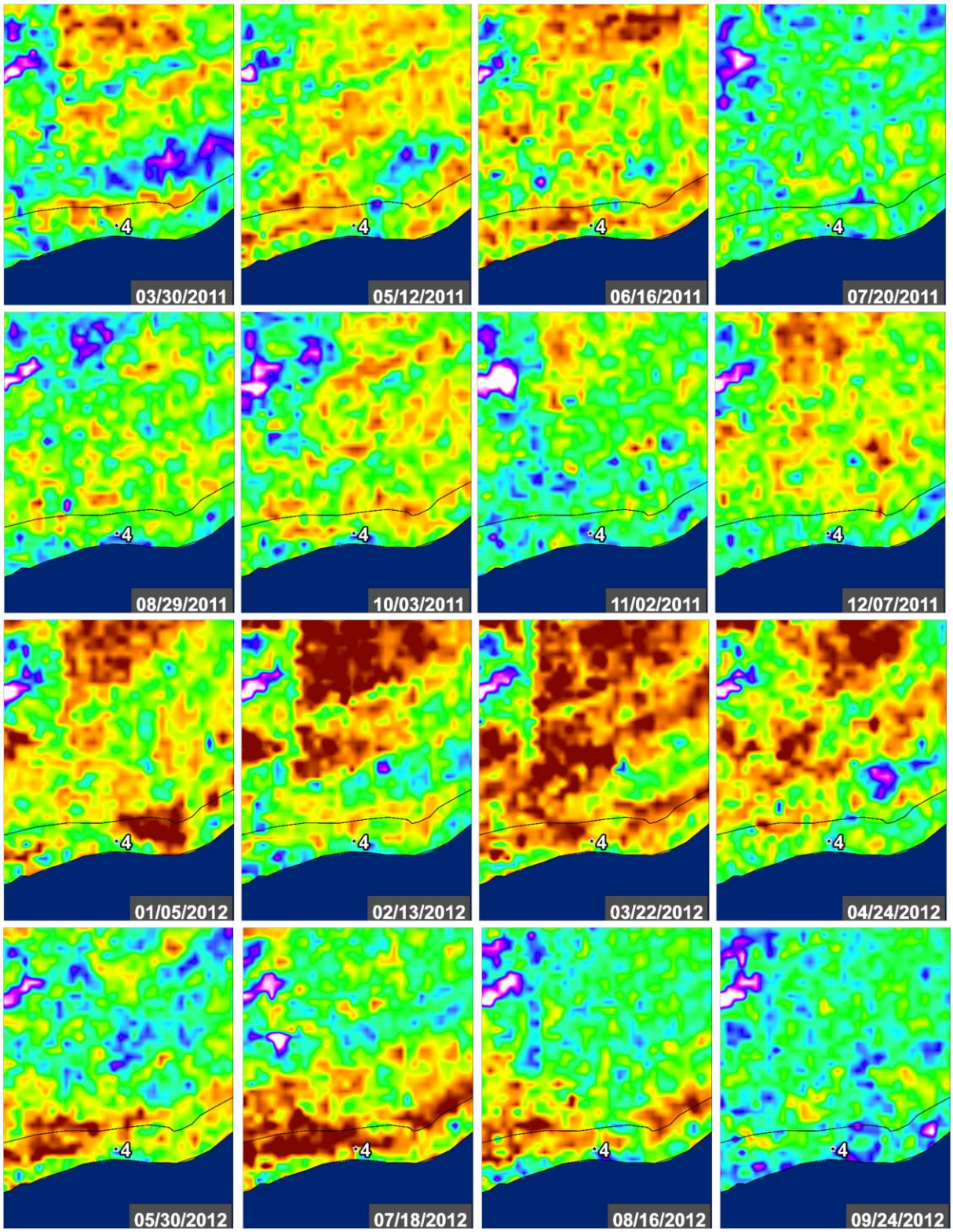

Figure 50C: Seep 4 – VV/HH Ratio – Line 15502

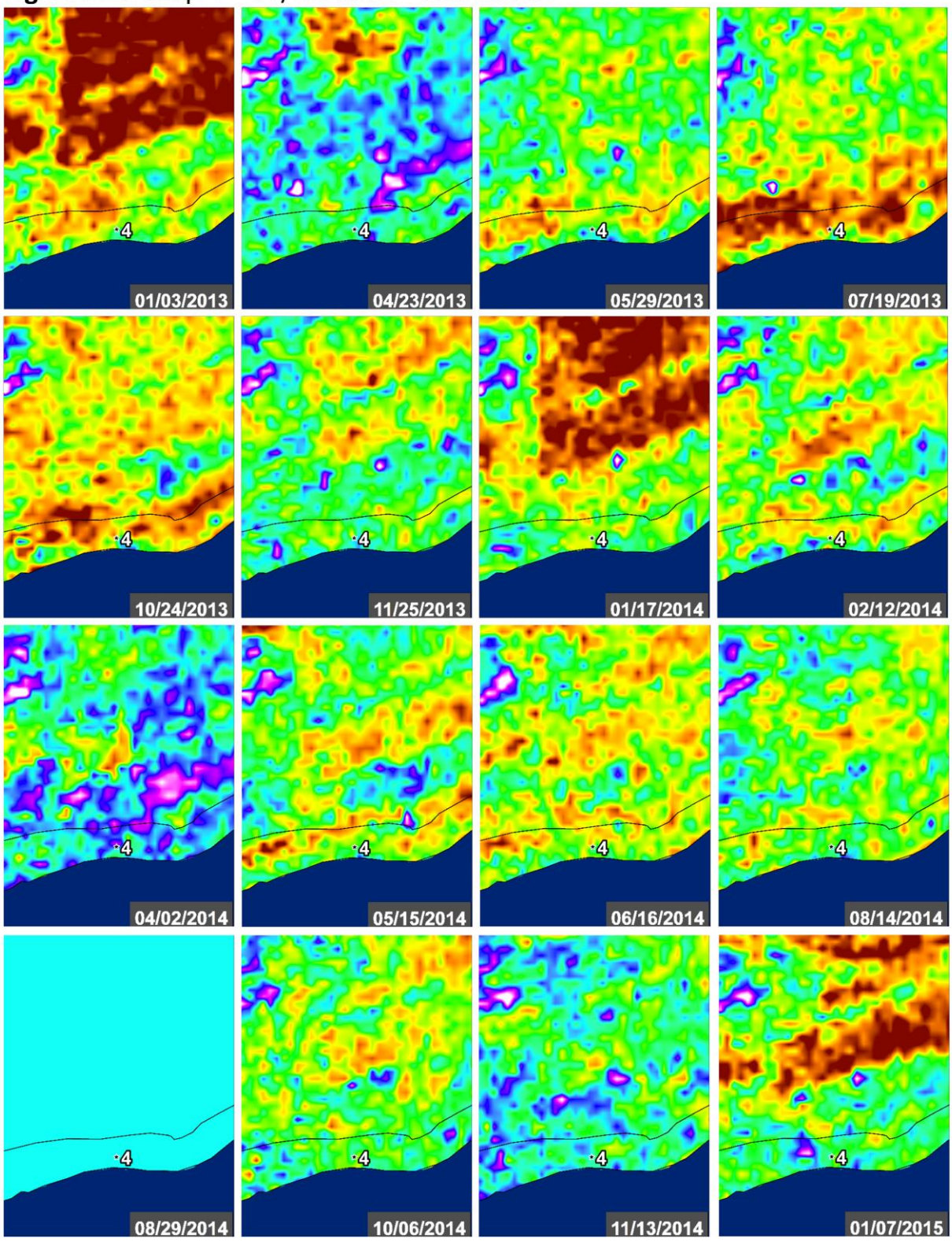

Figure 50D: Seep 4 – VV/HH Ratio – Line 15502

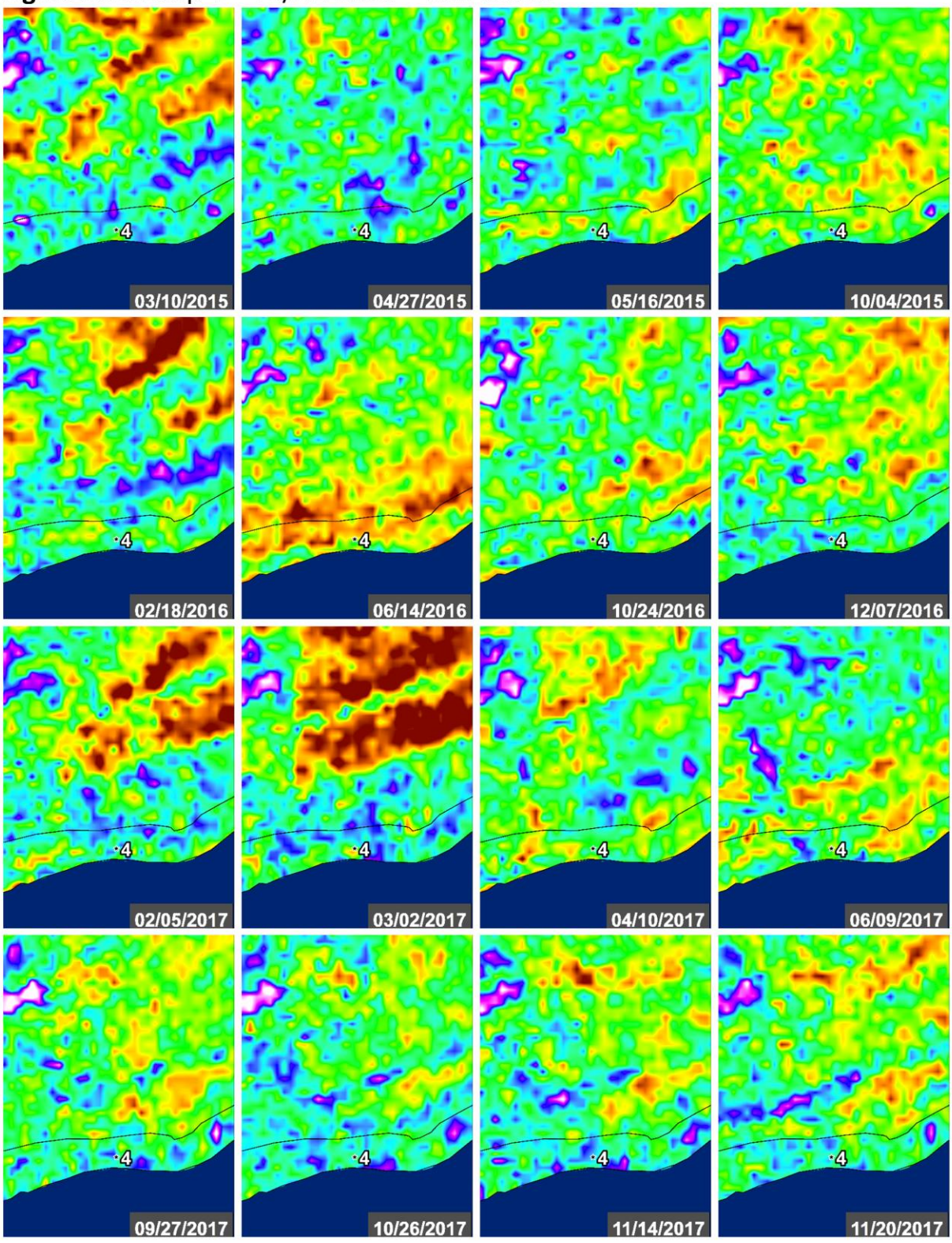

Figure 50E: Seep 4 – VV/HH Ratio – Line 15502

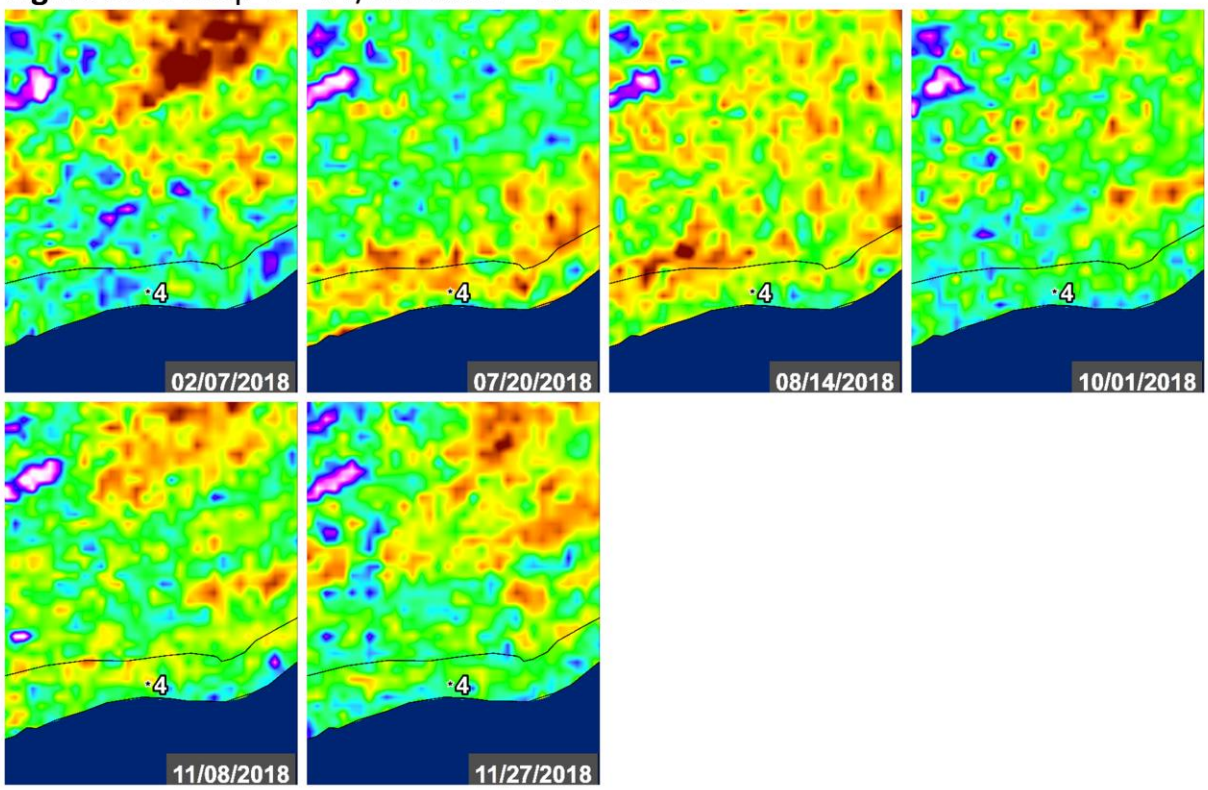

Figure 51A: Seep 4 – VV/HH Ratio – Line 33502

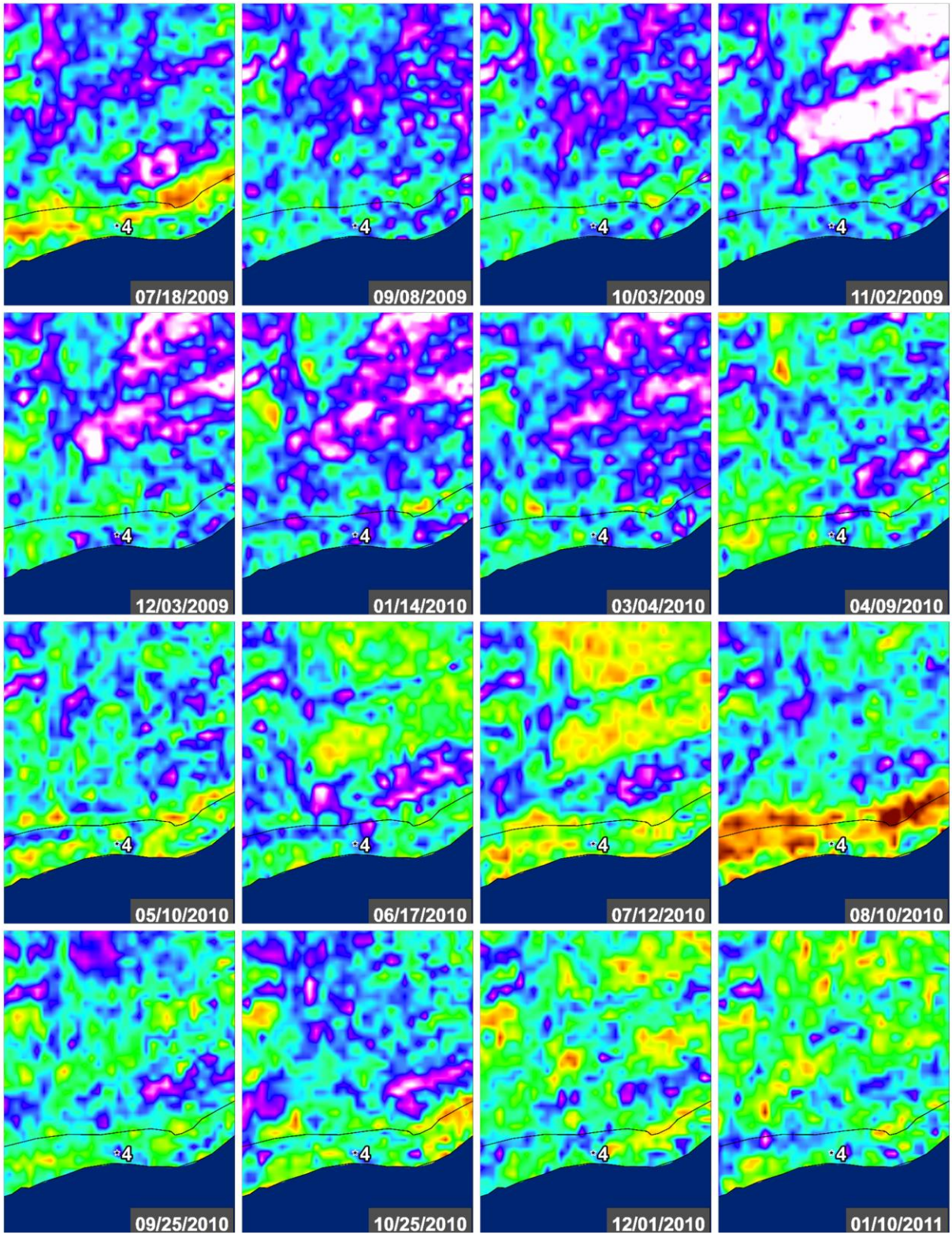

Figure 51B: Seep 4 – VV/HH Ratio – Line 33502

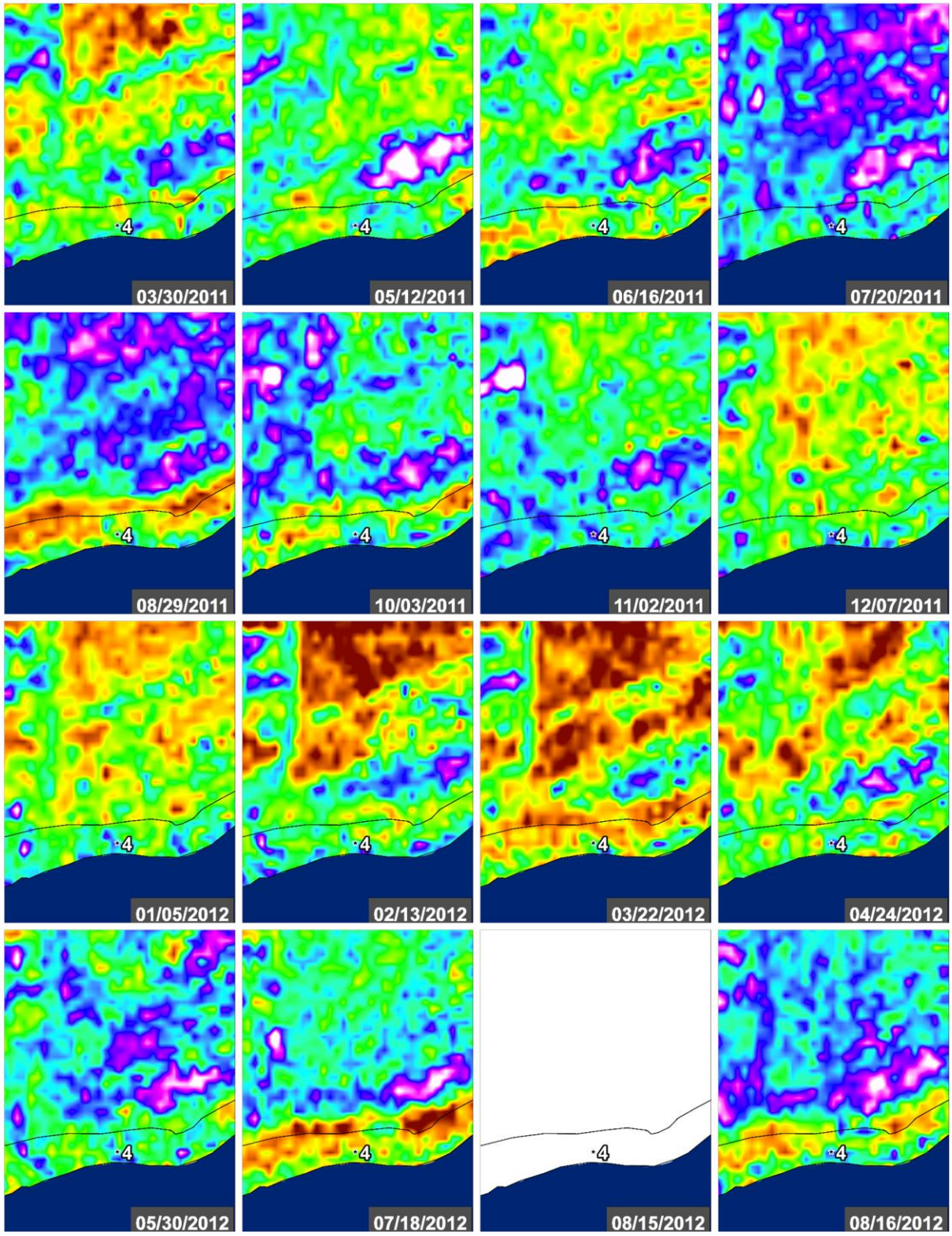

Figure 51C: Seep 4 – VV/HH Ratio – Line 33502

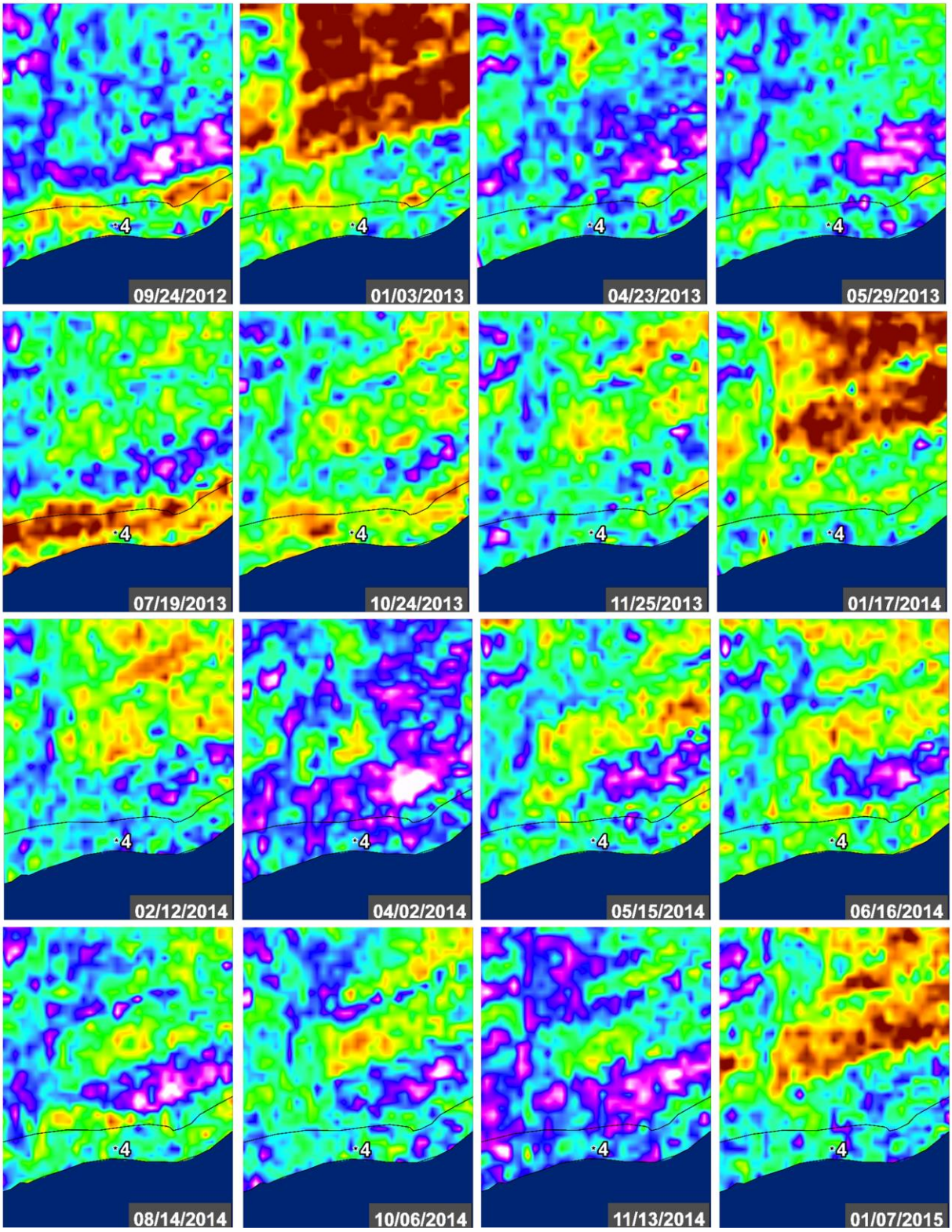

Figure 51D: Seep 4 – VV/HH Ratio – Line 33502

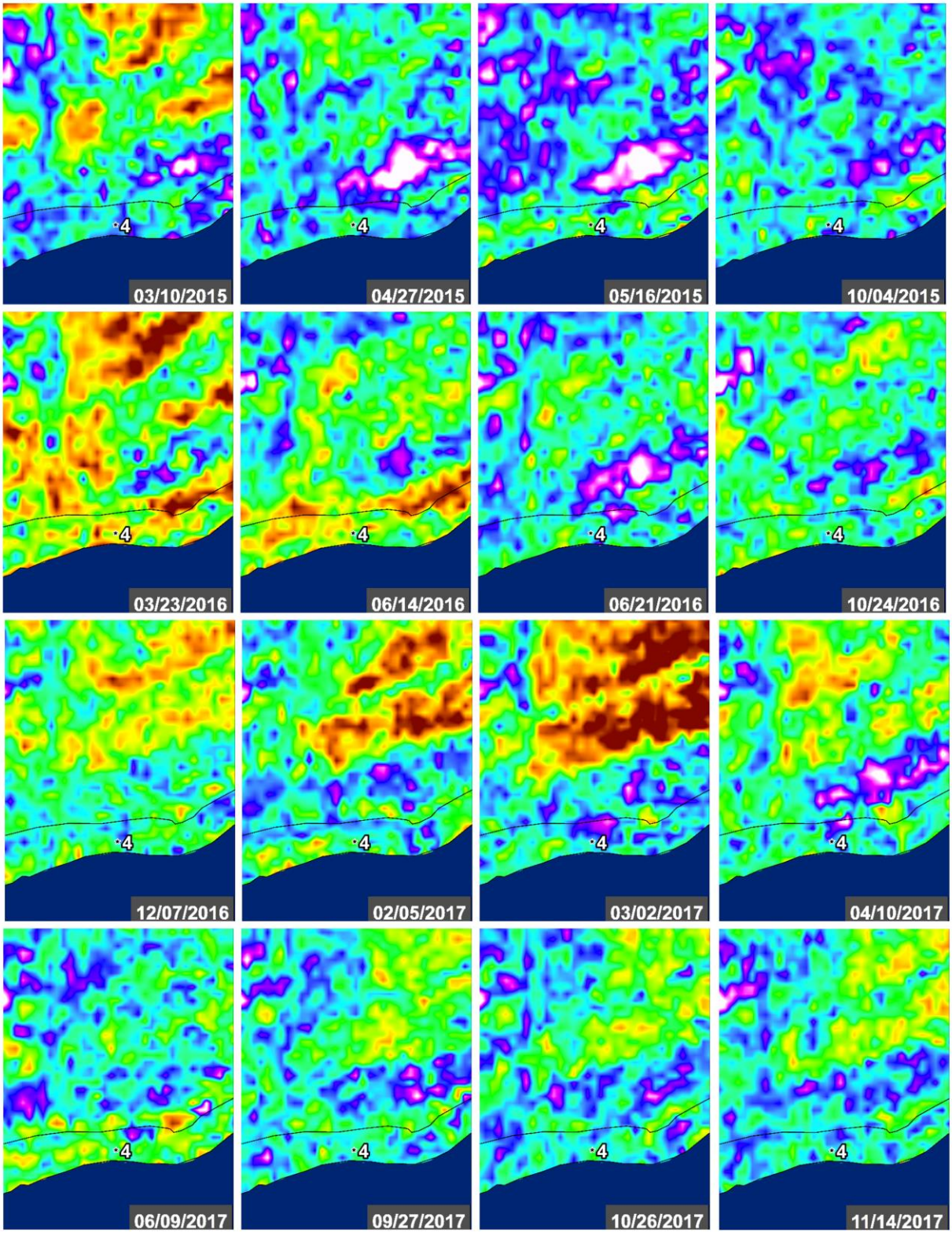

Figure 51E: Seep 4 – VV/HH Ratio – Line 33502

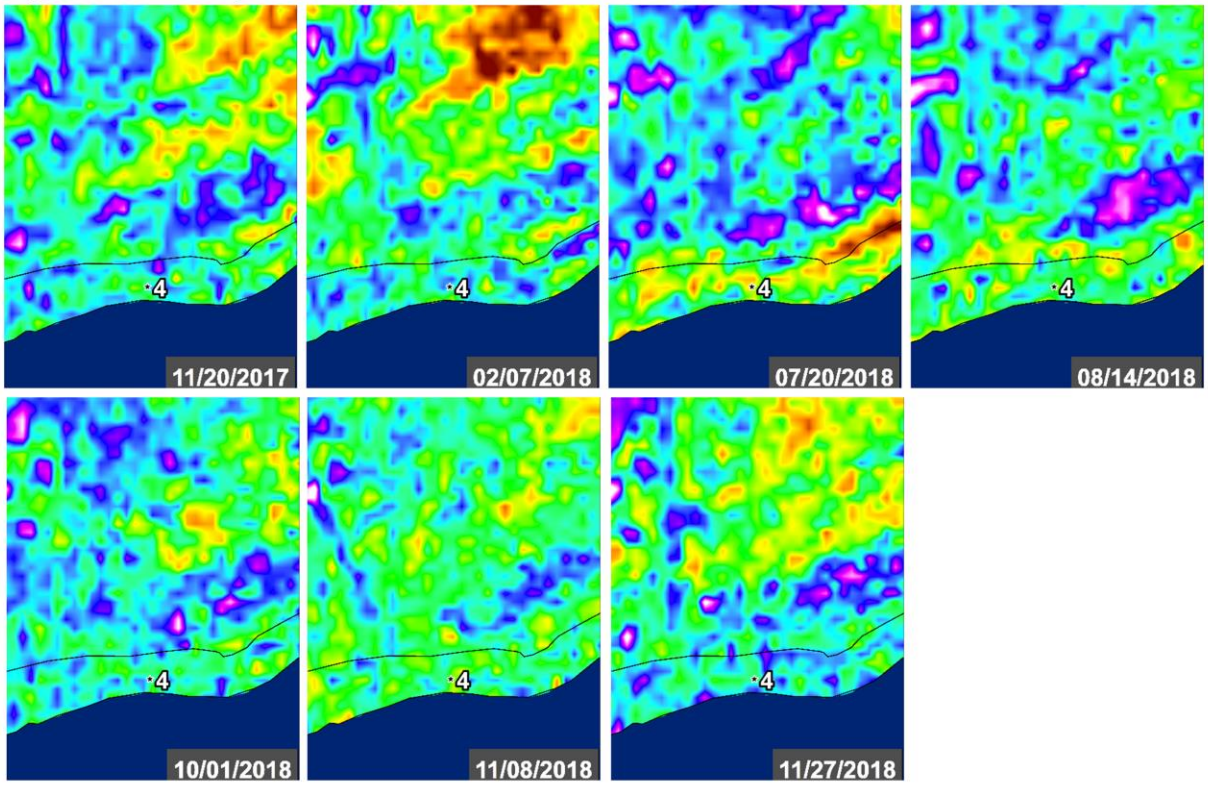

Figure 52A: Seep 4 – VV/HH Ratio – Line 23518

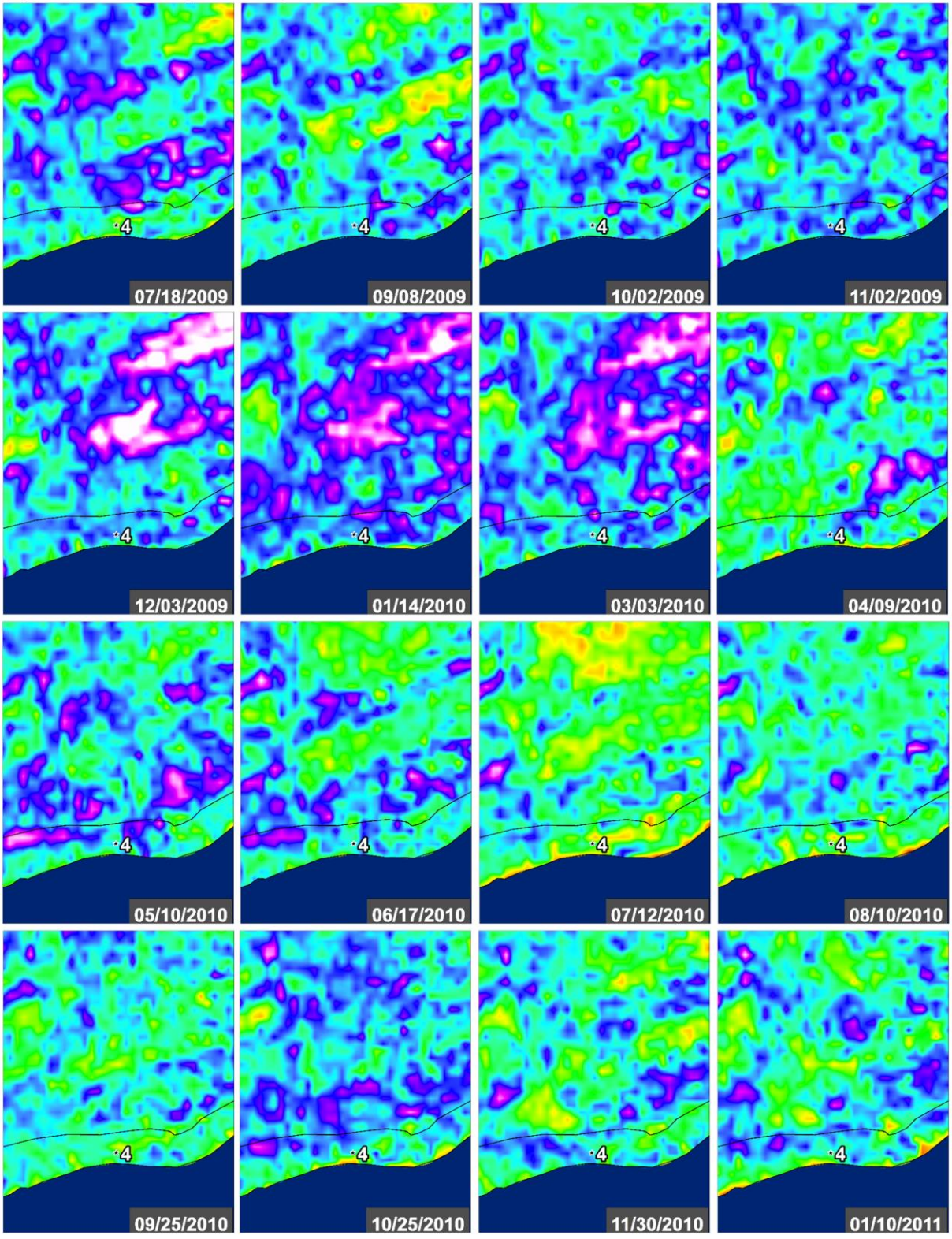

Figure 52B: Seep 4 – VV/HH Ratio – Line 23518

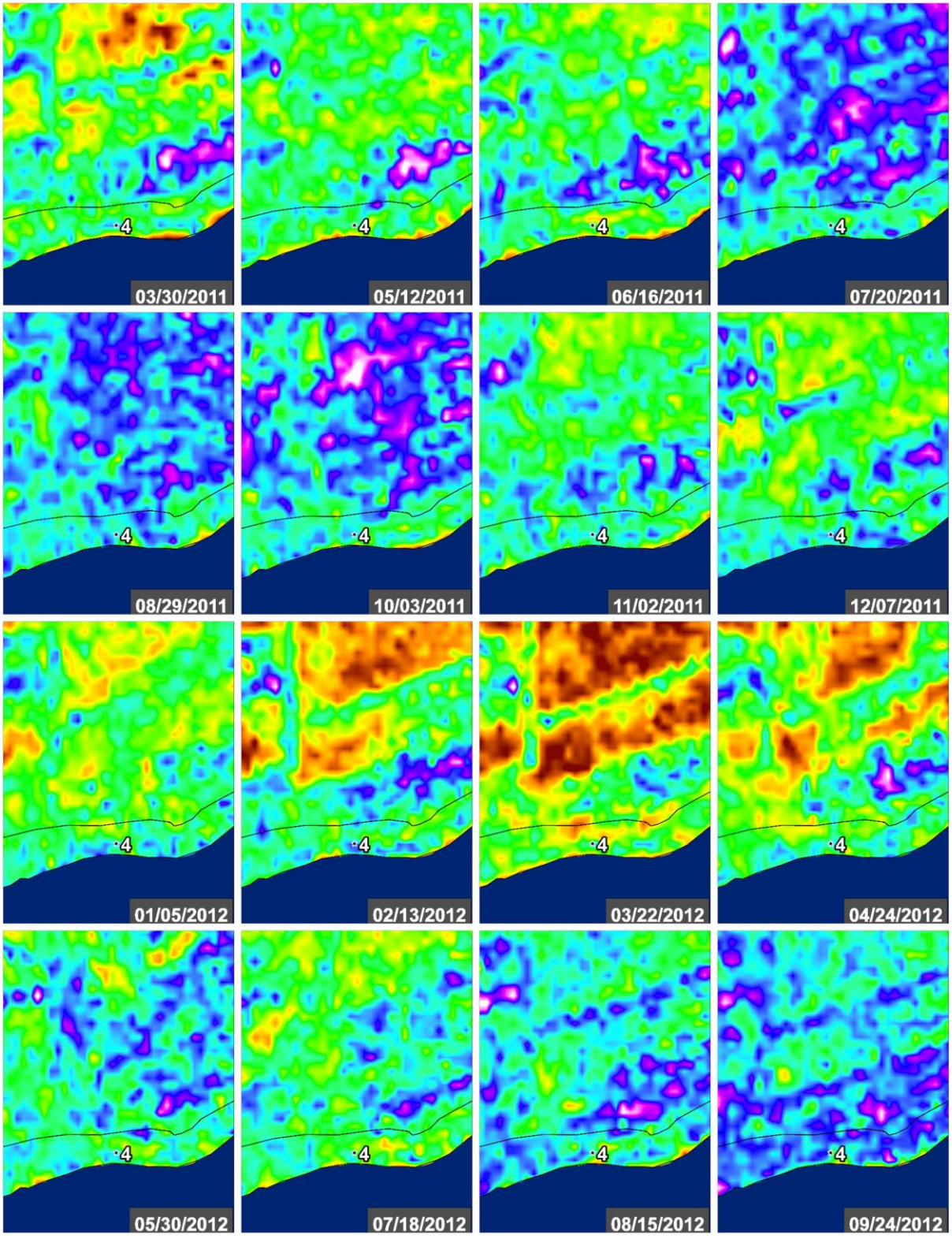

Figure 52C: Seep 4 – VV/HH Ratio – Line 23518

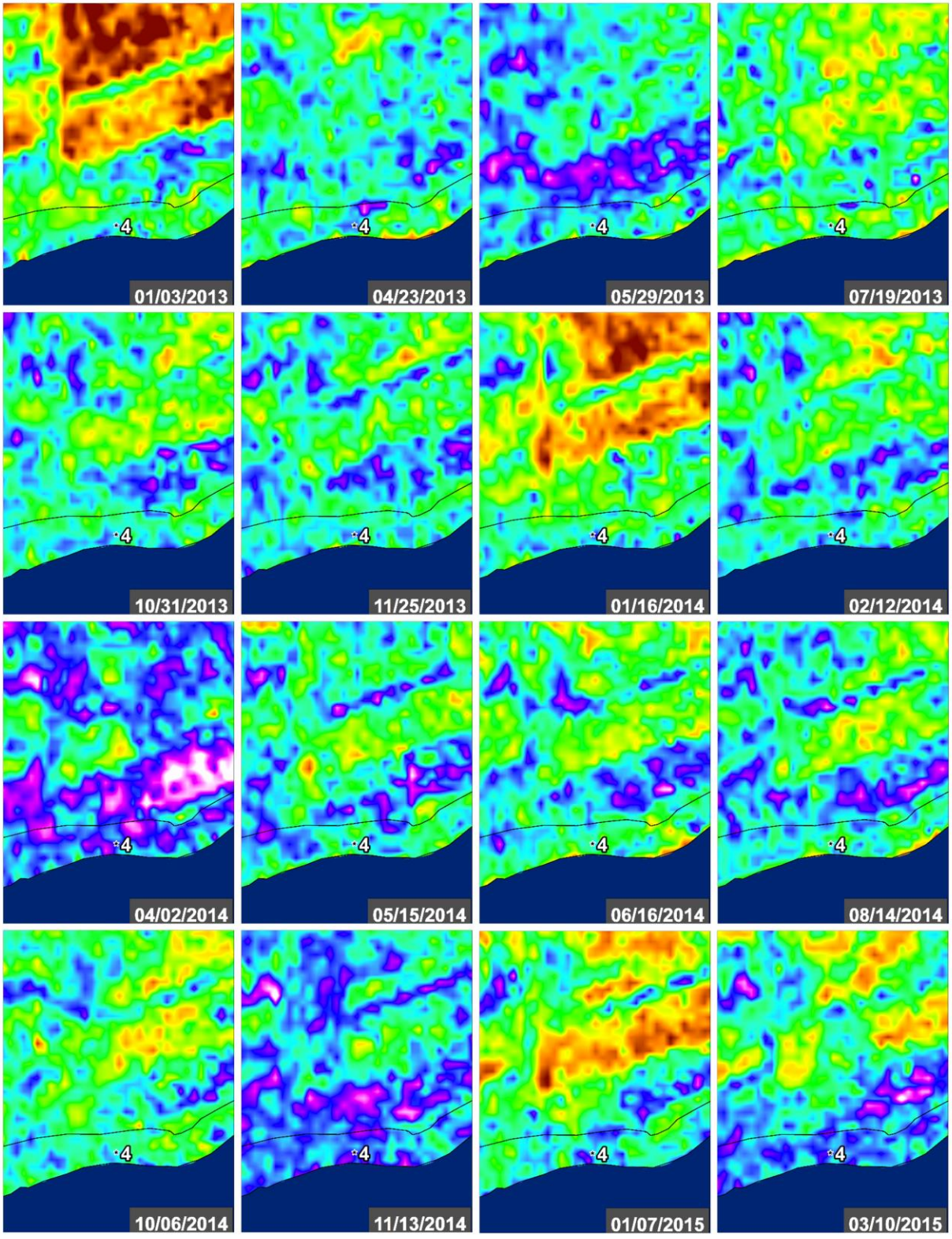

Figure 52D: Seep 4 – VV/HH Ratio – Line 23518

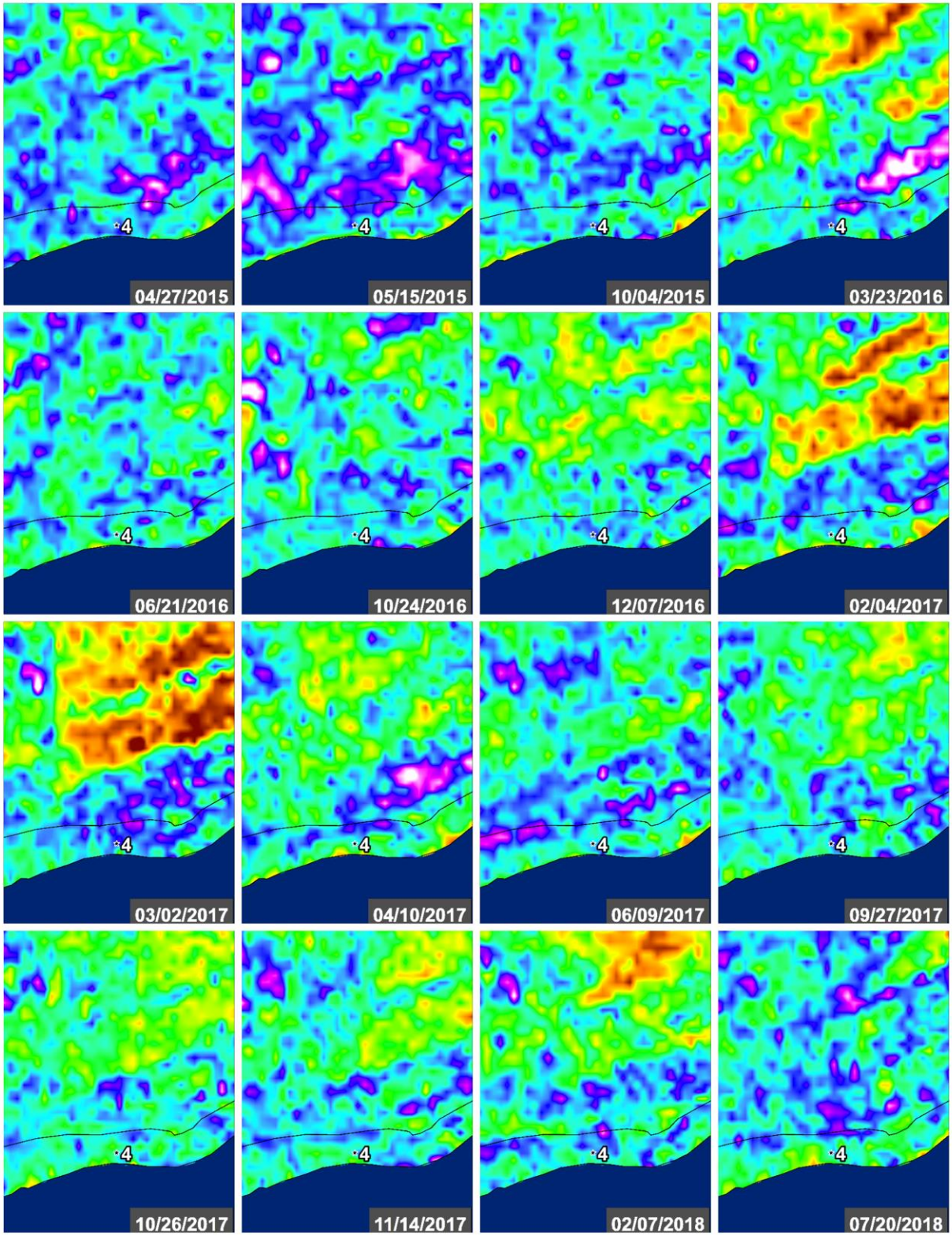

Figure 52E: Seep 4 – VV/HH Ratio – Line 23518

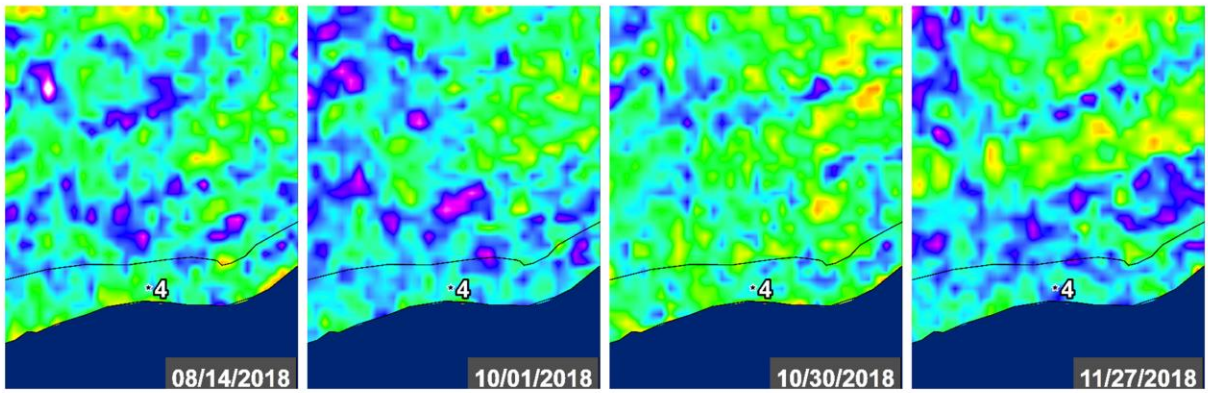

Figure 53: Study area overview for Seep 5 along the California Aqueduct.

Figure 54A: Seep 5– Google Earth Imagery

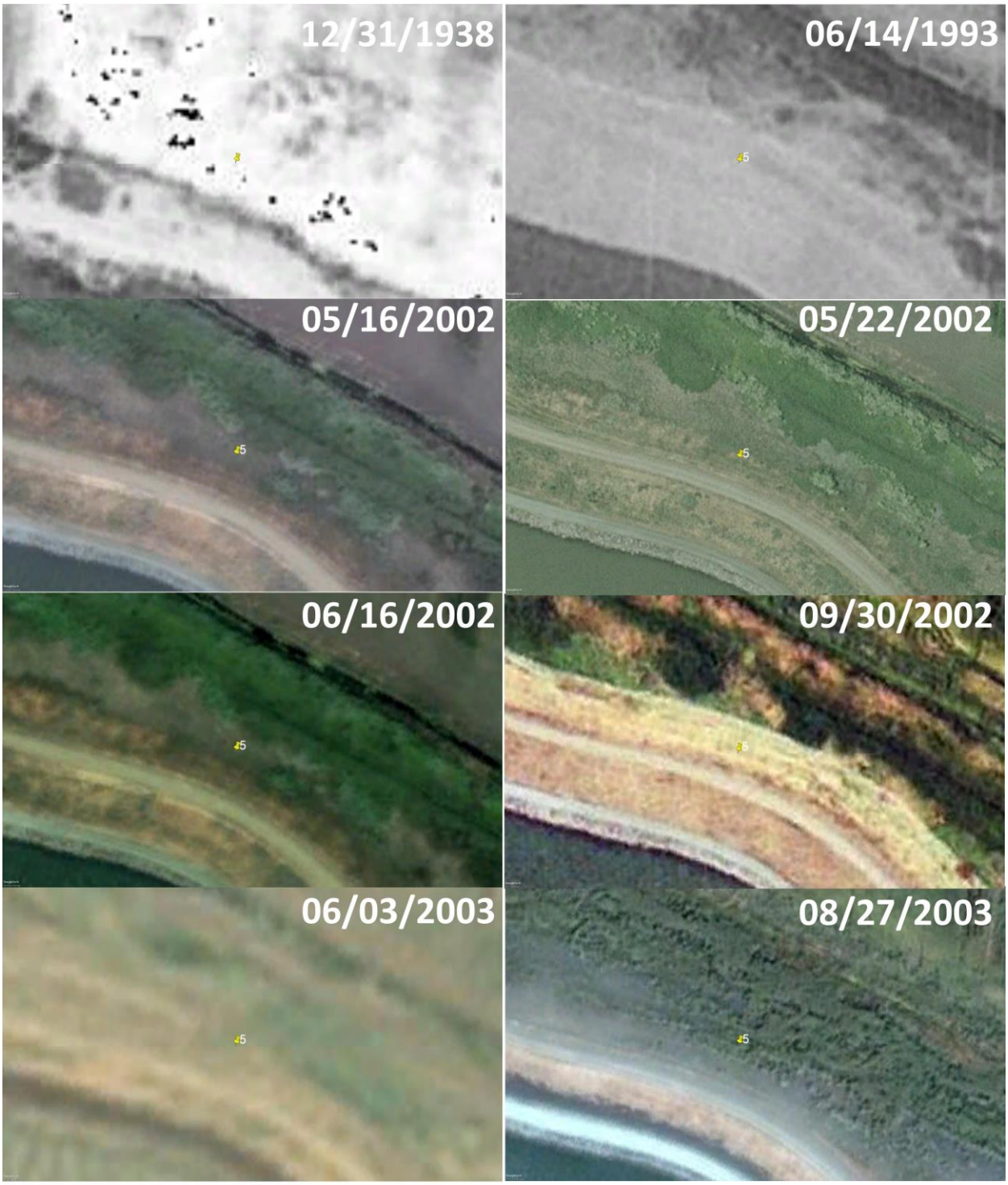

Figure 54B: Seep 5– Google Earth Imagery

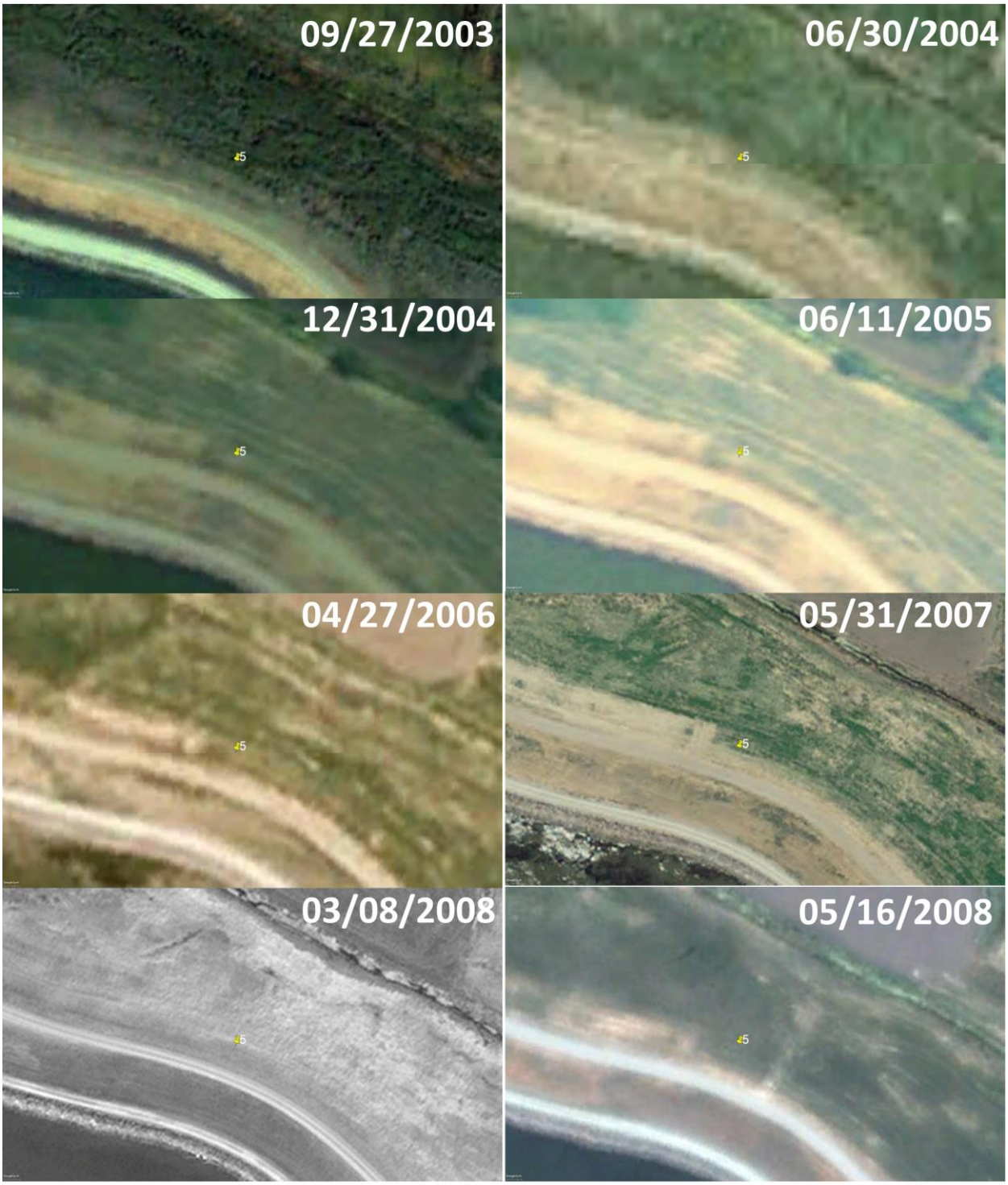

Figure 54C: Seep 5– Google Earth Imagery

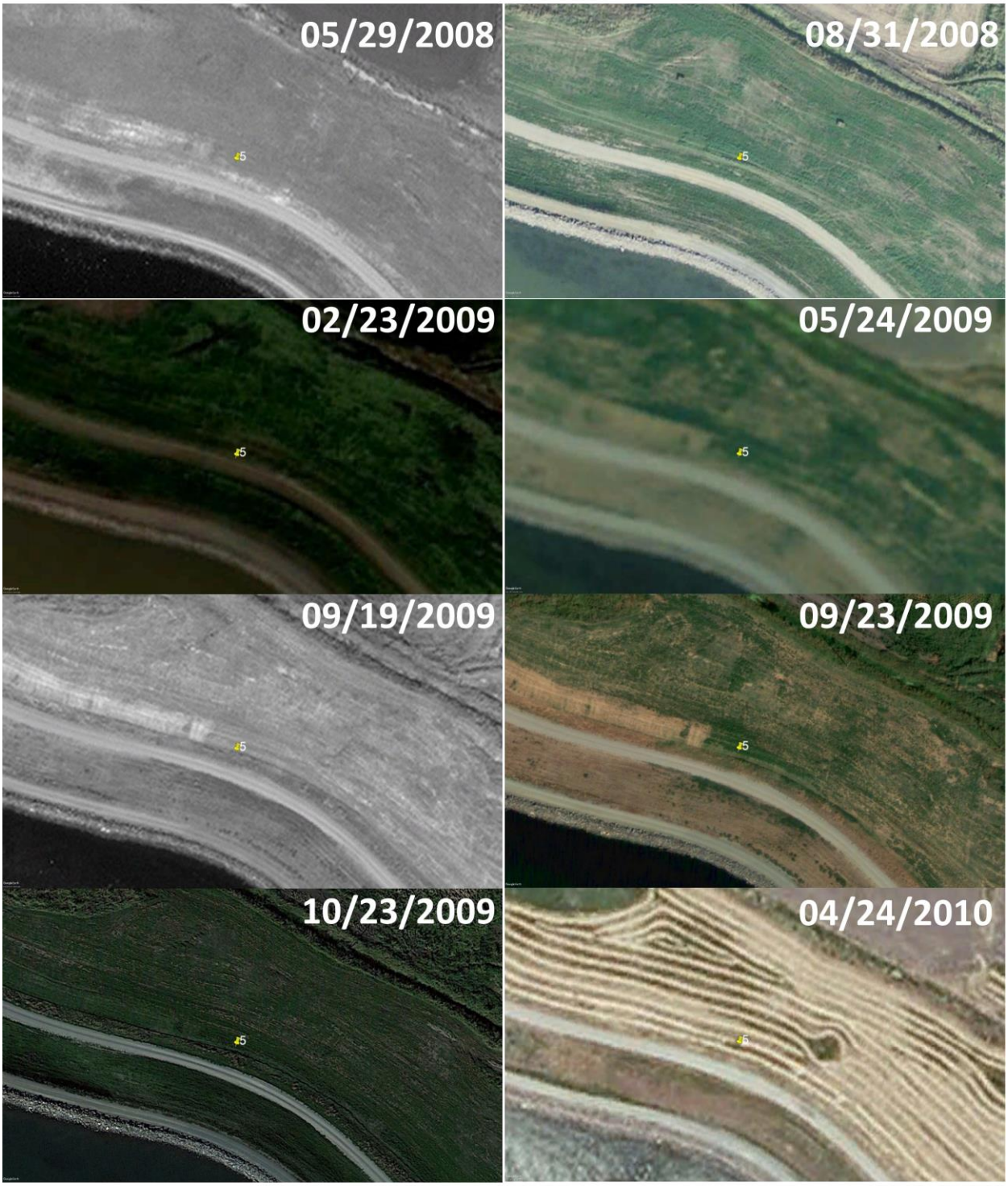

Figure 54D: Seep 5– Google Earth Imagery

Figure 54E: Seep 5– Google Earth Imagery

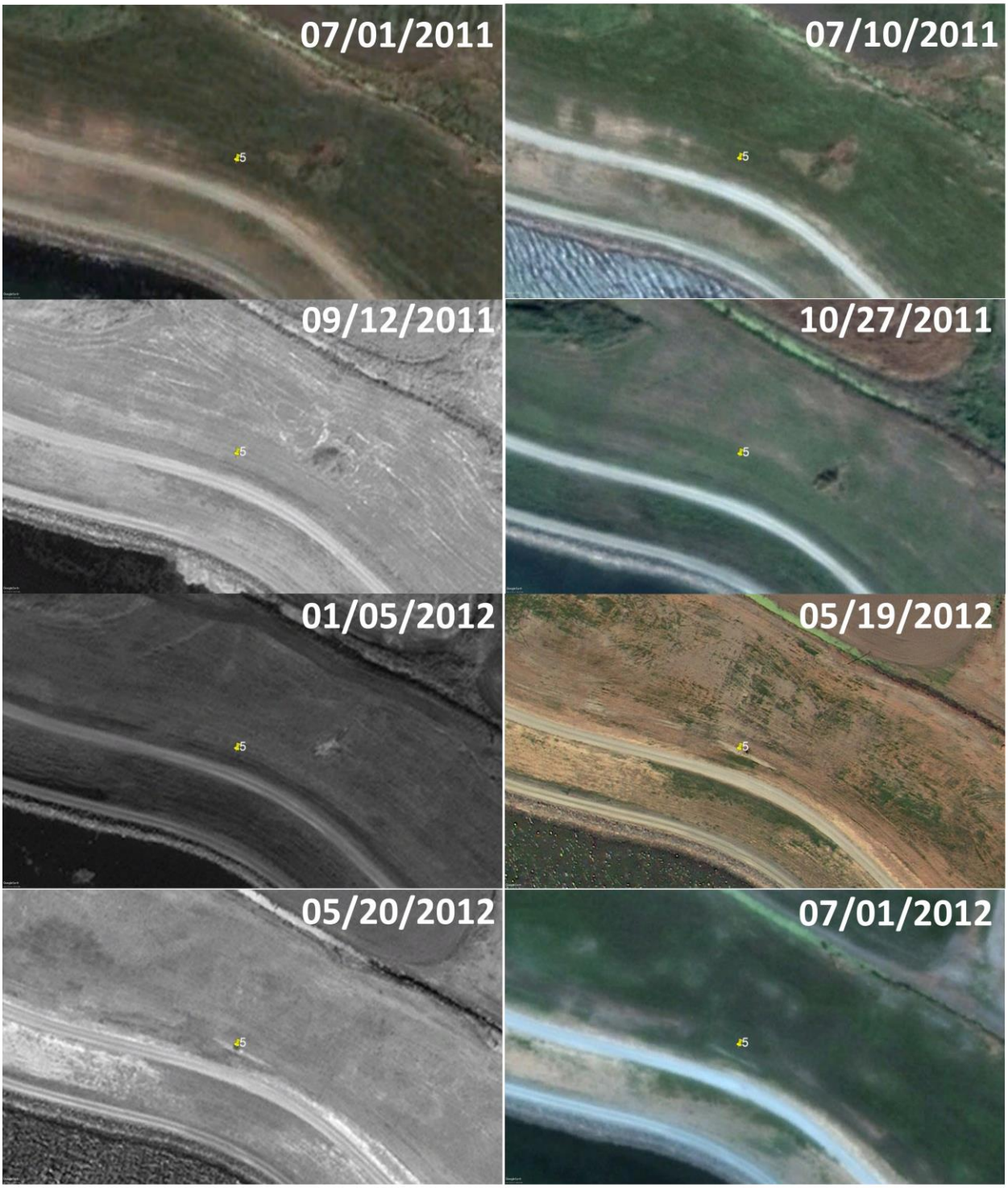

Figure 54F: Seep 5– Google Earth Imagery

Figure 54G: Seep 5– Google Earth Imagery

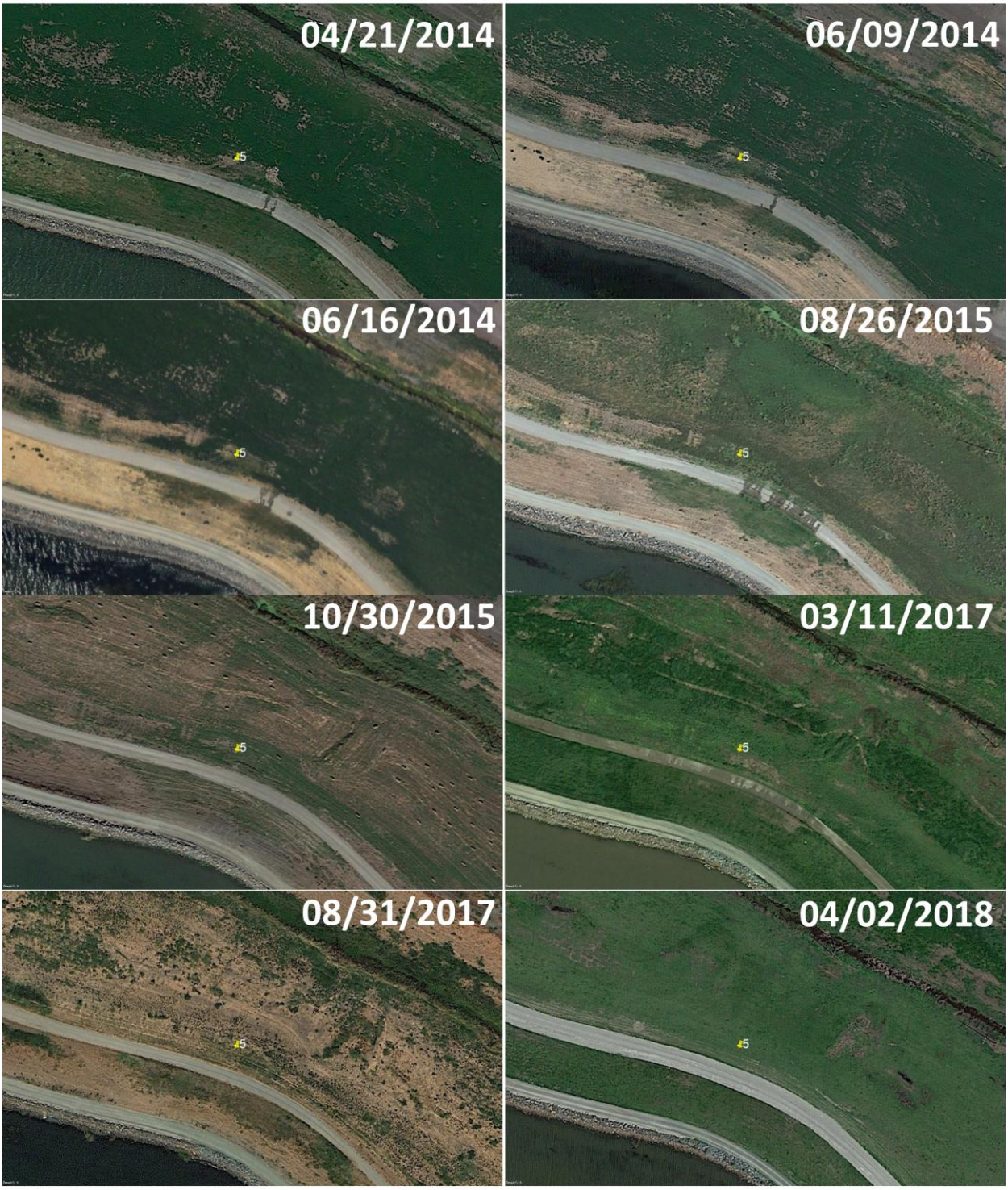

Figure 54H: Seep 5– Google Earth Imagery

Figure 55: Legends for NDWI and PolSAR data products.

Figure 56A: Seep 5 – NDWI

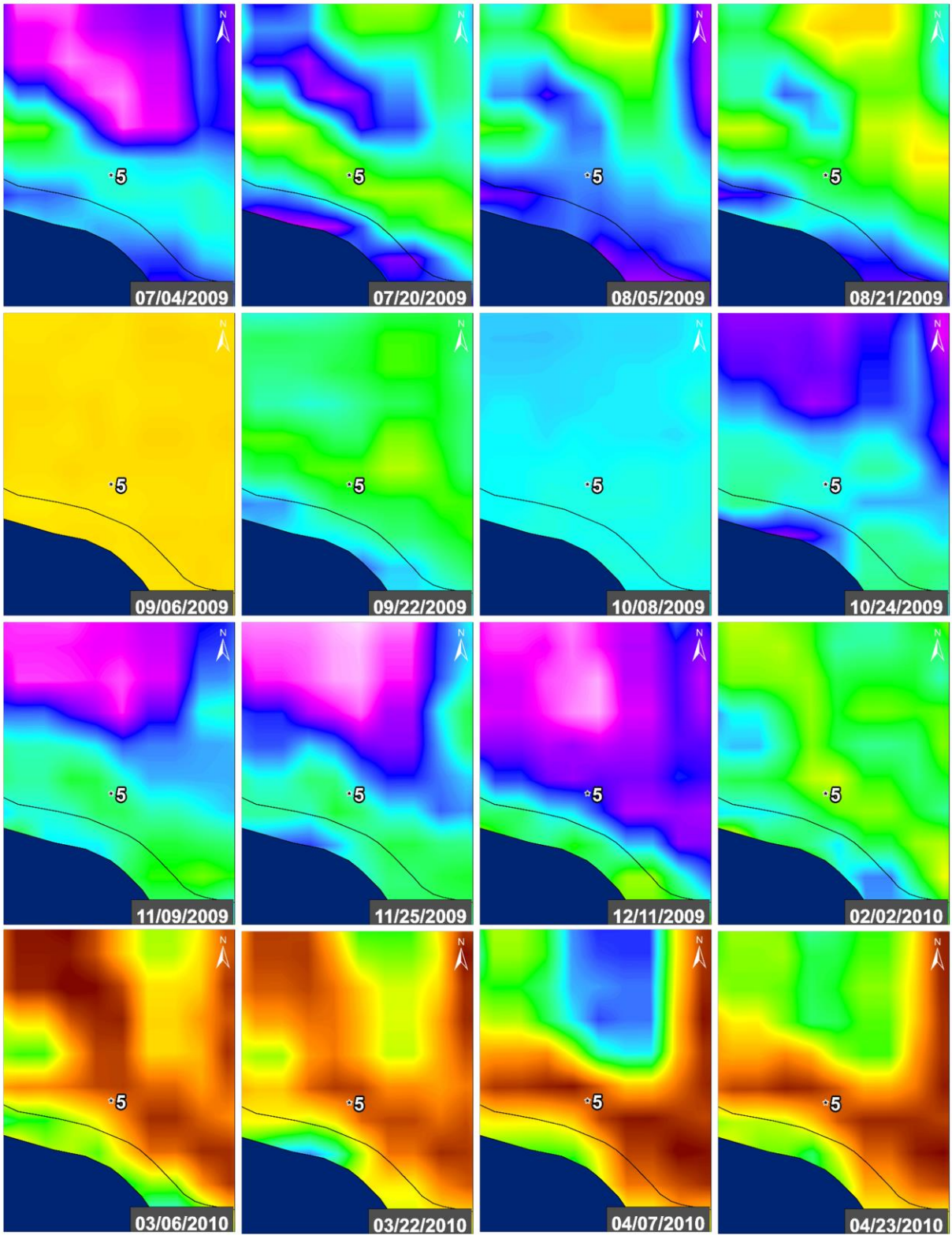

Figure 56B: Seep 5 – NDWI

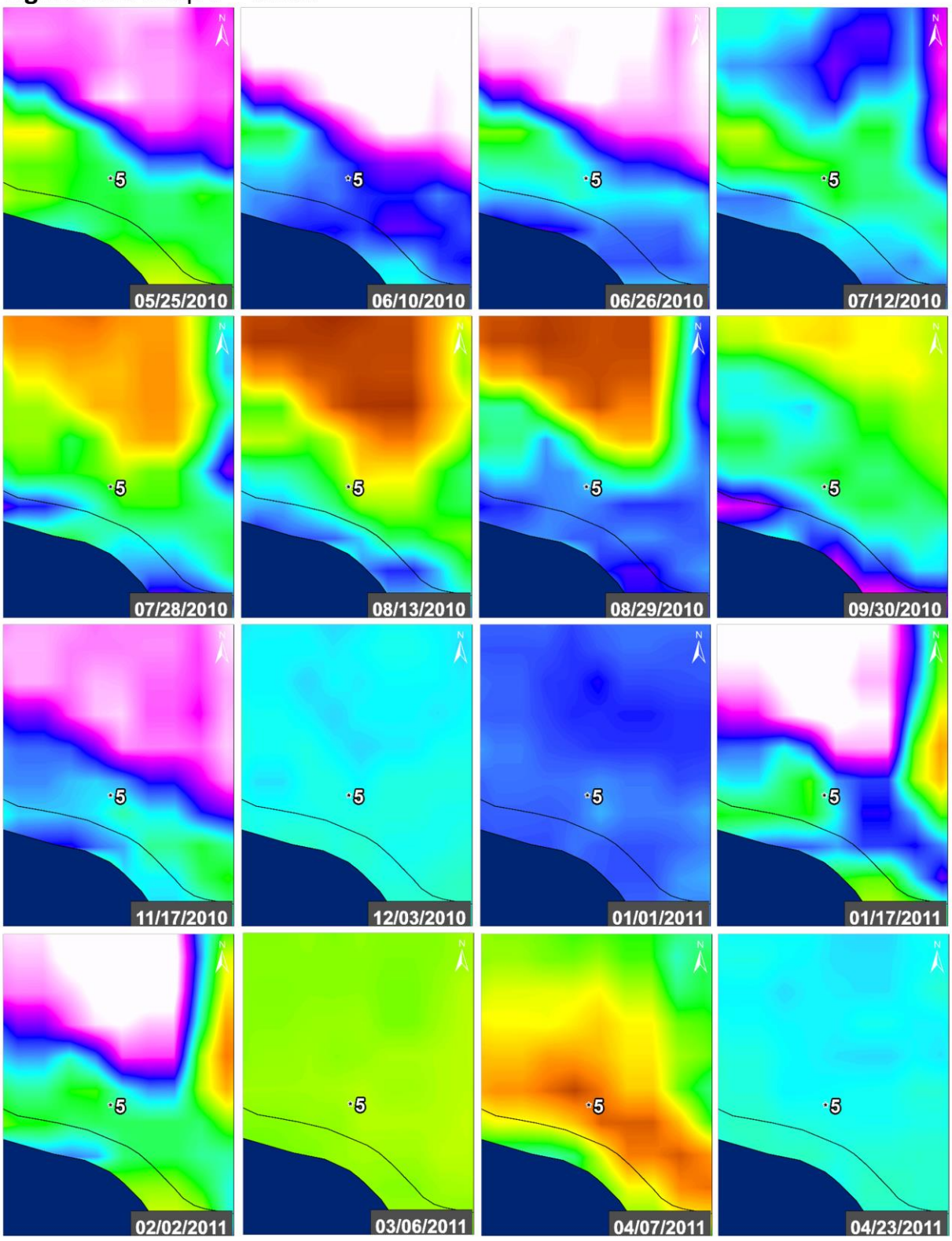

Figure 56C: Seep 5 – NDWI

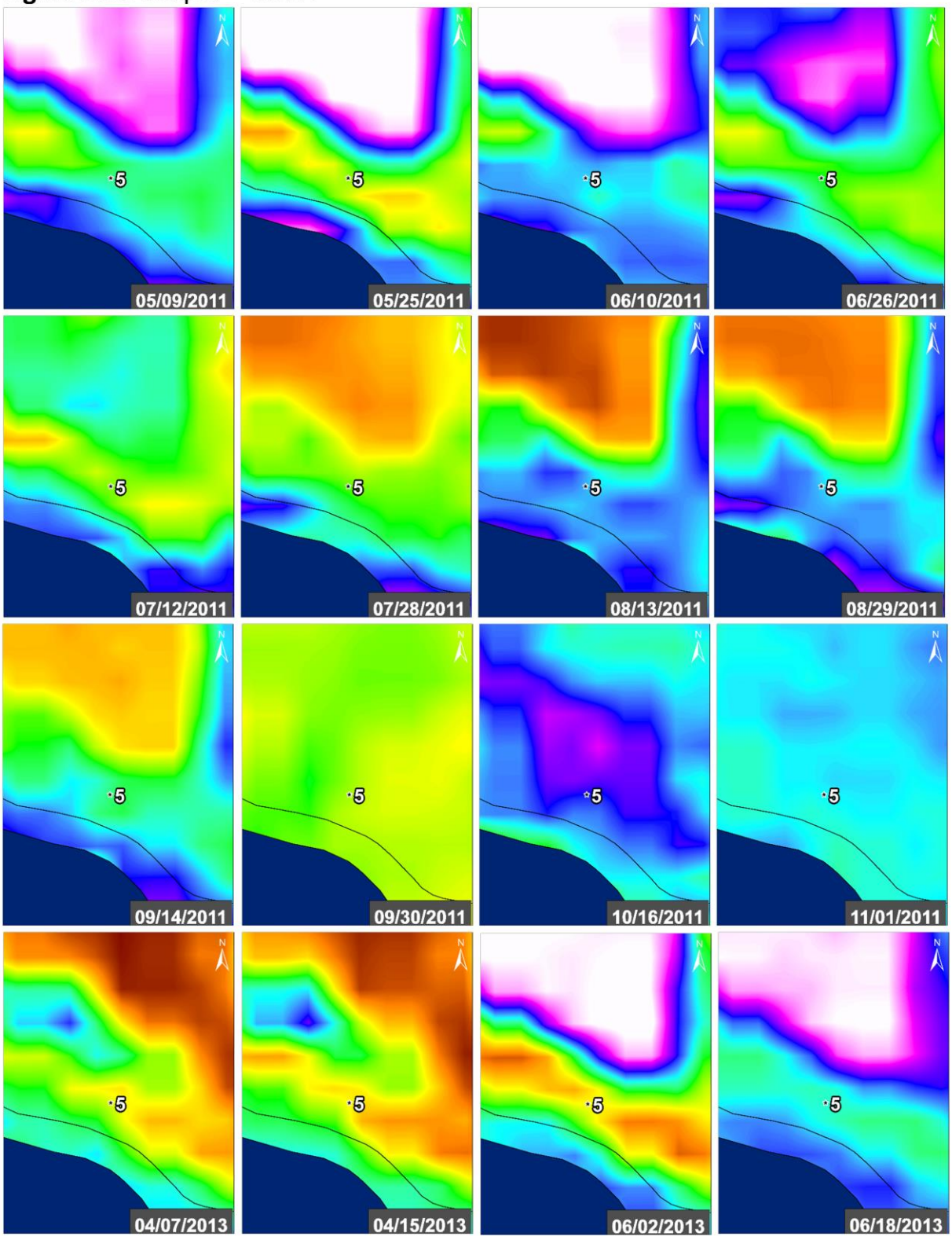

Figure 56D: Seep 5 – NDWI

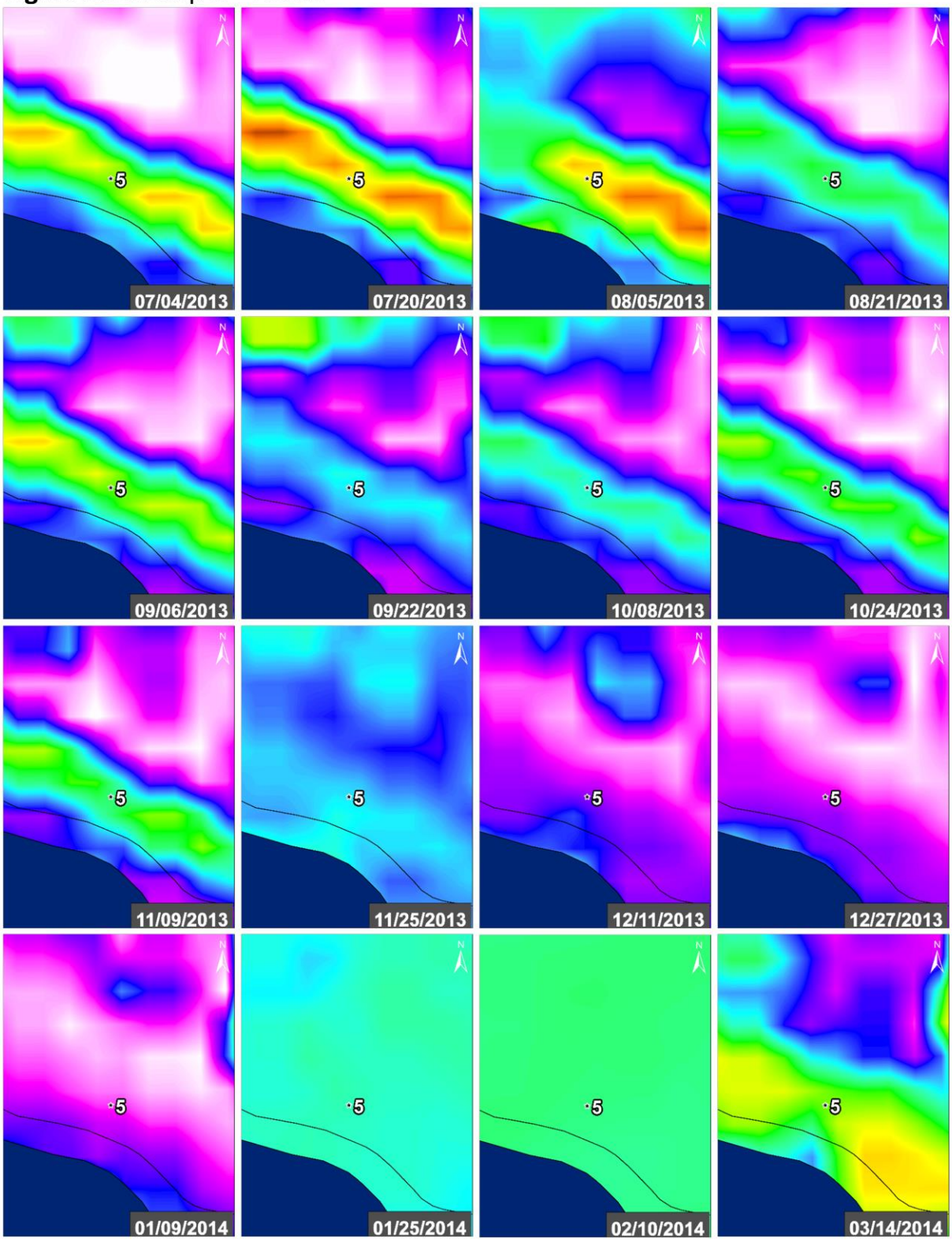

Figure 56E: Seep 5 – NDWI

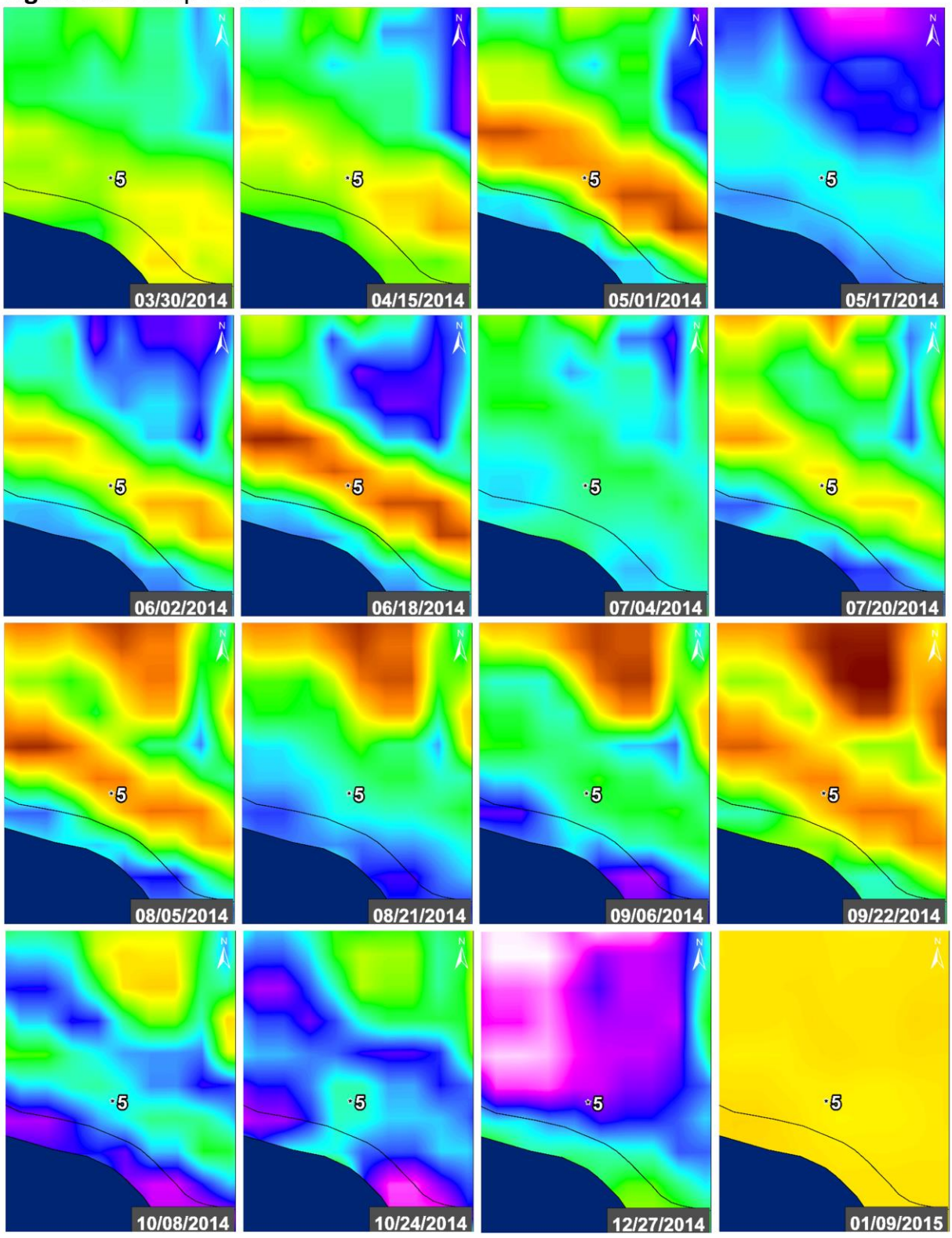

Figure 56F: Seep 5 – NDWI

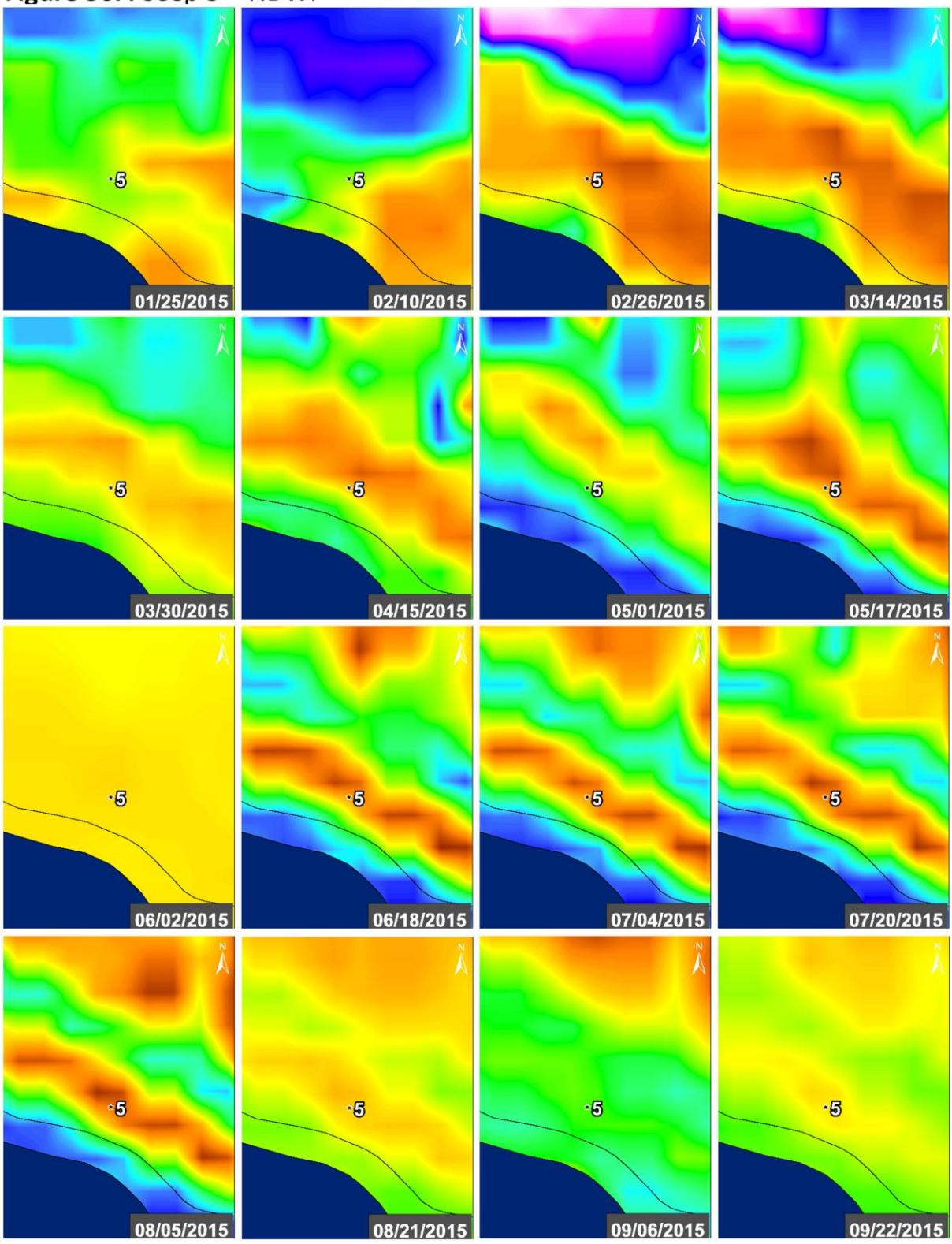

Figure 56G: Seep 5 – NDWI

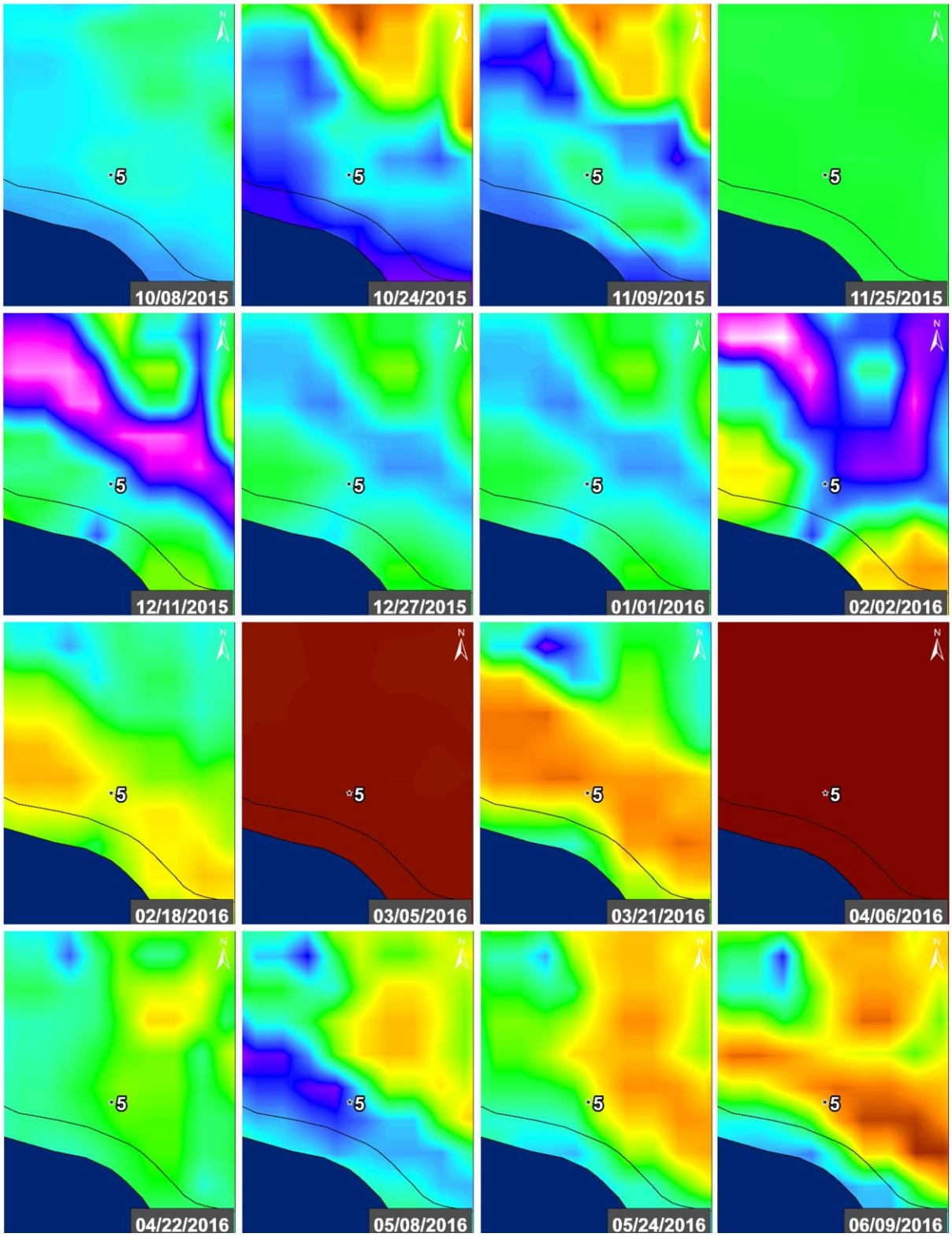

Figure 56H: Seep 5 – NDWI

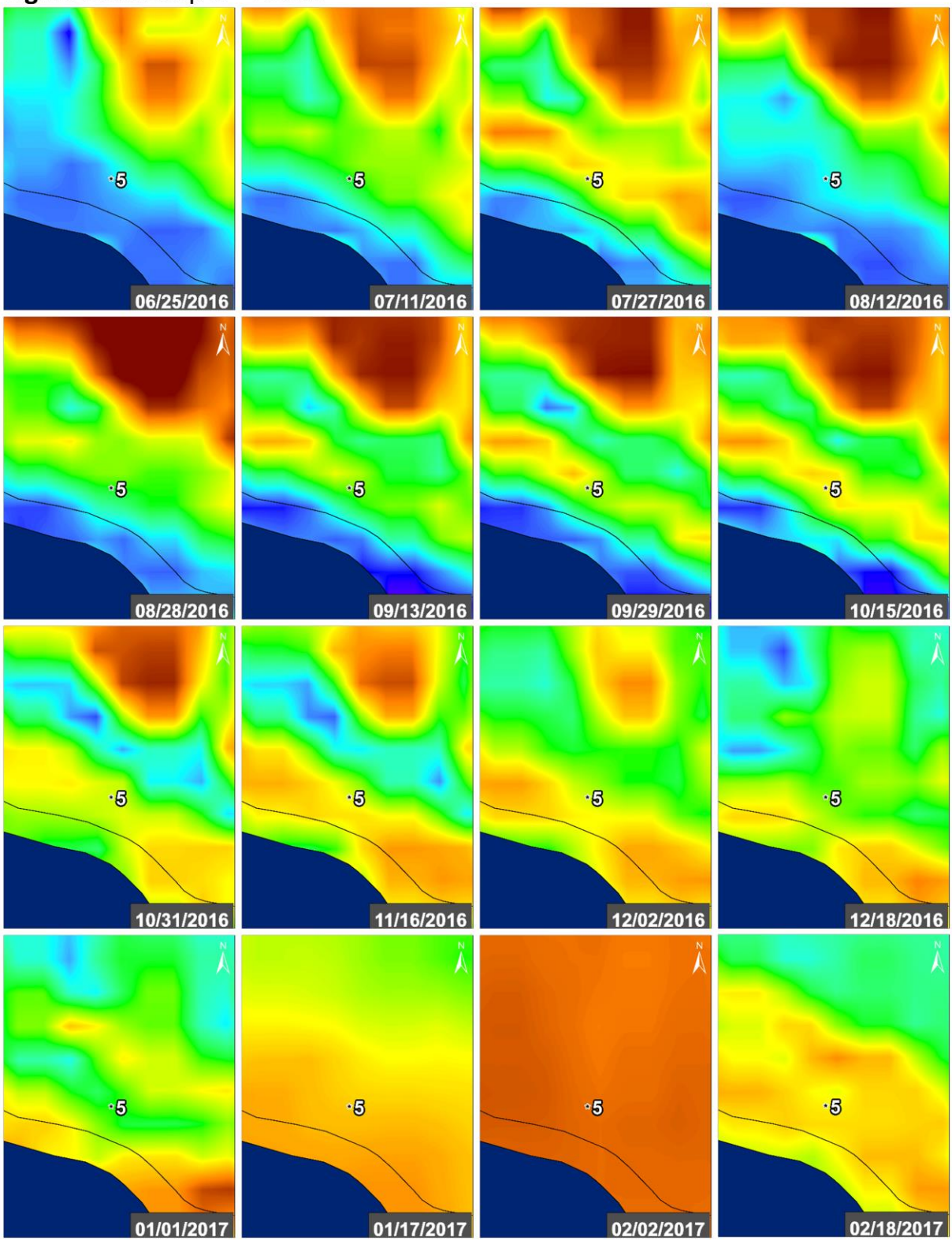

Figure 56I: Seep 5 – NDWI

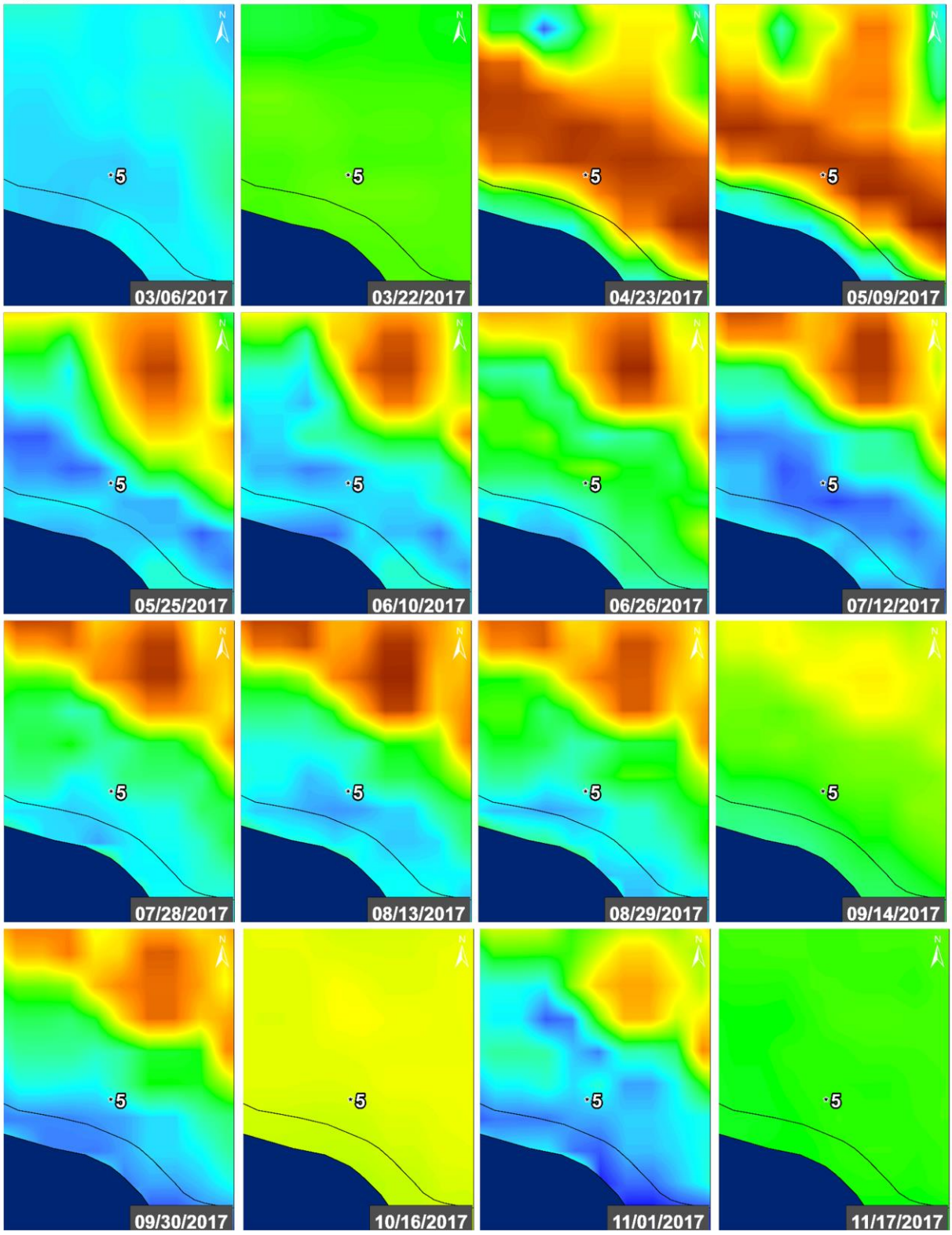

Figure 56J: Seep 5 – NDWI

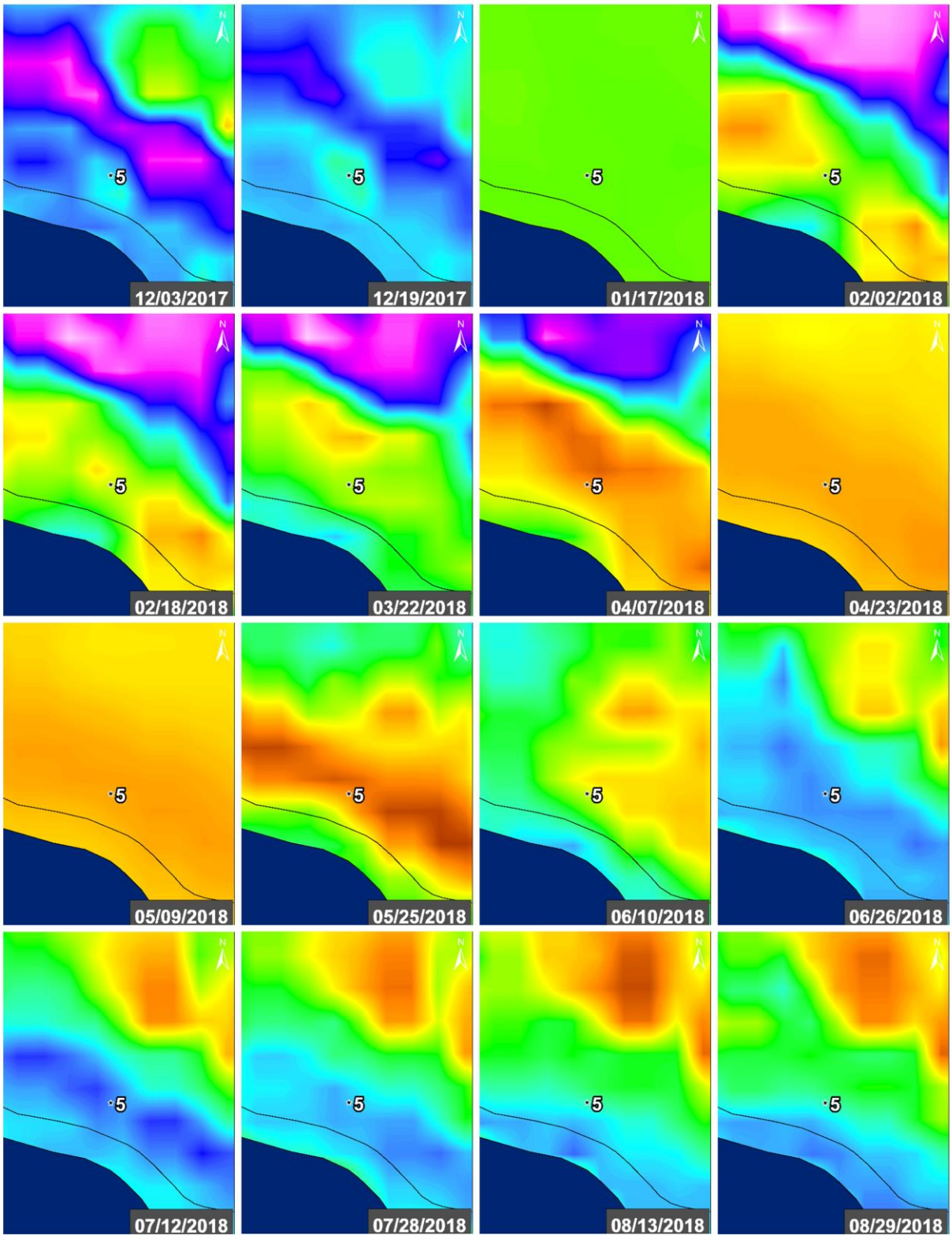

Figure 56K: Seep 5 – NDWI

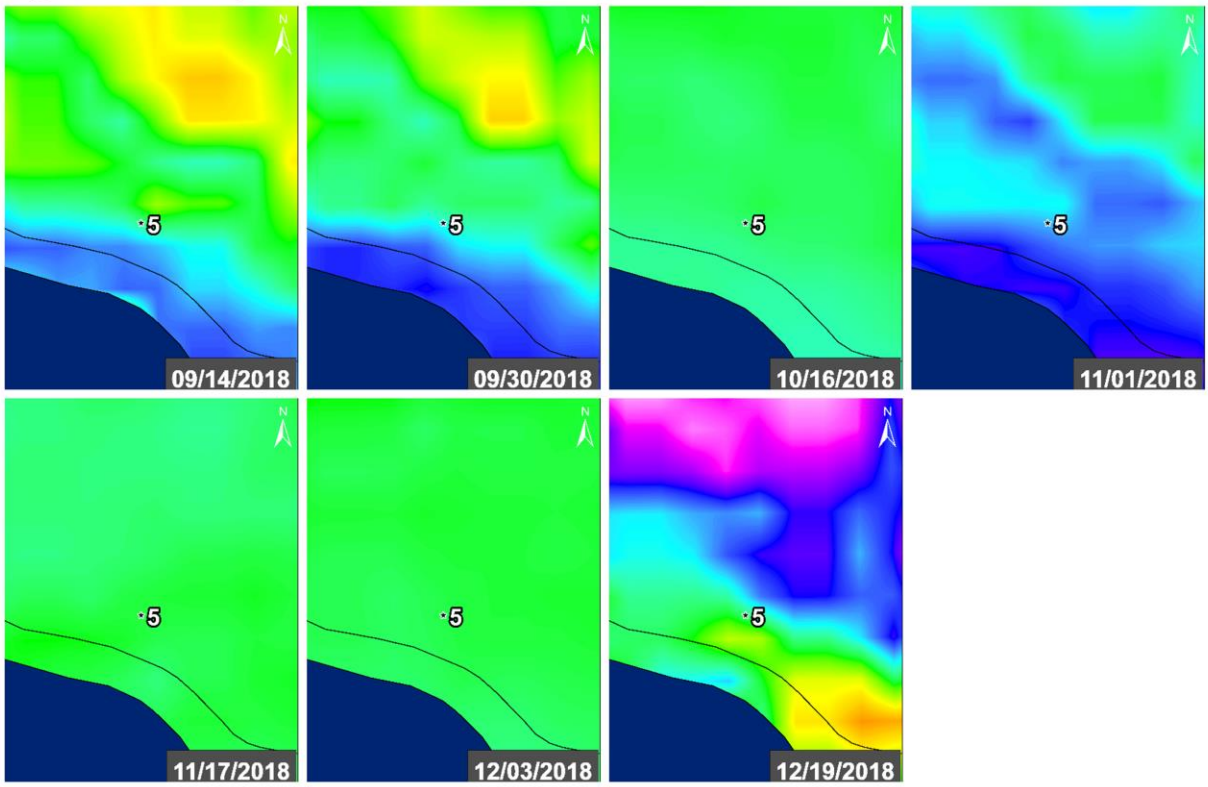

Figure 57A: Seep 5 – VV/HH Ratio – Line 05519

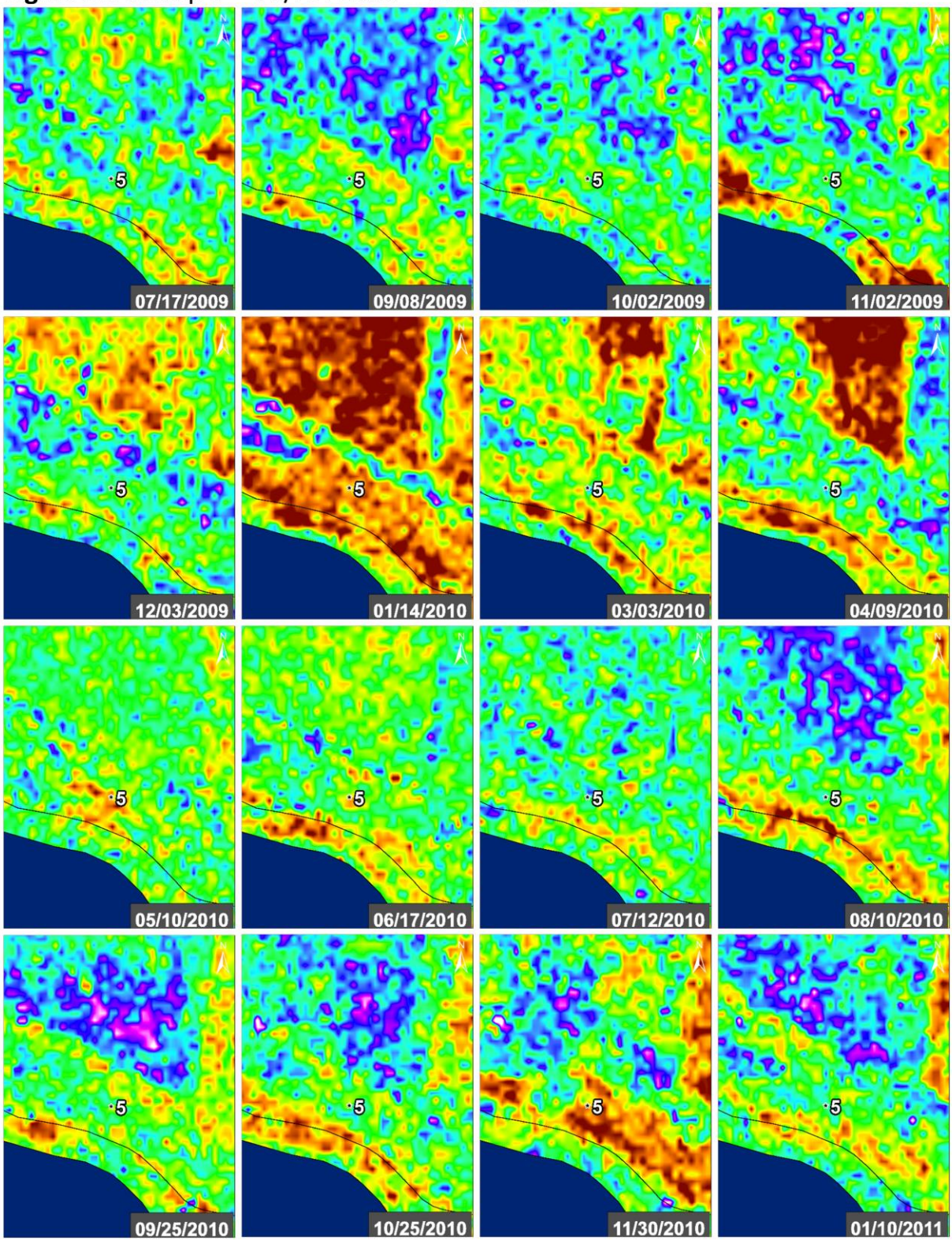

Figure 57B: Seep 5 – VV/HH Ratio – Line 05519

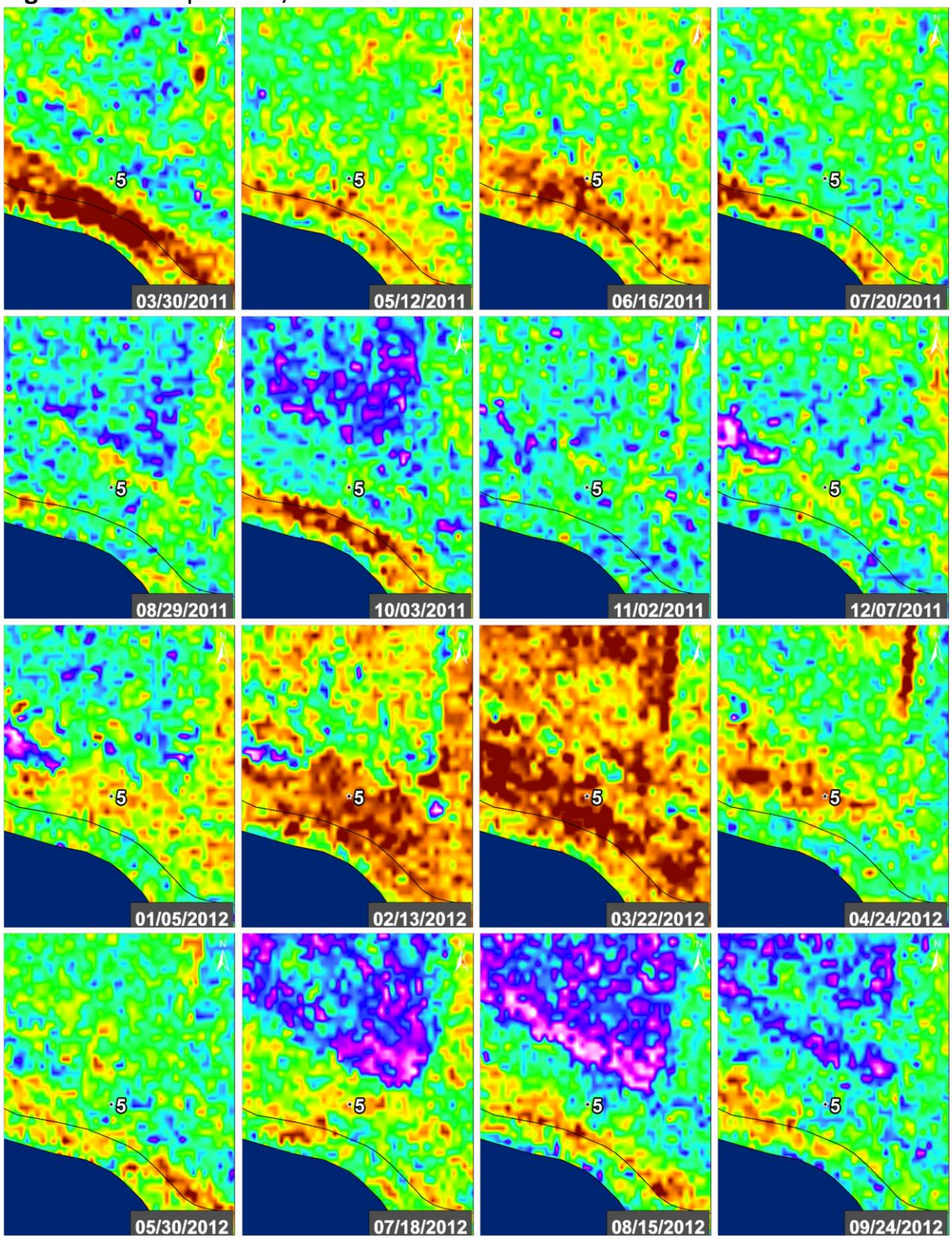

Figure 57C: Seep 5 – VV/HH Ratio – Line 05519

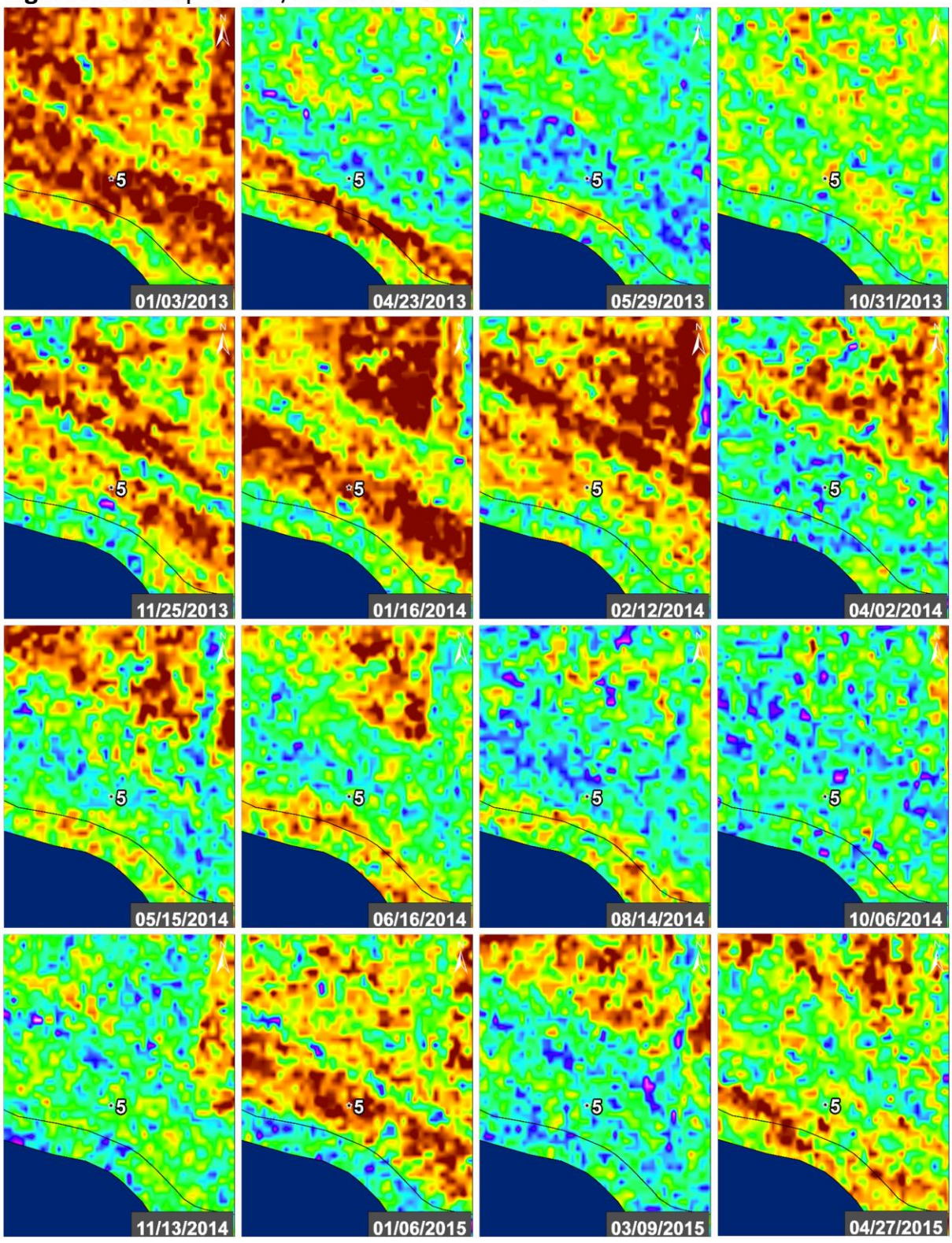

Figure 57D: Seep 5 – VV/HH Ratio – Line 05519

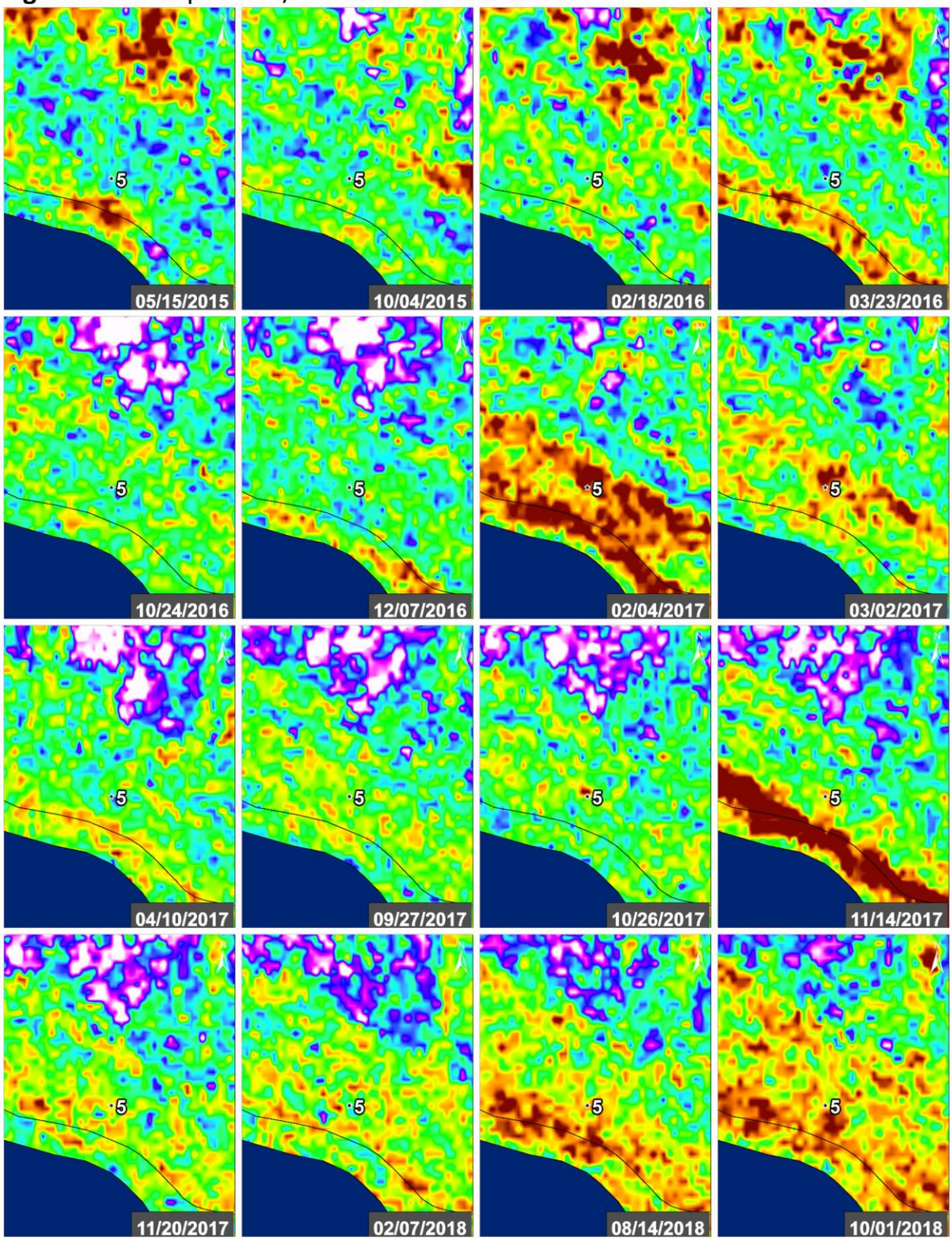

Figure 57E: Seep 5 – VV/HH Ratio – Line 05519

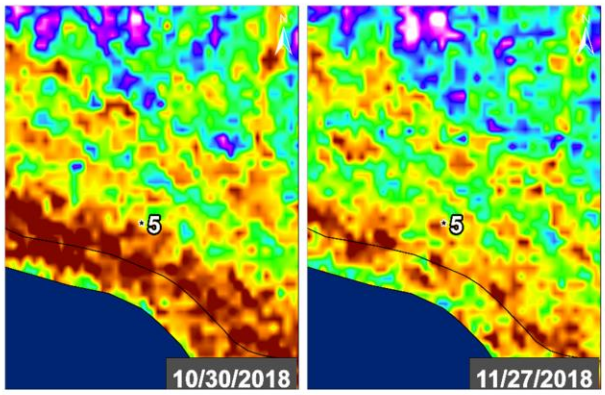

Figure 58A: Seep 5 – VV/HH Ratio – Line 15502

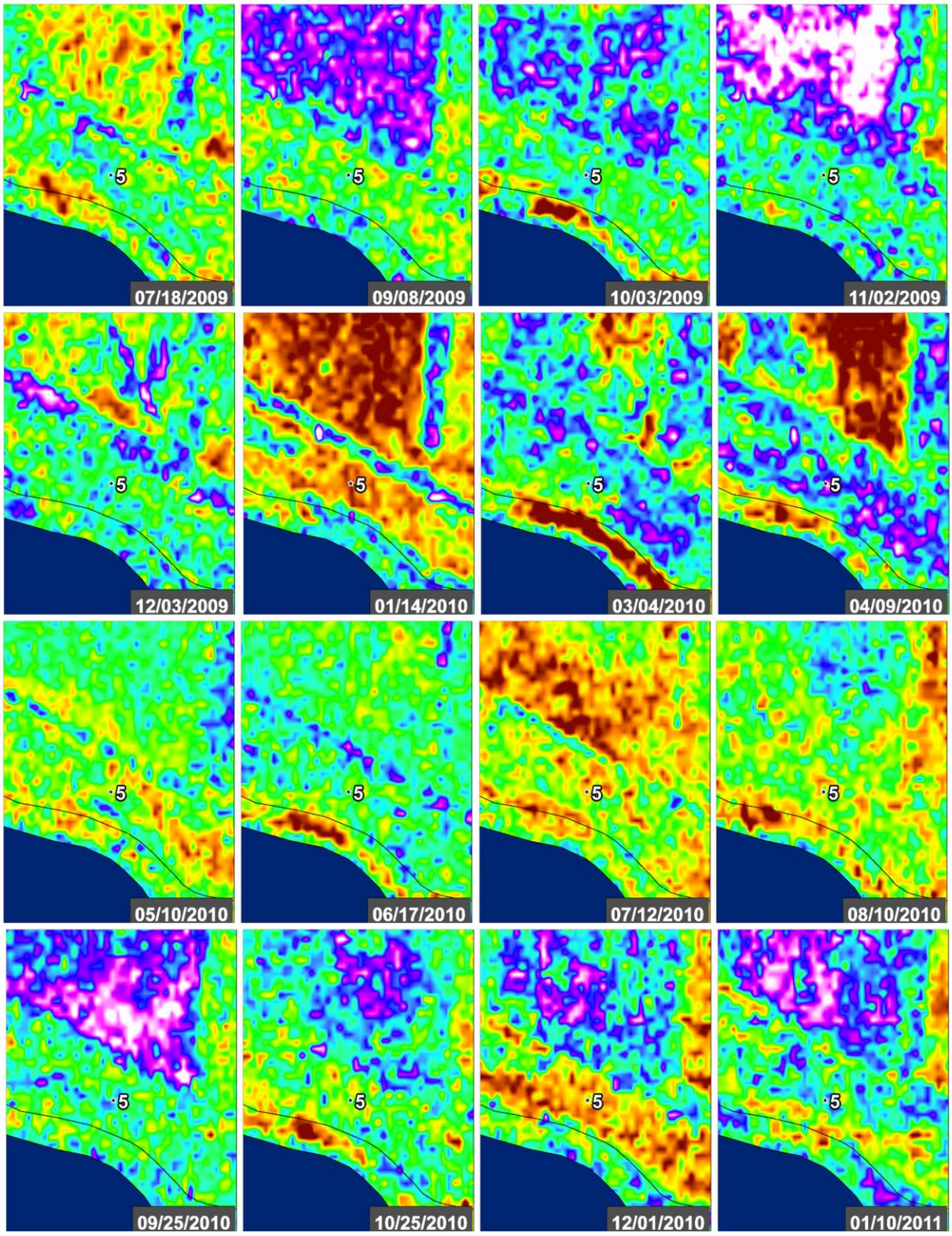

Figure 58B: Seep 5 – VV/HH Ratio – Line 15502

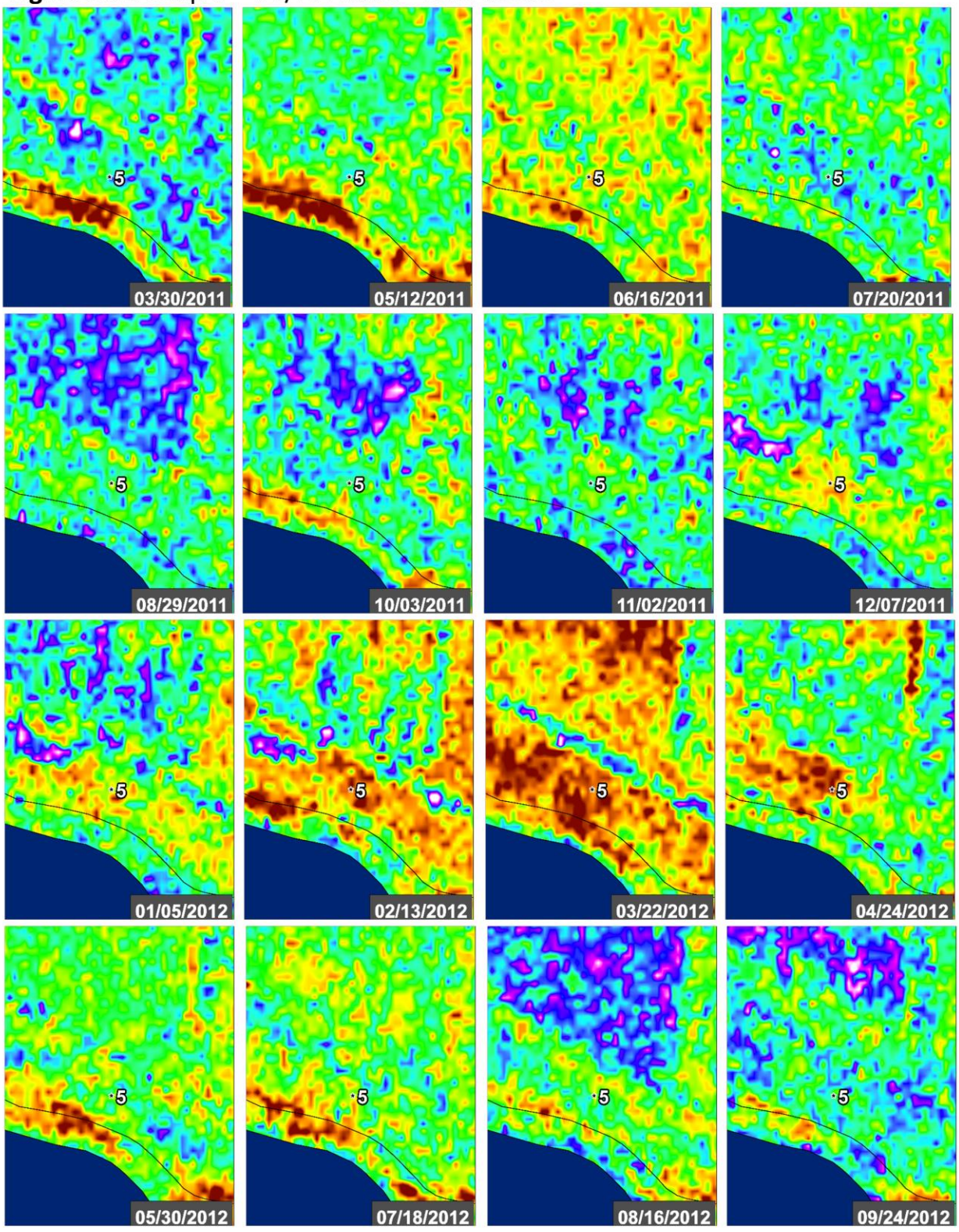

Figure 58C: Seep 5 – VV/HH Ratio – Line 15502

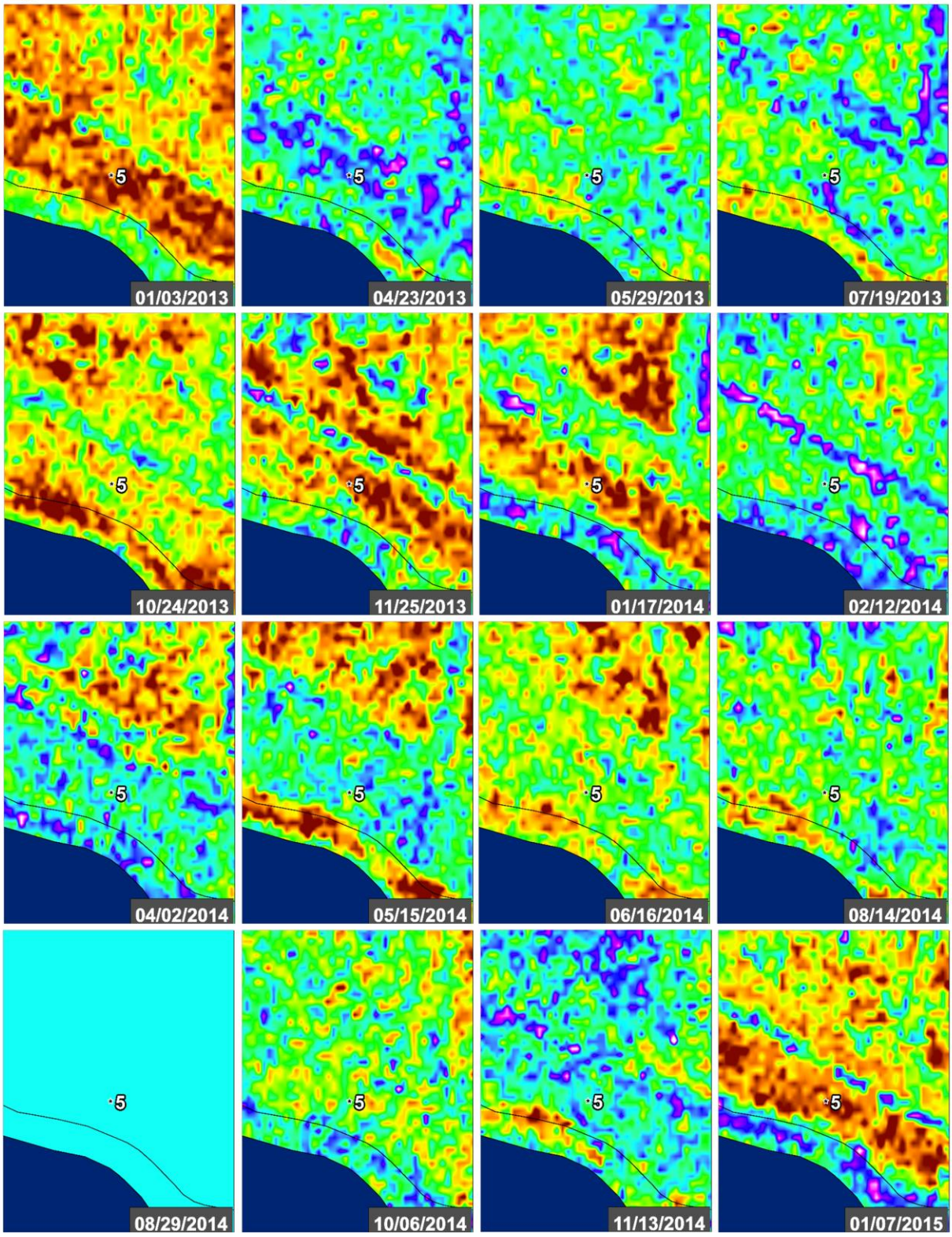

Figure 58D: Seep 5 – VV/HH Ratio – Line 15502

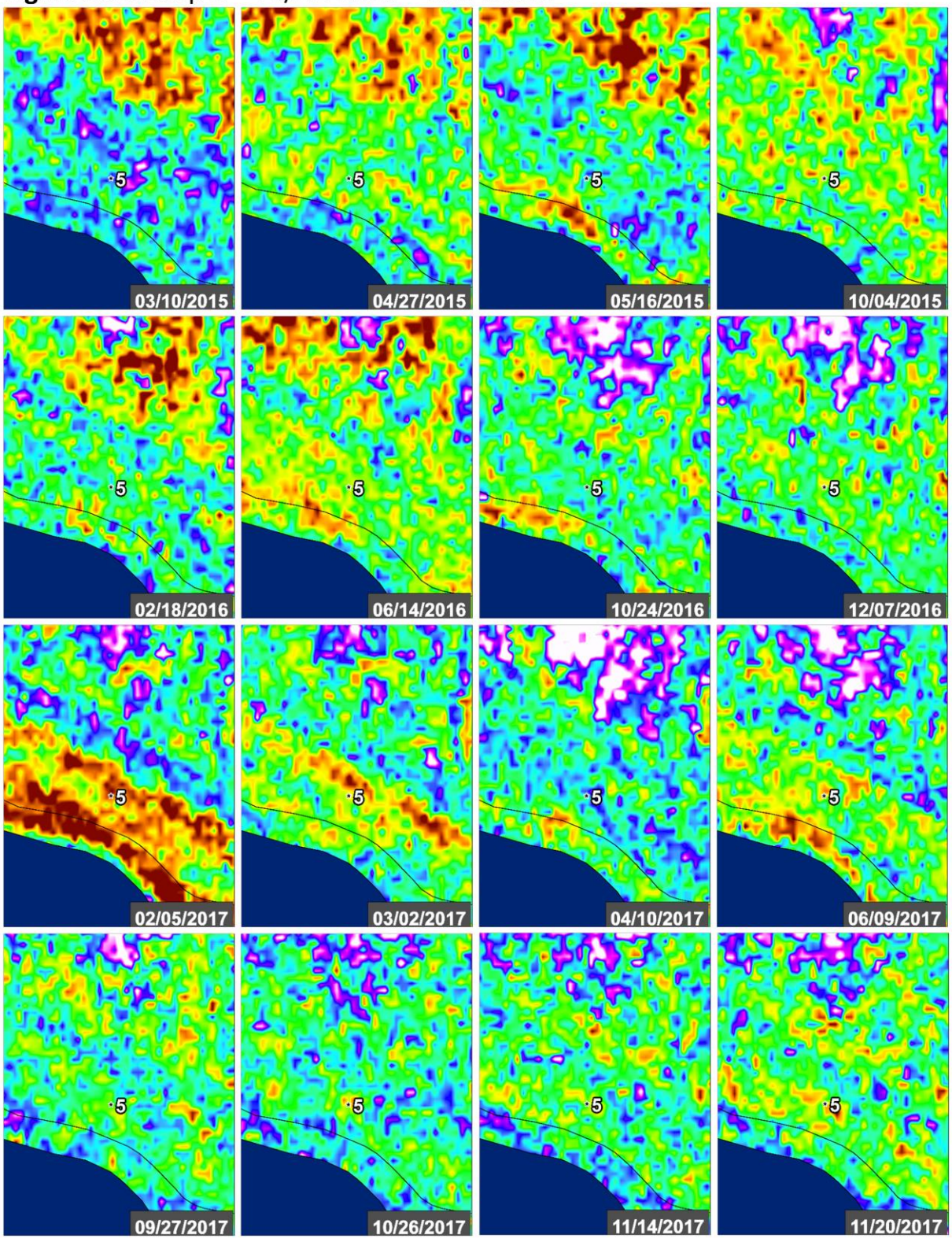

Figure 58E: Seep 5 – VV/HH Ratio – Line 15502

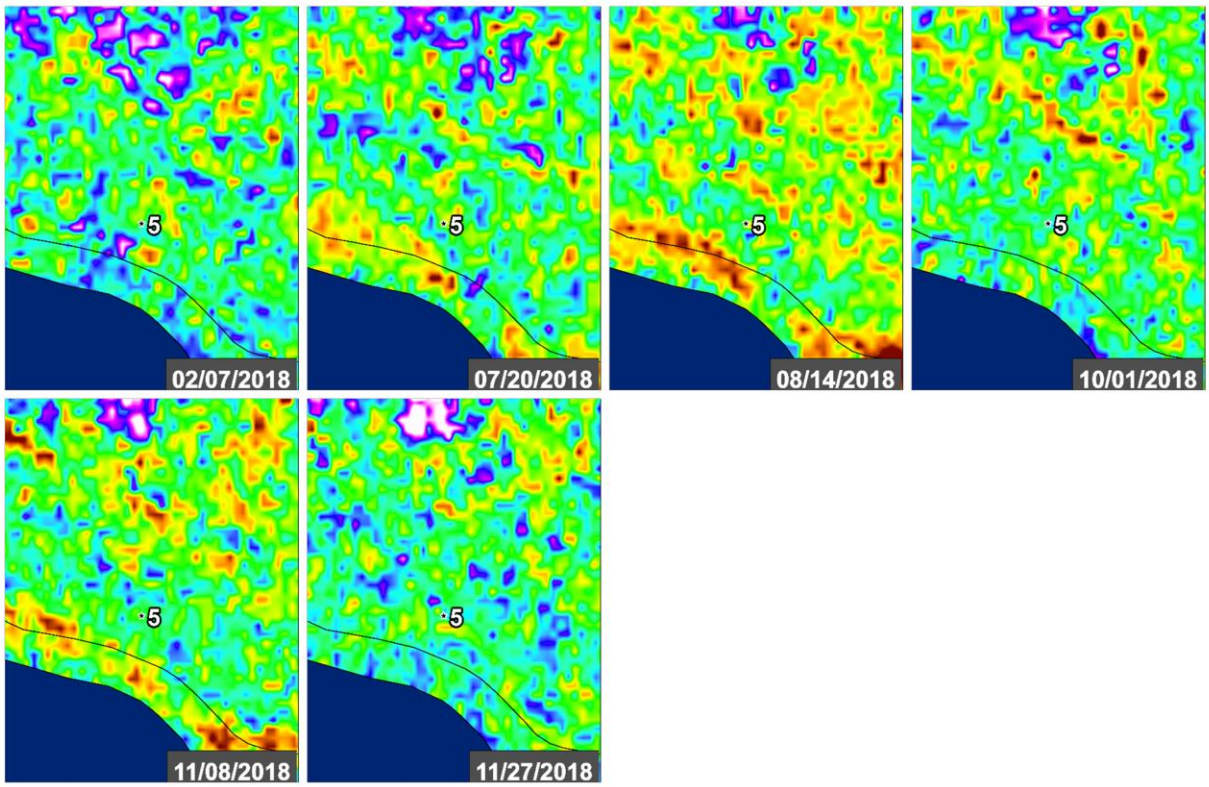

Figure 59A: Seep 5 – VV/HH Ratio – Line 15503

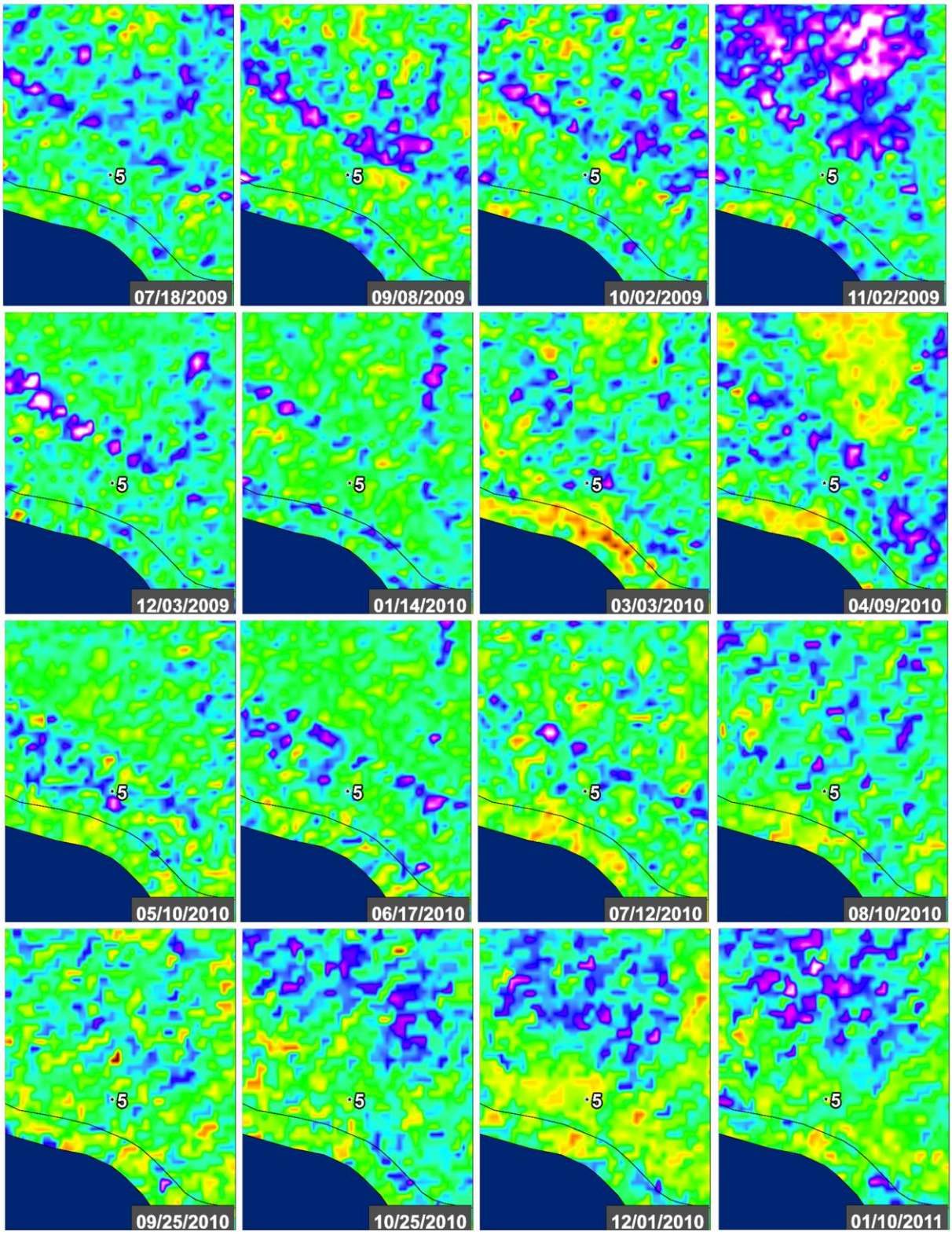

Figure 59B: Seep 5 – VV/HH Ratio – Line 15503

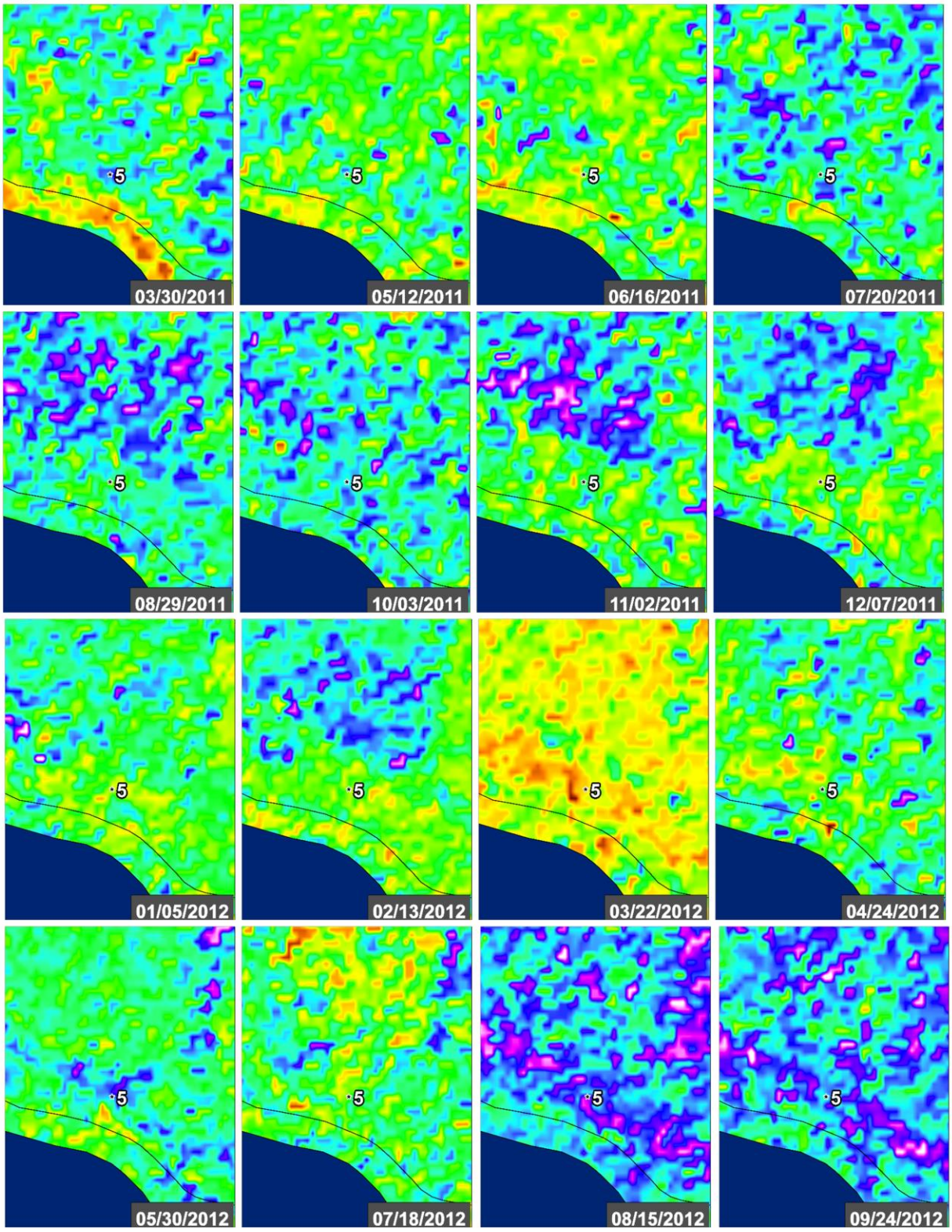

Figure 59C: Seep 5 – VV/HH Ratio – Line 15503

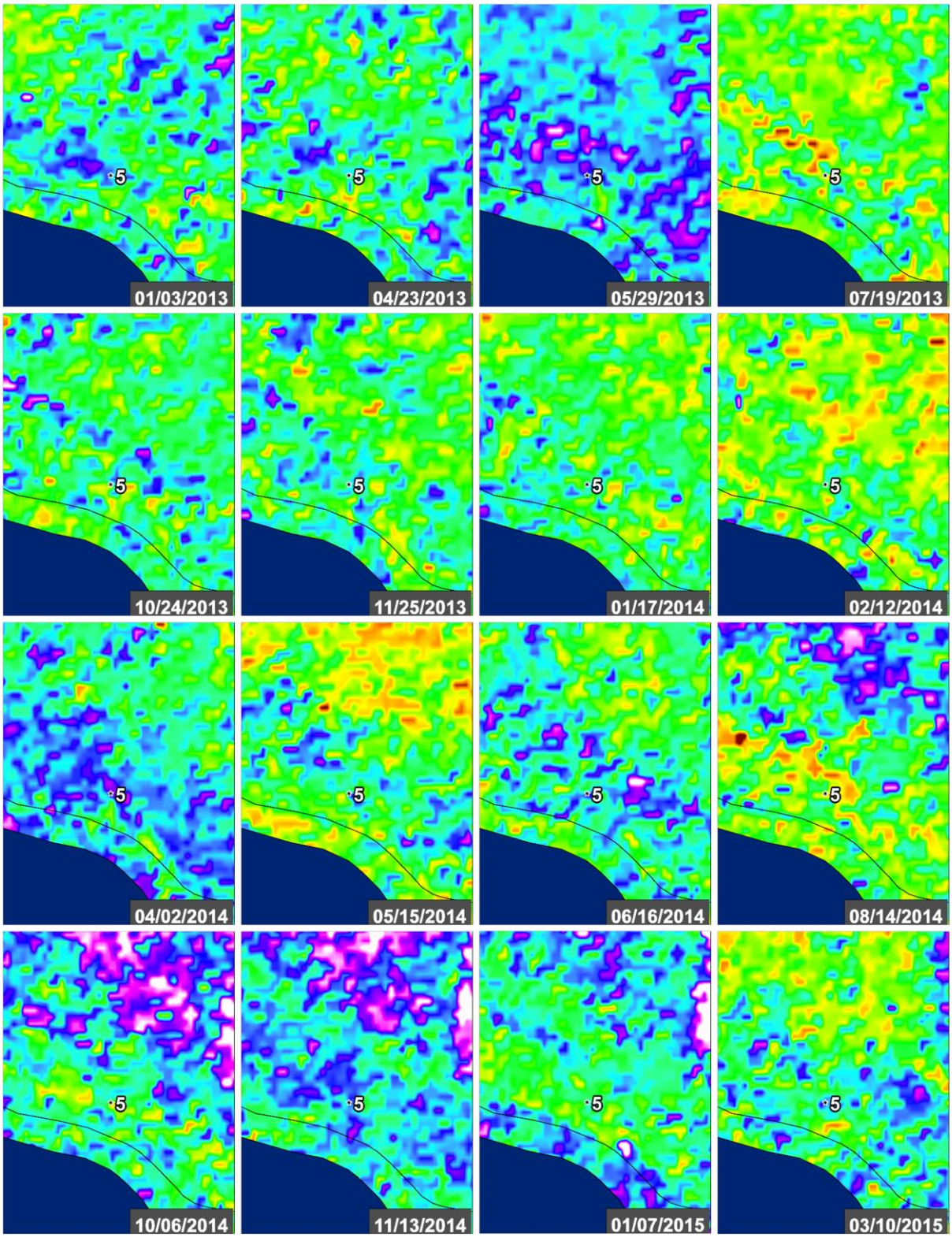

Figure 59D: Seep 5 – VV/HH Ratio – Line 15503

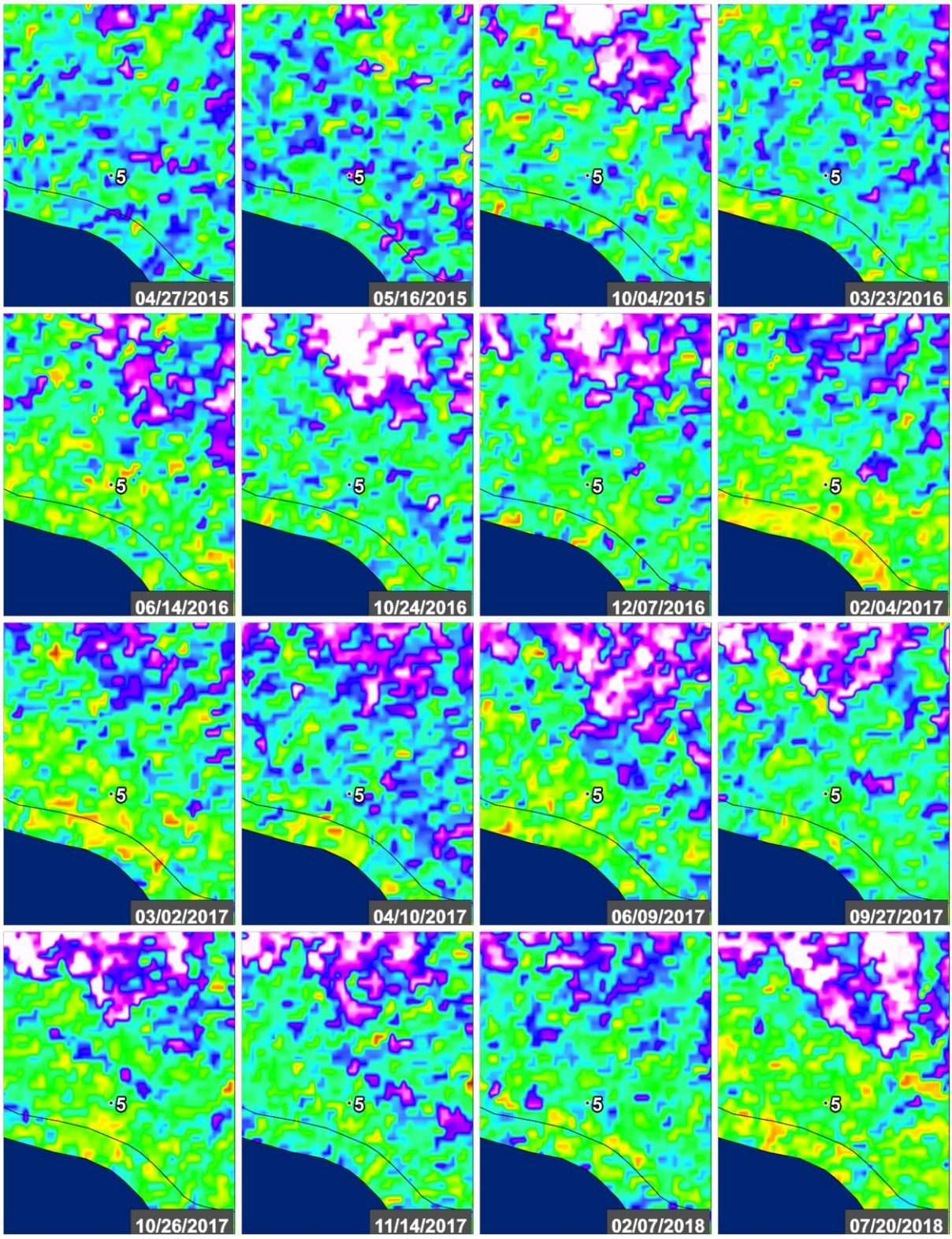

Figure 59E: Seep 5 – VV/HH Ratio – Line 15503

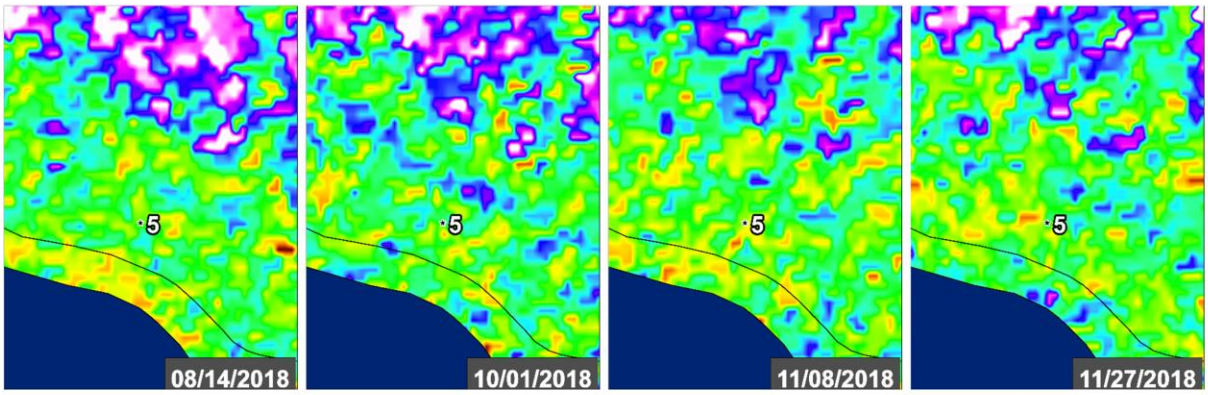

Figure 60A: Seep 5 – VV/HH Ratio – Line 33502

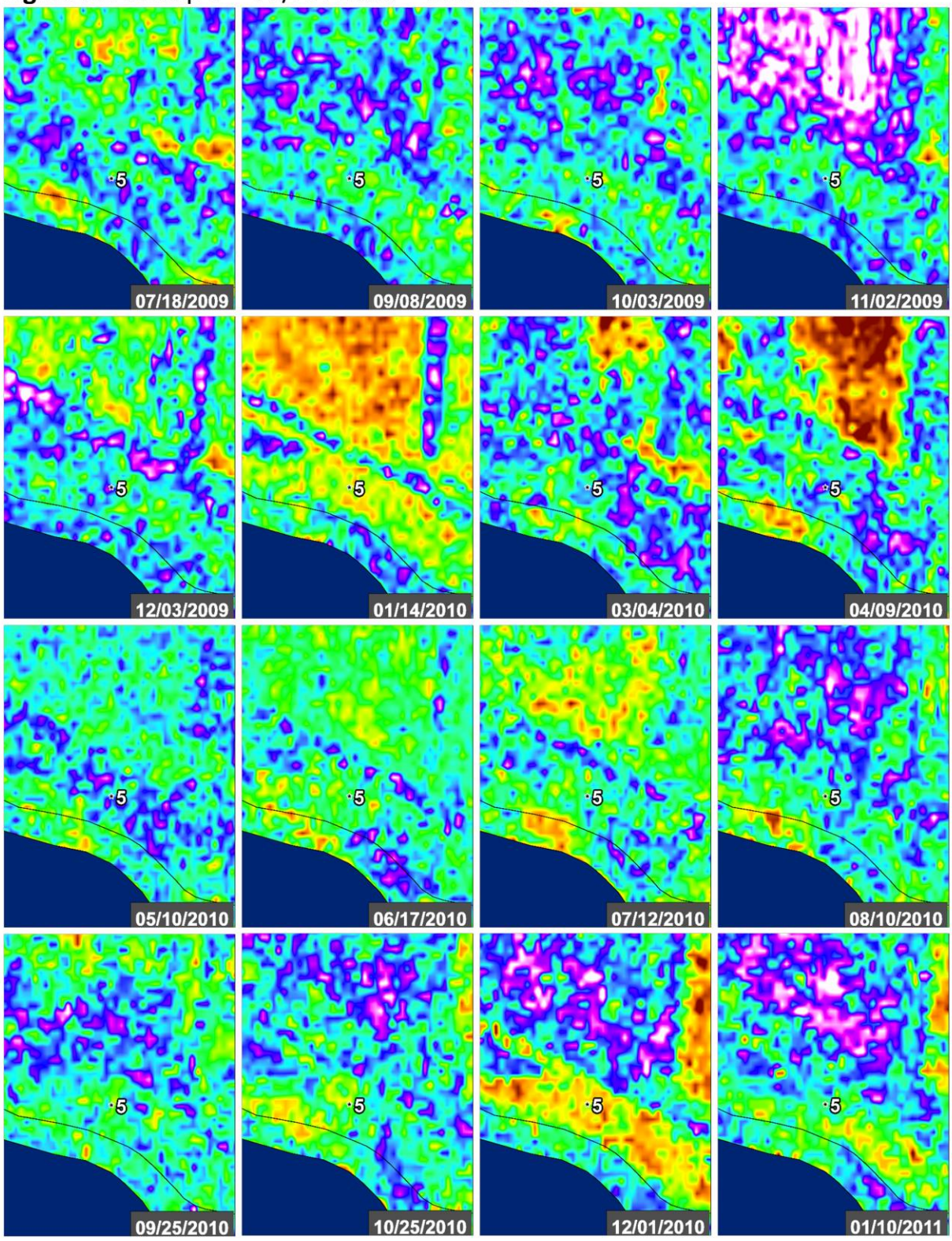

Figure 60B: Seep 5 – VV/HH Ratio – Line 33502

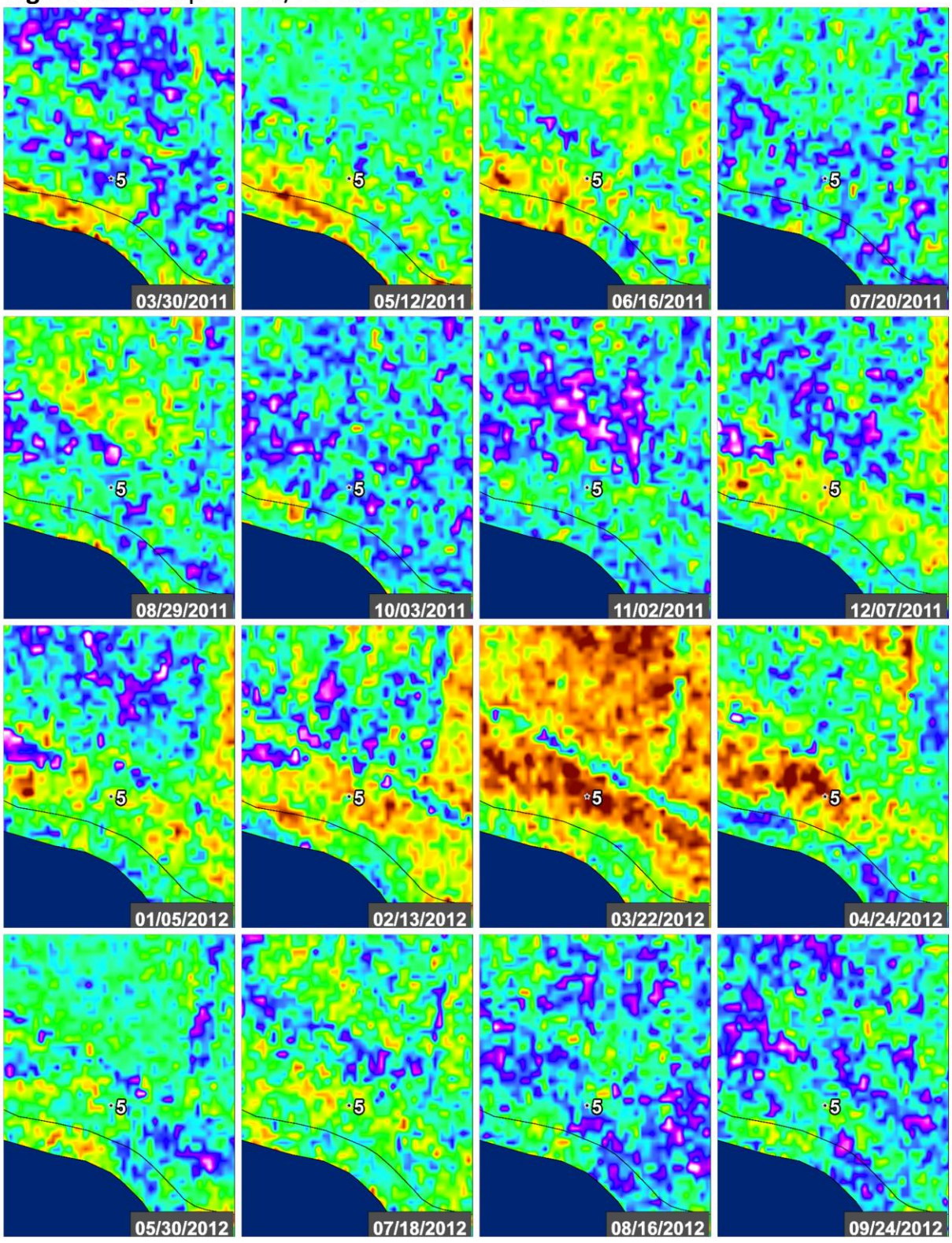

Figure 60C: Seep 5 – VV/HH Ratio – Line 33502

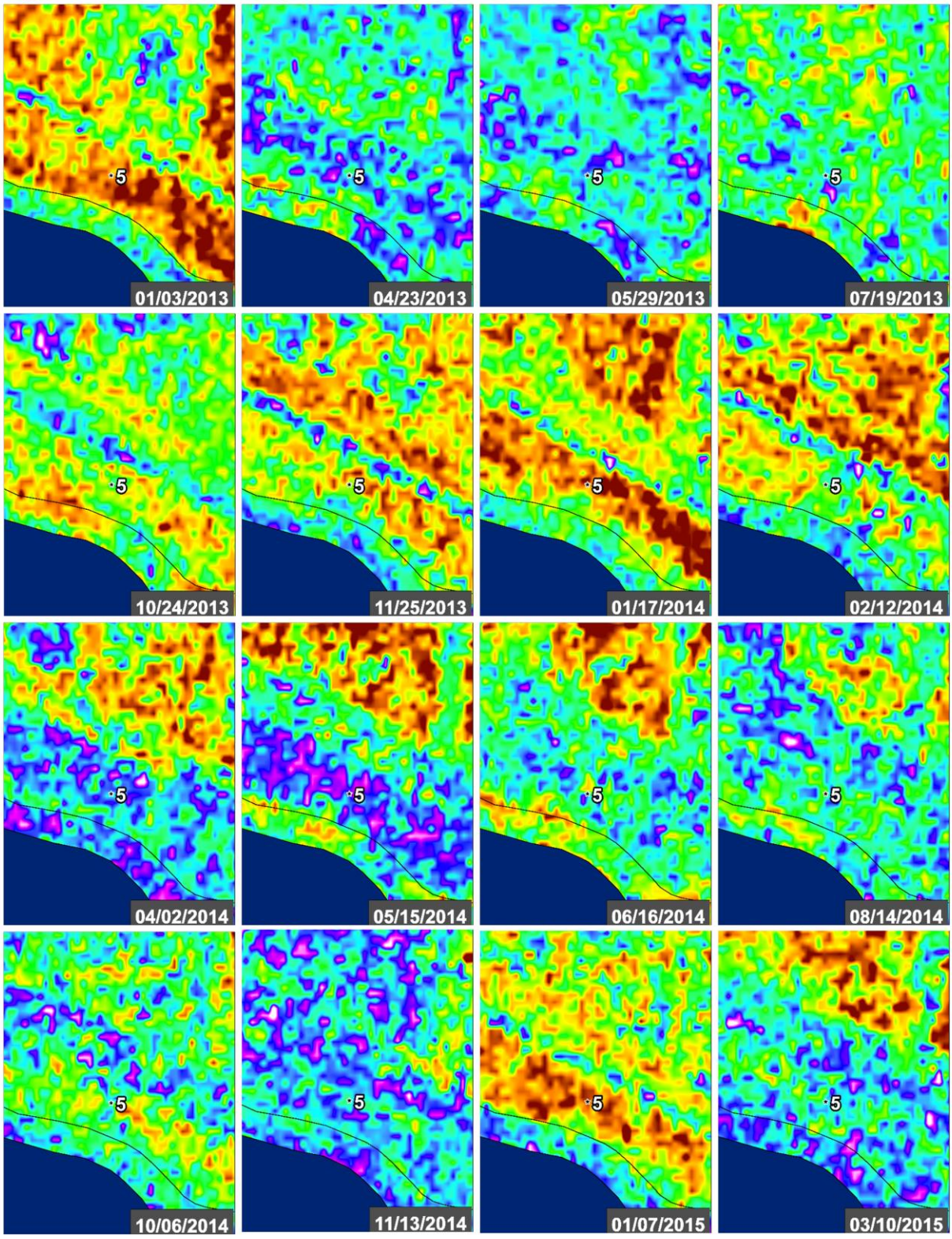

Figure 60D: Seep 5 – VV/HH Ratio – Line 33502

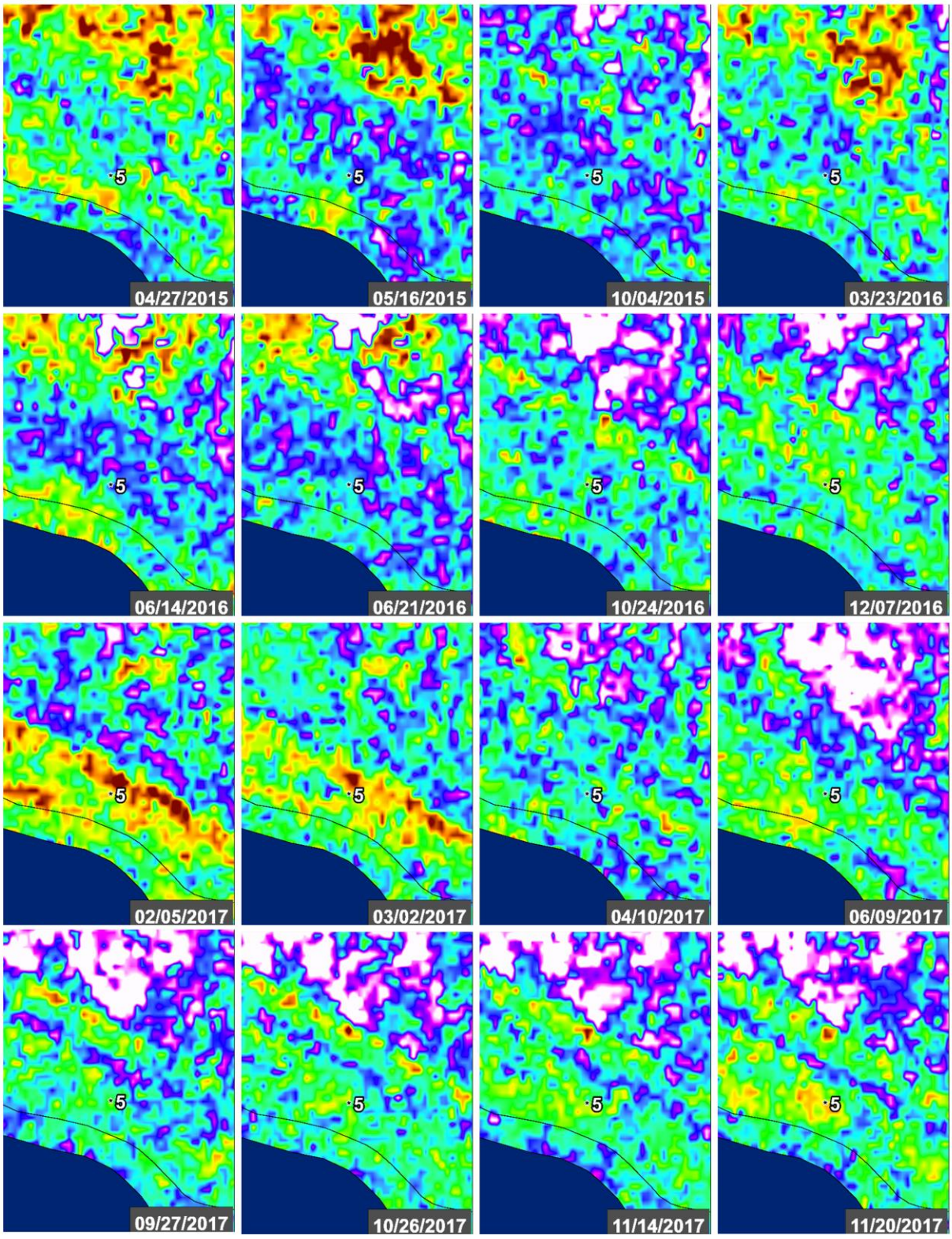

Figure 60E: Seep 5 – VV/HH Ratio – Line 33502

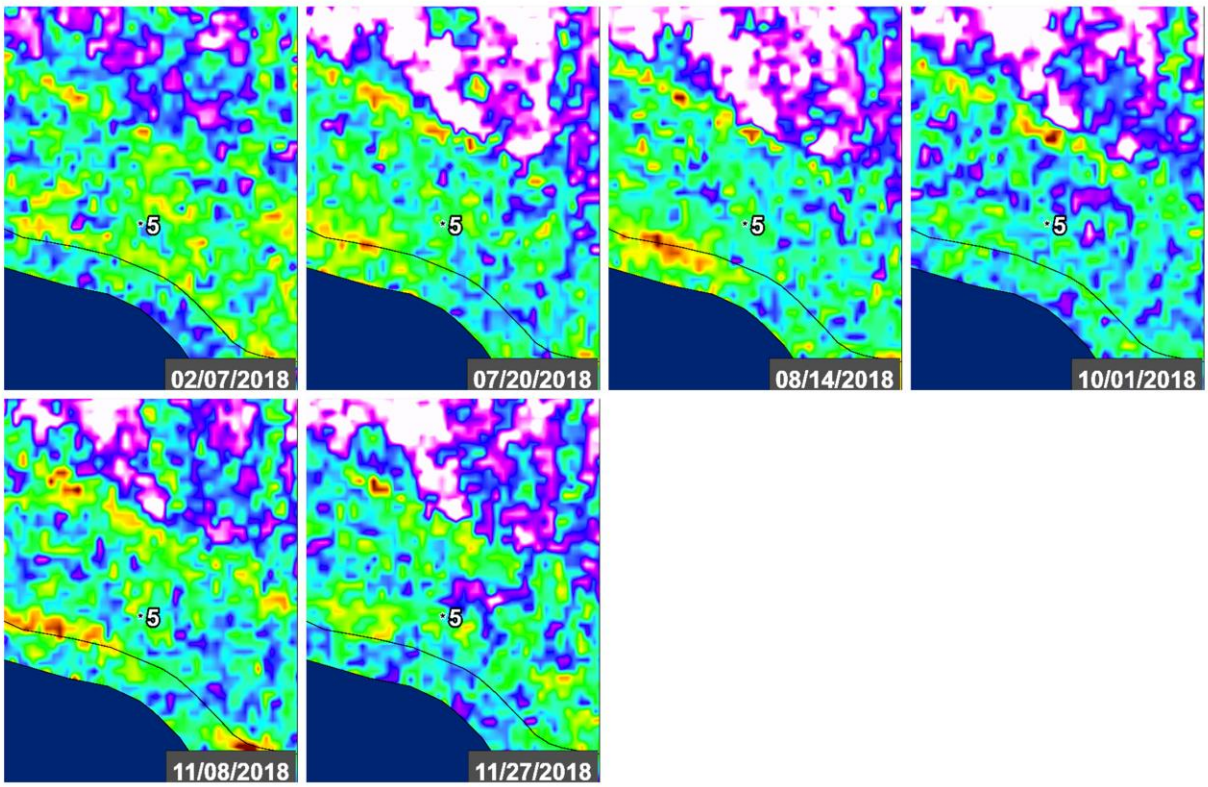

Figure 61A: Seep 5 – VV/HH Ratio – Line 23518

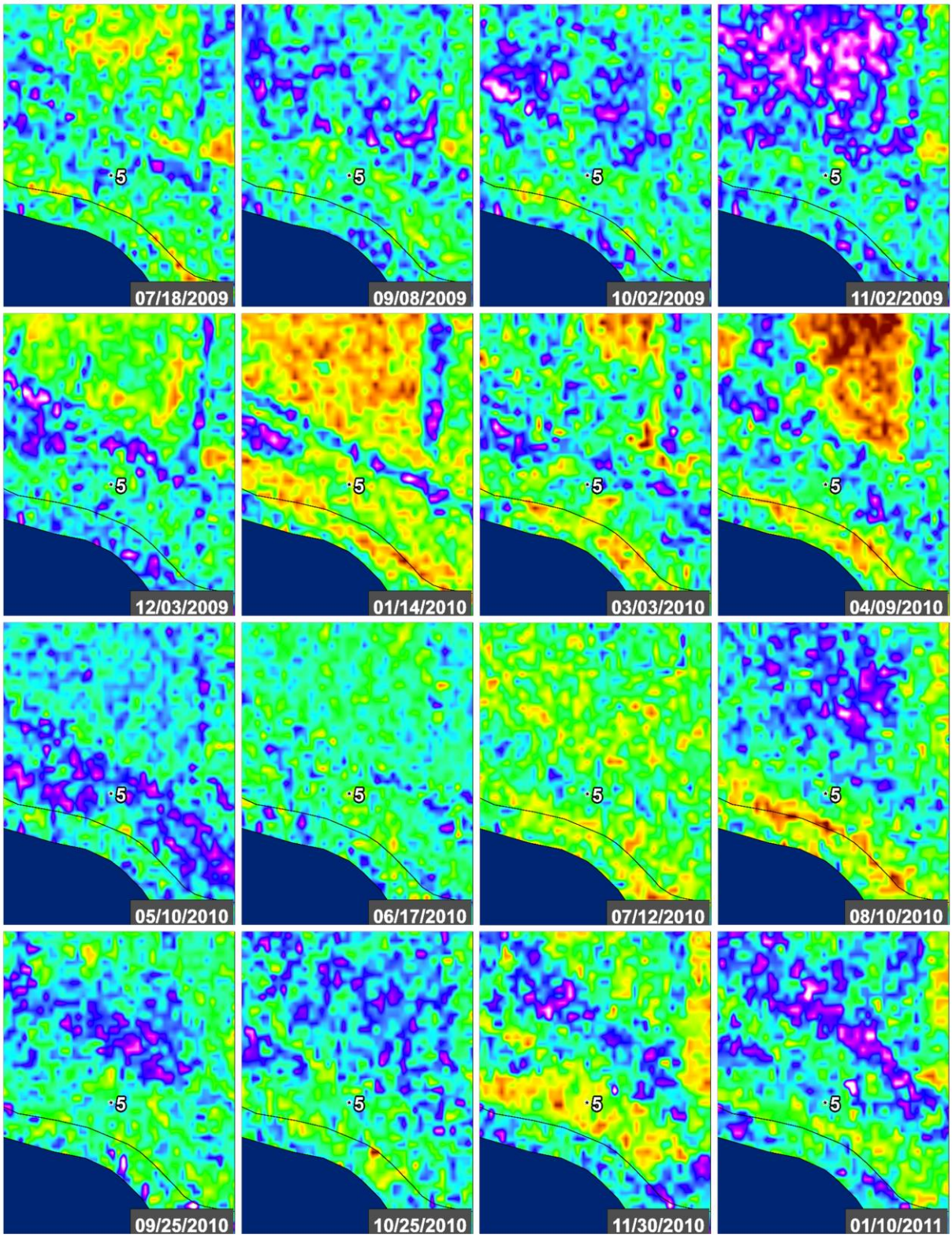

Figure 61B: Seep 5 – VV/HH Ratio – Line 23518

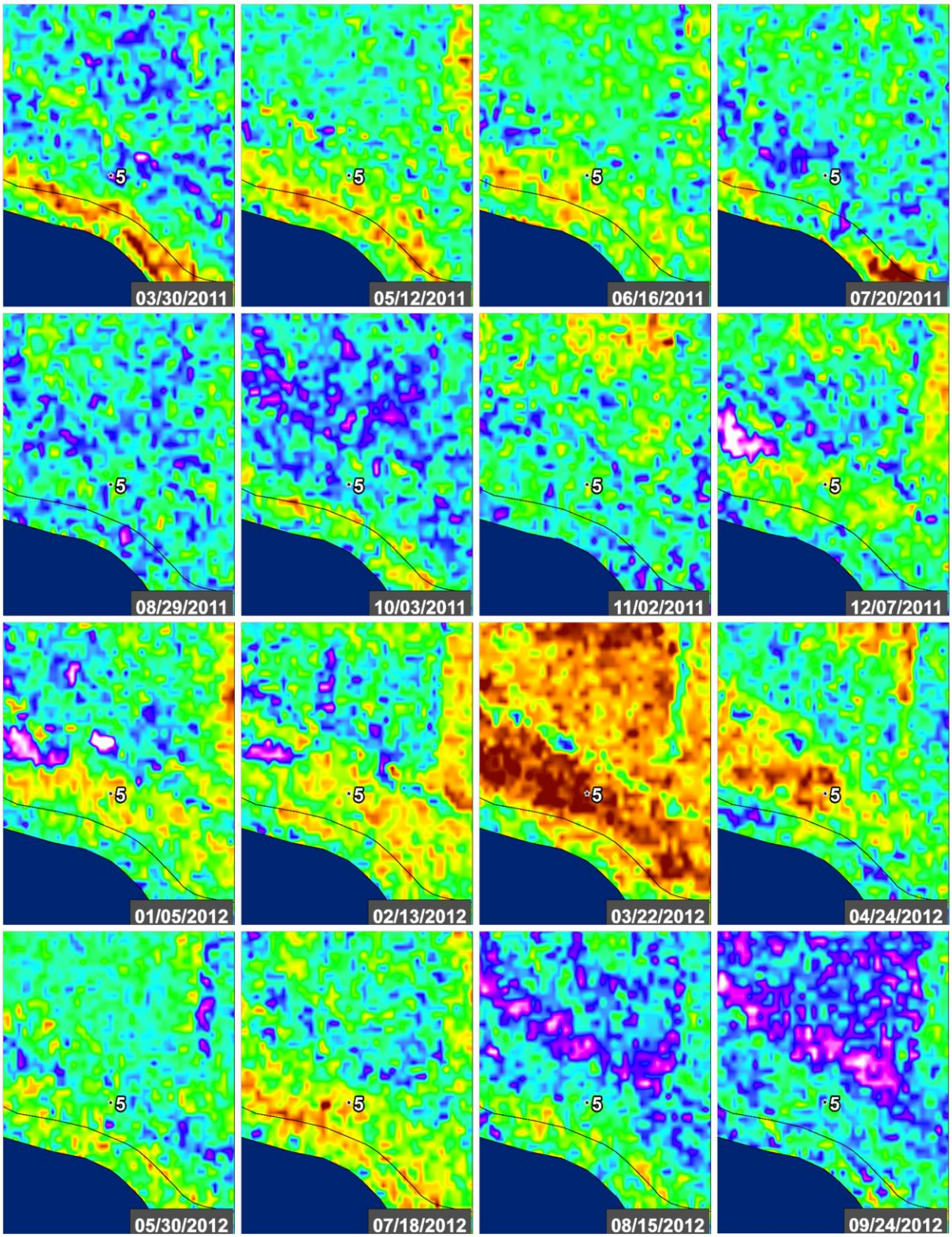

Figure 61C: Seep 5 – VV/HH Ratio – Line 23518

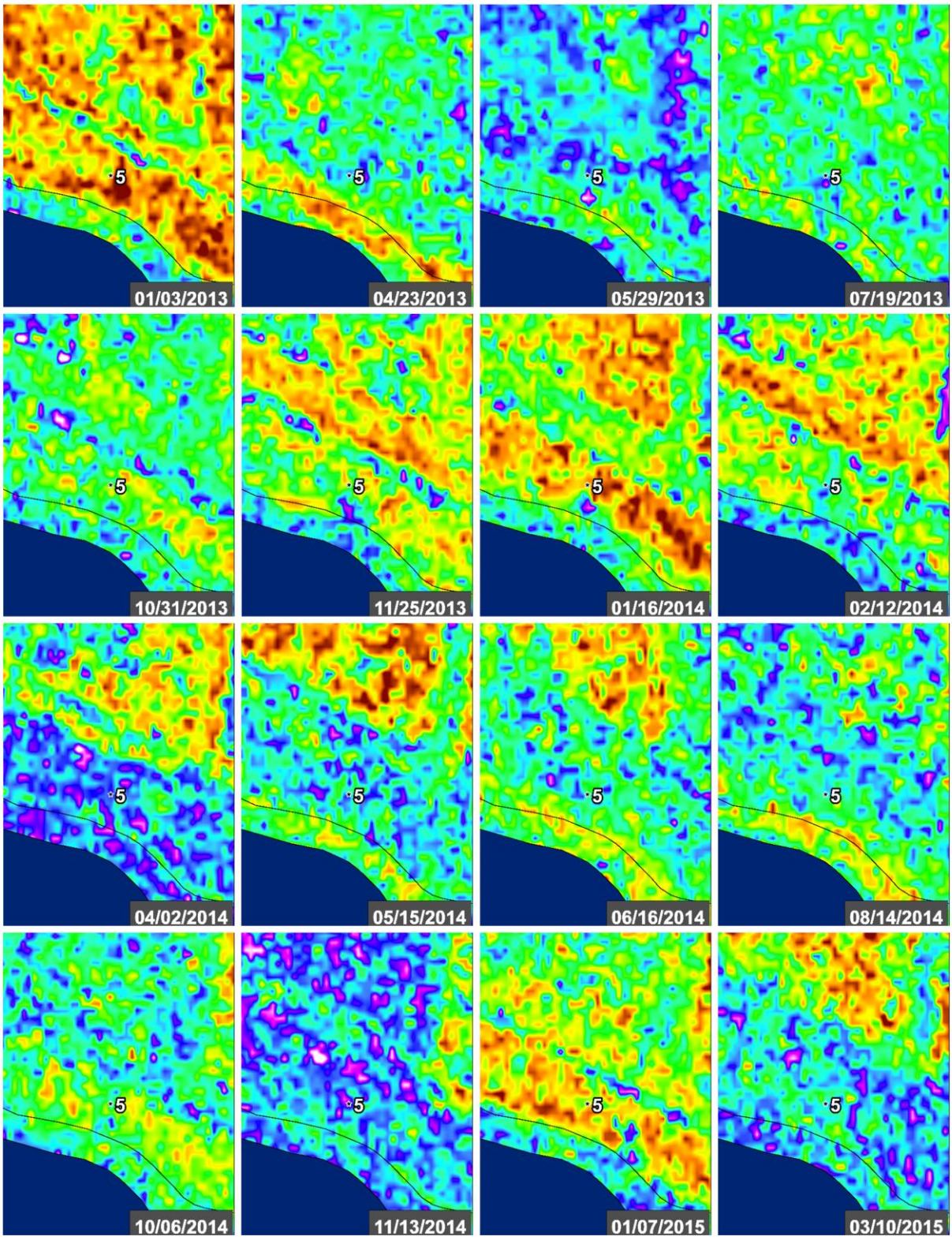

Figure 61D: Seep 5 – VV/HH Ratio – Line 23518

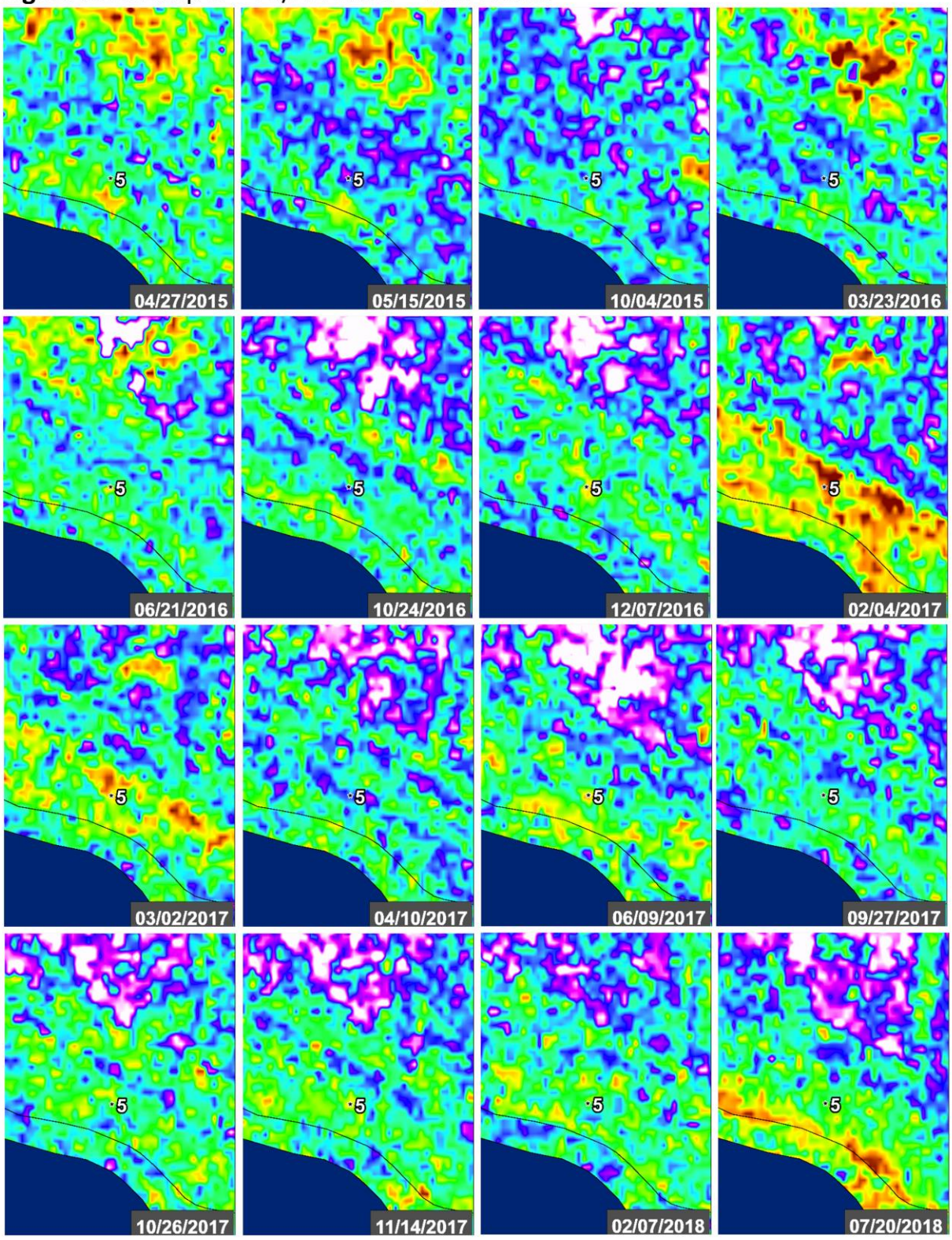

Figure 61E: Seep 5 – VV/HH Ratio – Line 23518

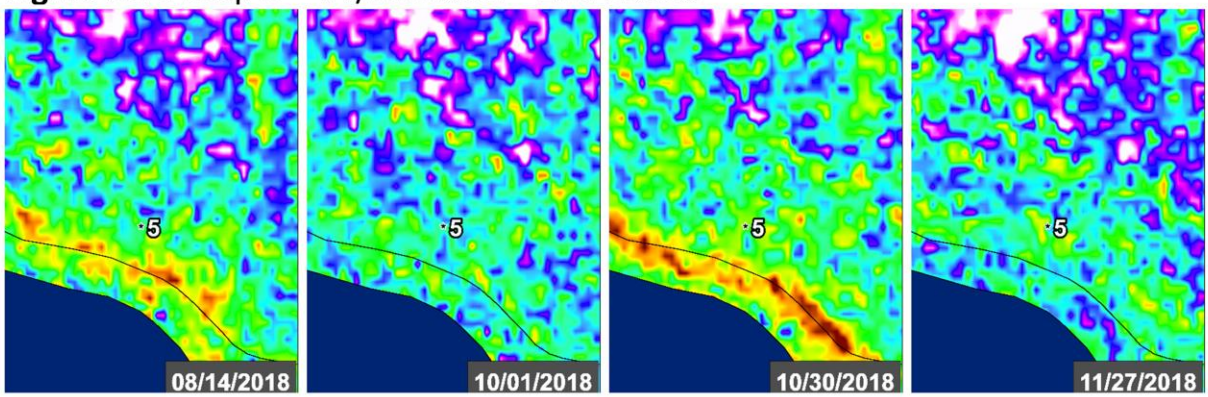

Figure 62: Field photos (by Cathleen Jones, JPL) of an active Seep #5 on Twitchell Island in June 2014.

References

Alberga, V. (2007). A study of land cover classification using polarimetric SAR parameters. *International Journal of Remote Sensing*, *28*(17), 3851-3870.

Barrett, B. W., Dwyer, E., & Whelan, P. (2009). Soil moisture retrieval from active spaceborne microwave observations: An evaluation of current techniques. *Remote Sensing*, *1*(3), 210-242.

Barrett, B., Whelan, P., & Dwyer, E. (2012). The use of C-and L-band repeat-pass interferometric SAR coherence for soil moisture change detection in vegetated areas. *Open Remote Sensing Journal*, *5*, 37-53.

Brooks, B. A., Bawden, G., Manjunath, D., Werner, C., Knowles, N., Foster, J., ... & Cayan, D. (2012). Contemporaneous subsidence and levee overtopping potential, Sacramento-San Joaquin Delta, California. *San Francisco Estuary and Watershed Science*, *10*(1).

Cloude, S. (2009). *Polarisation: applications in remote sensing*. OUP Oxford. doi:10.1093/acprof:oso/9780199569731.001.0001

Cloude, S. R., & Pottier, E. (1996). A review of target decomposition theorems in radar polarimetry. *IEEE transactions on geoscience and remote sensing*, *34*(2), 498-518.

Engman, E. T., & Chauhan, N. (1995). Status of microwave soil moisture measurements with remote sensing. *Remote Sensing of Environment*, *51*(1), 189-198.

Fang, B., & Lakshmi, V. (2014). Soil moisture at watershed scale: Remote sensing techniques. *Journal of hydrology*, *516*, 258-272.

Gao, B. C. (1996). NDWI—A normalized difference water index for remote sensing of vegetation liquid water from space. *Remote sensing of environment*, *58*(3), 257-266.

Hensley, S., Michel, T., Van Zyl, J., Muellerschoen, R., Chapman, B., Oveisgharan, S., ... & Mladenova, I. (2011, July). Effect of soil moisture on polarimetric-interferometric repeat pass observations by UAVSAR during 2010 Canadian soil moisture campaign. In *2011 IEEE International Geoscience and Remote Sensing Symposium* (pp. 1063-1066). IEEE.

Hensley, S., Jones, C., & Lou, Y. (2012, July). Prospects for operational use of airborne polarimetric SAR for disaster response and management. In *2012 IEEE International Geoscience and Remote Sensing Symposium* (pp. 103-106). IEEE.

Ingebritsen, S. E. (2000). *Delta subsidence in California: the sinking heart of the state*. US Department of the Interior, US Geological Survey.

Jain, A., Singh, D., & Rajput, N. S. (2015, July). Use of polarimetric indices for estimating soil moisture. In *2015 IEEE International Geoscience and Remote Sensing Symposium (IGARSS)* (pp. 696-699). IEEE.

Jones, C. E., Bawden, G., Deverel, S., Dudas, J., Hensley, S., & Yun, S. H. (2012, November). Study of movement and seepage along levees using DINSAR and the airborne UAVSAR instrument. In *SAR Image Analysis, Modeling, and Techniques XII* (Vol. 8536, p. 85360E). International Society for Optics and Photonics.

Jones, C. E. (2016). A practical guide to synthetic aperture radar for engineering and environmental geologists. *Applied Geology in California, Special Publication*, *26*.

Jones, C. E., Dudas, J., & Bawden, G. W. (2016). Application of remote sensing to assessment of water conveyance infrastructure integrity. *Applied geology in California, Special Publication*, *26*.

Kim, Y., & van Zyl, J. J. (2009). A time-series approach to estimate soil moisture using polarimetric radar data. *IEEE Transactions on Geoscience and Remote Sensing*, *47*(8), 2519-2527.

Marapareddy, R., Aanstoos, J. V., & Younan, N. H. (2016). Advanced Unsupervised Classification Methods to Detect Anomalies on Earthen Levees Using Polarimetric SAR Imagery. *Sensors*, *16*(6), 898.

McFeeters, S. K. (1996). The use of the Normalized Difference Water Index (NDWI) in the delineation of open water features. *International journal of remote sensing*, *17*(7), 1425-1432.

Mount, J., & Twiss, R. (2005). Subsidence, sea level rise, and seismicity in the Sacramento–San Joaquin Delta. *San Francisco Estuary and Watershed Science*, *3*(1).

Oh, Y. (2004). Quantitative retrieval of soil moisture content and surface roughness from multipolarized radar observations of bare soil surfaces. *IEEE Transactions on Geoscience and Remote Sensing*, *42*(3), 596-601.

Oh, Y., Sarabandi, K., & Ulaby, F. T. (1992). An empirical model and an inversion technique for radar scattering from bare soil surfaces. *IEEE transactions on Geoscience and Remote Sensing*, *30*(2), 370-381.

Poland, J. F., Ireland, R. L., Lofgren, B. E., & Pugh, R. G. (1975). Land subsidence in the San Joaquin Valley, California, as of 1972.

Robock, A., Vinnikov, K. Y., Srinivasan, G., Entin, J. K., Hollinger, S. E., Speranskaya, N. A., ... & Namkhai, A. (2000). The global soil moisture data bank. *Bulletin of the American Meteorological Society*, *81*(6), 1281-1300.

Sehat, S., Vahedifard, F., Aanstoos, J. V., Dabbiru, L., & Hasan, K. (2014). Using in situ soil measurements for analysis of a polarimetric SAR-based classification of levee slump slides in the Lower Mississippi River. *Engineering geology*, *181*, 157-168.

Service, R. F. (2007). Delta blues, California style. *Science*, *317*(5837), 442-445.

Ulaby, F. T., Dubois, P. C., & Van Zyl, J. (1996). Radar mapping of surface soil moisture. *Journal of hydrology*, *184*(1-2), 57-84.

Van Zyl, J. J., Zebker, H. A., & Elachi, C. (1987). Imaging radar polarization signatures: Theory and observation. *Radio science*, *22*(04), 529-543.

Vereecken, H., Huisman, J. A., Pachepsky, Y., Montzka, C., Van Der Kruk, J., Bogena, H., ... & Vanderborght, J. (2014). On the spatio-temporal dynamics of soil moisture at the field scale. *Journal of Hydrology*, *516*, 76-96.

Wang, H., Magagi, R., Goita, K., Jagdhuber, T., & Hajnsek, I. (2016). Evaluation of simplified polarimetric decomposition for soil moisture retrieval over vegetated agricultural fields. *Remote Sensing*, *8*(2), 142.

Water Education Foundation. (Accessed 2020, August 27). California Aqueduct. Retrieved from https://www.watereducation.org/aquapedia/california-aqueduct

Woodhouse, I. H. (2005). *Introduction to microwave remote sensing*. CRC press.

Xu, H. (2006). Modification of normalised difference water index (NDWI) to enhance open water features in remotely sensed imagery. *International journal of remote sensing*, *27*(14), 3025-3033.

CHAPTER FIVE

Developing open source flood disaster response toolkits and tutorials using UAVSAR and NISAR-simulated data

Abstract

The rise of global extreme water events is largely being combatted by engineered structures such as dams and levees, whose monitoring efforts rely on inefficient field surveys. Radar remote sensing of critical flood infrastructure offers a cost-effective solution to identifying vulnerable pre-flood conditions, such as levee seeps or subsidence near dams, as well as post-flood disaster response by identifying impacted structures such as overtopped bridges or levee breaks. Floods are chosen as the disaster of focus, being the most destructive natural disaster in terms of deaths and property damage, and because cascading or simultaneous events such as landslides can occur. This study proposes the use of publicly available interferometric and polarimetric datasets from NASA's UAVSAR (Uninhabited Aerial Vehicle Synthetic Aperture Radar) instrument to develop open source tutorials and toolkits for flood response agencies to effectively and rapidly direct resources. Interferometric radar products can be used to identify water elevation changes quickly after an event, with longer time period products able to measure structural deformation or nearby subsidence before an event. Polarimetric radar classification maps can be used to identify areas severely flooded and overtopped levees and bridges. The combination of these products along with relevant geographic information system (GIS) datasets such as roads, bridges, hospitals, schools, etc. will be synthesized into tutorials, tools, and datasets to best serve disaster prevention and recovery. The development of these tools includes use of NISAR-simulated (NASA-ISRO Synthetic Aperture Radar) data from the upcoming mission in 2022 and previews its global capability to provide timely observations for response of

various hazards.

Introduction

Satellite remote sensing of natural hazards can offer a global observation strategy to help mitigate the devastating socioeconomic impacts of natural disasters. The use of synthetic aperture radar (SAR) remote sensing for disaster response can help to overcome the limitations of optical imagery given appropriate visualization of derived products for response agencies. Unlike optical sensors, SAR-capable instruments are not limited by atmospheric weather conditions such as clouds, haze, and smoke which are common during floods and wildfires. However, common low-level SAR products are notoriously difficult to process and interpret, which is not ideal for time-sensitive disaster response applications. For example, commonly used interferograms of surface motion depict fringes of movement that are not easily understood by the lay-person. This work will use critical flood infrastructure as a testbed for improving visualization of existing interferometric (InSAR) and polarimetric SAR (PolSAR) datasets, and producing useful toolkits for the disaster response community, with applicability to other types of hazards.

Ten percent of the global population lives in low elevation coastal regions (less than ten meters above sea level) and face continuing coastal land loss and more frequent flooding from sea level rise (McGranahan et al., 2007). Global extreme coastal water level exposure is estimated to affect 190 million people by 2100, three times as many people as previously estimated (Kulp et al., 2019). It is widely suggested that the sustainability of coastal areas will depend on engineered solutions such as dams and levees (Tessler et al., 2015). However, these structures may be built on compressible soils or areas already subsiding and will need continual monitoring. The importance of monitoring such coastal hazards is prioritized in the U.S. National

Academy of Sciences' 2017 Decadal Survey for Earth Science and Applications from Space (National Academies of Sciences, 2019), which acknowledges the risk of increased storm activity to coastal areas protected by infrastructure to be a significant societal challenge.

This work's primary goal is to develop improved urgent response visualizations and open source toolkits for monitoring critical flood infrastructure after a disaster event. By using a suite of available SAR products from NASA's UAVSAR (Uninhabited Aerial Vehicle Synthetic Aperture Radar) instrument, this work will focus on both disaster prevention and response. Precursors to flood damage such as levee seepage or subsidence near a dam can be detected with existing PolSAR and InSAR products. User-friendly, open-source Jupyter notebook tutorials and GIS toolkits for relevant agencies can be produced to incorporate into flood response strategies. On the response side, a standard workflow can be developed that ingests standard UAVSAR products and outputs interpretable maps of post-disaster damage and inundation, alongside relevant GIS layers. NISAR-simulated datasets can be compared to their original UAVSAR sources to understand future global limitations of resolution and noise. Doing so will improve upon interpretability of existing products in flood-prone areas. And lastly, this work can provide optimized flight track information to the UAVSAR flight planning team based on GIS (geographic information system) datasets and improved visualization.

The NASA Earth Science Applied Sciences Disasters Program centers its focus on community resilience and disaster response, stating that "remote sensing is invaluable for effective hazard monitoring, mitigation design, disaster response and recovery" (NASA Applied Sciences). This work directly contributes to this purpose by investigating the capabilities of NASA's upcoming long wavelength radar space satellite, NISAR (NASA-ISRO Synthetic Aperture Radar). In fact, its prototype UAVSAR has already been contributing to disaster

response, quickly collecting data after Hurricane Florence in the Carolinas (Molthan and Bell, 2019) and the California wildfires in recent years (Donnellan et al., 2018). Since UAVSAR is the prototype for NISAR, these goals directly align with the space satellite's Level 1 "Baseline" Science requirements, to support "response to major natural or anthropogenic disasters" and "providing revised scheduling for new acquisitions within 24 hours of an event or an event forecast notification and delivering data within 5 hours of being collected" (NISAR). In particular, monitoring of critical infrastructure including levees and dams is listed as a major application of NISAR to provide early warnings of movement and seepage before a disaster.

Materials and Methods

Over the past few decades, remote sensing has been monitoring natural hazards from earthquakes to volcanoes, floods and landslides, coastal inundation, severe weather events, and wildfires (Tralli et al., 2005). Of these, floods have the largest socioeconomic impact of all hazards, causing more deaths and property damage than any other natural disaster (CEOS and Wood, 2003). Historically, flood management focused on field monitoring of precipitation and river discharge to predict the event itself, and still many parts of the world lack the resources for such expensive sensor networks (Rahman and Di, 2017). Flood infrastructure also typically involves in-person field monitoring. For example, methods of assessing and maintaining levee conditions remain largely ground-based with sparse spatial and temporal coverage, in most cases relying on day-to-day monitoring accomplished through visual surveys, augmented by measurements made at discrete locations (Bernardy and Sanoski, 2012). Although modernized geodetic methods employing Global Position System (GPS) and Light Distancing and Ranging (LiDAR) are now used in many areas, theodolite surveys with or without electronic distancing capability are still used. Furthermore, most methods are labor intensive, making it effectively

impossible to obtain a continual long-term, regional view of levee conditions.

Remote sensing information has been applied in recent decades during all stages of a flood: pre-flood warning, response during the event, post-flood recovery, and prevention. During a flood event, the different Landsat sensors over the years have been used for inundation mapping by utilizing the near-infrared band to highlight flooded areas (Wang et al., 2002). However, cloud cover during stormy weather and inability to see below forest cover are hindrances for optical imagers such as Landsat, AVHRR, and MODIS, leading to the use of SAR sensors such as ERS, RADARSAT, TerraSAR-X, etc. Water acts as a specular reflector in the microwave spectrum, appearing dark in radar imagery, and also has a high dielectric constant, increasing radar reflectivity in wet, flooded soils. This work will focus on SAR capability at all flood stages: measuring deformation at critical infrastructure pre-flood, inundation during a flood, and damage post-flood.

Many SAR image processing techniques have been developed to help distinguish flooded areas. Visual interpretation with multitemporal filters, image histogram thresholding of radar backscatter, and applying texture transforms are a few of the algorithms being used to identify inundated areas (Dasgupta et al., 2018). Change detection before and after a disaster event is also well-suited for regularly required SAR products. High spatial resolution single polarization datasets from Sentinel-1 have been shown to effectively detect flood inundation with automated algorithms using classification approaches (Clement et al., 2018). Both SAR intensity and coherence images have been used to perform change detection of flooded areas, and especially in urban areas, acquiring pre-flood imagery during dry conditions helps to differentiate false positive inundation from specular reflectors and shadows (Giustarini et al., 2012).

For flood infrastructure, InSAR has been used to some extent for levee health monitoring,

particularly making use of multiple polarizations of the radar pulses (Sehat et al., 2014) and applying InSAR time series analysis in urban settings (Dixon et al., 2006). The surface position surveys have largely used persistent scatterer InSAR (PSInSAR) to look at levees with hard surfaces and at a limited number of locations in urban areas. The main limitation is that short wavelength SARs (X, C band) experience rapid temporal decorrelation (Zebker and Villasenor, 1992), and so are challenged to detect small movements or distinguish surface movement below vegetation, while the longer wavelength SAR instruments (L-band) available in the past have not had the resolution to image the levees directly. This limitation can be addressed with L-band instruments such as UAVSAR and the upcoming spaceborne NISAR mission.

This work is divided between both mitigation and response techniques since consistent monitoring of pre-hazard conditions helps to efficiently determine post-hazard conditions. In a similar vein, preparing for the launch of the NISAR mission requires further understanding of its data quality limitations as compared to its prototype. This project will focus on the implementation of existing UAVSAR datasets to a flood response system and procedure, and integration of modern cartography and information visualization methods to improve product usability. The NISAR-simulated datasets produced by the UAVSAR team will also be used, where available. Major storms such as Hurricane Harvey and Florence will be used as the primary testbed since proof of concept already exists for these datasets to identify inundation and structural damage. Future study areas will be determined during the course of the project, with the opportunity to process additional NISAR-simulated data from the UAVSAR archive.

Disaster Prevention

In areas most vulnerable to flooding, having pre-flood imagery as a baseline is especially critical in urban areas when identifying inundation extent. The UAVSAR flight planning team

has expressed interest in optimizing flight tracks across areas most prone to flooding or containing flood infrastructure. A GIS repository will be created for specific sites by downloading publicly available datasets such as water surface boundaries, topography, and water infrastructure layers (e.g. levees and dams). Investigating flood-vulnerable areas alongside supporting GIS information can help to determine the optimal extent and direction of the flight line. For example, the orientation of a dam or levee/dike system relative to the flight direction can affect both the backscattered signal strength and the sensitivity to ground deformation. This procedure can be applied to other hazards as well, for example using topography data to predict the direction of landslides.

Aging critical flood infrastructure require continuous monitoring to ensure that they can withstand a major event. PolSAR and InSAR products from UAVSAR have been used to study small-scale structures such as levees due to the high spatial resolution of the airborne sensor. PolSAR products from UAVSAR include fully polarized imagery as ground projected files that have been projected to a coordinate system and are easily digestible into a GIS program such as Esri's ArcMap, ArcMap Pro, or an open-source platform such as QGIS. The HH (horizontally emitted and received pulses) and VV (vertically emitted and received pulses) polarizations can be used to identify water, with VV being the most sensitive to surface roughness (Henry et al., 2006). HH and VV have also been shown to be the most effective at discerning between different land types, and a simple ratio of the two polarizations has been used to identify levee seepages (Jones et al., 2017). UAVSAR also has InSAR products at varying resolutions and formats which can be used to study subsidence near flood infrastructure, as has been presented in the Sacramento Delta and other areas such as New Orleans (Jones et al., 2016). Figure 1 shows land subsidence occurring along critical flood infrastructure in New Orleans, using an interferogram

from 2009-2012. This information can directly inform flood mitigation experts of structures in need of immediate maintenance against storms such as Hurricane Katrina.

Both PolSAR and InSAR products are easily accessible online, and Jupyter-style notebooks and GIS toolkits for using them will be developed during this project. These tutorials and toolkits will center on certain study areas or events, e.g. the Sacramento Delta and Hurricane Harvey, but be applicable for other sites. Jupyter notebooks are fully compatible with the ArcGIS API for Python and can be made publicly available via a GitHub repository. This provides a fully executable environment for anyone to access. For each notebook, there will be clear step-by-step instructions on how to download datasets, ingest them into a GIS program, and easily interpret the data. This procedure will look different for various agencies depending on their familiarity with GIS programs. Also, agencies will have a greater or lesser need for open source software, and so there will be multiple versions of the tutorial. The format of these tutorials will be applied to other types of hazard mitigation in the future.

Disaster Response

The highest priority during an actual disaster event is generally reducing the latency between data acquisition and product delivery (Schumann et al., 2018). However, equally important for integrating SAR into disaster response is conveying information in a manner and format that is easily usable without specialized training.

This project will help to develop a standard workflow for UAVSAR information products to be delivered to disaster responders during an event. This work builds upon the previous tutorials developed for risk mitigation since the relevant datasets would already exist. More relevant GIS layers such as the location of hospitals, schools, police and fire stations, emergency shelters, etc. can be implemented to pinpoint areas experiencing the most inundation or damage,

or where these have the greatest impact on critical functions. Furthermore, roads shapefiles, which are available from the U.S. Census, can be used in conjunction with network datasets in ArcMap to map out evacuation routes to avoid the most impacted areas. Figure 2 depicts three prisons that flooded in Otey, Texas during Hurricane Harvey, identified in VV intensity imagery, with a GIS roads dataset shown alongside for identifying potential escape routes. Network analysis tools can be applied to the roads layer to add restriction attributes, such as avoiding flooded roads. These procedures can be similarly applied to other hazards as well, for example, the aftermath of volcanic eruptions also requires evacuation route information. Easily interpretable legends and highlighted features expedite understanding of these maps during a time-sensitive situation.

The same PolSAR and InSAR products can be used for disaster response as in disaster prevention. PolSAR data is very effective at distinguishing between wet and dry areas, especially if pre-flood imagery is available showing normal conditions. Single VV imagery has been shown to quickly identify flooded areas and even overtopped bridges (Figure 3). Here, the progression of a bridge in Lake Houston overtopping during the height of Hurricane Harvey is shown with VV imagery. The unnecessary legend with radar jargon is included to emphasize the need for more interpretable information by responders. Polarimetric decomposition methods can also be used to differentiate between open water, flooded vegetation, and damaged infrastructure. For InSAR, coherence maps can be used to determine inundation extent and water elevation changes can be detected with a single interferogram (Figure 4). Changing water levels can be seen here along the Neches River, and the reverse patterns encircled indicate that water levels are higher in the north and flowing south. This figure shows a typical flood response product, an interferogram, in unfamiliar units and fringe patterns not easily understood by responders. Tutorials instructing

proper interpretation will be created alongside figures similar to Figure 2, where irrelevant legends are omitted and only damage related information is highlighted.

The recently released NISAR-simulated datasets from UAVSAR will be important in understanding the difference in quality between the different instruments' information products. The simulated products have reduced spatial resolution as well as increased noise, which is to be expected from the space mission. NISAR polarimetric data has been released for several areas around the world, including the Sacramento Delta and parts of the Gulf Coast. These datasets will be compared to their UAVSAR counterparts to conclude the scale at which NISAR will be able to effectively image structures such as levees.

New Techniques

The novel aspect of this project is the integration of GIS datasets and high resolution SAR products for improved visualization of disaster response toolkits and tutorials. Demographic information on population density and location of points of interest (schools, hospitals, shelters, police stations, etc.) can help to focus the damage assessment on the most vulnerable areas. Even information on roofing materials for buildings could offer information on the likelihood of vertical evacuations during a flood (Rahman and Di, 2017). The vector overlays of the GIS datasets described above, such as points of interests, should add detail to the map without overcrowding the image.

In addition to integrating SAR and GIS datasets, improved map design will contribute greatly to user interpretability. Cartographic design methods based on modern mapping techniques such as deciding the visual hierarchy of map elements, balancing empty spaces, and choosing an appropriate spatial projection are small details that greatly affect the usefulness of a map (Brewer, 2004). Element borders, fonts, symbology, colorbar intervals, etc., are unique to a

map's purpose, and excessive decoration may impede on a responder's speed when interpreting the image. For maps intended for wide distribution, color schemes for map legends must be carefully selected to accommodate visually impaired audiences. These improved mapping and information visualization tactics are directly applicable to other hazards measurable by UAVSAR, for example, coherence changes have been used to map damage from earthquakes (Hoffmann, 2007), fire scar extent, and severe debris flows from landslides (Donnellan et al., 2018).

The main challenges to flood disaster response are maintaining application readiness and interoperability of data products (Schumann et al., 2018). For the first time, NISAR will offer a long wavelength radar instrument capable of imaging critical flood infrastructure around the world at regular intervals. A major conclusion from this project will be to provide improved visualizations of UAVSAR and NISAR data to best fit into the currently available flood response services using optical and microwave remote sensing products. Some examples from NASA Applied Sciences include the Advanced Rapid Imaging and Analysis (ARIA) Program, NASA WorldWind Quake Hunter, and RECOVER DSS (NASA Earth Science). A top priority action item that emerged from a NASA Flood Response Workshop in 2016 (Schumann, 2016) was the need for a "one-stop-shop" data portal for flood response. Currently, UAVSAR is not a part of any major flood response application, but with the upcoming global capability of NISAR, both instruments can play a large role in rapid response assessment, especially in remote areas. NISAR can be widely applicable to a variety of disasters if it contains on-board processing for urgent response products. The integration of UAVSAR and NISAR into existing flood response assessments requires an improved interpretability of the datasets that will be accomplished through open-source, GIS-friendly visualization techniques and tutorials.

Expected Results

This project will optimize existing data from the airborne SAR instrument UAVSAR and preview the capabilities of its upcoming space satellite NISAR by improving usability and interpretability for urgent response. Improved flight track boundaries will be provided to the UAVSAR team in consideration of flood-prone areas and the surrounding infrastructure. A similar approach can be used to improve flight paths for areas focused on other hazards, such as earthquakes and wildfires. Successful detection of flood inundation and damage with SAR datasets will be published in peer-reviewed journals specializing in remote sensing and GIS. GIS-based tools and tutorials will be created and shared with response agencies, and training sessions with relevant responders can be held to familiarize them with the InSAR and PolSAR products that will be produced during a flood event. Special focus will be paid to flooded infrastructure such as dams, levees, roads, and bridges. The ability to identify sites of refuge for temporary shelters or evacuation zones can also be included.

A major priority of this work is to produce easily interpretable, useful, and reliable information for end-users to direct resources for response. These tools are meant for emergency responders at all levels (local to federal jurisdictions) but can also be made publicly available for policy makers to apply to disaster scenarios, prevention planning, and response protocol. For these toolkits and tutorials to be effective, the response community must have the opportunity for continuous feedback because during an event, the latency between data acquisition and delivery of inundation or damage maps is most critical. The toolkits will include both PolSAR and InSAR products overlaid with relevant GIS datasets and be made publicly available via open-source domains such as GitHub and Binder. Based on feedback from response agencies, the most optimal map layouts will be provided during a disaster scenario to aid in rapid response. Flood

infrastructure is the focus of this project due to the disaster's potential to cause other hazards such as landslides, but the methods of data visualization can be applied to other SAR-detectable hazards in the future.

Figures

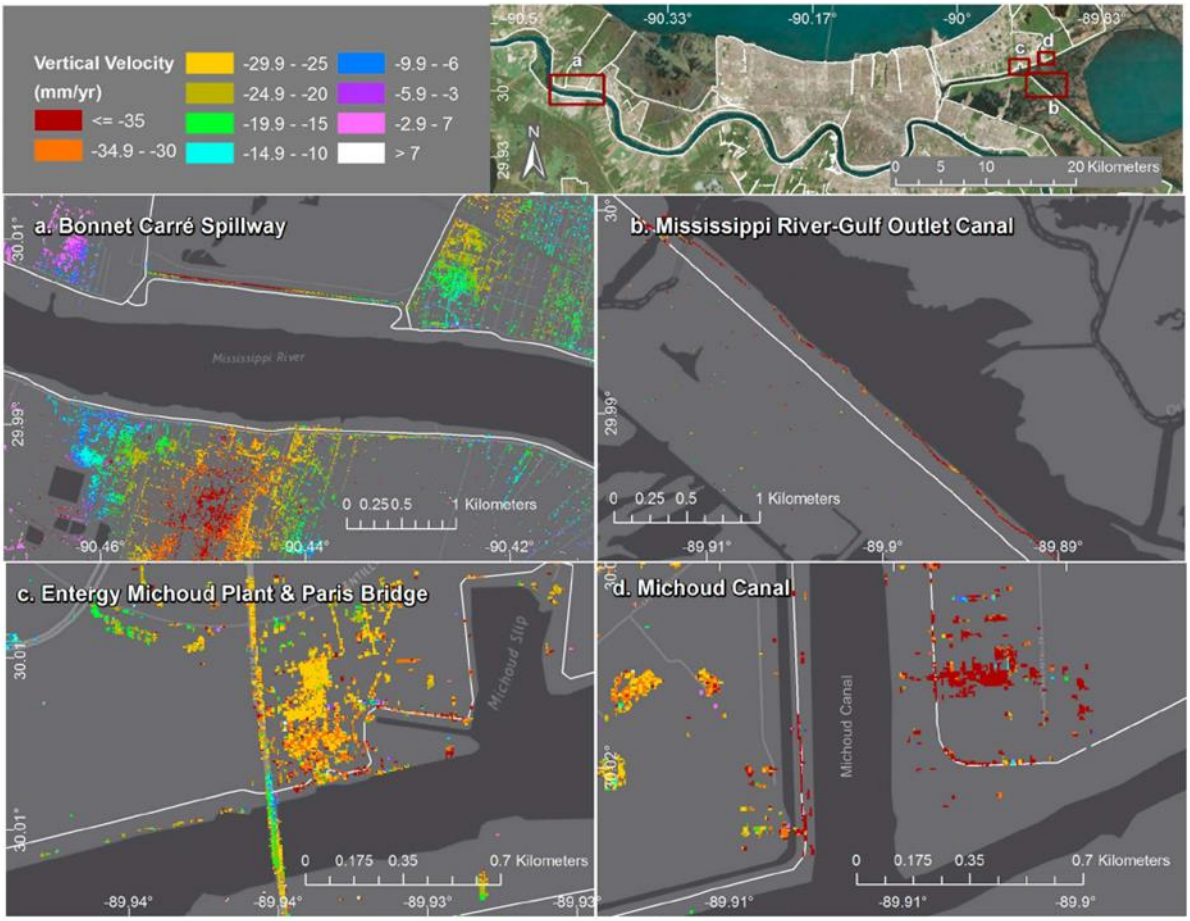

Figure 1: Vertical velocity rates from 2009-2012 for critical flood infrastructure in New Orleans, Louisiana for (A) Bonnet Carre Spillway, (B) Mississippi River-Gulf Outlet Canal, (C) Entergy Michoud Plant & Paris Bridge, and (D) Michoud Canal.

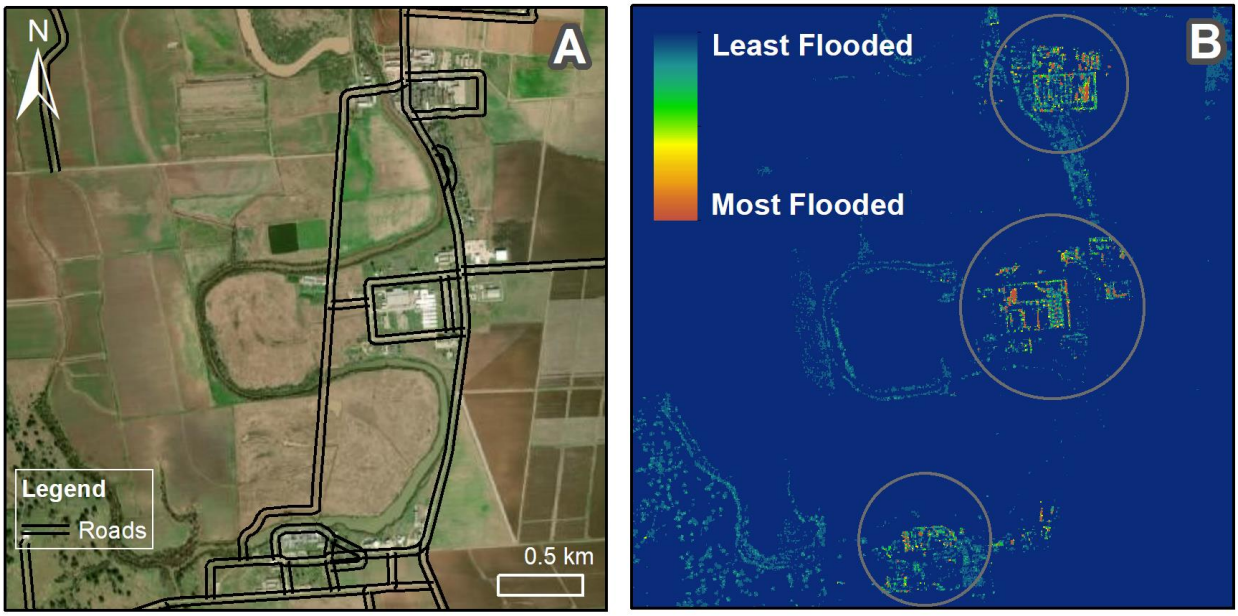

Figure 2: Single vertical polarization image for three prisons in Otey, Texas during Hurricane Harvey. (A) Optical imagery from ArcMap showing normal conditions and a roads line shapefile from the U.S. Census. (B) VV imagery from UAVSAR acquired on September 1, 2017.

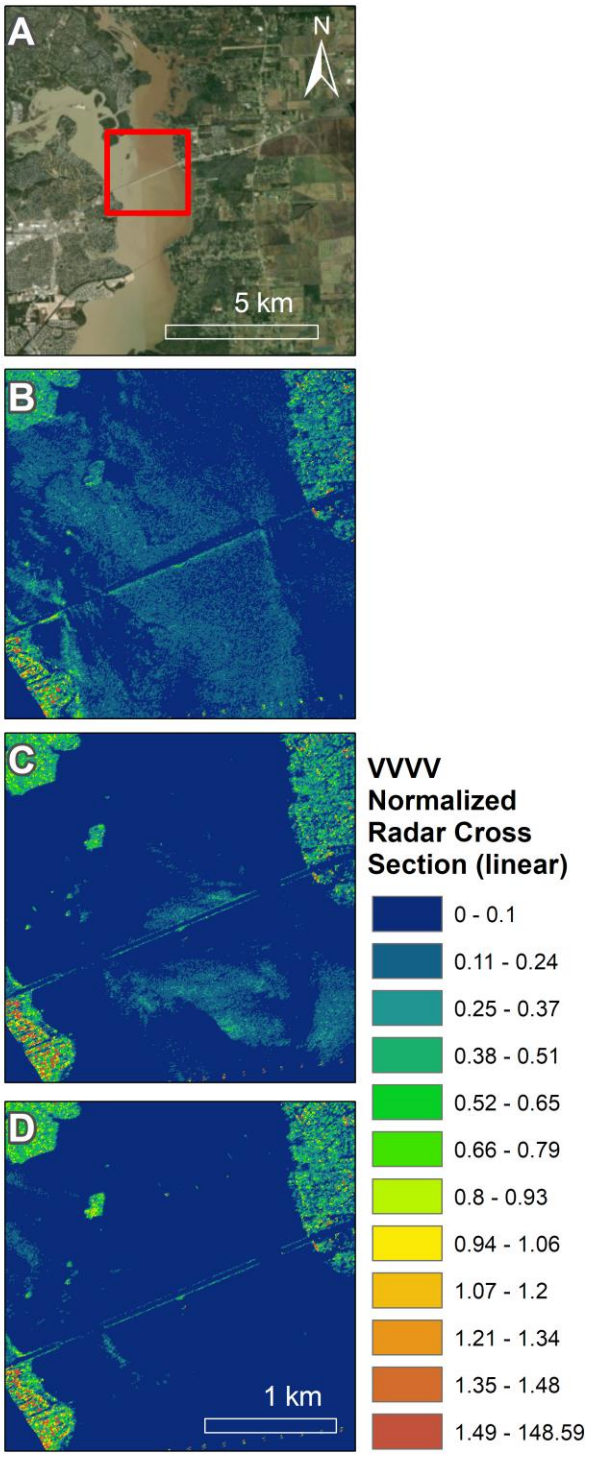

Figure 3: Single vertical polarization imagery for a bridge overtopping in Lake Houston during Hurricane Harvey. (A) Optical imagery from ArcMap showing normal conditions, with a red extent indicator for the next three panels. VV imagery from UAVSAR acquired on (A) August 31, 2017, (B) September 1, 2017, and (C) September 2, 2017.

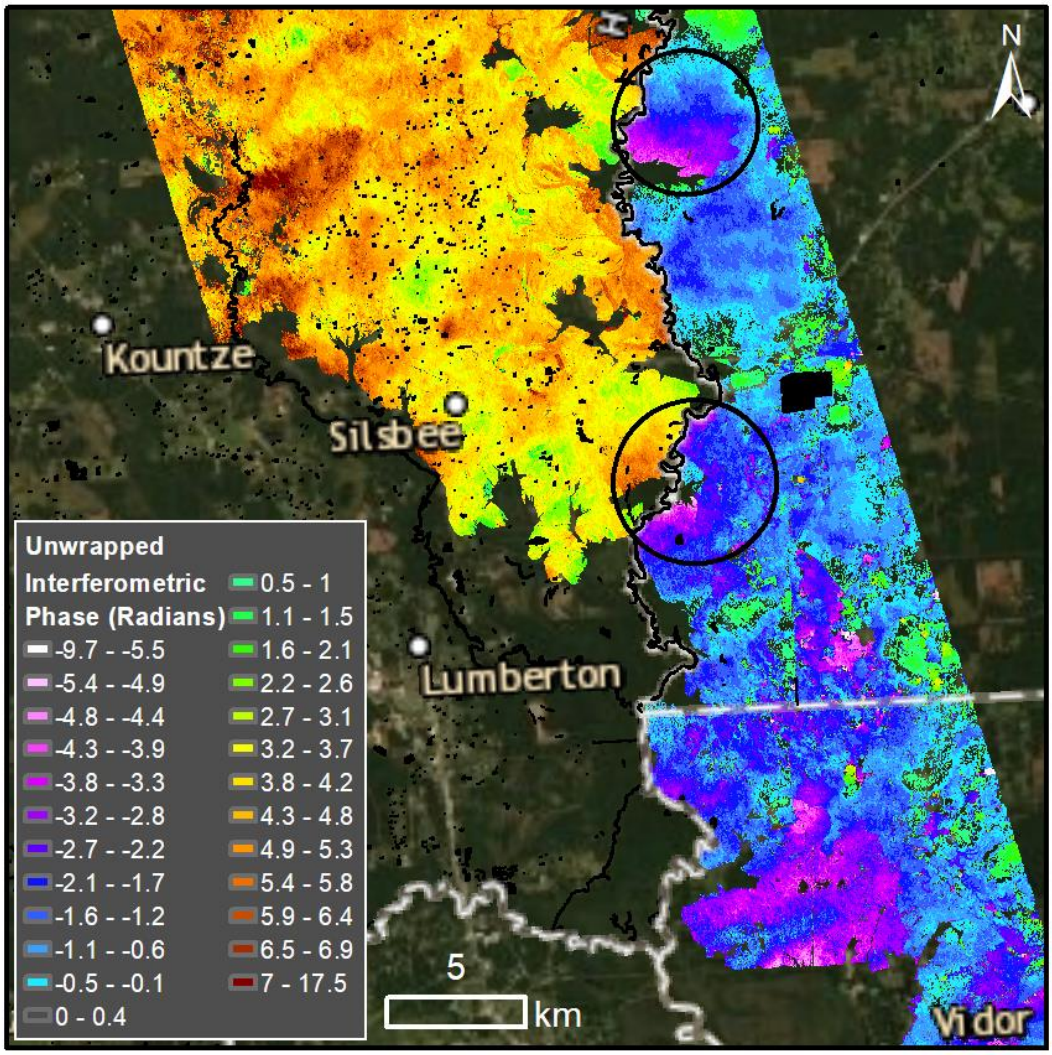

Figure 4 – Unwrapped InSAR phase product from UAVSAR acquired on September 1 and 2, 2017 during Hurricane Harvey. Changing water levels are seen (encircled) along the Neches River.

References

Bernardy, T., Sanoski, D. (2012). Levee threat monitoring guidelines: State of California, Dept. of Water Resources, 31 p.

Board, S. S., & National Academies of Sciences, Engineering, and Medicine. (2019). *Thriving on our changing planet: A decadal strategy for Earth observation from space*. National Academies Press.

Brewer, C. (2004). *Designing better Maps: A Guide for GIS users*. Environmental Systems Research.

CEOS Disaster Management Support Group, & Wood, H. M. (2003). *The Use of Earth Observing Satellites for Hazard Support: Assessments & Scenarios: Final Report of the CEOS Disaster Management Support Group: Chair's Overview*. National Oceanic and Atmospheric Administration, US Department of Commerce.

Clement, M. A., Kilsby, C. G., & Moore, P. (2018). Multi-temporal synthetic aperture radar flood mapping using change detection. *Journal of Flood Risk Management*, *11*(2), 152-168.

Dasgupta, A., Grimaldi, S., Ramsankaran, R. A. A. J., Pauwels, V. R., Walker, J. P., Chini, M., ... & Matgen, P. (2018). Flood mapping using synthetic aperture radar sensors from local to global scales. *Global Flood Hazard: Applications in Modeling, Mapping, and Forecasting*, 55-77.

Dixon, T. H., Amelung, F., Ferretti, A., Novali, F., Rocca, F., Dokka, R., ... & Whitman, D. (2006). Subsidence and flooding in New Orleans. *Nature*, *441*(7093), 587-588.

Donnellan, A., Parker, J., Milliner, C., Farr, T. G., Glasscoe, M., Lou, Y., ... & Hawkins, B. (2018). UAVSAR and optical analysis of the Thomas fire scar and Montecito debris flows: Case study of methods for disaster response using remote sensing products. *Earth and Space Science*, *5*(7), 339-347.

Giustarini, L., Hostache, R., Matgen, P., Schumann, G. J. P., Bates, P. D., & Mason, D. C. (2012). A change detection approach to flood mapping in urban areas using TerraSAR-X. *IEEE transactions on Geoscience and Remote Sensing*, *51*(4), 2417-2430.

Henry, J. B., Chastanet, P., Fellah, K., & Desnos, Y. L. (2006). Envisat multi-polarized ASAR data for flood mapping. *International Journal of Remote Sensing*, *27*(10), 1921-1929.

Hoffmann, J. (2007). Mapping damage during the Bam (Iran) earthquake using interferometric coherence. *International Journal of Remote Sensing*, *28*(6), 1199-1216.

Jones, C. E., An, K., Blom, R. G., Kent, J. D., Ivins, E. R., & Bekaert, D. (2016). Anthropogenic and geologic influences on subsidence in the vicinity of New Orleans, Louisiana. *Journal of Geophysical Research: Solid Earth*, *121*(5), 3867-3887.

Jones, C. E., Bekaert, D., & An, K. (2017, July). From flood to drought: Utilizing sar to assess

the status of levees and aqueducts. In *2017 IEEE International Geoscience and Remote Sensing Symposium (IGARSS)* (pp. 5889-5892). IEEE.

Kulp, S. A., & Strauss, B. H. (2019). New elevation data triple estimates of global vulnerability to sea-level rise and coastal flooding. *Nature communications*, *10*(1), 1-12.

McGranahan, G., Balk, D., & Anderson, B. (2007). The rising tide: assessing the risks of climate change and human settlements in low elevation coastal zones. *Environment and urbanization*, *19*(1), 17-37.

Molthan, A., & Bell, J. (2019). NASA Earth Science Activities Supporting Analysis and Response to Hurricanes Florence and Michael.

NISAR Level 1 Science Requirements. (accessed 2020, June 19). Retrieved from https://nisar.jpl.nasa.gov/mission/mission-requirements/level-1-science-requirements/

NASA Applied Sciences - What We Do. (accessed 2020, June 19). Retrieved from https://appliedsciences.nasa.gov/what-we-do/disasters

NASA Earth Science Disasters Program - Tools. (accessed 2020, June 19). Retrieved from https://disasters.nasa.gov/tools

Rahman, M. S., & Di, L. (2017). The state of the art of spaceborne remote sensing in flood

management. *Natural Hazards*, *85*(2), 1223-1248.

Schumann, G., Bates, P. D., Apel, H., & Aronica, G. T. (2018). Global flood hazard mapping, modeling, and forecasting: challenges and perspectives. *Global Flood Hazard: Applications in Modeling, Mapping, and Forecasting*, 239-244.

Schumann, G. J. P. (2016, June). Flood response using Earth observation data and products. In *Proceedings of the NASA Flood Response Workshop, Greenbelt, ML, USA* (pp. 14-16).

Schumann, G. J., Brakenridge, G. R., Kettner, A. J., Kashif, R., & Niebuhr, E. (2018). Assisting flood disaster response with earth observation data and products: A critical assessment. *Remote Sensing*, *10*(8), 1230.

Sehat, S., Vahedifard, F., Aanstoos, J. V., Dabbiru, L., & Hasan, K. (2014). Using in situ soil measurements for analysis of a polarimetric SAR-based classification of levee slump slides in the Lower Mississippi River. *Engineering geology*, *181*, 157-168.

Tessler, Z. D., Vörösmarty, C. J., Grossberg, M., Gladkova, I., Aizenman, H., Syvitski, J. P. M., & Foufoula-Georgiou, E. (2015). Profiling risk and sustainability in coastal deltas of the world. *Science*, *349*(6248), 638-643.

Tralli, D. M., Blom, R. G., Zlotnicki, V., Donnellan, A., & Evans, D. L. (2005). Satellite remote sensing of earthquake, volcano, flood, landslide and coastal inundation hazards. *ISPRS Journal*

of Photogrammetry and Remote Sensing, *59*(4), 185-198.

Wang, Y., Colby, J. D., & Mulcahy, K. A. (2002). An efficient method for mapping flood extent in a coastal floodplain using Landsat TM and DEM data. *International Journal of Remote Sensing*, *23*(18), 3681-3696.

Zebker, H. A., & Villasenor, J. (1992). Decorrelation in interferometric radar echoes. *IEEE Transactions on geoscience and remote sensing*, *30*(5), 950-959.

CHAPTER SIX

Dissertation Summary

The high spatial resolution of today's airborne instruments has improved by at least a factor of 10 from the first SAR images created by early spaceborne missions. The progress of using this technology for a wide variety of applications has made InSAR an indispensable tool in earth science remote sensing, and the queue of future spaceborne missions reflects the continuation of this trend. Chapter 1 reviews a brief history of microwave remote sensing, and explains the basic principles and limitations of InSAR before focusing on case studies that have used interferometry to monitor land subsidence in wet and dry environments. Particular focus is spent on northern California's Sacramento-San Joaquin Delta, the main study area of the dissertation. Emerging applications of InSAR also point to more direct comparisons with field datasets and informative geographic information systems (GIS) data to explain the intricate features seen in SAR imagery.

In Chapter 2, a UAVSAR-derived map of cumulative elevation change identifies areas of anomalous and rapid subsidence close to critical levee infrastructure. The time series product can be used to monitor historic levee breaks sites whose repairs result in more stability compared to the surroundings. With a priori knowledge of repair sites, the InSAR time-series method is able to differentiate between short-term settling after a levee break and ongoing subsidence. This study shows the feasibility of high resolution monitoring of a levee system using an L-band radar instrument, and contrasted InSAR- and lidar-based methods. The SAR and lidar observations are not always measuring the same physical process, with levee repair work in the lidar data often masking large subsidence signals seen in the SAR data. Though the lidar surveys offer high-resolution elevation data, they were shown to detect elevation gain at levee repair sites due to the

addition of fill material.

The island interiors are studied in a separate chapter from the levees since levees are man-made structures that are composed of different material. Chapter 3 ventures into the Delta island interiors and investigates small-scale subsidence features as compared with a GIS repository. The same lidar and InSAR datasets from Chapter 2 are compared with: elevation, soil organic matter, and land cover type. Typically, due to the constant drainage of agricultural soils, subsidence and thick peat soils tend to be concentrated near the center of many islands. This did not seem to be the case for most islands, at least for the most rapid observed subsidence, since the subsidence hot spots occurred more often close to the levee. However, this observation could be skewed by the addition of fill material near levees, which causes compression of peat soils below for these hot spots. Elevation seemed to have a strong relationship with subsidence in general. Since low elevation can be proxy for previous subsidence, if these areas continue to subside, the elevation will lower even further than current levels. For many islands, the soil organic matter outlines also matched fairly well with large subsidence signals. This indicates more compressible soils that may be more prone to subsidence, and that soil type boundaries, not just organic matter content, may also be a determining factor for subsidence. However, many islands did not show more subsidence in more compressible soils, so there appear to be other factors at play, such as land cover and land use. It was visually evident that some apparent subsidence and uplift features followed closely the shape and size of agricultural fields, and that on average certain crops grow at lower elevations with lower average subsidence values. Further investigation into how different crops impact subsidence through different agricultural practices may be helpful in explaining more subsidence features.

The polarimetric capabilities of UAVSAR are then presented in Chapter 4 to investigate the possibilities of levee seep detection in the Delta. Examples on Twitchell Island are previewed by examples of seeps along the California Aqueduct, a dry testbed environment. The optical imagery and polarimetric radar products compared in this study show that seep detection is successful for certain environmental conditions. For the California Aqueduct, the HH polarization showed large scene shifts of value ranges, but still shows the ability for seep tracking. The VV single polarization is more sensitive to surface roughness, and is also able to track seeps effectively, especially for the California Aqueduct. The HV ratio is most sensitive to vegetation changes, and was not able to detect the seep features effectively, showing changes in agriculture instead. The VV ratio, on the other hand, was able to reduce effects of surface roughness and highlight seep features prominently. This VV ratio is then chosen to study seeps in the Delta as the most effective PolSAR product. The entropy product was able to show that as a seep grows, more scattering mechanisms begin to take place. The anisotropy product did not show most seeps clearly, suggesting that only one dominant scattering type was present. The mean alpha angle showed a variety of values for the aqueduct seeps, indicating that the seeps are characterized by different scattering mechanisms. The Twitchell Island results were visually much noisier than those of the California Aqueduct, likely due to wetter conditions overall. Although the Google Earth imagery was effective at tracking active seeps over time, with many images showing the seep traveling over roads and increases in green vegetation nearby, optical imagery is insufficient for seep tracking. Seeps most commonly occur during large floods, which usually accompany stormy weather. As seen by the many missing acquisitions for the NDWI product, cloud cover obscures data collection for optical sensors. Relying solely on optical imagery for seep detection during a storm may not result in successful seep detection. For a large

flood event, seepage features will be much larger and easily detectable by PolSAR, which is especially compatible with UAVSAR's emergency response capabilities.

Future disaster response applications of this work are outlined in Chapter 5. The rise of global extreme water events is largely being combatted by engineered structures such as dams and levees, whose monitoring efforts rely on inefficient field surveys. Radar remote sensing of critical flood infrastructure offers a cost-effective solution to identifying vulnerable pre-flood conditions, such as levee seeps or subsidence, as well as post-flood response by identifying impacted structures such as overtopped bridges or levee breaks. Floods are the most destructive natural disaster in terms of deaths and property damage, and because cascading or simultaneous events such as landslides can occur. Publicly available interferometric and polarimetric datasets from UAVSAR can be used alongside GIS datasets to develop open source tutorials and toolkits for flood response agencies to effectively and rapidly direct resources. InSAR can be used to identify water elevation changes quickly after an event, with longer time period products able to measure structural deformation or nearby subsidence before an event. Chapters 2 and 3 showed the capability of high resolution InSAR to identify levee deformation and land subsidence, respectively. PolSAR classification maps can be used to identify areas severely flooded and overtopped levees and bridges. Chapter 4 showed the capability of high resolution PolSAR to identify small-scale seeps, and large flood extent will be more easily captured by PolSAR. The combination of InSAR and PolSAR along with relevant geographic information system (GIS) datasets such as roads, bridges, hospitals, schools, etc. will be synthesized into tutorials, tools, and datasets to best serve disaster prevention and recovery. The development of these tools includes use of NISAR-simulated data from the upcoming mission in 2022 and previews its global capability to provide timely observations for response of various hazards.